FACILITATING, UNDERSTANDING, AND CONTROLLING THE OXYGEN REDUCTION REACTION FOR FUEL CELL TECHNOLOGY USING (1) LACCASE-INSPIRED TRICOPPER MOLECULAR CATALYSTS, (2) A HIGH TEMPERATURE AND PRESSURE REACTION VESSEL, AND (3) A HYBRID BILAYER MEMBRANE ELECTROCHEMICAL PLATFORM

BY

CHUN MING EDMUND TSE

DISSERTATION

Submitted in partial fulfillment of the requirements
for the degree of Doctor of Philosophy in Chemistry
in the Graduate College of the
University of Illinois at Urbana-Champaign, 2016

Urbana, Illinois

Doctoral Committee:

Professor Andrew A. Gewirth, Chair
Professor Thomas B. Rauchfuss
Professor Catherine J. Murphy
Professor Paul A. J. Kenis

Abstract

The objectives of my thesis were to investigate three major facets of the oxygen reduction reaction (ORR: $O_2 + 4\ H^+ + 4\ e^- \rightarrow 2\ H_2O$). First, I developed new tri-copper catalysts for the ORR with a specific focus on the active site present in multi-copper oxidases, which are the most active enzymes for the ORR. Second, I evaluated the ORR kinetics at high temperature (between 100 and 200 °C) and under pressurized conditions (between 0.7 and 3.4 MPa). Third, I designed and prepared a hybrid bilayer membrane (HBM) electrochemical platform to control the ORR mechanism by modulating the proton flux.

In Chapter 1, I provide background information to the field of alternative energy conversion schemes and lay out the challenges and limitations at present in the field of fuel cell technology. In Chapter 2, I present the general experimental procedures I utilized for the synthesis and electrochemical investigation of organometallic complexes and the physical characterization and activity measurement of heterogeneous catalysts.

In Chapter 3, I describe our efforts in collaboration with the Rauchfuss group to prepare multicopper molecular model complexes inspired by the structure and function of the active site of blue copper oxidase, a class of enzymes containing multiple copper ions that catalyzes the four-electron four-proton reduction of dioxygen to water very efficiently. Cu complexes of 2,2'-dipicolylamine (DPA) were prepared and tested as electrocatalysts for the ORR (Figure 0.1). To study the effect of multinuclearity on the ORR, two Cu-DPA units were connected with a flexible linker, and a third metal-binding pocket was installed in the ligand framework. ORR onset potentials and the diffusion-limited current densities of di- and tri-copper complexes of DPA derivatives were found to be comparable to those of the simpler Cu-DPA system. Electrochemical analyses, crystallographic data, and metal-substitution studies suggested that Cu

complexes of DPA derivatives reacted with O_2 via a binuclear intermolecular pathway, but that the Cu center in the third binding site did not participate in the ORR process. This chapter highlighted the viability of utilizing Cu-DPA complexes to mimic the T3-site of laccase, and this study served as a guide for designing future laccase models.

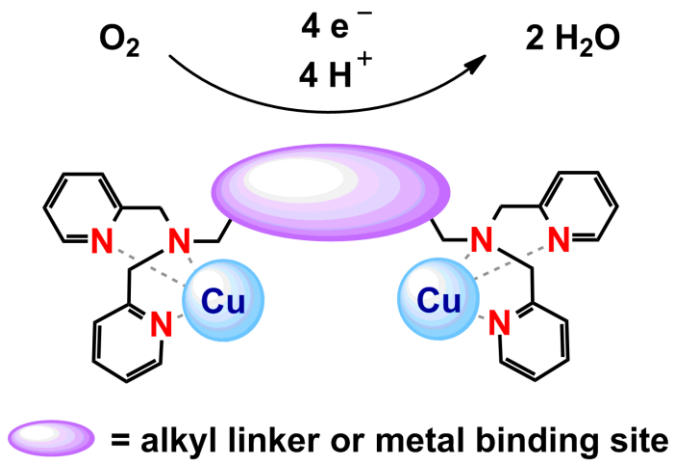

Figure 0.1. The design blueprint used to mimic the structure of the active site of laccase by connecting two copper-bearing 2,2'-dipicolylamine units together with either an alkyl linker or a third metal-binding pocket installed in the ligand framework.

In Chapter 4, I present my electrochemical results recorded at elevated temperatures and high pressures. A fundamental understanding of the ORR in aqueous medium at temperatures above 100 °C is lacking due to the practical limitations related to the harsh experimental conditions. In this chapter, the challenge to suppress water from boiling was overcome by conducting the electrochemical investigation under pressurized conditions. A striking improvement in the kinetics of the electrocatalytic reduction of O_2 by about 150 fold relative to room temperature and pressure was recorded under an O_2 pressure of 3.4 MPa at 200 °C in basic aqueous environment. To deconvolute the combined effect of temperature and pressure, the underlying variables that dictate the observed O_2 reduction kinetics of Pt and carbon electrodes

were examined individually. O_2 availability at the electrode-solution interface was controlled by the interplay between the diffusion coefficient and concentration of O_2. An accurate knowledge of the temperature and pressure dependence of O_2 availability at the electrode surface, the Tafel slope, the transfer coefficient, and the electrochemical active surface area was required to correctly account for the enhanced O_2 reduction kinetics.

In Chapter 5, I discuss the insights from kinetic isotope effect (KIE) studies on aqueous oxygen chemistry. Earth-abundant and inexpensive catalysts with low overpotential and high durability are central to the development of efficient water splitting electrolyzers and high power density fuel cell units. However, improvements in catalyst design and preparation are currently hampered by the lack of detailed understanding of the reaction mechanisms of both the ORR and the oxygen evolution reaction (OER) facilitated by non-precious metal (NPM) catalysts. In this chapter, we conducted a KIE study in an effort to identify the rate-determining step (RDS) of these intricate electrocatalytic reactions involving multiple proton-coupled electron transfer (PCET) processes. A KIE of about 2 for the ORR catalyzed by a NPM material was observed, but no KIE was observed for Pt or Pd supported on carbon. We found an inverse KIE for OER catalyzed by Ni and Co electrodes. These results contribute to a more complete understanding of the ORR and OER mechanisms and allow for future development of improved NPM catalysts.

In Chapters 6 to 12, I present our efforts in collaboration with the Zimmerman group to devise an electrochemical platform based on a HBM to control proton kinetics in PCET processes (Figure 0.2). To construct a HBM system, we prepared the first example of a synthetic NPM ORR catalyst based on a dinuclear Cu complex of 3,5-diamino-1,2,4-triazole that forms a self-assembled monolayer (SAM) on Au surfaces. We then embedded this Cu catalyst inside a HBM by depositing a monolayer of lipid on the SAM. By incorporating an alkyl proton carrier in

the lipid layer of a HBM, proton transport to a Cu-based molecular ORR catalyst was regulated. This electrochemical platform allows the precise and independent control of both the thermodynamics and kinetics of proton and electron transfers to a molecular catalyst.

Figure 0.2. Concept art depicting protons traversing lipid membranes.

In Chapter 6, I describe our attempt to prepare a pH-sensitive on-off switch for gating proton flux across lipid membranes, which could then reversibly modulate the activity of a lipid-buried ORR catalyst. Our HBM approach revealed unique mechanistic insights into PCET reactions that are relevant to both biological systems and energy conversion processes. In Chapter 7, I provide detailed electrochemical and physical characterization data of the lipid-modified Au electrodes employed.

PCET reactions typically are studied by varying the electron transfer thermodynamics and kinetics. Proton transfer thermodynamics can also be used to perturb PCET processes. However, *proton transfer kinetics* represents a largely unexplored territory to regulate PCET reactions. Table 0.1 summaries the techniques utilized in this thesis to examine PCET processes.

In Chapter 8, I present our efforts to control the selectivity of PCET reactions by tuning the proton transfer rate. NPM ORR catalysts are promising candidates to enable the widespread implementation of fuel cells. However, robust catalysts must exhibit high selectivity for the four-electron four-proton reduction of O_2 to H_2O without generating deleterious reactive side products including H_2O_2 and O_2^-. To modulate proton transport, we utilize lipid-modified electrodes. The results corroborated our hypothesis that the source of undesired ORR side products for NPM catalysts is a mismatch between the proton and electron transfer rates. Whereas fast proton transfer kinetics induce H_2O_2 formation and sluggish proton flux produces O_2^-, proton transfer rates commensurate with O-O bond breaking rates ensure that only H_2O forms. This fundamental insight applies to a multitude of NPM catalysts including the Fe-N-C material with the lowest ORR overpotential and aids in the development of future ORR catalysts that exhibit enhanced selectivity.

Table 0.1. Experimental handles to modulate the thermodynamics and kinetics of electron and proton transfer processes.

Attributes	Electron Transfer	Proton Transfer
Thermodynamics	Electrode Potential	Solution pH
Kinetics	Self-assembled Monolayer	Proton Carriers in Lipids

Since the HBM platform requires the proton carrier to deliver a proton across a lipid membrane, the mechanism by which protons are transported is therefore a crucial piece of knowledge. In Chapter 9, together with the Zimmerman group, we probed the mechanism of so-called "flip-flop" diffusion of proton carriers across the lipid layer of a HBM. The "flip-flop" diffusion rates of the proton carriers dictate the kinetics of O_2 reduction by the electrocatalyst. By varying both the tail lengths of the proton carriers and the lipids, we find the combination of

lengths which maximize the "flip-flop" diffusion rate. These experimental results combined with biophysical modeling studies allow us to propose a detailed mechanism for transmembrane "flip-flop" diffusion in HBM systems, which involves the bending of the alkyl tail of the proton carrier during the rate-determining step. Additional studies with an unbendable proton carrier further validate these mechanistic findings.

Molecular switches gate many fundamental processes in natural and artificial systems. To control proton delivery across biological membranes, in Chapter 10 we rationally designed a photo-responsive molecular switch incorporated in the lipid monolayer of a HBM (Figure 0.3). This proton gate was reversibly activated by adopting a Z conformation upon illumination with 390 nm light and then deactivated by taking an E conformation under 360 nm irradiation. We demonstrated that by incorporating this photo-responsive proton gate into the lipid layer, we turned on and off a lipid-buried O_2 reduction electrocatalyst by regulating the proton flux with irradiation on demand. We anticipate this proof-of-concept light-induced proton delivery system to play an important role in future development of functional organic-inorganic nano-devices.

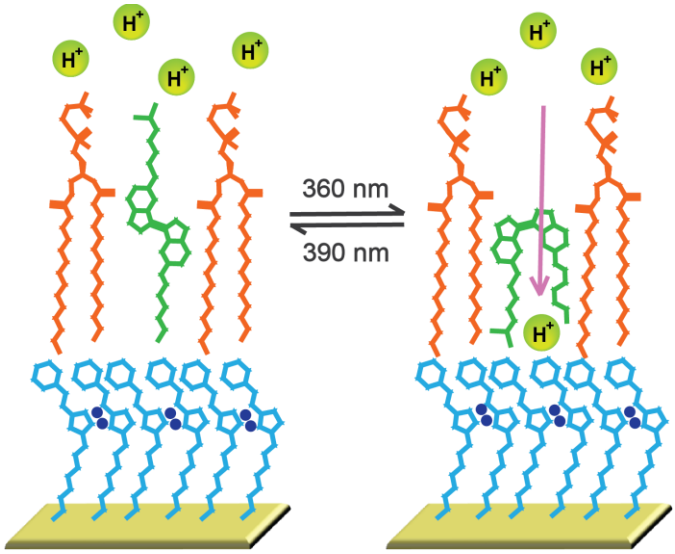

Figure 0.3. Schematic displaying light-triggered proton delivery across lipid membrane.

In the work presented in Chapters 6 to 10, we utilized lipid-modified electrodes to examine the assisted transport of protons, which are cationic species. We wondered if we can extend our investigation to interrogate unaided anion diffusion across biological membranes. In Chapter 11, we used a HBM as an analytical platform to assess anion diffusion through a lipid monolayer (Figure 0.4). We performed cyclic voltammetry (CV) using different anions in bulk solution and extracted thermodynamic and kinetic information about anion transport by interrogating the Cu(I)/Cu(II) redox covalently-bound to the SAM layer. We evaluated the empirical results using linear combinations of fundamental chemical trends, and determined that anion transport quantitatively correlates to polarity and basicity, a relationship we formalize as the lipid permeability parameter. In addition, we discussed how our findings can be understood according to the two leading mechanisms describing ion permeability across biological membranes. Our results demonstrated that anion transport through the lipid monolayer of a HBM is best described by the solubility-diffusion mechanism, not the pore mechanism.

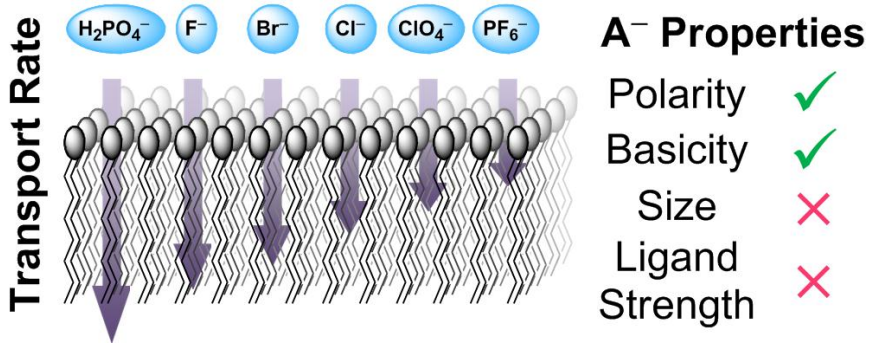

Figure 0.4. Illustration relating attributes of anions to transmembrane anion diffusion rates.

PCET reactions are ubiquitous in biochemistry and alternative energy schemes. Natural enzymes utilize quinones in proton transfer chains and energy conversion processes. In Chapter 12, we utilized a bio-inspired organic-inorganic HBM system to control the reaction mechanism

of a quinone molecule covalently bound to an electrode surface. In particular, by impeding proton access to the quinone moiety, we changed the reaction pathway from a PCET process to a pure electron transfer step. We further altered the reaction pathway to a stepwise PCET process by controlling the proton flux through the use of an alkyl proton carrier incorporated in the lipid membrane. We demonstrated that modulating proton kinetics dictates reaction pathway of a non-catalytic process. This work provides exclusive insight into stoichiometric PCET reactions and a unique electrochemical platform for interrogating them.

To a world

without war and disease

but instead filled

with love and compassion

ACKNOWLEDGEMENTS

First and foremost I would like to take the opportunity to thank my two dear advisors, **Professor Andrew A. Gewirth** and **Professor Thomas B. Rauchfuss** for their vision, wisdom, guidance, suggestions, and encouragement over the past five years. They kindly admitted me as a joint student and granted me access to resources in both laboratories. With their unfailing support and timely advice, I took on and completed several captivating yet challenging projects that allowed for my intellectual capacity and writing skills to grow substantially. I greatly enjoyed my stimulating Ph.D. experience and I will always cherish the time I spent at the University of Illinois at Urbana-Champaign (UIUC).

Next, I would like to thank my other thesis committee members, **Professor Catherine J. Murphy** and **Professor Paul J. A. Kenis**. I regard both professors as my role models and I learned a tremendous amount from the academic career paths of both professors. I hope that one day I could excel in any direction I undertake, similar to what Professor Murphy and Professor Kenis have demonstrated over the years. The knowledge I acquired during my B.Sc. and Ph.D. training will be indispensable for me to solve challenges and overcome hurdles in the years to come.

I owe my sincerest gratitude to **Professor Steven C. Zimmerman**. Without Professor Zimmerman's consent, support, and tutelage, the collaboration project on "Hybrid Bilayer Membrane" (HBM) between the Zimmerman group and the Gewirth group would not have happened. This HBM initiation is a highly-collaborative effort to address one fundamental aspect in a broad class of reactions that is critical to the survival of organisms on Earth and the advancement in renewable energy conversion schemes. Without this HBM collaboration, I would probably not have met **Dr. Ying Li**, who holds an irreplaceable position for me and

always cheered me up during our time together in graduate school. Without the help from Professor Zimmerman and Ying, I would probably still be struggling to synthesize the molecule that is central to this HBM study. Thus far, this collaboration has been a fruitful one. In terms of scientific research, we have made several key discoveries. In the sense of personal development, I am also grateful to have had the chance to be enlightened by **Dr. Ali Hosseini** in New Zealand. I am inspired by Ali's constant attention to details.

Without a doubt, I am indebted to **Dr. Christopher J. Barile** (also in the Gewirth group), the mastermind pulling the strings behind the scene. Chris is my dearest colleague in the Gewirth group, yet he also acts as a well-respected mentor to me. I learned much about experimental designs and strategies from Chris. Working in the laboratory with Chris is an incredible experience. I feel sorry for the new Gewirth group members who are not as fortunate as me to have the opportunity to learn from this wonderful young gentleman. Chris is truly a wonder kid. Not only can he revive seemingly impossible assignments to a meaningful investigation, he also constantly seeks ways to solve unanswered scientific problems. I, of course, look forward to our collaboration in the future and work on all the crazy ideas that we have accumulated over the years.

Together with Chris and Ying, we were fortunate enough to mentor a number of creative, bright, intelligent, diligent, and hardworking undergraduate students: **Katherine Sieradzki**, **Thomas B. Sobyra**, **John P. Gewargis**, **Nicholas A. Kirchschlager**, and **Benjamin J. Pedretti**. The HBM projects would not have advanced to today's stage without their time and effort. I absolutely enjoyed the discussion sessions we had on science-related subjects and I cherished our time together both in lab and at conferences. I wish the undergraduate group members the best of luck in all their future endeavors.

Hereby I include my vote of thanks to my colleagues and friends for an unforgettable journey in the past five years. I genuinely thank **Dr. David Schilter**, **Dr. Peter Sempsrott**, **Brian Trihn**, **Lien Nguyen**, **Dr. Xiaoyuan Zhou**, **Dr. Andrey Tregubov**, and **Geoffrey Chambers** for their enduring help, ceaseless suggestions and countless tips on organic and inorganic syntheses. Furthermore, I thank **Dr. Claire E. Tornow, Dr. Matt Thorseth**, **Dr. Matt Thorum**, **Dr. Hadi Tavassol**, **Dr. Laura Huff**, and **Dr. Justin Oberst** for getting my feet wet in the Gewirth group and passing along essential electrochemical characterization techniques. Here is a special shout-out to all the visiting scholars including **Dr. Ricardo T. Venegas** (Chile), **Dr. Yair Cohen** (Israel), **Dr. Renato Canha** (Brazil), **Dr. Camilo Angelucci** (Brazil), **Takashi Nakazono** (Japan), **Liu Lin** (Japan) for sharing their lab experiences from all around the globe.

I greatly appreciate the time and effort that **Thao Hoang**, **Jason Varnell**, and I spent together working on mind-boggling ventures and potentially-hazardous missions. Thank you for keeping the accident count to zero. I also thank **Elizabeth Miller**, **Ryan Rooney**, **Minjeong Shin**, and other **Gewirth and Rauchfuss group members** for being wonderful labmates. I thank **Dr. Heng-Liang Wu** for his encouraging pep talk and our valuable discussion on lipid-related project development. I thank **Dr. Adele Pacquette** for sharing her words of wisdom and experience on research and in job searching. I miss the days (and nights to be exact) that Heng, Adele, and I spent together discussing subjects related to both science and the NBA Finals. I thank Heng for "the sacrifice" so we could watch an NBA game live together. I thank **Kevin Schmitt** for teaching me how to conduct potential-dependent Raman spectroscopy for an electrochemical experiment *in situ*. I wish him good luck in finding a job. I also have to thank **Bruno Nicolau** for his wealth of knowledge in spectroscopy and his experience in cleaning glass slides. I wish Bruno all the best in his artificial monolayer studies. Bruno, do keep me posted

because I am very interested in that fundamental exploration. Last for this paragraph but definitely not the least, I would like to thank **Jen Esbenshade**, an incredible coworker who has shared the same office space with me for the past five years. I enjoy listening to her life lessons and hiking experience. Jen has contributed much to maintaining the serenity and silence in the office amidst the bustling lab that is necessary for high working efficiency and allow us to concentrate and focus on writing. I wish Jen all the best in securing the teaching-research position that she dreams of.

Furthermore, I would like to thank **Professor Robert B. Gennis**, **Professor Sharon Hammes-Schiffer**, **Professor Zaida Luthey-Schulten**, **Professor Hyunjoon Kong**, **Professor Kenneth S. Suslick**, **Professor Ralph G. Nuzzo**, **Professor Yi Lu**, **Professor Gregory S. Girolami**, and **Professor Joaquin Rodríguez-López**, **Dr. Dean Olson**, **Dr. Danielle L. Gray**, **Dr. Furong Sun**, **Dr. Haijun Yao**, **Dr. Richard T. Haasch**, **Dr. Julio Soares**, **Dr. Rudiger Laufhutte**, **Dr. Elizabeth Eves**, **Dr. Ratna Dutta**, **Dr. Marie E. Keel**, **Connie J. Knight**, **Beth L. Myler**, **Theresa E. Struss**, **Karen E. Watson**, and **Stacy K. Dudzinski** for their assistance during my time in UIUC and their input to my thesis projects, original research proposals, literature seminar, and potential collaboration plans.

I also would like to take this opportunity to thank multiple funding sources. First, I thank the **Croucher Foundation** for a scholarship during my PhD studies. I am grateful to receive the **Theron Standish Piper Award** for PhD students in the Inorganic division. The **Eastman Travel Grant** enabled me to attend a Gordon Research Conference (GRC) at Ventura, CA together with Chris. At the GRC, we were fortunate to gather valuable comments from **Dr. Cedric Tard** at the Laboratoire d'Electrochimie Moleculaire at CNRS in Paris, France. I am also indebted to the generosity of the donors of the **Harry S. Drickamer** Fellowship, the **Walter**

Brown Fellowship, the **James R. Beck** Fellowship, and the **Therald Moellar** Scholarship. I would also extend my gratitude to the **U.S. Department of Energy** for funding my research related to enabling next-generation fuel cell technologies. I thank the **International Institute for Carbon-Neutral Energy Research** (I^2CNER) for granting me the opportunity to visit the Kyushu University in Japan. I gratefully acknowledge **Professor Sasaki**, **Professor Hayashi**, **Professor Nishihara**, and **Professor Hagiwara** for their hospitality.

I would not be where I am right now if not for the training I received during my time as an undergraduate student. I will never forget the terrific opportunity to work as a summer intern in a research lab for the first time in my life offered by **Professor Chi-Ming Che** at the University of Hong Kong (HKU). I learned a great deal from Professor Che and **Dr. Vanessa K. Y. Lo**, my mentor-turned-lifelong-friend. I owe my sincerest gratitude to **Professor T. Brent Gunnoe**, my undergraduate advisor at the University of Virginia (UVA), where I picked up my organometallics background. I was very fortunate to learn synthetic and characterization techniques from **Dr. Joanna R. Webb** and **Dr. Brandon Quillian**, my two great mentors who both are now professors. The influence of these exceptional individuals has been instrumental in my academic career path. I owe a tremendous amount to these brilliant scientists mentioned above.

Outside of lab, I enjoy spending time at the gym mainly to preserve my sanity. I met quite a number of incredible people on the "**A-team**" badminton team, including Dr. Chun-Ho Wong, Juspreet Sandhu, Hanting Wang, Muhuan Liu, Jun Kit Wong, Yong Bing Chong, Dingfeng Zhang, Kun-ta Lee, Xiaolong Han, Ying, Chee Kang Yew, Ching-Pei Lee, Kaiwen Hsiao, Sunnie Huang, Yilin Ren, Raymond Ke, Lup Yee Wong, Dr. Yunzi Luo, Dr. Rui Wu, Dr. Kejia Chen, Angela Wu and many more. I treasure both our on-court practice and fitness training

sessions. I will not forget the particular occasion when we finally captured our first team championship after three times of asking. To our future teammates: keep up the good work and train persistently. **Jus** is an inventive physicist and **Xiaolong** is a talented mathematician. I am eager to read their theses and learn of their innovative work in the future.

Squash is my other favorite sport. **Tam Kal Wai**, who assisted me in the process of assembling the squash team from scratch at the Diocesan Boys' School (DBS), was an exchange student at UIUC for one semester. Despite our best effort to improve the ranking of DBS from being almost last in the league to second place, for six years we were not able to claim the ultimate glory for our alma mater. Fate had given Wai and me a second chance to reunite at UIUC and strive for the best again together as comrades. This time, my brother-in-arms and I made no mistake and clinched our very first gold trophy together for the UIUC squash team at the inaugural Jester's Mid America Collegiate Cup. We were overjoyed and we continued to improve UIUC's ranking at the Nationals.

UVA was an amazing place. I came to know a number of amazing individuals. I had an amazing time at the Virginia Club Badminton (VCB) participating in various tournaments together with **Alexander Nguyen**, **Anita Or**, **Michael Chen**, and **Simon Zhang**. I treasure every annual reunion ski trip and I thank Alex, Anita, and Anita's dad for their hospitality in hosting me. I feel as if I have a third home in Virginia/Maryland. I would also like to thank **Mae Li** for re-igniting my passion in badminton and watching badminton matches, the Olympic Games and among other sports events together virtually. I wish our friendship with the VCB crew will grow in depth and breadth with the passage of time.

Three of my awesome friends in UVA truly pulled me through my undergraduate and graduate studies. **Jimmy Yeu**, now a high school history teacher, always provides words of

wisdom that are mainly quotes from present and former US presidents. **Jonathan Lui**, my dearest buddy, and I share countless memories and indescribable stories together. **Dr. Nicholas Wu** is my role-model who is always a step ahead of everyone else. I will cherish all the movie nights at your apartment basement and the "late-night study sessions" at Clemons library, Alderman library, Gilman hall, Lambeth computer room, and the chemistry study room. I thank Jimmy, Jonathan, and Nick for their endless moral support and career counseling. I hope the bond between us will transcend the sands of time.

This acknowledgement would not be complete without devoting my gratitude to my family and friends from *afar, 7,879 miles* to be exact according to Google Maps. Despite the almost *12 hour* time difference between us, I treasure every video call with **Alvin Chan** and **David Lam**. We seem to turn back the hands of time and return to our care-free world. Those moments are the source of my strength that has propelled me to march forward. I hope we will still enjoy our "victory ice-cream" many years from now. I also would like to thank **Jonathan Wong**, **Eric Pun**, and **Alvin Kan** for their exceptional opinions on both scientific and political matters. For numerous circumstances, I was lost in my life. Time and time again, **Ivy Lee**, my dearest pen-pal, set my head straight, gave me a sense of purpose, and guided me through the haze and maze like a beacon of light in the mist. In return, I wish her a fruitful soul-searching process.

I cannot express how much I owe **my parents**, **grandparents** and **relatives** for their unfaltering support and untiring love, no matter how many times I have given them false hopes or have failed their expectations. I did not spend adequate amount of time around my parents even when I was in Hong Kong back then, and now I am away from home for almost 8 years. I am by no measure the "good" son that my parents deserve, but I hope one day that I will become

the son that my parents can be proud of. I wish my parents good health physically, mentally, and spiritually. I hope that I will have the chance to repay my parents. I am also indebted to **my sister**, who worked extremely hard after her graduation to pay for my college tuition. I wish my sister and her husband a family of perpetual comfort, harmony, and happiness.

Despite knowing that this lengthy acknowledgement section and my PhD thesis will never surmount to the unconditional love and ever-lasting support from my dearest family members and friends from all around the world, I would like to end this section by delivering this final message, "Thank you for coloring my memories and brightening up my life."

Table of Contents

Chapter 1

Introduction to Alternative Energy Conversion Schemes

1.1 Global Warming, Worldwide Energy Demand, and Strategies to Address Both

The quest for renewable energy sources is one of the central research themes in the 21st century due to the detrimental environmental consequences of consuming fossil fuels, including but not limited to global warming,[1-3] rising sea level,[4] adverse climate change,[5] escalating greenhouse gas emissions,[6,7] food shortage,[8] and infectious disease threat.[9] One viable strategy to combat the rising energy demand and mitigate detrimental impacts on our ecosystem, public health, and economy is to utilize clean energy technology in the transportation and power generation sectors. Widespread adoption of alternative energy schemes, in principle, should lead to a sustainable energy economy, maintain food security, and reduce the dependence on foreign oil supplies in the future.[10] Fuel cells provide a feasible route to enable clean energy usage with minimal generation of undesired pollutants.

Fuel cells are electrochemical devices that convert chemical energy directly into electrical energy using an external fuel source.[11] Fuel cells are not heat engines, and therefore fuel cells are not limited by the Carnot cycle, which sets the upper boundary for the thermodynamic efficiency of heat engines.[11] The theoretical efficiency of fuel cells can reach as high as 90 %.[11] With this superior efficiency and capacity, fuel cells are projected to be the energy conversion devices of choice for future transportation applications, provided that certain design problems can be solved.[12,13] These devices have utility in outer-space applications, but the costs remain too high for more conventional uses on Earth.[14] Fuel cell technology is a rapidly-

growing industry, and the global fuel cell market is predicted to grow to 15.7 billion USD by 2017.[13]

1.2 Fuel Cells as Efficient Energy Conversion Devices

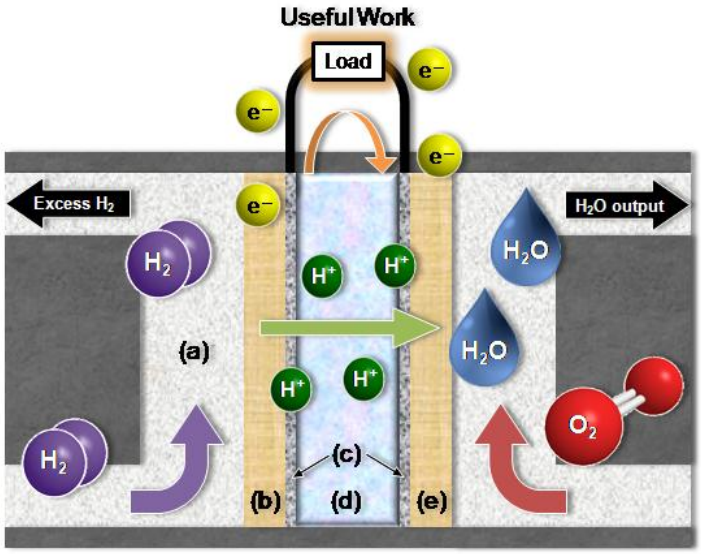

Figure 1.1. Functional components of a hydrogen PEMFC. (a) gas diffusion flow-field, (b) anode, where the facile oxidation of fuel occurs, (c) layer of catalysts immobilized on a conductive support bound by a binder component, (d) proton-exchange membrane, and (e) cathode, where the sluggish O_2 reduction occurs.

Fuel cells are classified into two major categories based on the operating temperature.[15] High temperature fuel cells operate at temperatures above 600 °C, and thus the potential applications are restricted to primarily stationary usages. In contrast, low temperature fuel cells typically operate at 80–200 °C. In particular, polymer electrolyte membrane fuel cells (PEMFCs) have a variety of potential portable applications, mainly in the transportation sector.[16] These relatively simple devices are comprised of a stack of ion-exchange membranes sandwiched between the cathode and anode, which are separated by a proton-conducting perfluoro-membrane commonly comprised of Nafion, with the catalysts deposited onto the electrode

surfaces (Figure 1.1).[17,18]

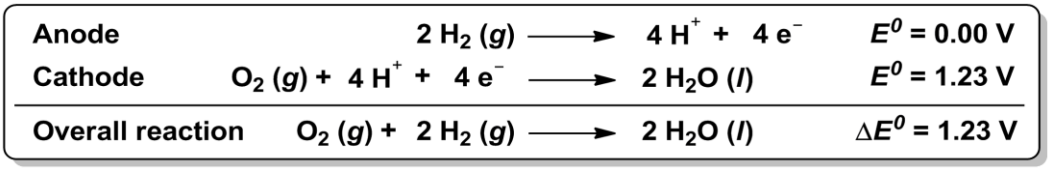

Figure 1.2. Standard cell potential of a hydrogen PEMFC at 1 atm and pH 0.

By incorporating fuel cell technology into a H_2 economy construct, our society would be able to achieve a sustainable system entirely free from fossil fuels.[19,20] Under the H_2 economy scenario, renewable energy sources such as solar and wind are converted into electrical energy in the first half of the cycle through concomitant water splitting to generate H_2 and O_2. To complete the H_2 economy cycle, H_2 is then oxidized on the anode of a fuel cell, where catalysts have already been developed to oxidize H_2 efficiently. O_2 is used as the terminal oxidant (electron acceptor) at the cathode. These two redox processes generate electricity captured by an external circuit to perform useful work. The driving force across the two electrodes is, in principle, dictated by the thermodynamic potentials of the two half cell reactions (Figure 1.2).[21] However at present, to obtain realistic power output, the half cell reaction at the cathode must operate at an overpotential of ~300 mV, i.e. E_{cell} drops to ~0.8 V.[11]

1.3 On the Slow Reaction Kinetics of the Oxygen Reduction Reaction

The PEMFC is superior to the conventional internal combustion engine, because the PEMFC overcomes the Carnot limitation on the conversion of heat to mechanical work, which is a manifestation of the second law of thermodynamics.[11] In addition to the attractive efficiency, PEMFCs also are environmentally friendly because water is the by-product. Despite their favorable qualities, PEMFCs are predominantly limited by fuel-crossover, a phenomenon that

lowers the cell voltage, and sluggish oxygen reduction kinetics at the cathode, among other engineering issues.[22-28] The former impediment is being addressed by advances in the membrane material research but the kinetic issue remains largely unsolved. Therefore, at present the performance of PEMFCs is practically inhibited by the sluggish kinetics of the oxygen reduction reaction (ORR) at the cathode.

At present, no artificial catalyst is capable of facilitating the ORR at virtually no overpotential. The ORR is an intricate process that requires a lot of energy to break the particularly strong O=O double bond (498 kJ/mol) and involves multiple proton-coupled electron transfer (PCET) steps.[11] Apart from the large energy input required for O=O bond cleavage and the complicated reaction mechanism, most catalysts do not selectively reduce O_2 by 4 e^- to H_2O. Instead, these catalysts generate a substantial amount of H_2O_2 as a deleterious side product via a 2 e^- process that leads to membrane degradation and catalyst decomposition.[19,26-30] These limitations contribute to the lack of an active, selective, and cost-effective catalyst for the ORR which prevents the large-scale commercial use of low temperature PEMFCs.[31,32]

1.4 Facilitating the ORR Kinetics by Precious Metal Catalysts

Catalysts are capable of lowering the kinetic barrier for the ORR, and precious metals such as Pt-group metals have long been used as an industrial standard to facilitate the ORR in fuel cells, especially those present in space shuttles and the international space station.[14] Current state-of-the-art fuel cells contain a high loading of Pt. However, the high cost and scarcity of Pt are two of the major impediments that have prohibited extensive commercialization of PEMFCs.[11] Another practical limitation of using Pt as the cathode catalyst is the 300 mV overpotential required to facilitate the ORR, a substantial energy loss that is higher than desired.

In an effort to achieve cost-effective ORR catalysts, a tremendous amount of effort has been invested in lowering the Pt loading. One research direction is to fabricate Pt alloys as ORR electrocatalysts.[11,17,33] Pt_3Ni is a successful example demonstrating the beneficial effect of doping a Pt lattice with Ni.[33-35] The incorporation of Ni improves the ORR onset potential of Pt by ca. 100 mV,[34,36,37] thus rendering Pt_3Ni the new activity benchmark while lowering the overall catalyst loading. Co, Fe and Mn are three other affordable transition metals employed to fine-tune the activity, selectivity, and durability of Pt-based catalysts.[18] There are two origins of the enhancement. First, a change in composition induces structural rearrangement, which in turn leads to an increase in the O_2 binding site availability and the binding strength between intermediate species and the catalyst surface.[33,34,36,38-50] Second, doping Pt with transition metals of different electron densities alters the d-band energy level of the resultant material, thus promoting more facile O-O bond cleavage and product removal as elicited by various computation methods.[51-55] However, these Pt alloys suffer from leaching of the less noble metal during ORR under typical PEMFC operating conditions.

Another route to lower the Pt loading absent of a dopant is through nano-engineering to generate Pt-skeleton morphologies.[33,34,36,39,45,50] These structures contain roughened features down to the atomic level are fabricated via co-deposition of Pt with another less-noble metal and subsequent leaching of the less-noble metal, leaving behind a highly porous material with an increased number of active sites. Pt skin and core-shell nanoparticles are two methodologies of particular interest to lower Pt loading.[56-59] These structures can be achieved via high temperature treatment or galvanic displacement of underpotential-deposited Cu or Pb with Pt.[59-64] However, these materials with hierarchical structures are not scalable. Extensive amount of research effort is also directed toward replacing Pt with Pd as the main component of the catalyst material.[65-69]

Utilizing the aforementioned alloying schemes and nano-structuring designs,[65,70-75] Pd-based materials exhibit attributes and ORR activities that can rival that of Pt.[56,67,76-79]

1.5 Non-precious Metal Heterogeneous Catalysts for ORR

An alternative approach is to search for, design, and prepare a more cost-effective catalyst that is comprised of non-precious metal (NPM) materials, such as those containing first-row transition metals, nitrogen and carbon (M-N-C).[80-89] The use of Fe, Co, Mn, and Ni to create NPM electrocatalysts has evolved into an area of intense study since the ORR activity of Co phthalocyanines was discovered.[90,91] In an effort to improve the ORR catalytic activity of these NPM catalysts, the pyrolysis of metal porphyrins/phthalocyanines as well as various metal salts with other N-containing compounds in the presence of a porous carbon support resulted in a remarkable enhancement in both the activity and the durability of the resultant catalysts.[31,89,92-101] The use of N-rich polymers as precursors, including but not limited to polyaniline, results in electrocatalysts with ORR performance resembling that of Pt.[29,30,93,102-108]

Despite the advancement in developing M-N-C as ORR electrocatalysts on a trial-and-error basis, the lack of a fundamental insight into the active site of the heterogeneous material and the absence of detailed mechanistic study of the ORR mechanism greatly hampered the progress in developing next-generation catalysts that build upon rational design. Many hypothetical proposals of the catalytic site structure have been suggested over the past decades.[89] First, the macrocycle is likely destroyed at 900 °C, but the metal ion site still resembles a Fe-N_4 coordination environment.[80,109-113] However, equally active M-N-C materials can be prepared by using non-macrocycles, thus disfavoring the Fe-N_4 postulation. Second, the ORR performance of metal-free N-doped carbon in basic condition rivals that of Pt and M-N-C, giving rise to the

supposition that the metal ion precursor merely serves as a templating agent to encourage the formation of active N-C network.[114] However, trace amount of metal impurities in the putative "metal-free" materials begs the question as to whether the metal contaminations contribute to the observed ORR activity or not.[115,116] Despite decades of research efforts, the controversy regarding the active site in these highly-heterogeneous materials still heavily restricts progress in enabling the widespread deployment of PEMFCs containing M-N-C electrocatalysts.[100,117]

To further identify the active site accountable for the observed ORR activity in these M-N-C materials, small molecules including CO, CN^-, N_3^-, and Cl^- were introduced to the electrolyte solution prior to or during the ORR.[118-120] These molecular poisons typically bind tightly to metal ions and occupy open coordination sites on the metal ions, thus effectively inhibiting O_2 from binding in other well-studied systems.[120-122] This poisoning effect is particularly apparent when CO reacts irreversibly with Fe porphyrins.[123] However, CO has no effect on the ORR activity of the NPM catalysts. Intriguingly, the ORR activity of the M-N-C materials poisoned by other small molecules can be restored easily by rinsing the pyrolyzed catalysts and replacing the electrolyte with fresh solution, suggesting that the active site of these heterogeneous materials is indeed metal-centered but not in the form of a bare metal ion. Further investigation and characterization efforts are underway.

1.6 Natural Enzymes Enables High ORR Activity

Scientists and engineers continue the pursuit of an alternative ORR catalyst that is more active than Pt and does not contain precious metals.[124] In nature, a handful of naturally-occurring enzymes with well-defined active sites reduce O_2 more efficiently than Pt.[125,126] One attractive target is a class of enzymes called multicopper oxidases of which laccase is the most well-known

example.[127] Laccase, a "blue oxidase" enzyme found in fungi, plants, and microorganisms, features a three-Cu active site where the ORR occurs.[128-133]

Laccases have been widely characterized with 105 resolved crystal structures existing in the RCSB Protein Data Bank.[134,135] The active site of laccase, where the ORR occurs, contains 1×T2 Cu and 2×T3 Cu centers.[136] The T2 Cu is bound by two histidine units, and can be three-coordinated with an extra H_2O or OH^- ligand, or it can bind an additional Cl^- ligand to give a four-coordinated square-planar geometry. Both of the T3 Cu centers are bound by three histidine units, and exhibit a distorted tetrahedral geometry in the resting state.[137] By examining the thermal-ellipsoids of the Cu atoms, oxygen is proposed to first bind to the two T3 Cu centers, as suggested by the perpendicular trajectory. The T2 Cu then approaches the peroxo species to break the O–O bond. An unanticipated observation is noted in the structure, where the bound peroxo species is not symmetrical between the two T3 sites.[138]

Artificially-modified laccases have been synthesized to further understand the reaction pathway of the ORR.[128-130] A T2-depleted sample was prepared to compare the bound peroxo intermediate to that observed in the natural enzyme.[139] Since minimal electronic and spectroscopic differences were noted, the authors suggested T3 coppers are crucial to the O_2 binding event. The T1 Cu site can be replaced by Hg(II), which is redox silent.[140] As no electron was supplied to the tri-Cu site, a long-lived peroxo species was trapped. A primary kinetic isotope effect was observed with ^{17}O NMR, thus O-O bond cleavage was determined to be the rate-determining step in the decomposition of the unnatural intermediate species.[140]

Laccase catalyzes the four-electron four-proton reduction of O_2 to H_2O, with minimal production of H_2O_2.[141-144] When immobilized onto gold surfaces using an anthracene-2-methanethiol linker, the enzyme functions as an efficient cathode catalyst at pH 7.[145] While

commercial Pt catalysts exhibit a substantial overpotential of ~300 mV, the laccase-modified electrode shows a promising overpotential of merely ~70 mV.[146] However, the overall performance of the laccase-modified electrode is limited by the immense size of laccase (~60 kDa), which significantly decreases the current density and the power output. Furthermore, laccase is only stable in physiological pH solutions and is unable to withstand the harsh operating conditions of PEMFCs (typically temperatures 80–200 °C, pH <2).[11] Laccase activity is greatly inhibited under non-physiological conditions.[147] Taken together the enormous size, low chemical tolerance, and intrinsic thermal instability of the laccases studied, direct utilization of laccase as a cathode catalyst in PEMFCs is not practical.

1.7 Bio-inspired ORR Catalysts as an Alternative Strategy

The vast literature on laccase, only partially reviewed above, provides information about the relationship between geometric features of the trinuclear Cu active site and the ORR activity of laccase. Since the direct utilization of laccase is plagued with inherent shortcomings and cannot deliver the power density necessary for practical uses,[11] molecular models of the active site may yield a robust, yet efficient, catalyst.[148] It is desirable to develop new bio-inspired Cu complexes as fuel cell catalysts that supersede the activity of traditional materials at a substantially lower cost.

Synthetic Cu complexes are well known to react with O_2,[11,149-152] although relatively few studies examine their ability to catalyze the reduction of O_2 to water. Recently, our group reported that the Cu complex of tris(2-pyridylmethyl)amine (TPA) catalyzes the ORR with an overpotential of 700 mV at pH 1, the lowest overpotential for a non-biological Cu complex at this pH.[153] Rational design of the ligand framework should allow further lowering of the ORR

overpotential. By tuning the steric environment and electronic properties of the primary and secondary coordination spheres,[154-165] Cu complexes with O_2 in various binding modes have been isolated and characterized with concomitant changes to the thermodynamic reduction potentials of the metal centers.[166-170] The key to synthesizing fruitful biomimetic ORR catalysts based on laccase requires the *precise positioning* (spatial) of the *three copper centers* (chemical) of the *appropriate reducing power* (potential) at the *exact moment* (temporal). To ensure cooperativity comparable to that of metalloproteins, future catalysts require sophisticated ligand scaffolds.[171-174] Quantitative structure-activity relationship between ligand flexibility and ORR activity should assist in the identification of a molecular template that encourages intramolecular O_2 interaction by preorganizing the Cu units.

1.8 Improving the ORR Rate under Harsh Reaction Conditions

At present, the catalytic activity of ORR catalysts under 1 atm at room temperature is described by a 2D theoretical volcano plot, a correlation between the M-O bond strength and the ORR onset potential.[175] It is preferable to further map out the temperature and pressure dependences of the ORR activity of each of the metal of interest. With a reaction enthalpy of 10 kcal/mol, the Arrhenius equation predicts a one-fold enhancement in ORR kinetics if the operating temperature of PEMFCs is raised from 80 °C to 160 °C.[176] However, PEMFCs are limited to temperatures below 100 °C due to the use of Nafion, a proton-conducting membrane that transfer protons only when hydrated.[177] To reach temperature beyond 100 °C, phosphoric acid with a boiling point of 158 °C was utilized. However, phosphoric acid fuel cells suffer from low activity due to the high binding affinity of phosphate towards Pt, rendering a deactivated Pt surface.[176,178,179]

Fundamental studies of the ORR in water at temperatures above 100 °C are limited due to the harsh experimental conditions.[180] Interrogating the ORR on Pt at above 100 °C provides valuable kinetic information including the temperature dependences of Tafel slopes and transfer coefficients. Apart from enhancing the ORR kinetics, raising the temperature can promote efficient Pt-OH bond cleavage. Knowledge of the strength of Pt-OH bonds at above 100 °C will provide clues to minimize the ORR overpotential on precious metal and NPM catalysts and allow a deeper understanding of the potential-driven, proton-coupled, temperature-assisted rate-limiting step.

1.9 ORR Falls under the Umbrella of Proton-coupled Electron Transfer Reactions

PCET reactions are fundamental to many energy conversion processes, in particular, the four-electron four-proton ORR to water is one of the most intensely studied PCET reactions.[181-190] Much experimental and computational work examines the underlying reaction mechanism of the ORR in an effort to develop more efficient fuel cell cathodes and understand the cellular respiration process.[11,191-193] One long-standing goal in the field of PCET is to delineate the individual roles of thermodynamics and kinetics of electron and proton transfers.

The thermodynamics of electron transfer can be independently modulated by tuning the electrode potential,[21] while the kinetics of electron transfer can be separately regulated by the length and identity of a self-assembled monolayer (SAM) grown on an electrode surface.[194-199] Conventionally, the pH of bulk solution and covalently-bound proton relays are used to probe the effect of proton transfer thermodynamics on PCET reactions.[187,200,201] However, a modification in pH results in concomitant alterations in proton transfer kinetics. Apart from being a synthetically challenging and burdensome task, the addition of exquisite proton relays often

associates with a simultaneous shift in redox potential of the metal center and a concurrent change in solubility, rendering a fair and direct comparison between the modified and original systems problematic.[124,152,153,202] Taken together the complications that arise with tuning the bulk solution pH, new approaches are necessary to deconvolute the unequivocal influence of proton flux on the mechanism of not only the ORR, but all PCET processes.

1.10 The Underappreciated Role of Proton Kinetics in PCET Processes

In nature, transport of charged species such as protons across lipid bilayers is facilitated only in the presence of specific ion channels or mediators.[191,203-208] A bio-inspired hybrid bilayer membrane (HBM) is a unique electrochemical platform that interrogates the explicit role of proton transfer kinetics by modulating the proton flux to a redox species that undergoes a PCET reaction.[209,210] In a HBM system, a monolayer of lipid molecules is appended to a SAM of alkanethiols, terminated with a redox probe, covalently attached to a Au electrode.[211-214] Gating the proton flux would enable more in-depth understanding of the PCET mechanism. Tuning the interplay between proton, electron, and photon transfer thermodynamics and kinetics to a redox reaction center may allow unprecedented control over the reaction pathway and consequently the product speciation.[215] The lipid-modified electrode can also serve as an analytical platform to assess transport of small molecules across lipid layers apart from protons.[216] The HBM experimental platform is envisioned to provide unique mechanistic insight into how proton transfer controls PCET processes and allow for the advancement in developing a unifying theoretical PCET framework that accounts for the Marcus theory of electron transfer.[195,217-221]

1.11 References

(1) Blois, J. L.; Zarnetske, P. L.; Fitzpatrick, M. C.; Finnegan, S. *Science* **2013**, *341*, 499.
(2) Moritz, C.; Agudo, R. *Science* **2013**, *341*, 504.
(3) Post, E.; Bhatt, U. S.; Bitz, C. M.; Brodie, J. F.; Fulton, T. L.; Hebblewhite, M.; Kerby, J.; Kutz, S. J.; Stirling, I.; Walker, D. A. *Science* **2013**, *341*, 519.
(4) Kintisch, E. *Science* **2013**, *341*, 480.
(5) Diffenbaugh, N. S.; Field, C. B. *Science* **2013**, *341*, 486.
(6) Appel, A. M.; Bercaw, J. E.; Bocarsly, A. B.; Dobbek, H.; DuBois, D. L.; Dupuis, M.; Ferry, J. G.; Fujita, E.; Hille, R.; Kenis, P. J. A.; Kerfeld, C. A.; Morris, R. H.; Peden, C. H. F.; Portis, A. R.; Ragsdale, S. W.; Rauchfuss, T. B.; Reek, J. N. H.; Seefeldt, L. C.; Thauer, R. K.; Waldrop, G. L. *Chem. Rev.* **2013**, *113*, 6621.
(7) Benson, E. E.; Kubiak, C. P.; Sathrum, A. J.; Smieja, J. M. *Chem. Soc. Rev.* **2009**, *38*, 89.
(8) Wheeler, T.; von Braun, J. *Science* **2013**, *341*, 508.
(9) Altizer, S.; Ostfeld, R. S.; Johnson, P. T. J.; Kutz, S.; Harvell, C. D. *Science* **2013**, *341*, 514.
(10) Chu, S.; Majumdar, A. *Nature* **2012**, *488*, 294.
(11) Gewirth, A. A.; Thorum, M. S. *Inorg. Chem.* **2010**, *49*, 3557.
(12) DeLuca, N. W.; Elabd, Y. A. *J. Polym. Sci., Part B: Polym. Phys.* **2006**, *44*, 2201.
(13) Carter, D.; Ryan, M.; Wing, J. *Fuel Cell Today* **2012**, 1.
(14) Chan, C. C. *Proc. IEEE* **2007**, *95*, 704.
(15) Zhang, J.; Xie, Z.; Zhang, J.; Tang, Y.; Song, C.; Navessin, T.; Shi, Z.; Song, D.; Wang, H.; Wilkinson, D. P.; Liu, Z.-S.; Holdcroft, S. *J. Power Sources* **2006**, *160*, 872.
(16) Sandy Thomas, C. E. *Int. J. Hydrogen Energ.* **2009**, *34*, 9279.
(17) Debe, M. K. *Nature* **2012**, *486*, 43.
(18) Wang, Y.; Chen, K. S.; Mishler, J.; Cho, S. C.; Adroher, X. C. *Applied Energy* **2011**, *88*, 981.
(19) Cheng, X.; Shi, Z.; Glass, N.; Zhang, L.; Zhang, J.; Song, D.; Liu, Z.-S.; Wang, H.; Shen, J. *J. Power Sources* **2007**, *165*, 739.
(20) Neburchilov, V.; Martin, J.; Wang, H.; Zhang, J. *J. Power Sources* **2007**, *169*, 221.
(21) Bard, A. J.; Faulkner, L. R. *Electrochemical Methods: Fundamentals and Applications*; Wiley, 2000.
(22) Li, H.; Shi, Z.; Zhang, J. In *Encyclopedia of Electrochemical Power Sources*; Garche, J., Ed.; Elsevier: Amsterdam, 2009, p 941.
(23) Gervasio, D. In *Encyclopedia of Electrochemical Power Sources*; Garche, J., Ed.; Elsevier: Amsterdam, 2009, p 806.
(24) Srouji, A.-K.; Mench, M. M. In *Polymer Electrolyte Fuel Cell Degradation*; Veziroglu, M. M. M. C. K. N., Ed.; Academic Press: Boston, 2012, p 293.
(25) El-kharouf, A.; Pollet, B. G. In *Polymer Electrolyte Fuel Cell Degradation*; Veziroglu, M. M. M. C. K. N., Ed.; Academic Press: Boston, 2012, p 215.
(26) Wu, J.; Yuan, X. Z.; Martin, J. J.; Wang, H.; Zhang, J.; Shen, J.; Wu, S.; Merida, W. *J. Power Sources* **2008**, *184*, 104.
(27) Wu, J.; Yuan, X. Z.; Martin, J. J.; Wang, H. In *Encyclopedia of Electrochemical Power Sources*; Garche, J., Ed.; Elsevier: Amsterdam, 2009, p 848.
(28) Coms, F. D. *ECS Trans.* **2008**, *16*, 235.

(29) Jaouen, F.; Proietti, E.; Lefevre, M.; Chenitz, R.; Dodelet, J.-P.; Wu, G.; Chung, H. T.; Johnston, C. M.; Zelenay, P. *Energy Environ. Sci.* **2011**, *4*, 114.
(30) Higgins, D. C.; Chen, Z. *Can. J. Chem. Eng.* **2013**, *91*, 1881.
(31) Bezerra, C. W. B.; Zhang, L.; Liu, H.; Lee, K.; Marques, A. L. B.; Marques, E. P.; Wang, H.; Zhang, J. *J. Power Sources* **2007**, *173*, 891.
(32) Cao, D.; Sun, Y.; Wang, G. *J. Power Sources* **2007**, *167*, 250.
(33) Stamenkovic, V.; Schmidt, T. J.; Ross, P. N.; Markovic, N. M. *J. Electroanal. Chem.* **2003**, *554*, 191.
(34) Stamenkovic, V. R.; Fowler, B.; Mun, B. S.; Wang, G.; Ross, P. N.; Lucas, C. A.; Marković, N. M. *Science* **2007**, *315*, 493.
(35) Debe, M. K.; Steinbach, A. J.; Vernstrom, G. D.; Hendricks, S. M.; Kurkowski, M. J.; Atanasoski, R. T.; Kadera, P.; Stevens, D. A.; Sanderson, R. J.; Marvel, E.; Dahn, J. R. *J. Electrochem. Soc.* **2011**, *158*, B910.
(36) Stamenkovic, V. R.; Mun, B. S.; Arenz, M.; Mayrhofer, K. J. J.; Lucas, C. A.; Wang, G.; Ross, P. N.; Markovic, N. M. *Nat. Mater.* **2007**, *6*, 241.
(37) Wang, C.; Markovic, N. M.; Stamenkovic, V. R. *ACS Catal.* **2012**, *2*, 891.
(38) Stamenkovic, V.; Mun, B. S.; Mayrhofer, K. J. J.; Ross, P. N.; Markovic, N. M.; Rossmeisl, J.; Greeley, J.; Norskov, J. K. *Angew. Chem. Int. Ed.* **2006**, *45*, 2897.
(39) Stamenkovic, V. R.; Mun, B. S.; Mayrhofer, K. J. J.; Ross, P. N.; Markovic, N. M. *J. Am. Chem. Soc.* **2006**, *128*, 8813.
(40) Anderson, A. B.; Roques, J.; Mukerjee, S.; Murthi, V. S.; Markovic, N. M.; Stamenkovic, V. *J. Phys. Chem. B* **2005**, *109*, 1198.
(41) Kattel, S.; Wang, G. *J. Chem. Phys.* **2014**, *141*.
(42) Strasser, P.; Koh, S.; Anniyev, T.; Greeley, J.; More, K.; Yu, C.; Liu, Z.; Kaya, S.; Nordlund, D.; Ogasawara, H.; Toney, M. F.; Nilsson, A. *Nat. Chem.* **2010**, *2*, 454.
(43) Beard, B. C.; Ross, P. N. *J. Electrochem. Soc.* **1990**, *137*, 3368.
(44) Paulus, U. A.; Wokaun, A.; Scherer, G. G.; Schmidt, T. J.; Stamenkovic, V.; Markovic, N. M.; Ross, P. N. *Electrochim. Acta* **2002**, *47*, 3787.
(45) Paffett, M. T.; Beery, J. G.; Gottesfeld, S. *J. Electrochem. Soc.* **1988**, *135*, 1431.
(46) Teliska, M.; Murthi, V. S.; Mukerjee, S.; Ramaker, D. E. *J. Electrochem. Soc.* **2005**, *152*, A2159.
(47) Mun, B. S.; Watanabe, M.; Rossi, M.; Stamenkovic, V.; Markovic, N. M.; Ross, P. N., Jr. *Surf. Rev. Lett.* **2006**, *13*, 697.
(48) Mun, B. S.; Watanabe, M.; Rossi, M.; Stamenkovic, V.; Markovic, N. M.; Ross, P. N. *J. Chem. Phys.* **2005**, *123*.
(49) Toda, T.; Igarashi, H.; Watanabe, M. *J. Electrochem. Soc.* **1998**, *145*, 4185.
(50) Watanabe, M.; Tsurumi, K.; Mizukami, T.; Nakamura, T.; Stonehart, P. *J. Electrochem. Soc.* **1994**, *141*, 2659.
(51) Greeley, J.; Stephens, I. E. L.; Bondarenko, A. S.; Johansson, T. P.; Hansen, H. A.; Jaramillo, T. F.; Rossmeisl, J.; Chorkendorff, I.; Norskov, J. K. *Nat. Chem.* **2009**, *1*, 552.
(52) Kitchin, J. R.; Norskov, J. K.; Barteau, M. A.; Chen, J. G. *J. Chem. Phys.* **2004**, *120*, 10240.
(53) Kitchin, J. R.; Norskov, J. K.; Barteau, M. A.; Chen, J. G. *Phys. Rev. Lett.* **2004**, *93*.
(54) Greeley, J.; Norskov, J. K.; Mavrikakis, M. *Annu. Rev. Phys. Chem.* **2002**, *53*, 319.
(55) Roques, J.; Anderson, A. B. *Surf. Sci.* **2005**, *581*, 105.

(56) Shao, M. H.; Huang, T.; Liu, P.; Zhang, J.; Sasaki, K.; Vukmirovic, M. B.; Adzic, R. R. *Langmuir* **2006**, *22*, 10409.
(57) Zhang, J.; Mo, Y.; Vukmirovic, M. B.; Klie, R.; Sasaki, K.; Adzic, R. R. *J. Phys. Chem. B* **2004**, *108*, 10955.
(58) Zhang, J. L.; Vukmirovic, M. B.; Xu, Y.; Mavrikakis, M.; Adzic, R. R. *Angew. Chem. Int. Ed.* **2005**, *44*, 2132.
(59) Adzic, R. R.; Zhang, J.; Sasaki, K.; Vukmirovic, M. B.; Shao, M.; Wang, J. X.; Nilekar, A. U.; Mavrikakis, M.; Valerio, J. A.; Uribe, F. *Top. Catal.* **2007**, *46*, 249.
(60) Brankovic, S. R.; Wang, J. X.; Adzic, R. R. *Surf. Sci.* **2001**, *474*, L173.
(61) Zhang, J.; Lima, F. H. B.; Shao, M. H.; Sasaki, K.; Wang, J. X.; Hanson, J.; Adzic, R. R. *J. Phys. Chem. B* **2005**, *109*, 22701.
(62) Brankovic, S. R.; Wang, J. X.; Adzic, R. R. *Electrochem. Solid-State Lett.* **2001**, *4*, A217.
(63) Srejic, I.; Smiljanic, M.; Grgur, B.; Rakocevic, Z.; Strbac, S. *Electrochim. Acta* **2012**, *64*, 140.
(64) Strbac, S.; Srejic, I.; Smiljanic, M.; Rakocevic, Z. *J. Electroanal. Chem.* **2013**, *704*, 24.
(65) Shao, M. *J. Power Sources* **2011**, *196*, 2433.
(66) Spendelow, J. S.; Wieckowski, A. *Phys. Chem. Chem. Phys.* **2007**, *9*, 2654.
(67) Antolini, E. *Energy Environ. Sci.* **2009**, *2*, 915.
(68) Gasteiger, H. A.; Kocha, S. S.; Sompalli, B.; Wagner, F. T. *Appl. Catal., B* **2005**, *56*, 9.
(69) Zamel, N.; Li, X. *Prog. Energy Combust. Sci.* **2011**, *37*, 292.
(70) Xiao, L.; Zhuang, L.; Liu, Y.; Lu, J.; Abruna, H. D. *J. Am. Chem. Soc.* **2009**, *131*, 602.
(71) Lima, F. H. B.; Zhang, J.; Shao, M. H.; Sasaki, K.; Vukmirovic, M. B.; Ticianelli, E. A.; Adzic, R. R. *J. Phys. Chem. C* **2007**, *111*, 404.
(72) Seo, M. H.; Choi, S. M.; Kim, H. J.; Kim, W. B. *Electrochem. Commun.* **2011**, *13*, 182.
(73) Erikson, H.; Sarapuu, A.; Alexeyeva, N.; Tammeveski, K.; Solla-Gullon, J.; Feliu, J. M. *Electrochim. Acta* **2012**, *59*, 329.
(74) Kim, J.; Park, J.-E.; Momma, T.; Osaka, T. *Electrochim. Acta* **2009**, *54*, 3412.
(75) Shao, M. H.; Sasaki, K.; Liu, P.; Adzic, R. R. *Z. Phys. Chem.* **2007**, *221*, 1175.
(76) Shao, M. H.; Sasaki, K.; Adzic, R. R. *J. Am. Chem. Soc.* **2006**, *128*, 3526.
(77) Fernandez, J. L.; Walsh, D. A.; Bard, A. J. *J. Am. Chem. Soc.* **2005**, *127*, 357.
(78) Fernandez, J. L.; Raghuveer, V.; Manthiram, A.; Bard, A. J. *J. Am. Chem. Soc.* **2005**, *127*, 13100.
(79) Shao, M.; Liu, P.; Zhang, J.; Adzic, R. *J. Phys. Chem. B* **2007**, *111*, 6772.
(80) Wiesener, K. *Electrochim. Acta* **1986**, *31*, 1073.
(81) Wiesener, K.; Ohms, D.; Neumann, V.; Franke, R. *Mater. Chem. Phys.* **1989**, *22*, 457.
(82) Shi, Z.; Zhang, J. *J. Phys. Chem. C* **2007**, *111*, 7084.
(83) Baker, R.; Wilkinson, D. P.; Zhang, J. *Electrochim. Acta* **2008**, *53*, 6906.
(84) Steiger, B.; Anson, F. C. *Inorg. Chem.* **1997**, *36*, 4138.
(85) Ouyang, J. B.; Shigehara, K.; Yamada, A.; Anson, F. C. *J. Electroanal. Chem.* **1991**, *297*, 489.
(86) Song, E. H.; Shi, C. N.; Anson, F. C. *Langmuir* **1998**, *14*, 4315.
(87) Cardenas-Jiron, G. I. *J. Phys. Chem. A* **2002**, *106*, 3202.
(88) Li, W.; Yu, A.; Higgins, D. C.; Llanos, B. G.; Chen, Z. *J. Am. Chem. Soc.* **2010**, *132*, 17056.
(89) Yeager, E. *Electrochim. Acta* **1984**, *29*, 1527.
(90) Jasinski, R. J. *Nature* **1964**, *201*, 1212.

(91) Jasinski, R. J. *J. Electrochem. Soc.* **1965**, *112*, 526
(92) Scherson, D. A.; Gupta, S. L.; Fierro, C.; Yeager, E. B.; Kordesch, M. E.; Eldridge, J.; Hoffman, R. W.; Blue, J. *Electrochim. Acta* **1983**, *28*, 1205.
(93) Chen, Z.; Higgins, D.; Yu, A.; Zhang, L.; Zhang, J. *Energy Environ. Sci.* **2011**, *4*, 3167.
(94) Bezerra, C. W. B.; Zhang, L.; Lee, K.; Liu, H.; Marques, A. L. B.; Marques, E. P.; Wang, H.; Zhang, J. *Electrochim. Acta* **2008**, *53*, 4937.
(95) Ladouceur, M.; Lalande, G.; Guay, D.; Dodelet, J. P.; Dignard-Bailey, L.; Trudeau, M. L.; Schulz, R. *J. Electrochem. Soc.* **1993**, *140*, 1974.
(96) Medard, C.; Lefevre, M.; Dodelet, J. P.; Jaouen, F.; Lindbergh, G. *Electrochim. Acta* **2006**, *51*, 3202.
(97) Jaouen, F.; Dodelet, J.-P. *J. Phys. Chem. C* **2009**, *113*, 15422.
(98) Baranton, S.; Coutanceau, C.; Roux, C.; Hahn, F.; Leger, J. M. *J. Electroanal. Chem.* **2005**, *577*, 223.
(99) Zagal, J. H. *Coor. Chem. Rev.* **1992**, *119*, 89.
(100) Van, V. J. A. R.; Visser, C. *Electrochim. Acta* **1979**, *24*, 921.
(101) Zagal, J.; Bindra, P.; Yeager, E. *J. Electrochem. Soc.* **1980**, *127*, 1506.
(102) Banham, D.; Ye, S.; Pei, K.; Ozaki, J.-i.; Kishimoto, T.; Imashiro, Y. *J. Power Sources* **2015**, *285*, 334.
(103) Tylus, U.; Jia, Q.; Strickland, K.; Ramaswamy, N.; Serov, A.; Atanassov, P.; Mukerjee, S. *J. Phys. Chem. C* **2014**, *118*, 8999.
(104) Li, S.; Hu, Y.; Xu, Q.; Sun, J.; Hou, B.; Zhang, Y. *J. Power Sources* **2012**, *213*, 265.
(105) Wu, G.; More, K. L.; Johnston, C. M.; Zelenay, P. *Science* **2011**, *332*, 443.
(106) Li, X.; Liu, G.; Popov, B. N. *J. Power Sources* **2010**, *195*, 6373.
(107) Feng, Y.; Alonso-Vante, N. *Phys. Status Solidi B* **2008**, *245*, 1792.
(108) Bashyam, R.; Zelenay, P. *Nature* **2006**, *443*, 63.
(109) Maldonado, S.; Stevenson, K. J. *J. Phys. Chem. B* **2004**, *108*, 11375.
(110) Gojkovic, S. L.; Gupta, S.; Savinell, R. F. *J. Electroanal. Chem.* **1999**, *462*, 63.
(111) Maldonado, S.; Stevenson, K. J. *J. Phys. Chem. B* **2005**, *109*, 4707.
(112) Matter, P. H.; Zhang, L.; Ozkan, U. S. *J. Catal.* **2006**, *239*, 83.
(113) Bagotzky, V. S.; Tarasevich, M. R.; Radyushkina, K. A.; Levina, O. A.; Andrusyova, S. I. *J. Power Sources* **1978**, *2*, 233.
(114) Zhang, J.; Dai, L. *ACS Catal.* **2015**, *5*, 7244.
(115) Wang, L.; Pumera, M. *Chem. Comm.* **2014**, *50*, 12662.
(116) Wang, L.; Ambrosi, A.; Pumera, M. *Angew. Chem. Int. Ed.* **2013**, *52*, 13818.
(117) Bouwkamp-Wijnoltz, A. L.; Visscher, W.; van Veen, J. A. R.; Boellaard, E.; van der Kraan, A. M.; Tang, S. C. *J. Phys. Chem. B* **2002**, *106*, 12993.
(118) Oberst, J. L.; Thorum, M. S.; Gewirth, A. A. *J. Phys. Chem. C* **2012**, *116*, 25257.
(119) Thorum, M. S.; Hankett, J. M.; Gewirth, A. A. *J. Phys. Chem. Lett.* **2011**, *2*, 295.
(120) Birry, L.; Zagal, J. H.; Dodelet, J.-P. *Electrochem. Commun.* **2010**, *12*, 628.
(121) von, D. D.; Singh, D.; King, J. C.; Ozkan, U. S. *Appl. Catal., B* **2012**, *113-114*, 126.
(122) Akhade, S. A.; Luo, W.; Nie, X.; Bernstein, N. J.; Asthagiri, A.; Janik, M. J. *Phys. Chem. Chem. Phys.* **2014**, *16*, 20429.
(123) Collman, J. P.; Brauman, J. I.; Halbert, T. R.; Suslick, K. S. *Proc. Natl. Acad. Sci. U.S.A.* **1976**, *73*, 3333.
(124) Thorseth, M. A.; Tornow, C. E.; Tse, E. C. M.; Gewirth, A. A. *Coor. Chem. Rev.* **2013**, *257*, 130.

(125) Dagys, M.; Haberska, K.; Shleev, S.; Arnebrant, T.; Kulys, J.; Ruzgas, T. *Electrochem. Commun.* **2010**, *12*, 933.
(126) Blanford, C. F.; Heath, R. S.; Armstrong, F. A. *Chem. Commun.* **2007**, 1710.
(127) Yoon, J.; Fujii, S.; Solomon, E. I. *Proc. Natl. Acad. Sci. U.S.A.* **2009**, *106*, 6585.
(128) Solomon, E. I.; Augustine, A. J.; Yoon, J. *Dalton Trans.* **2008**, 3921.
(129) Solomon, E. I.; Randall, D. W.; Glaser, T. *Coor. Chem. Rev.* **2000**, *200*, 595.
(130) Solomon, E. I.; Sundaram, U. M.; Machonkin, T. E. *Chem. Rev.* **1996**, *96*, 2563.
(131) Solomon, E. I.; Kirk, M. L.; Gamelin, D. R.; Pulver, S. In *Biochemical Spectroscopy*; Academic Press Inc.: San Diego, CA, 1995; Vol. 246, p 71.
(132) Solomon, E. I.; Lowery, M. D.; Lacroix, L. B.; Root, D. E. *Metallobiochemistry, Part C* **1993**, *226*, 1.
(133) Solomon, E. I.; Hare, J. W.; Gray, H. B. *Proc. Natl. Acad. Sci. U.S.A.* **1976**, *73*, 1389.
(134) Piontek, K.; Antorini, M.; Choinowski, T. *J. Biol. Chem.* **2002**, *277*, 37663.
(135) Ducros, V.; Brzozowski, A. M.; Wilson, K. S.; Ostergaard, P.; Schneider, P.; Svendson, A.; Davies, G. J. *Acta Crystallogr. D: Biol. Crystallogr.* **2001**, *57*, 333.
(136) Hakulinen, N.; Kiiskinen, L.-L.; Kruus, K.; Saloheimo, M.; Paananen, A.; Koivula, A.; Rouvinen, J. *Nat. Struct. Mol. Biol.* **2002**, *9*, 601.
(137) Kallio, J. P.; Gasparetti, C.; Andberg, M.; Boer, H.; Koivula, A.; Kruus, K.; Rouvinen, J.; Hakulinen, N. *FEBS J.* **2011**, *278*, 2283.
(138) Hakulinen, N.; Andberg, M.; Kallio, J.; Koivula, A.; Kruus, K.; Rouvinen, J. *J. Struct. Biol.* **2008**, *162*, 29.
(139) Ducros, V.; Brzozowski, A. M.; Wilson, K. S.; Brown, S. H.; Ostergaard, P.; Schneider, P.; Yaver, D. S.; Pedersen, A. H.; Davies, G. J. *Nat. Struct. Mol. Biol.* **1998**, *5*, 310.
(140) Palmer, A. E.; Lee, S. K.; Solomon, E. I. *J. Am. Chem. Soc.* **2001**, *123*, 6591.
(141) Silva, C. S.; Damas, J. M.; Chen, Z.; Brissos, V.; Martins, L. O.; Soares, C. M.; Lindley, P. F.; Bento, I. *Acta Crystallogr. D: Biol. Crystallogr.* **2012**, *68*, 186.
(142) Nogala, W.; Szot, K.; Burchardt, M.; Jönsson-Niedziolka, M.; Rogalski, J.; Wittstock, G.; Opallo, M. *Bioelectrochemistry* **2010**, *79*, 101.
(143) Bento, I.; Silva, C.; Chen, Z.; Martins, L.; Lindley, P.; Soares, C. *BMC Struct. Biol.* **2010**, *10*, 28.
(144) Blanford, C. F.; Foster, C. E.; Heath, R. S.; Armstrong, F. A. *Faraday Discuss.* **2009**, *140*, 319.
(145) Thorum, M. S.; Anderson, C. A.; Hatch, J. J.; Campbell, A. S.; Marshall, N. M.; Zimmerman, S. C.; Lu, Y.; Gewirth, A. A. *J. Phys. Chem. Lett.* **2010**, *1*, 2251.
(146) Schweiger, H.; Vayner, E.; Anderson, A. B. *Electrochem. Solid-State Lett.* **2005**, *8*, A585.
(147) Toledo-Núñez, C.; López-Cruz, J. I.; Hernández-Arana, A. *Biophys. Chem.* **2012**, *167*, 36.
(148) Spiccia, L.; Graham, B.; T. W. Hearn, M.; Lazarev, G.; Moubaraki, B.; S. Murray, K.; R. T. Tiekink, E. *Dalton Trans.* **1997**, 4089.
(149) Mirica, L. M.; Ottenwaelder, X.; Stack, T. D. P. *Chem. Rev.* **2004**, *104*, 1013.
(150) Lewis, E. A.; Tolman, W. B. *Chem. Rev.* **2004**, *104*, 1047.
(151) Hatcher, L. Q.; Karlin, K. D. In *Adv. Inorg. Chem.*; Eldik, R. v., Reedijk, J., Eds.; Academic Press: 2006; Vol. Volume 58, p 131.
(152) Hatcher, L. Q.; Karlin, K. D. *J Biol Inorg Chem* **2004**, *9*, 669.

(153) Thorseth, M. A.; Letko, C. S.; Rauchfuss, T. B.; Gewirth, A. A. *Inorg. Chem.* **2011**, *50*, 6158.
(154) Harata, M.; Hasegawa, K.; Jitsukawa, K.; Masuda, H.; Einaga, H. *Bull. Chem. Soc. Japan* **1998**, *71*, 1031.
(155) Schatz, M.; Becker, M.; Thaler, F.; Hampel, F.; Schindler, S.; Jacobson, R. R.; Tyeklár, Z.; Murthy, N. N.; Ghosh, P.; Chen, Q.; Zubieta, J.; Karlin, K. D. *Inorg. Chem.* **2001**, *40*, 2312.
(156) Jacobson, R. R.; Tyeklar, Z.; Farooq, A.; Karlin, K. D.; Liu, S.; Zubieta, J. *J. Am. Chem. Soc.* **1988**, *110*, 3690.
(157) Kitajima, N.; Fujisawa, K.; Morooka, Y.; Toriumi, K. *J. Am. Chem. Soc.* **1989**, *111*, 8975.
(158) Kitajima, N.; Moro-oka, Y. *Chem. Rev.* **1994**, *94*, 737.
(159) Maiti, D.; Fry, H. C.; Woertink, J. S.; Vance, M. A.; Solomon, E. I.; Karlin, K. D. *J. Am. Chem. Soc.* **2007**, *129*, 264.
(160) Maiti, D.; Woertink, J. S.; Narducci Sarjeant, A. A.; Solomon, E. I.; Karlin, K. D. *Inorg. Chem.* **2008**, *47*, 3787.
(161) Tyeklar, Z.; Jacobson, R. R.; Wei, N.; Murthy, N. N.; Zubieta, J.; Karlin, K. D. *J. Am. Chem. Soc.* **1993**, *115*, 2677.
(162) Thorseth, M. A.; Letko, C. S.; Tse, E. C. M.; Rauchfuss, T. B.; Gewirth, A. A. *Inorg. Chem.* **2012**, *52*, 628.
(163) Fujii, H. *J. Am. Chem. Soc.* **1993**, *115*, 4641.
(164) Kitajima, N.; Fujisawa, K.; Fujimoto, C.; Morooka, Y.; Hashimoto, S.; Kitagawa, T.; Toriumi, K.; Tatsumi, K.; Nakamura, A. *J. Am. Chem. Soc.* **1992**, *114*, 1277.
(165) Blackman, A. G.; Tolman, W. B. *Struct. Bonding* **2000**, *97*, 179.
(166) Nagao, H.; Komeda, N.; Mukaida, M.; Suzuki, M.; Tanaka, K. *Inorg. Chem.* **1996**, *35*, 6809.
(167) Blackman, A. G. *Euro. J. Inorg. Chem.* **2008**, *2008*, 2633.
(168) Chuang, C.-l.; Lim, K.; Chen, Q.; Zubieta, J.; Canary, J. W. *Inorg. Chem.* **1995**, *34*, 2562.
(169) Chuang, C.-L.; Lim, K.; Canary, J. W. *Supramol. Chem.* **1995**, *5*, 39.
(170) Sorrell, T. N.; Jameson, D. L. *Inorg. Chem.* **1982**, *21*, 1014.
(171) Maiti, D.; Woertink, J. S.; Ghiladi, R. A.; Solomon, E. I.; Karlin, K. D. *Inorg. Chem.* **2009**, *48*, 8342.
(172) Tsui, E. Y.; Kanady, J. S.; Day, M. W.; Agapie, T. *Chem. Commun.* **2011**, *47*, 4189.
(173) Tsui, E. Y.; Day, M. W.; Agapie, T. *Angew. Chem. Int. Ed.* **2011**, *50*, 1668.
(174) Lionetti, D.; Day, M. W.; Agapie, T. *Chem. Sci.* **2013**, *4*, 785.
(175) Nørskov, J. K.; Rossmeisl, J.; Logadottir, A.; Lindqvist, L.; Kitchin, J. R.; Bligaard, T.; Jónsson, H. *J. Phys. Chem. B* **2004**, *108*, 17886.
(176) Lee, K.-S.; Yoo, S. J.; Ahn, D.; Kim, S.-K.; Hwang, S. J.; Sung, Y.-E.; Kim, H.-J.; Cho, E.; Henkensmeier, D.; Lim, T.-H.; Jang, J. H. *Electrochim. Acta* **2011**, *56*, 8802.
(177) Yang, C.; Costamagna, P.; Srinivasan, S.; Benziger, J.; Bocarsly, A. B. *J. Power Sources* **2001**, *103*, 1.
(178) Tanaka, A. A., R.; Nikolic, B. *J. Serb. Chem. Soc.* **1999**, *64*, 695−705.
(179) He, Q.; Yang, X.; Chen, W.; Mukerjee, S.; Koel, B.; Chen, S. *Phys. Chem. Chem. Phys.* **2010**, *12*, 12544.
(180) Parthasarathy, A.; Srinivasan, S.; Appleby, A. J.; Martin, C. R. *J. Electrochem. Soc.* **1992**, *139*, 2530.

(181) Mayer, J. M.; Rhile, I. J. *BBA-Bioenergetics* **2004**, *1655*, 51.
(182) Mayer, J. M. *Annu. Rev. Phys. Chem.* **2004**, *55*, 363.
(183) Wenger, O. S. *Acc. Chem. Res.* **2013**, *46*, 1517.
(184) Weinberg, D. R.; Gagliardi, C. J.; Hull, J. F.; Murphy, C. F.; Kent, C. A.; Westlake, B. C.; Paul, A.; Ess, D. H.; McCafferty, D. G.; Meyer, T. J. *Chem. Rev.* **2012**, *112*, 4016.
(185) Soudackov, A.; Hammes-Schiffer, S. *J. Chem. Phys.* **2000**, *113*, 2385.
(186) Sjödin, M.; Styring, S.; Wolpher, H.; Xu, Y.; Sun, L.; Hammarström, L. *J. Am. Chem. Soc.* **2005**, *127*, 3855.
(187) Irebo, T.; Reece, S. Y.; Sjödin, M.; Nocera, D. G.; Hammarström, L. *J. Am. Chem. Soc.* **2007**, *129*, 15462.
(188) Costentin, C.; Robert, M.; Savéant, J.-M. *Chem. Rev.* **2010**, *110*, PR1.
(189) Chen, Z.; Vannucci, A. K.; Concepcion, J. J.; Jurss, J. W.; Meyer, T. J. *Proc. Natl. Acad. Sci. U.S.A.* **2011**, *108*, E1461.
(190) Huynh, M. H. V.; Meyer, T. J. *Chem. Rev.* **2007**, *107*, 5004.
(191) Chang, C. J.; Chang, M. C. Y.; Damrauer, N. H.; Nocera, D. G. *BBA-Bioenergetics* **2004**, *1655*, 13.
(192) Migliore, A.; Polizzi, N. F.; Therien, M. J.; Beratan, D. N. *Chem. Rev.* **2014**, *114*, 3381.
(193) Hammes-Schiffer, S.; Soudackov, A. V. *J. Phys. Chem. B* **2008**, *112*, 14108.
(194) Chidsey, C. E. D. *Science* **1991**, *251*, 919.
(195) Henstridge, M. C.; Laborda, E.; Rees, N. V.; Compton, R. G. *Electrochim. Acta* **2012**, *84*, 12.
(196) Smalley, J. F.; Feldberg, S. W.; Chidsey, C. E. D.; Linford, M. R.; Newton, M. D.; Liu, Y.-P. *J. Phys. Chem.* **1995**, *99*, 13141.
(197) Collman, J. P.; Devaraj, N. K.; Eberspacher, T. P. A.; Chidsey, C. E. D. *Langmuir* **2006**, *22*, 2457.
(198) Collman, J. P.; Devaraj, N. K.; Decréau, R. A.; Yang, Y.; Yan, Y.-L.; Ebina, W.; Eberspacher, T. A.; Chidsey, C. E. D. *Science* **2007**, *315*, 1565.
(199) Eckermann, A. L.; Feld, D. J.; Shaw, J. A.; Meade, T. J. *Coor. Chem. Rev.* **2010**, *254*, 1769.
(200) Rosenthal, J.; Nocera, D. G. *Acc. Chem. Res.* **2007**, *40*, 543.
(201) Bediako, D. K.; Solis, B. H.; Dogutan, D. K.; Roubelakis, M. M.; Maher, A. G.; Lee, C. H.; Chambers, M. B.; Hammes-Schiffer, S.; Nocera, D. G. *Proc. Natl. Acad. Sci. U.S.A.* **2014**, *111*, 15001.
(202) McCrory, C. C. L.; Ottenwaelder, X.; Stack, T. D. P.; Chidsey, C. E. D. *J. Phys. Chem. A* **2007**, *111*, 12641.
(203) Denning, E. J.; Beckstein, O. *Chem. Phys. Lipids* **2013**, *169*, 57.
(204) Hu, X.-B.; Chen, Z.; Tang, G.; Hou, J.-L.; Li, Z.-T. *J. Am. Chem. Soc.* **2012**, *134*, 8384.
(205) Barboiu, M.; Le Duc, Y.; Gilles, A.; Cazade, P.-A.; Michau, M.; Marie Legrand, Y.; van der Lee, A.; Coasne, B.; Parvizi, P.; Post, J.; Fyles, T. *Nat. Commun.* **2014**, *5*.
(206) Suarez-Isla, B. A.; Wan, K.; Lindstrom, J.; Montal, M. *Biochemistry* **1983**, *22*, 2319.
(207) Saier, M. H. *Microbiol. Mol. Biol. Rev.* **2000**, *64*, 354.
(208) Aqvist, J.; Warshel, A. *Biophys. J.* **1989**, *56*, 171.
(209) Hosseini, A.; Barile, C. J.; Devadoss, A.; Eberspacher, T. A.; Decreau, R. A.; Collman, J. P. *J. Am. Chem. Soc.* **2011**, *133*, 11100.
(210) Barile, C. J.; Tse, E. C. M.; Li, Y.; Sobyra, T. B.; Zimmerman, S. C.; Hosseini, A.; Gewirth, A. A. *Nat. Mater.* **2014**, *13*, 619.

(211) Plant, A. L. *Langmuir* **1993**, *9*, 2764.
(212) Plant, A. L. *Langmuir* **1999**, *15*, 5128.
(213) Twardowski, M.; Nuzzo, R. G. *Langmuir* **2003**, *19*, 9781.
(214) Twardowski, M.; Nuzzo, R. G. *Langmuir* **2003**, *20*, 175.
(215) Li, Y.; Tse, E. C. M.; Barile, C. J.; Gewirth, A. A.; Zimmerman, S. C. *J. Am. Chem. Soc.* **2015**, *137*, 14059.
(216) Tse, E. C. M.; Barile, C. J.; Gewargis, J. P.; Li, Y.; Zimmerman, S. C.; Gewirth, A. A. *Anal. Chem.* **2015**, *87*, 2403.
(217) Hammes-Schiffer, S. *Acc. Chem. Res.* **2009**, *42*, 1881.
(218) Marcus, R. A. *Rev. Mod. Phys.* **1993**, *65*, 599.
(219) Marcus, R. A. *J. Electroanal. Chem.* **2000**, *483*, 2.
(220) Marcus, R. A. *J. Chem. Phys.* **1965**, *43*, 679.
(221) Marcus, R. A.; Sutin, N. *BBA-Bioenergetics* **1985**, *811*, 265.

Chapter 2

General Experimental Procedures

2.1 General Synthetic Procedures

Reaction Conditions

Chemicals were obtained from commercial sources and used without further purification unless otherwise specified. All reactions were conducted under a dry argon atmosphere using standard Schlenk line techniques or inside an Ar-filled glove-box. Dry tetrahydrofuran (THF), dichloromethane (DCM), and dimethyl sulfoxide (DMSO) were used directly from solvent delivery systems in the Rauchfuss group and the Zimmerman group just prior to use. All other solvents were of reagent grade or better and used without further purification. Reported reaction temperatures refer to the temperature of the heating medium. The progress of reactions was monitored by silica gel thin layer chromatography (TLC) using 0.2 mm silica 60 coated, plastic plates with F254 indicator purchased from EM Science. Chromatography was performed using either Ultra Pure SiliaFlash® P60 230-400 mesh (40-63 μm) silica gel (SiO_2) or aluminum oxide

(puriss., ≥98% Al_2O_3 basis). Specific synthetic procedures for small molecules, organic ligands, and organometallic complexes were presented in Chapter 3. Heterogeneous materials was prepared according to published methods (Figure 2.1).[1]

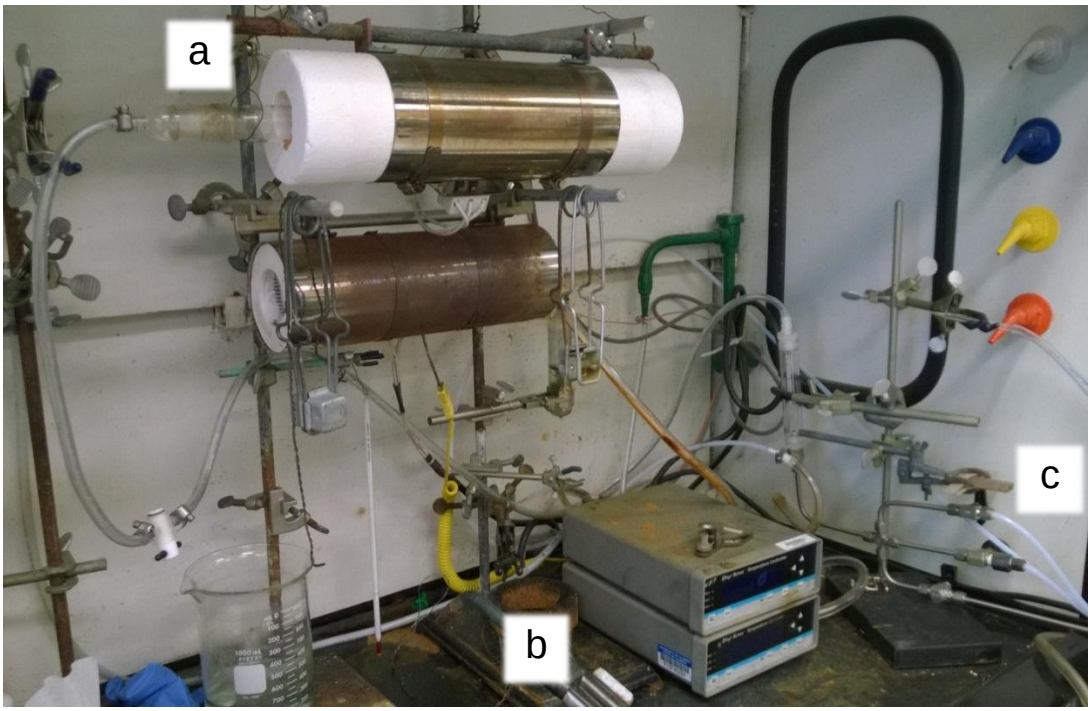

Figure 2.1. (a) A tube furnace for pyrolysis with (b) a temperature controller and (c) a manifold for premixing gases.

Characterization Methods

NMR spectra were performed predominantly in chloroform-*d* and acquired using a Varian Unity 500 MHz instrument in the VOICE laboratory at the University of Illinois at Urbana-Champaign (UIUC). Chemical shifts (δ) and coupling constants (*J*) were reported in parts per million (ppm) and hertz (Hz), respectively. For ^{1}H spectra, chemical shifts were referenced to the residual proton solvent peak: 7.26 ppm for chloroform-*d*. For ^{13}C spectra, chemical shifts were referenced to the solvent peak at 77.5 ppm in chloroform-*d*. Electrospray

ionization mass spectrometry (ESI-MS) data were collected using a Quattro II instrument (Waters) at UIUC. Elemental analysis (EA: C, H, N, Cl, B, S, P, Cu, Fe, and etc.), thermogravimetric analysis (TGA), and differential scanning calorimetry (DSC) were conducted by research specialists at the microanalysis facility at UIUC.

Caution! *Perchlorate salts are potentially explosive. Only small amounts of materials should be prepared. HF is extremely corrosive and should be handled with care.*

Solutions and Electrolytes Preparation

Aqueous solutions were prepared using Milli-Q purified water (>18 MΩ cm). Experiments at pH 1 and 13 were performed in $HClO_4$ (0.1 M, 70 wt% optima grade $HClO_4$, Fisher Scientific) and in NaOH or KOH (0.1 M, analytical titration grade, Fisher Scientific) diluted with Milli-Q water, respectively. Potassium phosphate buffers (100 mM, pH 5 or 7) were sparged with Ar or O_2 for 30 min prior to each experiment. Experiments at pH 4-10 were performed in Britton-Robinson buffer (BR) consisting of H_3BO_3 (0.04 M, 99.999%, Sigma-Aldrich), CH_3COOH (0.04 M, 99.99%, Sigma-Aldrich), H_3PO_4 (0.04 M, 85 wt% in H_2O, 99.99%, Sigma-Aldrich), and $NaClO_4$ (0.1 M, 99.9%, Sigma-Aldrich). The pH was adjusted to 4, 7, and 10 using NaOH (10 M, analytical titration grade, Fisher Scientific). Aqueous solutions of $KClO_4$, KF, KCl, KBr, KPF_6, and KH_2PO_4 were prepared using Milli-Q water and adjusted to pH 5 using $HClO_4$, HF, HCl, HBr, HPF_6, H_3PO_4, and KOH. Solutions were sparged with Ar (99.999%, ultra high purity, S. J. Smith Welding Supply) or O_2 (99.999%, ultra high purity, S. J. Smith Welding Supply) for 30 min prior to each experiment.

2.2 General Electrochemical Procedures

Potentiostats Used

Electrochemical investigations were carried out using CH Instruments 760C, 760D, and 760E Electrochemical Workstations (Austin, TX) at room temperature (24 °C to 26 °C). All experiments performed were at least triplicated. Voltammograms shown were from representative trials. Error bars presented represent standard deviations of all trials. The onset potential of O_2 reduction was defined as the potential at which 5% of the maximum current was reached. Unless otherwise stated, the scan rate was 10 mV/s. Electrochemical impedance spectra (EIS) for iR correction were collected using a SP-150 potentiostat (Bio-Logic, LLC). The uncompensated solution resistance, R, was typically ca. 3 Ω, and iR correction was done following published procedures.[2-4] Tafel analysis was carried out using iR-corrected Tafel plots.

Three-electrode Setup

Oxygen reduction reaction (ORR) experiments were performed in a three-compartment cell (Figure 2.2) with an aqueous "no-leak" Ag/AgCl (3 M KCl, eDAQ, Inc.) reference electrode separated from the working electrode by a Luggin capillary. A deviation of ca. 1.3 mV in the electrode potential of the Ag/AgCl reference was expected due to a fluctuation of 2 °C in room temperature.[5] Electrochemical potentials were reported relative to the reversible hydrogen electrode (RHE), the value of which was measured by sparging the solution with H_2 (1 atm) and monitoring the open circuit potential between the Ag/AgCl reference and a Pt wire introduced following the measurement.[6] A carbon rod counter electrode was separated from the working electrode by a glass frit. For oxygen evolution reaction (OER), experiments were performed in a sealed cell with a Pt mesh counter electrode and a "no-leak" Ag/AgCl reference electrode. The

measured potential by the Ag/AgCl reference electrode did not shift in proteo and deutero solutions, as confirmed by the peak position of the Fe(II)/Fe(III) couple of $K_3Fe(CN)_6$.[7]

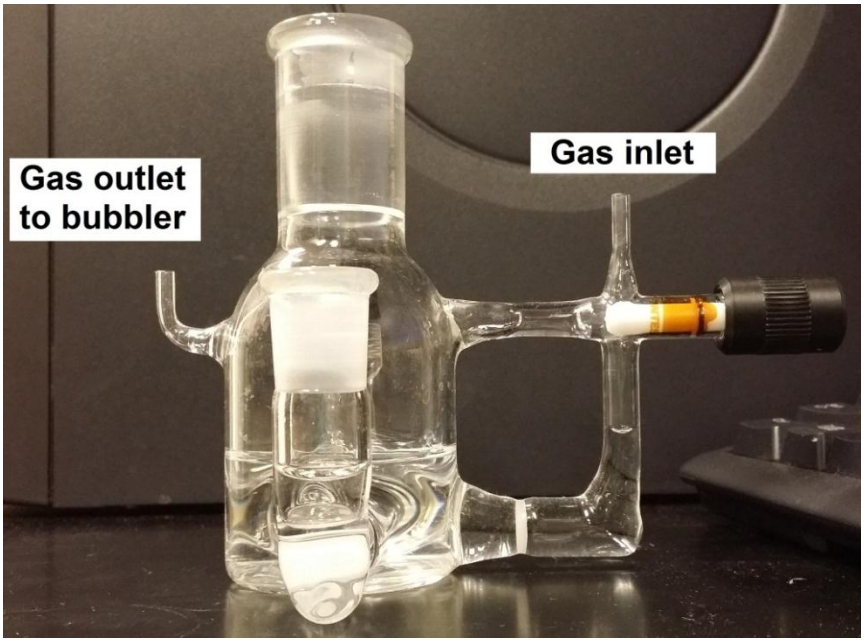

Figure 2.2a. Side-view of a three-compartment glass cell for electrochemical investigation showing the gas inlet, control valve, a frit separating the gas inlet and the main solution compartment, and the gas outlet to a bubbler.

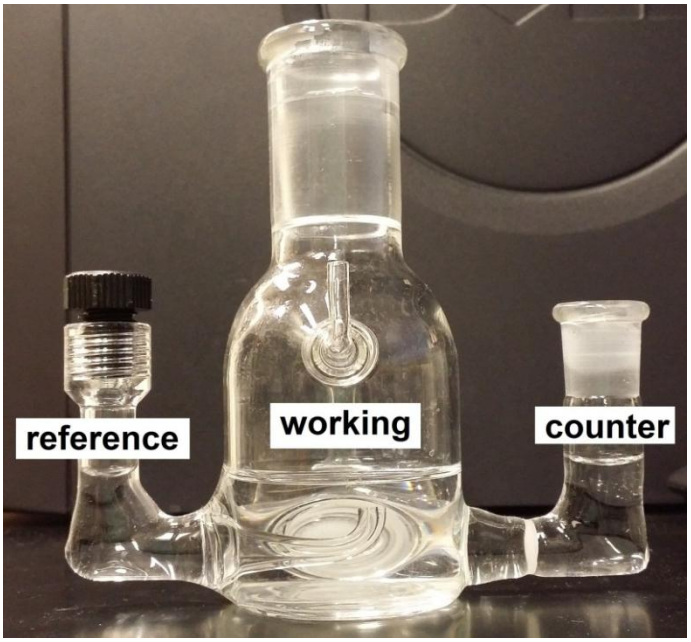

Figure 2.2b. Front-view of a three-compartment glass cell for electrochemical investigation showing the compartments where the electrodes should be situated.

Rotation Studies

Rotating ring-disk electrode (RRDE) experiments were performed using a ring-disk assembly with an interchangeable disk (E5 series, Pine instruments) connected to a MSRX rotator (Pine instruments, Figures 2.3a and 2.3b). The GC disk electrode (A = 0.196 cm^2, Figure 2.3c) was polished sequentially with 0.25 μm and 0.05 μm diameter diamond polish (MetaDi Supreme, Buehler), and sonicated in water after each stage. A Au disk electrode (Figure 2.3d) could be used in place of the GC electrode for RRDE experiments of catalysts that were self-assembled on the Au electrode surface at a rotation rate of 400 rpm. The Au electrode was polished sequentially using 9 μm, 3 μm, 1 μm, 0.25 μm, and 0.05 μm diameter diamond polish and sonicated in water after each stage.

The Pt ring electrode (A = 0.093 cm^2, Pine Instruments) was cleaned electrochemically by cycling from –0.4 V to +1.7 V vs. Ag/AgCl reference at 100 mV/s in an aqueous solution of $HClO_4$ (0.1 M) until the current of oxide stripping at ~ +0.35 V vs. Ag/AgCl reference remained constant. A GC electrode was used as a standard for the 2 e^- reduction of O_2, which was described previously.[8] The collection efficiency of the ring electrode, which was held at 1.2 V vs. RHE, was usually about 18%. An ink of typically 5 or 10 μL was applied to the GC disk and dried under a stream of Ar or N_2.

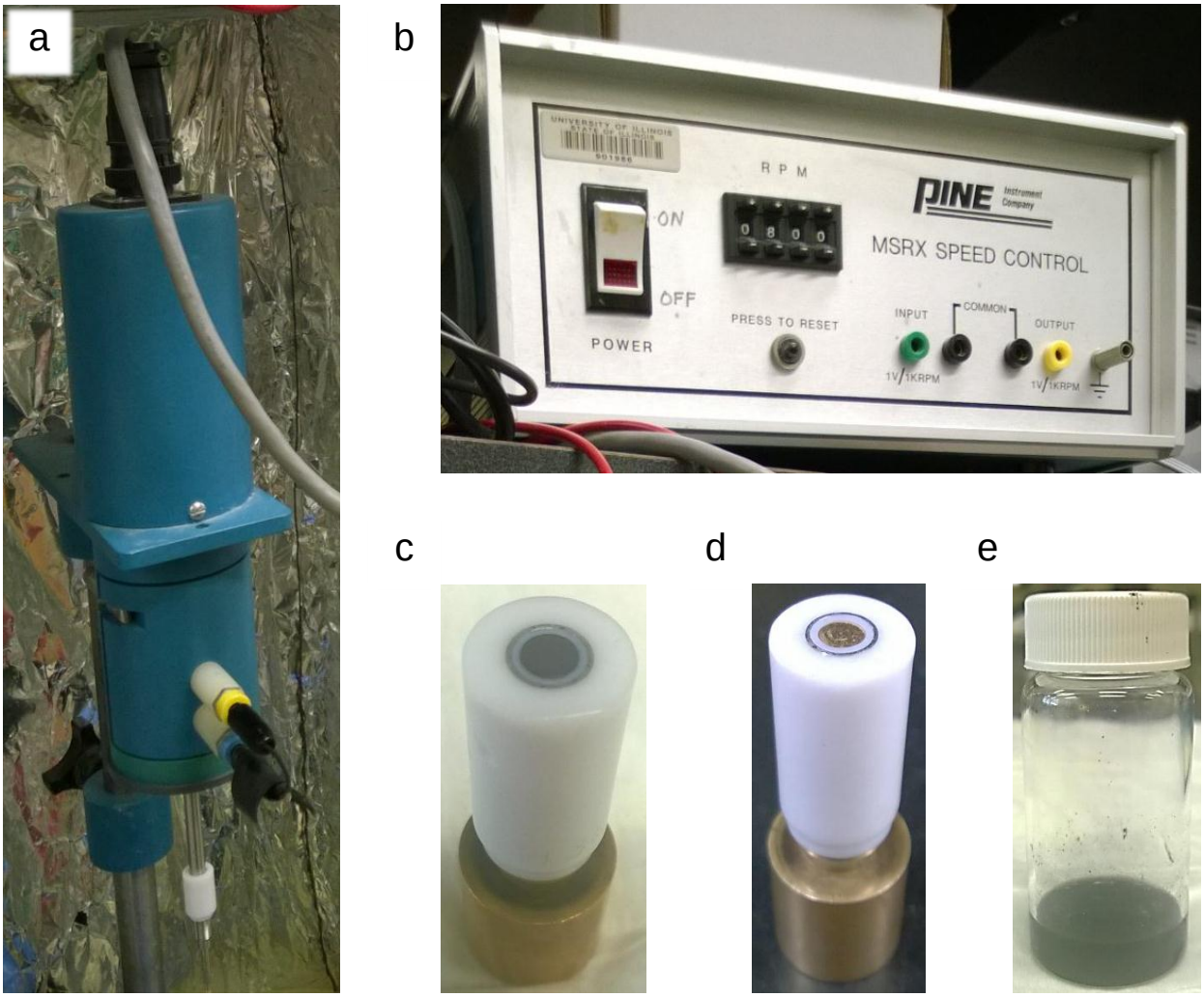

Figure 2.3. (a) Pine rotator; (b) MSRX speed controller; (c) GC and (d) Au RRDE assembly utilized for electrochemical investigation showing the working electrode and the concentric Pt ring for product detection; and (e) ink slurry containing the redox species or electrocatalysts of interest.

2.3 General High Temperature and High Pressure Procedures

Caution! *Experiments at high temperature and pressure can lead to personal injury and property damage. Studies that potentially generate* H_2 *or* H_2O_2 *in situ under a highly oxidizing atmosphere should be carried out with extreme caution inside a chemical fume hood with a blast shield properly installed.*

A modified version of a near- and supercritical system with a stationary three-electrode cell configuration previously described was used.[9] High temperature and pressure electrochemical studies were carried out using a #4590 micro reactor (Parr Instruments, Figure 2.4) with a removable PTFE insert (50 mL, Parr Instruments). Temperature was varied (± 1 °C) with an integrated #4848 control panel (Parr Instruments, Figure 2.5).

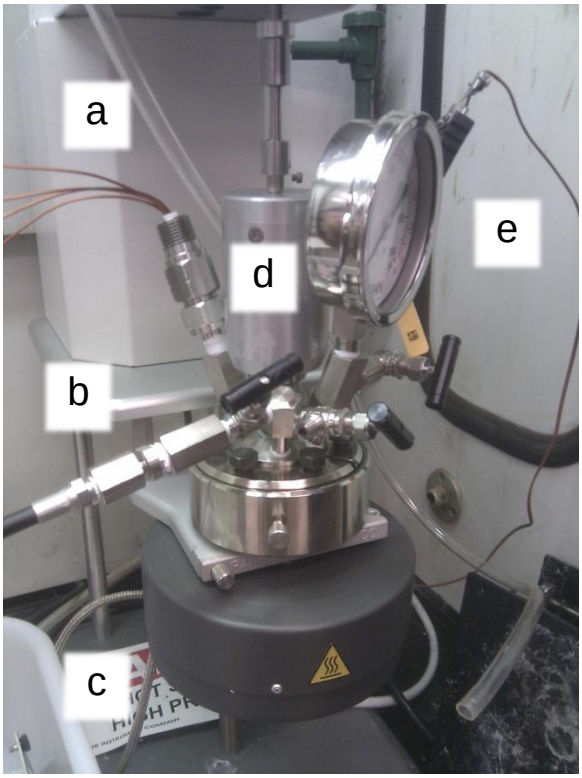

Figure 2.4. House-modified Parr micro stirred reactor (#4590, 50 mL) with (a) electrical feedthroughs connected to a potentiostat, (b) high-pressure gas inlet and tubing, (c) heating mantle connected to a control panel (Figure 2.5), (d) pressure gauge, and (e) thermal couple.

Figure 2.5. Parr #4848 control panel for temperature regulation.

The rationale behind choosing this particular high temperature and pressure electrochemical system was as follows. Studies on ORR at elevated temperatures and pressurized conditions were rare for several reasons. First, the highly oxidizing nature of O_2 was detrimental to the integrity of the reaction vessel.[9] At high temperature, O_2 possibly causes undesired formation of oxides, leaching of metal components, and contamination. In addition to the problems at high temperature, high pressure of O_2 potentially induces crack formation in the reactor and eventually leads to incidences of cell fractures and failures.[10]

Second, the choice of electrode sealant material was another obstacle. Typical sealant materials, such as PTFE and CTFE, cannot withstand the H_2 flaming procedure. Unlike polymers, borosilicate glass can be flamed. However, borosilicate glass conducts e^- at high temperature, resulting in stray currents that distort CVs of the redox reaction of interest.[10] The pursuit for a sealant material that has a similar thermal expansion coefficient as the working electrode, a high melting/softening temperature, and does not allow e^- leakage remains one of the most pressing needs in the field of high temperature electrochemical investigations.

In summary, the desired electrochemical setup should be mechanically tough to withstand high pressure, and chemically robust to resist a highly-oxidizing environment at high temperature. Taken together these considerations, we chose to modify a Parr reactor that was capable of withstanding pressure up to 17.2 MPa and temperature up to 250 °C, restricted by the melting point of reactor sealant material. Ar was used instead of N_2 to avoid N_2 reduction, which was possible at high temperatures under pressurized conditions.[9]

The electrodes were connected to the Cu wire feedthroughs by mechanical contact. This method allowed for easy disassembling and cleaning of the cell and electrodes. Electrical junctions were covered with Teflon tape, leaving only the electrodes exposed. The Teflon tape retains its integrity at temperatures below 250 °C.[9] A solution volume of 15 mL was used for each experiment. After heating to the desired temperature, the system was equilibrated for 1 h to minimize thermal gradients and convection.[9]

For Pt studies, Pt wires (99.95 %, Alfa Aesar) were used as both working and counter electrodes. Pt wires were soaked in freshly prepared aqua regia (3:1 HCl/HNO_3, AR® ACS grade, Macron Fine Chemicals) overnight, and then fresh $HClO_4$ (70%, Ultrex II UltraPure reagent grade, J. T. Baker). The Pt wires were subsequently rinsed with Milli-Q water and flamed using a H_2 torch (99.9999%, research grade, S. J. Smith Welding Supply), and used immediately. Electrode areas were determined by using the characteristic H_2 adsorption and desorption waves at 20 °C under an Ar pressure of 0.1 MPa and were typically ca. 0.37 cm^2.

For carbon studies, a glassy carbon (GC) disk with an embedded metal pin (modified MF-2012, Bioanalytical Systems Inc.) and a carbon rod (spectroscopically pure, grade 1, Ted Pella Inc.) were used as the working and counter electrodes, respectively. The GC disk working electrode was polished successively with 9 μm, 3 μm, 1 μm, 0.25 μm, and 0.05 μm diameter

diamond polish, and sonicated in water after each stage. The carbon rod counter electrode was polished with 400-grit sandpaper (Buehler).

Electrochemical potentials were measured and reported with respect to a tungsten wire reference electrode.[11,12] A tungsten wire (99.95%, Alfa Aesar) was freshly cut and immersed in KOH (0.1 M) for 60 min prior to use.[13] As the focus of this investigation was the effect of temperature and pressure on the current response, no effort was made to report the electrochemical potentials with respect to the RHE.[9] Typical aqueous Ag/AgCl reference electrode was not used in this study for the following reasons. Commercial "no-leak" Ag/AgCl reference electrode was not stable at temperatures higher than 80 °C, and custom-made Ag/AgCl reference electrode may fracture at high pressure due to unbalanced pressure inside and outside of the electrode. Moreover, the combined effect of temperature and pressure may accelerate Cl^- leaking out of the reference electrode to bind on the surface of the Pt working electrode.[14]

Attempts to use other bare or oxide-covered metal wires (Ag, Pt, Pd, Ir, Ni, Au, Cu, and Ta) as reference electrodes were unsuccessful. More sophisticated internal and external reference electrodes have been developed for electrochemistry at unconventional conditions. However, each of the designs faces limitations of its own. In particular, most of the design contains Cl^- (aq), Hg (l) or H_2 (g), which either poisons the Pt surface, or causes chemical or explosion hazard. Macdonald *et al.*, leaders in reference electrode technology at high subcritical (300 °C < T < 374.15 °C) and in supercritical (T > 374.15 °C) conditions, admitted that no stable reference electrode with predictable potential drift at high temperature and pressure for aqueous electrochemical investigations was available.[15]

All O_2 reduction LSVs at high temperature and high pressure were collected at a scan rate of 50 mV/s, and corrected for uncompensated Ohmic resistance (R_u), which was obtained from

EIS measurements. We followed published methods to minimize R_u, including increasing the solution conductivity, shortening the distance between RE and WE, and building a symmetrical cell design.[3] We chose 0.1 M KOH for our system because 0.1 M KOH was proven to be conductive enough at high temperature and pressure—R_u decreases as temperature increases.[4] Furthermore, we placed the electrodes as close to each other as possible, and we used identical Pt wires as working and counter electrodes. There were other methods to measure and correct for R_u. However, these methods exhibited intrinsic problems of their own.[3] For example, positive feedback loop suffered from time lag due to phase shifts, exhibited chance of over or under compensation, added noise to data due to ringing, and risked losing control by overshooting, and damaged working electrode if oscillations occur. The interruptor method required a region with no faradaic reaction, large faradaic capacitance, and slow sampling speed that limited the scan rate used. This method also increased the chance of adding noise to data. The EIS method allowed for accurate measurement and efficient correction after data collection.[4]

2.4 General Hybrid Bilayer Membrane Procedures

For HBM studies in aqueous and ethanolic solutions, a cone cell (Figure 2.6) was used with a carbon rod counter electrode. Au working electrodes (0.219 cm^2 exposed area restricted by the size of the rubber o-ring) were deposited using an electron-beam vacuum deposition apparatus (Figure 2.7). A Ti adhesion layer (20-50 nm), followed by a Au layer (150-250 nm), was deposited on Pyrex glass slides (Figure 2.8). Pt working electrodes (0.219 cm^2) were fabricated from Pyrex glass slides modified on one side using DC magnetron sputter deposition of Ti (20 nm) followed by Pt (200 nm). The electrodes were rinsed with water and EtOH prior to use.

Figure 2.6a. Teflon cone cells with aluminum bases and wire for electrical contact.

Figure 2.6b. Teflon cone cells before (right) and after (left) assembling.

Figure 2.7. Temescal six-pocket e-beam evaporation system at the Materials Research Laboratories (MRL) at UIUC. Typical deposition rate was about 1 Å/s at a vacuum level of 2 × 10−6 Torr or better. A tungsten filament was used as the e^- source and a quartz crystal balance was utilized to measure the thickness of the deposited film.

Self-assembled monolayers (SAMs) of the Cu catalysts were attached to the Au working electrodes in three steps. First, the thiol group was deprotected to give free BTT by adding the tritylated thiol (1.0 mg) to neat trifluroacetic acid (100 μL), resulting in a yellow solution. Triethylsilane (~100 μL) was added dropwise until the solution became colorless. The resulting solution was then diluted with Ar-sparged EtOH (7.0 mL). The Au electrodes were immersed in the BTT solution for 2 h and washed with EtOH. The BTT-Au surfaces were immersed in an ethanolic $Cu(ClO_4)_2$ solution (6.7 mM) for 1 h. The electrodes were rinsed 3 times with EtOH and 3 times with pH 7 buffer solution.

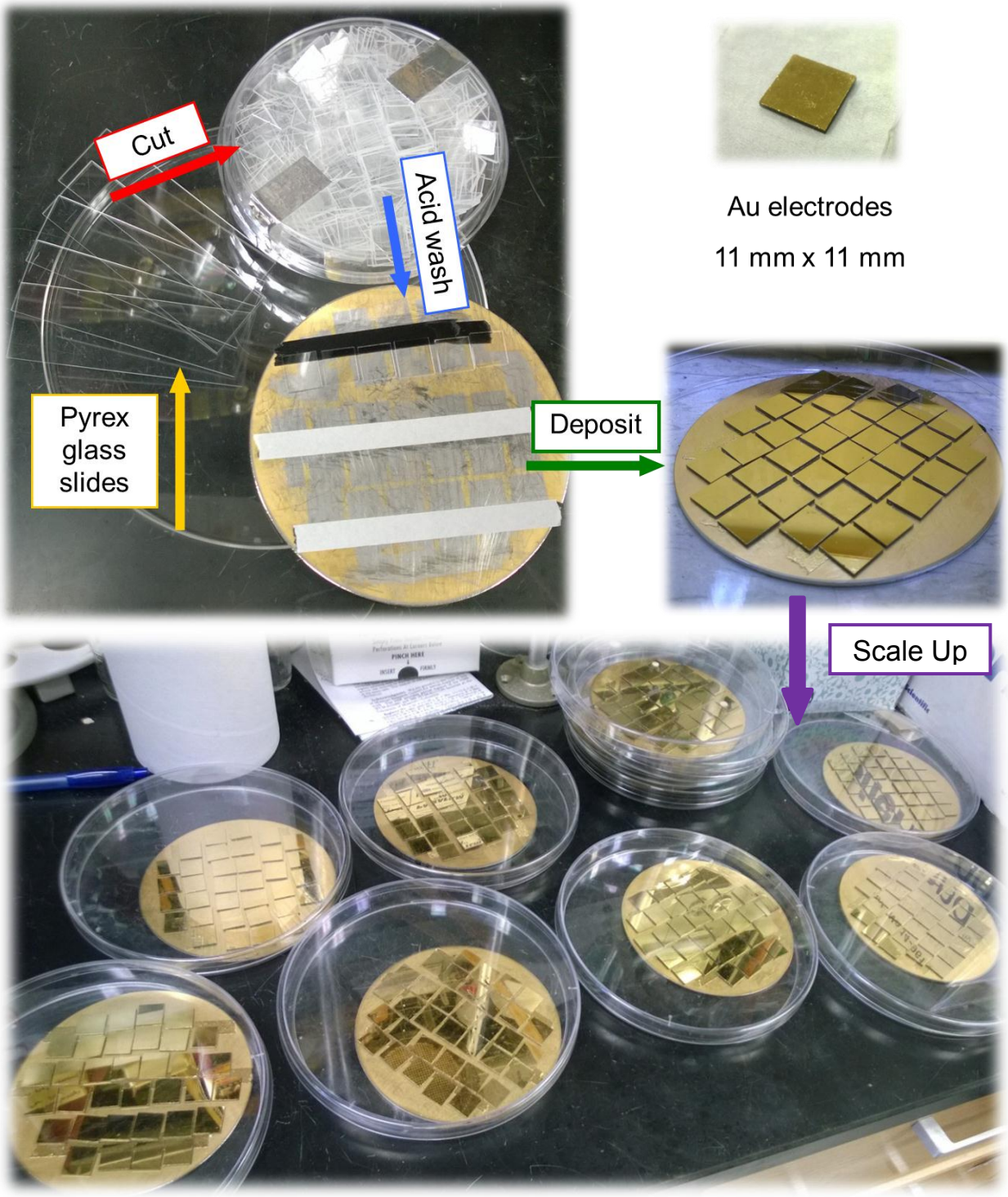

Figure 2.8. Scheme showing steps to fabricate Au electrodes on glass slides. Hot Piranha acid solution (3:1 conc. H_2SO_4:30% H_2O_2) was used to clean the glass squares, which were then affixed on e-beam target plates using carbon tape prior to e-beam deposition of Au.

The Cu complex of BTT was embedded in a HBM using a previously reported procedure with pure DMPC or DMPC with 1 equivalent of alkyl proton carrier relative to DMPC.[16-20] Patience was the key toward reproducibly preparing a working lipid-forming solution for the vesicle fusion process. In other words, slow evaporation, slow addition, and slow swirling were necessary. Briefly, 5 mg of lipid of choice was weighed out in a clean scintillation vial (20 mL). 1 molar equivalent of proton carrier was added if necessary. The lipid and proton carrier were dissolved in $CHCl_3$ (about 2 mL). Other solvent choices such as EtOH or isopropyl alcohol (IPA) were possible as long as the lipid and proton carrier were soluble. Diethyl ether and acetone were poor choices because either the lipid or the proton carrier was not soluble. The solution was then dried under a gentle stream of Ar or N_2 to afford a clear film in the bottom of the vial. In the presence of proton carrier, the film typically appeared cloudy or translucent. However, a ring of lipid and proton carrier localized predominantly at the junction between the bottom and the side wall of the vial was undesirable and gave irreproducible results. The experiment was almost guaranteed to fail if the lipid or proton carrier precipitated out as clumps or powder. Typically, re-dissolving the clumps in a different solvent or drying at a slower rate could resolve the problem. The dried film was then transferred to a desiccator to dry further under house vacuum for 30 min to get rid of $CHCl_3$. Residual $CHCl_3$ was found to be detrimental to the vesicle formation process.

IPA or EtOH (84 μL) was added to redissolve the dried film while applying a circular swirling motion manually or mechanically with the use of a Teflon stir bar. The wetted film was then heated to above the gel-phase transition temperature of the corresponding lipid utilized. Addition of more alcohol was necessary for certain lipids, such as DPPC which has a lower critical micelle concentration (CMC) than DMPC. [**critical step**] pH 7 potassium phosphate

buffer (100 mM, 1 mL) was added ***DROPWISE*** via a syringe and a 25-gauge needle with swirling in between each drop, i.e. wait until the aqueous drop was completely dissolved or dispersed in the alcohol solution before adding another drop. A syringe pump might work as long as the parameters were set up appropriately. During the first 1 (or more) mL addition of buffer, the solution turned cloudy. The degree of cloudiness depends on the lipid used, the amount of proton carrier incorporated, and the rates of buffer addition and mixing. An exceedingly slow addition ratecoupled with strong mixing, however, typically resulted in bubble formation, which inhibited the vesicle formation process for unidentified reasons. The addition of too much alcohol (800+ μL) possibly resulted in a situation where the CMC could not be reached and the solution remained clear. After the solution turned turbid, the next 4 mL of buffer was added at a faster rate (2~3 drops per swirling motion). The last 5.5 mL of buffer was then added all at once by aiming at the side wall of the vial. Directly spraying at the solution usually resulted in bubble formation and should be avoided. The solution was sonication for 30 min and cooled to RT. The solution was then ready for use and could be stored in the fridge (8 °C) and reused by warming in a sonicator for about 2 min. Three lipid solutions were shown in Figure 2.9 as examples.

Switch Experiments

Chronoamperometry was performed in O_2-saturated pH 7 buffer solutions (2.6 mL). The pH of the solution was adjusted to 5 *in situ* with an Ar-sparged solution of H_3PO_4 (15 μL). The pH of the solution was adjusted back to 7 with an Ar-sparged solution of KOH (15 μL). An Ar-sparged solution of pH 7 buffer (15 μL) was added instead of acid or base in control experiments. Before and after chronoamperometry, blocking experiments with CV at a scan rate of 50 mV/s using a solution of $K_3Fe(CN)_6$ (1 mM) with KCl (100 mM) as supporting electrolyte

were performed to confirm that the integrity of the lipid layer of the HBM was not compromised. An additional control experiment in which an Ar-sparged solution of pH 7 buffer (15 μL) was added twice before the addition of an Ar-sparged solution of H_3PO_4 (15 μL) further demonstrated that the increase in O_2 reduction current at pH 5 was not due to the degradation of the HBM. To evaluate the pH switch, the difference in the percentage change in current before and 5 s after addition were calculated. These values were then normalized for the percentage change in current observed in the control experiments with an added Ar-sparged solution of pH 7 buffer.

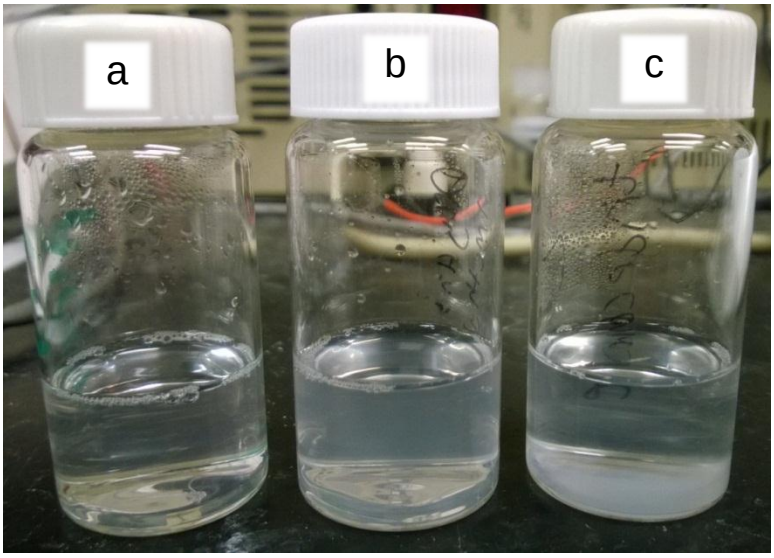

Figure 2.9. (a) A clear and (b) a cloudy lipid-forming solution. (c) A lipid-forming solution containing precipitated white powder at the bottom of the vial. Typically, solution (a) and (c) do not form a complete lipid monolayer on the CuBTT SAM. Solution (b) was desired. The lipid-forming solutions could be characterized using dynamic light scattering techniques. The size of the vesicles could further be controlled by passing through size-exclusion filters and columns. However, for successful vesicle fusion process, the size of the vesicles was not a major factor.

Controlled-temperature Experiments

Studies at above RT were performed in an oven (Figure 2.10a) with the temperature

monitored by a thermometer through a drilled port at the top of the oven and a thermometer in solution. Studies below RT were performed either in a refrigerator (Figure 2.10b), an ice-salt bath, an ice bath (Figure 2.10c), or a cold water bath with the temperature monitored by a thermometer. Both the oven and the refrigerator were equipped with ports for wires for electrical contact and gas inlets for O_2 and Ar.

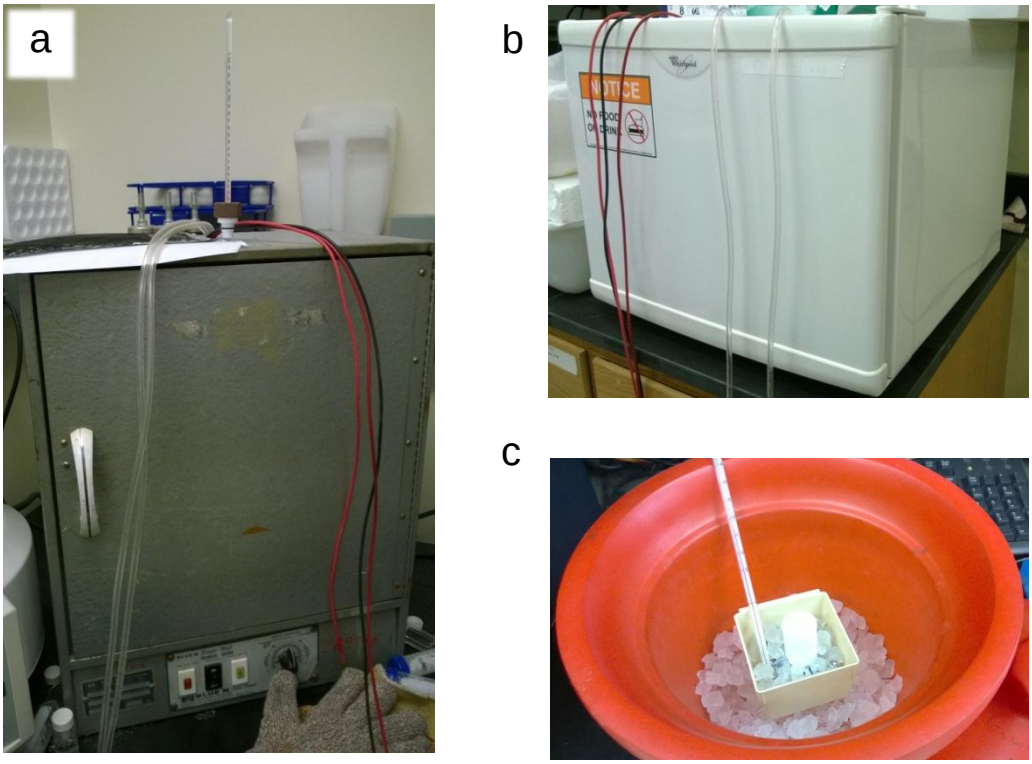

Figure 2.10. (a) A modified oven, (b) a refrigerator, and (c) an ice bath adapted for controlled-temperature electrochemical investigations.

Photoelectrochemical Studies

For interconversion experiments monitored using NMR techniques, the irradiation times for the *E*-to-*Z* and *Z*-to-*E* conversions were 40 and 30 min, respectively ([analyte] = 2 mg/mL). All optical apparatuses including mounted LEDs (M385L2 and M365L2, max current limit = 700 mA), power source drivers (DC2100), collimators (COP1-A), adaptors (SM1A2), couplers (SM2T2), and band pass filters (390 nm and 360 nm, FWHM = 10 nm) were purchased from

Thorlabs, Inc. All photoelectrochemical experiments were conducted inside a Faraday cage (Figure 2.11) in a dark room. The deprotection of MIDA-protected molecules was performed by dissolving the desired molecule (5.4 mol) in THF (0.2 mL). NaOH (0.01 mL, 10 M) was added, and the resulting solution was stirred vigorously for 15 min at room temperature. NH_4Cl (9 mL, saturated aqueous solution) was added, and the mixture was stirred vigorously for 5 min. Ether (9 mL × 3) was added to extract the organic layer, which was then combined and dried. All procedures involving light-sensitive molecules were conducted in the dark with all glassware wrapped with aluminum foil.

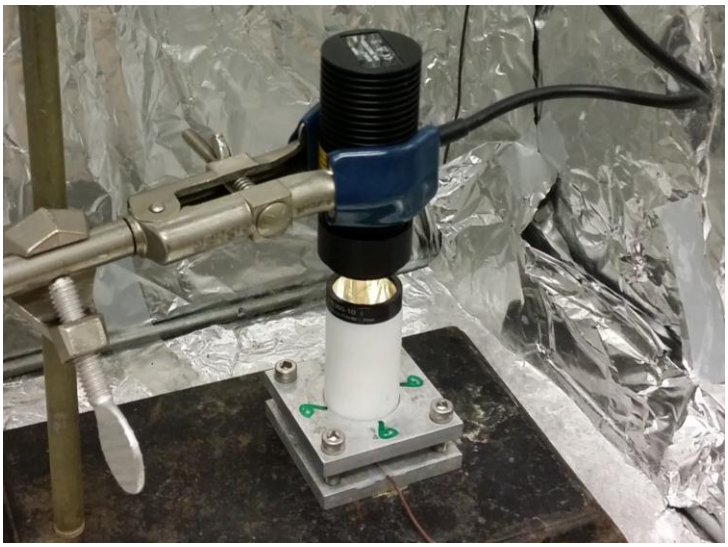

Figure 2.11. Experimental setup for photoelectrochemical investigations.

Quinone Studies

All quinone experiments were conducted inside an Ar-filled glove box (Figures 2.12 and 2.13). Solutions were sparged with Ar overnight and stored in the glove box prior to each experiment. A SAM of BHQ or N_2-BHQ was prepared by immersing a Au electrode in a solution of BHQ or N_2-BHQ in EtOH (1 mM) for 2 h. The electrode was rinsed with EtOH and then with pH 7 BR buffer before further use. Preparation of the HBM system with and without

MDP was reported earlier in this thesis chapter (*vide supra*).

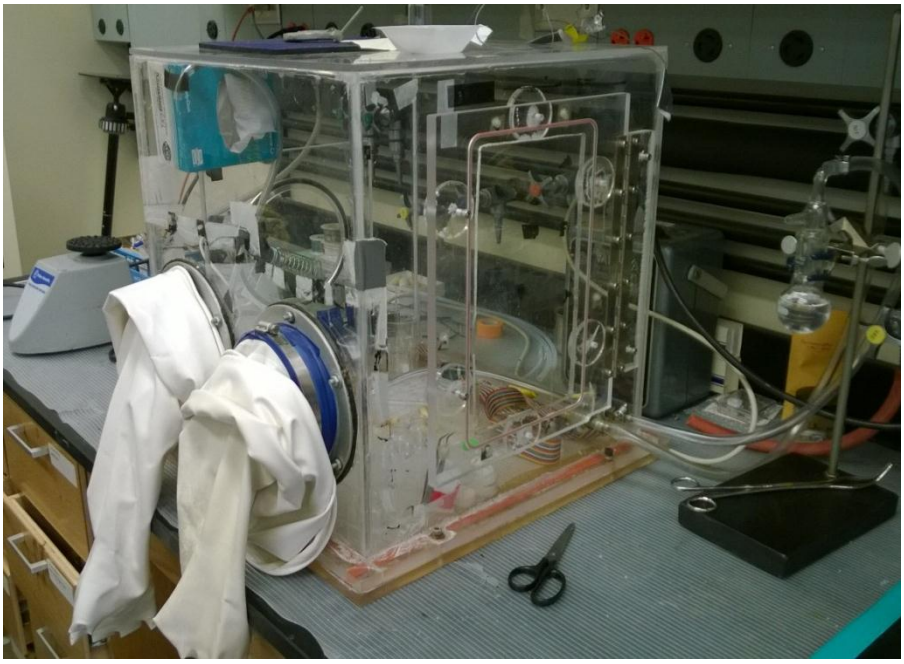

Figure 2.12. A multi-purpose reaction chamber equipped with a vortexer and electrical feedthroughs for HBM studies under an Ar atmosphere.

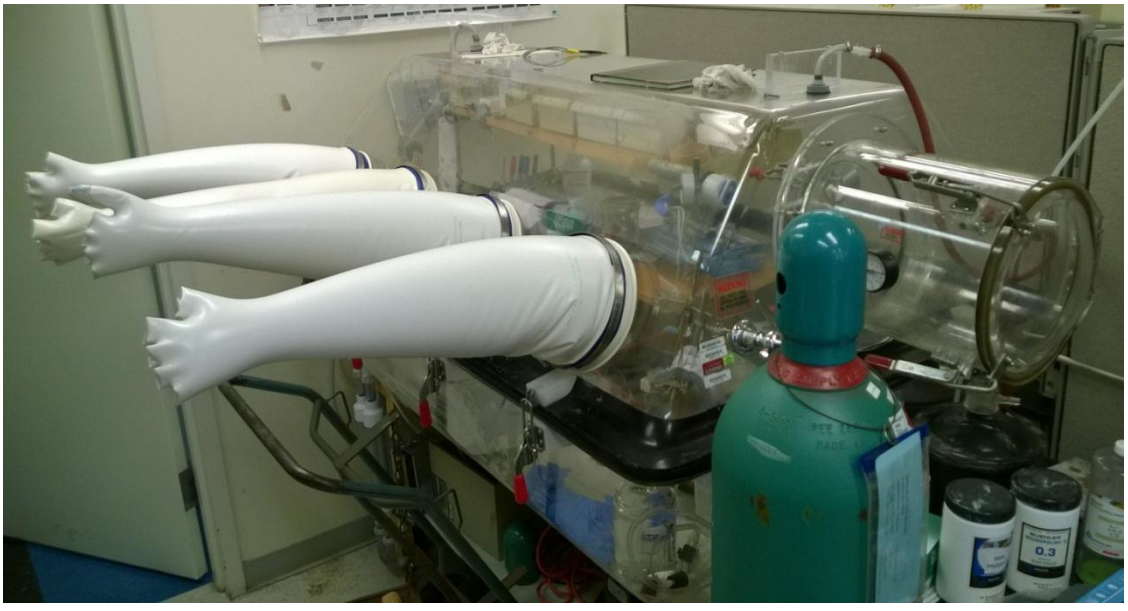

Figure 2.13. A wet box assembled by Dr. Christopher J. Barile and Edmund C. M. Tse. The glove box, which was equipped with an antechamber, allows for aqueous electrochemistry under an inert N_2 atmosphere.

2.5 General Surface Characterization Procedures

Surface Topology Investigations

Contact-mode atomic force microscopy (AFM) was conducted using a Series 5500 multipurpose AFM/SPM probe and controller (Agilent Technologies). Au(111) evaporated onto freshly-cleaved mica substrates were utilized for AFM measurements (N9807A and N9805A, Keysight Technologies). Prior to use, the Au(111) substrates were annealed slightly using a H_2 flame (99.9999%, research grade, S. J. Smith Welding Supply). The SiN cantilever (DNP-S10, Bruker) with a spring constant of 0.35 N/m was used to acquire AFM images and force curves. While maintaining contact with the sample, the AFM tip with minimum force was applied on the surface during data collection to avoid any surface damage. All AFM images were recorded at 256 × 256 pixel resolution at a scan rate of 1 Hz and were flattened using PicoView 1.14 (Agilent Technologies). The cantilever deflection versus piezo-position curves were converted to force-distance curves. The cantilever deflection sensitivity was obtained according to published procedures by pressing the AFM tip against a glass substrate.[21] The AFM and force-distance curve measurements were carried out in pH 7 phosphate buffer solutions.

Scanning tunneling microscopy (STM) was carried out using a Nanoscope III E (Digital Instrument Corporation) system under ambient conditions. STM tips were prepared by electrochemical etching of tungsten wire (0.25 mm in diameter) in 2.0 M NaOH. The tips were then rinsed with water and dried under a gentle stream of Ar. STM images were acquired using constant current mode with a tunneling current of 3.0 nA and a tip bias of 50 mV. Mean roughness values were calculated using WSxM 5.0 Develop 6.4 software. Scanning electron microscopy (SEM) was performed using a Hitachi S-4700 Cold FE-SEM (Hitachi High Technologies) with an acceleration voltage of 20 kV.

Membrane Thickness Measurements

Ellipsometry was performed using a Gaertner Ellipsometer L116C equipped with a He-Ne laser (632.8 nm) set at an incidence angle of 70°. An average of four measurements was used, each of which was taken at a different spot on the Au electrodes. A two-layer transparent film model was used for the thickness calculations based on pseudosubstrate constants measured on clean Au substrates. The refractive index of the organic SAM film was fixed at 1.5.

Surface Composition Analysis

Energy-dispersive X-ray Spectroscopy (EDX) was performed with an Oxford Instruments ISIS EDX Microanalysis System. X-ray photoelectron spectroscopy (XPS) was conducted using an AXIS Ultra spectrometer (Kratos Analytical) with a monochromatic Al Kα (1486.6eV) X-ray source (Figure 2.14).

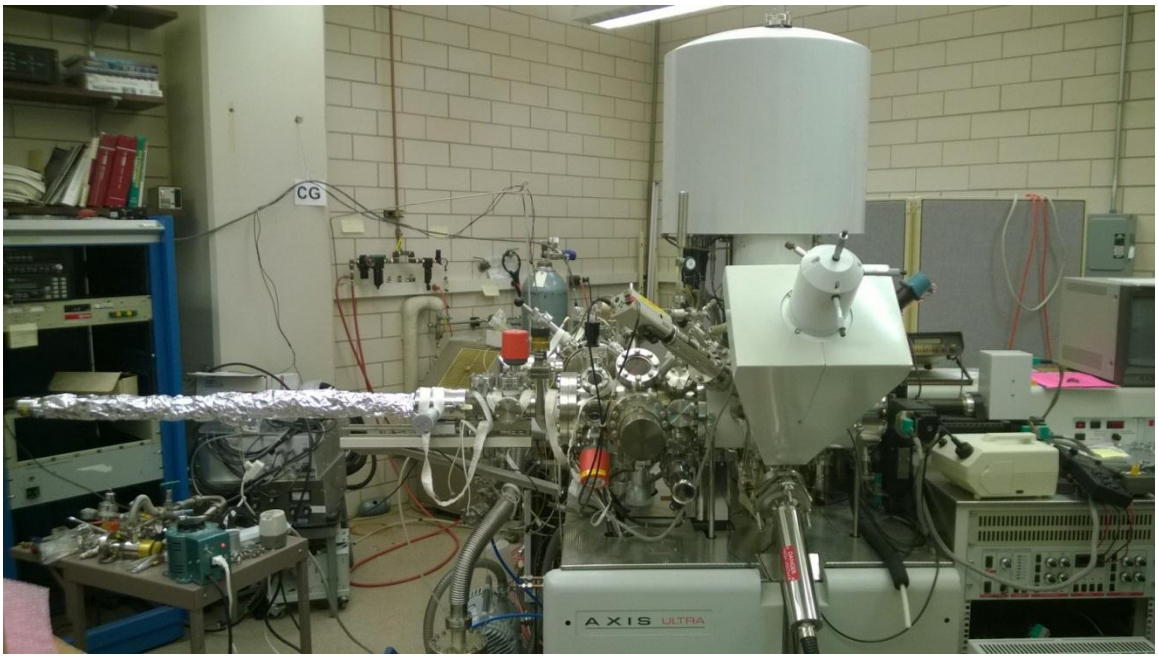

Figure 2.14. The X-ray photoelectron spectrometer at MRL at UIUC.

Surface-Enhanced Raman Spectroscopy

Polycrystalline Au disk working electrode was sequentially polished using 9 μm, 3 μm, 1 μm, 0.25 μm, and 0.05 μm diamond suspensions to a mirror finish. After each 5-min polishing step, the electrode was sonicated in Milli-Q water for 5 min and thoroughly rinsed. The Au disk was flamed using a H_2 torch and quenched in Milli-Q water. The flamed Au electrode was then electrochemically roughened in a cell consisting of an aqueous "no-leak" Ag/AgCl reference electrode, a Au counter electrode, and a 0.5 M KCl electrolyte by cycling between −0.25 V and 1.3 V vs. Ag/AgCl for twenty-five roughening cycles as previously described.[22,23] The roughened Au disk was then electrochemically cycled for six times between 0 to 1.85 V vs. Ag/AgCl in a cell consisting of an aqueous "no-leak" Ag/AgCl reference electrode, a Au counter electrode, and a 0.1 M HNO_3 electrolyte. Electrochemical active surface area (ECSA) of the Au electrode was determined by using the characteristic cathodic stripping peak at about 0.75 V vs. Ag/AgCl and was typically ca. 6.61 cm^2. For investigations involving water-insoluble catalysts, the metal complexes dissolved in $CHCl_3$ or acetone (1 mM, 40 μL) was casted onto the Au surface. The electrode was air-dried and rinsed with water before use.

In situ Electrochemical Raman Spectroscopy Procedure

In situ surface-enhanced Raman spectroscopy (SERS) measurements were conducted using a spectroelectrochemical cell described previously.[24] For studies involving metal complexes, a He–Ne laser (50 mW, 632.8 nm, Meredith Instruments) was used to provide sample excitation at an incident angle of approximately 45° relative to an 85 mm f/1.2 collection lens (Canon). For studies involving highly-fluorescent porphyrin-based molecules, a diode laser (75 mW, 784.5 nm, Ondax) was used instead. The scattered radiation was then focused using an

f/1.2 lens to the 50 μm slit of a SpectraPro 2300i monochromator (Princeton Instruments) with grating of 1200 grooves per mm. The CCD detector (Andor) was thermoelectrically cooled to −80 °C. Acquisition time for the spectra reported was 1 min. The complete Raman experimental set-up was presented in Figures 2.15 and 2.16.

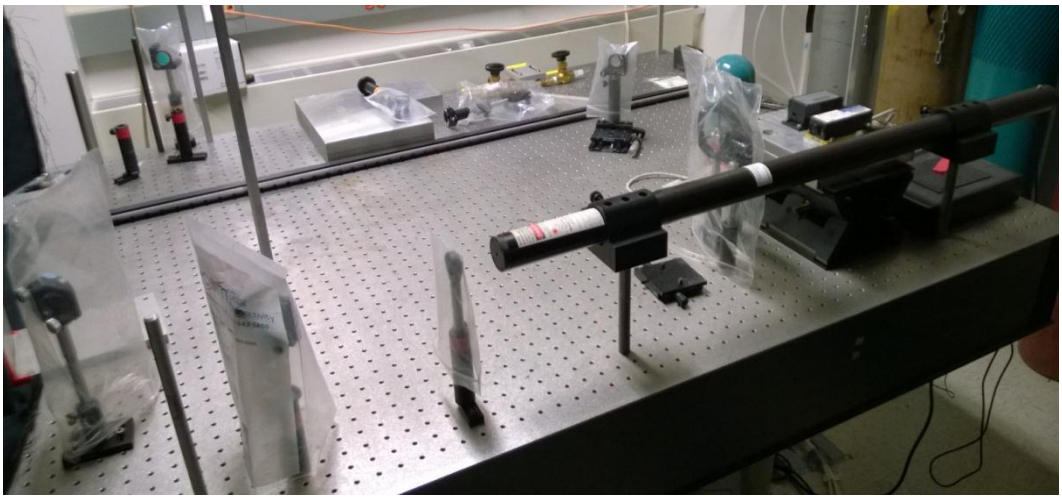

Figure 2.15. Raman experimental set-up showing the lasers and reflecting mirrors.

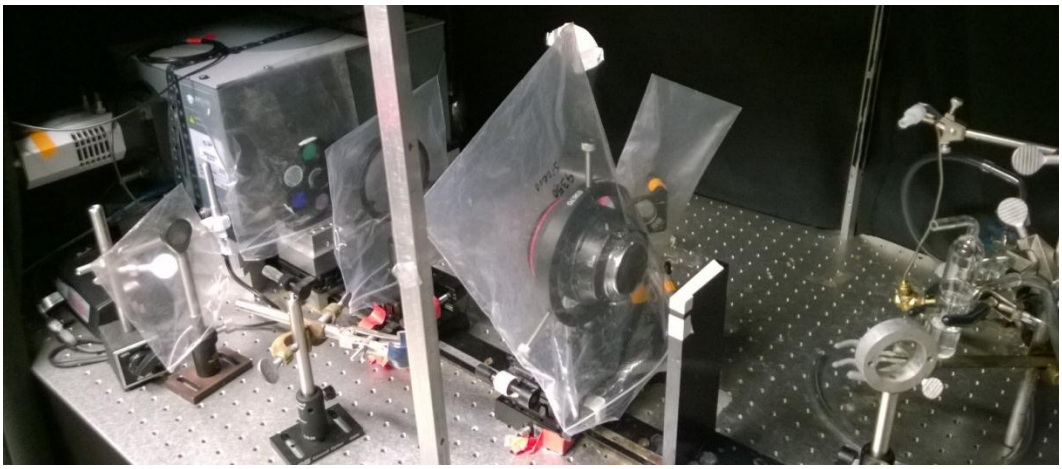

Figure 2.16. Raman experimental set-up showing a CCD detector, a notch filter, and a set of focusing lenses.

2.6 References

(1) Wu, G.; More, K. L.; Johnston, C. M.; Zelenay, P. *Science* **2011**, *332*, 443.
(2) Tse, E. C. M.; Gewirth, A. A. *J. Phys. Chem. A* **2015**, *119*, 1246.

(3) Bard, A. J.; Faulkner, L. R. *Electrochemical Methods: Fundamentals and Applications, 2nd Edition*; Wiley Global Education, 2000.
(4) van der Vliet, D.; Strmcnik, D. S.; Wang, C.; Stamenkovic, V. R.; Markovic, N. M.; Koper, M. T. M. *J. Electroanal. Chem.* **2010**, *647*, 29.
(5) Bard, A. J.; Parsons, R.; Jordan, J. *Standard Potentials in Aqueous Solution*; Taylor & Francis, 1985.
(6) Thorseth, M. A.; Letko, C. S.; Tse, E. C. M.; Rauchfuss, T. B.; Gewirth, A. A. *Inorg. Chem.* **2012**, *52*, 628.
(7) Weaver, M. J.; Nettles, S. M. *Inorg. Chem.* **1980**, *19*, 1641.
(8) Gong, K.; Du, F.; Xia, Z.; Durstock, M.; Dai, L. *Science* **2009**, *323*, 760.
(9) McDonald, A. C.; Fan, F. R. F.; Bard, A. J. *J. Phys. Chem.* **1986**, *90*, 196.
(10) Liu, C.-y.; Snyder, S. R.; Bard, A. J. *J. Phys. Chem. B* **1997**, *101*, 1180.
(11) Ashraf-Khorassani, M.; Braun, R. D. *Corrosion* **1987**, *43*, 32.
(12) Lvovich, V.; Scheeline, A. *Anal. Chem.* **1997**, *69*, 454.
(13) Zeuthen, T. *Med. Biol. Eng. Comput.* **1978**, *16*, 483.
(14) Schmidt, T. J.; Paulus, U. A.; Gasteiger, H. A.; Behm, R. J. *J. Electroanal. Chem.* **2001**, *508*, 41.
(15) Bosch, R. W.; Féron, D.; Celis, J. P. *Electrochemistry in Light Water Reactors: Reference Electrodes, Measurement, Corrosion and Tribocorrosion Issues*; Elsevier Science, 2007.
(16) Tse, E. C. M.; Barile, C. J.; Gewargis, J. P.; Li, Y.; Zimmerman, S. C.; Gewirth, A. A. *Anal. Chem.* **2015**, *87*, 2403.
(17) Hosseini, A.; Barile, C. J.; Devadoss, A.; Eberspacher, T. A.; Decreau, R. A.; Collman, J. P. *J. Am. Chem. Soc.* **2011**, *133*, 11100.
(18) Li, Y.; Tse, E. C. M.; Barile, C. J.; Gewirth, A. A.; Zimmerman, S. C. *J. Am. Chem. Soc.* **2015**, *137*, 14059.
(19) Hosseini, A.; Collman, J. P.; Devadoss, A.; Williams, G. Y.; Barile, C. J.; Eberspacher, T. A. *Langmuir* **2010**, *26*, 17674.
(20) Barile, C. J.; Tse, E. C. M.; Li, Y.; Sobyra, T. B.; Zimmerman, S. C.; Hosseini, A.; Gewirth, A. A. *Nat. Mater.* **2014**, *13*, 619.
(21) Garcia-Manyes, S.; Sanz, F. *BBA-Biomembranes* **2010**, *1798*, 741.
(22) Gao, P.; Gosztola, D.; Leung, L.-W. H.; Weaver, M. J. *J. Electroanal. Chem. Interfacial Electrochem.* **1987**, *233*, 211.
(23) Thorum, M. S.; Anderson, C. A.; Hatch, J. J.; Campbell, A. S.; Marshall, N. M.; Zimmerman, S. C.; Lu, Y.; Gewirth, A. A. *J. Phys. Chem. Lett.* **2010**, *1*, 2251.
(24) Schultz, Z. D.; Feng, Z. V.; Biggin, M. E.; Gewirth, A. A. *J. Electrochem. Soc.* **2006**, *153*, C97.

Chapter 3

Multicopper Models for the Laccase Active Site:

Effect of Nuclearity on Electrocatalytic Oxygen Reduction

3.1 Introduction

Low-temperature polymer electrolyte membrane (PEM) fuel cells represent an attractive power source for clean and sustainable transportation.[1-3] Unlike conventional combustion engines, fuel cells do not exhibit the Carnot limitation on the conversion of heat to mechanical work.[4,5] The development of fuel cells has been hampered by several design issues.[6-10] From a technical standpoint, the key to fuel cell viability is efficient mediation of the oxygen reduction reaction (ORR) to water: $O_2 + 4\ e^- + 4\ H^+ \rightarrow 2\ H_2O$.[11] Presently, cathodes of choice feature Pt or one of its alloys, these being neither cheap nor sufficiently active and robust.[12-15]

Synthetic Cu complexes exhibit rich reactivity towards O_2, and several Cu-O_2 binding modes have been identified for mono- and multicopper systems.[16-21] In view of the essential role of Cu in O_2-activating enzymes,[22] it is no surprise that Cu complexes have been well-studied in the context of ORR catalysis.[23] For example, the facile oxygenation of $[Cu(TPA)]^+$ (tris(2-pyridylmethyl)amine = TPA) and its derivatives led to the discovery that $[Cu(TPA)(H_2O)]^{2+}$ complex has the lowest ORR overpotential at pH 1 of any synthetic Cu catalysts.[24-26] Through

pyrolysis and reconstitution studies, we showed that ORR activity necessitates the Cu centers to be attached to the *N*-donor ligands.[27] Further studies, however, showed that variations of the TPA platform do not strongly affect the ORR onset potential, even though the Cu(I/II) couple is affected.[27] In view of the modest effects of substituents on ORR catalysis by the Cu-TPA platform, further development requires more drastic changes in the design of catalysts based on the Cu-TPA motif.

The design of new ORR catalysts could benefit from more faithful mimicry of biological catalysts for the same reaction. Cu enzymes catalyze the four-electron four-proton reduction of O_2 to water very efficiently.[28-30] Often found in fungi (e.g. *Melanocarpus albomyces*,[31] *Rigidoporus lignosus*,[32] and *Trametes versicolor*[33]), laccases are ORR catalysts that feature a characteristic tricopper O_2-binding site supplemented by a fourth Cu center. Upon immobilization onto an electrode, laccase exhibits an ORR overpotential of only ~100 mV, which is even better than Pt-based catalysts.[23,34-39] However, due to the large size of laccase (160 nm^3),[33,40,41] electrodes decorated with these enzymes cannot deliver the power densities required for practical use.[42] Furthermore, laccases denature under operating conditions typical of PEM fuel cells.[43,44] Synthetic models of the trinuclear Cu active site could possibly replicate the high activity of laccase while exhibiting the durability and power density necessary for PEM fuel cell applications.[5] Such functional tricopper active site models have, however, not yet been reported.[45]

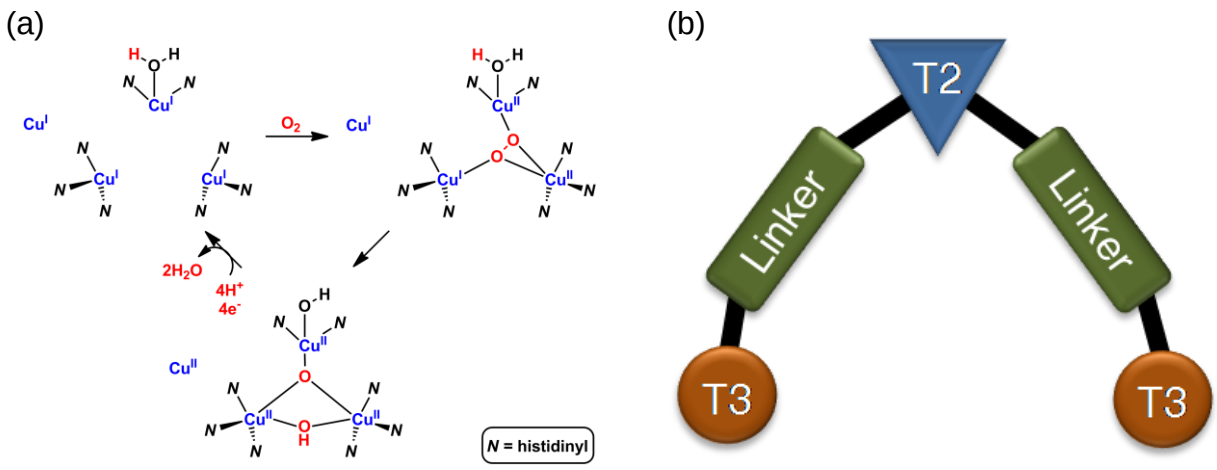

Figure 3.1. (a) Schematic of the laccase active site,[46] and (b) design principle for models of the laccase tricopper site.

The laccase active site features two Cu centers each bound to three histidine residues (denoted 'T3' sites) and a third Cu existing in a pocket with two histidine ligands, a 'T2' site (Figure 3.1a).[46] The tricopper O_2-binding site is dynamic, i.e. the Cu—Cu distances change from ~5 Å in the fully reduced state to ~3.5 Å in the oxygenated state.[31,33,45] Synthetic tricopper complexes often form very stable μ_3-hydroxy species, e.g. $[Cu^{II}_3(\mu_3\text{-}OH)(trz)_3(OH)_2(H_2O)_4]\cdot 4.5\ H_2O$ (Htrz = 1,2,4-triazole) and $[Cu_3(\mu_3\text{-}OH)(\mu\text{-}pz)_3(HCOO)_2(Hpz)_2]$ (Hpz = pyrazole), such motifs typically being inactive towards ORR.[47,48] The design of appropriately ligated tricopper catalysts thus remains an unsolved area of research. Whereas many ligand scaffolds feature three equivalent Cu binding sites, few designs accommodate the asymmetry of the laccase active site.[49]

In addition to the tricopper site that binds O_2, laccase features a fourth copper, labeled T1. When the T1 site (not depicted) is substituted with Hg(II), which is redox-inactive, laccase loses its catalytic activity, although it still binds but does not cleave O_2.[50] The T1 copper functions as an electron reservoir, which can in principle be replicated with an electrode in model systems.

In this report we describe initial efforts to construct and test ensembles of T2 and T3 sites, as inspired by laccase. Figure 3.1b shows our design concept for the laccase active site: T2 and T3 sites are connected by flexible linkers. The T3 centers feature coordination of Cu by three *N*-donor groups while the T2 center features Cu coordination by two *N*-donor groups. Given the high ORR activity afforded by the TPA ligand,[26,27] its derivative, 2,2'-dipicolylamine (DPA, **1**) was used to simulate the T3 site mimics while we used 2,2'-bipyridine (bipy) and 2,2':6',2''-terpyridine (terpy) for the T2 site mimic. Figure 3.2 shows the ligands used in this study (including the new species **4**, a prototypical T3-T2-T3 mimic), each of which incorporate DPA fragments as surrogates for the native tris(imidazolyl) binding pockets.

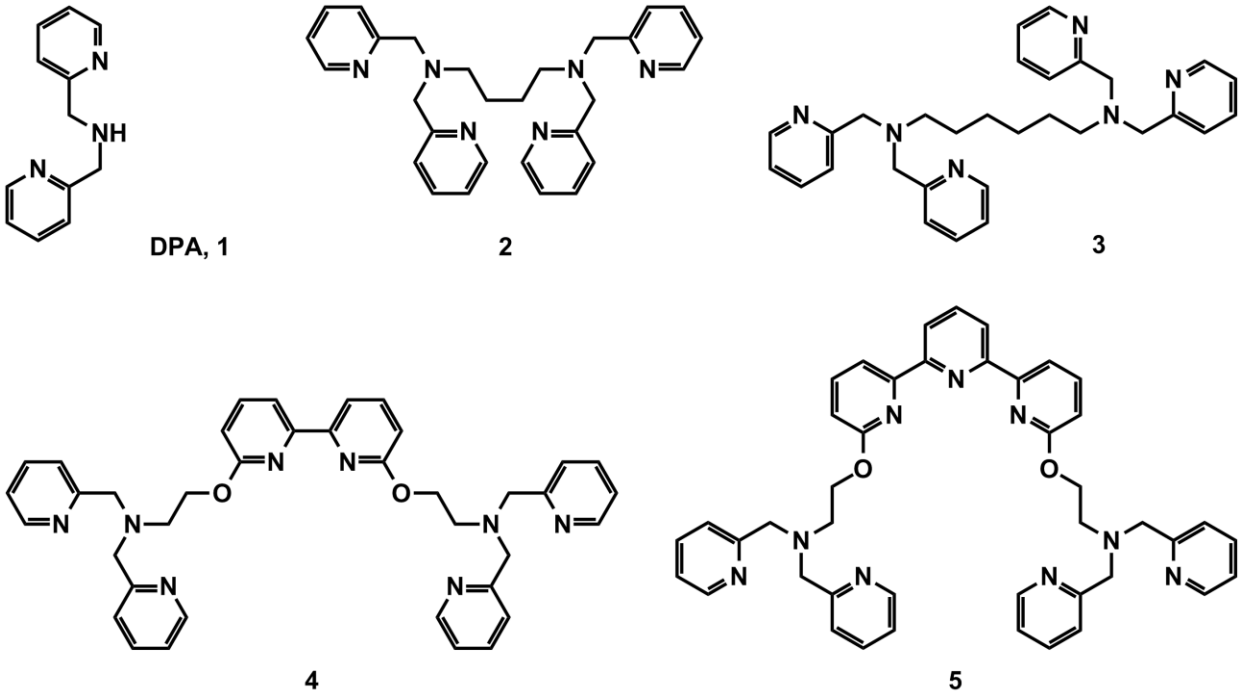

Figure 3.2. Ligands used in this study: 2,2'-dipicolylamine (DPA, **1**), *N*,*N*,*N*',*N*'-tetra(pyridin-2-ylmethyl)butane-1,4-diamine (**2**), *N*,*N*,*N*',*N*'-tetra(pyridin-2-ylmethyl)hexane-1,6-diamine (**3**), 2,2'-([2,2'-bipyridine]-6,6'-diylbis(oxy))bis(*N*,*N*-bis(pyridin-2-ylmethyl)ethanamine) (**4**), and 2,2'-([2,2':6',2''-terpyridine]-6,6''-diylbis(oxy))bis(*N*,*N*-bis(pyridin-2-ylmethyl)ethanamine) (**5**).

3.2 Materials and Methods

Unless otherwise stated, all chemicals were purchased from commercial sources and used as received. The ligands *N*,*N*,*N'*,*N'*-tetra(pyridin-2-ylmethyl)butane-1,4-diamine (**2**) and *N*,*N*,*N'*,*N'*-tetra(pyridin-2-ylmethyl)hexane-1,6-diamine (**3**) were prepared according to a published procedure,[51] using NMe_4I instead of $[N(C_{12}H_{25})Me_3]Cl$ as the catalyst. The trinucleating ligand 2,2'-([2,2':6',2"-terpyridine]-6,6"-diylbis(oxy))bis(*N*,*N*-bis(pyridin-2-ylmethyl)ethanamine) (**5**) and its tricopper complex $[Cu_3Cl_6(\mathbf{5})]$ were also prepared using a modified literature procedure, using KO^tBu in THF instead of KOH in DMSO.[52] The monocopper complexes $[Cu(\mathbf{1})](NO_3)_2$ and $[Cu(\mathbf{1})Cl_2]$ were prepared following literature methods.[53,54] Degassed MeCN and THF were dried through columns of activated alumina and stored over molecular sieves. ^{1}H NMR spectra were recorded on a Varian VXR500 spectrometer at 500 MHz. A Waters Micromass Quattro II spectrometer was used to acquire ESI-MS data for analytes in dilute MeOH solution. CHN analytical data were acquired using an Exeter Analytical CE-440 elemental analyzer.

Caution! *Perchlorate salts of metal ion complexes are potentially explosive. Only small amounts of materials should be prepared.*

3.3 Synthesis and Characterization of Model Complexes

2,2'-([2,2'-bipyridine]-6,6'-diylbis(oxy))bis(N,N-bis(pyridin-2-ylmethyl)ethanamine) (**4**)

Under an atmosphere of dry N_2, a stirred solution of *N*,*N'*-di(2-picolyl)ethanolamine (73.0 mg, 0.300 mmol) in THF (1 mL) was treated with KO^tBu (37.0 mg, 0.330 mmol) suspended in THF (2 mL). After 30 min, 6,6'-dibromo-2,2'-bipyridine (31.4 mg, 0.100 mmol) suspended in

THF (2 mL) was added and the mixture stirred for 96 h at room temperature, before the mixture was heated and the solvent boiled off. The oily residue was extracted with CH_2Cl_2 (5 mL), and the solution washed with H_2O (3 × 10 mL), dried over Na_2SO_4 and evaporated to dryness to leave a pale oil. Recrystallization from warm Me_2CO afforded the product as off-white plates (42.2 mg, 66.0 μmol, 66%). ^{1}H NMR ($CDCl_3$): 8.49 (m, 4H, py-H6), 7.80 (m, 2H, bipy-H3), 7.65 – 7.50 (m, 10H, py-H3,4/bipy-H4), 7.10 (m, 4H, py-H5), 6.69 (m, 2H, bipy-H5), 4.58 (t, $^3J_{HH}$ = 6 Hz, 4H, OCH_2), 3.99 (s, 8H, pyCH_2), 3.08 (t, $^3J_{HH}$ = 6 Hz, 4H, OCH_2CH_2) ppm. ESI-MS: *m*/*z* 639.3 $[M + H]^+$, 320.4 $[M + 2H]^{2+}$. Anal. Calcd for $C_{38}H_{38}N_8O_2$: C, 71.45; H, 6.00; N, 17.54. Found: C, 71.32; H, 5.97; N, 16.82.

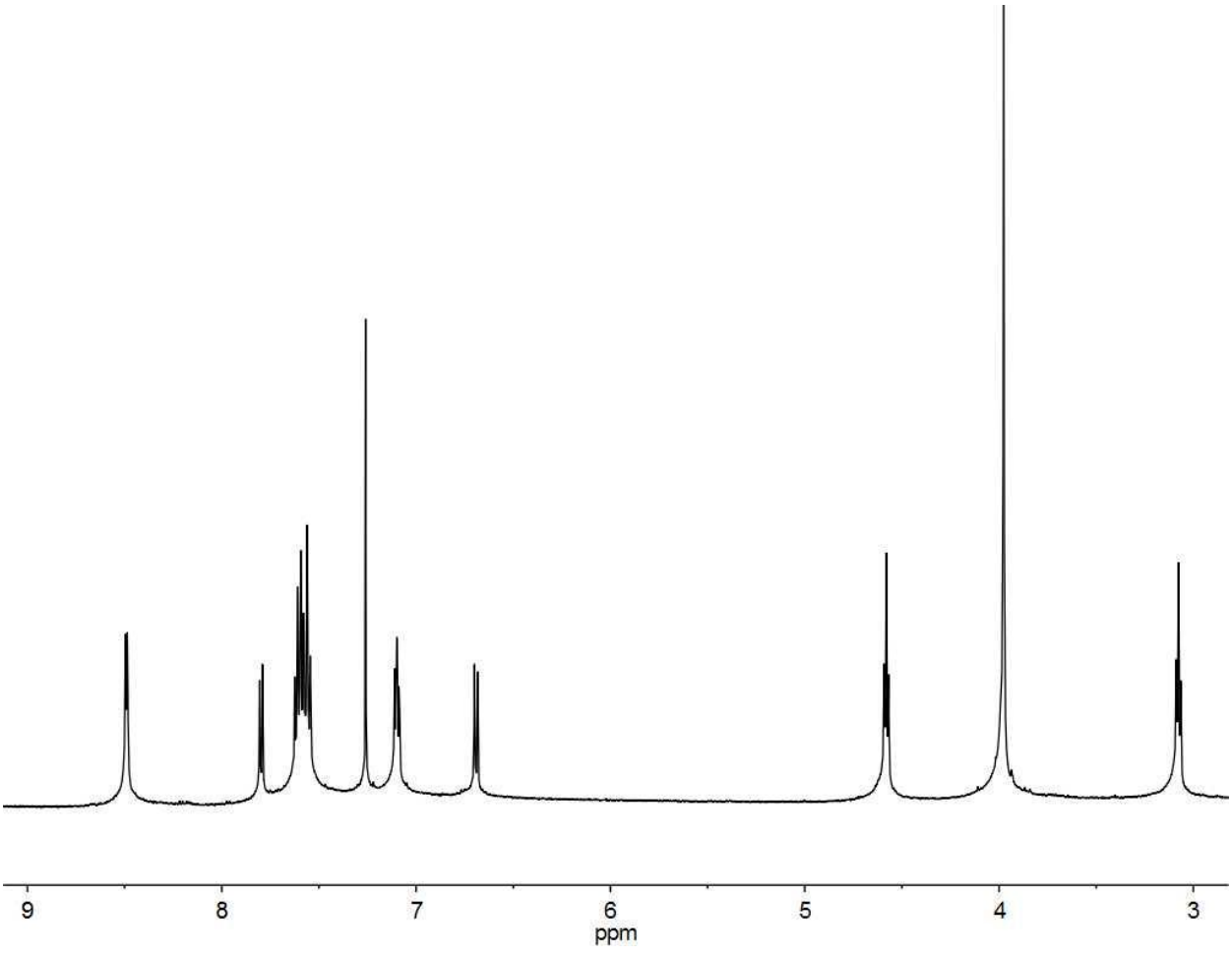

Figure 3.3. ^{1}H NMR spectrum of **4** in $CDCl_3$.

*[Cu(MeCN)(**1**)]BF_4*

Under an atmosphere of dry N_2, $[Cu(MeCN)_4]BF_4$ (62.9 mg, 200 μmol) and **1** (39.9 mg, 200 μmol) were dissolved in MeCN (2 mL) with stirring. After 10 min, the solution was layered with Et_2O (15 mL) and allowed to stand at –28°C for 1 h. The solid that formed was isolated by filtration, washed with Et_2O (2 × 2 mL), and dried briefly to give the title compound as a yellow microcrystalline powder (68.8 mg, 176 μmol, 88%). ^{1}H NMR (CD_3CN) 8.56 (m, 2H, H6), 7.80 (m, 2H, H4), 7.36 (m, 2H, H5), 7.32 (m, 2H, H3), 4.03 (s, 4H, C*H*$_2$), 3.87 (s, 1H, N*H*), 1.96 (s, CH_3) ppm. ESI-MS: *m*/*z* 303.0 $[M - BF_4^-]^+$, 262.0 $[M - MeCN - BF_4^-]^+$. Anal. Calcd for $C_{14}H_{16}BCuF_4N_3$–MeCN: C, 41.23; H, 3.75; N, 12.02. Found: C, 41.22; H, 3.68; N, 11.79 (the MeCN ligand is readily lost under vacuum).

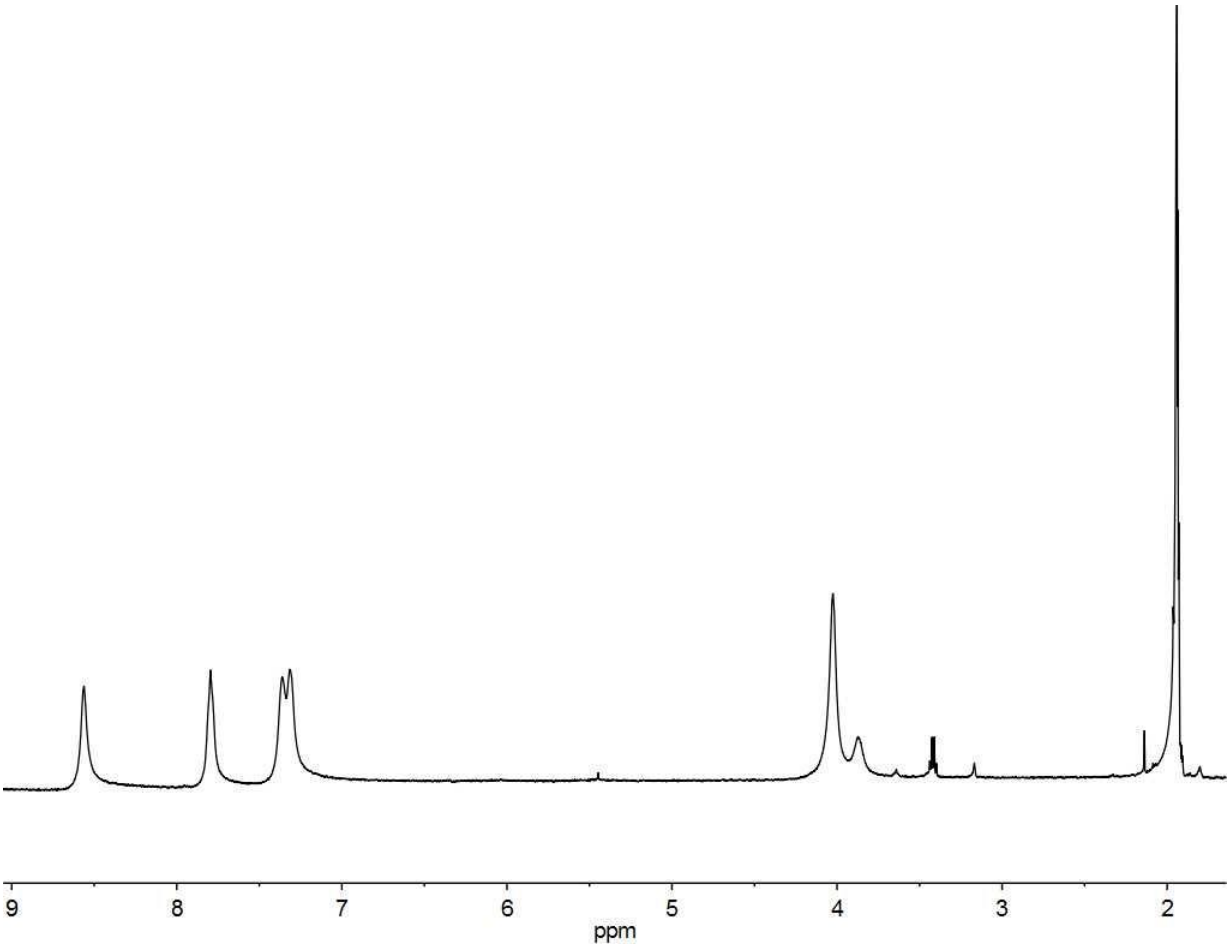

Figure 3.4. ^{1}H NMR spectrum of [Cu(MeCN)(**1**)]BF_4 in CD_3CN.

*[Cu_2(MeCN)$_2$(**2**)](BF_4)$_2$*

Under an atmosphere of dry N_2, [Cu(MeCN)$_4$]BF_4 (251.6 mg, 800 μmol) and **2** (192.3 mg, 400 μmol) were dissolved in MeCN (5 mL) with stirring. After 2 h, the solution was layered with Et_2O (15 mL) and allowed to stand at –28°C for 1 h. The solid that formed was isolated by filtration, washed with Et_2O (2 × 2 mL), and dried briefly to give the title compound as a yellow microcrystalline powder (325.1 mg, 389 μmol, 97%). ^{1}H NMR (CD_3CN): d8.56 (d, $^{3}J_{HH}$ = 5.0 Hz, 4H, H6), 7.83 (dt, $^{3}J_{HH}$ = 7.7 Hz, $^{4}J_{HH}$ = 1.7 Hz, 4H, H4), 7.41 (t, $^{3}J_{HH}$ = 6.3 Hz, 4H, H5), 7.35 (d, $^{3}J_{HH}$ = 7.8 Hz, 4H, H3), 3.79 (s, 8H, pyCH_2), 2.70 (t, $^{3}J_{HH}$ = 7.4 Hz, 4H, NCH_2), 1.97 (s, 6H, CH_3), 1.56 (m, 8H, NCH_2CH_2) ppm. ESI-MS: *m*/*z* 665.1 [M – MeCN – BF_4^-]$^+$, 309.6 [M –

$2BF_4^-]^{2+}$, 289.1 [M – MeCN – $2BF_4^-]^{2+}$. Anal. calcd for $C_{32}H_{38}B_2Cu_2F_8N_8$·0.5MeCN: C, 46.31; H, 4.65; N, 13.91. Found: C, 46.44; H, 4.72; N, 13.84.

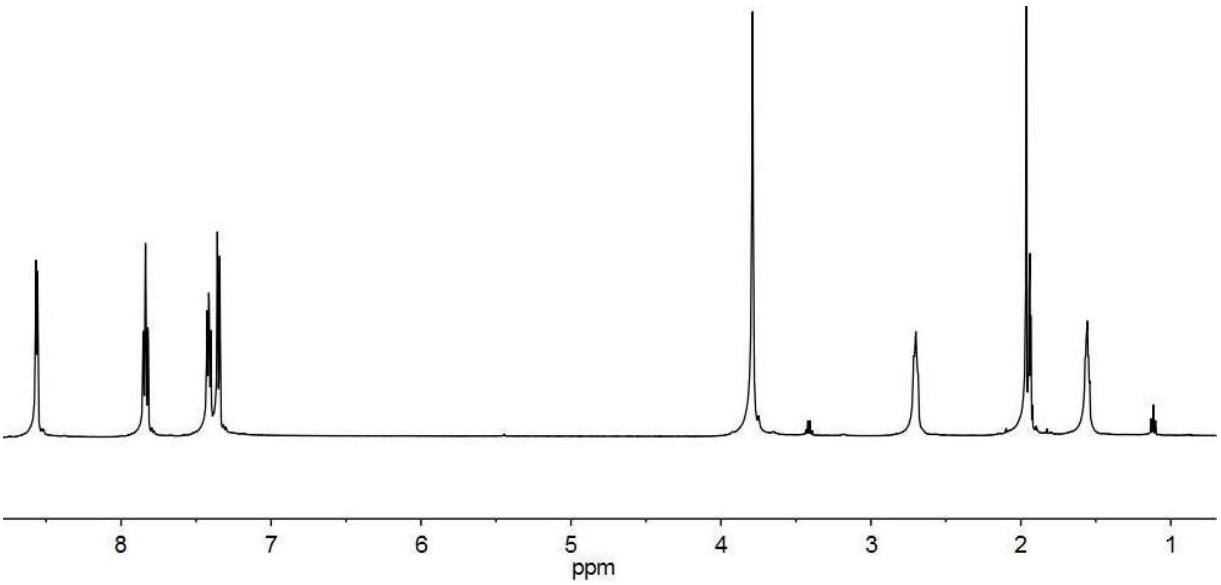

Figure 3.5. ^{1}H NMR spectrum of $[Cu_2(MeCN)_2(\mathbf{2})](BF_4)_2$ in CD_3CN. Resonances at 3.42, 1.12 ppm are from residual Et_2O.

$[Cu_2(MeCN)_2(\mathbf{3})](BF_4)_2$.

This compound was prepared analogously to $[Cu_2(MeCN)_2(\mathbf{2})](BF_4)_2$, instead using **3** as the precursor. A sticky golden semi-solid was obtained, which was purified by crystallization from MeCN/Et_2O. Yield: 92%, yellow powder. ^{1}H NMR (CD_3CN): 8.57 (m, 4H, H6), 7.84 (t, $^3J_{HH}$ = 6.9 Hz, 4H, H4), 7.41 (t, $^3J_{HH}$ = 6.1 Hz, 4H, H5), 7.36 (d, $^3J_{HH}$ = 7.3 Hz, 4H, H3), 3.80 (s, 8H, pyCH_2), 2.70 (t, $^3J_{HH}$ = 7.8 Hz, 4H, NCH_2), 1.96 (s, 6H, CH_3), 1.54 (m, 8H, $NCH_2CH_2CH_2$), 1.20 (m, 8H, $NCH_2CH_2CH_2$) ppm. ESI-MS: *m*/*z* 693.0 [M – MeCN – $BF_4^-]^+$, 303.0 [M – MeCN – $2BF_4^-]^{2+}$. Anal. Calcd for $C_{34}H_{42}B_2Cu_2F_8N_8$: C, 47.29; H, 4.90; N, 12.98. Found: C, 46.96; H, 4.82; N, 12.66.

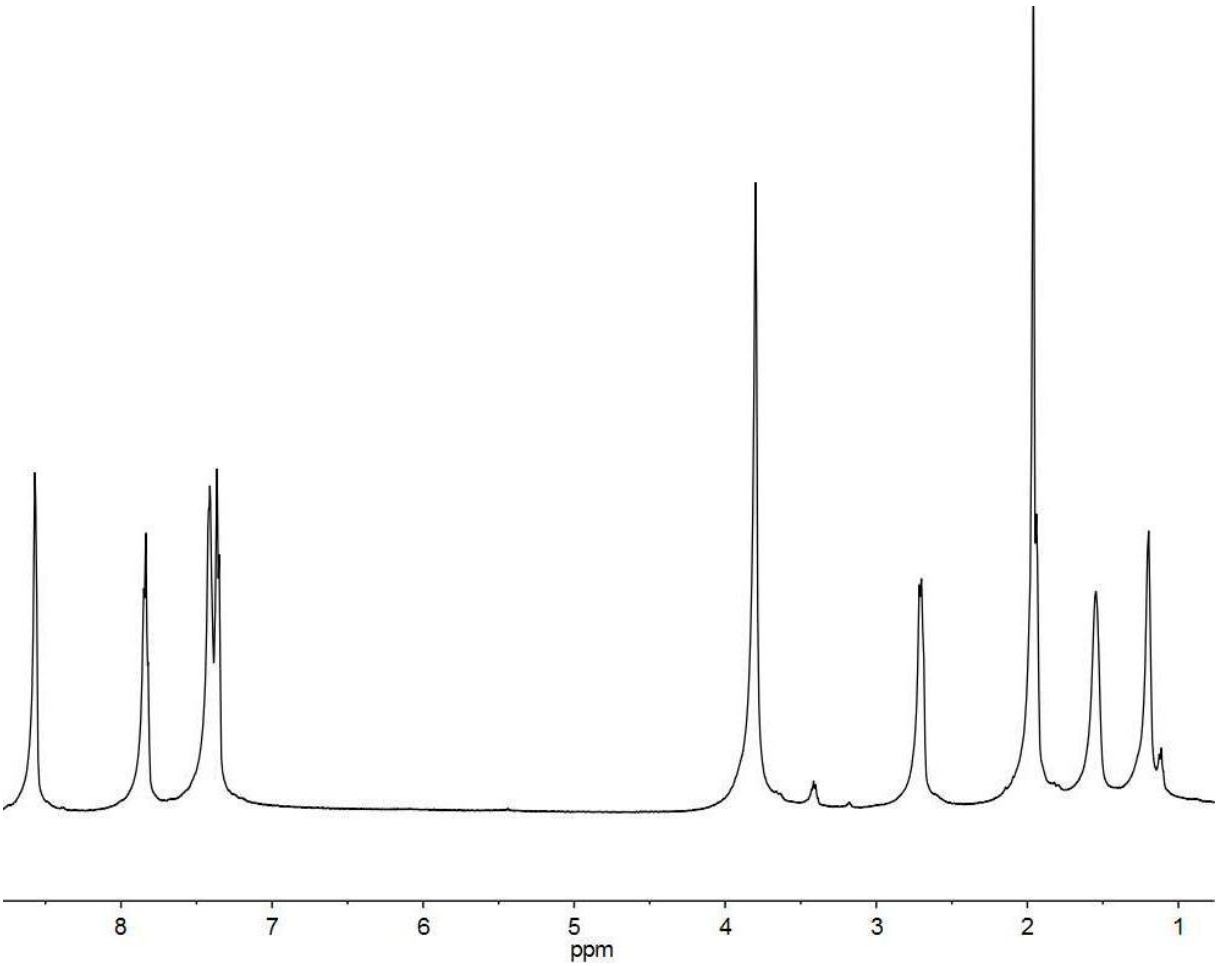

Figure 3.6. ^{1}H NMR spectrum of $[Cu_2(MeCN)_2(\mathbf{3})](BF_4)_2$ in CD_3CN. Resonances at 3.42, 1.12 ppm are from residual Et_2O.

$[Cu_2(NO_3)_4(\mathbf{2})]$

A solution of $Cu(NO_3)_2{\cdot}2.5H_2O$ (93.0 mg, 400 μmol) in boiling MeOH (1 mL) was treated with **2** (90.5 mg, 200 μmol) in MeOH (2 mL) with stirring. A pale blue solid precipitated from the deep blue mixture. Upon cooling to room temperature, the solid was isolated by filtration and washed with MeOH (2 mL) to give the product as a blue microcrystalline powder (157.3 mg, 190 μmol, 95%). ESI-MS: *m*/*z* 764.6 $[M - NO_3^-]^+$. Anal. calcd for $C_{28}H_{32}Cu_2N_{10}O_{12}$: C, 40.63; H, 3.90; N, 16.92. Found: C, 40.57; H, 3.81; N, 16.43.

*[$Cu_2(NO_3)_4$(**3**)]*

This compound was prepared analogously to [$Cu_2(NO_3)_4$(**2**)], instead using **3** as the precursor. Yield: 96%, blue powder. ESI-MS: *m*/*z* 792.6 [M – NO_3^-]$^+$, 365.3 [M – $2NO_3^-$]$^{2+}$. Anal. calcd for $C_{30}H_{36}Cu_2N_{10}O_{12}$·1.25$H_2O$: C, 41.03; H, 4.42; N, 15.95. Found: C, 41.09; H, 4.27; N, 15.48.

*[Cu_2Cl_4(**2**)]*

A solution of $CuCl_2$·2H_2O (68.2 mg, 400 μmol) in boiling MeOH (1 mL) was treated with **2** (90.5 mg, 200 μmol) in MeOH (2 mL) with stirring. Upon cooling to room temperature, the deep blue mixture was treated with Et_2O (15 mL) and the resulting solid isolated by filtration and washed with Et_2O (2 mL) to give the product as a baby blue crystals (127.1 mg, 176 μmol, 88%). ESI-MS: *m*/*z* 685.5 [M – Cl^-]$^+$, 325.4 [M – $2Cl^-$]$^{2+}$. Anal. calcd for $C_{28}H_{32}Cl_4Cu_2N_6$·2MeOH: C, 44.84; H, 5.27; N, 10.46. Found: C, 45.15; H, 5.15; N, 10.36.

*[Cu_2Cl_4(**3**)]*

This compound was prepared analogously to [Cu_2Cl_4(**2**)], instead using **3** as the precursor. Yield: 85%, teal powder. ESI-MS: *m*/*z* 712.7 [M – Cl^-]$^+$. Anal. calcd for $C_{30}H_{36}Cl_4Cu_2N_6$·0.5H_2O: C, 47.50; H, 4.92; N, 11.08. Found: C, 47.53; H, 4.90; N, 10.75. Blue prisms of [Cu_2Cl_4(**3**)]·2MeOH formed upon slow diffusion of Et_2O vapor into a MeOH solution of the title compound. One crystal (0.493 × 0.308 × 0.202 mm^3) was subjected to X-ray diffraction studies.

*[$Cu_2(ClO_4)_4$(**2**)]*

$Cu(ClO_4)_2 \cdot 6H_2O$ (74.1 mg, 200 μmol) in boiling MeOH (1 mL) was treated with **2** (45.3 mg, 100 μmol) in MeOH (1 mL) with stirring. Upon cooling to room temperature, the deep blue mixture was treated with Et_2O (15 mL) and the resulting solid isolated by filtration and washed with Et_2O (2 mL) to give the product as a purple microcrystalline powder (93.4 mg, 95.6 μmol, 96%). ESI-MS: *m*/*z* 877.4 $[M - ClO_4^-]^+$, 389.4 $[M - 2ClO_4^-]^{2+}$. Anal. calcd for $C_{28}H_{32}Cl_4Cu_2N_6O_{16} \cdot 7H_2O$: C, 30.47; H, 4.20; N, 7.62. Found: C, 30.46; H, 3.65; N, 7.16.

$[Cu_2(ClO_4)_4(\mathbf{3})]$

This compound was prepared analogously to $[Cu_2(ClO_4)_4(\mathbf{2})]$, instead using **3** as the precursor. Addition of Et_2O was not required to precipitate the product. Yield: 82%, blue powder. ESI-MS: *m*/*z* 905.0 $[M - ClO_4^-]^+$, 403.0$[M - 2ClO_4^-]^{2+}$. Anal. calcd for $C_{30}H_{36}Cl_4Cu_2N_6O_{16} \cdot 4H_2O$: C, 33.44; H, 4.12; N, 7.80. Found: C, 33.40; H, 3.93; N, 7.68.

$[Cu_4(OH)_4(\mathbf{2})_2](BF_4)_4$

Under an atmosphere of dry N_2, $[Cu_2(MeCN)_2(\mathbf{2})](BF_4)_2$ (83.5 mg, 100 μmol) was dissolved in MeCN (1 mL). The solution was then cooled to –78°C and placed under O_2 (1 atm), after which the solution, now a blue-green color, was allowed to warm to room temperature. The solution was treated with Et_2O (5 mL) and allowed to stand at –28 °C for 1 h, the resulting solid isolated by filtration, washed with Et_2O (2 × 2 mL) and dried briefly to give the title compound as blue-green crystals (71.7 mg, 45.6 μmol, 91%). ESI-MS: *m*/*z* 699.2 $[M - 2BF_4^-]^{2+}$, 437.9 $[M - 3BF_4^-]^{3+}$, 306.6 $[M - \mathbf{2} - 2Cu^{2+} - 2OH^- - 4BF_4^-]^{2+}$. Anal. calcd for $C_{56}H_{68}B_4Cu_4F_{16}N_{12}O_4 \cdot H_2O$: C, 42.23; H, 4.43; N, 10.55. Found: C, 41.92; H, 4.17; N, 10.25.

$[Cu_4(OH)_4(\mathbf{3})_2](BF_4)_4$

This compound was prepared analogously to $[Cu_4(OH)_4(\mathbf{2})_2](BF_4)_4$, instead using $[Cu_2(MeCN)_2(\mathbf{3})](BF_4)_2$ as the precursor. Yield: 87%, blue-green crystals. ESI-MS: *m*/*z* 727.0 $[M - \mathbf{3} - 2Cu^{2+} - 2OH^- - 3BF_4^-]^+$, 320.0 $[M - \mathbf{3} - 2Cu^{2+} - 2OH^- - 4BF_4^-]^{2+}$. Anal. calcd for $C_{60}H_{76}B_4Cu_4F_{16}N_{12}O_4$: C, 43.24; H, 4.84; N, 10.08. Found: C, 43.43; H, 4.42; N, 9.69. Blue prisms of $[Cu_4(OH)_4(\mathbf{3})_2](BF_4)_4 \cdot 4MeCN \cdot 4H_2O$ formed upon slow diffusion of Et_2O vapor into a MeCN solution of the title compound. One crystal (0.1323 × 0.0621 × 0.0435 mm^3) was subjected to X-ray diffraction studies.

$[Cu_2Cl_4(\mathbf{4})]$

$CuCl_2 \cdot 2H_2O$ (17.0 mg, 100 μmol) in MeOH (0.5 mL) was treated with **4** (31.9 mg, 50 μmol) in warm MeOH (1 mL) with stirring. The blue solution was treated with Et_2O (15 mL) and the resulting solid that formed was isolated by filtration, washed with Et_2O (2 mL) and dried briefly to give the product as a baby blue powder (42.7 mg, 47 μmol, 94%). ESI-MS: *m*/*z* 871.2 $[M - Cl^-]^+$, 418.0 $[M - 2Cl^-]^{2+}$.

$[Cu_3Cl_6(\mathbf{4})]$

This compound was prepared analogously to $[Cu_3Cl_6(\mathbf{5})]$,[52] instead using **4** as the precursor. Yield: 81%, blue-green powder. ESI-MS: *m*/*z* 1005.8 $[M - Cl^-]^+$, 971.0 $[M - Cl - Cl^-]^+$, 871.0 $[M - Cu^{2+} - Cl^-]^+$, 485.5 $[M - 2Cl^-]^{2+}$, 418.0 $[M - Cu^{2+} - 4Cl^-]^{2+}$.

$[Cu_2Ag(NO_3)_5(\mathbf{4})]$

$Cu(NO_3)_2 \cdot 2.5H_2O$ (23.3 mg, 100 μmol) and $AgNO_3$ (8.5 mg, 50 μmol) in MeOH (1 mL) were treated with **4** (31.9 mg, 50 μmol) in warm MeOH (1 mL) with stirring in the absence of light. After 5 min, the teal mixture was treated with Et_2O (15 mL) and allowed to stand overnight in the absence of light. The solid that formed was isolated by filtration, washed with Et_2O (2 mL) and dried briefly to give the product as a green microcrystalline powder (49.9 mg, 42 μmol, 84%). ESI-MS: *m*/*z* 1121.2 $[M - NO_3^-]^+$, 529.5 $[M - 2NO_3^-]^{2+}$. Anal. calcd for $C_{28}H_{32}Cl_4Cu_2N_6O_{16} \cdot MeOH$: C, 38.53; H, 3.48; N, 14.98. Found: C, 38.59; H, 3.06; N, 14.48.

3.4 Ink Preparation Methods for General Electrochemical Investigations

A suspension of finely ground Vulcan XC-72 (90 mg, Cabot Corp.) and $Cu(ClO_4)_2 \cdot 6H_2O$ (18.5 mg, 50.0 μmol) in boiling MeOH (2 mL) was treated with ligand **1** (50.0 μmol), **2**/**3** (25.0 μmol), or **4**/**5** (16.7 μmol) in MeOH (1 mL). The mixture was briefly sonicated, treated with Et_2O (15 mL), and the solids were isolated by centrifugation before being dried in vacuo (80 °C, 3 h). A fraction (3.6 mg) of the resulting carbon-supported catalyst was suspended in EtOH (1 mL) and treated with Nafion (4 μL, 5 wt% in alcohols, Sigma-Aldrich), the resulting slurry being sonicated for 30 min. This ink (10 μL) was then deposited on a glassy carbon (GC) electrode, which was dried under a stream of Ar.

3.5 Ink Preparation Methods for Anion Effect Study

Inks of monocopper complexes were prepared from *in situ* generated species. Thus, solutions of **1** (3.4 mg, 17 μmol) in EtOH (2.5 mL) were treated separately with $Cu(ClO_4)_2 \cdot 6H_2O$ (6.3 mg, 17 μmol), $Cu(NO_3)_2 \cdot 2.5H_2O$ (4.0 mg, 17 μmol), $CuSO_4 \cdot 5H_2O$ (4.2 mg, 17 μmol), $CuCl_2$ (2.3 mg, 17 μmol), $Cu(HCO_2)_2 \cdot xH_2O$ (4.0 mg, ~17 μmol) and $Cu(OAc)_2 \cdot H_2O$ (3.4 mg, 17 μmol).

After sonicating each solution for 10 min, finely ground Vulcan XC-72 (9 mg, Cabot Corp.) was added, and the suspensions sonicated for a further 10 min. A solution of Nafion (10 μL, 5 wt% in alcohols, Sigma-Aldrich) was added to the suspensions, and the resulting slurries sonicated for 30 min. The inks (10 μL) were then deposited on a GC electrode, which was dried under a stream of Ar.

3.6 Structure Determination by X-ray Crystallography

Single-crystal X-ray diffraction data were collected on compounds $[Cu_2Cl_4(\mathbf{3})]\cdot 2H_2O$ and $[Cu_4(OH)_4(\mathbf{3})_2](BF_4)_4\cdot 4MeCN\cdot 4H_2O$ with the use of graphite-monochromatized Mo Kα radiation (λ = 0.71073 Å) at 168 K and 183 K respectively. For each crystal, four ω scan frame series were collected on a Bruker platform APEX II CCD diffractometer.[55] The collection of intensity data, cell refinement and data reduction were carried out with the APEX2 suite of programs.[55] Face-indexed absorption corrections were performed numerically with the use of the program XPREP.[56] Then the program SADABS was employed to make incident beam and decay corrections.[56] The structures were solved with the direct methods program SHELXS and refined with the full-matrix least-squares program SHELXL of the SHELXTL suite of programs.[57] Both structures contained disordered solvate molecules whose positions could not be solved, so the "squeeze" routine in the program Platon was used to remove the solvate contributions from the structures.[58] Additional experimental details and selected metrical data are shown in Tables 3.1 and 3.2.

Table 3.1. Crystal Data and Structure Refinement.

	$[Cu_2Cl_4(\mathbf{3})]\cdot 2H_2O$	$[Cu_4(OH)_4(\mathbf{3})_2](BF_4)_4\cdot 4MeCN\cdot 4H_2O$
formula mass (amu)	813.61	2000.21
space group	P2(1)/c	Pī
Z	2	1
a (Å)	11.361(2)	9.8961(8)
b (Å)	11.795(2)	16.716(1)
c (Å)	14.008(2)	16.885(1)
α (°)	90	62.202(1)
β (°)	105.165(2)	87.664(1)
γ (°)	90	73.505(1)
V (Å^3)	1811.6(5)	2355.2(3)
T (K)	183(2)	168(2)
λ (Å)	0.71073	0.71073
ρ_c (g cm^{-3})	1.492	1.410
μ (cm^{-1})	15.07	9.8
$R(F)^a$	0.0374	0.0431
$R_w(F^2)^b$	0.1094	0.1257

[a] $R(F) = \Sigma||F_o| - |F_c||/\Sigma|F_o|$ for $F_o^2 > 2\sigma(F_o^2)$.
[b] $R_w(F_o^2) = [\Sigma\, w(F_o^2 - F_c^2)^2/\Sigma w F_o^4]$, $w^{-1} = \sigma^2(F_o^2) + (q(F_o^2 + 2F_c^2)/3)^2 + r((F_o^2 + 2F_c^2)/3)$ for $F_o^2 \geq 0$;
$w^{-1} = \sigma^2(F_o^2)$ for $F_o^2 < 0$.
For $[Cu_2Cl_4(\mathbf{3})]$, q = 0.0640, r = 0.5623. For $[Cu_4(OH)_4(\mathbf{3})_2](BF_4)_4$, q = 0.0750, r = 0.

Table 3.2. Hydrogen bond distances (Å) and angles (°) for $[Cu_4(OH)_4(\mathbf{3})_2](BF_4)_4\cdot 4MeCN\cdot 4H_2O$.

D-H...A	d(D-H)	d(H···A)	d(D···A)	<(DHA)
O(2)-H(2)...F(4)	0.83(1)	2.10(2)	2.879(5)	155(4)
O(2)-H(2)...F(4B)	0.83(1)	2.14(2)	2.95(2)	165(4)
O(1)-H(1)...F(3)#2	0.82(1)	2.17(2)	2.960(8)	160(3)
O(1)-H(1)...F(3B)#2	0.82(1)	2.07(2)	2.87(1)	164(3)

Symmetry transformations used to generate equivalent atoms:
#1 -x+1,-y+1,-z #2 x-1,y,z

3.7 Cu Complex of DPA as T3 Site Mimic

3.7.1 Voltammetry under Ar

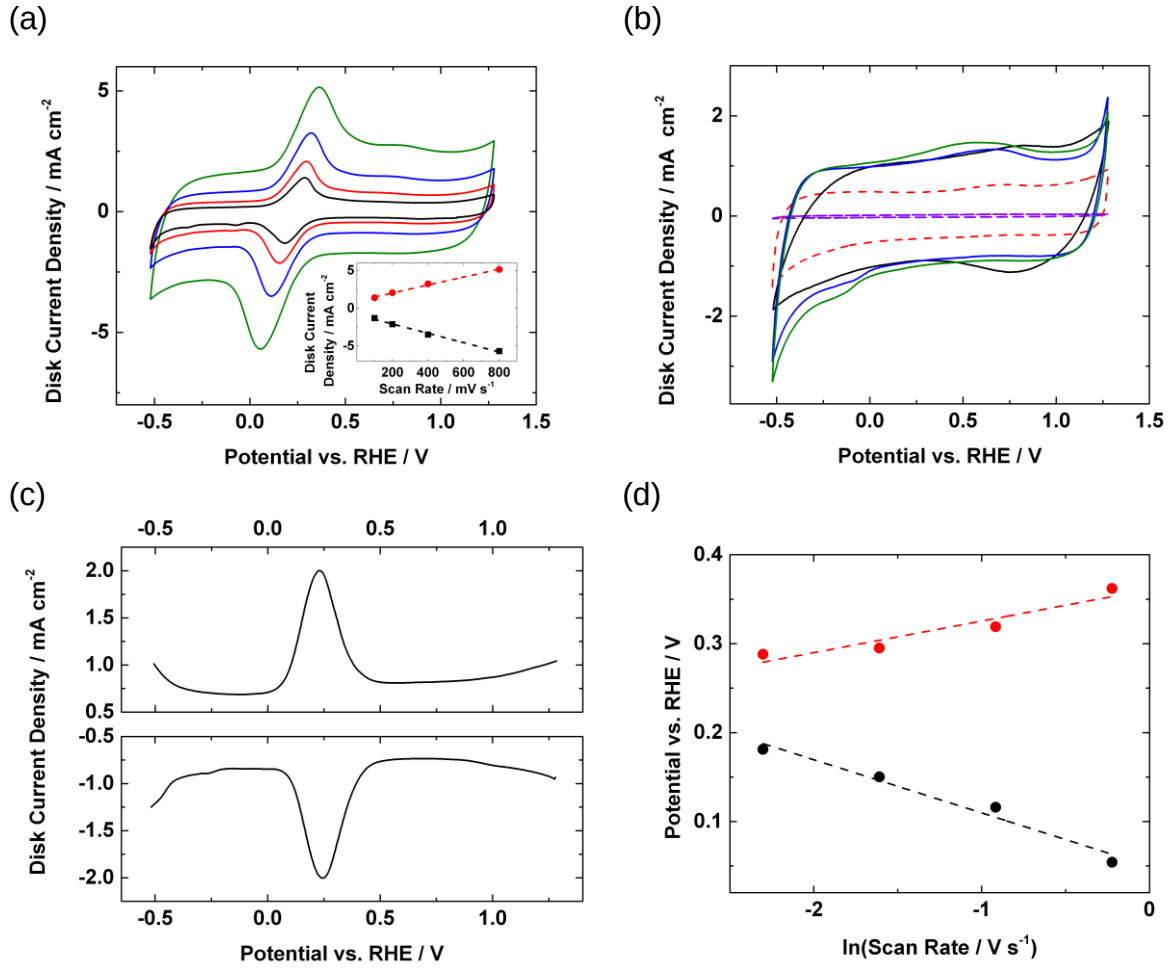

Figure 3.7a. Cyclic voltammograms (CVs) of $[Cu(\mathbf{1})]^{2+}$ with scan rates of 100 (black), 200 (red), 400 (blue), 800 (green) mV/s. Randles-Sevcik plots (inset) of $[Cu(\mathbf{1})]^{2+}$ projected from the cathodic (black dots) and anodic (red dots) peak current densities. **Figure 3.7b.** CVs of **1** (black), **3** (blue), **4** (green), Vulcan-XC72 blank (red, dash), and bare GC electrode (purple, dash) with scan rates of 200 mV/s. **Figure 3.7c.** Differential pulse voltammogram (DPV) of $[Cu(\mathbf{1})]^{2+}$. **Figure 3.7d.** Plot of cathodic (black) and anodic (red) peak potential of $[Cu(\mathbf{1})]^{2+}$ vs. natural log of scan rate. Studies were conducted in pH 4 Ar-sparged Britton-Robinson buffer.

Towards a functional model of laccase, we tested the feasibility of using $[Cu(\mathbf{1})]^{2+}$ to mimic the T3 unit of the tricopper active site. We collected voltammograms of $[Cu(\mathbf{1})]^{2+}$ (Figure 3.7a) and **1** (Figure 3.7b, black trace), both supported on XC-72 carbon in Ar-sparged pH 4

Britton-Robinson buffer. Whereas free DPA and other DPA derivatives are redox-inactive, $[Cu(\mathbf{1})]^{2+}$ exhibits a reversible wave at a midpoint potential $E_{½}$ = +0.23 V vs. RHE, this wave being assigned to the Cu(I/II) couple. This behavior is comparable to that for $[Cu(TPA)(H_2O)]^{2+}$ ($E_{½}$ = +0.23 V) studied previously.[26] Differential pulse voltammetry (DPV) shows a single redox wave centered at +0.23 V (Figure 3.7c), confirming the peak observed by cyclic voltammetry (CV).

The inset to Figure 3.7a shows the Randles-Sevcik plot obtained for $[Cu(\mathbf{1})]^{2+}$. The cathodic (black) and anodic (red) absolute peak currents were found to scale linearly with scan rate, indicating the analyte to be surface-bound, as reported for $[Cu(TPA)(H_2O)]^{2+}$.[26] Interestingly, the potentials of $[Cu(\mathbf{1})]^{2+}$ redox peaks are dependent on ln(scan rate), although $E_{½}$ values remain constant. Figure 3.7d shows the linear dependence of both the cathodic (black) and anodic (red) absolute peak potentials with ln(scan rate). This linearity is interpreted using expressions (1) and (2) derived from the Butler-Volmer equation to calculate symmetry factors (αn and $(1-\alpha)n$), charge transfer coefficient (α), and apparent electron transfer rate constant (k_{app}).[59,60] Here, F is the Faraday constant, $\upsilon_{c,a}$ are the cathodic and anodic scan rates, respectively, T is the temperature, and R is the gas constant.

$$E_{\mathrm{pc}} = E_{\mathrm{c}}^{0} - \left(\frac{\mathrm{RT}}{\alpha n \mathrm{F}}\right) \ln\left[\frac{\alpha n \mathrm{F} \upsilon_{\mathrm{c}}}{\mathrm{RT} k_{app}}\right] \qquad (1)$$

$$E_{\mathrm{pa}} = E_{\mathrm{a}}^{0} - \left(\frac{\mathrm{RT}}{(1-\alpha) n \mathrm{F}}\right) \ln\left[\frac{(1-\alpha) n \mathrm{F} \upsilon_{\mathrm{a}}}{\mathrm{RT} k_{app}}\right] \qquad (2)$$

The cathodic αn and the anodic $(1-\alpha)n$ were calculated from the slopes of the black and red dashed lines to be 0.43 and 0.72 respectively (Figure 3.7d). The sum of the two symmetry

factors (1.15) is close to that expected for a reversible $1e^-$ redox event (1.0).[61] Assuming a single electron transfer (n = 1), the average charge transfer coefficient (α = 0.35) indicates the energy barrier of the Cu(I/II) couple to be slightly asymmetric.[62] The y-intercepts correspond to the rate constants with cathodic k_{app} = 1.5 s^{-1} and anodic k_{app} = 2.0 s^{-1}. These rate constants are very low relative to 6×10^8 s^{-1} for an outer-sphere electron transfer (ET) process of ferrocene/ferrocenium ($Fc^{0/+}$) tethered to a Au surface with a short-chain thiolate,[63] and even small relative to 73.7 s^{-1} for a proton-coupled electron transfer (PCET) process for a quinone-derivative tethered to a Au electrode via a short-chain thiolate.[61] However, the rates seen in Cu complexes of **1**, **2**, **3**, **4**, and **5** (Figure 3.8) are comparable to those obtained for $Fc^{0/+}$ linked to Au via a *long-chain* thiolate (2.1 s^{-1}).[64] The slowness is likely associated with the complex undergoing an inner-sphere ET process with major reorganization in coordination geometry, as suggested by the asymmetric energy barrier of the Cu(I/II) couple.[65,66] Also, ET rate may be further attenuated by the nature of a heterogeneous electrode surface with physisorbed Cu complexes bound inside a carbon-Nafion matrix.

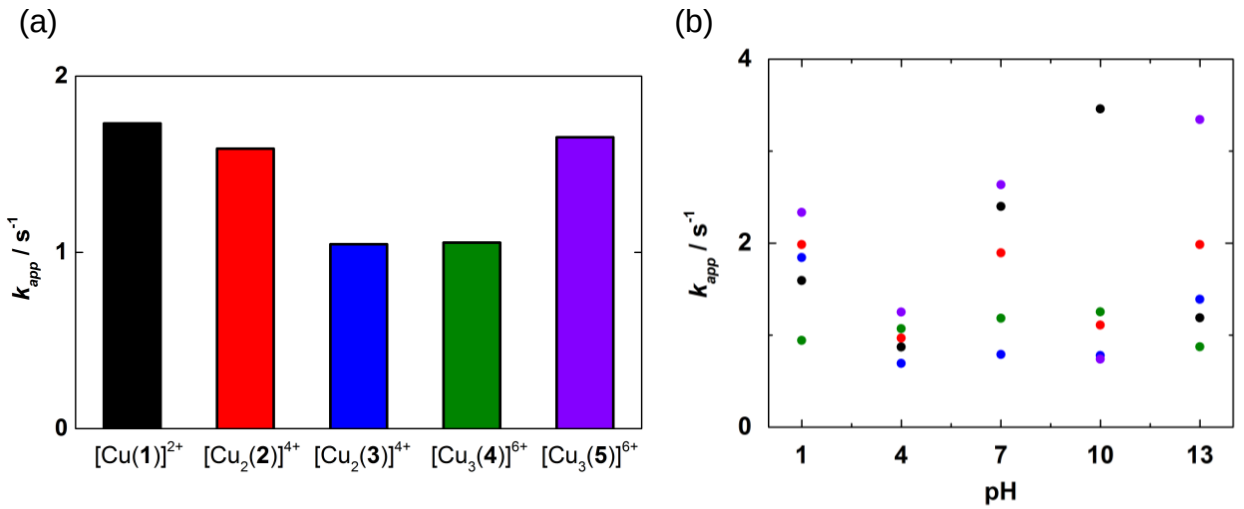

Figure 3.8. (a) Apparent electron transfer rate constants (k_{app}) of $[Cu(\mathbf{1})]^{2+}$ (black), $[Cu_2(\mathbf{2})]^{4+}$ (red), $[Cu_2(\mathbf{3})]^{4+}$ (blue), $[Cu_3(\mathbf{4})]^{6+}$ (green), and $[Cu_3(\mathbf{5})]^{6+}$ (purple). (b) k_{app} of these complexes versus pH.

3.7.2 Rotating Ring-Disk Electrode (RRDE) Measurements under O_2

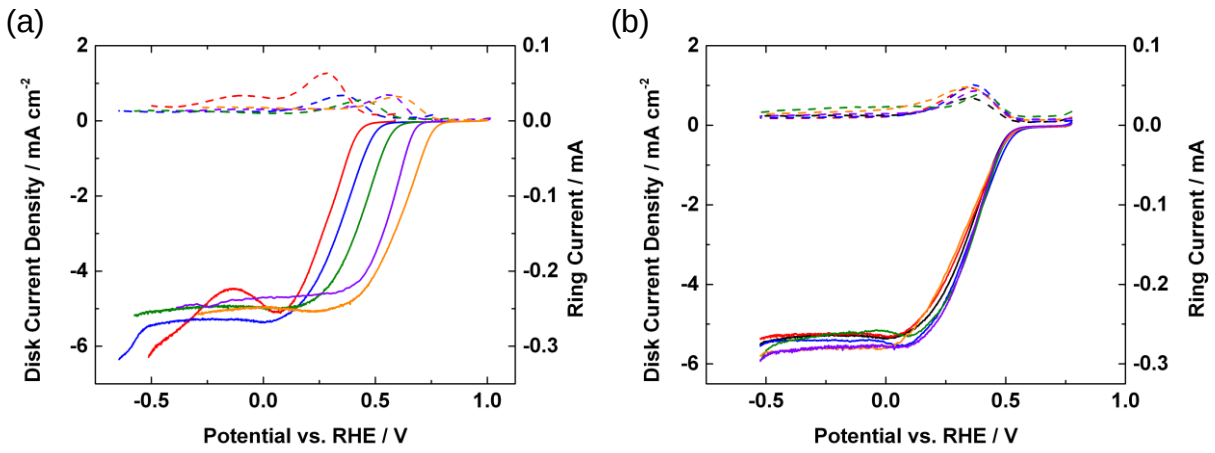

Figure 3.9a. Rotating ring-disk electrode (RRDE) experiments of $[Cu(\mathbf{1})]^{2+}$ in pH 1 (red), 4 (blue), 7 (green), 10 (purple), and 13 (orange) O_2-sparged solutions at 1600 rpm with a scan rate of 10 mV/s. **Figure 3.9b.** RRDE experiments of $[Cu(\mathbf{1})]^{2+}$ in pH 4 O_2-sparged Britton-Robinson buffer solution at 1600 rpm with a scan rate of 10 mV/s with ClO_4^- (black), NO_3^- (red), SO_4^{2-} (blue), Cl^- (green), HCO_2^- (orange), and AcO^- (purple) as counterions.

Figure 3.9 depicts RRDE measurements obtained for Vulcan-supported $[Cu(\mathbf{1})]^{2+}$ at various pH values and in the presence of various anions. $[Cu(\mathbf{1})]^{2+}$ exhibits an ORR onset potential, which is defined as the potential at which 5% of the diffusion-limited current is reached, at 0.41 V vs. RHE at pH 1 (Figure 3.9a). The observed ORR onset potential for $[Cu(\mathbf{1})]^{2+}$ is 120 mV more negative than $[Cu(TPA)(H_2O)]^{2+}$, which is presently the best synthetic Cu ORR catalyst at pH 1.[26] In the pH 4-7 range, $[Cu(\mathbf{1})]^{2+}$ exhibits ORR onset potentials ~100 mV more negative than [Cu(2,9-dimethyl-1,10-phenanthroline)]$^{2+}$ on graphite, which is one of the Cu ORR catalysts with the lowest ORR overpotential in the pH 4-7 range.[67-70] In the pH 10 to 13 range, $[Cu(\mathbf{1})]^{2+}$ exhibits ORR onset potentials ~140 mV more negative than the dinuclear Cu complex of 3,5-diamino-1,2,4-triazole, which is the benchmark synthetic Cu ORR catalyst between pH 10-13.[71] The ORR activity of $[Cu(\mathbf{1})]^{2+}$ is unaffected by changing the counteranion

used in the preparation step, e.g. ClO_4^-, NO_3^-, SO_4^{2-}, Cl^-, HCO_2^-, and AcO^- (Figure 3.9b) – neither Lewis basicity nor charge has any effect on ORR activity.

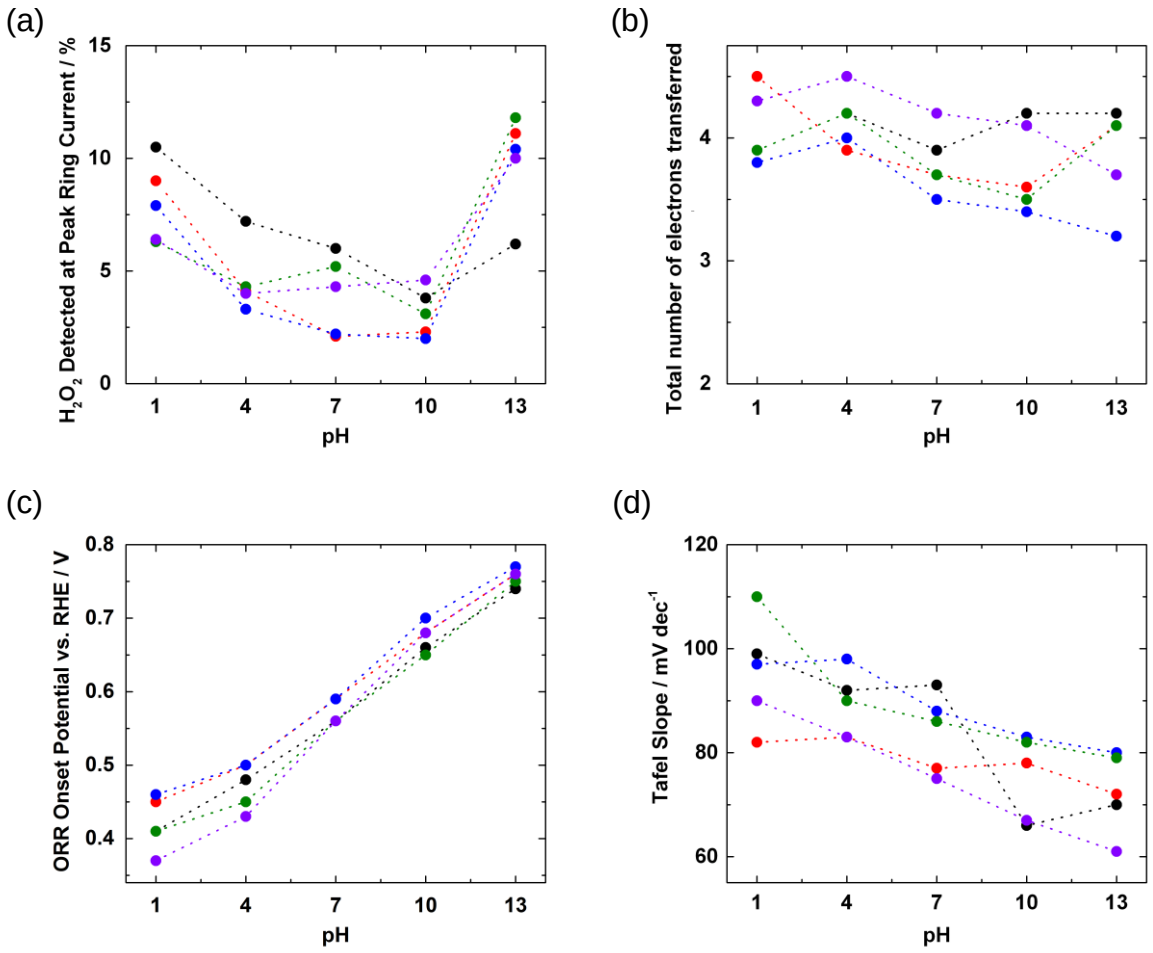

Figure 3.10. Plots of (a) peak percentages of H_2O_2 detected by the Pt ring, (b) total number of electrons transferred per catalytic cycle in the diffusion-limited region calculated from Koutecky-Levich analyses, (c) ORR onset potentials obtained from RRDE measurements, and (d) Tafel slopes acquired from linear sweep voltammograms (LSVs) of $[Cu(\mathbf{1})]^{2+}$ (black), $[Cu_2(\mathbf{2})]^{4+}$ (red), $[Cu_2(\mathbf{3})]^{4+}$ (blue), $[Cu_3(\mathbf{4})]^{6+}$ (green), and $[Cu_3(\mathbf{5})]^{6+}$ (purple) vs. pH of the bulk solution.

As the pH is varied between 1-13 for $[Cu(\mathbf{1})]^{2+}$, the maximum amount of H_2O_2 detected ranges from 13% to 5.4% (Figure 3.10a, black), while the amount of H_2O_2 detected in the diffusion-limited region ranges from 3.0% to 1.0%. The complex $[Cu(TPA)(H_2O)]^{2+}$ exhibited

comparable results.[26] Koutecky-Levich analysis of the RRDE data allows the determination of the number of electrons transferred during the ORR (Figure 3.11). Over the pH 1-13 range, about 4 e^- are transferred per catalytic cycle in the diffusion-limited current region, indicating that $[Cu(\mathbf{1})]^{2+}$ reduces O_2 to H_2O (Figure 3.10b, black). A correlation exists between the ORR onset potentials of the present system and the pH of the bulk solution (Figure 3.10c, black), with the potential scaling linearly by about 30 mV/pH. This correlation suggests that the rate-determining step involves protonation, as is characteristic of PCET processes.[72-77] Indeed, the onset potentials of all non-precious metal catalysts examined to date exhibit pH-dependence.[23,78,79] Notably, the shape of the voltammogram varies with pH (Figure 3.9a). In acidic medium, $[Cu(\mathbf{1})]^{2+}$ exhibits a Tafel slope of about 100 mV/dec (Figure 3.10d, black), which is close to 120 mV/dec. The value 120 mV/dec is indicative of a 1 e^- rate-determining step as observed for $[Cu(\mathbf{1})]^{2+}$ at pH 1.[26] At pH 10-13, the Tafel slopes of $[Cu(\mathbf{1})]^{2+}$ decrease to about 70 mV/dec (Figure 3.10d, black), consistent with a 2 e^- RDS. This change was not observed for Cu systems of TPA and related derivatives.[27] A change in the Tafel slope is usually associated with a change in mechanism.[80]

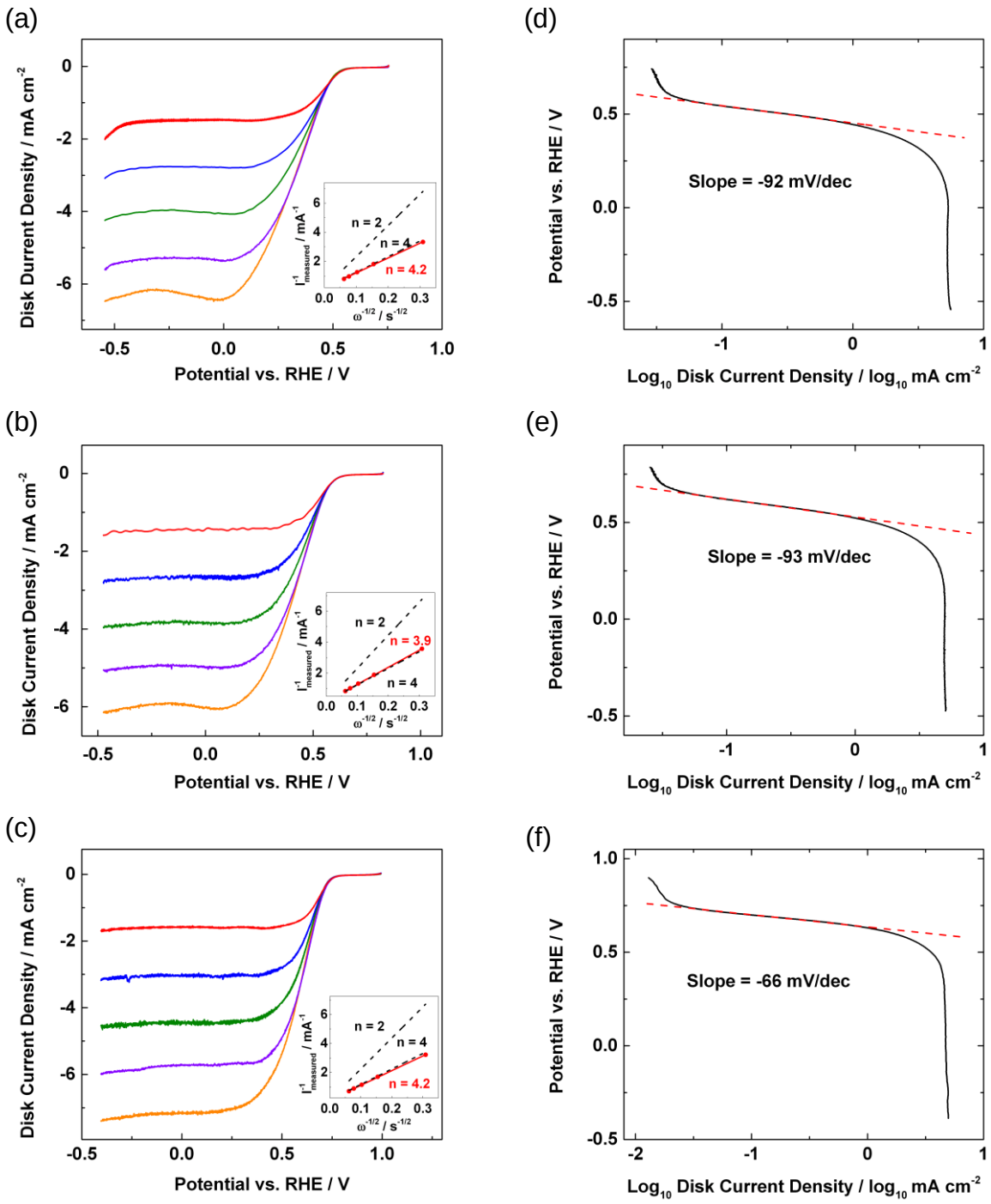

Figure 3.11. RDE voltammograms and Koutecky-Levich plots (inset) of $[Cu(\mathbf{1})]^{2+}$ supported on Vulcan XC-72 in (a) pH 4, (b) pH 7, and (c) pH 10 O_2-saturated Britton-Robinson buffer solutions with a scan rate of 10 mV/s at 100 (red), 400 (blue), 900 (green), 1600 (violet), and 2500 rpm (orange). Tafel plots $[Cu(\mathbf{1})]^{2+}$ supported on Vulcan XC-72 in (d) pH 4, (e) pH 7, and (f) pH 10 O_2-saturated Britton-Robinson buffer solutions (10 mV/s, 1600 rpm).

3.7.3 Summary of Mononuclear Cu Complex

$[Cu(\mathbf{1})]^{2+}$ exhibits a well-defined redox couple under an Ar atmosphere and catalyzes the ORR at an overpotential slightly larger than the related $[Cu(TPA)(H_2O)]^{2+}$. Both the RRDE measurements and the Koutecky-Levich analysis suggest that $[Cu(\mathbf{1})]^{2+}$ effects 4 e^- reduction of O_2, mirroring the activity of the analogous $[Cu(TPA)(H_2O)]^{2+}$. In acidic media, the Tafel behavior of $[Cu(\mathbf{1})]^{2+}$ is comparable to that of $[Cu(TPA)(H_2O)]^{2+}$, further supporting the use of DPA to replace TPA as a viable T3-site mimic for the rest of this study.

3.8 Dinuclear Systems - Cu Complexes with Linked DPA Units

3.8.1 Voltammetry under Ar

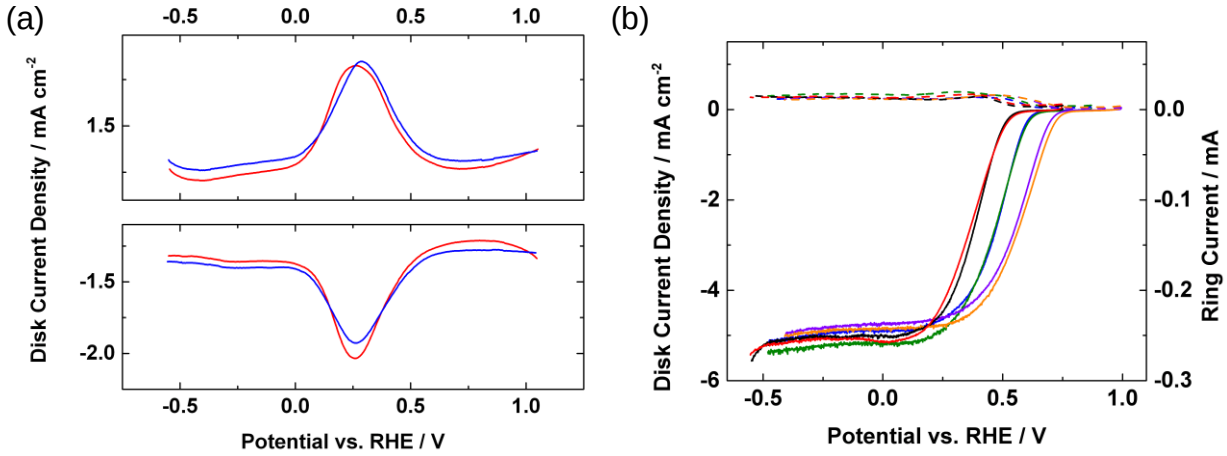

Figure 3.12a. DPVs for dinuclear complexes $[Cu_2(\mathbf{2})]^{4+}$ (red) and $[Cu_2(\mathbf{3})]^{4+}$ (blue) in pH 4 Ar-sparged Britton-Robinson buffer solution. **Figure 3.12b.** RRDE experiments for $[Cu_2(\mathbf{2})]^{4+}$ in pH 4 (black), pH 7 (blue), and pH 10 (purple), and $[Cu_2(\mathbf{3})]^{4+}$ in pH 4 (red), pH 7 (green), and pH 10 (orange) O_2-sparged Britton-Robinson buffer solution at 1600 rpm with a scan rate of 10 mV/s.

The Cu—Cu cooperativity implicit in the multicopper oxidases inspired us to test ligands incorporating two DPA moieties. Figure 3.12a shows the DPVs of the dicopper(II) complexes of **2** and **3**. Both complexes exhibit a single redox wave at about 0.25 V vs. RHE, a value similar to that for $[Cu(\mathbf{1})]^{2+}$ system (Figure 3.7c), and thus indicating that the sites are equivalent.

3.8.2 RRDE Measurements under O_2

Figure 3.12b presents LSVs and RRDE measurements of $[Cu_2(\mathbf{2})]^{4+}$ and $[Cu_2(\mathbf{3})]^{4+}$. The ORR onset potentials and the diffusion-limited currents for $[Cu_2(\mathbf{2})]^{4+}$ (Figure 3.12b, black) and $[Cu_2(\mathbf{3})]^{4+}$ (Figure 3.12b, red) are similar to those of $[Cu(\mathbf{1})]^{2+}$ at pH 4 (Figure 3.9a, blue). At pH 7 and 10, the ORR onset potentials for $[Cu_2(\mathbf{2})]^{4+}$ (Figure 3.12b, blue and purple) and $[Cu_2(\mathbf{3})]^{4+}$ (Figure 3.12b, green and orange) are about 20 mV more positive than those of $[Cu(\mathbf{1})]^{2+}$ (Figure 3.9a, green and purple). However, the slight differences observed in the diffusion-limited currents can be attributed to variation in different ink casts onto the GC electrode. The dicopper complexes produce less H_2O_2 (Figure 3.12b, dashed lines), indicating that they mediate 4 e^- reduction even in the Tafel region.

Figure 3.10b summarizes the Koutecky-Levich results for $[Cu_2(\mathbf{2})]^{4+}$ (red) and $[Cu_2(\mathbf{3})]^{4+}$ (blue). The complexes catalyze 4 e^- reduction of O_2 in the diffusion-limited region (Figures 3.13 and 3.14), with a pH-dependence (~30 mV/pH, Figure 3.10c) for the ORR onset in both $[Cu_2(\mathbf{2})]^{4+}$ (red) and $[Cu_2(\mathbf{3})]^{4+}$ (blue) systems. As expected, the Tafel slopes for $[Cu_2(\mathbf{2})]^{4+}$ (red) and $[Cu_2(\mathbf{3})]^{4+}$ (blue) vary with the bulk solution pH (Figure 3.10d). Taken together, these results show that the ORR activities of the dicopper complexes are similar if not identical to that of the mononuclear system.

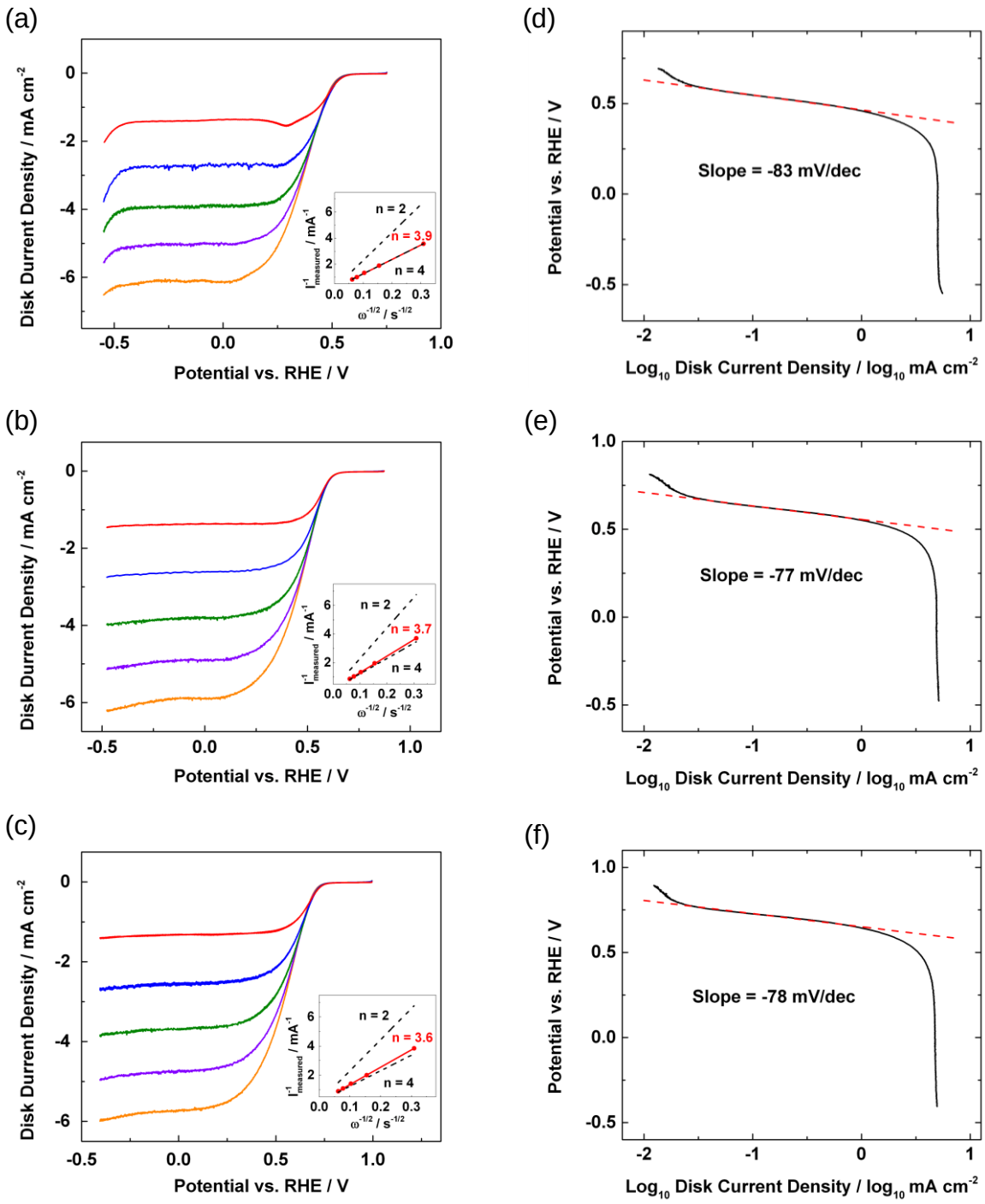

Figure 3.13. RDE voltammograms and Koutecky-Levich plots (inset) of $[Cu_2(\mathbf{2})]^{4+}$ supported on Vulcan XC-72 in (a) pH 4, (b) pH 7, and (c) pH 10 O_2-saturated Britton-Robinson buffer solutions with a scan rate of 10 mV/s at 100 (red), 400 (blue), 900 (green), 1600 (violet), and 2500 rpm (orange). Tafel plots of $[Cu_2(\mathbf{2})]^{4+}$ on Vulcan XC-72 in (d) pH 4, (e) pH 7, and (f) pH 10 O_2-saturated Britton-Robinson buffer solutions (10 mV/s, 1600 rpm).

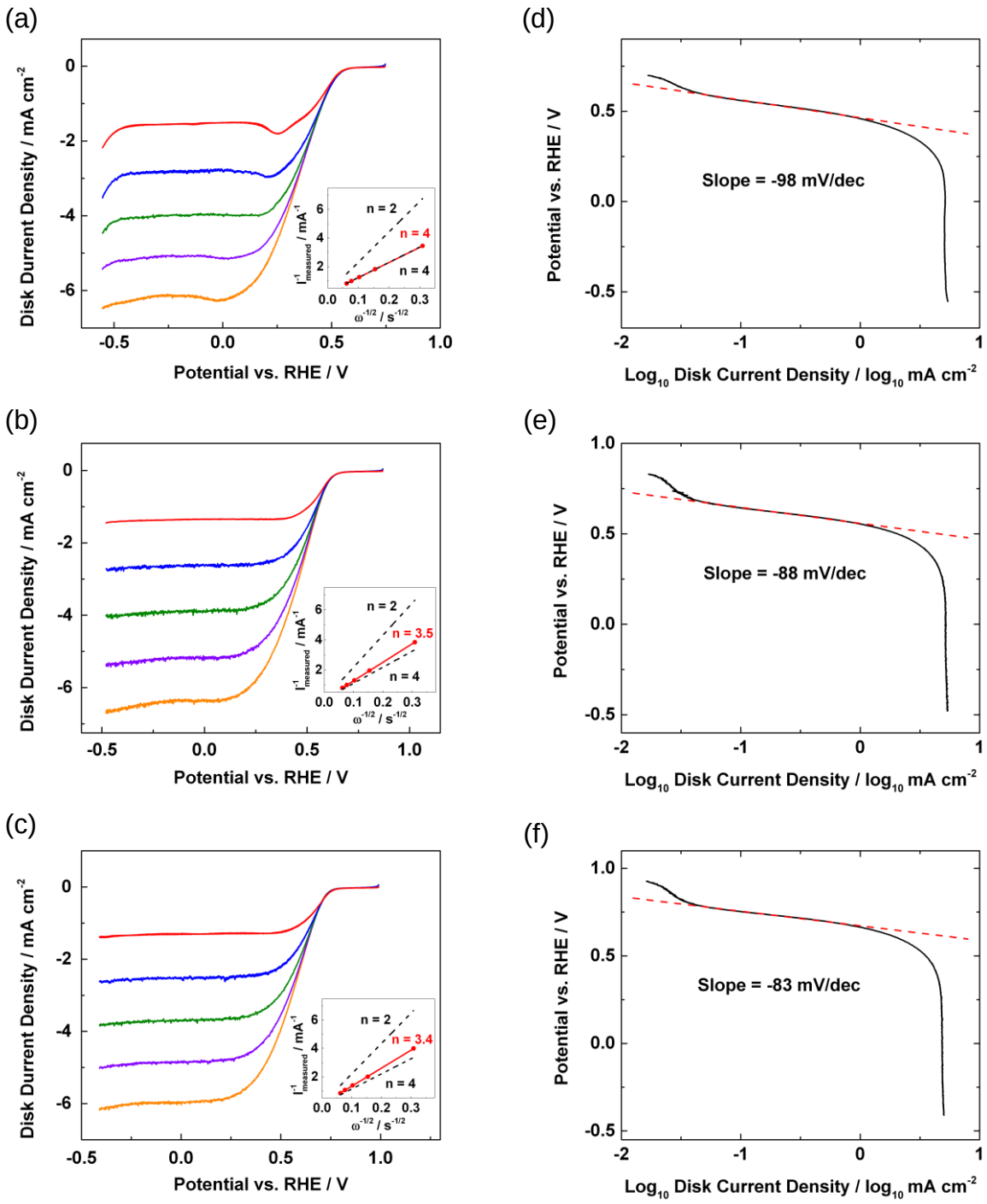

Figure 3.14. RDE voltammograms and Koutecky-Levich plots (inset) of $[Cu_2(\mathbf{3})]^{4+}$ supported on Vulcan XC-72 in (a) pH 4, (b) pH 7, and (c) pH 10 O_2-saturated Britton-Robinson buffer solutions with a scan rate of 10 mV/s at 100 (red), 400 (blue), 900 (green), 1600 (violet), and 2500 rpm (orange). Tafel plots of $[Cu_2(\mathbf{3})]^{4+}$ supported on Vulcan XC-72 in (d) pH 4, (e) pH 7, and (f) pH 10 O_2-saturated Britton-Robinson buffer solutions (10 mV/s, 1600 rpm).

3.8.3 Crystal Structures of Dinuclear Cu Complex of 3 Before and After Oxygenation

To gain further insights into the reactivity displayed by $[Cu_2(\mathbf{2})]^{4+}$ and $[Cu_2(\mathbf{3})]^{4+}$, two examples of these species were examined crystallographically. The structure of $[Cu_2Cl_4(\mathbf{3})]$ reveals a centrosymmetric complex with two equivalent Cu centers linked by the polymethylene chain (Figure 3.15).

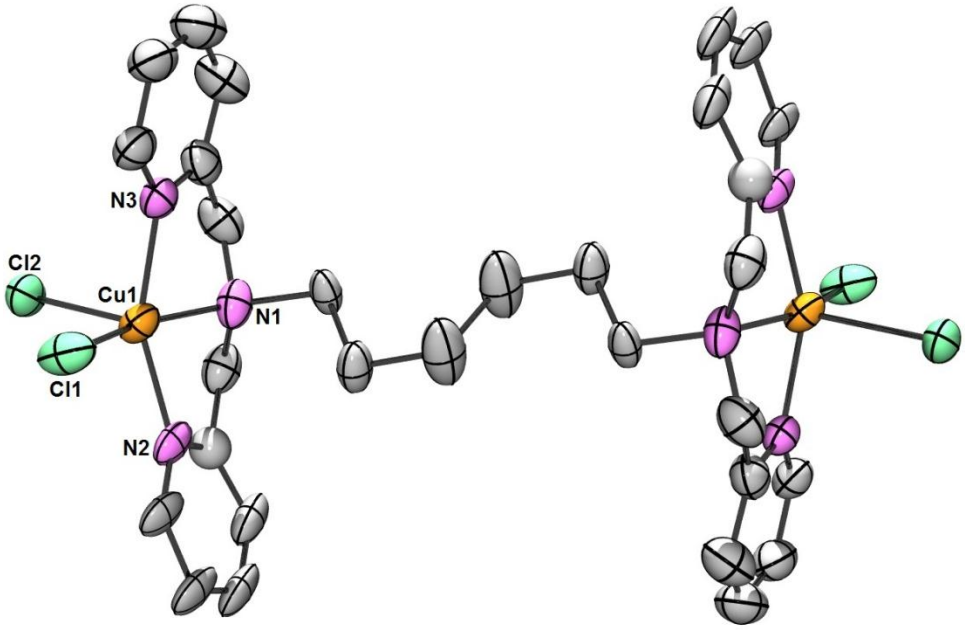

Figure 3.15. ORTEP of $[Cu_2Cl_4(\mathbf{3})]\cdot 2H_2O$ with ellipsoids drawn at the 50% probability level. The solvate molecules and H atoms are omitted for clarity. Selected distances (Å): Cu1-N1, 2.058(2); Cu1-N2, 2.026(6); Cu1-N3, 2.013(2); Cu1-Cl1, 2.254(1); Cu1-Cl2, 2.511(4). Selected angles (°): Cl1-Cu1-N1, 160.87(7); N2-Cu1-N3, 155.9(5).

The coordination geometry of each Cu(II) is best described as a distorted square pyramidal, with the Addison τ parameter (the difference between the angles Cl1-Cu1-N1 and N2-Cu1-N3 divided by 60°) being 0.08, indicating a low degree of trigonality. Jahn-Teller distortion is indicated by the apical Cl2 being more distant from the metal center (2.511(4) Å)

than is the basal Cl1 (2.254(1) Å). The inter-copper distance is large at 10.500(8) Å but the linker is flexible.

As expected for copper(II) species, [Cu_2Cl_4(**3**)] is unreactive towards O_2. The relevant reactivity was thus sought with the analogous dicopper(I) complex, which was generated by combining [$Cu(MeCN)_4$]BF_4 and **3** (0.5 equiv.). The product [$Cu_2(MeCN)_2$(**3**)]$(BF_4)_2$ is a pale yellow solid, exhibiting characteristic ^{1}H NMR and ESI-MS data. The material is extremely sensitive to air. Exposure of [$Cu_2(MeCN)_2$(**3**)]$(BF_4)_2$ in MeCN solution to O_2 (1 atm) instantaneously afforded a green-blue solution, an identical observation also being found if the experiment was conducted at low temperature (–78 °C). Analysis of the solution by ESI-MS allowed for the detection of the cation [[$Cu_2(OH)_2$(**3**)]BF_4]$^+$ (*m*/*z* 727.0). This dinuclear species was thought to form upon the cleavage of O_2 by the cooperative active of two copper species, the metal centers of which are concomitantly oxidized to the Cu(II) state. The origin of the O*H*$^-$ atoms is unclear, and H· abstraction from MeCN or adventitious H_2O cannot be ruled out. Layering the MeCN solution with Et_2O garnered blue-green single crystals suitable for X-ray diffraction, the results of this analysis being presented in Figure 3.16.

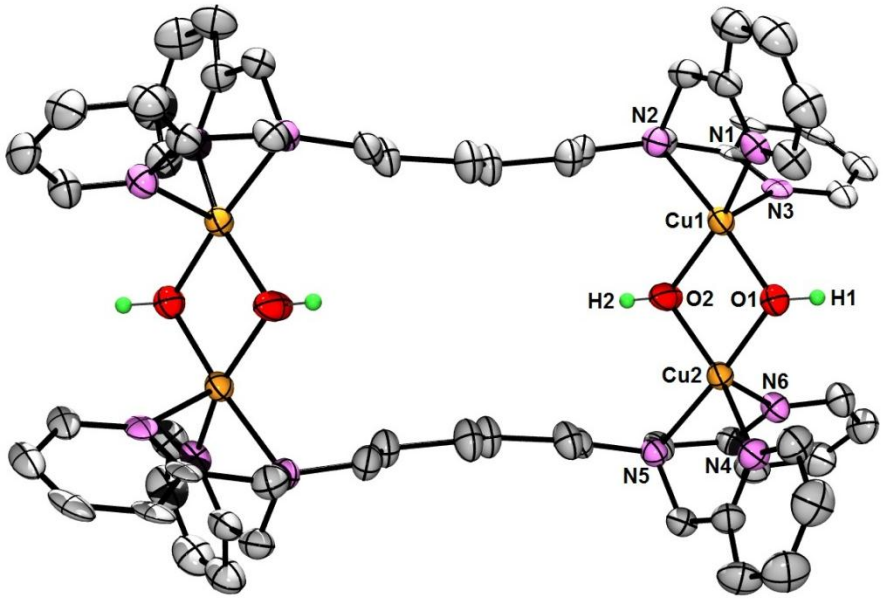

Figure 3.16. ORTEP of $[Cu_4(OH)_4(\mathbf{3})_2](BF_4)_4 \cdot 4MeCN \cdot 4H_2O$ with ellipsoids drawn at the 50% probability level. The BF_4^- anions, solvate molecules and non-hydroxyl H atoms are omitted for clarity. Selected distances (Å): Cu1-O1, 1.926(2); Cu1-O2, 1.927(2); Cu1-N1, 2.010(3); Cu1-N2, 2.049(2); Cu1-N3, 2.272(5); Cu2-O1, 1.938(2); Cu2-O2, 1.924(2); Cu2-N4, 1.997(4); Cu2-N5, 2.071(2); Cu2-N6, 2.254(2); Cu1-Cu2, 2.9361(5), 10.0917(6). Selected angles (°): Cu1-O1-Cu2, 98.92(9); Cu1-O2-Cu2, 99.35(9); O1-Cu1-N1, 96.2(2); O2-Cu1-N3, 105.8(4); O1-Cu2-N4, 95.8(3); O2-Cu2-N5, 97.36(8).

While disordered solvent, counterions and polymethylene chains resulted in the crystal data being relatively poor, the connectivity of the rather surprising $[Cu_4(OH)_4(\mathbf{3})_2](BF_4)_4$ product could be ascertained. The species can be viewed as a tetranuclear metallacycle incorporating two **3** ligands and four copper centers, each being ligated to a DPA fragment as well as two bridging OH^- groups in a distorted square pyramidal coordination geometry ($\tau_{Cu1} = 0.26$, $\tau_{Cu2} = 0.26$). The hydroxyl H atoms were located in the difference map, with further confirmation being found in O-H···F-BF_3^- interactions (O2-F4 @ 2.879(6) Å) and the average Cu-O distances (1.929(8) Å). Thus, the metallacycle features two Cu(II)(μ-$OH)_2$Cu(II) units that, along with related Cu(II)(μ-O_2)Cu(II) and Cu(III)(μ-$O)_2$Cu(III) cores, are common motifs in copper enzymes.[17,81-83] The tetranuclear solid state structure contrasts the dinuclear species identified by ESI-MS and it is

possible that dinuclear species 'wraps' together to bind O_2, and further dimerizes to relieve ring strain. Alternatively, the dicopper(I) complex elongates (the polymethylene chain adopts a more staggered conformation relative to that in $[Cu_2Cl_4(\mathbf{3})]\cdot 2H_2O$) and functions in concert with an additional dicopper species. It is interesting to note that exposure of the shorter analog $[Cu_2(MeCN)_2(\mathbf{2})](BF_4)_2$ to O_2 afforded, in addition to an ion assigned to a dihydroxo dicopper(II) fragment (*m*/*z* 306.6), allowed for detection of the tetracopper complex (*m*/*z* 699.2, 437.9). Clearly, the shorter derivative favors the formation of a tetranuclear species, as a single dinculear species with a shorter linker is not suited to 'wrapping' around to bind O_2.

3.8.4 Summary of Dinuclear Cu Complexes

The complexes $[Cu_2(\mathbf{2})]^{4+}$ and $[Cu_2(\mathbf{3})]^{4+}$ exhibit very similar ORR activity (*vide supra*). Crystal structures of the Cu complex of **3** before and after oxygenation provide clues to the reactivity of these complexes. The analyses indicate that the dicopper complex of **3** (and likely the dicopper complex of **2**) reacts with O_2 at the T3 DPA sites intermolecularly. This chemistry is reminiscent of the Kitagawa system, in which two [Cu[tri[2-(6-picolyl)]amine]]$^+$ units bind O_2 to afford the peroxodicopper(II) species $[Cu_2[\text{tri(6-picolyl)methane})]_2(\mu\text{-}\eta^2\text{:}\eta^2\text{-}O_2)]^{2+}$,[82,84,85] and other systems involving TPA-derivatives observed by Karlin and Fukuzumi.[86] Kodera reported a more stable peroxodicopper(II) complex, in which tethered tridentate sites hold the Cu centers in close proximity leading to enhanced (and *reversible*) O_2 binding.[87-89] Notably, the Kodera complexes have negligible ORR activity,[26] while the dinuclear complexes reported here are catalytically competent, possibly a result of the *irreversible* nature of O_2 binding in the present case. This high reactivity of DPA-bound copper(I) fragments we ascribe to the inability of DPA

to occupy three sites at a tetrahedrally coordinated copper(I); instead DPA is well-suited to bind copper(II) in a planar fashion.

3.9 Trinuclear Systems – Cu Complexes Bearing the T3-T2-T3 Paradigm

3.9.1 Voltammetry under Ar

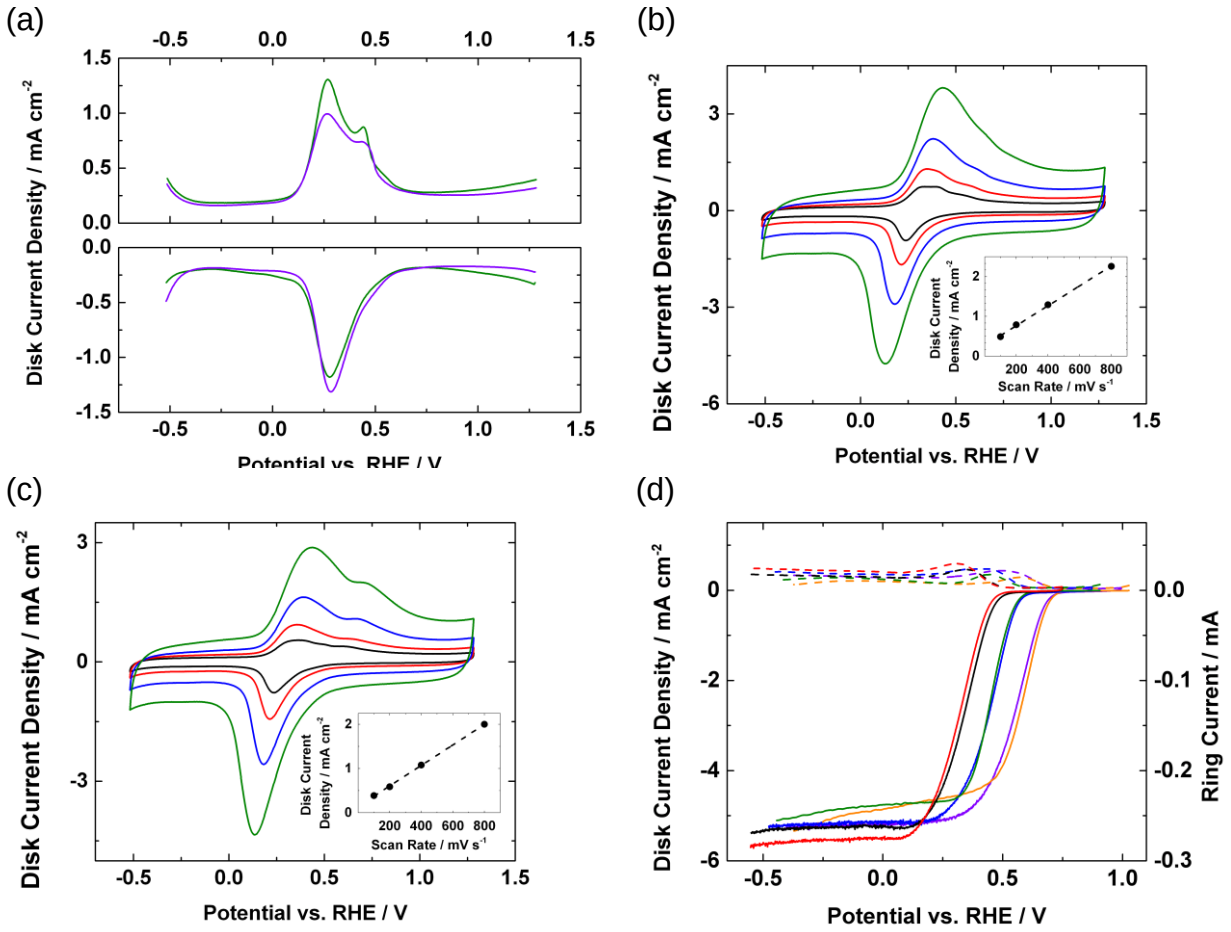

Figure 3.17. DPVs (a) of trinuclear complexes $[Cu_3(\mathbf{4})]^{6+}$ (green) and $[Cu_3(\mathbf{5})]^{6+}$ (purple). CVs of $[Cu_3(\mathbf{4})]^{6+}$ (b) and $[Cu_3(\mathbf{5})]^{6+}$ (c) with scan rates of 100 (black), 200 (red), 400 (blue), 800 (green) mV/s. Randles-Sevcik plots of $[Cu_3(\mathbf{4})]^{6+}$ (b, inset) and $[Cu_3(\mathbf{5})]^{6+}$ (c, inset) projected from the anodic (black circles) current densities of the peak/shoulder at above 0.5 V vs. RHE. These three studies were conducted in pH 4 Ar-sparged Britton-Robinson buffer solutions. **Figure 3.17d.** RRDE data for $[Cu_3(\mathbf{4})]^{6+}$ in pH 4 (black), pH 7 (blue), and pH 10 (purple), and $[Cu_3(\mathbf{5})]^{6+}$ in pH 4 (red), pH 7 (green), and pH 10 (orange) O_2-sparged Britton-Robinson buffer solution at 1600 rpm with a scan rate of 10 mV/s.

In view of the tricopper active site present in several oxidases, we examined two tricopper complexes with pairs of DPA groups. Figure 3.17a reports the DPVs for $[Cu_3(\mathbf{4})]^{6+}$ and $[Cu_3(\mathbf{5})]^{6+}$. The cathodic scans (Figure 3.17a, lower box) for both complexes reveal a single reduction at 0.28 V vs. RHE, this reduction wave being attributed to reduction of all cupric centers to the cuprous state. The anodic scan of $[Cu_3(\mathbf{4})]^{6+}$ reveals *two* oxidation waves (upper box, green). The oxidation at 0.27 V is assigned to the Cu(I/II) couple at the DPA site, based on its similarity to that of $[Cu(\mathbf{1})]^{2+}$. The remaining event at 0.44 V is thus attributed to bipy-bound Cu(I/II). Analogous behavior was observed for $[Cu_3(\mathbf{5})]^{6+}$ (lower box, purple), with waves at 0.27 (Cu(I/II)-DPA) and 0.45 V (Cu(I/II)-terpy). In Figure 3.17a, the ratio of the total reductive to oxidative charge is 1:1, supporting the hypothesis that the waves are reversible. Also in Figure 3.17a, the ratio of the area under the peak at 0.27 V to the other oxidative peak is about 2:1, confirming the distribution of the Cu ions in the ligand – one Cu ion at each of the two DPA sites, and one Cu ion at the bipy or terpy site. Apart from electrochemical characterization techniques, mass spectrometry of the tricopper complexes and elemental analysis of the tricopper complexes physisorbed on Vulcan XC-72 both confirm the Cu:ligand ratio to be 3:1.

Cyclic voltammograms and Randles-Sevcik plots for trinuclear complexes $[Cu_3(\mathbf{4})]^{6+}$ (Figure 3.17b) and $[Cu_3(\mathbf{5})]^{6+}$ (Figure 3.17c) were analyzed to establish their redox properties. The Randles-Sevcik plots (insets) show the linear relationship between the oxidative peaks/shoulders at about +0.7 V and the scan rate. This proportionality indicates that the oxidative peaks/shoulders are due to surface-bound redox centers. The similarity of the reductive and oxidative currents indicates reversibility.

3.9.2 RRDE Measurements under O_2

Figure 3.17d shows the LSVs and RRDE measurements for $[Cu_3(\mathbf{4})]^{6+}$ and $[Cu_3(\mathbf{5})]^{6+}$. At pH 4, the onset potentials for both $[Cu_3(\mathbf{4})]^{6+}$ (Figure 3.17d, black) and $[Cu_3(\mathbf{5})]^{6+}$ (Figure 3.17d, red) are about 30 mV negative of that for $[Cu(\mathbf{1})]^{2+}$. At pH 7, both $[Cu_3(\mathbf{4})]^{6+}$ and $[Cu_3(\mathbf{5})]^{6+}$ exhibit onset potentials similar to that of $[Cu(\mathbf{1})]^{2+}$ and generate less H_2O_2 than $[Cu(\mathbf{1})]^{2+}$ (Figure 3.17d, blue and green lines). The diffusion-limited currents observed for $[Cu_3(\mathbf{4})]^{6+}$ and $[Cu_3(\mathbf{5})]^{6+}$ are similar to that for $[Cu(\mathbf{1})]^{2+}$ at both pH 4 and 7. At pH 10, $[Cu_3(\mathbf{4})]^{6+}$ (Figure 3.17d, purple) exhibits an ORR onset at ~10 mV negative than $[Cu(\mathbf{1})]^{2+}$, while $[Cu_3(\mathbf{5})]^{6+}$ (Figure 3.17d, orange) exhibits an ORR onset at ~15 mV more positive and displays lower diffusion-limited currents than $[Cu(\mathbf{1})]^{2+}$, with all catalysts generating similar amounts of H_2O_2 (Figure 3.17d, purple and orange dashed lines) at pH 10.

To further understand the ORR activity of these trinuclear Cu complexes, we carried out Koutecky-Levich analyses on $[Cu_3(\mathbf{4})]^{6+}$ and $[Cu_3(\mathbf{5})]^{6+}$ (Figures 3.18 and 3.19). Figure 3.10b summarizes the results from Koutecky-Levich analyses. These Koutecky-Levich plots reveal for both complexes that about 4 e^- are transferred at the diffusion-limited region within pH 1-13 range, confirming that both complexes undergo a 4 e^- pathway. Figure 3.10d reports the Tafel slopes of both complexes. Similar to $[Cu(\mathbf{1})]^{2+}$, $[Cu_2(\mathbf{2})]^{4+}$ and $[Cu_2(\mathbf{3})]^{4+}$, the Tafel slopes change from ~100 mV/dec to ~70 mV/dec. These results indicate that $[Cu_3(\mathbf{4})]^{6+}$ and $[Cu_3(\mathbf{5})]^{6+}$ behave as ORR catalysts the same way as $[Cu(\mathbf{1})]^{2+}$.

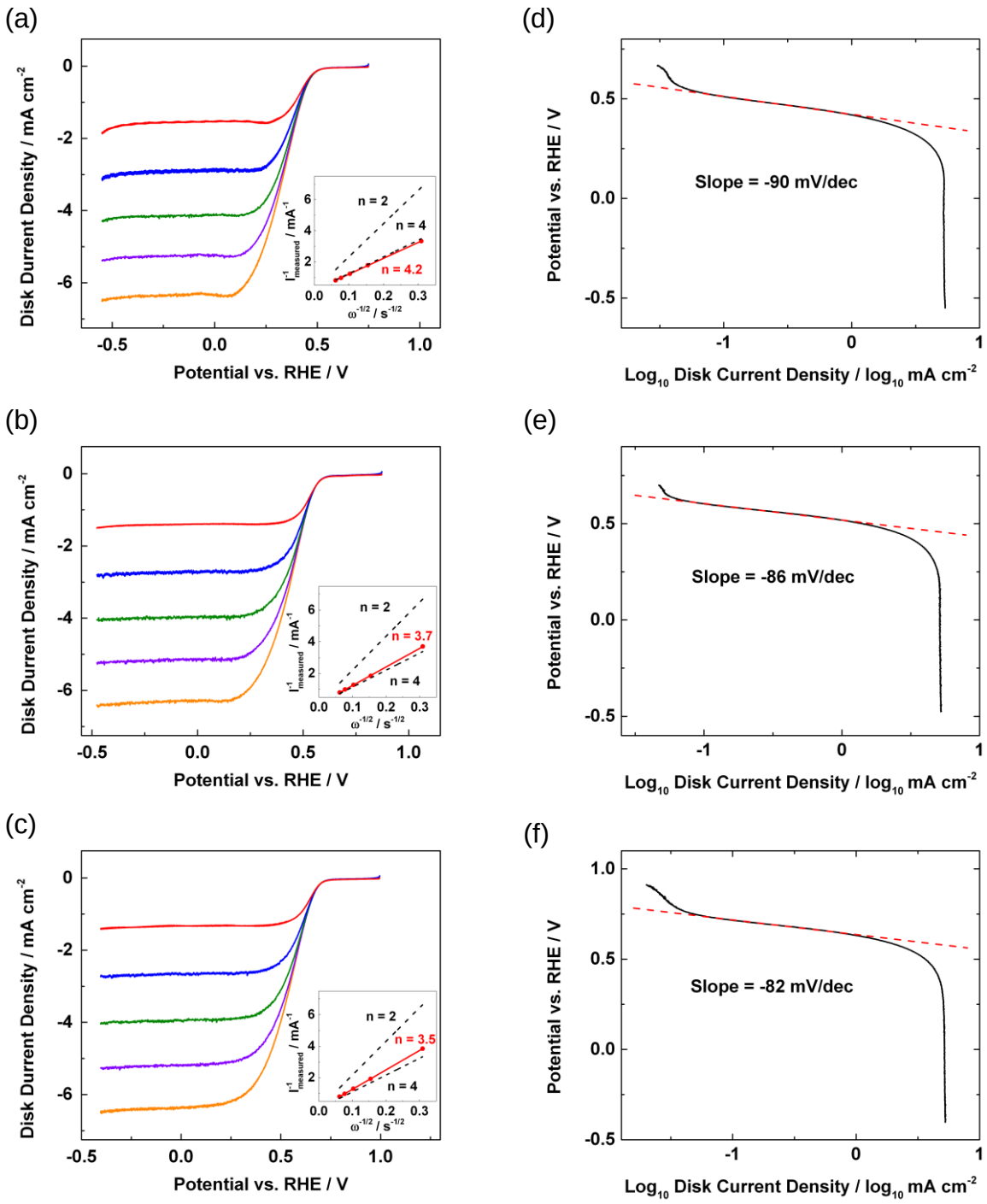

Figure 3.18. RDE voltammograms and Koutecky-Levich plots (inset) of $[Cu_3(\mathbf{4})]^{6+}$ supported on Vulcan XC-72 in (a) pH 4, (b) pH 7, and (c) pH 10 O_2-saturated Britton-Robinson buffer solutions with a scan rate of 10 mV/s at 100 (red), 400 (blue), 900 (green), 1600 (violet), and 2500 rpm (orange). Tafel plots of $[Cu_3(\mathbf{4})]^{6+}$ supported on Vulcan XC-72 in (d) pH 4, (e) pH 7, and (f) pH 10 O_2-saturated Britton-Robinson buffer solutions (10 mV/s, 1600 rpm).

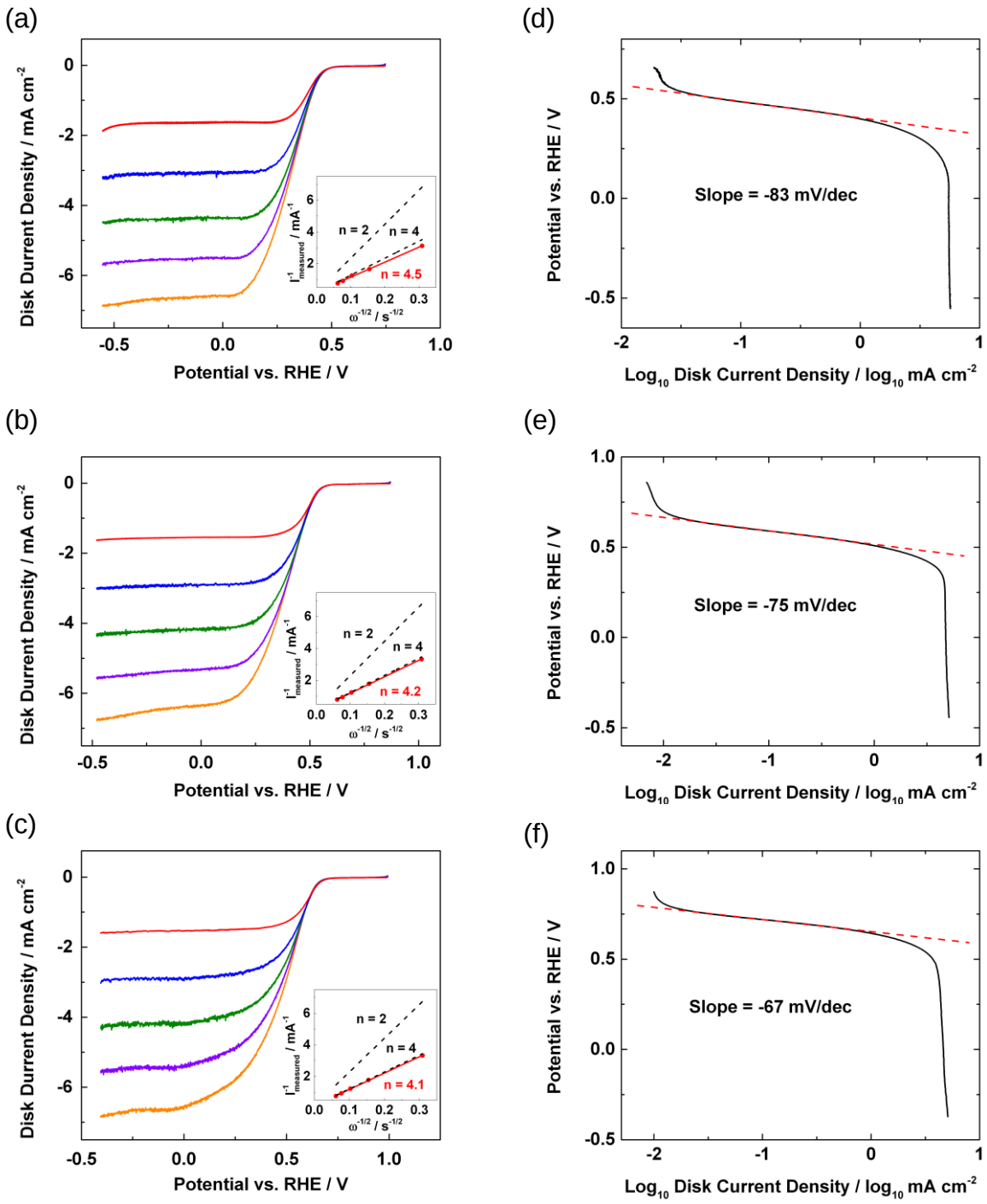

Figure 3.19. RDE voltammograms and Koutecky-Levich plots (inset) of $[Cu_3(\mathbf{5})]^{6+}$ supported on Vulcan XC-72 in (a) pH 4, (b) pH 7, and (c) pH 10 O_2-saturated Britton-Robinson buffer solutions with a scan rate of 10 mV/s at 100 (red), 400 (blue), 900 (green), 1600 (violet), and 2500 rpm (orange). Tafel plots of $[Cu_3(\mathbf{5})]^{6+}$ supported on Vulcan XC-72 in (d) pH 4, (e) pH 7, and (f) pH 10 O_2-saturated Britton-Robinson buffer solutions (10 mV/s, 1600 rpm).

3.9.3 Metal Substitution Studies

We next investigate possible reasons that the ORR activity for these trinuclear Cu complexes is no better than that found with $[Cu(\mathbf{1})]^{2+}$. We were unable to obtain crystal structures of the trinuclear Cu complexes, in either oxygenated or deoxygenated form. From the similar ORR activities among the complexes of DPA and its derivatives, we hypothesize that the O_2 reduction process occurs at the DPA sites via an intermolecular pathway, while the third Cu (in either a bipy or terpy site) does not participate in the ORR. To evaluate this claim, we conducted a series of electrochemical tests with trinuclear mixed metal complexes.

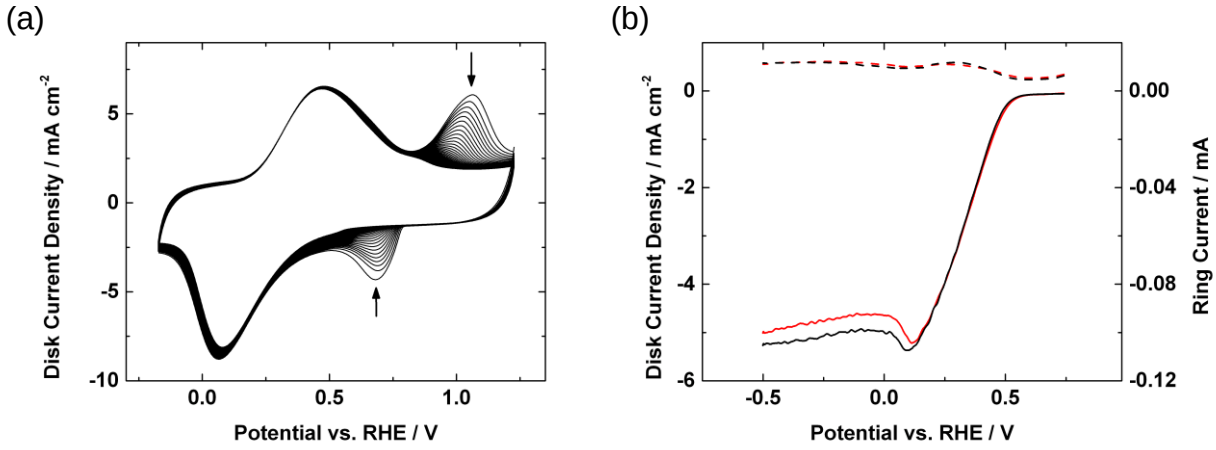

Figure 3.20a. CVs of $[AgCu_2(\mathbf{4})]^{5+}$ in pH 4 Ar-sparged Britton-Robinson buffer solution with a scan rate of 200 mV/s for 50 cycles. **Figure 3.20b.** RRDE experiments of $[AgCu_2(\mathbf{4})]^{5+}$ in pH 4 O_2-sparged Britton-Robinson buffer solution at 1600 rpm with a scan rate of 10 mV/s before (black) and after (red) 50 cycles under Ar.

Given the greater affinity of DPA moieties for Cu(II) over Ag(I),[90] we generated $AgCu_2$ derivatives by treating 1:2 mixtures of the metal nitrates with **4**. It is predicted that two Cu(II) ions bind the tridentate DPA unit, with the Ag(I) ion coordinated to the bidentate bipy unit. Figure 3.20a shows the CV of $[AgCu_2(\mathbf{4})]^{5+}$ with two visible reversible waves. The Cu(I/II) couple of $[AgCu_2(\mathbf{4})]^{5+}$ at 0.25 V vs. RHE is comparable to the redox couple of a Cu ion bound

by a DPA unit, e.g. $[Cu(\mathbf{1})]^{2+}$, $[Cu_2(\mathbf{2})]^{4+}$, and $[Cu_2(\mathbf{3})]^{4+}$. The lack of an oxidative shoulder at 0.44 V vs. RHE indicates that no Cu ion is present in the bipy unit. We assign the remaining redox wave with a $E_{½}$ of 0.8 V vs. RHE to be the Ag(0/I) couple of the $[AgCu_2(\mathbf{4})]^{5+}$. The ratio of the charges of the redox waves at 0.25 V and 0.8 V vs. RHE is 2:1, which matches with the 2:1 Cu:Ag ratio from the EA results. Taken together, the CV results confirm our proposed formulation of $[AgCu_2(\mathbf{4})]^{5+}$, with two Cu ions bound by the two DPA units of **4** and a Ag ion situated in the bipy pocket.

Figure 3.20b shows the LSVs of $[AgCu_2(\mathbf{4})]^{5+}$ with an ORR onset at 0.45 V vs. RHE at pH 4, which is similar to that of $[Cu(\mathbf{1})]^{2+}$ and $[Cu_3(\mathbf{4})]^{6+}$. The amount of H_2O_2 detected by the ring (Figure 3.20b, black dashed line) and the diffusion-limited currents (Figure 3.20b, black solid line) of $[AgCu_2(\mathbf{4})]^{5+}$ are both comparable to that of $[Cu(\mathbf{1})]^{2+}$ and $[Cu_3(\mathbf{4})]^{6+}$. We then electrochemically remove the Ag(I) ions from the electrode surface by cycling for 50 times in the absence of O_2. Figure 3.20a shows the disappearance of the Ag(0/I) redox wave at 0.8 V vs. RHE upon cycling. Figure 3.20b red lines show that the resulting complex exhibits ORR activity similar to that found before Ag leaching.

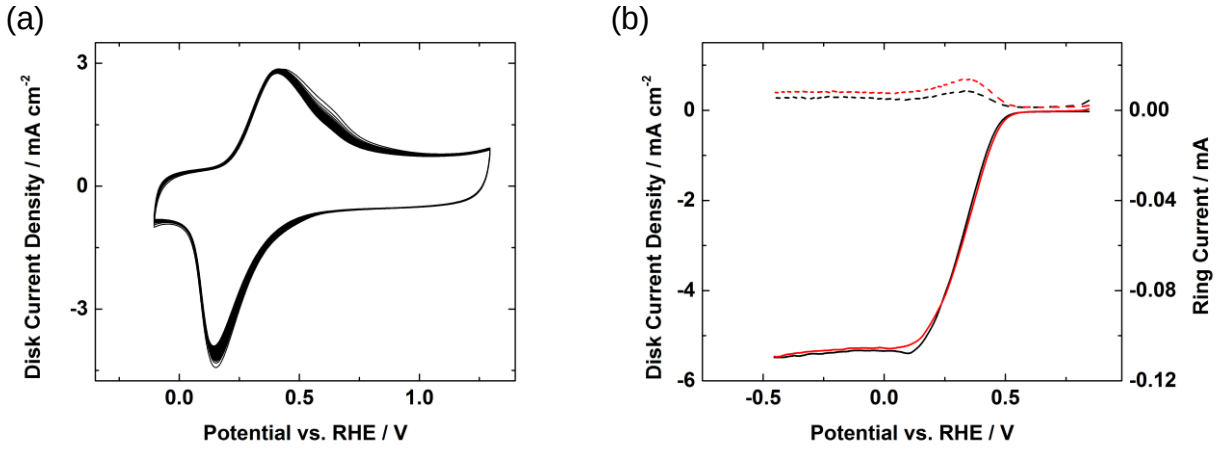

Figure 3.21a. CVs of $[Cu_2(\mathbf{4})]^{4+}$ in pH 4 Ar-sparged Britton-Robinson buffer solution with a scan rate of 200 mV/s for 50 cycles. **Figure 3.21b.** RRDE experiments of $[Cu_2(\mathbf{4})]^{4+}$ in pH 4 O_2-

sparged Britton-Robinson buffer solution at 1600 rpm with a scan rate of 10 mV/s before (black) and after (red) 50 cycles under Ar.

Control experiments were conducted with $[Cu_2(\mathbf{4})]^{4+}$. Mass spectrometry of $[Cu_2(\mathbf{4})]^{4+}$ and elemental analysis of $[Cu_2(\mathbf{4})]^{4+}$ physisorbed on Vulcan XC-72 both confirm the Cu:ligand ratio to be 2:1. Figure 3.21a shows the CV of $[Cu_2(\mathbf{4})]4^{+}$ under Ar. The redox wave at 0.25 V vs. RHE is assigned to the Cu(I/II) couple for the Cu ions in the DPA sites, because the potential of the redox wave is similar to that of the Cu(I/II) couple observed for $[Cu(\mathbf{1})]^{2+}$ (*vide supra*). The lack of a redox wave at about 0.8 V vs. RHE further confirms that such wave observed in $[AgCu_2(\mathbf{4})]^{5+}$ is in fact due to the Ag(0/I) couple.

Figure 3.21b shows the LSVs of $[Cu_2(\mathbf{4})]^{4+}$ with an ORR onset at 0.45 V vs. RHE at pH 4, which is similar to that of $[AgCu_2(\mathbf{4})]^{5+}$. The amount of H_2O_2 detected by the ring (Figure 3.21b, black dashed line) and the diffusion-limited currents (Figure 3.21b, black solid line) are both comparable to that of $[AgCu_2(\mathbf{4})]^{5+}$. We then cycle $[Cu_2(\mathbf{4})]^{4+}$ for 50 times using the exact procedure for Ag leaching. The charge under the curve remains relatively constant (Figure 3.21a), suggesting that $[Cu_2(\mathbf{4})]^{4+}$ does not degrade over the course of the experiment. Figure 3.21b shows the linear voltammogram (red solid line) and RRDE measurements (red dashed line) of $[Cu_2(\mathbf{4})]^{4+}$ after potential cycling. The ORR activities of the post-cycled and the pre-cycled $[Cu_2(\mathbf{4})]^{4+}$ are comparable, suggesting there is minimal degradation resulting from potential cycling.

3.9.4 Summary of Trinuclear Cu Complexes

Cu complexes of **4**, in which the bipy site is vacant, or occupied by Cu or Ag, exhibit very similar ORR activity, suggesting that metal ions in the T2-mimicking site of our ligand do

not actively engage in ORR. Hence, we hypothesis that trinuclear complexes $[Cu_3(\mathbf{4})]^{6+}$ and $[Cu_3(\mathbf{5})]^{6+}$ also react with O_2 through the T3 DPA sites via an intermolecular pathway, i.e. in a similar fashion as dinuclear complexes $[Cu_2(\mathbf{2})]^{4+}$ and $[Cu_2(\mathbf{3})]^{4+}$ and mononuclear complex $[Cu(\mathbf{1})]^{2+}$.

3.10 Conclusions

The ORR activity of $[Cu(\mathbf{1})]^{2+}$ is comparable to that of $[Cu(TPA)(H_2O)]^{2+}$ previously reported by our group. However, the ET rate between $[Cu(\mathbf{1})]^{2+}$ and electrode surface is low, indicating that more coupling to the electrode may be required for efficient ORR. Covalently linking two $[Cu(DPA)]^{2+}$ cores together results in ORR activities no better than $[Cu(\mathbf{1})]^{2+}$ alone. Crystallographic studies confirm the competency of dinuclear complexes $[Cu_2(\mathbf{2})]^{4+}$ and $[Cu_2(\mathbf{3})]^{4+}$ to activate O_2, although no advantage is conferred by linking the Cu sites. The challenges in this area are further illustrated by our tests on DPA as a synthon for the T3 sites, and bipy or terpy for the T2 site. However, trinuclear complexes $[Cu_3(\mathbf{4})]^{6+}$ and $[Cu_3(\mathbf{5})]^{6+}$ did not exhibit enhanced ORR activity, as compared to $[Cu(\mathbf{1})]^{2+}$. We show via metal substitution that the metal in the T2 equivalent site does not participate in the ORR process. Hence, more elaborate ligand design is imperative to fully mimic both the intricate structure of the active site of laccase and the remarkable ORR activity of laccase. The relationship of inter-site flexibility and cooperativity is long recognized;[91] it is insufficient to simply connect reactive Cu sites. To ensure cooperativity comparable to that of metalloproteins, future catalysts require more sophisticated designs than those tested in this report.

3.11 References

(1) Mehta, V.; Cooper, J. S. *J. Power Sources* **2003**, *114*, 32.
(2) Thomas, C. E. *Int. J. Hydrogen Energy* **2009**, *34*, 6005.
(3) Sandy Thomas, C. E. *Int. J. Hydrogen Energy* **2009**, *34*, 9279.
(4) Campanari, S.; Manzolini, G.; Garcia de la Iglesia, F. *J. Power Sources* **2009**, *186*, 464.
(5) Gewirth, A. A.; Thorum, M. S. *Inorg. Chem.* **2010**, *49*, 3557.
(6) Gervasio, D. In *Encyclopedia of Electrochemical Power Sources*; Garche, J., Ed.; Elsevier: Amsterdam, 2009, p 806.
(7) Wu, J.; Yuan, X. Z.; Martin, J. J.; Wang, H.; Zhang, J.; Shen, J.; Wu, S.; Merida, W. *J. Power Sources* **2008**, *184*, 104.
(8) Li, H.; Shi, Z.; Zhang, J. In *Encyclopedia of Electrochemical Power Sources*; Garche, J., Ed.; Elsevier: Amsterdam, 2009, p 941.
(9) Li, H.; Tang, Y.; Wang, Z.; Shi, Z.; Wu, S.; Song, D.; Zhang, J.; Fatih, K.; Zhang, J.; Wang, H.; Liu, Z.; Abouatallah, R.; Mazza, A. *J. Power Sources* **2008**, *178*, 103.
(10) Wu, J.; Yuan, X. Z.; Martin, J. J.; Wang, H. In *Encyclopedia of Electrochemical Power Sources*; Garche, J., Ed.; Elsevier: Amsterdam, 2009, p 848.
(11) Bergens, S. H.; Markiewicz, M. E. P. In *Encyclopedia of Electrochemical Power Sources*; Garche, J., Ed.; Elsevier: Amsterdam, 2009, p 616.
(12) Borup, R. L.; Davey, J. R.; Garzon, F. H.; Wood, D. L.; Inbody, M. A. *J. Power Sources* **2006**, *163*, 76.
(13) Cai, M.; Ruthkosky, M. S.; Merzougui, B.; Swathirajan, S.; Balogh, M. P.; Oh, S. H. *J. Power Sources* **2006**, *160*, 977.
(14) Shao, Y.; Yin, G.; Gao, Y. *J. Power Sources* **2007**, *171*, 558.
(15) Zhang, S.; Yuan, X.-Z.; Hin, J. N. C.; Wang, H.; Friedrich, K. A.; Schulze, M. *J. Power Sources* **2009**, *194*, 588.
(16) Blackman, A. G.; Tolman, W. B. *Struct. Bonding* **2000**, *97*, 179.
(17) Hatcher, L.; Karlin, K. *J. Biol. Inorg. Chem.* **2004**, *9*, 669.
(18) Mirica, L. M.; Ottenwaelder, X.; Stack, T. D. P. *Chem. Rev.* **2004**, *104*, 1013.
(19) Lewis, E. A.; Tolman, W. B. *Chem. Rev.* **2004**, *104*, 1047.
(20) Q. Hatcher, L.; D. Karlin, K. In *Adv. Inorg. Chem.*; Eldik, R. v., Reedijk, J., Eds.; Academic Press: 2006; Vol. Volume 58, p 131.
(21) Cramer, C. J.; Tolman, W. B. *Acc. Chem. Res.* **2007**, *40*, 601.
(22) Dagys, M.; Haberska, K.; Shleev, S.; Arnebrant, T.; Kulys, J.; Ruzgas, T. *Electrochem. Commun.* **2010**, *12*, 933.
(23) Thorseth, M. A.; Tornow, C. E.; Tse, E. C. M.; Gewirth, A. A. *Coor. Chem. Rev.* **2013**, *257*, 130.
(24) Jensen, M. P.; Que, E. L.; Shan, X.; Rybak-Akimova, E.; Que, J. L. *Dalton Trans.* **2006**, 3523.
(25) Karlin, K. D.; Wei, N.; Jung, B.; Kaderli, S.; Niklaus, P.; Zuberbuehler, A. D. *J. Am. Chem. Soc.* **1993**, *115*, 9506.
(26) Thorseth, M. A.; Letko, C. S.; Rauchfuss, T. B.; Gewirth, A. A. *Inorg. Chem.* **2011**, *50*, 6158.
(27) Thorseth, M. A.; Letko, C. S.; Tse, E. C. M.; Rauchfuss, T. B.; Gewirth, A. A. *Inorg. Chem.* **2013**, *52*, 628.
(28) Messerschmidt, A.; Luecke, H.; Huber, R. *J. Mol. Biol.* **1993**, *230*, 997.

(29) Solomon, E. I.; Sundaram, U. M.; Machonkin, T. E. *Chem. Rev.* **1996**, *96*, 2563.
(30) McGuirl, M. A.; Dooley, D. M. *Curr. Opin. Chem. Biol.* **1999**, *3*, 138.
(31) Hakulinen, N.; Andberg, M.; Kallio, J.; Koivula, A.; Kruus, K.; Rouvinen, J. *J. Struct. Biol.* **2008**, *162*, 29.
(32) Garavaglia, S.; Teresa Cambria, M.; Miglio, M.; Ragusa, S.; Iacobazzi, V.; Palmieri, F.; D'Ambrosio, C.; Scaloni, A.; Rizzi, M. *J. Mol. Biol.* **2004**, *342*, 1519.
(33) Piontek, K.; Antorini, M.; Choinowski, T. *J. Biol. Chem.* **2002**, *277*, 37663.
(34) Schweiger, H.; Vayner, E.; Anderson, A. B. *Electrochem. Solid-State Lett.* **2005**, *8*, A585.
(35) Mano, N.; Soukharev, V.; Heller, A. *J. Phys. Chem. B* **2006**, *110*, 11180.
(36) Pita, M.; Shleev, S.; Ruzgas, T.; Fernández, V. M.; Yaropolov, A. I.; Gorton, L. *Electrochem. Commun.* **2006**, *8*, 747.
(37) Blanford, C. F.; Heath, R. S.; Armstrong, F. A. *Chem. Commun.* **2007**, 1710.
(38) Blanford, C. F.; Foster, C. E.; Heath, R. S.; Armstrong, F. A. *Faraday Discuss.* **2009**, *140*, 319.
(39) Thorum, M. S.; Anderson, C. A.; Hatch, J. J.; Campbell, A. S.; Marshall, N. M.; Zimmerman, S. C.; Lu, Y.; Gewirth, A. A. *J. Phys. Chem. Lett.* **2010**, *1*, 2251.
(40) Murphy, M. E. P.; Lindley, P. F.; Adman, E. T. *Protein Sci.* **1997**, *6*, 761.
(41) Ducros, V.; Brzozowski, A. M.; Wilson, K. S.; Ostergaard, P.; Schneider, P.; Svendson, A.; Davies, G. J. *Acta Crystallogr., Sect D: Biol. Crystallogr.* **2001**, *57*, 333.
(42) Cracknell, J. A.; Vincent, K. A.; Armstrong, F. A. *Chem. Rev.* **2008**, *108*, 2439.
(43) Toledo-Núñez, C.; López-Cruz, J. I.; Hernández-Arana, A. *Biophys. Chem.* **2012**, *167*, 36.
(44) St-Pierre, J. In *Encyclopedia of Electrochemical Power Sources*; Garche, J., Ed.; Elsevier: Amsterdam, 2009, p 901.
(45) Hakulinen, N.; Kiiskinen, L.-L.; Kruus, K.; Saloheimo, M.; Paananen, A.; Koivula, A.; Rouvinen, J. *Nat. Struct. Mol. Biol.* **2002**, *9*, 601.
(46) Solomon, E. I.; Augustine, A. J.; Yoon, J. *Dalton Trans.* **2008**, 3921.
(47) Casarin, M.; Corvaja, C.; Di Nicola, C.; Falcomer, D.; Franco, L.; Monari, M.; Pandolfo, L.; Pettinari, C.; Piccinelli, F. *Inorg. Chem.* **2005**, *44*, 6265.
(48) Ouellette, W.; Yu, M. H.; O'Connor, C. J.; Hagrman, D.; Zubieta, J. *Angew. Chem. Int. Ed.* **2006**, *45*, 3497.
(49) Maiti, D.; Woertink, J. S.; Ghiladi, R. A.; Solomon, E. I.; Karlin, K. D. *Inorg. Chem.* **2009**, *48*, 8342.
(50) Palmer, A. E.; Lee, S. K.; Solomon, E. I. *J. Am. Chem. Soc.* **2001**, *123*, 6591.
(51) Erturk, H.; Hofmann, A.; Puchta, R.; van Eldik, R. *Dalton Trans.* **2007**, 2295.
(52) Suntharalingam, K.; Hunt, D. J.; Duarte, A. A.; White, A. J. P.; Mann, D. J.; Vilar, R. *Chem. Eur. J.* **2012**, *18*, 15133.
(53) Humphreys, K. J.; Karlin, K. D.; Rokita, S. E. *J. Am. Chem. Soc.* **2002**, *124*, 8055.
(54) Choi, K.-Y.; Ryu, H.; Sung, N.-D.; Suh, M. *J. Chem. Crystallogr.* **2003**, *33*, 947.
(55) Bruker *APEX2*; Bruker AXS, Inc., Madison, Wisconsin, USA., 2010.
(56) Bruker *SAINT*, *SHELXTL*, *SADABS*, *XCIF*, *XPREP*; Bruker AXS, Inc., Madison, Wisconsin, USA, 2005.
(57) Sheldrick, G. M. *Acta Cryst.* **2008**, *A64*, 112.
(58) Spek, A. L.; van der Sluis, P. *Acta Cryst.* **1990**, *A46*, 194.
(59) Laviron, E. *J. Electroanal. Chem. Interfacial Electrochem.* **1979**, *101*, 19.

(60) Eckermann, A. L.; Feld, D. J.; Shaw, J. A.; Meade, T. J. *Coor. Chem. Rev.* **2010**, *254*, 1769.
(61) Park, W.-C.; Hong, H.-G. *Bull. Korean Chem. Soc.* **2006**, *27*, 381.
(62) Bard, A. J.; Faulkner, L. R. *Electrochemical Methods: Fundamentals and Applications*; Wiley, 2000.
(63) Smalley, J. F.; Feldberg, S. W.; Chidsey, C. E. D.; Linford, M. R.; Newton, M. D.; Liu, Y.-P. *J. Phys. Chem.* **1995**, *99*, 13141.
(64) Hosseini, A.; Collman, J. P.; Devadoss, A.; Williams, G. Y.; Barile, C. J.; Eberspacher, T. A. *Langmuir* **2010**, *26*, 17674.
(65) Rorabacher, D. B. *Chem. Rev.* **2004**, *104*, 651.
(66) Vande Linde, A. M. Q.; Westerby, B. C.; Ochrymowycz, L. A.; Rorabacher, D. B. *Inorg. Chem.* **1993**, *32*, 251.
(67) Zhang, J.; Anson, F. C. *Electrochim. Acta* **1993**, *38*, 2423.
(68) Lei, Y.; Anson, F. C. *Inorg. Chem.* **1994**, *33*, 5003.
(69) Lei, Y.; Anson, F. C. *Inorg. Chem.* **1995**, *34*, 1083.
(70) McCrory, C. C. L.; Ottenwaelder, X.; Stack, T. D. P.; Chidsey, C. E. D. *J. Phys. Chem. A* **2007**, *111*, 12641.
(71) Thorum, M. S.; Yadav, J.; Gewirth, A. A. *Angew. Chem. Int. Ed.* **2009**, *48*, 165.
(72) Cukier, R. I.; Nocera, D. G. *Annu. Rev. Phys. Chem.* **1998**, *49*, 337.
(73) Mayer, J. M. *Annu. Rev. Phys. Chem.* **2004**, *55*, 363.
(74) Madhiri, N.; Finklea, H. O. *Langmuir* **2006**, *22*, 10643.
(75) Huynh, M. H. V.; Meyer, T. J. *Chem. Rev.* **2007**, *107*, 5004.
(76) Rosenthal, J.; Nocera, D. G. *Acc. Chem. Res.* **2007**, *40*, 543.
(77) Weinberg, D. R.; Gagliardi, C. J.; Hull, J. F.; Murphy, C. F.; Kent, C. A.; Westlake, B. C.; Paul, A.; Ess, D. H.; McCafferty, D. G.; Meyer, T. J. *Chem. Rev.* **2012**, *112*, 4016.
(78) Zhang, J.; Anson, F. C. *J. Electroanal. Chem.* **1992**, *341*, 323.
(79) Nagao, H.; Komeda, N.; Mukaida, M.; Suzuki, M.; Tanaka, K. *Inorg. Chem.* **1996**, *35*, 6809.
(80) Fletcher, S. *J. Solid State Electrochem.* **2009**, *13*, 537.
(81) Mahapatra, S.; Kaderli, S.; Llobet, A.; Neuhold, Y. M.; Palanche, T.; Halfen, J. A.; Young, V. G.; Kaden, T. A.; Que, L.; Zuberbuhler, A. D.; Tolman, W. B. *Inorg. Chem.* **1997**, *36*, 6343.
(82) Hayashi, H.; Fujinami, S.; Nagatomo, S.; Ogo, S.; Suzuki, M.; Uehara, A.; Watanabe, Y.; Kitagawa, T. *J. Am. Chem. Soc.* **2000**, *122*, 2124.
(83) Cahoy, J.; Holland, P. L.; Tolman, W. B. *Inorg. Chem.* **1999**, *38*, 2161.
(84) Mizuno, M.; Hayashi, H.; Fujinami, S.; Furutachi, H.; Nagatomo, S.; Otake, S.; Uozumi, K.; Suzuki, M.; Kitagawa, T. *Inorg. Chem.* **2003**, *42*, 8534.
(85) Taki, M.; Teramae, S.; Nagatomo, S.; Tachi, Y.; Kitagawa, T.; Itoh, S.; Fukuzumi, S. *J. Am. Chem. Soc.* **2002**, *124*, 6367.
(86) Fukuzumi, S.; Karlin, K. D. *Coor. Chem. Rev.* **2013**, *257*, 187.
(87) Kodera, M.; Kajita, Y.; Tachi, Y.; Katayama, K.; Kano, K.; Hirota, S.; Fujinami, S.; Suzuki, M. *Angew. Chem. Int. Ed.* **2004**, *43*, 334.
(88) Kodera, M.; Kano, K. *Bull. Chem. Soc. Jpn.* **2007**, *80*, 662.
(89) Kodera, M.; Katayama, K.; Tachi, Y.; Kano, K.; Hirota, S.; Fujinami, S.; Suzuki, M. *J. Am. Chem. Soc.* **1999**, *121*, 11006.

(90) Zuckerman, J. J.; Hagen, A. P. *Inorganic Reactions and Methods, The Formation of Bonds to N,P,As,Sb,Bi*; Wiley, 2009.
(91) Collman, J. P. *Acc. Chem. Res.* **1977**, *10*, 265.

Chapter 4

Effect of Temperature and Pressure on the Kinetics of the Oxygen Reduction Reaction

4.1 Introduction

Polymer electrolyte membrane (PEM) fuel cells are attractive portable power conversation devices for clean and sustainable transportation in the near future.[1-3] Unlike combustion engines, fuel cells are not limited by the thermodynamic aspects of the Carnot cycle on the conversion of heat to mechanical work.[4,5] Despite the intrinsic advantage offered by fuel cells, the widespread deployment of fuel cells has been hindered by several technical problems and design issues.[6-10] One of the major impediments is the sluggish oxygen reduction reaction (ORR) to water: $O_2 + 4\ e^- + 4\ H^+ \rightarrow 2\ H_2O$ (in acid), and $O_2 + 4\ e^- + 2\ H_2O \rightarrow 4\ OH^-$ (in base). While both forms of the ORR are kinetically slow, the acidic version is particularly so.[11]

At present, Pt or one of its alloys is the catalyst of choice to efficiently mediate the kinetically slow ORR in the fuel cell industry.[12-15] In the field of academic research, Pt is the standard benchmark for non-precious metal and metal-free ORR catalysis. However, the performance of Pt is still far from satisfactory for practical fuel cell applications—with an overpotential of ~ 300 mV. The origin of the observed overpotential lies in the strong binding affinity of OH^- for Pt surfaces at potentials above 0.9 V vs. RHE,[16] a claim reinforced by DFT calculations.[17-19] Much prior work is dedicated to destabilizing the Pt-OH bond by incorporating

alloy elements. Pt_3Ni,[20] currently the best Pt-based ORR catalyst among other Pt-alloys,[21] suffers from Ni dissolution under operating conditions.[22]

Pt also serves as a standard catalyst in fuel cell anodes. The material suffers from poisoning issues by adventitious CO in the H_2 stream remaining from the reforming process.[23,24] 10 ppm of CO is detrimental to H_2 oxidation kinetics.[25] By raising the cell temperature to 130 °C, CO tolerance is enhanced up to 1,000 ppm. We wondered if we could apply a similar strategy to promote Pt-OH bond dissociation at intermediate temperatures (100–200 °C).

Temperature-programmed desorption (TPD) results demonstrate that CO desorbs from Pt surface at ~ 230 °C,[26] with an activation energy of ~ 130 kJ/mol for CO desorption from Pt.[27] On the other hand, OH^- desorbs from Pt at > 600 °C, with an activation barrier of ~ 210 kJ/mol.[28-36] The drastic difference between CO and OH^- desorption is due to the formation of intricate hydrogen-bonded hexagonal networks or multilayer islands of H_2O with surface OH^- groups to form complex structures that increase the desorption activation energy of OH^-.[34,37,38] Laser-induced fluorescence (LIF) studies provide further evidence for the exceptionally strong Pt-OH bond. OH^- dissociation involves either a charged species or leaves behind a charged surface which is energetically highly unfavorable.[36,39] This analysis suggests that direct elimination of OH^- from a Pt surface at intermediate temperatures is unlikely.

A close examination of the Pt-CO poisoning studies reveals that the Pt-CO bond is significantly destabilized at 130 °C, which is ca. 100 °C lower than the desorption temperature (*vide supra*), suggesting that the poisoning effect of CO is sufficiently mitigated at temperatures well-below the CO desorption temperature. To our surprise, H_2O desorbs from an oxide-covered Pt surface at ~ 130 °C,[40-42] which is even lower than that of CO from Pt, with an activation energy of ~ 80 kJ/mol.[43] In essence, Pt-OH_2 is the protonated form of Pt-OH. In conjunction with

the TPD results, another study concludes that Pt-OH bonds are weaker at a liquid-solid junction than at a gas-solid interface.[44] Hence, facilitating the release of H_2O from Pt surface at intermediate temperatures appears to be a relevant and compelling strategy to enhance the activity of Pt.

Apart from the opportunity to enable efficient cleavage of the Pt-OH bonds, raising the operating temperature can potentially enhance the ORR kinetics of Pt, as predicted by the Arrhenius equation.[45] Both full and half cell studies suggest that the power density of Pt increases at elevated temperatures (< 100 °C).[46] However, polymer electrolyte membrane requires hydrated condition to conduct protons efficiently.[25,47] Hence, the operating cell temperature is limited to temperatures below which the relative humidity is high.[48,49] In combination with fuel cell studies, new membrane materials that allow H^+ conduction in dehumidified conditions are actively being investigated.[50] Another approach to reach temperatures beyond 100 °C is the use of high-boiling solvents, but these ionic liquids, organic or inorganic solvents are more expensive, less conductive, or more likely to poison the catalyst, as compared to water.[51-53]

The use of phosphoric acid, which has a boiling point of 160 °C, is another attempt to raise the cell temperature. However, phosphate ions are site-specific poisons that compete with O_2 for binding sites on Pt,[54] thus rendering the Pt surface less reactive towards ORR relative to more weakly coordinating anions.[55-58] FT-IR,[59,60] EQCM,[61] and *in situ* X-ray absorption spectroscopy[55] indicated that phosphate poisoning is still in effect up to 160 °C within a wide range of working cell voltages (from 300 to 800 mV).[45,62] It is desirable to examine ORR kinetics on Pt absent the poisoning effects of phosphate.

Electrochemical studies at high temperature and pressure have been limited to simple reversible reactions in MeCN,[63,64] SO_2,[65] ammonia,[66-68] and H_2SO_4 or $NaHSO_4$ solutions[69] under near- and supercritical conditions—all of which were conducted in the absence of O_2.[70] Studies examining the ORR, an intricate catalytic cycle involving multiple proton-coupled electron transfer steps, have yet to be reported.

In this paper we examine ORR kinetics on Pt at temperatures between 100 and 200 °C. Water boiling is suppressed by raising the internal pressure of the reaction vessel. To avoid complications due to anion decoration on Pt surfaces,[71-75] we study the behavior of Pt in basic solutions with only OH^- anions. Cations adsorb onto Pt to a much lower extent than anions, with a trend $Li^+ > Na^+ > K^+$,[76] so we conducted our experiments in KOH.

4.2 Electrochemistry of Pt at Elevated Temperatures and Pressures

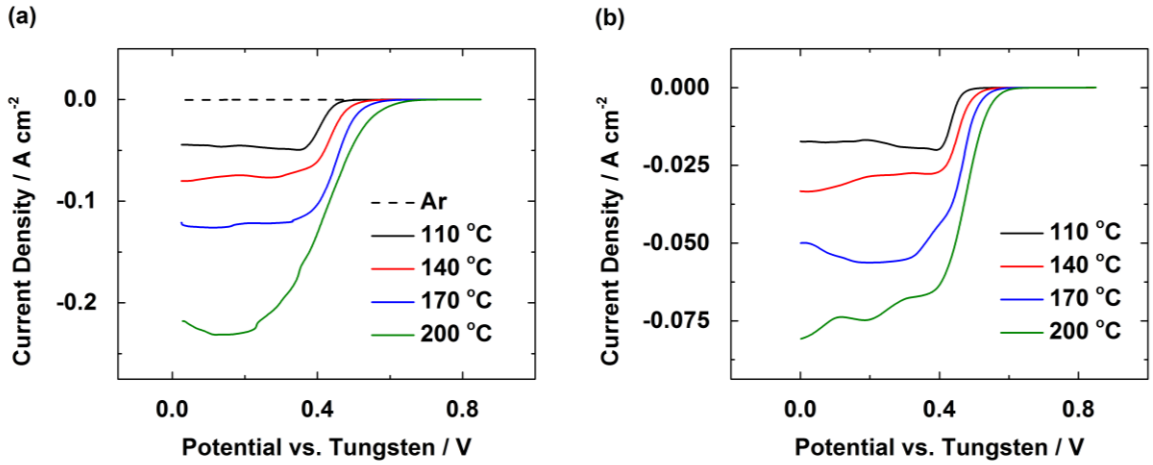

Figure 4.1. Linear sweep voltammograms (LSVs) of Pt in 0.1 M KOH with a scan rate of 50 mV/s at 110 °C (black), 140 °C (red), 170 °C (blue), and 200 °C (green) with an initial Ar (dashed line) and O_2 (solid lines) pressure of (a) 3.4 and (b) 1.4 MPa at 20 °C.

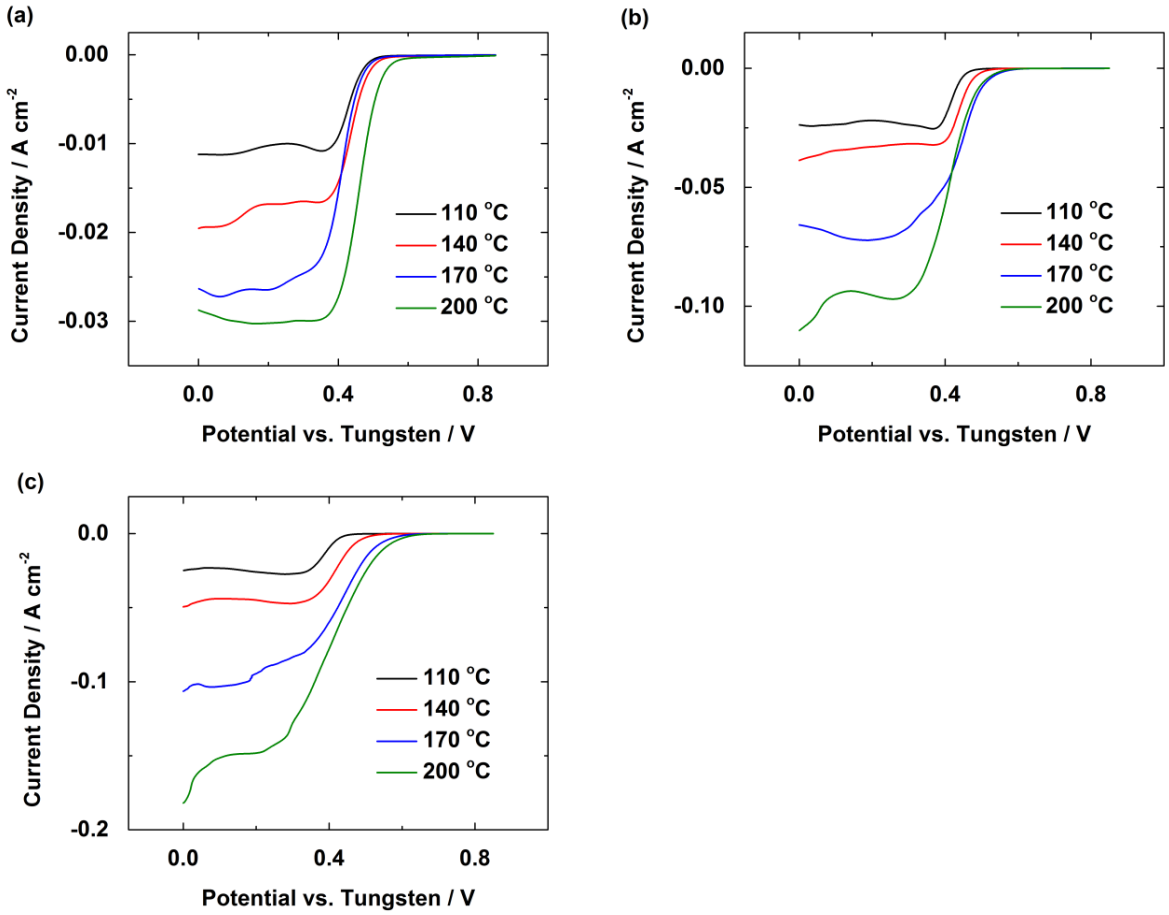

Figure 4.2. O_2 reduction LSVs of Pt at 110 °C (black), 140 °C (red), 170 °C (blue), and 200 °C (green) with an initial O_2 pressure of (a) 0.7, (b) 2.1, and (c) 2.8 MPa at 20 °C in 0.1 M KOH with a scan rate of 50 mV/s.

Figure 4.1a shows a representative set of LSVs obtained from a Pt wire immersed in a solution of 0.1 M KOH at temperatures between 110 and 200 °C with an initial O_2 pressure of 3.4 MPa at 20 °C. Figure 4.1a also displays an LSV obtained at 200 °C with an initial Ar pressure of 3.4 MPa at 20 °C (dashed line). The lack of substantial response from the Ar saturated electrolyte (seen at all temperatures) means that the cathodic current seen in the presence of O_2 is associated with the ORR. The figure demonstrates that as the temperature increases, the current increases as well. Figure 4.1b shows LSVs obtained from the same electrolyte but with an initial O_2 pressure at 20 °C of 1.4 MPa. The lower O_2 pressure used in

Figure 4.1b corresponds to lower currents relative to Figure 4.1a. The oscillatory response seen at higher temperatures is associated with mass transport due to minor thermal convection.[77] Figures 4.2 report the temperature-dependent O_2 reduction LSVs of Pt with an initial O_2 pressure of 0.7, 2.1, and 2.8 MPa at 20 °C.

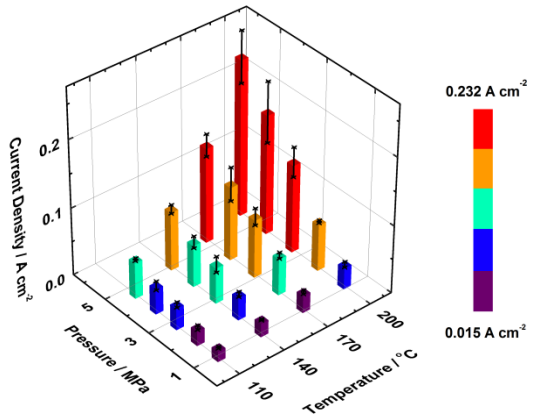

Figure 4.3. Tridimensional plot of O_2 reduction current density of Pt in 0.1 M KOH vs. O_2 pressure vs. cell temperature. The color scheme quantifies the O_2 reduction current density.

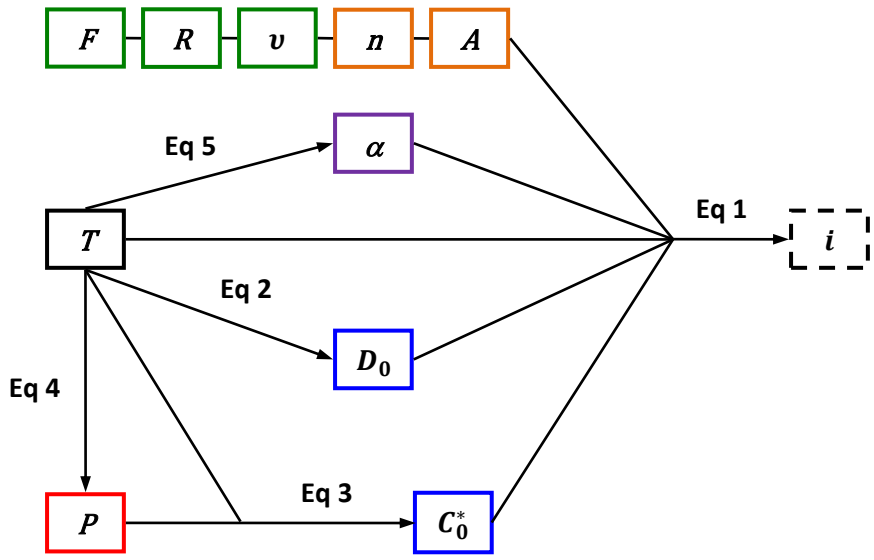

Scheme 4.1. Constants and variables affecting the measured current. i = current (A), F = Faraday's constant (C mol^{-1}), R = ideal gas constant (J mol^{-1} K^{-1}), υ = scan rate (V s^{-1}), n =

number of electrons, A = electrode area (cm^2), α = transfer coefficient, D_0 = diffusion coefficient ($cm^2\ s^{-1}$), C_0^* = bulk concentration ($mol\ cm^{-3}$), T = temperature (K), P = pressure (MPa).

The experimental correlation between temperature, pressure and current is presented in Figure 4.3. This correlation indicates qualitatively that ORR current density is a function of O_2 pressure and temperature. Scheme 4.1 shows the essential components affecting the measured current in LSVs. F and R are constants, and υ is held at 50 mV/s and 100 mV/s for voltammetries under O_2 and Ar, respectively. We chose a scan rate of 50 mV/s for the O_2 reduction LSVs for two reasons. First, we observed undesirable oscillatory current response at scan rate slower than 50 mV/s, as shown in Figure 4.4. Second, fast scan rates result in high iR_u loss, which can be minimized by lowering the amount of current passing through R_u. Slower scan rates yield lower current. Taken together, a trade-off between high and low scan rates is necessary. We optimize our current response by lowering both the signal noise and the uncompensated Ohmic drop. A scan rate of 50 mV/s is the result of compromise.

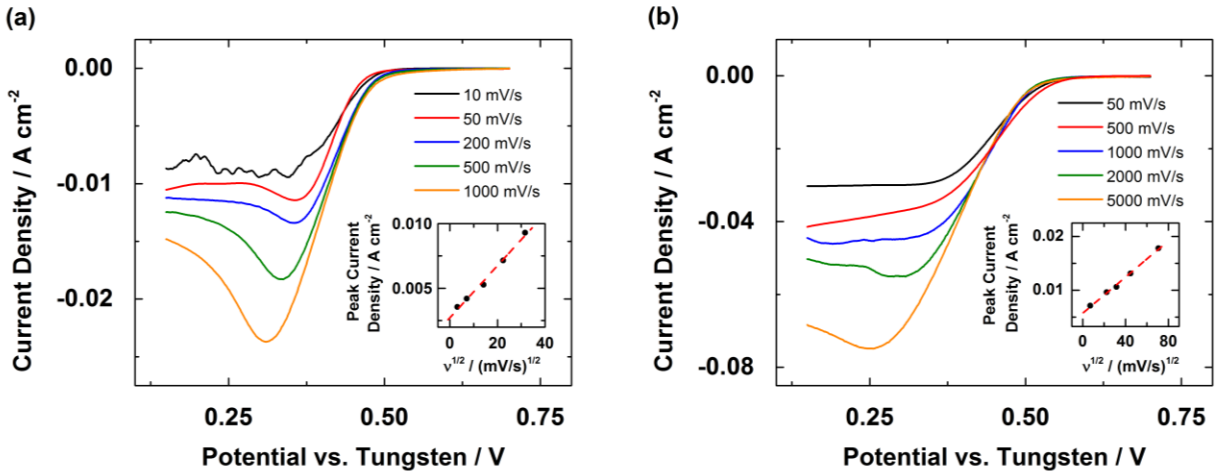

Figure 4.4. O_2 reduction LSVs of Pt at (a) 110 and (b) 200 °C with an initial O_2 pressure of 0.7 MPa at 20 °C in 0.1 M KOH at various scan rates. Insets (black circles = data, red dashed line = best-fit line) show plots of peak current densities versus the square roots of scan rates.

n is assumed to be 4, because polycrystalline Pt catalyzes the ORR via a $4e^-$ pathway.[78] Electrochemical active surface area measured prior to each experiment is taken as *A*, and is assumed to be constant throughout the experiment. α, D_0, and C_0^* are temperature-dependent.[79] *P* is also influenced by *T*, and indirectly affects the current measured by affecting the bulk concentration. We aim to elucidate the effect of *T*, the independent variable, on *i*, the observable quantity.

4.3 Modeling the ORR Activity of Pt at Elevated Temperatures and Pressures

To quantify the relationship between temperature, pressure and current, we search for a mathematical expression that includes variables listed in Scheme 4.1 to describe the trend observed in Figure 4.3. The LSVs in Figures 4.1 and 4.2 exhibit microelectrode-like steady-state current behavior, not macroelectrode-like peak current behavior. One straightforward method to discern the differences between the two behaviors is to vary the scan rate. Steady-state current is independent of scan rate, but peak current is scan-rate dependent. Figure 4.4 shows the O_2 reduction LSVs of Pt at various scan rates. At high scan rates, we observed LSVs with typical peaking behavior for an irreversible process. We attribute the limiting current behavior observed at low scan rates to the excess availability of O_2 at the surface. At slow scan rates, O_2 depletion at the surface is relatively slow compare to O_2 diffusion from bulk solution to surface. The fast replenishment of O_2 is due to the combined effect of high O_2 concentration and increased O_2 mobility at high temperature and high pressure conditions. The inset of Figure 4.4 describes the linear relationship between the square roots of scan rates and the observed peak current densities. This linear relationship suggests that our system is in the macroelectrode regime, allowing us to

calculate the theoretical limiting current using the peak current equation for irreversible electrochemical processes (Eq. 1).[80]

$$i = 0.4958\, F^{3/2}\, R^{-1/2}\, v^{1/2}\, n\, A\, C_0^*\, D_0^{1/2}\, \alpha^{1/2}\, T^{-1/2} \qquad (1)$$

Eq. 1 shows that in addition to the direct dependence on temperature, current is further indirectly affected by temperature through the temperature dependence of D_0, C_0^*, and α. To accurately predict the temperature dependence of the current, knowledge of $D_0(T)$, $C_0^*(T)$, and $\alpha(T)$ is necessary. These will be discussed below.

First, the diffusion coefficient of O_2 (D_0) does not depend on the pressure of O_2 (P_{O_2}),[81] so we directly compute D_0 at various temperatures using Eq. 2.[82]

$$log_{10}\, D_0 = -4.410 + \frac{773.8}{T} - \left(\frac{506.4}{T}\right)^2 \qquad (2)$$

Next, Eq. 3 establishes the connection between the temperature dependence of C_0^* and P_{O_2},[83] which is also temperature-dependent by our experimental design. We determine the change in pressure by applying the van der Waals equation (Eq. 4), allowing us to compute C_0^* using Eq. 3, where a (m^6 Pa mol^{-2}) and b (m^3 mol^{-1}) are van der Waals constants of O_2,[84] n_g is the number of moles of O_2, and V (m^3) is the volume of the head space in the reactor.

$$C_0^* = P_{O_2} \exp\left[\frac{0.046\, T^2 + 203.35\, T\, \ln\left(\frac{T}{298}\right) - (299.378 + 0.092\, T)\,(T - 298) - 20591}{8.3144\, T}\right] \qquad (3)$$

$$\left[P + \frac{a\,(n_g)^2}{V^2}\right]\left(V - n_g\, b\right) = n_g\, R\, T \qquad (4)$$

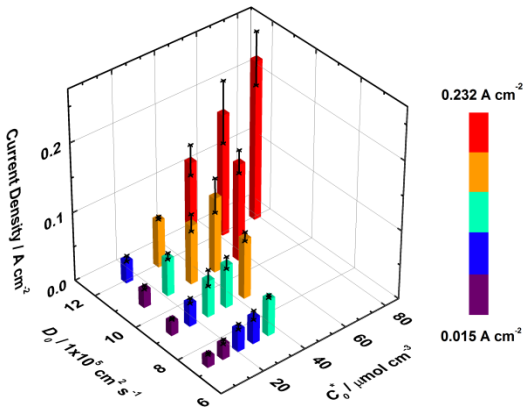

Figure 4.5. Tridimensional plot of O_2 reduction current density in 0.1 M KOH vs. O_2 diffusion coefficient vs. O_2 bulk concentration. The color scheme quantifies the O_2 reduction current density.

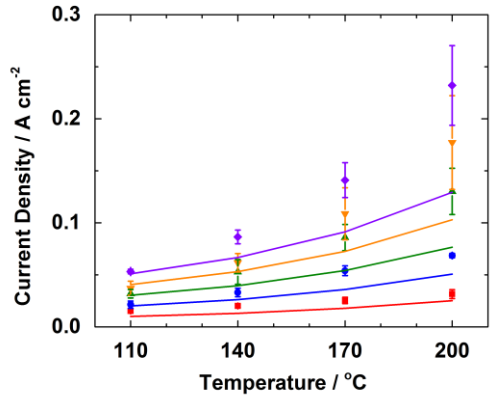

Figure 4.6. Experimental (symbols) and theoretical (lines) ORR current densities of Pt with initial O_2 pressures of 0.7 (red), 1.4 (blue), 2.1 (green), 2.8 (orange), and 3.4 (purple) MPa at 20 °C in 0.1 M KOH, assuming $\alpha = 0.5$.

The values of D_0 and C_0^* for O_2 together determines the availability of O_2 at the electrode surface. Figure 4.5 describes the relationship between observed O_2 reduction current with the diffusion coefficient of O_2 and the bulk concentration of O_2. Figure 4.6 shows the comparison between the experimental and calculated ORR current densities of Pt. The calculated values are found using Eq. 1 with the calculated $D_0(T)$ and $C_0^*(T)$ of O_2, assuming $\alpha = 0.5$. The general trend is correctly predicted, yet the calculated values deviate from the observed values,

suggesting α is likely not 0.5. To obtain values of α, we measure the Tafel slopes of the O_2 reduction LSVs of Pt at intermediate temperatures.

$$\eta = \frac{R\,T}{\alpha\, n_a\, F}\ln i_0 - \frac{R\,T}{\alpha\, n_a\, F}\ln i \qquad (5)$$

Eq. 5 shows the Tafel slope equation with η = overpotential, n_a = number of electron transferred in the rate-determining step (RDS), and i_0 = the exchange current density. Rearranging the Tafel slope equation yields Eq. 6.

$$\eta = \frac{R\,T}{\alpha\, n_a\, F}\ln i_0 - \frac{R\,T}{\alpha\, n_a\, F}\ln i$$

$$E - E^0 = \frac{R\,T}{\alpha\, n_a\, F}\ln i_0 - \frac{R\,T}{\alpha\, n_a\, F}\ln i \qquad (6)$$

However, E^0 vs. tungsten (at > 100 °C, > 0.7 MPa) is unknown in our experiment. Due to the lack of a stable reference electrode at high temperature with predictable potential drift, η cannot be computed accurately. Hence, we use an alternate form of the Tafel slope equation (Eq. 7).

$$E = \left(\frac{R\,T}{\alpha\, n_a\, F}\ln i_0 + E^0\right) - \frac{R\,T}{\alpha\, n_a\, F}\ln i \qquad (7)$$

with $y = E$, $m = -\frac{R\,T}{\alpha\, n_a\, F}$, $x = \ln i$, and $c = \left(\frac{R\,T}{\alpha\, n_a\, F}\ln i_0 + E^0\right)$

Without the knowledge of E^0 at the experimental conditions, i_0 cannot be computed from the intercept. Without i_0, apparent enthalpy of activation cannot be calculated using the Arrhenius approach.[85] The electrochemical community has not yet reached a consensus whether the Tafel slope or the transfer coefficient of the ORR is temperature-sensitive.[86] A study proposed that a Tafel slope of about 60 mV/dec in the low current density region, where Temkin adsorption kinetics dominate on an oxide-covered Pt surface, is sensitive towards temperature.[25] In the high current density region where Langmuirian conditions are favored on an oxide-free Pt

surface, a temperature-insensitive Tafel slope of about 120 mV/dec is observed.[25] However, other studies suggested otherwise.[87-89]

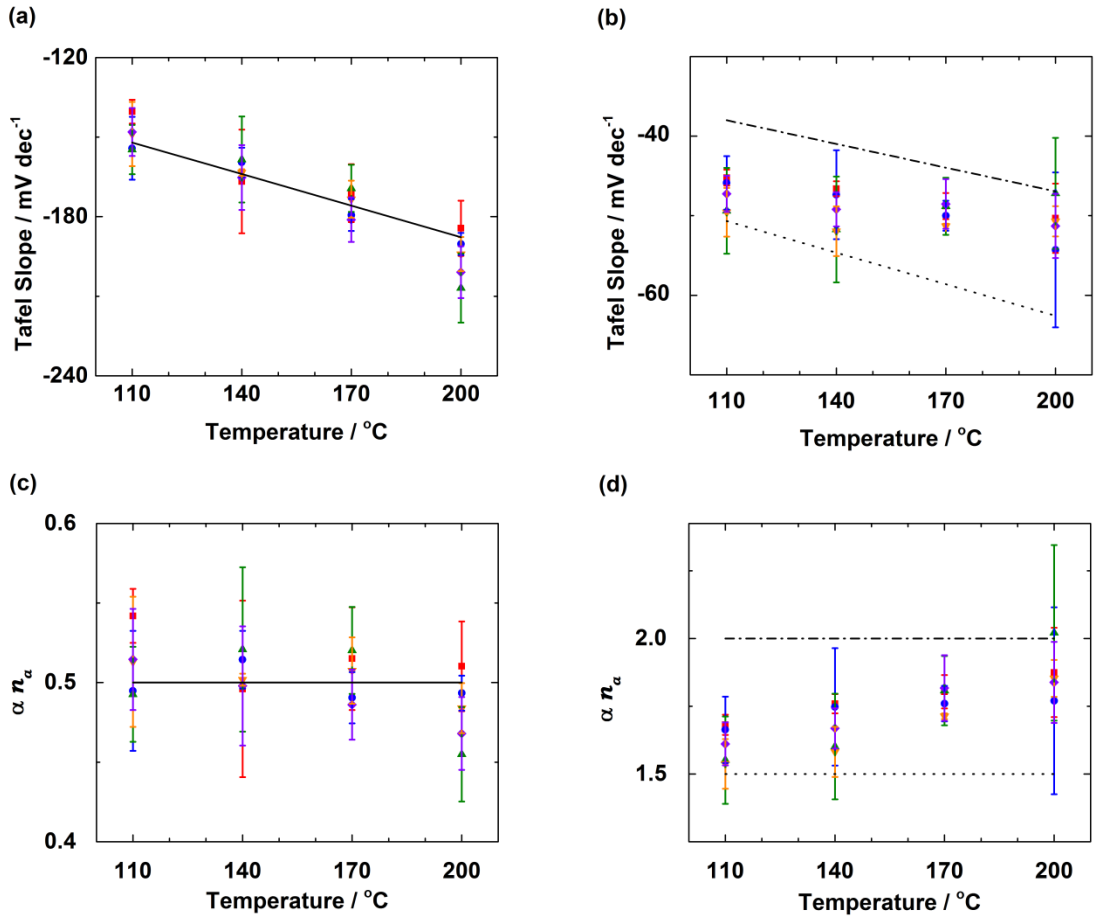

Figure 4.7. Experimental Tafel slopes in the (a) Langmuir and (b) Temkin region and $\alpha\ n_a$ in the (c) Langmuir and (d) Temkin region of ORR catalyzed by Pt in 0.1 M KOH (symbols) with initial O_2 pressures of 0.7 (red), 1.4 (blue), 2.1 (green), 2.8 (orange), and 3.4 (purple) MPa at 20 °C. Theoretical values are predicted with n_a = 1 (black solid line), 3 (black dotted line) or 4 (black dashed-dotted line).

First, we compare the observed Tafel slopes in both the Langmuir and Temkin regions to the theoretical Tafel slopes predicted from Eq. 7. Figures 4.7a and 4.7b show the observed (colored symbols) and predicted (n_a = 1, 3, 4, black lines) Tafel slopes, assuming α is 0.5. The observed Tafel slopes are temperature-dependent and match with the predicted Tafel slopes in

the Langmuir region, but are temperature-insensitive and deviate from the predicted Tafel slopes in the Temkin region. These observations contradict a published report,[90] likely due to differences in experimental conditions. The ORR kinetics in ref. [90] are likely altered by a contamination effect from the polymer electrolyte, as pointed out by authors in another study.[91] Since the observed Tafel slopes in the Temkin region are temperature-independent, we suspect that the transfer coefficient, α, instead is temperature-dependent. Figures 4.7c and 4.7d show the $\alpha\ n_a$ values calculated from the observed Tafel slopes in the Langmuir and Temkin regions, respectively. We found $\alpha\ n_a$ to be close to 0.5, indicating that α = 0.5 and n_a = 1 in the Langmuir region. These values are consistent with results suggesting that the ORR catalyzed by Pt proceeds via a $1e^-$ step in the Langmuir region.[92] Experimentally, we find α is about 0.5 ± 0.1, which is within the typical range of $0.3 \leq \alpha \leq 0.7$.[80] The Temkin region for Pt ORR typically refers to a $2e^-$ reduction process.[79] Assuming n_a = 2, α increases from 0.7 to 1 as temperature raises from 110 to 200 °C. An α of unity in the Temkin region is not uncommon—previous studies suggest a fast electron-transfer step which is followed by a chemical RDS.[86,87]

4.4 Electrochemistry of Glassy Carbon at Elevated Temperatures and Pressures

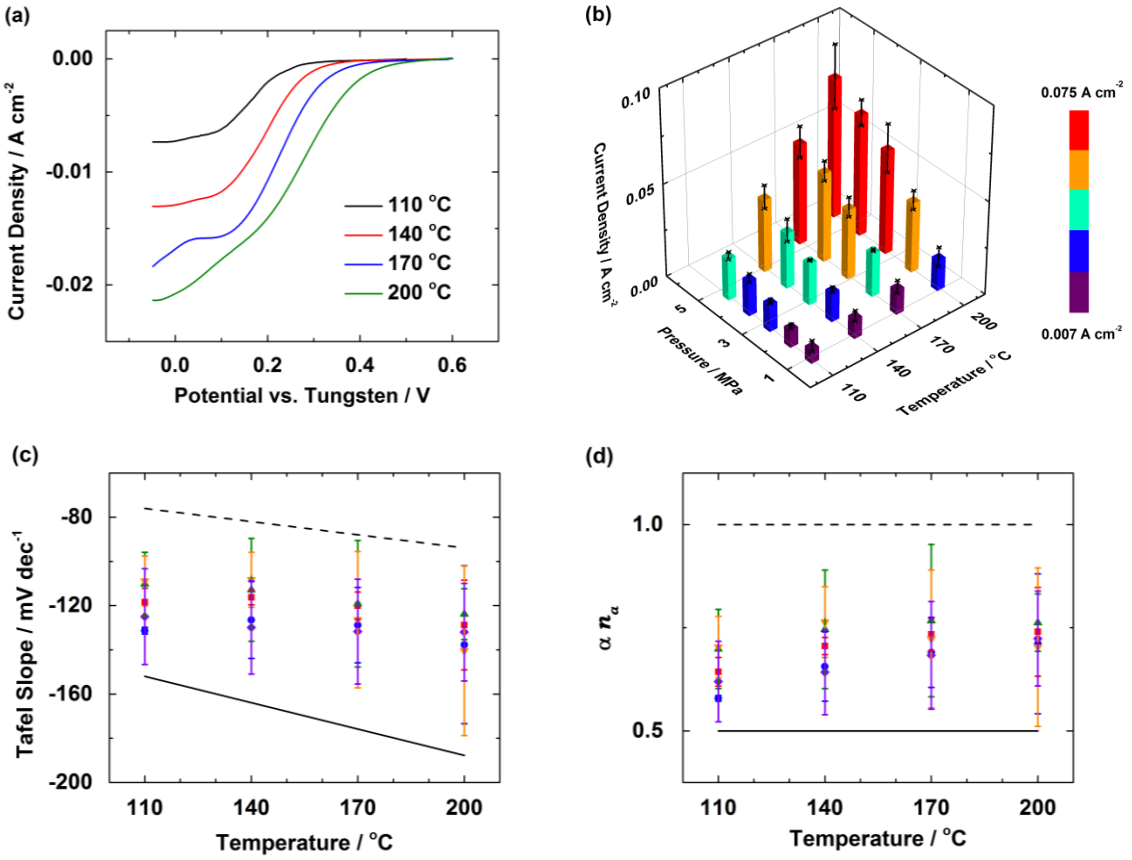

Figure 4.8. (a) LSVs of GC in 0.1 M KOH with a scan rate of 50 mV/s at 110 °C (black), 140 °C (red), 170 °C (blue), and 200 °C (green) with an initial O_2 pressure of 0.7 MPa at 20 °C. (b) Tridimensional plot of O_2 reduction current density of GC in 0.1 M KOH vs. O_2 pressure vs. cell temperature. The color scheme quantifies the O_2 reduction current density. (c) Experimental (symbols) Tafel slopes and (d) $\alpha\, n_a$ of ORR catalyzed by GC in 0.1 M KOH. Theoretical values (lines) are predicted with n_a = 1 (black solid line) or 2 (black dashed line).

In order to validate our observations on Pt and to avoid complications attendant two different Tafel slopes, we next use glass carbon (GC) as a simpler test system. Figure 4.8a displays a representative set of LSVs obtained from a GC electrode immersed in a solution of 0.1 M KOH at temperatures between 110 and 200 °C with an initial O_2 pressure of 0.7 MPa at 20 °C. Similar to the case of Pt, the ORR limiting current density on GC increases as a function of

temperature. The experimental correlation between temperature, pressure and current is described in Figure 4.8b. This correlation indicates that ORR current density on GC is a function of O_2 pressure and temperature. Figure 4.8c shows the observed Tafel slope of GC (colored symbols) and the predicted Tafel slope (black line), assuming α is 0.5. The figure demonstrates that the experimental ORR Tafel slope of GC is temperature-independent. Given this condition, we then study the effect of temperature on $\alpha\ n_a$. Figure 4.8d shows the $\alpha\ n_a$ values calculated from the Tafel slopes. The product of α and n_a is slightly temperature-sensitive, and lies between the theoretical values calculated with α = 0.5 and n_a = 1 or 2. The typical n_a value of GC is 1,[88] which equals to the observed n_a at 0.1 MPa, 20 °C. Hence, we conclude the α values of GC increases with temperature, albeit the magnitude of change in α is smaller relative to that from Pt obtained in the Temkin region.

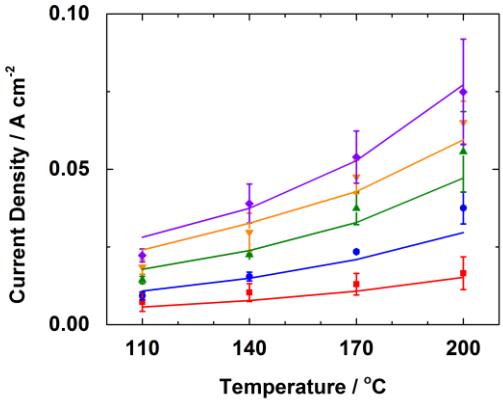

Figure 4.9. Experimental (symbols) and theoretical (lines) ORR current densities of GC with initial O_2 pressures of 0.7 (red), 1.4 (blue), 2.1 (green), 2.8 (orange), and 3.4 (purple) MPa at 20 °C in 0.1 M KOH. α values are obtained from Tafel slopes at each temperature.

Equipped with a new set of knowledge on the temperature dependence of α, we recalculate the theoretical temperature dependence of the ORR current density by using Eq. 1.

Figure 4.9 shows the experimental (symbols) and predicted (lines) ORR current densities of GC. By compensating for the temperature dependence of α, the predicted values are in close agreement with the experimental values. We conclude that Eq. 1 accurately describes the ORR activity of GC at intermediate temperatures in a pressurized system, if we account for the temperature effect on α.

4.5 Tafel Slope Analysis of the ORR Activity of Pt at Elevated Temperatures and Pressures

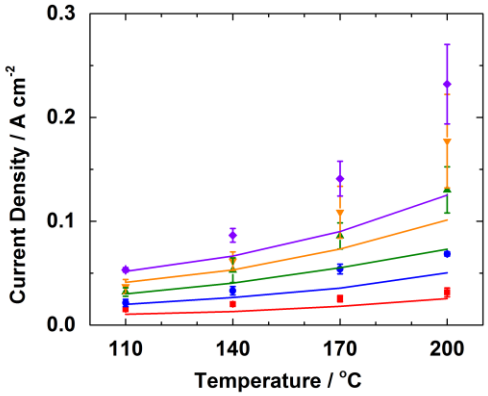

Figure 4.10. Experimental (symbols) and theoretical (lines) ORR current densities of Pt with initial O_2 pressures of 0.7 (red), 1.4 (blue), 2.1 (green), 2.8 (orange), and 3.4 (purple) MPa at 20 °C in 0.1 M KOH. α values are obtained from Tafel slopes in the Langmuir region at each temperature.

We next address Pt. As mentioned above, the Pt system is complicated due to the presence of two Tafel slopes, requiring use of two sets of α values. In the Langmuir region, we obtain α values ≈ 0.5 from the temperature-dependent Tafel slopes. Using these α values centered at 0.5 yields calculated ORR current densities (Figure 4.10) similar to those predicted in Figure 4.6 that do not match with the observed values.

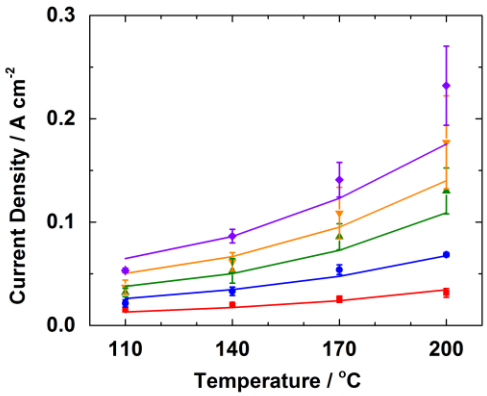

Figure 4.11. Experimental (symbols) and theoretical (lines) ORR current densities of Pt with initial O_2 pressures of 0.7 (red), 1.4 (blue), 2.1 (green), 2.8 (orange), and 3.4 (purple) MPa at 20 °C in 0.1 M KOH. α values are obtained from Tafel slopes in the Temkin region at each temperature.

We use α values obtained from the Temkin region to predict the ORR current density. Figure 4.11 shows a comparison of the calculated and experimental temperature dependence of the current density for the ORR on Pt using α values obtained from the Temkin region. Indeed, by taking into account of the temperature effect on α, the predicted values are in good agreement with the experimental values, with the exception of one condition at 200 °C, which will be addressed later.

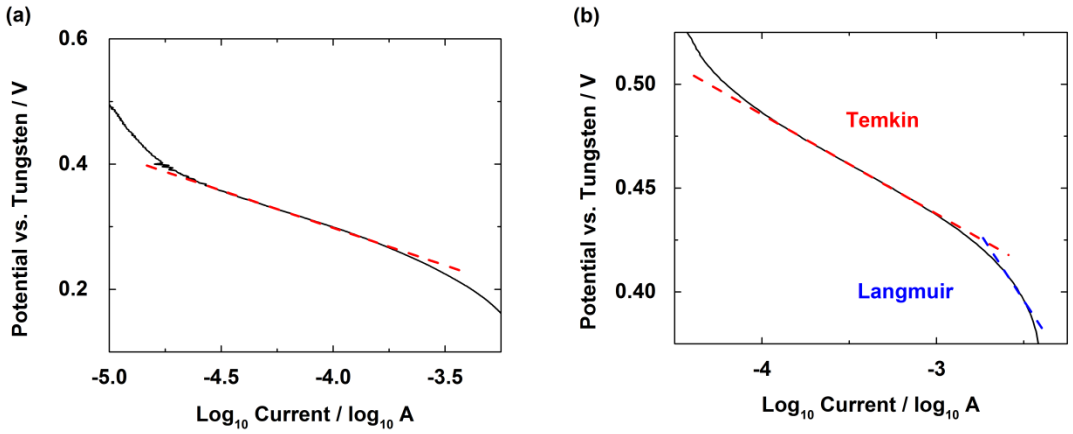

Figure 4.12. Tafel plot of (a) GC and (b) Pt, showing the Temkin and Langmuir regions, in 0.1 M KOH with a scan rate of 50 mV/s at 110 °C with an initial O_2 pressure of 0.7 MPa.

We next justify the use of α values from the Temkin region (Figure 4.12). We propose three reasons to justify the use of α values from the Temkin region. Our first two reasons are based on the GC control. Accurate prediction of the peak ORR current densities of GC requires the use of temperature-sensitive α values obtained from temperature-insensitive Tafel slopes. Our results demonstrate that Tafel slopes are insensitive to temperature in the Temkin region (*vide supra*), implying that the α values in the Temkin region are temperature-sensitive. Apart from the nature of α, we focus on the potential range where the Tafel slope is measured. For the GC control, we measure the Tafel slopes at the plateau region in the Tafel plots, which translate to a potential between 0.4-0.2 V in the actual LSVs (Figure 4.12a). The Tafel slope measured at potentials more negative than 0.2 V is larger than 300 mV/dec, suggestive of an electrochemical RDS.[93] The potential range of 0.4-0.2 V is adjacent to and negative of the ORR onset. The Temkin region observed in the Pt system (Figure 4.12b) is equivalent to the potential range where relevant Tafel slope is measured in the GC control. Our third reason to support the use of α values from the Temkin region is related to our experimental setup. As we did not pretreat our Pt chemically or electrochemically to expose bare Pt surface, we anticipate our Pt electrode inside the reactor at intermediate temperature under O_2 pressure to be covered by surface oxide or hydroxide.[94] ORR kinetics of a catalyst is dominated by the surface condition of the electrode,[95] which is likely to be Pt-OH in our system. Taken together, we decide that α values obtained from the Pt-OH region are relevant in our prediction.

4.6 Investigating the Deviations between Predicted and Experimental Values under High Temperature and Pressure Conditions

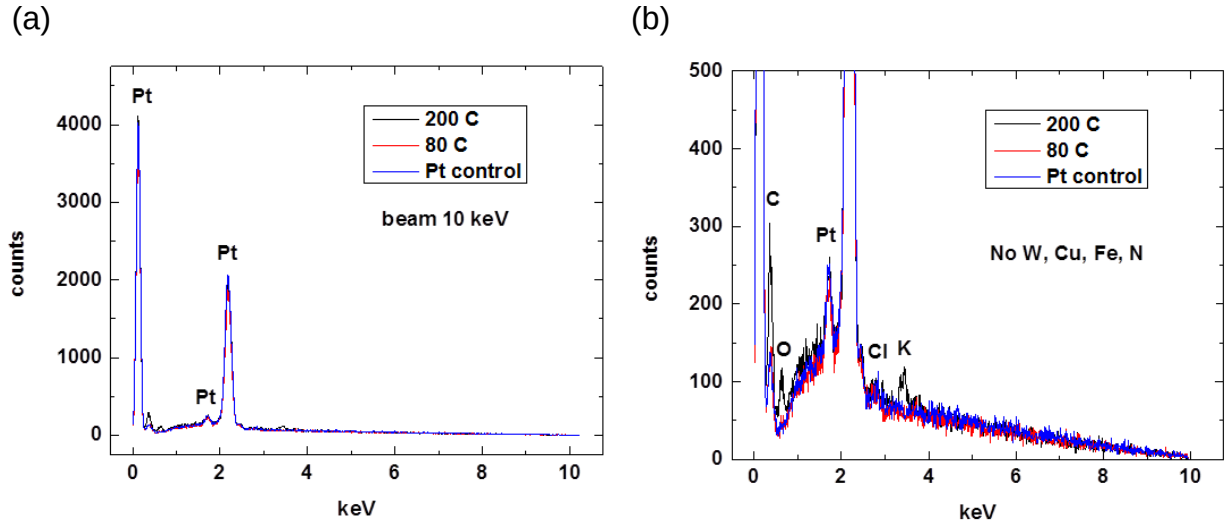

Figure 4.13. (a) Zoomed-out and (b) zoomed-in EDX of the Pt working electrode that is freshly cleaned (blue), heated to 80 °C at 0.1 MPa of O_2 (red), and heated to 200 °C at an initial O_2 pressure of 3.4 MPa (black).

Moving forward, we investigate the deviation between the experimental and calculated ORR current densities observed at 200 °C. Under high pressure of O_2 at 200 °C, reactor components including the tungsten wire, the thermocouple, and the electrical feedthroughs might corrode or leach.[77,96] To verify if the observed enhanced ORR activity is due to formation of Pt surface alloys from metal impurities, we examine the surface composition of the Pt wire by using energy-dispersive X-ray spectroscopy (EDX). Pt wire, which is freshly cleaned, heated to 80 °C at 0.1 MPa of O_2, or heated to 200 °C at an initial O_2 pressure of 3.4 MPa, exhibits no formation of W, Fe, Cu, or N alloys (Figure 4.13). No elements other than Pt, C, O, K and Cl were detectable by EDX. Minor concentration of contaminants below the detection limit of EDX (1%) is possible, but dopant levels higher than 10% are typically required to enhance the ORR

performance.[97-100] We thus corroborate that the formation of surface alloy is not the cause to the enhanced ORR current density observed at 200 °C.

Our prediction model accounts for temperature effects on α, D_0, and C_0^*, assuming n and A to be constant. We wonder if the deviation stems from unanticipated changes in n or A at intermediate temperature under a pressurized O_2 atmosphere. Studies indicate that Pt generates less H_2O_2 as temperature increases,[101] thus the assumption that n remains as 4 at high temperature and pressure is valid. A, measured before pressurizing and heating, is assumed to be constant. Thermal expansion of the solvent to increase the submerged surface area of the Pt wire is possible. However, a Pt disk electrode produces the same result as a Pt wire, suggesting that the change in water level does not significantly alter the submerged area of the Pt wire.

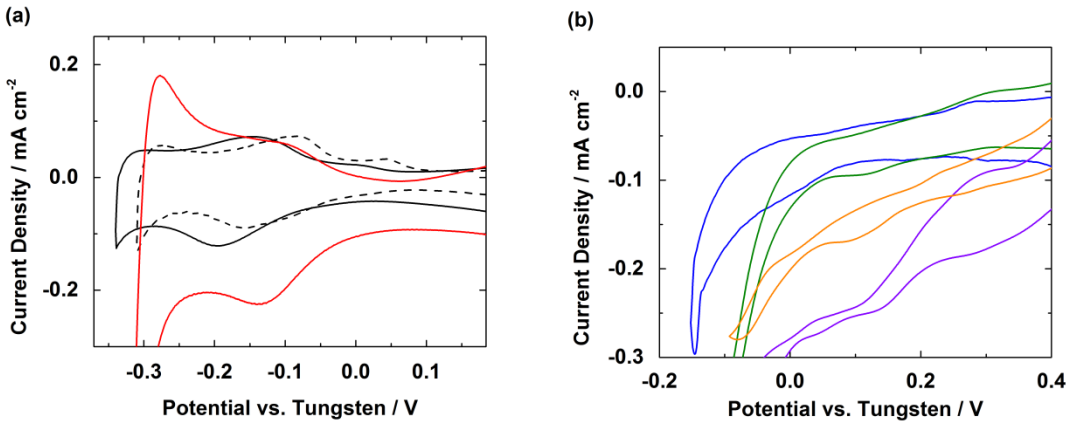

Figure 4.14. CVs of Pt in 0.1 M KOH with a scan rate of 100 mV/s (a) at 20 °C (black dashed line) under 0.1 MPa of Ar, at 20 °C under 3.4 MPa of Ar (black solid line), 50 °C (red line) with an initial Ar pressure of 3.4 MPa at 20 °C, and (b) at 110 (blue), 140 (green), 170 (yellow), and 200 (purple) °C with an initial Ar pressure of 3.4 MPa at 20 °C. See S. I. note 6 for extended discussion on the disappearance of Pt-H_{upd} feature.

Instead of a macroscopic change in the Pt surface area, we hypothesize that the deviation in observed and predicted current densities is a consequence of microscopic changes on the Pt surface. To this end, we monitor the change in electrochemical active surface area (ECSA) of Pt. To measure the ECSA of Pt *in situ*, we collect CVs of Pt under Ar at intermediate temperatures. We then calculate the ECSA of Pt by integrating the charge in the region where underpotential deposition of H_2 on Pt (Pt-H_{upd}) occurs. Figure 4.14a displays the CVs focusing on the hydrogen adsorption-desorption region of Pt under Ar up to 50 °C. The temperature dependence of the potential range and shape of the Pt-H_{upd} feature is similar to those reported in literature.[44,102,103] Surprisingly, at temperatures above 110 °C, we observe the disappearance of the Pt-H_{upd} feature (Figure 4.14b), which has not been reported before. Bard *et al.* observed disappearance of anion adsorption feature in solutions containing 0.2 M KCl or 0.2 M KBr.[77] The magnitude of the polarizable limits of Pt electrodes decreases as temperature increases, i.e. a positive shift in potential of the hydrogen evolution reaction and a negative shift of the oxygen evolution reaction. Bard *et al.* also observed similar slantedness and noise in CV, which were attributed to alterations in interelectronic resistance and capacitance.[77,104] This observation is in agreement with TPD data, which indicates that Pt-H bond dissociates at 90 °C under vacuum.[27] Due to the disappearance of the Pt-H_{upd} features at intermediate temperatures, our attempt to monitor changes in ECSA of Pt *in situ* under Ar is not fruitful.

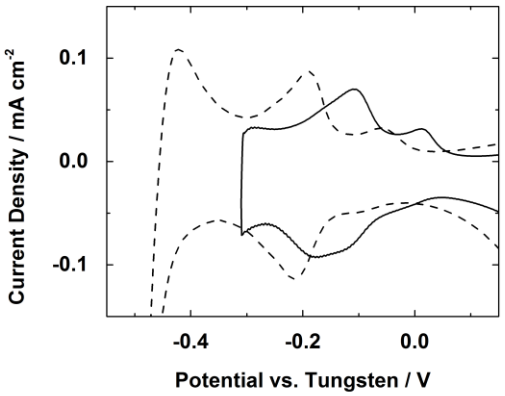

Figure 4.15. CVs of Pt at 20 °C under 0.1 MPa of Ar in 0.1 M KOH with a scan rate of 100 mV/s before (solid line) and after (dashed line) heating to 200 °C with an initial O_2 pressure of 3.4 MPa at 20 °C.

Instead of monitoring the changes in ECSA of Pt *in situ*, we measure ECSA of Pt after the experiment. We let the reactor cool to room temperature, and then depressurize the system. Figure 4.15 displays the Pt-H_{upd} region before (solid line) and after (dashed line) heating to 200 °C with an initial O_2 pressure of 3.4 MPa at 20 °C. The ECSA of Pt increases by 28 % after heating to 200 °C. By using the ECSA of Pt obtained after heating to 200 °C, the experimental current density becomes 0.18 ± 0.03 A cm^{-2}, which is comparable to the calculated current density. We use *ex situ* scanning electron microscopy (SEM) to monitor changes to the surface morphology of the Pt wire. Figure 4.16 shows a collection of *ex situ* SEM images of Pt wire that is freshly cleaned, heated to 80 °C at 0.1 MPa of O_2, or heated to 200 °C with an initial O_2 pressure of 3.4 MPa. SEM image reveals 10 μm chevron features on the Pt surface, possibly due to lack of mechanical polishing of the Pt wire prior to use. After conducting an experiment at 80 °C at 0.1 MPa, the chevron patterns on the Pt surface persist and grow to about 20 μm. However, after heating to 200 °C with an initial O_2 pressure of 3.4 MPa, the chevron markings coalesce to form terraces and steps. In other parts of the Pt wire, we observe a rough Pt surface with pores of various sizes (1-10 μm). The *ex situ* SEM images of Pt working electrodes before and after high

temperature and pressure experiments under various conditions further supports the notion that the difference in observed and predicted ORR current densities of Pt is likely related to changes in surface area. With the predicted current densities being consistent with the observed values, we conclude that at intermediate temperatures, the peak current equation is valid and the intrinsic catalytic ORR activity of Pt remains unchanged.

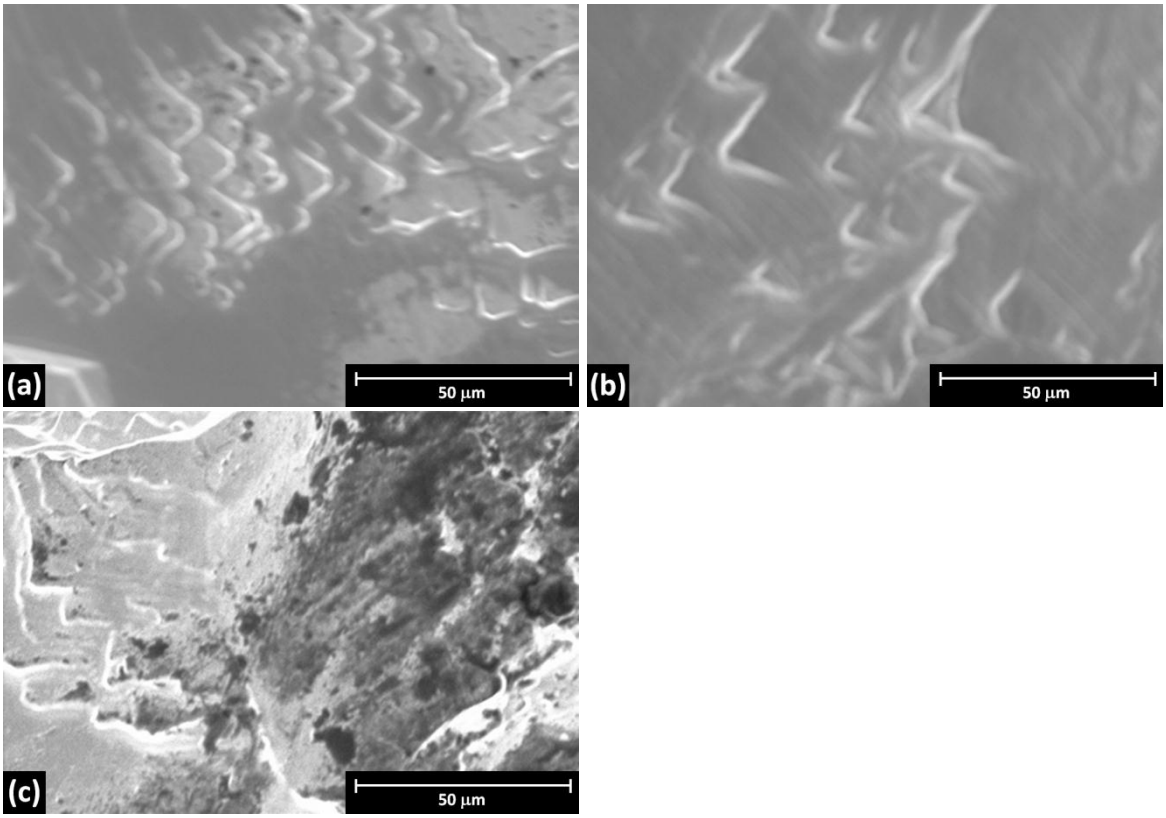

Figure 4.16. SEM images of Pt electrode that is (a) freshly cleaned, (b) heated to 80 °C at 0.1 MPa of O_2, and (c) heated to 200 °C with an initial O_2 pressure of 3.4 MPa.

4.7 Conclusions

In this report, we have studied the electrocatalytic reduction of O_2 at temperatures above 100 °C and pressures beyond 0.7 MPa in 0.1 M KOH aqueous medium. Our results demonstrate that the O_2 reduction kinetics is a function of both temperature and pressure; variables which

together modulate the availability of O_2 at the electrode surface. Apart from the diffusion coefficient and solubility of O_2, we investigate the temperature dependence of the ORR Tafel slopes. In the Temkin region, we observe temperature-insensitive Tafel slope, suggesting that α, the transfer coefficient, is temperature-dependent. An increase in electrochemical active surface area of Pt electrode at 200 °C during ORR likely reflects Pt instability at elevated temperatures. Correct accounting for the many temperature- and pressure-dependent variables leads to accurate prediction of the enhanced ORR activity observed at intermediate temperatures under pressurized conditions. We subject glassy carbon to the same experimental conditions as Pt and observe similar temperature-dependent behavior of the Tafel slopes and α values. GC electrode reduces O_2 via a 2 e^- process even at high temperatures. Under an O_2 pressure of 3.4 MPa at 200 °C, the ORR activity of both Pt and glassy carbon electrodes improves by ca. 150 fold relative to room temperature and pressure.

4.8 References

(1) Mehta, V.; Cooper, J. S. *J. Power Sources* **2003**, *114*, 32.
(2) Thomas, C. E. *Int. J. Hydrogen Energ.* **2009**, *34*, 6005.
(3) Sandy Thomas, C. E. *Int. J. Hydrogen Energ.* **2009**, *34*, 9279.
(4) Campanari, S.; Manzolini, G.; Garcia de la Iglesia, F. *J. Power Sources* **2009**, *186*, 464.
(5) Gewirth, A. A.; Thorum, M. S. *Inorg. Chem.* **2010**, *49*, 3557.
(6) Gervasio, D. In *Encyclopedia of Electrochemical Power Sources*; Garche, J., Ed.; Elsevier: Amsterdam, 2009, p 806.
(7) Wu, J.; Yuan, X. Z.; Martin, J. J.; Wang, H.; Zhang, J.; Shen, J.; Wu, S.; Merida, W. *J. Power Sources* **2008**, *184*, 104.
(8) Li, H.; Shi, Z.; Zhang, J. In *Encyclopedia of Electrochemical Power Sources*; Garche, J., Ed.; Elsevier: Amsterdam, 2009, p 941.
(9) Li, H.; Tang, Y.; Wang, Z.; Shi, Z.; Wu, S.; Song, D.; Zhang, J.; Fatih, K.; Zhang, J.; Wang, H.; Liu, Z.; Abouatallah, R.; Mazza, A. *J. Power Sources* **2008**, *178*, 103.
(10) Wu, J.; Yuan, X. Z.; Martin, J. J.; Wang, H. In *Encyclopedia of Electrochemical Power Sources*; Garche, J., Ed.; Elsevier: Amsterdam, 2009, p 848.
(11) Bergens, S. H.; Markiewicz, M. E. P. In *Encyclopedia of Electrochemical Power Sources*; Garche, J., Ed.; Elsevier: Amsterdam, 2009, p 616.

(12) Borup, R. L.; Davey, J. R.; Garzon, F. H.; Wood, D. L.; Inbody, M. A. *J. Power Sources* **2006**, *163*, 76.
(13) Cai, M.; Ruthkosky, M. S.; Merzougui, B.; Swathirajan, S.; Balogh, M. P.; Oh, S. H. *J. Power Sources* **2006**, *160*, 977.
(14) Shao, Y.; Yin, G.; Gao, Y. *J. Power Sources* **2007**, *171*, 558.
(15) Zhang, S.; Yuan, X.-Z.; Hin, J. N. C.; Wang, H.; Friedrich, K. A.; Schulze, M. *J. Power Sources* **2009**, *194*, 588.
(16) Hsueh, K. L.; Gonzalez, E. R.; Srinivasan, S. *Electrochim. Acta* **1983**, *28*, 691.
(17) Nørskov, J. K.; Rossmeisl, J.; Logadottir, A.; Lindqvist, L.; Kitchin, J. R.; Bligaard, T.; Jónsson, H. *J. Phys. Chem. B* **2004**, *108*, 17886.
(18) Marković, N. M.; Ross Jr, P. N. *Surf. Sci. Rep.* **2002**, *45*, 117.
(19) Hansen, H. A.; Viswanathan, V.; Nørskov, J. K. *J. Phys. Chem. C* **2014**, *118*, 6706.
(20) Stamenkovic, V. R.; Fowler, B.; Mun, B. S.; Wang, G.; Ross, P. N.; Lucas, C. A.; Marković, N. M. *Science* **2007**, *315*, 493.
(21) Debe, M. K.; Steinbach, A. J.; Vernstrom, G. D.; Hendricks, S. M.; Kurkowski, M. J.; Atanasoski, R. T.; Kadera, P.; Stevens, D. A.; Sanderson, R. J.; Marvel, E.; Dahn, J. R. *J. Electrochem. Soc.* **2011**, *158*, B910.
(22) Stevens, D. A.; Mehrotra, R.; Sanderson, R. J.; Vernstrom, G. D.; Atanasoski, R. T.; Debe, M. K.; Dahn, J. R. *J. Electrochem. Soc.* **2011**, *158*, B905.
(23) Oettel, C. S., K.; Rihko-Struckmann, L. *J. Fuel Cell Sci. Technol* **2012**, *9*, 1.
(24) Li, Q.; He, R.; Gao, J.-A.; Jensen, J. O.; Bjerrum, N. J. *J. Electrochem. Soc.* **2003**, *150*, A1599.
(25) Zhang, J.; Xie, Z.; Zhang, J.; Tang, Y.; Song, C.; Navessin, T.; Shi, Z.; Song, D.; Wang, H.; Wilkinson, D. P.; Liu, Z.-S.; Holdcroft, S. *J. Power Sources* **2006**, *160*, 872.
(26) Kizhakevariam, N.; Stuve, E. M. *Surf. Sci.* **1993**, *286*, 246.
(27) Collins, D. M.; Spicer, W. E. *Surf. Sci.* **1977**, *69*, 85.
(28) Yang, H.; Whitten, J. L. *J. Phys. Chem. B* **1997**, *101*, 4090.
(29) Dalbeck, R.; Buschmann, H. W.; Vielstich, W. *J. Electroanal. Chem.* **1994**, *369*, 233.
(30) Fridell, E.; Rosen, A.; Kasemo, B. *Langmuir* **1994**, *10*, 699.
(31) Fridell, E.; Elg, A.-P.; Rosén, A.; Kasemo, B. *J. Chem. Phys.* **1995**, *102*, 5827.
(32) Hsu, D. S. Y.; Hoffbauer, M. A.; Lin, M. C. *Langmuir* **1986**, *2*, 302.
(33) Mooney, C. E.; Anderson, L. C.; Lunsford, J. H. *J. Phys. Chem.* **1993**, *97*, 2505.
(34) Karp, E. M.; Campbell, C. T.; Studt, F.; Abild-Pedersen, F.; Nørskov, J. K. *J. Phys. Chem. C* **2012**, *116*, 25772.
(35) Patrito, E. M.; Olivera, P. P.; Sellers, H. *Surf. Sci.* **1994**, *306*, 447.
(36) Talley, L. D.; Sanders, F. W. A.; Bogan, D. J.; Lin, M. C. *J. Chem. Phys.* **1981**, *75*, 3107.
(37) Shavorskiy, A.; Eralp, T.; Gladys, M. J.; Held, G. *J. Phys. Chem. C* **2009**, *113*, 21755.
(38) Vasić, D.; Pašti, I.; Gavrilov, N.; Mentus, S. *Russ. J. Phys. Chem. A* **2013**, *87*, 2214.
(39) Maclagan, R. G. A. R. *J. Mol. Struc.-Theochem.* **2001**, *536*, 117.
(40) Mitchell, G. E.; Akhter, S.; White, J. M. *Surf. Sci.* **1986**, *166*, 283.
(41) Ogle, K. M.; White, J. M. *Surf. Sci.* **1986**, *169*, 425.
(42) Creighton, J. R.; White, J. M. *Surf. Sci.* **1982**, *122*, L648.
(43) Hellsing, B.; Kasemo, B.; Zhdanov, V. P. *J. Catal.* **1991**, *132*, 210.
(44) Marković, N. M.; Schmidt, T. J.; Grgur, B. N.; Gasteiger, H. A.; Behm, R. J.; Ross, P. N. *J. Phys. Chem. B* **1999**, *103*, 8568.

(45) Lee, K.-S.; Yoo, S. J.; Ahn, D.; Kim, S.-K.; Hwang, S. J.; Sung, Y.-E.; Kim, H.-J.; Cho, E.; Henkensmeier, D.; Lim, T.-H.; Jang, J. H. *Electrochim. Acta* **2011**, *56*, 8802.
(46) Gasteiger, H. A.; Kocha, S. S.; Sompalli, B.; Wagner, F. T. *Appl. Catal. B-Environ.* **2005**, *56*, 9.
(47) Gatto, I.; Stassi, A.; Passalacqua, E.; Aricò, A. S. *Int. J. Hydrogen Energ.* **2013**, *38*, 675.
(48) Yang, C.; Costamagna, P.; Srinivasan, S.; Benziger, J.; Bocarsly, A. B. *J. Power Sources* **2001**, *103*, 1.
(49) Aricò, A. S.; Di Blasi, A.; Brunaccini, G.; Sergi, F.; Dispenza, G.; Andaloro, L.; Ferraro, M.; Antonucci, V.; Asher, P.; Buche, S.; Fongalland, D.; Hards, G. A.; Sharman, J. D. B.; Bayer, A.; Heinz, G.; Zandonà, N.; Zuber, R.; Gebert, M.; Corasaniti, M.; Ghielmi, A.; Jones, D. J. *Fuel Cells* **2010**, *10*, 1013.
(50) Lee, S.-Y.; Ogawa, A.; Kanno, M.; Nakamoto, H.; Yasuda, T.; Watanabe, M. *J. Am. Chem. Soc.* **2010**, *132*, 9764.
(51) Bose, S.; Kuila, T.; Nguyen, T. X. H.; Kim, N. H.; Lau, K.-t.; Lee, J. H. *Prog. Polym. Sci.* **2011**, *36*, 813.
(52) MacFarlane, D. R.; Tachikawa, N.; Forsyth, M.; Pringle, J. M.; Howlett, P. C.; Elliott, G. D.; Davis, J. H.; Watanabe, M.; Simon, P.; Angell, C. A. *Energ. Environ. Sci.* **2014**, *7*, 232.
(53) Noda, A.; Susan, M. A. B. H.; Kudo, K.; Mitsushima, S.; Hayamizu, K.; Watanabe, M. *J. Phys. Chem. B* **2003**, *107*, 4024.
(54) Teliska, M.; Murthi, V. S.; Mukerjee, S.; Ramaker, D. E. *J. Phys. Chem. C* **2007**, *111*, 9267.
(55) He, Q.; Yang, X.; Chen, W.; Mukerjee, S.; Koel, B.; Chen, S. *Phys. Chem. Chem. Phys.* **2010**, *12*, 12544.
(56) Tanaka, A. A., R.; Nikolic, B. *J. Serb. Chem. Soc.* **1999**, *64*, 695−705.
(57) Ross, P. N.; Andricacos, P. C. *J. Electroanal. Chem. Interfacial Electrochem.* **1983**, *154*, 205.
(58) Hsueh, K. L.; Chang, H. H.; Chin, D. T.; Srinivasan, S. *Electrochim. Acta* **1985**, *30*, 1137.
(59) Weber, M.; Nart, F. C.; de Moraes, I. R.; Iwasita, T. *J. Phys. Chem.* **1996**, *100*, 19933.
(60) Zelenay, P.; Habib, M. A.; Bockris, J. O. *Langmuir* **1986**, *2*, 393.
(61) Santos, M. C.; Miwa, D. W.; Machado, S. A. S. *Electrochem. Commun.* **2000**, *2*, 692.
(62) Kaserer, S.; Caldwell, K. M.; Ramaker, D. E.; Roth, C. *J. Phys. Chem. C* **2013**, *117*, 6210.
(63) Crooks, R. M.; Bard, A. J. *J. Electroanal. Chem. Interfacial Electrochem.* **1988**, *243*, 117.
(64) Cabrera, C. R.; Bard, A. J. *J. Electroanal. Chem. Interfacial Electrochem.* **1989**, *273*, 147.
(65) Cabrera, C. R.; Garcia, E.; Bard, A. J. *J. Electroanal. Chem. Interfacial Electrochem.* **1989**, *260*, 457.
(66) Crooks, R. M.; Bard, A. J. *J. Phys. Chem.* **1987**, *91*, 1274.
(67) Crooks, R. M.; Fan, F. R. F.; Bard, A. J. *J. Am. Chem. Soc.* **1984**, *106*, 6851.
(68) Crooks, R. M.; Bard, A. J. *J. Electroanal. Chem. Interfacial Electrochem.* **1988**, *240*, 253.
(69) Flarsheim, W. M.; Tsou, Y. M.; Trachtenberg, I.; Johnston, K. P.; Bard, A. J. *J. Phys. Chem.* **1986**, *90*, 3857.

(70) Toghill, K. E.; Méndez, M. A.; Voyame, P. *Electrochem. Commun.* **2014**, *44*, 27.
(71) El Kadiri, F.; Faure, R.; Durand, R. *J. Electroanal. Chem. Interfacial Electrochem.* **1991**, *301*, 177.
(72) Grgur, B. N.; Marković, N. M.; Ross, P. N. *Can. J. Chemistry* **1997**, *75*, 1465.
(73) Maciá, M. D.; Campiña, J. M.; Herrero, E.; Feliu, J. M. *J. Electroanal. Chem.* **2004**, *564*, 141.
(74) Perez, J.; Villullas, H. M.; Gonzalez, E. R. *J. Electroanal. Chem.* **1997**, *435*, 179.
(75) Schmidt, T. J.; Paulus, U. A.; Gasteiger, H. A.; Behm, R. J. *J. Electroanal. Chem.* **2001**, *508*, 41.
(76) StrmcnikD; KodamaK; van der Vliet, D.; GreeleyJ; Stamenkovic, V. R.; Marković, N. M. *Nat. Chem.* **2009**, *1*, 466.
(77) McDonald, A. C.; Fan, F. R. F.; Bard, A. J. *J. Phys. Chem.* **1986**, *90*, 196.
(78) Strbac, S. *Electrochim. Acta* **2011**, *56*, 1597.
(79) Parthasarathy, A.; Martin, C. R.; Srinivasan, S. *J. Electrochem. Soc.* **1991**, *138*, 916.
(80) Bard, A. J.; Faulkner, L. R. *Electrochemical Methods: Fundamentals and Applications, 2nd Edition*; Wiley Global Education, 2000.
(81) Parthasarathy, A.; Srinivasan, S.; Appleby, A. J.; Martin, C. R. *J. Electrochem. Soc.* **1992**, *139*, 2856.
(82) Han, P.; Bartels, D. M. *J. Phys. Chem.* **1996**, *100*, 5597.
(83) Tromans, D. *Hydrometallurgy* **1998**, *48*, 327.
(84) Haynes, W. M. *CRC Handbook of Chemistry and Physics, 95th Edition*; Taylor & Francis, 2014.
(85) Sepa, D. B.; Vojnovic, M. V.; Vracar, L. M.; Damjanovic, A. *Electrochim. Acta* **1986**, *31*, 97.
(86) Parthasarathy, A.; Srinivasan, S.; Appleby, A. J.; Martin, C. R. *J. Electrochem. Soc.* **1992**, *139*, 2530.
(87) Sepa, D. B.; Vracar, L. M.; Vojnovic, M. V.; Damjanovic, A. *Electrochim. Acta* **1986**, *31*, 1401.
(88) Yeager, E. *Electrochim. Acta* **1984**, *29*, 1527.
(89) Damjanovic, A. *J. Electroanal. Chem.* **1993**, *355*, 57.
(90) Uribe, F. A.; Springer, T. E.; Gottesfeld, S. *J. Electrochem. Soc.* **1992**, *139*, 765.
(91) Paulus, U. A.; Schmidt, T. J.; Gasteiger, H. A.; Behm, R. J. *J. Electroanal. Chem.* **2001**, *495*, 134.
(92) Sepa, D. B.; Vojnovic, M. V.; Damjanovic, A. *Electrochim. Acta* **1980**, *25*, 1491.
(93) Fletcher, S. *J. Solid State Electr.* **2009**, *13*, 537.
(94) Damjanovic, A.; Brusic, V. *Electrochim. Acta* **1967**, *12*, 615.
(95) Koper, M.; Wieckowski, A. *Fuel Cell Catalysis: A Surface Science Approach*; Wiley, 2009.
(96) Zhang, J.; Vukmirovic, M. B.; Sasaki, K.; Nilekar, A. U.; Mavrikakis, M.; Adzic, R. R. *J. Am. Chem. Soc.* **2005**, *127*, 12480.
(97) Mukerjee, S.; Srinivasan, S.; Soriaga, M. P.; McBreen, J. *J. Electrochem. Soc.* **1995**, *142*, 1409.
(98) Liu, Z.; Ma, L.; Zhang, J.; Hongsirikarn, K.; Goodwin, J. G. *Cataly. Rev.* **2013**, *55*, 255.
(99) Stamenkovic, V.; Mun, B. S.; Mayrhofer, K. J. J.; Ross, P. N.; Markovic, N. M.; Rossmeisl, J.; Greeley, J.; Nørskov, J. K. *Angew. Chem. Int. Ed.* **2006**, *45*, 2897.

(100) Stephens, I. E. L.; Bondarenko, A. S.; Gronbjerg, U.; Rossmeisl, J.; Chorkendorff, I. *Energ. Environ. Sci.* **2012**, *5*, 6744.
(101) Schmidt, T. J.; Stamenkovic, V.; Ross, J. P. N.; Markovic, N. M. *Phys. Chem. Chem. Phys.* **2003**, *5*, 400.
(102) Gómez, R.; Orts, J. M.; Álvarez-Ruiz, B.; Feliu, J. M. *J. Phys. Chem. B* **2003**, *108*, 228.
(103) Zolfaghari, A.; Villiard, F.; Chayer, M.; Jerkiewicz, G. *J. Alloy Compd.* **1997**, *253–254*, 481.
(104) Flarsheim, W. M.; Bard, A. J.; Johnston, K. P. *J. Phys. Chem.* **1989**, *93*, 4234.

Chapter 5

Inverted and Normal Kinetic Isotope Effects in Oxygen Evolution and Oxygen Reduction Electrochemistry

The work in this chapter was accomplished in collaboration with Thao T. H. Hoang, Jason A. Varnell, and Professor Andrew A. Gewirth.

5.1 Introduction

5.1.1 The Importance of Aqueous Oxygen Chemistry

The ability to control the chemistry of oxygen represents a major step toward the utilization of sustainable energy from renewable energy sources.[1] To materialize this vision, facilitating the oxygen evolution reaction (OER, $4OH^- \rightarrow 2H_2O + 4e^- + O_2$ in alkaline or $2H_2O \rightarrow O_2 + 4H^+ + 4e^-$ in acid) and the oxygen reduction reaction (ORR, $2H_2O + 4e^- + O_2 \rightarrow 4OH^-$ in alkaline or $O_2 + 4e^- + 4H^+ \rightarrow 2H_2O$ in acid) at low overpotential is necessary to the widespread deployment of electrolyzers and fuel cells, respectively.[2] An electrolyzer is an energy conversion device that splits water into H_2 and O_2 via the following two half reactions: the anodic OER and the cathodic hydrogen evolution reaction (HER, $2H^+ + 2e^- \rightarrow H_2$).[3] In a fuel cell, the reverse of these two half reactions occurs.[4] In both devices, the performance is not limited by the reaction involving hydrogen, but is limited by the sluggish kinetics of the reaction involving oxygen.[1-4] Oxygen chemistry has thus attracted a tremendous amount of attention over the past fifty years to prepare robust, scalable and competent OER and ORR catalysts.[5-10] Despite

the extensive effort expended in these areas, a complete understanding of the reaction mechanism has not been achieved.

The kinetic isotope effect (KIE) is a general method to study the reaction mechanism of many types of chemical transformations.[11,12] Specifically, the substitution of hydrogen with deuterium has been carried out extensively due to the large differences in reaction rates arising from the reduced mass differences between the isotopes.[13,14] For electrocatalysis involving protons, Conway et al. investigated KIE of the HER catalyzed by Pt and Yeager et al. conducted a similar KIE study on ORR catalyzed by Pt.[15-18] However, KIE studies are not prevalent in the field of electrochemistry. Therefore, we seek to expand the use KIE studies to further understand the OER and ORR processes at the molecular level.

5.1.2 Current Understanding of the ORR Mechanism

The ORR is central to the development of alternative energy conversion devices.[5,19] Currently, state-of-the-art fuel cells utilize Pt or one of its alloys to facilitate the ORR.[4] Unfortunately, these precious materials degrade or are poisoned during operation and despite being the best catalysts still exhibit overpotentials of about 300 mV. An alternate strategy to promote efficient O_2 reduction is to utilize low-cost and poison-resistant non-precious metal (NPM) catalysts.[5,20,21] State-of-the-art NPM ORR catalysts are prepared via pyrolysis of transition metal/N/C precursors,[6] which results in a highly heterogeneous surface structure. Due to the structural complexity of the catalyst material,[22] optimization of the ORR performance cannot be achieved using conventional structure-activity relationship approaches.[23] Apart from the incomplete structural information of the active site, the formation pathways of deleterious side products such as O_2^- and H_2O_2 that lead to degradation of fuel cell membranes and other

components are also elusive.[24,25] A unified understanding of the ORR and degradation mechanism undoubtedly will benefit future catalyst design.

Understanding the ORR mechanism is instrumental to lowering the activation barrier of ORR. Over the past decade, there are few substantive attempts to elucidate the mechanism of ORR.[26] However, the relationship between the reaction pathway and catalytic performance remains poorly understood. The rate-determining step (RDS) of ORR catalyzed by Pt is generally accepted to be the first electron transfer step, as evidenced by a 120 mV/dec Tafel slope and supported by DFT calculations.[2] The onset potential of ORR by Pt is not pH-dependent,[27] further providing evidence that the RDS is not a proton-coupled electron transfer (PCET) step. Yeager et al. demonstrated that Pt does not exhibit a KIE during ORR.[18] The absence of a KIE signifies that the steps at or before the RDS do not involve protons/deuterons.[18] One recent report found that Au(100) exhibits a substantial KIE during ORR at pH < 7, but no KIE at pH > 7.[28] This finding is suggestive of a change in proton-participation in the ORR mechanism upon pH changes. Recent studies of NPM catalysts have shown that the ORR onset potential is pH-dependent,[8,21,23] suggesting that protons are involved in the RDS. However, a comprehensive, comparative study of carbon-supported catalysts is lacking.

5.1.3 Current Understanding of the OER Mechanism

Redox reactions involving multiple PCET steps are ubiquitous and have gathered a significant amount of interest over the past decades.[29,30] Using renewable sources to power water-splitting electrolyzers offers a promising scheme to generate H_2 with almost no carbon footprint.[31-33] The efficiency of the overall reaction is dictated by the OER overpotential at the anode and the stability of the anode material.[34,35] Ir and Ru are the anodes of choice in acidic

electrolyte with low OER overpotentials.[36] However, their widespread application of Ir/Ru-based anodes is hindered by the prohibitive high cost and poor long-term stability of these precious metal catalysts.

Ni, Co, and their alloys are attractive OER electrocatalysts for OER in alkaline electrolyte, because these relatively inexpensive NPM materials are abundant and durable in basic condition.[37-39] However, OER overpotentials using Ni/Co-based materials range from ca. 50 to 150 mV relative to the thermoneutral potential of 1.48 V versus RHE.[31,40] Real-world thermodynamic efficiencies for water splitting are only ~75% with currently available Ni-based catalysts.[31] However, catalyst design to eliminate the high OER overpotential is still limited because insight into the OER mechanism is missing.[38]

Currently, tremendous effort is put in to elucidate the identity and surface structure of the bulk anode materials used to facilitate the OER.[39,41] Reports suggest that surface oxides and oxyhydroxides which are formed on the metal prior to the OER are the active catalytic species.[42] Compositional and morphological changes upon redox cycling of these porous thin film OER catalysts have been investigated using various techniques, including but not limited to voltammetric studies,[36,43,44] Raman spectroscopy,[45-48] X-ray photoelectron spectroscopy (XPS),[49-52] X-ray diffraction (XRD),[53,54] X-ray absorption spectroscopy (XAS),[55-57] scanning electron microscopy (SEM) and transmission electron microscopy (TEM),[54,58] scanning tunneling microscopy (STM),[59] ellipsometry,[60,61] atomic force microscopy (AFM),[62,63] electrochemical quartz crystal microbalance (EQCM),[64-67] and *in situ* stress measurement.[68]

In order to understand the OER mechanism on oxidized metals, it is important to interrogate the OER process at the molecular level. Density functional theory (DFT) calculations predicted that the binding energy of surface oxygen species such as $^{*}O$, $^{*}OH$, $^{*}OOH$ controls the

OER activity.[32,38,42] This result sparks the following question: does the kinetics of deprotonation determine the overall OER rate? To the best of our knowledge, literature report on the KIE of the OER process is lacking.

5.1.4 KIE Studies of ORR and OER

Here, we launched comprehensive and comparative KIE studies of several precious and NPM ORR and OER catalysts to gain direct mechanistic insight into these intricate reactions involving multiple PCET steps. In particular, we examined the effect of deuteration on the ORR process in three different pH regimes: acidic condition that is relevant to proton-conducting polymer electrolyte membrane fuel cells, neutral condition that is found commonly in biological systems, and basic condition that is essential for alkaline fuel cell. We further interrogated the difference in OER response of NPM OER catalysts in the condition at which they are stable and active. We envision these results to provide unique information that will allow the development of next-generation, high-performance, durable, and affordable ORR and OER catalysts for practical energy conversion devices under operation conditions in the near future.

5.2 Experimental Procedures for Studies in Proteo and Deutero Solutions

Chemicals were obtained from commercial sources and used without further purification unless otherwise specified. All proteo and deutero aqueous solutions were prepared freshly each day using Milli-Q water (> 18 MΩ cm) and D_2O, respectively. For experiments at pH 0.3 and pD 0.3, H_2SO_4 (500 mM) and D_2SO_4 (500 mM) solutions were used, respectively. For experiments at pH 7 and pD 7, proteo potassium phosphate buffer solution (H-phos, 100 mM) and deutero potassium phosphate buffer solution (D-phos, 100 mM) were used, respectively. For experiments at pH 13 and pD 13, NaOH (100 mM) and NaOD (100 mM) solutions were used, respectively.

For experiments at pH 14 and pD 14, NaOH (1 M) and NaOD (1 M) solutions were used, respectively. Solutions were sparged with Ar or O_2, both of which were dried using a drying tube, for 30 min prior to each experiment.

PANI-Fe-C was prepared according to published procedure.[6] Ink slurries were prepared using Nafion 117 solution (5 wt % in alcohols, Sigma-Aldrich) or solution made of Nafion powder (Sigma-Aldrich). To prepare the binder solution from Nafion powder, Nafion powder (5 mg) was dissolved in IPA or IPA-D8 (95 mg). After sonicating the mixture for 10 min and heating to 70 °C for 1 min, PEG200 (5 mg) was added. PANI-Fe-C (7.2 mg), Pt supported on Vulcan XC-72 (Pt/C, 7.2 mg, 20 wt. %, E-Tek Inc.), or Pd supported on Vulcan XC-72 (Pd/C, 7.2 mg, 20 wt. %, E-Tek Inc.) was dispersed in EtOH (500 μL) or EtOD (500 μL). After sonicating for 20 min, Nafion solution (10 μL) was added. For the binderless cases, the inks were prepared in analogous manner in the absence of Nafion solution. The resultant suspension was further sonicated for 20 min to afford an ink slurry, which was deposited onto a GC electrode and then dried under a stream of Ar.

For OER studies, Au substrates were fabricated from glass microscope coverslips (Gold Seal No. 1, 150 μm thick) modified on one side by electron beam deposition of 20 nm Ti followed by 200 nm Au. The geometric areas of the electrodes were typically ca. 1 cm^2. The Au electrodes were annealed with a H_2 flame prior to use. The Ni films (~ 300 nm) were electrodeposited onto Au cantilevers in an aqueous bath of $NiSO_4$ (0.5 M) and H_3BO_3 (0.4 M) adjusted to pH 3 using H_2SO_4 using a pulse deposition method: held at -4 mA cm^{-2} for 100 s followed by 10 s of resting time, and repeated for two more times. [68] For studies in deutero solutions, the bath was prepared using D_3BO_3 (0.4 M) in D_2O and adjusted to pD 3 using D_2SO_4. Co films (~ 300 nm) were prepared in an analogous manner using $CoSO_4$ (0.5 M) instead.

5.3 Results and Discussion

5.3.1 ORR in Proteo and Deutero Solutions

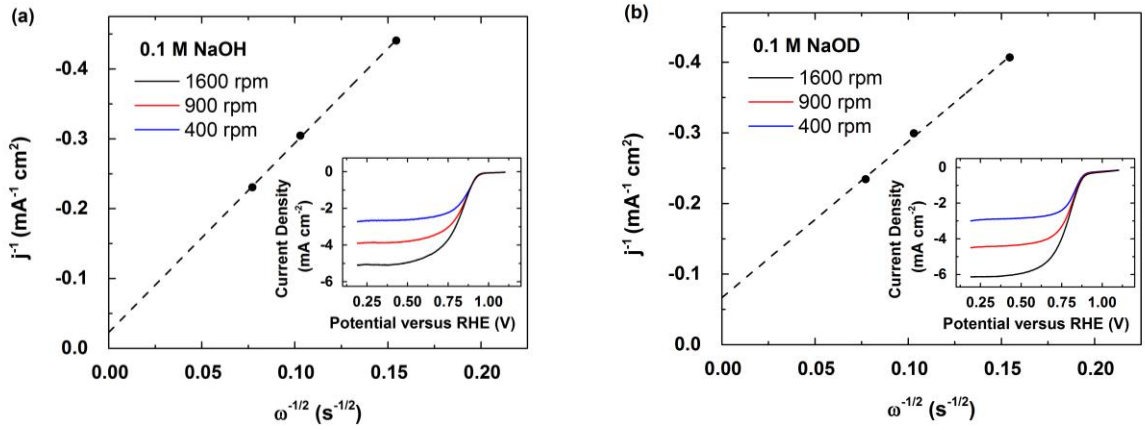

Figure 5.1. Koutecky-Levich plots and rotating disk electrode (RDE) voltammograms (insets) of PANI-Fe-C in (a) pH 13 and (b) pD 13 O_2-saturated solutions with a scan rate of 10 mV s^{-1} at 400 (blue), 900 (red), and 1600 (black) rpm.

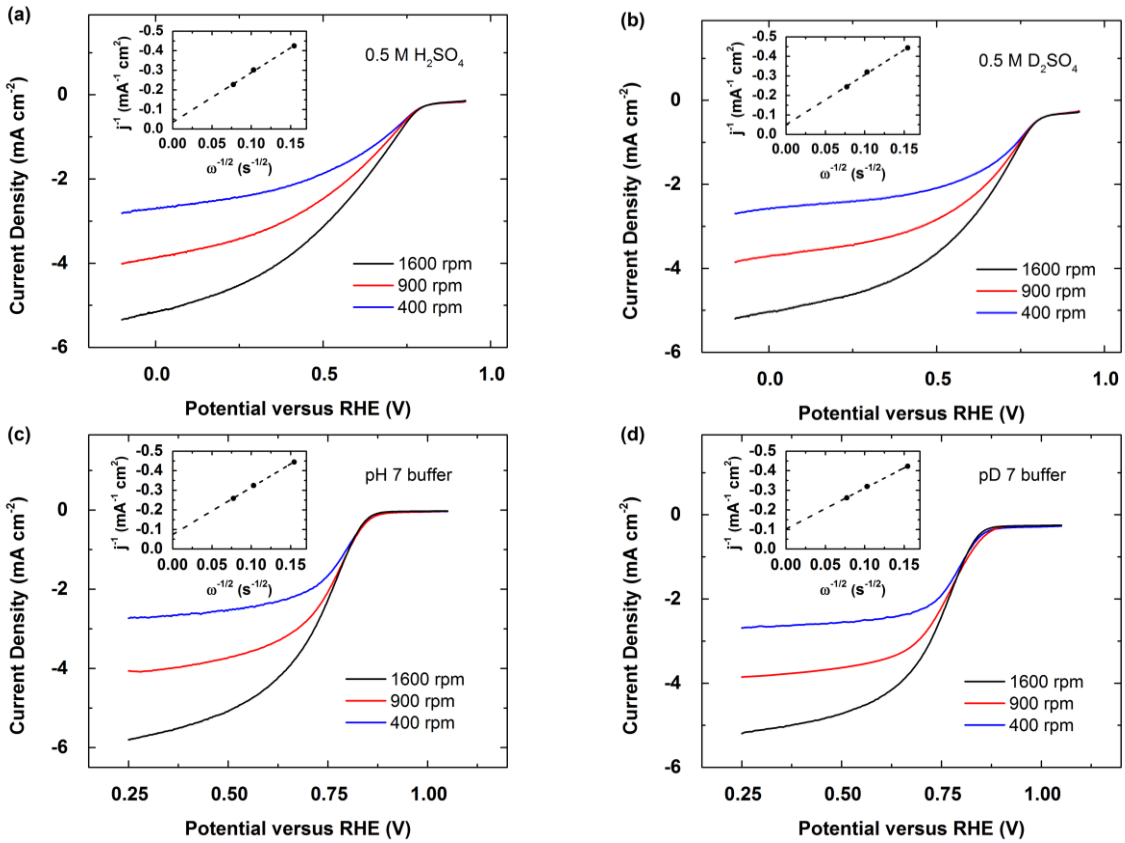

Figure 5.2. RDE voltammograms and Koutecky-Levich plots (insets) of PANI-Fe-C with inks prepared with Nafion powder in (a) pH 0.3, (b) pD 0.3, (c) pH 7, and (d) pD 7 O_2-saturated solutions with a scan rate of 10 mV/s at 400 (blue), 900 (red), and 1600 (black) rpm.

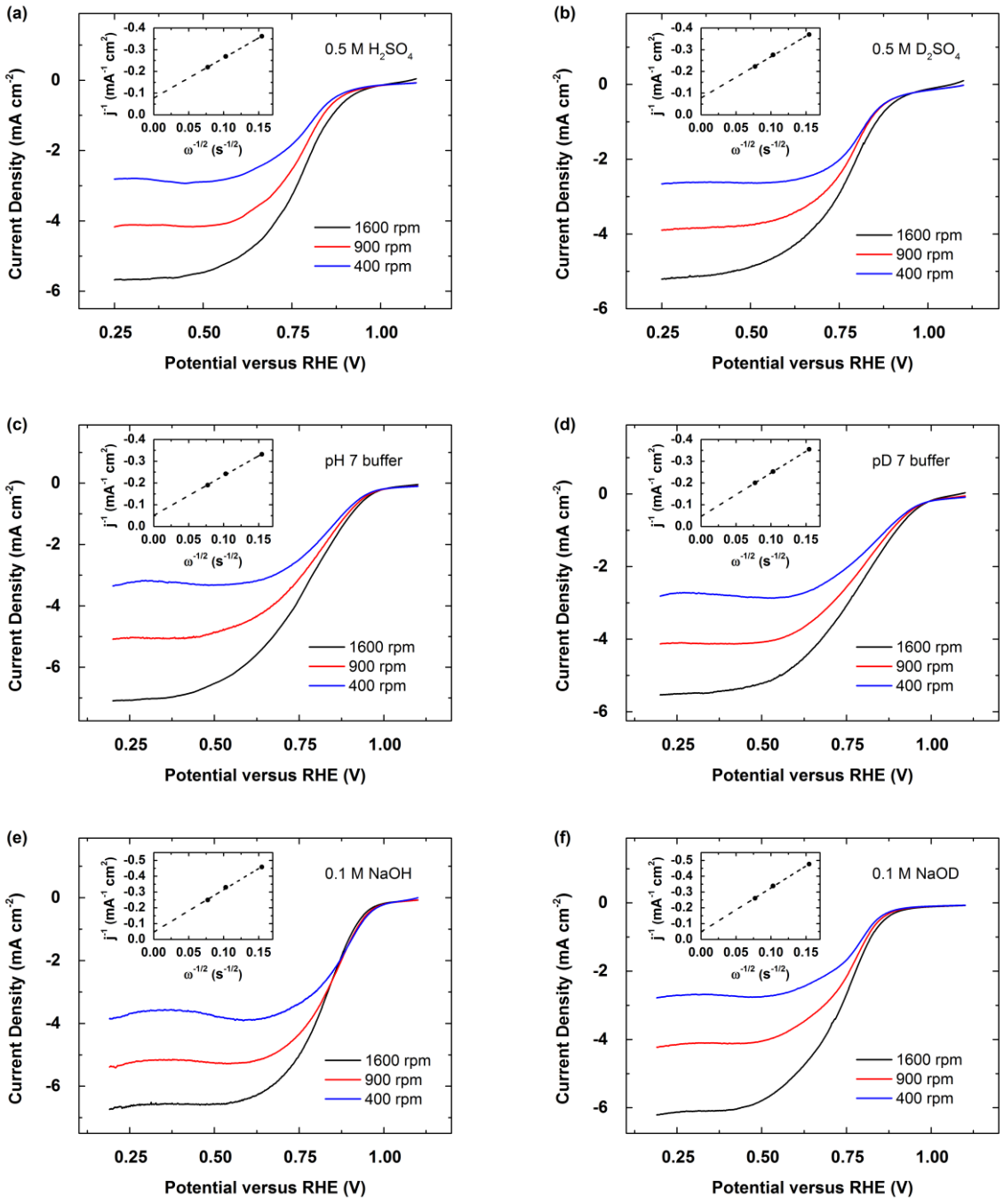

Figure 5.3. RDE voltammograms and Koutecky-Levich plots (insets) of 20 wt.% Pt supported on Vulcan XC-72 with inks prepared with Nafion powder in (a) pH 0.3, (b) pD 0.3, (c) pH 7, (d) pD 7, (e) pH 13, and (f) pD 13 O_2-saturated solutions with a scan rate of 10 mV/s at 400 (blue), 900 (red), and 1600 (black) rpm.

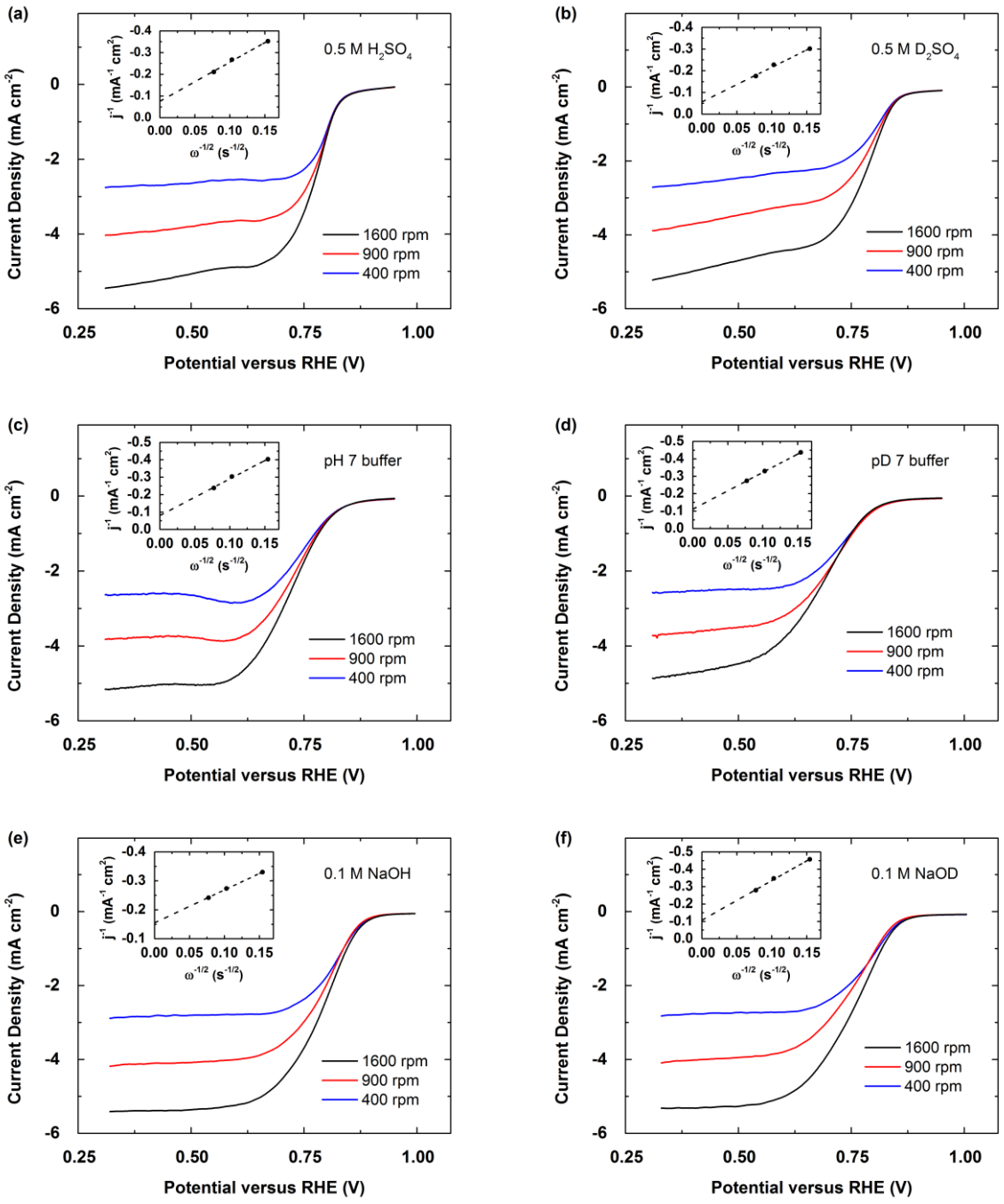

Figure 5.4. RDE voltammograms and Koutecky-Levich plots (insets) of 20 wt.% Pd supported on Vulcan XC-72 with inks prepared with Nafion powder in (a) pH 0.3, (b) pD 0.3, (c) pH 7, (d) pD 7, (e) pH 13, and (f) pD 13 O_2-saturated solutions with a scan rate of 10 mV/s at 400 (blue), 900 (red), and 1600 (black) rpm.

To determine the role of protons in the RDS for the ORR, we carried out Koutecky-Levich analysis in proteo and deutero solutions. The voltammograms of O_2 reduction catalyzed by PANI-Fe-C, Pt/C, and Pd/C under various rotation regimes in acidic, neutral, and basic conditions and the corresponding Koutecky-Levich plots are shown in Figures 5.1-4. We note that in some cases the O_2-diffusion limited current densities observed in proteo solution are different from those found in deutero solution. However, the difference in the mass transport limited current density does not directly relate to the KIE. The KIE was determined from the voltammograms by comparing the kinetically limited current density (j_K) given by the Koutecky-Levich equation.[69]

$$\frac{1}{j} = \frac{1}{j_K} + \frac{1}{j_{l,c}}$$

$$limiting\ cathodic\ current\ density = \ j_{l,c} = 0.62nFD_{O_2}^{2/3}\omega^{1/2}v^{-1/6}C_{O_2}^{*}$$

$$kinetically\ limited\ current\ density = \ j_K = nFk_fC_{O_2}^{*}$$

Where j = current density, n = number of electrons transferred, F = Faraday's constant, D_{O_2} = diffusion coefficient of O_2, ω = electrode rotation rate, v = kinematic viscosity, $C_{O_2}^{*}$ = the bulk concentration of O_2, and $k_f = k_0\, e^{-\frac{\alpha F\eta}{RT}}$ = heterogeneous rate constant for reduction.

$j_{l,c}$ represents the current density obtained under totally mass-transfer-limited conditions and thus involves terms related to diffusion, bulk concentration, kinematic viscosity and rotation rate. j_K describes the current density measured under the kinetic limitation when the mass transfer is efficient enough to keep the concentration of reactants at the electrode surface equal to the bulk value. The current density absent any mass-transfer effects is a prerequisite to study kinetic isotope effect.

Plotting $y = \frac{1}{j}$ and $x = \frac{1}{\omega^{1/2}}$ gives:

$$slope = \frac{1}{0.62nFD_{O_2}^{2/3}v^{-1/6}C_{O_2}^{*}}$$

$$intercept = \frac{1}{j_K} = \frac{1}{nFk_fC_{O_2}^{*}}$$

Dividing j_K^H obtained in proteo solution by j_K^D obtained in deutero solution gives:

$$\frac{j_0^H}{j_0^D} = \frac{n^H k_f^H C_{O_2}^{*,H}}{n^D k_f^D C_{O_2}^{*,D}}$$

Following established methods,[70,71] the solvomolalities of O_2 in H_2O and D_2O at 298.15 K are converted to bulk concentrations of O_2 in H_2O ($C_{O_2}^{*,H}$) and in D_2O ($C_{O_2}^{*,D}$) to yield

$$\frac{C_{O_2}^{*,H}}{C_{O_2}^{*,D}} = 0.908$$

Calculating the KIE at constant overpotentials and assuming the total number of electrons transferred and the transfer coefficients to be similar yields:

$$\frac{k_0^H}{k_0^D} = \frac{j_0^H C_{O_2}^{*,D}}{j_0^D C_{O_2}^{*,H}} = \frac{j_0^H}{j_0^D}\frac{1}{0.908}$$

Changes in O_2 diffusion limited current is due to differences in O_2 diffusion coefficients, kinematic viscosity, and bulk O_2 concentration between H and D solutions. Similar changes in the peak current can be observed for the case without rotation.

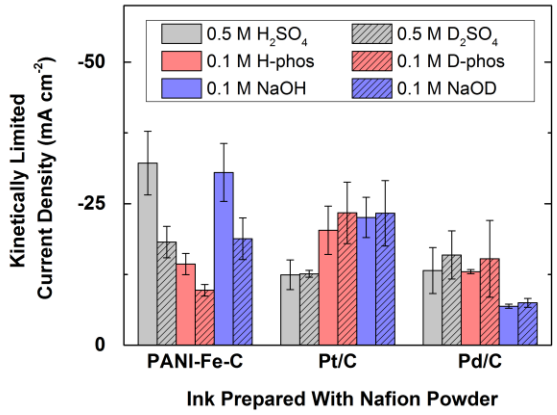

Figure 5.5. Bar graphs summarizing the kinetically limited current densities obtained from Koutecky-Levich analyses of O_2 reduction voltammograms for PANI-Fe-C, Pt/C and Pd/C with inks prepared with Nafion powder in O_2-saturated 0.5 M H_2SO_4 (gray), 0.5 M D_2SO_4 (gray with strips), 0.1 M pH 7 phosphate buffer (red), 0.1 M pD 7 phosphate buffer (red with strips), 0.1 M NaOH (blue), and 0.1 M NaOD (blue with strips) solutions.

Figure 5.5 shows bar graphs that summarizes the kinetically limited current densities of PANI-Fe-C, Pt/C, and Pd/C in O_2-saturated acidic, neutral and basic solutions. The observed kinetically limited current densities are comparable to the values found for conventional heterogeneous ORR catalysts.[72-74] We observe a dramatic decrease in the ORR kinetically limited current density for the deutero case relative to the proteo case for PANI-Fe-C in all three pH regimes. By way of contrast, the ORR j_K for Pt/C and Pd/C exhibits only a slight dependence on whether the electrolyte is deuterated or not, which is attributed to the difference in bulk concentration of O_2 in proteo and deutero solvents. By accounting for the differences in the value of $C_{O_2}^*$ in the two solutions, the kinetic isotope effects for the ORR catalyzed by PANI-Fe-C, Pt/C and Pd/C can be calculated.

Table 5.1. Summary of the kinetic isotope effect of ORR catalyzed by PANI-Fe-C, Pt/C, and Pd/C in acidic (0.5 M sulfuric acid), neutral (0.1 M, pH 7 phosphate buffer) and basic (0.1 M NaOH/(D)) conditions.

Catalysts	PANI-Fe-C	Pt/C	Pd/C
Acidic	1.9 ± 0.5	1.1 ± 0.2	0.9 ± 0.4
Neutral	1.6 ± 0.3	1.0 ± 0.3	0.9 ± 0.4
Basic	1.8 ± 0.5	1.0 ± 0.3	1.0 ± 0.2

The majority of the decrease in the kinetically limited current density observed for the NPM catalyst is therefore attributed to a KIE. Table 5.1 shows the KIE corrected for the differences in $C_{O_2}^*$ in proteo and deutero solutions observed for PANI-Fe-C, Pt/C and Pd/C catalysts. For PANI-Fe-C, a KIE of approximately 2 was observed while for Pt/C a KIE of 1 was observed in all three pH regimes. The observed KIEs for the non-precious metal catalyst demonstrate the involvement of protons from solution at or before the RDS of the ORR. Pt/C exhibits a fairly low overpotential for the ORR, while that for PANI-Fe-C is somewhat higher. We wanted to test whether a higher overpotential for the ORR might be correlated with sensitivity to deuteration. Experiments using Pd/C, a catalyst that exhibits a higher overpotential for ORR than Pt/C, also show a KIE of 1, indicating that for these precious metal ORR catalysts (Pt/C and Pd/C) the RDS is a proton-independent electron transfer process.

In order to verify the kinetic effect of the replacement of hydrogen with deuterium, inks were prepared using Nafion powder to eliminate the effect of trapped protons in the catalyst film and the results are presented in Figures 5.6-13 and Table 5.2-4.

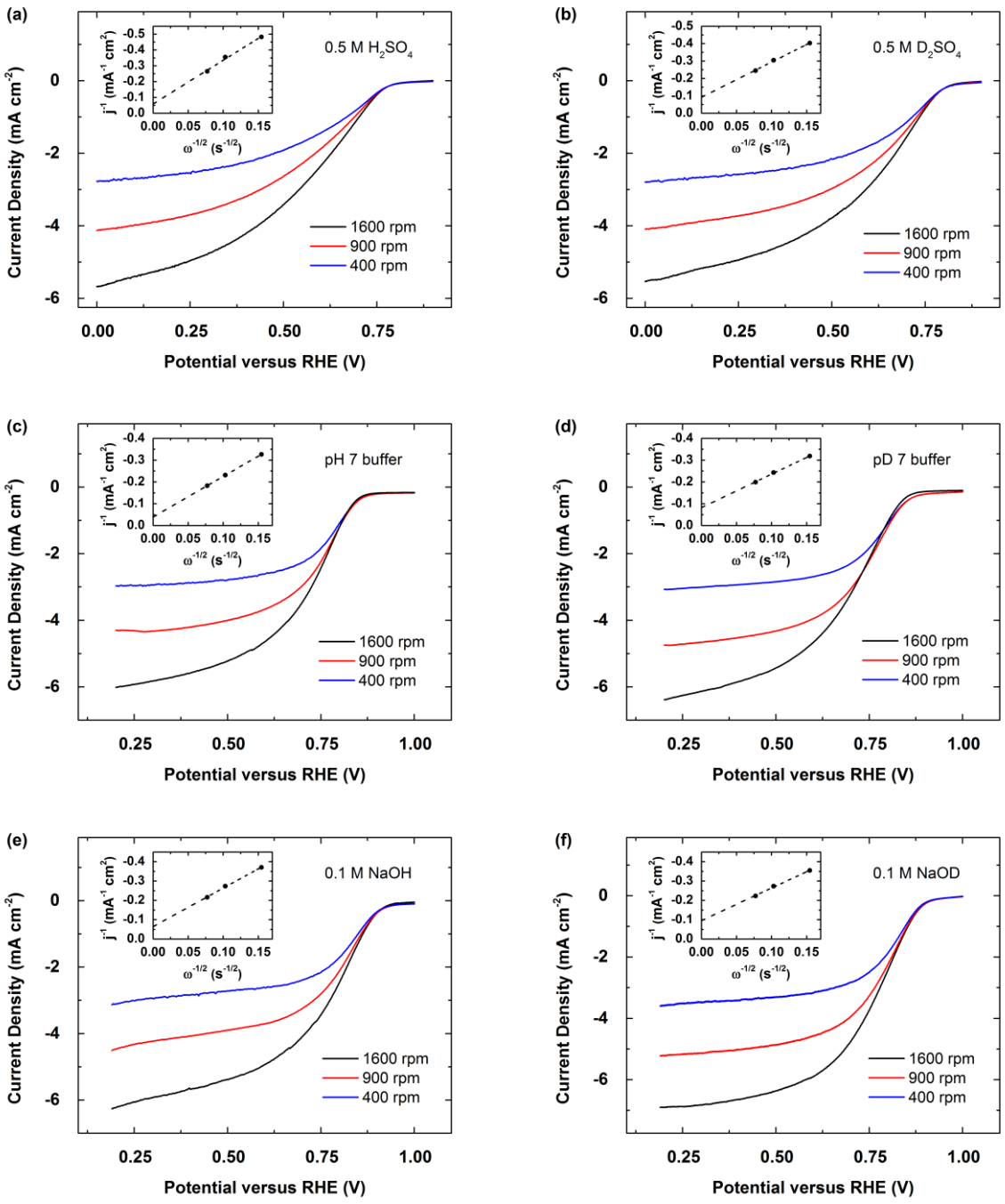

Figure 5.6. RDE voltammograms and Koutecky-Levich plots (insets) of PANI-Fe-C without binder in (a) pH 0.3, (b) pD 0.3, (c) pH 7, (d) pD 7, (e) pH 13, and (f) pD 13 O_2-saturated solutions with a scan rate of 10 mV/s at 400 (blue), 900 (red), and 1600 (black) rpm.

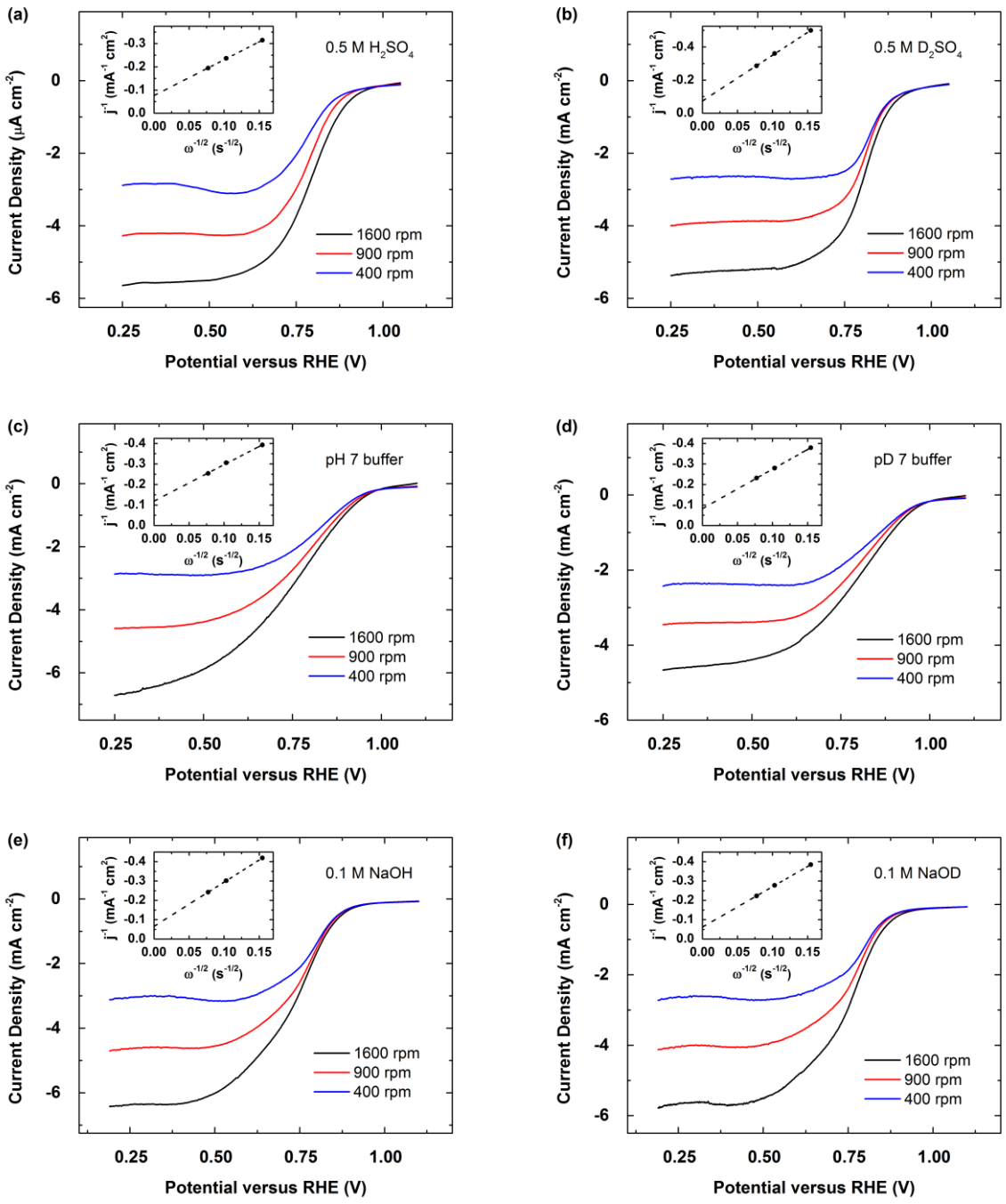

Figure 5.7. RDE voltammograms and Koutecky-Levich plots (insets) of 20 wt.% Pt supported on Vulcan XC-72 without binder in (a) pH 0.3, (b) pD 0.3, (c) pH 7, (d) pD 7, (e) pH 13, and (f) pD 13 O_2-saturated solutions with a scan rate of 10 mV/s at 400 (blue), 900 (red), and 1600 (black) rpm.

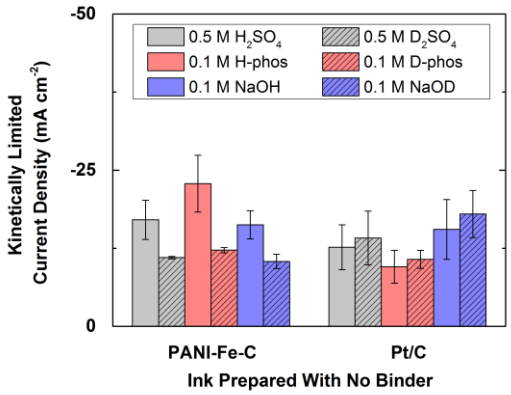

Figure 5.8. Bar graphs summarizing the kinetically limited current densities obtained from Koutecky-Levich analyses of O_2 reduction voltammograms for PANI-Fe-C, Pt/C and Pd/C with inks prepared with without binder in O_2-saturated 0.5 M H_2SO_4 (gray), 0.5 M D_2SO_4 (gray with stripes), 0.1 M pH 7 phosphate buffer (red), 0.1 M pD 7 phosphate buffer (red with stripes), 0.1 M NaOH (blue), and 0.1 M NaOD (blue with stripes) solutions.

In an effort to minimize the effect of binder on protons or deuterons delivery to the catalytic site during the ORR process, we study the ORR activity of PANI-Fe-C and Pt/C in proteo and deutero solutions using various ink preparation methods (Figures 5.6-13). Figure 5.8 compares the kinetically limited current densities calculated from Koutecky-Levich plots of PANI-Fe-C and Pt/C using inks without Nafion powder. We observe lower ORR kinetically limited current densities by PANI-Fe-C in deutero solutions as compared to proteo solutions. For Pt/C, the ORR kinetically limited current densities are similar in both deutero and proteo solutions. These results are similar to those obtained from inks prepared using Nafion powder as binders.

Table 5.2. Summary of the kinetic isotope effect of ORR catalyzed by PANI-Fe-C, Pt/C, and Pd/C with inks prepared without binder in acidic (0.5 M sulfuric acid), neutral (0.1 M, pH 7 phosphate buffer) and basic (0.1 M NaOH/(D)) conditions.

Catalysts	**PANI-Fe-C**	**Pt/C**
Acidic	1.7 ± 0.3	1.0 ± 0.4
Neutral	2.1 ± 0.4	1.0 ± 0.3
Basic	1.7 ± 0.3	0.9 ± 0.4

Table 5.2 displays the kinetic isotope effects calculated using values in Figure 5.8. In all three pH regimes, the kinetic isotope effects measured for PANI-Fe-C and Pt/C are ca. 2 and 1, respectively. The kinetic isotope effects are very similar for both inks with Nafion powder as binder and inks without binder, further confirming our conclusion above that protons are involved at or before the RDS of the ORR catalyzed by non-precious metal catalyst PANI-Fe-C but not for the case of Pt/C.

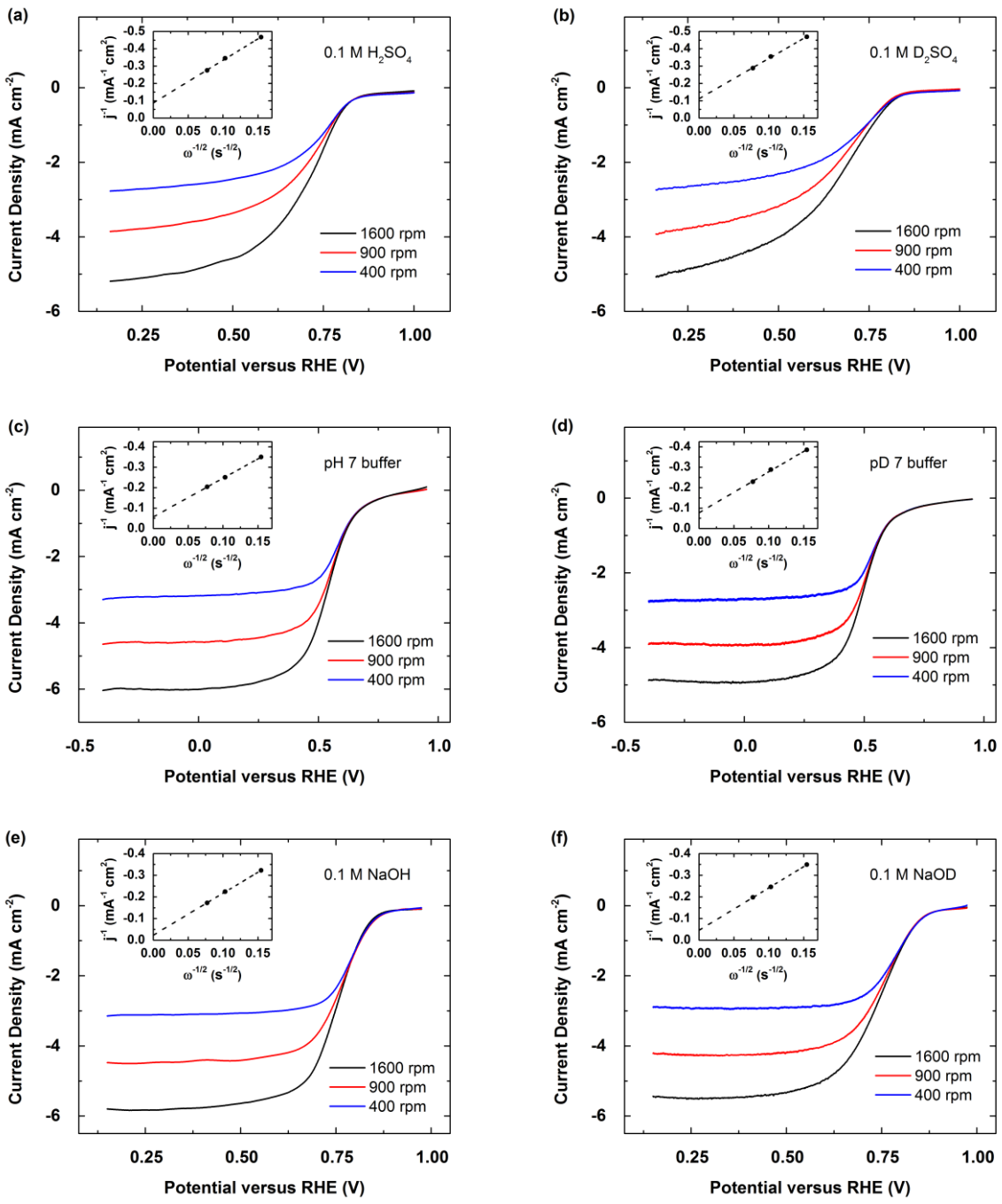

Figure 5.9. RDE voltammograms and Koutecky-Levich plots (insets) of PANI-Fe-C with inks prepared using Nafion 117 solution in EtOH in (a) pH 0.3, (b) pD 0.3, (c) pH 7, (d) pD 7, (e) pH 13, and (f) pD 13 O_2-saturated solutions with a scan rate of 10 mV/s at 400 (blue), 900 (red), and 1600 (black) rpm.

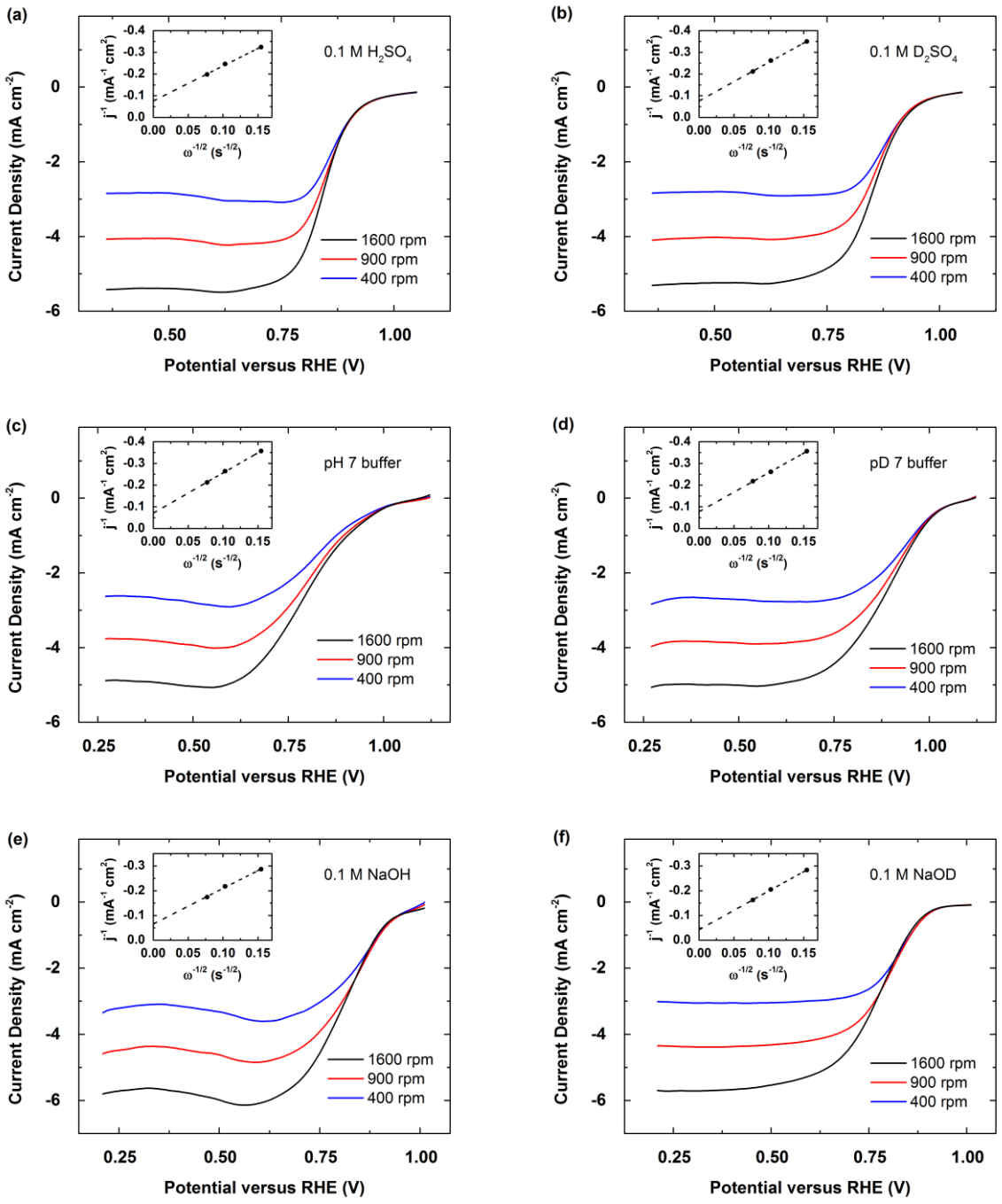

Figure 5.10. RDE voltammograms and Koutecky-Levich plots (insets) of 20 wt.% Pt supported on Vulcan XC-72 with inks prepared using Nafion 117 solution in EtOH in (a) pH 0.3, (b) pD 0.3, (c) pH 7, (d) pD 7, (e) pH 13, and (f) pD 13 O_2-saturated solutions with a scan rate of 10 mV/s at 400 (blue), 900 (red), and 1600 (black) rpm.

To further investigate the effect of trapped protons in binders, we formulate inks using Nafion 117 solution saturated with protons. Figures 5.9 and 5.10 display the ORR LSVs and Koutecky-Levich plots of PANI-Fe-C and Pt/C with inks saturated with protons. Using inks saturated with protons, we observed no change in the O_2 reduction voltammetries and the kinetically limited current densities.

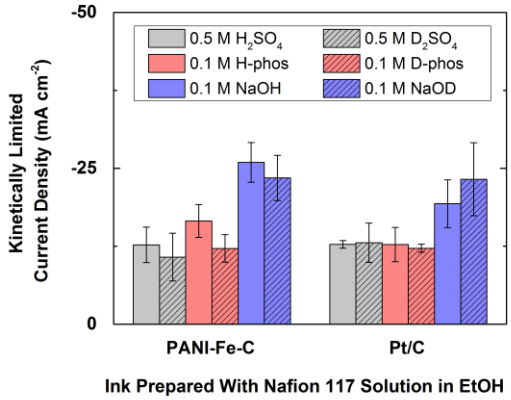

Figure 5.11. Bar graphs summarizing the kinetically limited current densities obtained from Koutecky-Levich analyses of O_2 reduction voltammograms for PANI-Fe-C and Pt/C with inks prepared using Nafion 117 solution in O_2-saturated 0.5 M H_2SO_4 (gray), 0.5 M D_2SO_4 (gray with stripes), 0.1 M pH 7 phosphate buffer (red), 0.1 M pD 7 phosphate buffer (red with stripes), 0.1 M NaOH (blue), and 0.1 M NaOD (blue with stripes) solutions.

Table 5.3. Summary of the kinetic isotope effect of ORR catalyzed by PANI-Fe-C and Pt/C with inks prepared using Nafion 117 solution in acidic (0.5 M sulfuric acid), neutral (0.1 M, pH 7 phosphate buffer) and basic (0.1 M NaOH/(D)) conditions.

Catalysts	**PANI-Fe-C**	**Pt/C**
Acidic	1.3 ± 0.5	1.1 ± 0.3
Neutral	1.5 ± 0.4	1.2 ± 0.3
Basic	1.2 ± 0.2	0.9 ± 0.3

Figure 5.11 shows the bar graphs summarizing the measured kinetically limited current densities of PANI-Fe-C and Pt/C with inks saturated with protons. Table 5.3 summaries the measured kinetically limited current densities and the calculated kinetic isotope effects of PANI-Fe-C and Pt/C with inks saturated with protons. Both PANI-Fe-C and Pt/C exhibit KIEs of ca. 1, suggesting that the presence of deuterons in bulk solution does not slow down nor speed up the ORR. These results suggest that by using inks prepared with the commercially available Nafion 117 solution, protons are trapped inevitably in the dried catalyst film on the electrode surface.

Since commercially available Nafion 117 solution results in trapped protons in the catalyst inks, we attempted to exchange out the trapped protons by using EtOD to prepare the inks. We also explored other methods to prepare the inks such as drying the Nafion 117 solution prior to preparing inks, but this method resulted in a translucent film that could not be redissolved upon addition of deuterated ethanol or isopropanol. Figure 5.12 compares the LSVs of an attempt to prepare deuterated inks using Nafion 117 solution diluted with EtOD. The corresponding bar graphs that summarize the kinetically limited current densities calculated from Koutecky-Levich plots are shown in Figure 5.13.

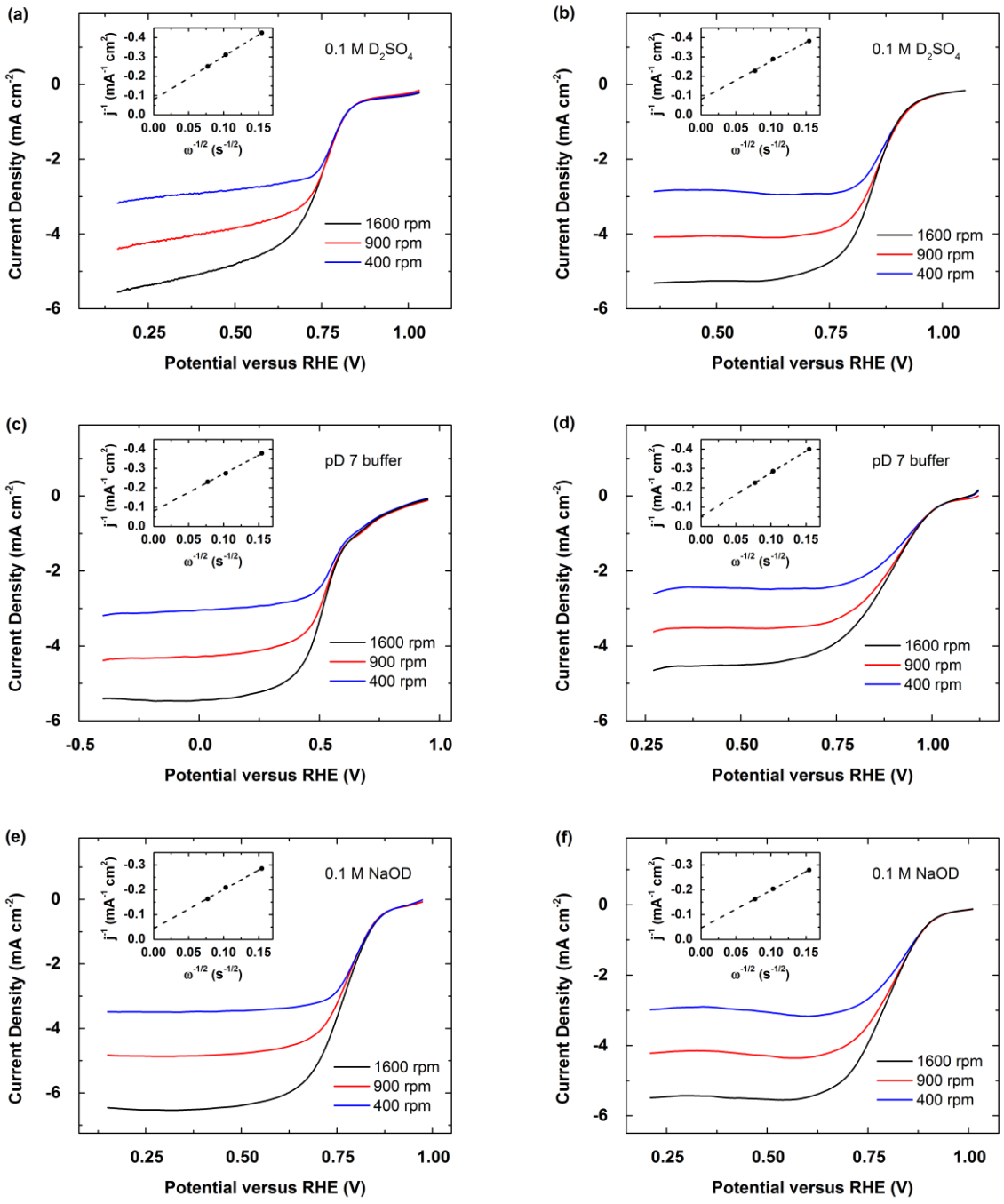

Figure 5.12. RDE voltammograms and Koutecky-Levich plots (insets) of PANI-Fe-C in (a) pD 0.3, (c) pD 7, and (e) pD 13 and 20 wt.% Pt supported on Vulcan XC-72 in (b) pD 0.3, (d) pD 7, and (f) pD 13 O_2-saturated solutions using inks prepared with Nafion 117 solution in EtOD with a scan rate of 10 mV/s at 400 (blue), 900 (red), and 1600 (black) rpm.

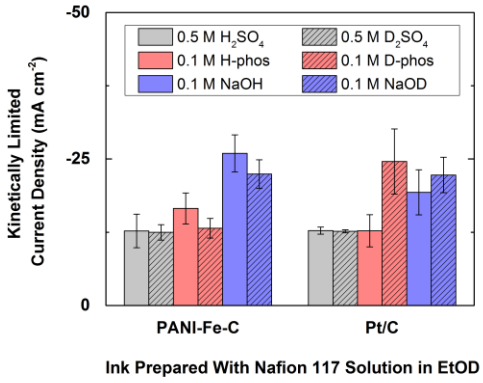

Figure 5.13. Bar graphs summarizing the kinetically limited current densities obtained from Koutecky-Levich analyses of O_2 reduction voltammograms for PANI-Fe-C and Pt/C with inks prepared using Nafion 117 solution in O_2-saturated 0.5 M H_2SO_4 (gray), 0.5 M D_2SO_4 (gray with stripes), 0.1 M pH 7 phosphate buffer (red), 0.1 M pD 7 phosphate buffer (red with stripes), 0.1 M NaOH (blue), and 0.1 M NaOD (blue with stripes) solutions.

Table 5.4. Summary of the kinetic isotope effect of ORR catalyzed by PANI-Fe-C and Pt/C with inks prepared using Nafion 117 solution with the deuterated inks containing EtOD in acidic (0.5 M sulfuric acid), neutral (0.1 M, pH 7 phosphate buffer) and basic (0.1 M NaOH/(D)) conditions.

Catalysts	PANI-Fe-C	Pt/C
Acidic	1.1 ± 0.3	1.1 ± 0.1
Neutral	1.4 ± 0.3	1.1 ± 0.2
Basic	1.3 ± 0.2	1.0 ± 0.2

Figure 5.13 shows the bar graphs summarizing the measured kinetically limited current densities of PANI-Fe-C and Pt/C with deuterated inks prepared using Nafion 117 solution diluted with EtOD. Table 5.4 summarizes the measured kinetically limited current densities and the calculated kinetic isotope effects of PANI-Fe-C and Pt/C with deuterated inks prepared using Nafion 117 solution diluted with EtOD. Both PANI-Fe-C and Pt/C exhibit KIEs of ca. 1, suggesting that the presence of deuterons in bulk solution does not slow down nor speed up the ORR. These results suggest that by using inks prepared with the Nafion 117 solution, protons are

trapped in the dried catalyst film on the electrode surface irrespective to the solvent used to dilute the ink.

5.3.2 Mechanistic Insight of the ORR

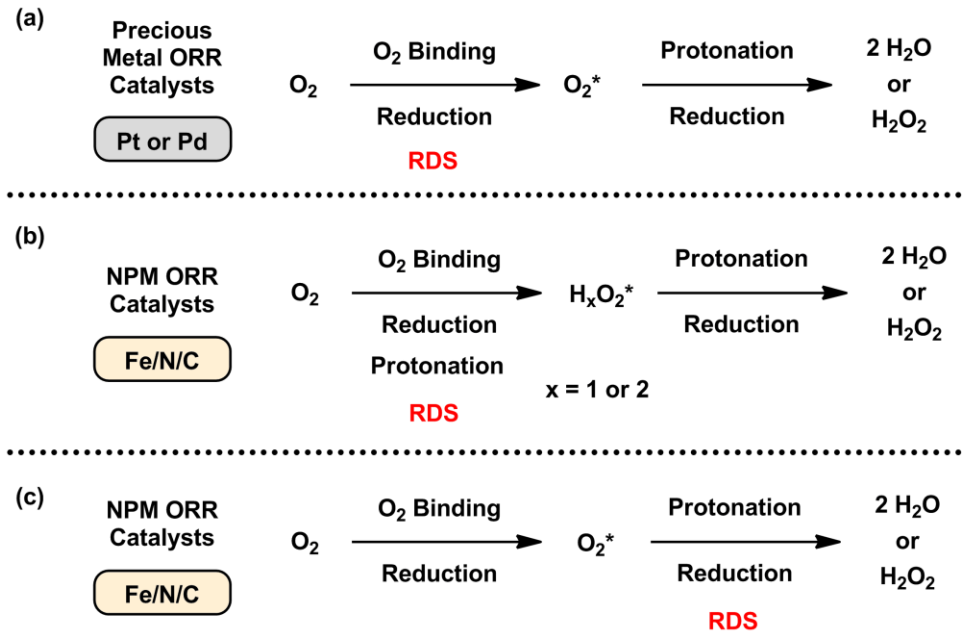

Figure 5.14. Possible mechanisms for the ORR on (a) precious metal and (b-c) non-precious metal materials. O_2^* and $H_xO_2^*$ represent surface-adsorbed, partially-reduced O_2 species without and with protonation, respectively. x = 1 or 2. RDS is shown in red.

Together, these findings suggest that the ORR proceeds by different mechanisms in the two classes of ORR catalysts investigated in this work. Figure 5.14 shows three possible mechanisms associated with the ORR catalyzed by either precious metals (Figure 5.14a) or a NPM ORR catalyst (Figures 5.14 b and c). The lack of a KIE in the precious metal catalysts indicates that protons do not participate in the RDS of the ORR, confirming that the RDS of O_2 reduction by Pt and Pd is an electron transfer step (Figure 5.14a), at least in the high overpotential region.[18,27] The presence of an electron-transfer-limited RDS is fully consistent

with the 120 mV dec^{-1} Tafel slope observed in the so-called Langmuir region of the ORR voltammetry.[2]

For the NPM ORR catalyst examined, the presence of a KIE ≈ 2 indicates that protons are involved at or before the RDS. Two possible general mechanisms are consistent with this insight. In the mechanism presented in Figure 5.14b, protons are associated with the initial reduction of O_2 during the RDS. Figure 5.14c displays a mechanism whereby protons likely interact with a bound partially-reduced O_2 species during the RDS. Unfortunately, our data cannot differentiate between the two proposed ORR pathways shown in Figures 5.14 b and c for NPM catalysts. Previous work has shown that the ORR onset potential of NPM catalysts is pH-dependent,[8,21,23] further supporting the involvement of at least one protonation step at or before the RDS in the ORR mechanism. Our experiments using PANI-Fe-C as a model NPM catalyst show the presence of a KIE, consistent with the proposed mechanisms.

The direct evidence demonstrated by our KIE studies that different ORR catalysts achieve the same reaction via different mechanisms provides an important distinction when considering the design of new catalyst materials. An electron transfer RDS suggests that proton transfer plays a negligible role in determining the ORR kinetics on Pt. Therefore, methods to improve the ORR activity of Pt include alloying Pt with Ni and other transition metals to destabilize the surface OH poisons instead of enhancing proton transfer kinetics.[75-77] Alternatively, the presence of a KIE on the NPM catalyst examined here suggests that improvements in catalyst performance require specific attention to proton transfer during the RDS in addition to the electron transfer step(s).

5.3.3 Electrodeposited Ni and Co OER Catalysts in Proteo and Deutero Solutions

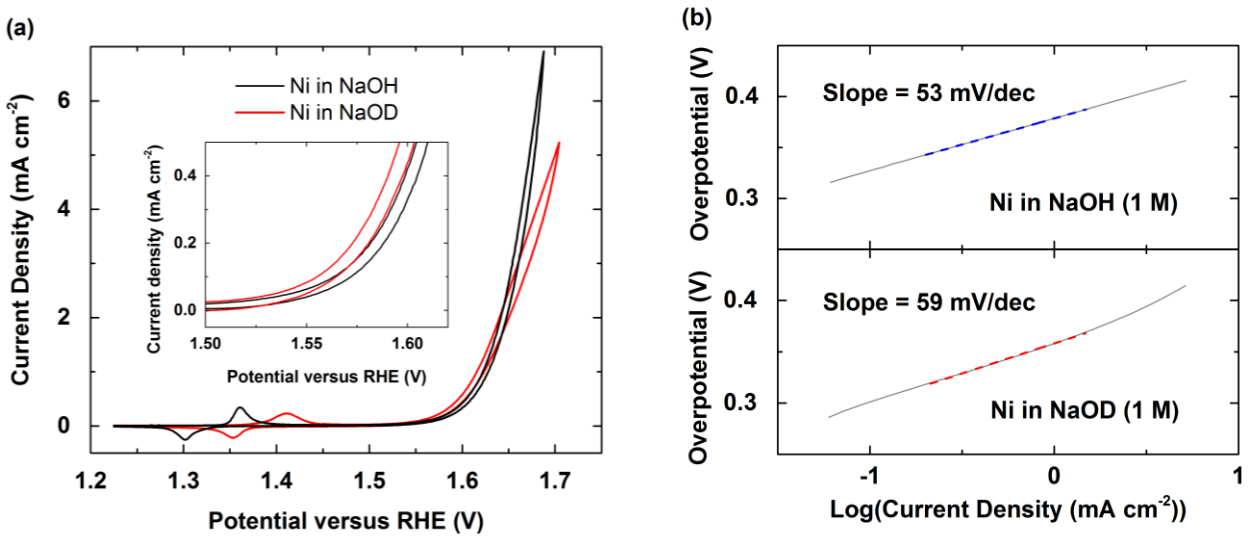

Figure 5.15. (a) IR-corrected CVs of Ni in NaOH (1 M) and NaOD (1 M) solutions. Inset displays the OER onset region. (b) Tafel plots of Ni in (top) 1 M NaOH and (bottom) 1 M NaOD solutions.

After examining proton involvement in the ORR, we next investigate the effect of protons on the OER. Figure 5.15a shows cyclic voltammograms (CVs) obtained from Ni in basic proteo and deutero solutions starting with the anodic sweep. Similar to previous reports in alkaline solutions,[33,78,79] Ni metal is spontaneously oxidized to Ni(II) hydroxide upon immersion,[53,80] and is then further oxidized to generate Ni(III) oxyhydroxide at 1.362 V. At 1.600 V, the electrodeposited Ni electrode delivers an OER current density of 0.5 mA cm^{-2}.

The black line in Figure 5.15a displays the $Ni(OH)_2$/NiOOH redox wave with a midpoint potential ($E_{1/2}$) of 1.333 V. The red line displays the $Ni(OD)_2$/NiOOD redox wave with a $E_{1/2}$ of 1.388 V. The position of the redox wave in deutero solution is ca. 55 mV more positive than that obtained in proteo solution, indicating that the oxidation of $Ni(OD)_2$ to NiOOD is thermodynamically more difficult than the oxidation of $Ni(OH)_2$ to NiOOH.

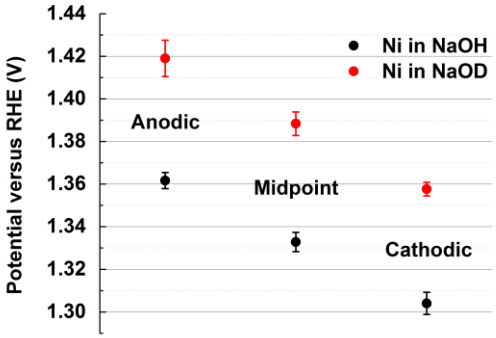

Figure 5.16. Anodic, cathodic, and midpoint potentials of the $Ni(OH)_2$/NiOOH wave in 1 M NaOH (black) and 1 M NaOD (red).

Figure 5.16 summarizes other information related to the Ni(II/III) redox wave. We note that the magnitudes of the isotope effects are less for the cases of surface catalysts, likely due to the planar geometry (as opposed to spherical geometry in the case for molecular compounds in solution) of the extended water network and solvation shell.[81-83]

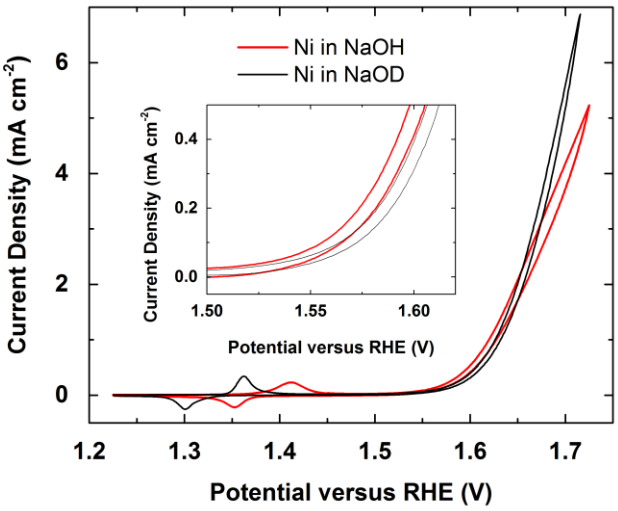

Figure 5.17. IR-uncorrected CVs of Ni in NaOH (1 M) and NaOD (1 M) solutions. Inset displays the OER onset region.

The CVs presented in Figure 5.17 are without IR-correction. We observe more OER current in proteo solution than deutero solution at potentials greater than 1.66 V for the case of Ni, likely because the diffusion coefficient of H_2O is larger than that of D_2O.[84,85] At potentials lower than 1.66 V, OER occurs at a slower rate and the interlayer $H(D)_2O$ inside the NiOOH(D) film is preferentially oxidized. At high potentials, interlayer $H(D)_2O$ is depleted and the gaps are replenished by bulk $H(D)_2O$. This bulk-to-interlayer diffusion process of $H(D)_2O$ likely limits the OER rates. We note that Co exhibits the same crossing behavior as Ni (*vide infra*), suggesting that this feature is likely not dependent on the identity of the OER catalysts, but rather a general phenomenon when running experiments in and comparing results between proteo and deutero solutions.

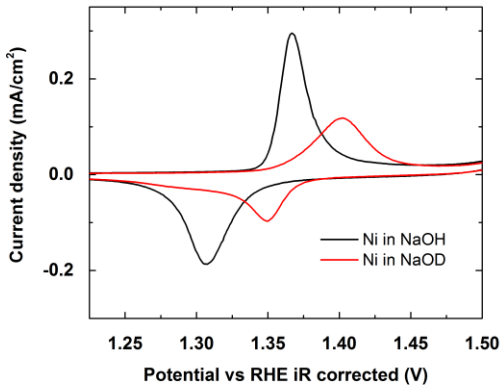

Figure 5.18. CVs of Ni foil in 1 M NaOH (black) and 1 M NaOD (red) solutions (zoomed into the Ni redox wave).

To confirm the shift in the Ni(II/III) wave with deuteration, we carried out similar experiments using Ni foil in proteo and deutero solutions and observed a 40 mV positive shift in deutero solution similar to the case using electrodeposited Ni (Figure 5.18). We note that these shifts in potential are not due to reference electrode effects, as confirmed by experiments with

$K_3Fe(CN)_6$ which demonstrated identical potentials for the Fe(II/III) wave in both proteo and deutero media.[83] The difference in current observed in Figure 5.18 could be due to many reasons, one of which could be the difference in surface roughness of the Ni foil used. The Ni foil was polished with sand paper and dipped into H_2SO_4 or D_2SO_4 to expose fresh Ni surfaces prior to electrochemical studies, so the geometric area used to calculate current density does not reflect the actual electrochemical active surface area. We would like to stress that the point of this experiment is to check whether the Ni(II/III) peak shifts depending on the bulk solution content—in particular H versus D. This experiment clearly demonstrates that the Ni(II/III) peak in deutero solution is more positive than the case in proteo solution.

Similar positive shifts upon deuteration have been observed for a variety of cationic transition metal complexes and are explained in two ways.[81-83] First, because the O-D bond is stronger than the O-H bond,[86] breaking the O-D bond is energetically more costly and the anodic wave shifts positive. Second, Ni(III) has a tighter solvation shell than Ni(II) and D_2O forms a stronger deuterium bonding network relative to the hydrogen bonding network of H_2O.[73] Therefore, there is a greater increase in entropy when the deuterated solvent structure relaxes during the reduction of Ni(III) to Ni(II).[83] Due to the more favorable change in entropy that occurs upon reducing Ni(III) to Ni(II) in deutero solutions, the cathodic wave shifts positive. Since both the anodic and cathodic waves shift positive, the $E_{1/2}$ shifts positive accordingly.

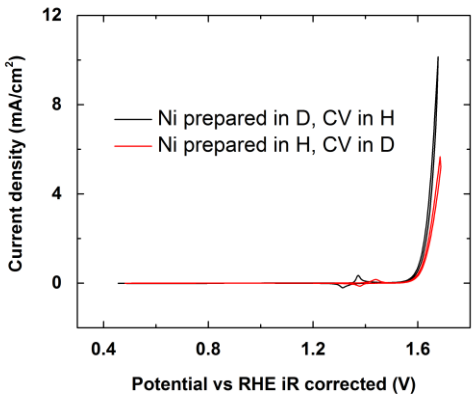

Figure 5.19. CVs of Ni prepared in proteo solution and ran CVs in NaOD (1 M) solution and prepared in deutero solution and ran in NaOH (1 M) solution.

Figure 5.19 shows the CVs of Ni prepared in proteo solution and interrogated in deutero solution and CVs of Ni prepared in deutero solution and interrogated in proteo solutions. The CVs show that Ni metal film prepared in H solution and interrogated in D solution exhibit a Ni(II/III) redox wave more positive than that found using a Ni metal film prepared in D solution and interrogated in H solution. This result suggests that the shift in redox potential does not depend on the solution in which the film is prepared. Instead, the shift depends upon the solution in which the voltammetry is recorded, a condition analogous to the case presented in Figure 5.15. This "cross" experiment further demonstrates that preparing Ni metal film in H and D solution does not leave a detectable trace amount of H or D residual in the electrodeposited film. Therefore, pulse deposition of Ni in pH- or pD-controlled solution likely leads to electrodeposits consisting of pure Ni metal films absent hydroxide, deuteroxide, oxyhydroxide, and/or oxydeuteroxide contamination.

The inset to Figure 5.15a shows a blowup of the OER onset region in both proteo and deutero solutions. Interestingly, the inset shows that the OER in D_2O exhibits a more negative onset and a lower overpotential at 0.5 mA cm^{-2} relative to the same system in H_2O. Figure 5.15b

shows the Tafel slopes of OER catalyzed by Ni in proteo and deutero basic solutions. The Tafel slope found in NaOD at the low overpotential region (where η ranges between 0.3 and 0.4 V) is 59 mV dec^{-1} (Figure 5.15b, top), a value that is somewhat greater than the corresponding slope (53 mV dec^{-1}) found in NaOH (Figure 5.15b, bottom). Recent Tafel slope values for the OER in NaOH on Ni at the low overpotential range from 51 to 54 mV dec^{-1}.[87] At higher overpotentials, the NaOH and NaOD OER traces cross at 1.65 V versus RHE, likely due to the faster diffusion rate of H_2O relative to D_2O from bulk solution to the electrode surface where they interact with the oxide layers during OER.[84,85] The contribution of differential diffusion rates at low overpotential is insignificant because there are enough reactants between the oxide layers when the rate of OER is low. Therefore for the KIE analysis, we focus at the low overpotential region where the kinetics of the reaction is not dominated by the mass diffusion from reactants from the bulk solution to the catalytic site on the electrode surface.

Table 5.5. Summary of the overpotential at 0.5 mA cm^{-2}, Tafel slope and kinetic isotope effect of OER catalyzed by Ni and Co in 1 M NaOH and 1 M NaOD solutions.

Condition	Overpotential at 0.5 mA cm^{-2} (V)	Tafel Slope (mV dec^{-1})	k_H/k_D
Ni in 1 M NaOH	0.370 ± 0.006	53 ± 1	0.6 ± 0.1
Ni in 1 M NaOD	0.337 ± 0.006	59 ± 1	
Co in 1 M NaOH	0.330 ± 0.007	57 ± 1	0.5 ± 0.1
Co in 1 M NaOD	0.285 ± 0.002	63 ± 1	

Table 5.5 lists the OER activity of Ni found in Figure 5.15a, the OER Tafel slope obtained at the low overpotential region from Tafel analysis (Figure 5.15b), and k_H/k_D of Ni in proteo and deutero solutions. The KIE of OER was determined from the voltammograms using the Tafel equation.[88]

$$overpotential = \eta = \frac{R\,T}{\alpha\, n_a\, F}\ln j_0 - \frac{R\,T}{\alpha\, n_a\, F}\ln j$$

where R = ideal das constant, T = temperature, α = transfer coefficient, n_a = number of electrons transferred during the rate-determining step, F = Faraday's constant, j_0 = exchange current density and j = current density.

Plotting $y = \eta$ and $x = \ln j$ gives:

$$slope = -\frac{R\,T}{\alpha\, n_a\, F}$$

$$intercept = \frac{R\,T}{\alpha\, n_a\, F}\ln j_0$$

$$intercept = (-slope)\ln j_0$$

$$j_0 = e^{\frac{intercept}{-slope}}$$

Exchange current density (j_0) is described by the following equation:[69]

$$j_0 = nFk_0C^*$$

where n = total number of electrons transferred, k_0 = standard heterogeneous rate constant, and C^* = bulk concentration of species.

Dividing j_0^H obtained in proteo solution by j_0^D obtained in deutero solution gives:

$$\frac{j_0^H}{j_0^D} = \frac{n^H k_0^H C^{*,H}}{n^D k_0^D C^{*,D}}$$

$C^{*,H} = C^{*,D}$ because the experiments were conducted in pH 14 and pD 14 solutions, i.e. the hydroxide and deuteroxide concentrations are the same.

Assuming n remains unchanged in proteo and deutero solutions:

$$\frac{j_0^H}{j_0^D} = \frac{k_0^H}{k_0^D}$$

Using Tafel slope analysis to calculate kinetic isotope effect is not meaningful at high overpotential because the reaction is limited by mass transport. Therefore, to obtain meaningful interpretation of the kinetic isotope effect of OER catalyzed by Ni and Co, we utilize Tafel slope analysis at overpotentials less than 0.5 V where the reaction is not limited by mass transport.

Using the Gibbs formation energy of D_2O,[89] the formal reduction potential for the reaction $2\ D_2 + O_2 \rightarrow 2\ D_2O$ is calculated to be 1.26 V, which is 30 mV greater than H_2O (1.23 V). The standard potential of a hydrogen redox couple on Pt differs from that of a deuterium redox couple on Pt by 4.3 mV at 298 K.[90]

For maintaining consistency in Tafel slope analysis, Tafel slopes are obtained in the same potential window for both proteo and deutero solutions where the second derivatives of the CV traces are zero. The Tafel slopes measured for proteo solutions at both low and high overpotentials match with literature reported values. Recent Tafel slope values for the OER on Ni at high overpotential range from 126 to 132 mV dec^{-1}.[87] However, we focus our attention to the low overpotential region where the kinetics of the reaction is not plagued by mass diffusion from bulk solution to the electrode surface then through the layered-structure of the metal oxides/oxyhydroxides/hydroxides. Using the Tafel slopes found, the calculated KIE is 0.6. A k_H/k_D value of below 1 is indicative of an inverse KIE.[13,14]

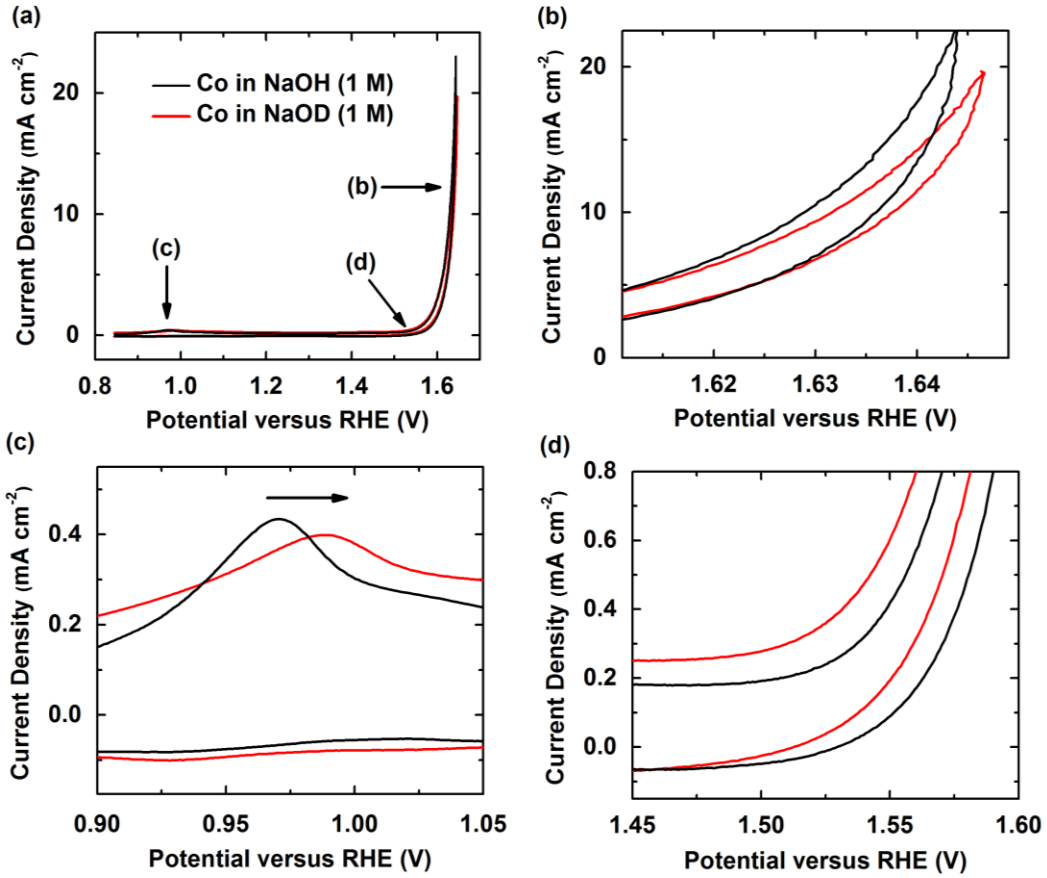

Figure 5.20. (a) IR-corrected CVs of Co in NaOH (1 M) and NaOD (1 M) solutions. (b), (c), and (d) display the blowups of the diffusion-controlled OER region, the Co(II/III) redox region, and the OER onset region, respectively.

To test the generality of the inverse KIE in alkaline OER catalysis, we next evaluate the effect of deuteration on the OER on Co electrodes. Figures 5.20a-d display the IR-corrected CVs of Co obtained in basic proteo and deutero solutions and Figures 5.21a-d show the corresponding uncorrected data. Our Co OER results match with previous reports.[45] Without IR-correction, we observe more OER current in proteo solution than deutero solution at potentials greater than 1.63 V for the case of Co, likely because the diffusion coefficient of H_2O is larger than that of D_2O.[84,85] Qualitatively similar to the case of Ni, interlayer H_2O or D_2O is depleted and the gaps are replenished by bulk H_2O or D_2O. This bulk-to-interlayer diffusion process of H_2O or D_2O

likely limits the OER rates at the high overpotential region. Since Co and Ni both exhibit the crossing behavior, we hypothesize that this feature is likely not dependent on the identity of the OER catalysts, but rather a common behavior when comparing results conducted in proteo and deutero solutions.

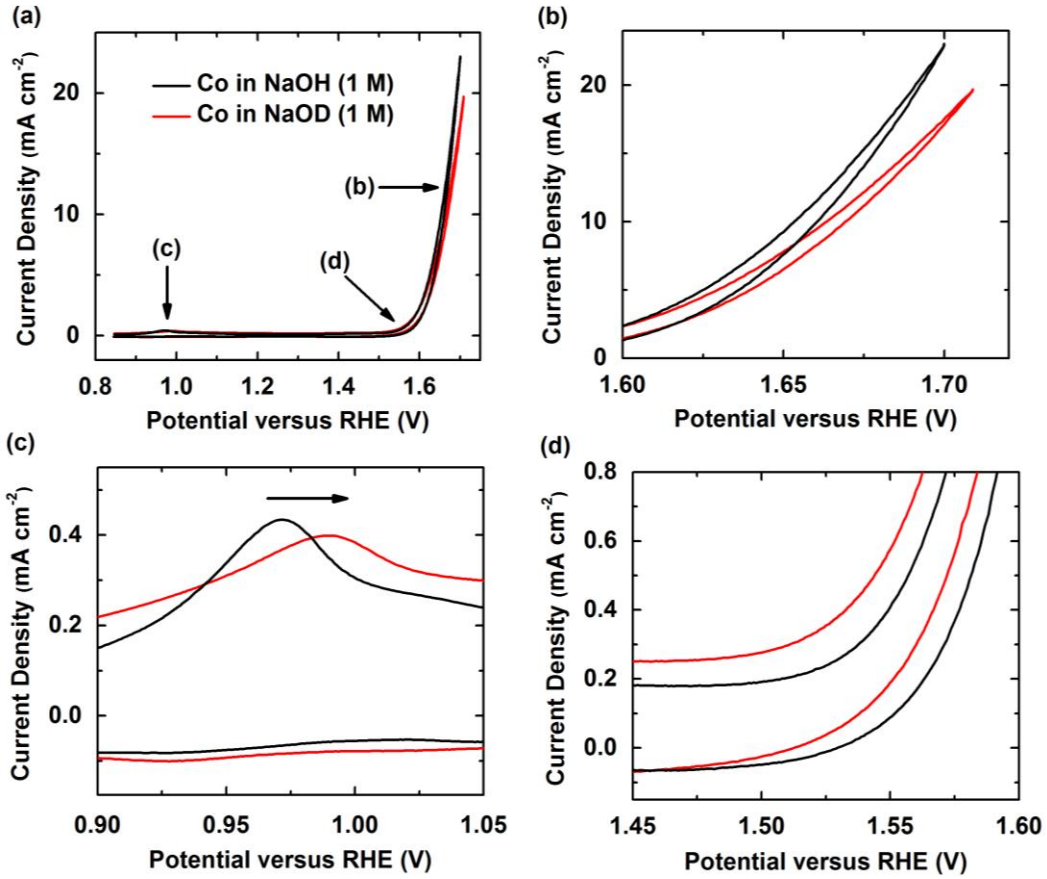

Figure 5.21. IR-uncorrected CVs of Co in NaOH (1 M) and NaOD (1 M) solutions. (b), (c), and (d) display the blowups of the diffusion-controlled OER region, the Co(II/III) redox region, and the OER onset region, respectively.

Figure 5.20c compares the anodic peak positions of the Co(II/III) wave in proteo and deutero basic solutions. Comparing to the Ni case (*vide supra*), the Co(II/III) anodic peak in 1 M NaOD is at 0.987 V versus RHE, which is slightly more positive relative to that found in 1 M

NaOH (0.978 V versus RHE). The difference between the OER current densities measured at high overpotential between proteo and deutero solutions found for Co is less apparent as compared to the Ni case. Although Ni and Co exhibit the same qualitative trends, the dissimilarities in the magnitude observed is likely due to the fact that Co forms multiple types of oxides and hydroxides before and during OER,[35] while Ni only forms $Ni(OH)_2$ and NiOOH in alkaline.[39] Table 5.5 lists the OER overpotentials of Co at 0.5 mA cm^{-2} obtained in proteo and deutero basic solutions, which are similar to those found using Ni as the OER catalyst. Figure 5.22 shows the Tafel plots of Co at the low overpotential region. The calculated KIE is about 0.5 (Table 5.5), which is similar to the KIE value found for the Ni case.

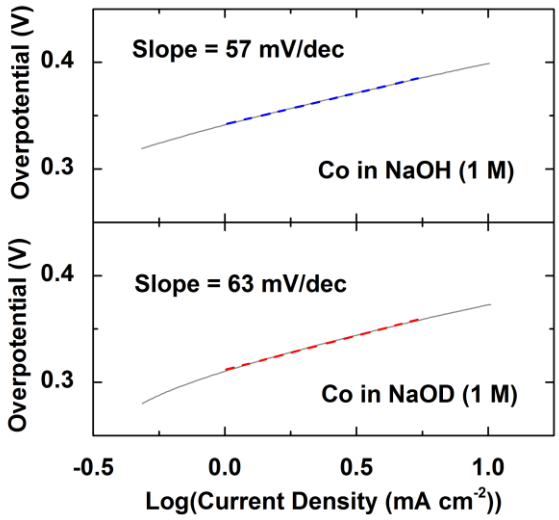

Figure 5.22. Tafel plots of Co in (a) 1 M NaOH and (b) 1 M NaOD solutions.

5.3.4 Origins of the Inverted KIE during the OER

We next address the possible origins of the inverse KIE found for the OER on Ni and Co in basic solutions. First, inverse KIEs are usually associated with differences in the steric environment of the active site caused by deuteration during the RDS.[14] For example,

interconversions of sterically-hindered biaryls typically exhibit inverse KIEs of ca. 0.8.[14,91-94] A comparison between the racemization rates of 2,2'-dibromo-4,4'-dicarboxybiphenyl and its 6,6'-dideutero derivative gives an inverse KIE of 0.85.[95-97] Another comparison of the inversion rates of 9,10-dihydroxy-4,5-dimethylphenanthrene and its derivative with the two methyl groups fully deuterated yields an inverse KIE of 0.86.[98,99] Translating this steric argument to the OER leads to a possible scenario shown in Figure 5.23a where surface crowding could lead to an inverse KIE. In this model, the O-D bond is stronger than the O-H bond.[86] This means that the O-D bond in MO(OD) is shorter than the O-H bond in MO(OH), where M = Ni or Co. The shorter O-D bond could lead to a less occluded active site, resulting in a less hindered pathway for reactants to diffuse to the MO(OD) surface as compared to the MO(OH) surface. As a result, the less bulky MO(OD) structure would exhibit faster OER kinetics. Our model shows a particular case in which a single metal center is the locus of reactivity, but this idea could easily be extended to a multi-metallic active site, as has been suggested in other work.[34,35,39,100-102]

A second origin of an inverse KIE results from a change from a less hybridized state to a more hybridized state (e.g. sp^2 to sp^3) during the RDS.[14] The typical observed KIE relating to this type of rehybridization is about 0.9. For example, solvolyses of methyl esters containing iodide and their deuterated derivatives lead to inverse KIEs of ca. 0.87.[103] A change in the hybridization state during the RDS leads to a larger difference in the Δ zero point energy (ZPE) of the transition state than in the Δ ZPE in the ground state. Figure 5.23b displays a possible scenario where a change in the coordination environment of M (Ni or Co) could result in an inverse KIE. In this model, the MO(OH) changes hybridization state upon binding of a $^{-}$OH. Therefore, the Δ ZPE for the case involving $^{-}$OD as the incoming species may be larger than that for the $^{-}$OH case.

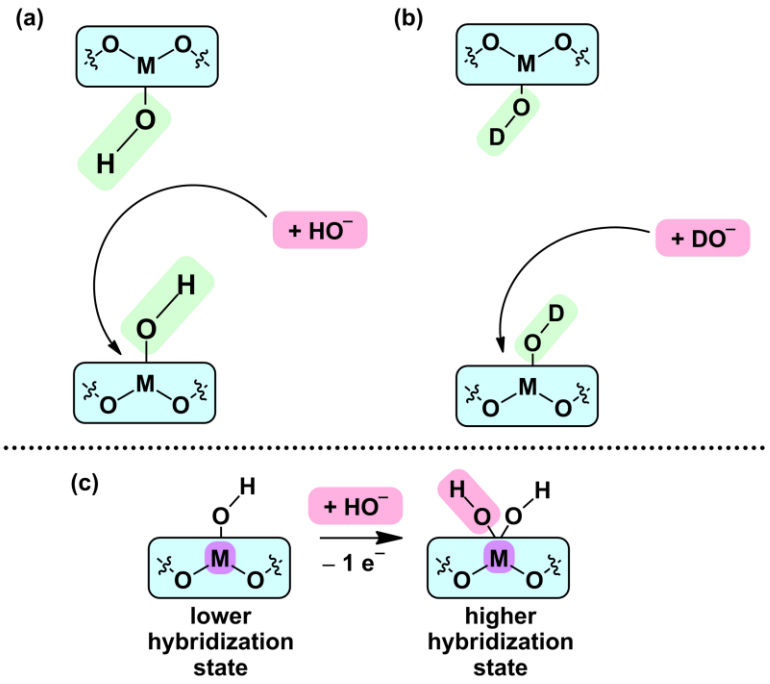

Figure 5.23. A possible scenario of the OER process catalyzed by M (Ni or Co) surface oxyhydroxides in which an inverse KIE can be observed highlighting (a) the hydroxide and (b) deuteroxide (green) that impart KIE on the adjacent bond forming or breaking site, and (c) the change in coordination environment and the corresponding rehybridization of the metal center (violet) upon accommodating an incoming $^{-}$OH species (pink).

A third explanation for an inverse KIE invokes an electronic argument.[14] The magnitude of an inductive KIE is typically about 0.95, a less significant effect than the two types of inverse KIEs previously discussed.[14,104] Deuterium substitution at a position more remote than β to the reaction center along an alkyl chain yields an inverse KIE of 0.97.[105,106] D is more electropositive than H, meaning that D is more electron releasing.[107,108] Due to the difference in electron donating ability, $^{-}$OD is more polar than $^{-}$OH, resulting in a higher $^{-}$OD flux towards the positively charged metal centers.

At this point, it is not possible to distinguish between the different origins of the inverted KIE as it applies to the OER. The relatively large inverse KIEs found for the OER catalyzed by

Ni and Co may result from a combination of all three effects mentioned above, as has been suggested in other systems.[14]

5.3.5 Mechanistic Implications for the OER

We next evaluated OER mechanism in the context of the inverted KIE. Many OER mechanisms have been proposed.[102] Here, by utilizing the insight we obtained from the KIE experiments, we attempt to identify the plausible RDS in four OER mechanisms commonly discussed in literature. The lack of a primary normal KIE indicates that O-H or O-D bonds are not cleaved during the RDS of the OER. Instead, the observed inverse KIE suggests that the RDS involves forming or breaking of a bond which (1) does not directly involve H or D, (2) is adjacent to an OH or OD moiety, and/or (3) requires a change from a less to a more hybridized state on the metal or oxygen center.

$$^{-}OH \longrightarrow (OH)_{ads} + e^{-} \quad (1)$$

$$(OH)_{ads} + {}^{-}OH \longrightarrow (O^{-})_{ads} + H_2O \quad (2)$$

$$(O^{-})_{ads} \longrightarrow (O)_{ads} + e^{-} \quad (3)$$

$$2\,(O^{-})_{ads} \longrightarrow O_2 \quad (4)$$

Figure 5.24. An OER mechanism focusing on the adsorbed species.[86,87]

First, we consider the simplest case that emphasizes adsorbed species.[101,109] The mechanism presented in Figure 5.24 considers the adsorbed reactants only and discounts the role of the underlying metal oxides. $^{-}$OH adsorbs on the surface upon oxidation and generates adsorbed O^{-} species upon deprotonation (steps 1 and 2). Two O^{-} species react to give off O_2 upon further oxidation (steps 3 and 4). Step 1 is not sterically hindered and step 2 contains direct

O-H bond breaking. No protons are adjacent to the bond breaking/forming sites in steps 3 and 4. Since none of the steps in this mechanism fits any of the criteria that leads to an inverse kinetic isotope effect, our data does not support any of the steps shown in the mechanism presented in Figure 5.24 to be rate-limiting. Several other papers dismiss the mechanism in Figure 5.24 as a prevalent OER mechanism on metal oxide surfaces.[34,39] One of the reasons steps in Figure 5.24 are not favored is the involvement of high energy species such as OH radicals and O atoms.[100]

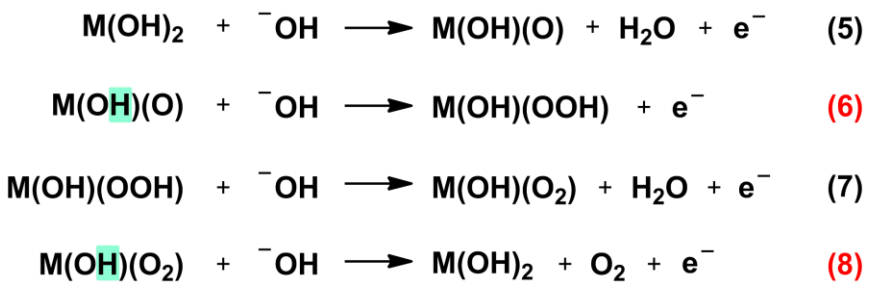

Figure 5.25. A mechanism of OER catalyzed by metal surfaces (M = Ni or Co) with neighboring bound OH species.[34,80] Plausible RDS are highlighted in red. Proton that imparts KIE on the adjacent bond forming or breaking site is highlighted in green.

Figure 5.25 displays an OER pathway that implicates adjacent OH species in the OER mechanism.[39,87] Steps 5 and 7 show the deprotonation of surface-bound OH and OOH species by aqueous $^{-}$OH. Since direct O-H bond cleavage exhibits a normal KIE,[13,14] steps 5 and 7 are likely not rate-limiting. Step 6 shows an attack of a bridging oxide or terminal oxo by $^{-}$OH with a neighboring surface-bound OH moiety, while step 8 displays an O_2 releasing step and a $^{-}$OH association step. Due to the heterogeneity of the metal surfaces and the ambiguity of the binding modes of the O, OOH and O_2 species,[45,68,110,111] the accurate assignment of the RDS in the case presented in Figure 5.25 is difficult. Since a sterically-hindering OH moiety is within the vicinity

of the bond breaking or forming site with a possible rehybridization event occurring, we cannot exclude the possibility that either step 6 or 8 can be rate-limiting.

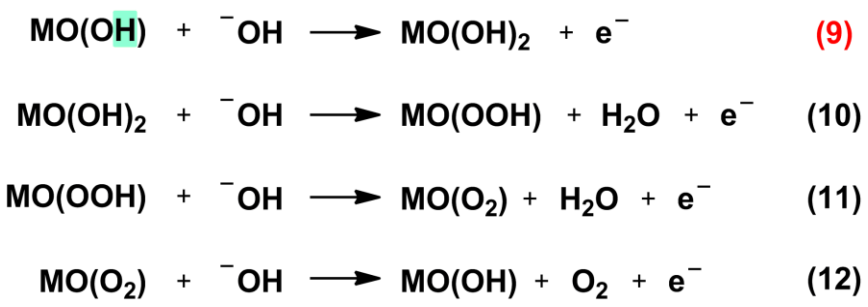

Figure 5.26. An OER mechanism that involves metal oxides (M = Ni or Co).[34,100,112] A plausible RDS is denoted in red. A proton that imparts an inverse KIE on the adjacent bond forming or breaking site is denoted in green.

Figure 5.26 shows an OER mechanism that involves an addition of a $^{-}$OH to the metal center and changes the geometry and the coordination number of the metal center.[34,100,112] Step 9 is likely a RDS because it involves the formation of a M-O bond next to an existing OH moiety, which provides the steric crowding required for the observed inverse KIE.[14] Steps 10 and 11 are not rate-limiting because they contain deprotonation steps and direct cleavage of an O-H bond should give a measurable normal KIE.[13] Step 12 involves an O_2 dissociation step and a $^{-}$OH addition step. However, the reaction site is not occluded by bound OH moieties, suggesting that step 12 is not rate-limiting.

Figure 5.27 shows a pathway less frequently discussed in literature. Intriguingly, this pathway invokes the involvement and release of a H_2O_2 intermediate.[34,100] Identical to step 9 presented in Figure 5.26, step 13 in Figure 5.27 is a plausible RDS because the formation of a M-O bond close to an existing OH group fits the criteria required to yield an inverse KIE.[14] The release of H_2O_2 depicted in step 14 likely results in a change of the metal center from a more

hybridized state to a less hybridized step, a change usually associated to a normal KIE.[13] Step 15 involves the addition of a $^{-}$OH to M without neighboring OH functionalities. Steps 15 and 16 contain deprotonation steps of species not directly attached to the electrode surface. Therefore, the likelihood of steps 14-16 to be rate-limiting is low.

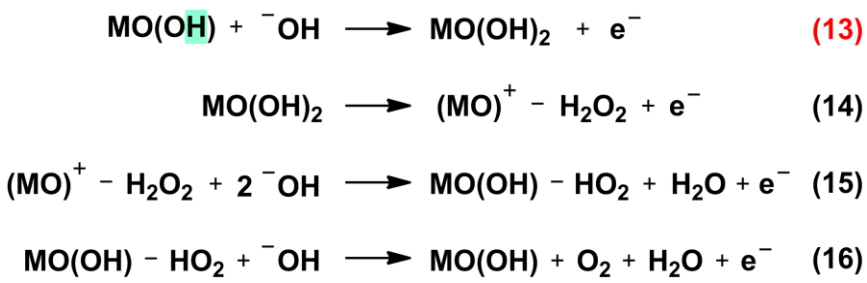

Figure 5.27. An OER mechanism that entails a H_2O_2 intermediate species.[29,88] Plausible RDS is represented in red. Proton that imparts KIE on the adjacent bond forming or breaking site is represented in green.

The goal of this section is not to disprove any mechanism proposed in the literature. Rather we intend to identify the plausible RDS in the many OER pathways suggested over the years. In Figures 5.24-27, we classify the many OER mechanisms previously proposed into four broad categories based on species involved in the process. Our observation of an inverse KIE for the OER suggest that the OER RDS likely involves breaking or forming a bond that (1) does not involve H or D directly, (2) occurs at an occluded site decorated by nearby OH or OD groups, and/or (3) requires a rehybridization of the reaction site to a more hybridized state. This observation provides constraints as to the nature of the RDS during the OER, constraints that must be addressed during the search for more competent OER catalysts.

5.4 Conclusions

In this report, we investigated the effect of deuteration on the ORR and the OER

activities of both precious and NPM catalysts. For the ORR on the precious metal catalysts Pt and Pd, we found a KIE of 1, in agreement with previous studies. For the ORR on Fe-based NPM catalysts, we found a KIE of 2 which demonstrates the involvement of protons at or before the RDS. For the OER on Ni and Co, we found an inverse KIE of 0.6 and 0.5, respectively. The OER results suggest that a rate-limiting bond breaking or forming event which does not involve the direct cleavage of an O-H bond, but likely occurs at an occluded site on the electrode surface with adjacent OH functionalities. The mechanistic insight gained from our KIE studies of the ORR and OER should be generally useful to the broad community that is interested in both the fundamental aspects of these PCET processes and the development of active, robust, and inexpensive catalysts for these energy-intensive reactions.

5.5 References

(1) Katsounaros, I.; Cherevko, S.; Zeradjanin, A. R.; Mayrhofer, K. J. J. *Angew. Chem. Int. Ed.* **2014**, *53*, 102.
(2) Zhang, J.; Xie, Z.; Zhang, J.; Tang, Y.; Song, C.; Navessin, T.; Shi, Z.; Song, D.; Wang, H.; Wilkinson, D. P.; Liu, Z.-S.; Holdcroft, S. *J. Power Sources* **2006**, *160*, 872.
(3) Carmo, M.; Fritz, D. L.; Mergel, J.; Stolten, D. *Int. J. Hydrogen Energy* **2013**, *38*, 4901.
(4) Gewirth, A. A.; Thorum, M. S. *Inorg. Chem.* **2010**, *49*, 3557.
(5) Jaouen, F.; Proietti, E.; Lefevre, M.; Chenitz, R.; Dodelet, J.-P.; Wu, G.; Chung, H. T.; Johnston, C. M.; Zelenay, P. *Energy Environ. Sci.* **2011**, *4*, 114.
(6) Wu, G.; More, K. L.; Johnston, C. M.; Zelenay, P. *Science* **2011**, *332*, 443.
(7) Bergmann, A.; Martinez-Moreno, E.; Teschner, D.; Chernev, P.; Gliech, M.; de Araujo, J. F.; Reier, T.; Dau, H.; Strasser, P. *Nat. Commun.* **2015**, *6*.
(8) Boulatov, R.; Collman, J. P.; Shiryaeva, I. M.; Sunderland, C. J. *J. Am. Chem. Soc.* **2002**, *124*, 11923.
(9) Barile, C. J.; Tse, E. C. M.; Li, Y.; Sobyra, T. B.; Zimmerman, S. C.; Hosseini, A.; Gewirth, A. A. *Nat. Mater.* **2014**, *13*, 619.
(10) Das, D.; Lee, Y.-M.; Ohkubo, K.; Nam, W.; Karlin, K. D.; Fukuzumi, S. *J. Am. Chem. Soc.* **2013**, *135*, 4018.
(11) Klinman, J. P. *FEBS Journal* **2014**, *281*, 489.
(12) Nelson, S. D.; Trager, W. F. *Drug Metab. Dispos.* **2003**, *31*, 1481.
(13) Gómez-Gallego, M.; Sierra, M. A. *Chem. Rev.* **2011**, *111*, 4857.
(14) Saunders, W. H.; Melander, L. R. *Reaction Rates of Isotopic Molecules*; Wiley: New York, 1980.

(15) Conway, B. E.; Salomon, M. *J. Chem. Phys.* **1964**, *41*, 3169.
(16) Salomon, M.; Conway, B. E. *Ber. Bunsen-Ges. Phys. Chem.* **1965**, *69*, 669.
(17) Krishtalik, L. I. *Electrochim. Acta* **2001**, *46*, 2949.
(18) Ghoneim, M. M.; Clouser, S.; Yeager, E. *J. Electrochem. Soc.* **1985**, *132*, 1160.
(19) Mayer, J. M.; Rhile, I. J. *BBA-Bioenergetics* **2004**, *1655*, 51.
(20) Thorseth, M. A.; Tornow, C. E.; Tse, E. C. M.; Gewirth, A. A. *Coord. Chem. Rev.* **2013**, *257*, 130.
(21) Tse, E. C. M.; Schilter, D.; Gray, D. L.; Rauchfuss, T. B.; Gewirth, A. A. *Inorg. Chem.* **2014**, *53*, 8505.
(22) Tylus, U.; Jia, Q.; Strickland, K.; Ramaswamy, N.; Serov, A.; Atanassov, P.; Mukerjee, S. *J. Phys. Chem. C* **2014**, *118*, 8999.
(23) Thorseth, M. A.; Letko, C. S.; Tse, E. C. M.; Rauchfuss, T. B.; Gewirth, A. A. *Inorg. Chem.* **2012**, *52*, 628.
(24) Inaba, M.; Kinumoto, T.; Kiriake, M.; Umebayashi, R.; Tasaka, A.; Ogumi, Z. *Electrochim. Acta* **2006**, *51*, 5746.
(25) Coms, F. D. *ECS Trans.* **2008**, *16*, 235.
(26) Nørskov, J. K.; Rossmeisl, J.; Logadottir, A.; Lindqvist, L.; Kitchin, J. R.; Bligaard, T.; Jónsson, H. *J. Phys. Chem. B* **2004**, *108*, 17886.
(27) Li, M. F.; Liao, L. W.; Yuan, D. F.; Mei, D.; Chen, Y.-X. *Electrochim. Acta* **2013**, *110*, 780.
(28) Mei, D.; He, Z. D.; Zheng, Y. L.; Jiang, D. C.; Chen, Y.-X. *Phys. Chem. Chem. Phys.* **2014**, *16*, 13762.
(29) Hammes-Schiffer, S.; Soudackov, A. V. *J. Phys. Chem. B* **2008**, *112*, 14108.
(30) Weinberg, D. R.; Gagliardi, C. J.; Hull, J. F.; Murphy, C. F.; Kent, C. A.; Westlake, B. C.; Paul, A.; Ess, D. H.; McCafferty, D. G.; Meyer, T. J. *Chem. Rev.* **2012**, *112*, 4016.
(31) Laguna-Bercero, M. A. *J. Power Sources* **2012**, *203*, 4.
(32) Man, I. C.; Su, H.-Y.; Calle-Vallejo, F.; Hansen, H. A.; Martínez, J. I.; Inoglu, N. G.; Kitchin, J.; Jaramillo, T. F.; Nørskov, J. K.; Rossmeisl, J. *ChemCatChem* **2011**, *3*, 1159.
(33) Doyle, R. L.; Godwin, I. J.; Brandon, M. P.; Lyons, M. E. G. *Phys. Chem. Chem. Phys.* **2013**, *15*, 13737.
(34) Lyons, M. E. G.; Brandon, M. P. *Int. J. Electrochem. Sci.* **2008**, *3*, 1386.
(35) Lyons, M. E. G.; Brandon, M. P. *Int. J. Electrochem. Sci.* **2008**, *3*, 1425.
(36) Reier, T.; Oezaslan, M.; Strasser, P. *ACS Catal.* **2012**, *2*, 1765.
(37) Hall, D. E. *J. Electrochem. Soc.* **1985**, *132*, 41C.
(38) Dau, H.; Limberg, C.; Reier, T.; Risch, M.; Roggan, S.; Strasser, P. *ChemCatChem* **2010**, *2*, 724.
(39) Lyons, M. E. G.; Brandon, M. P. *J. Electroanal. Chem.* **2010**, *641*, 119.
(40) Miles, M. H.; Kissel, G.; Lu, P. W. T.; Srinivasan, S. *J. Electrochem. Soc.* **1976**, *123*, 332.
(41) Godwin, I. J.; Lyons, M. E. G. *Electrochem. Commun.* **2013**, *32*, 39.
(42) Rossmeisl, J.; Logadottir, A.; Nørskov, J. K. *Chem. Phys.* **2005**, *319*, 178.
(43) Jaksic, M. M.; Johansen, B.; Tunold, R. *Int. J. Hydrogen Energy* **1994**, *19*, 321.
(44) Behl, W. K.; Toni, J. E. *J. Electroanal. Chem. Interfacial Electrochem.* **1971**, *31*, 63.
(45) Yeo, B. S.; Bell, A. T. *J. Phys. Chem. C* **2012**, *116*, 8394.
(46) Melendres, C. A.; Xu, S. *J. Electrochem. Soc.* **1984**, *131*, 2239.
(47) Desilvestro, J.; Corrigan, D. A.; Weaver, M. J. *J. Electrochem. Soc.* **1988**, *135*, 885.

(48) Bewick, A.; Gutiérrez, C.; Larramona, G. *J. Electroanal. Chem.* **1992**, *333*, 165.
(49) Ismail, K. M.; Badawy, W. A. *J. Appl. Electrochem.* **2000**, *30*, 1303.
(50) Kötz, R.; Neff, H.; Stucki, S. *J. Electrochem. Soc.* **1984**, *131*, 72.
(51) Peuckert, M. *Electrochim. Acta* **1984**, *29*, 1315.
(52) Foelske, A.; Strehblow, H.-H. *Surf. Interface Anal.* **2002**, *34*, 125.
(53) Medway, S. L.; Lucas, C. A.; Kowal, A.; Nichols, R. J.; Johnson, D. *J. Electroanal. Chem.* **2006**, *587*, 172.
(54) Pralong, V.; Delahaye-Vidal, A.; Beaudoin, B.; Gerand, B.; Tarascon, J. M. *J. Mater. Chem.* **1999**, *9*, 955.
(55) Hillman, A. R.; Skopek, M. A.; Gurman, S. J. *Phys. Chem. Chem. Phys.* **2011**, *13*, 5252.
(56) Totir, D.; Mo, Y.; Kim, S.; Antonio, M. R.; Scherson, D. A. *J. Electrochem. Soc.* **2000**, *147*, 4594.
(57) Mo, Y.; Stefan, I. C.; Cai, W.-B.; Dong, J.; Carey, P.; Scherson, D. A. *J. Phys. Chem. B* **2002**, *106*, 3681.
(58) Li, X.; Walsh, F. C.; Pletcher, D. *Phys. Chem. Chem. Phys.* **2011**, *13*, 1162.
(59) Yau, S.-L.; Fan, F.-R. F.; Moffat, T. P.; Bard, A. J. *J. Phys. Chem.* **1994**, *98*, 5493.
(60) Kong, F.; Kostecki, R.; McLarnon, F.; Muller, R. H. *Thin Solid Films* **1998**, *313–314*, 775.
(61) Lu, P. W. T.; Srinivasan, S. *J. Electrochem. Soc.* **1978**, *125*, 1416.
(62) Hu, Y.; Scherson, D. A. *J. Phys. Chem. B* **1997**, *101*, 5370.
(63) Kowal, A.; Niewiara, R.; Perończyk, B.; Haber, J. *Langmuir* **1996**, *12*, 2332.
(64) Mo, Y.; Hwang, E.; Scherson, D. A. *J. Electrochem. Soc.* **1996**, *143*, 37.
(65) Birss, V. I.; Elzanowska, H.; Gottesfeld, S. *J. Electroanal. Chem. Interfacial Electrochem.* **1991**, *318*, 327.
(66) Juodkazytė, J.; Šebeka, B.; Stalnionis, G.; Juodkazis, K. *Electroanalysis* **2005**, *17*, 1734.
(67) Zhen, C.-H.; Sun, S.-G.; Fan, C.-J.; Chen, S.-P.; Mao, B.-W.; Fan, Y.-J. *Electrochim. Acta* **2004**, *49*, 1249.
(68) Hoang, T. T. H.; Cohen, Y.; Gewirth, A. A. *Anal. Chem.* **2014**, *86*, 11290.
(69) Bard, A. J.; Faulkner, L. R. *Electrochemical Methods: Fundamentals and Applications, 2nd Edition*; Wiley Global Education, 2000.
(70) Ivanov, E. V.; Abrosimov, V. K. *Russ. J. Gen. Chem.* **2005**, *75*, 1851.
(71) Battino, R.; Rettich, T. R.; Tominaga, T. *J. Phys. Chem. Ref. Data* **1983**, *12*, 163.
(72) Ye, H.; Crooks, J. A.; Crooks, R. M. *Langmuir* **2007**, *23*, 11901.
(73) Zurilla, R. W.; Sen, R. K.; Yeager, E. *J. Electrochem. Soc.* **1978**, *125*, 1103.
(74) Ci, S.; Wu, Y.; Zou, J.; Tang, L.; Luo, S.; Li, J.; Wen, Z. *Chinese Sci. Bull.* **2012**, *57*, 3065.
(75) Stamenkovic, V. R.; Fowler, B.; Mun, B. S.; Wang, G.; Ross, P. N.; Lucas, C. A.; Marković, N. M. *Science* **2007**, *315*, 493.
(76) Huang, X.; Zhao, Z.; Cao, L.; Chen, Y.; Zhu, E.; Lin, Z.; Li, M.; Yan, A.; Zettl, A.; Wang, Y. M.; Duan, X.; Mueller, T.; Huang, Y. *Science* **2015**, *348*, 1230.
(77) Cao, L.; Mueller, T. *J. Phys. Chem. C* **2015**, *119*, 17735.
(78) Lyons, M. E. G.; Doyle, R. L.; Godwin, I.; O'Brien, M.; Russell, L. *J. Electrochem. Soc.* **2012**, *159*, H932.
(79) Trotochaud, L.; Ranney, J. K.; Williams, K. N.; Boettcher, S. W. *J. Am. Chem. Soc.* **2012**, *134*, 17253.

(80) Pourbaix, M. *Atlas of electrochemical equilibria in aqueous solutions*; National Association of Corrosion Engineers, 1974.
(81) Weaver, M. J.; Tyma, P. D.; Nettles, S. M. *J. Electroanal. Chem.* **1980**, *114*, 53.
(82) Frank, H. S.; Wen, W.-Y. *Discuss. Faraday Soc.* **1957**, *24*, 133.
(83) Weaver, M. J.; Nettles, S. M. *Inorg. Chem.* **1980**, *19*, 1641.
(84) Franks, F. *The Physics and Physical Chemistry of Water*; Springer US, 2012.
(85) Liu, H.; Macedo, E. A. *J. Supercrit. Fluids* **1995**, *8*, 310.
(86) Boyarkin, O. V.; Koshelev, M. A.; Aseev, O.; Maksyutenko, P.; Rizzo, T. R.; Zobov, N. F.; Lodi, L.; Tennyson, J.; Polyansky, O. L. *Chem. Phys. Lett.* **2013**, *568–569*, 14.
(87) Lyons, M. E. G.; Cakara, A.; O'Brien, P.; Godwin, I.; Doyle, R. L. *Int. J. Electrochem. Sci.* **2012**, *7*, 11768.
(88) Shinagawa, T.; Garcia-Esparza, A. T.; Takanabe, K. *Scientific Reports* **2015**, *5*, 13801.
(89) Wagman, D. D. *The NBS Tables of Chemical Thermodynamic Properties: Selected Values for Inorganic and C1 and C2 Organic Substances in SI Units*; American Chemical Society and the American Institute of Physics for the National Bureau of Standards, 1982.
(90) Gary, R.; Bates, R. G.; Robinson, R. A. *J. Phys. Chem.* **1964**, *68*, 1186.
(91) Carter, R. E.; Dahlgren, L. *Acta Chem. Scand.* **1969**, *23*, 504.
(92) Bartell, L. S. *J. Am. Chem. Soc.* **1961**, *83*, 3567.
(93) Bartell, L. S. *Tetrahedron Lett.* **1960**, *1*, 13.
(94) Carter, R. E.; Dahlgren, L. *Acta Chem. Scand.* **1970**, *24*, 633.
(95) Melander, L.; Carter, R. E. *Acta Chem. Scand.* **1964**, *18*, 1138.
(96) Westheimer, F. H. *J. Chem. Phys.* **1947**, *15*, 252.
(97) Westheimer, F. H.; Mayer, J. E. *J. Chem. Phys.* **1946**, *14*, 733.
(98) Mislow, K.; Graeve, R.; Gordon, A. J.; Wahl, G. H. *J. Am. Chem. Soc.* **1964**, *86*, 1733.
(99) Mislow, K.; Graeve, R.; Gordon, A. J.; Wahl, G. H. *J. Am. Chem. Soc.* **1963**, *85*, 1199.
(100) Juodkazis, K.; Juodkazytė, J.; Vilkauskaitė, R.; Jasulaitienė, V. *J. Solid State Electrochem.* **2008**, *12*, 1469.
(101) Bocca, C.; Barbucci, A.; Cerisola, G. *Int. J. Hydrogen Energy* **1998**, *23*, 247.
(102) Mom, R. V.; Cheng, J.; Koper, M. T. M.; Sprik, M. *J. Phys. Chem. C* **2014**, *118*, 4095.
(103) Llewellyn, J. A.; Robertson, R. E.; Scott, J. M. W. *Can. J. Chem.* **1960**, *38*, 222.
(104) Shiner, V. J.; Humphrey, J. S. *J. Am. Chem. Soc.* **1963**, *85*, 2416.
(105) Collins, C. J.; Bowman, N. S. *Isotope effects in chemical reactions*; Van Nostrand Reinhold, 1971.
(106) Jewett, J. G.; Dunlap, R. P. *J. Am. Chem. Soc.* **1968**, *90*, 809.
(107) Clough, S. A.; Beers, Y.; Klein, G. P.; Rothman, L. S. *J. Chem. Phys.* **1973**, *59*, 2254.
(108) Brittain, A. H.; Cox, A. P.; Duxbury, G.; Hersey, T. G.; Jones, R. G. *Mol. Phys.* **1972**, *24*, 843.
(109) Sadiek, I. M.; Mohammad, A. M.; El-Shakre, M. E.; El-Deab, M. S. *Int. J. Hydrogen Energy* **2012**, *37*, 68.
(110) Zhu, Y.; Li, H.; Koltypin, Y.; Gedanken, A. *J. Mater. Chem.* **2002**, *12*, 729.
(111) Schrebler Guzmán, R. S.; Vilche, J. R.; Arvía, A. J. *J. Electrochem. Soc.* **1978**, *125*, 1578.
(112) Cibrev, D.; Jankulovska, M.; Lana-Villarreal, T.; Gómez, R. *Int. J. Hydrogen Energy* **2013**, *38*, 2746.

Chapter 6

Proton Switch for Modulating Oxygen Reduction by a Copper Electrocatalyst Embedded in a Hybrid Bilayer Membrane

Reprinted with permission from Barile, C. J.;[†] Tse, E. C. M.;[†] Li, Y; Sobyra, T. B.; Zimmerman, S. C.; Hosseini, A.; Gewirth, A. A. *Nature Materials* **2014**, *13*, 619−623.

[†] C. J. B. and E. C. M. T. contributed equally.

6.1 Introduction

Molecular switches regulate many functions in biology, chemistry, and physics, and the development of artificial switches is an important goal in these fields. In nanotechnology, chemical switches are used in the construction of molecular machines[1,2] and computers.[3,4] In biological systems, switches are fundamental to gene regulation,[5] vision,[6] and cellular trafficking.[7] Frequently, such biological switches modulate proton transfer occurring in enzymes and across cellular membranes.[8] The protons regulated by these switches are frequently involved in proton-coupled electron transfer (PCET) reactions.

PCET reactions are also fundamental to many energy conversion processes such as N_2 fixation, H_2O oxidation, and CO_2 reduction.[9-12] The four-electron four-proton oxygen reduction reaction (ORR) to water is one of the most intensely studied reactions involving PCET.[13] Much experimental and computational work examines the mechanism of the ORR in an effort to

construct more efficient fuel cell cathodes.[14] However, in many cases, the mechanism of ORR remains poorly understood.

At present, since proton transfer is hard to switch on and off, the effect of proton transfer on catalysis and other reactions cannot be easily evaluated. Traditionally, the pH of the bulk solution is varied in order to affect the thermodynamics of redox couples in the catalyst.[11,15-17] The accompanying redox shift, however, gives little information about the influence of proton flux on the mechanism of the catalytic process. The role of covalently-bound proton relays in ORR catalysts has also been explored.[18-20] A hybrid bilayer membrane (HBM) is a unique electrochemical platform that can be used to interrogate the role of proton flux on a molecular ORR catalyst without altering neither its molecular structure nor the contents of the bulk solution.[21] In a HBM system, a monolayer of lipid molecules is appended to a self-assembled monolayer (SAM) of alkanethiols covalently attached to a Au electrode.[22-25] The role of proton flux in affecting the reactivity of a molecular ORR catalyst remains largely unexplored.

In this paper, we design and prepare a robust, active, dinuclear Cu ORR catalyst specifically tailored to be embedded inside a HBM system. We demonstrate that proton delivery to the catalyst through the lipid layer can be controlled through the use of an alkyl phosphate proton carrier and explore how this proton carrier can be used as a pH-sensitive switch.

6.2 Ligand Design and Synthesis

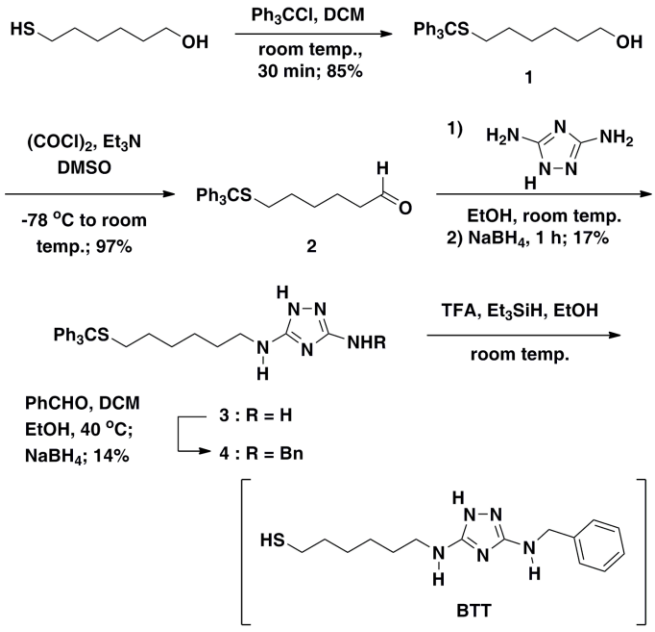

Scheme 6.1. Synthesis of BTT.

We first designed a new ligand to support an active Cu O_2 reduction catalyst in a HBM system. Scheme 6.1 illustrate the preparation of 6-((3-(benzylamino)-1,2,4-triazol-5-yl)amino)hexane-1-thiol (BTT). Ying Li in the Zimmerman group prepared BTT. The BTT ligand features three active regions, each with a specific function. First, the Cu coordination site is based on 3,5-diamino-1,2,4-triazole (DAT), which upon coordination to Cu forms an efficient O_2 reduction catalyst over a wide pH range.[26]

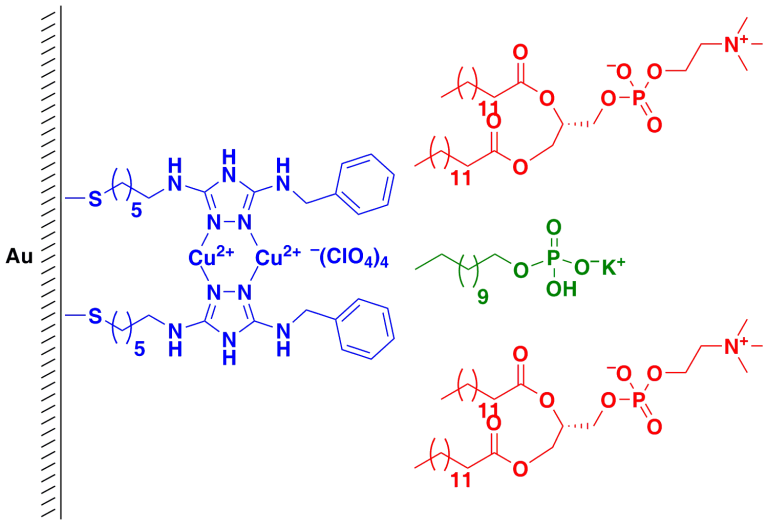

Figure 6.1. The HBM used in this study is composed of the Cu complex of BTT (blue), the 1,2-dimyristoyl-*sn*-glycero-3-phosphocholine (DMPC) lipid layer (red), and the alkyl phosphate proton carrier (green).

The second feature of BTT is a terminal benzyl moiety. Our initial attempts to deposit a lipid layer on a hydrophilic amino-terminated ligand were unsuccessful. We hypothesized that unfavorable interactions between the hydrophilic ends of the amino-terminated ligand and the hydrophobic tails of the lipid hinder the formation of a HBM in this case. Therefore, we attached a hydrophobic benzyl moiety onto BTT to append the lipid layer, allowing us to construct the electrochemical platform described in Figure 6.1.

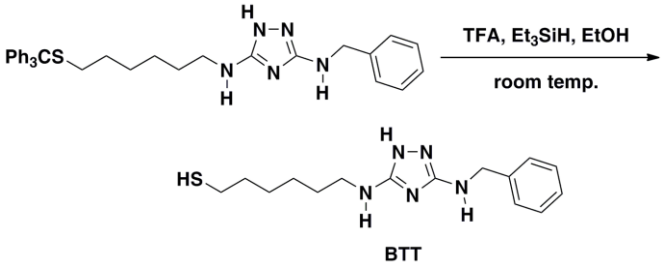

Figure 6.2. Synthesis of BTT.

Finally, we equipped BTT with a hexylthiol chain to allow for the formation of a well-packed SAM on Au electrodes. Electron transfer through this short-chained thiol is facile, eliminating it as the rate-limiting step for O_2 reduction.[27] A full monolayer of BTT on Au electrodes was formed through the *in situ* deprotection of the tritylated thiol using trifluoroacetic acid and triethylsilane (Figure 6.2).[28] O_2 reduction on the BTT-Au surface is greatly suppressed compared to a bare Au surface, demonstrating that the SAM layer is well-formed and effectively passivates the Au electrode (Figure 6.3).

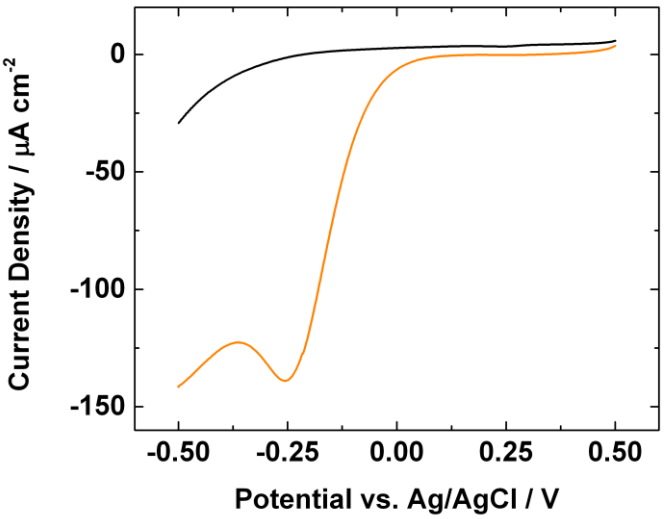

Figure 6.3. Linear sweep voltammograms (LSVs) of O_2 reduction by a bare Au surface (orange) and a BTT SAM on Au (black) in pH 7 buffer solution at a scan rate of 10 mV/s at 26 °C.

6.3 O_2 Reduction Catalysis

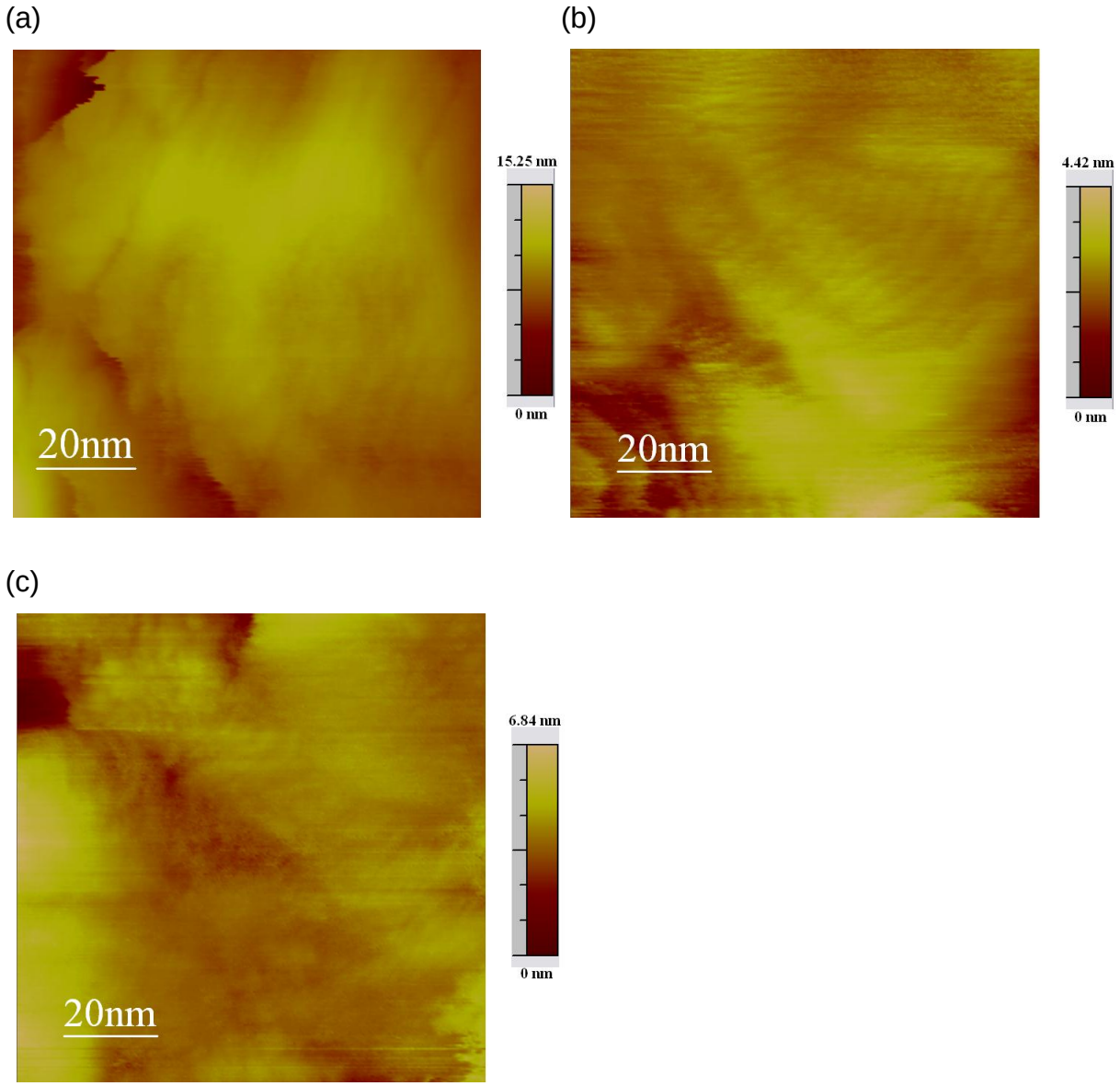

Figure 6.4. Representative scanning tunneling microscopy images of surfaces of bare Au (**a**), BTT on Au (**b**), and the Cu complex of BTT on Au (**c**). The average roughness across five images was (1.50 ± 0.41) nm for bare Au, (1.74 ± 0.86) nm for BTT on Au, and (1.43 ± 0.51) nm for the Cu complex of BTT on Au.

To form an active O_2 reduction catalyst, we subsequently immersed the BTT-Au surface in a solution of $Cu(ClO_4)_2$ to form a dinuclear Cu complex with two triazole units. Scanning tunneling microscopy (STM) reveals that the roughness of the bare Au and BTT-Au surfaces

with and without Cu do not deviate significantly, suggesting that the BTT monolayer is well-packed and its uniformity is not perturbed by the addition of Cu (Figure 6.4).

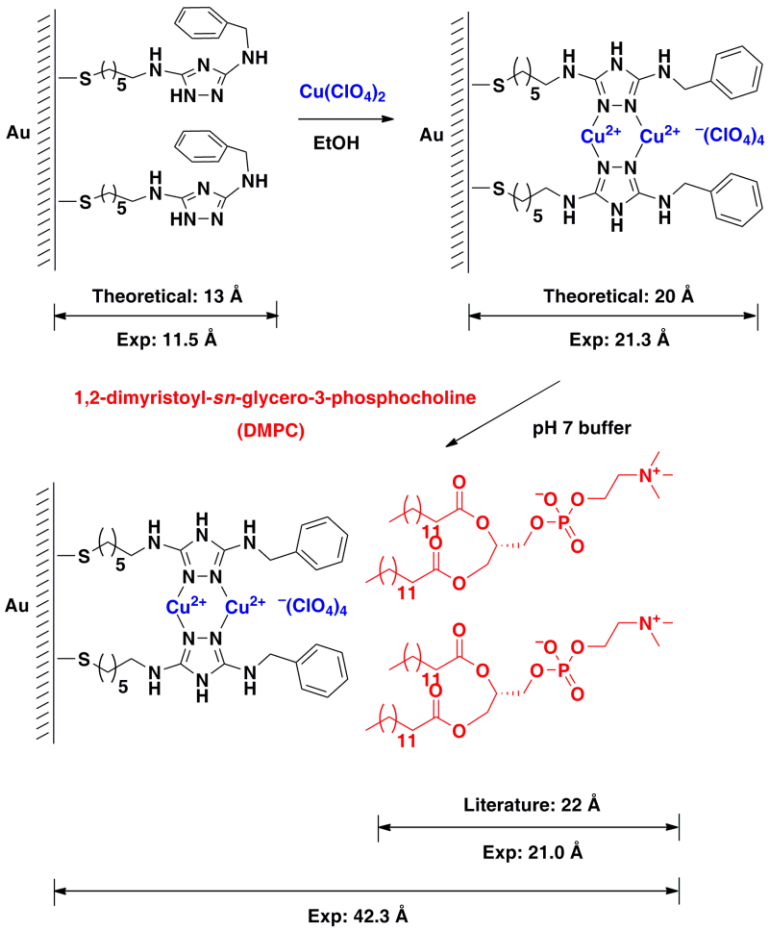

Figure 6.5. Modeling of ellipsometric measurements of a BTT SAM, a SAM of the Cu complex, and the HBM containing the Cu complex on Au.

Ellipsometric measurements are also consistent with the formation of a full monolayer as the length of the Cu complex of BTT on Au is 21 Å, comparable to the value obtained from theoretical modeling of the SAM (Figure 6.5). The film thicknesses obtained match with theoretical modeling and literature values.[9] Theoretical modeling was accomplished using Spartan ’08 v. 1.2.0 (Wavefunction, Inc.). We hypothesize that the BTT SAM is not fully

extended so that the phenyl rings can participate in favorable π-π stacking interactions. Upon addition of Cu, the complex is more rigid, and the phenyl rings are fully extended.

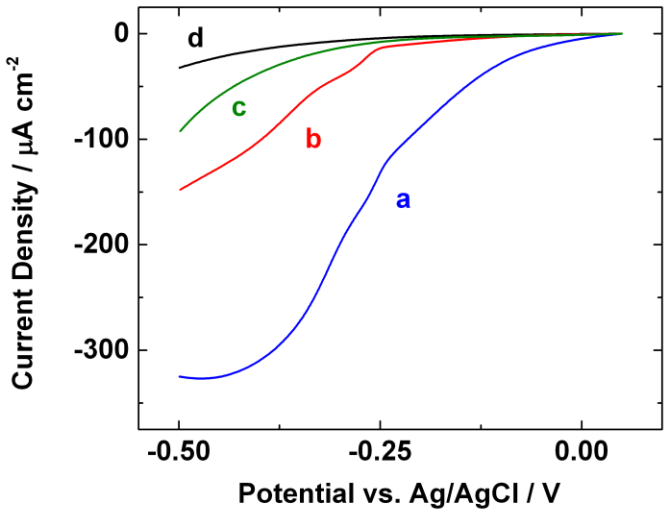

Figure 6.6. LSVs of O_2 reduction by a SAM of the Cu complex of BTT (blue, a), the HBM containing the Cu complex with DMPC only in the lipid layer (red, b), the HBM containing the Cu complex with 1 equivalent of MDP incorporated in the lipid layer (green, c), and a BTT SAM (black, d) on Au at 26 °C in pH 7 buffer solution at a scan rate of 10 mV/s.

O_2 reduction by the Cu complex of BTT on Au displays an onset potential of −70 mV vs. Ag/AgCl at pH 7 (Figure 6.6, blue). The Cu complex of BTT on Au reduces O_2 by an average of 3.7 ± 0.2 electrons, whereas a bare Au surface reduces O_2 by an average of 2.9 ± 0.1 electrons (Figure 6.7). The number of electrons by which O_2 is reduced and the onset potential of the Cu complex of BTT are similar to the values reported for the Cu complex of DAT on carbon black.[26] These observations demonstrate that modifying the Cu complex of DAT with alkylthiol and benzyl moieties does not perturb its catalytic activity.

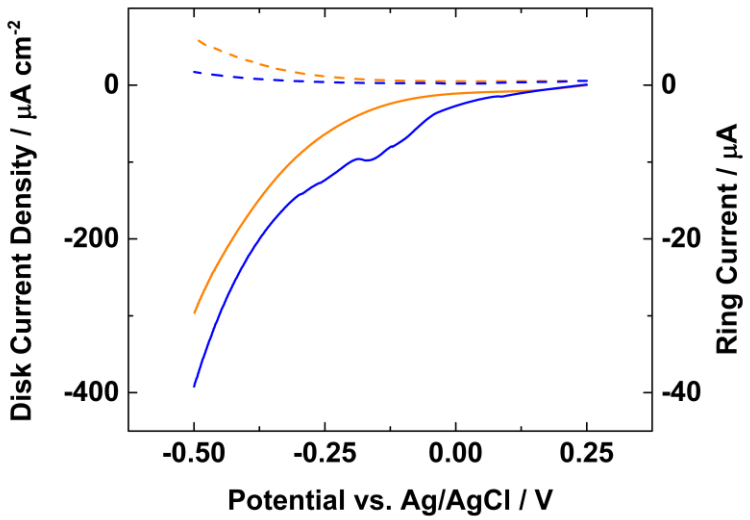

Figure 6.7. Rotating ring-disk LSVs (solid) and ring currents (dash) of the Cu complex of BTT on Au (blue) and a bare Au surface (orange) in pH 5 buffer solution sparged with O_2 at a scan rate of 10 mV/s at 26 °C.

Under an atmosphere of Ar, the BTT-Au surface in the absence of Cu is redox-active (Figure 6.8a, black). Presented in Figure 6.8b, the CV trace collected under Ar in the absence of O_2 shows that O_2 does not involve or contribute to the redox waves observed in Figure 6.8a. We hypothesize that the redox wave for the case of BTT-modified Au is due to the reversible one-electron reduction of the triazole ring, which has been reported for other triazole derivatives.[29] Protected BTT (**4**) and DAT both exhibit redox waves at similar potentials in an ethanolic solution, further supporting this hypothesis (Figure S6.8c).

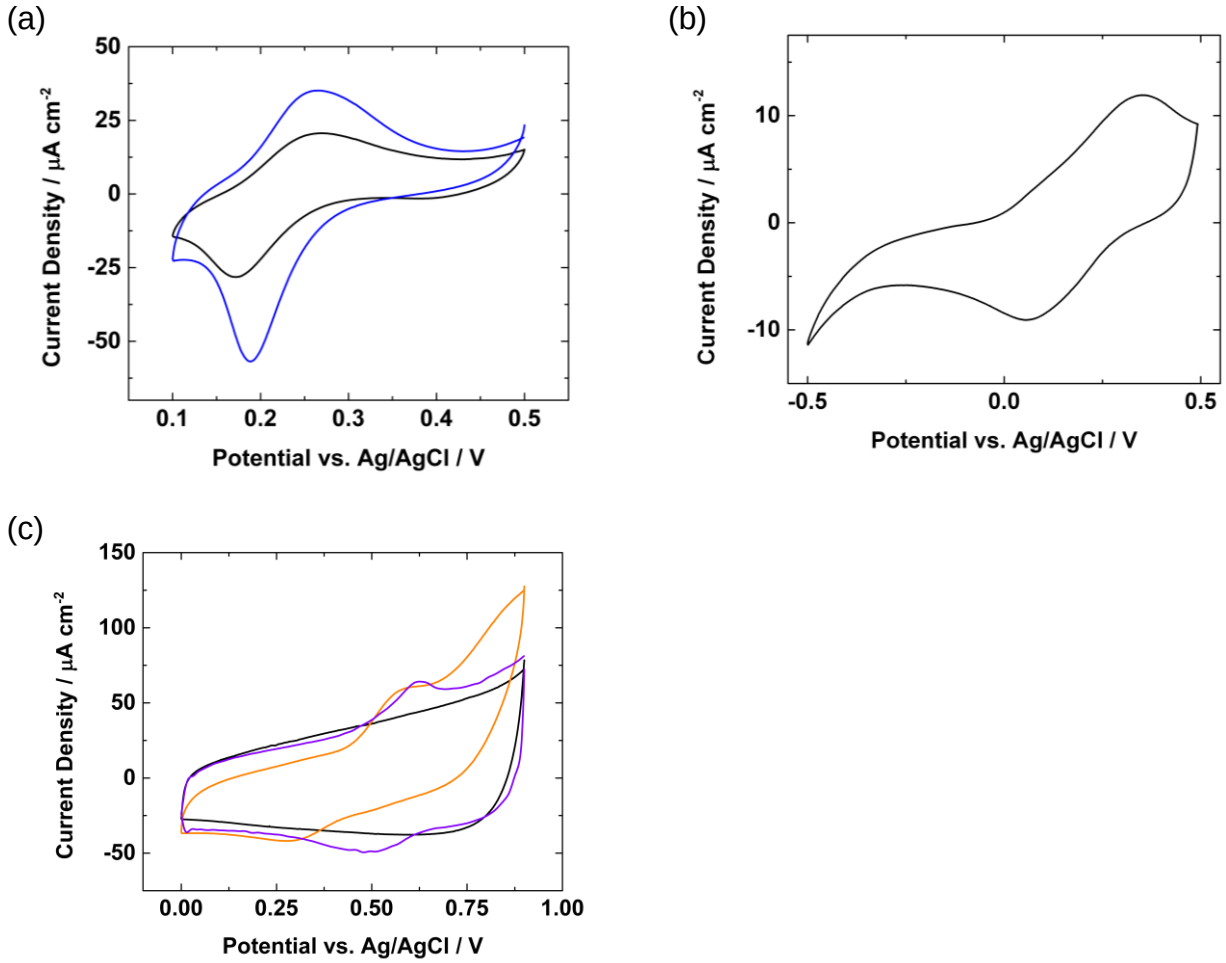

Figure 6.8. Cyclic voltammograms (CVs) at 26 °C of a BTT SAM (**a**, black) and a SAM of the Cu complex (**a**, blue) in pH 7 buffer solution sparged with Ar at a scan rate of 100 mV/s and the Cu complex of BTT (**b**) in KCl (100 mM) solution sparged with Ar at a scan rate of 10 mV/s. (**c**) CVs of a bare glassy carbon electrode (black), DAT (orange), and protected BTT (**4**, purple) in an ethanolic solution containing $LiClO_4$ (100 mM) at a scan rate of 100 mV/s at 26 °C.

Upon the formation of the Cu complex on the BTT-Au surface, the charge under the redox wave nearly doubles (Figure 6.8a, blue). This phenomenon reflects an additional one-electron Cu(I)/Cu(II) couple occurring at a similar potential as the free BTT-Au wave. By correcting for the contribution of the BTT, the surface coverage of the Cu complex of BTT on Au is 3.4×10^{-11} mol cm^{-2}, which is similar to the value expected for a full monolayer calculated using Spartan '08 (Wavefunction, Inc.) v. 1.2.0. The calculated cross-sectional area of a Cu

complex of BTT with coordinated EtOH molecules is 350 $Å^2$. Assuming a smooth Au surface, the surface coverage based upon this area is 4.7×10^{-11} mol cm^{-2}, which is comparable to the experimentally observed Cu coverage. We note that the O_2 reduction onset potential of Cu BTT on Au is about 300 mV more negative than the Cu(I)/Cu(II) couple. This negative shift is expected because O_2 reduction is an intricate process involving multiple proton delivery, electron transfer, and binding steps.

6.4 Hybrid Bilayer Membrane Construction

To construct a platform containing a molecular switch, we embedded the catalyst in a lipid layer composed of 1,2-dimyristoyl-*sn*-glycero-3-phosphocholine (DMPC), which is stable in the pH 5-9 range, to form a HBM. Ellipsometric measurements demonstrate that the length of the appended lipid layer is 21Å (Figure 6.5), and the double-layer current of the electrode decreases upon formation of the HBM (Figure 6.9). These two findings are consistent with the formation of a well-formed DMPC monolayer.[30] Figure 6.9 also shows that the amount of charge under the BTT and Cu(I)/Cu(II) waves decreases substantially upon HBM formation. This behavior arises because the anions ($H_2PO_4^-$/HPO_4^{2-}) from the aqueous-lipid interface are slow to diffuse through the lipid layer and compensate for the positive charge on the Cu complex, consistent with previous studies examining the transport properties of anions in HBM systems.[30,31]

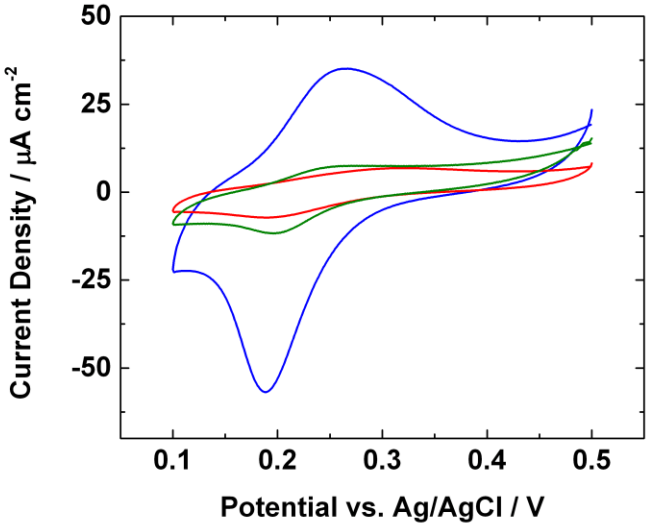

Figure 6.9. CVs of a SAM of the Cu complex (blue), the HBM containing the Cu complex (red), and the HBM containing the Cu complex with 1 equivalent of MDP incorporated in the lipid layer (green) in pH 7 buffer solution sparged with Ar at a scan rate of 100 mV/s at 26 °C.

At pH 7, the addition of a lipid layer to the Cu complex shifts the onset potential for O_2 reduction ~300 mV negative compared to the onset of the Cu complex without lipid, significantly decreasing the catalytic current (Figure 6.6, red). We hypothesize that the observed negative shift in the O_2 reduction onset potential is due to changing the local environment of the catalyst from an aqueous medium to the hydrophobic lipid interior. O_2 reduction in the HBM is not limited by the diffusion of O_2 in DMPC because the diffusion coefficients of O_2 in DMPC and pH 7 buffer are comparable at room temperature.[32-34] O_2 has a partition coefficient of greater than 2 in DMPC relative to water at 25 °C.[32] The diffusion coefficient of O_2 at 25 °C in a DMPC bilayer is 1.8×10^{-5} cm^2/s,[33] which is comparable to that of water (1.9×10^{-5} cm^2/s).[34] The time required for a molecule of O_2 to diffuse through 21 Å (the experimental length of the lipid layer as determined by ellipsometry) of the HBM can be calculated using Eq. 1 and is less than 2 ns.[35] The experimental time scales are in the range of 1 s.

$$t = \frac{\langle x \rangle^2 \pi}{4D} \qquad (1)$$

where D is the diffusion coefficient of O_2 in DMPC, x is the average distance traveled by an O_2 molecule, and t is the time elapsed

O_2 has a partition coefficient of 0.4 in DMPC relative to water at 10 °C.[32] Using this partition coefficient, the diffusion coefficient of O_2 at 10 °C in a DMPC bilayer is calculated to be 2.5×10^{-5} cm^2/s using the method described by Hyde and Subczynski.[36] Given the partition coefficient of O_2 between DMPC and water and that the solubility of O_2 in water is 0.24 mM at 25 °C,[15] the concentration of O_2 in the HBM is estimated to be 0.48 mM. Therefore, O_2 is expected to readily permeate through the lipid layer.

The cross-sectional area calculated using Spartan '08 of a DMPC and a MDP molecule is 65 $Å^2$. The experimental length of the HBM as determined by ellipsometry is 42 Å. Assuming 1 equivalent of MDP relative to DMPC and using the Henderson-Hasselbalch equation, the equilibrium concentration of MDP existing as RH_2PO_4 inside the HBM is 3.8 mM at pH 5 and 0.038 mM at pH 7. We note that these calculated values are equilibrium values describing how MDP exists at the lipid-water interface in the absence of catalysis, and do not take into account the rate of "flip-flop" diffusion of MDP through the DMPC layer.

There are two remaining possibilities as to the origin of the decreased O_2 reduction rate in the HBM. These possibilities relate to the inefficient delivery of either protons or electrons to the catalyst. The Cu complex of BTT without a lipid layer exhibits facile O_2 reduction, signifying that electron delivery from the Au electrode is not rate determining in the HBM. Unlike O_2, however, hydrophilic protons do not readily diffuse through the hydrophobic lipid layer of the HBM. In biological systems, protons are only shuttled across lipid bilayers with the aid of

specific channels or mediators.[37] This observation suggests that sluggish proton transfer through the lipid layer is responsible for the large negative shift of the onset potential for O_2 reduction by the catalyst when it is placed inside a HBM. Indeed, the slow and steady current rise we observe resembles the O_2 reduction profiles of Fe porphyrins appended to SAMs exhibiting slow electron transfer.[38,39]

6.5 Proton Carrier Incorporation

We next incorporate an alkyl phosphate, mono-*N*-dodecyl phosphate (MDP), in our HBM system to facilitate proton transport to the embedded catalyst and to act as a molecular switch. Proton carriers, such as aliphatic acids and amines, orient themselves with their polar head groups toward the lipid-water interface.[40] However, in the presence of a driving force such as a pH gradient, they deliver protons across the membrane via "flip-flop" diffusion.[41,42] Proton shuttling is important in many biological systems such as mitochondrial membranes.[8] We incorporate MDP in the HBM as a unique proton carrier since it is diprotic and hence its ability to transport protons can be modulated by changes in pH unlike previously used acids and amines. We confirm the presence of MDP in the lipid layer of the HBM using mass spectrometry (Figure 6.10).

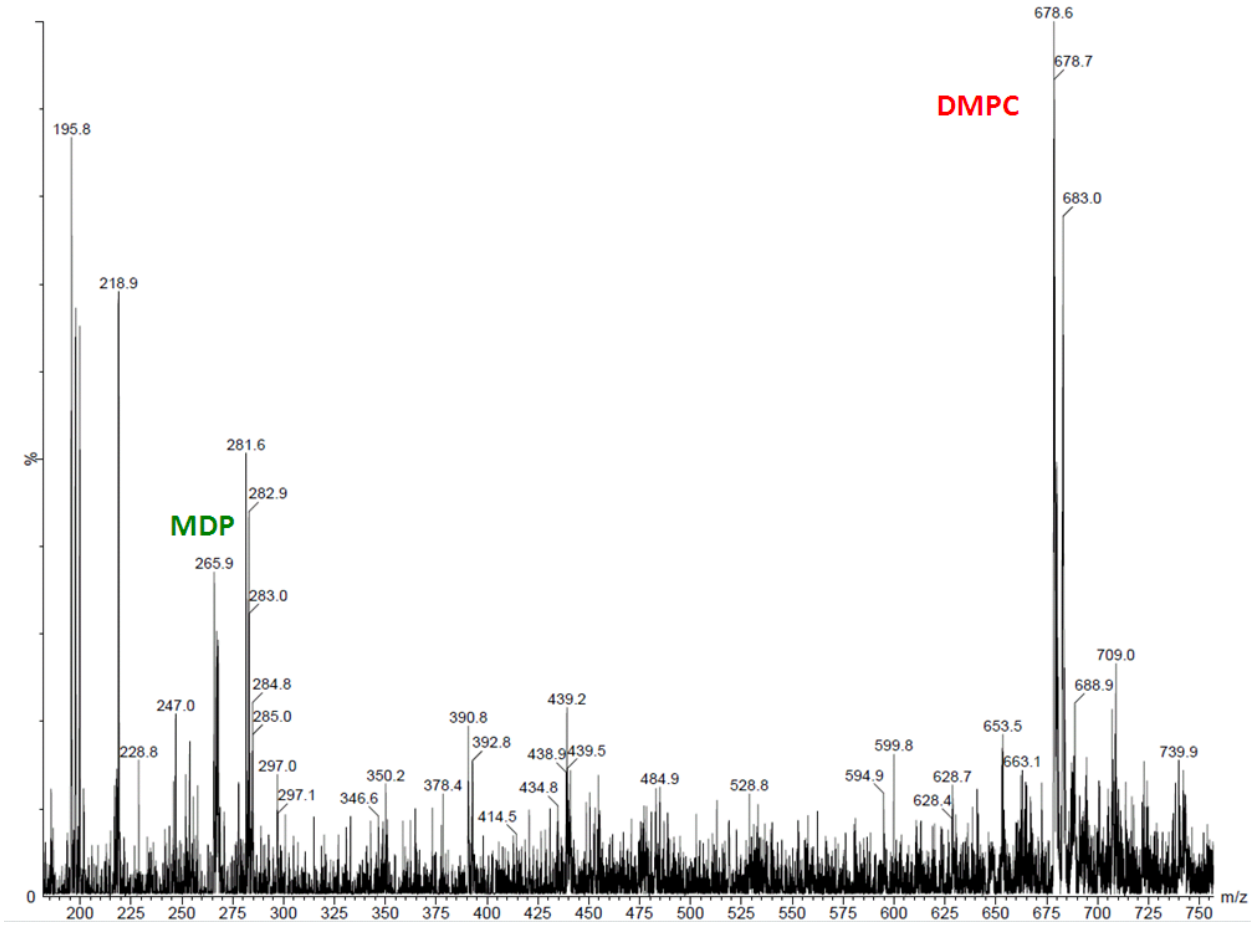

Figure 6.10. Electrospray ionization-mass spectrometry of DMPC and MDP extracted with EtOH and $CHCl_3$ from a HBM after O_2 reduction.

The green line in Figure 6.6 demonstrates that incorporating 1 equivalent of MDP into the lipid layer of the HBM inhibits the O_2 reduction activity of the Cu complex of BTT further at pH 7. At pH 7, MDP exists as an equilibrium mixture of $RHPO_4^-$/RPO_4^{2-}.[43] Protonation of this equilibrium mixture is dominated by the conversion of RPO_4^{2-} to $RHPO_4^-$. $RHPO_4^-$ is a poor proton carrier as the transport of charged species through the hydrophobic interior of the lipid layer is energetically unfavorable.[35]

However, at pH 5, MDP exists predominantly as $RHPO_4^-$. This species can then be protonated to give neutral RH_2PO_4, which can facilitate proton transport across the lipid layer of the HBM. This enhancement in proton transfer kinetics is confirmed by an increased O_2 reduction current by the embedded catalyst at pH 5 when 1 equivalent of MDP is incorporated in the lipid layer of the HBM (Figure 6.11, green). We hypothesize that the presence of MDP in the lipid layer increases the rate of proton delivery to the catalyst. Although the O_2 reduction current increases, it is not revived to the amount observed for the Cu complex of BTT without lipid because O_2 reduction inside the HBM is still limited by proton transport. However, the onset potential of the catalyst remains unchanged, indicating that the incorporation of a proton carrier does not change the thermodynamics of the catalyst in the HBM system, but rather enhances the kinetics of proton transport.

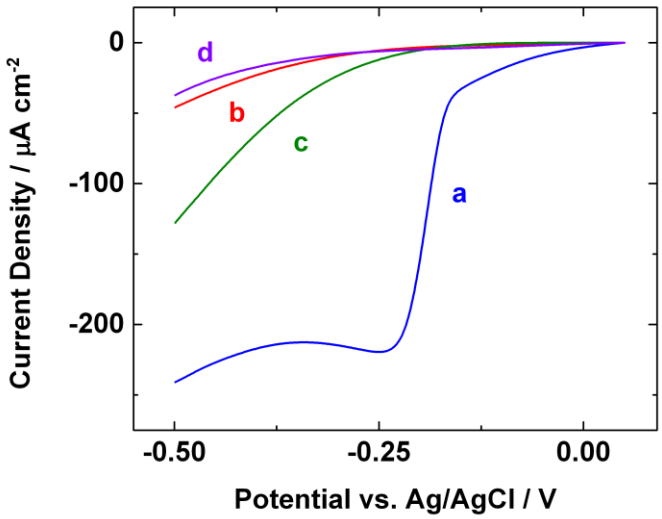

Figure 6.11. LSVs of O_2 reduction by a SAM of the Cu complex at 26 °C (blue, a), the HBM containing the Cu complex with DMPC only in the lipid layer at 26 °C (red, b), and the HBM containing the Cu complex with 1 equivalent of MDP incorporated in the lipid layer at 26 °C (green, c) and 10 °C (purple, d) on Au in pH 5 buffer solution at a scan rate of 10 mV/s.

To further interrogate the mechanism of proton transport inside the HBM, we studied the O_2 reduction activity of Cu BTT at 10 °C. At this temperature, DMPC monolayers exist in the gel phase[44] where "flip-flop" diffusion is suppressed,[45] but the O_2 diffusion rate across the lipid layer is similar to that at room temperature (*vide supra*). Unlike at 26 °C, the O_2 reduction current of the HBM with 1 equivalent of MDP at 10 °C (Figure 6.11, purple) is similar to that of the HBM with DMPC only at 10 °C (Figure 6.12, red) and 26 °C (Figure 6.11, red). We hypothesize that since MDP cannot undergo "flip-flop" diffusion at 10 °C, it is not an effective proton carrier and hence does not enhance the O_2 reduction activity of the catalyst. However, when the surface is warmed to 26 °C after being cooled, MDP is reactivated as a proton carrier, resulting in revived O_2 reduction activity (Figure 6.12, green).

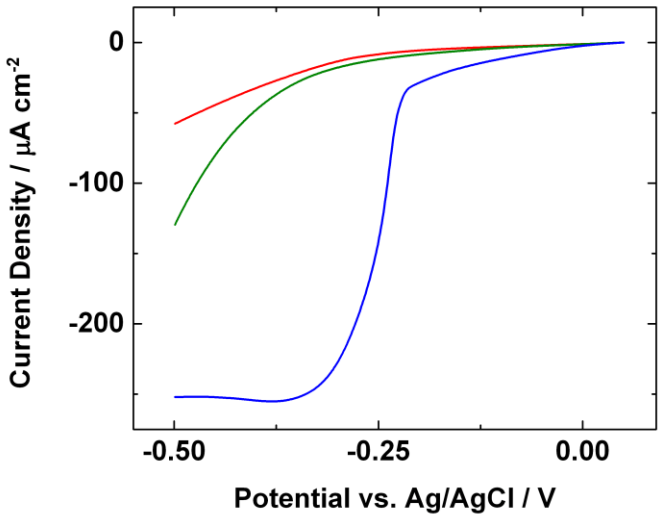

Figure 6.12. LSVs of O_2 reduction by a SAM of the Cu complex at 10 °C (blue), the HBM containing the Cu complex with DMPC only in the lipid layer at 10 °C (red), and the HBM containing the Cu complex with 1 equivalent of MDP incorporated in the lipid layer kept at 10 °C for 30 min and then ran at 26 °C (green) on Au in pH 5 buffer solution at a scan rate of 10 mV/s.

The integrity of the lipid layer is examined by blocking experiments with a solution of $K_3Fe(CN)_6$ (Figure 6.13).[46] In the absence of the lipid layer, we observe a combination of Fe(II)/Fe(III), Cu(I)/Cu(II), and BTT redox couples in the cyclic voltammogram. The current significantly decreases upon addition of DMPC, suggesting the presence of a well-packed monolayer of lipid on the SAM.[46] More importantly, the current originating from the Fe(II)/Fe(III) couple is similar for both the lipid-only HBM and the HBM with MDP, indicating that the incorporation of MDP does not adversely affect the integrity of the lipid layer. This important finding corroborates that MDP does not phase segregate in DMPC at pH 5 and 7. Acids have been shown to phase segregate only when they are fully protonated, and MDP exists predominantly as charged species in our system.[43, 44]

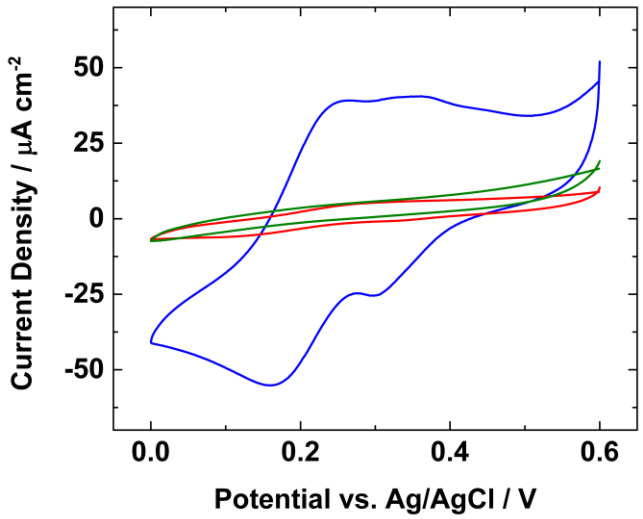

Figure 6.13. CVs of a SAM of the Cu complex (blue), the HBM containing the Cu complex (red), and the HBM containing the Cu complex with 1 equivalent of MDP incorporated in the lipid layer (green) in a solution of $K_3Fe(CN)_6$ (1 mM) with KCl (100 mM) at a scan rate of 50 mV/s at 26 °C.

6.6 pH-Sensitive Switch

The $RH_2PO_4/RHPO_4^-/RPO_4^{2-}$ equilibrium combined with the hindered proton transport

by $RHPO_4^-$ allows MDP to act as a pH-dependent switch for O_2 reduction inside the HBM. To evaluate the viability of MDP as a reversible switch for proton transport, we change the pH of the bulk solution *in situ* while monitoring the O_2 reduction activity of the Cu complex of BTT using chronoamperometry (Figure 6.14).

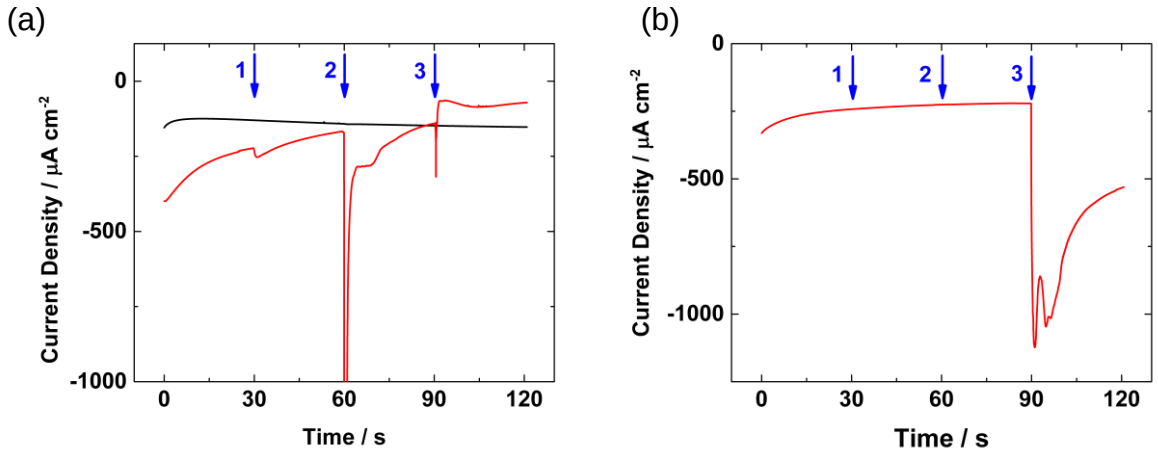

Figure 6.14. Chronoamperometry at 26 °C of the Cu complex of BTT on Au with lipid (black) and lipid with MDP (red) at –0.5 V starting in pH 7 buffer solution sparged with O_2. (a) pH 7 buffer solution (1), acid (2), and base (3) were added after 30, 60, and 90 s respectively. (b) pH 7 buffer solution (1), pH 7 buffer solution (2), and acid (3) were added after 30, 60, and 90 s respectively.

The amount of O_2 reduction current by the catalyst increases substantially upon changing the solution from pH 7 to pH 5. By acidifying the solution, the MDP proton carrier switch is turned on, increasing the flux of rate-limiting proton transfer to the catalyst, thus increasing the O_2 reduction current. The O_2 reduction activity of the catalyst is then shut down by turning off the MDP switch. Indeed, upon readjusting the solution to pH 7, the O_2 reduction current decreases to within 5% of its original value at pH 7, demonstrating that MDP is a reversible switch for proton transport in a HBM (Figure 6.15, red circles). In the absence of MDP, the lipid layer of the HBM effectively blocks proton transport to the catalyst. Therefore, the O_2 reduction

current in the absence of MDP is not sensitive to changes in the pH of the bulk solution (Figure 6.15, black squares).

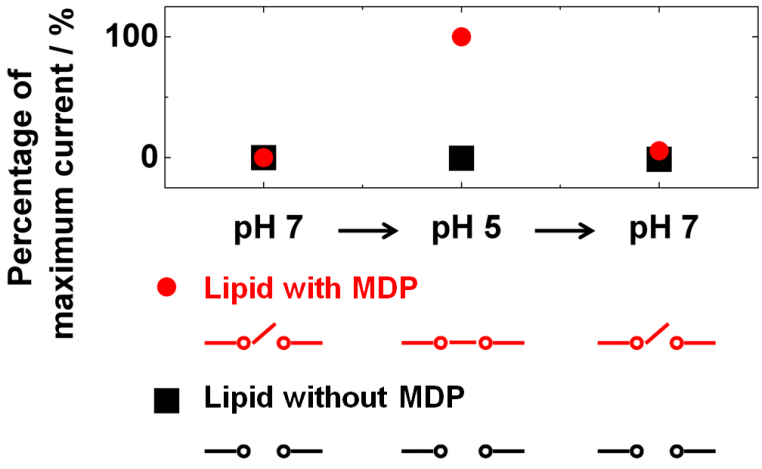

Figure 6.15. Percentage of maximum current of O_2 reduction at –0.5 V by the Cu complex of BTT with lipid (black squares) and lipid with the MDP switch (red circles).

6.7 Conclusions

For the first time, we have constructed a system in which a proton transfer switch is utilized to turn on and off a molecular catalyst by controlling proton flux to the catalyst. By changing the pH of the bulk solution, the ability of MDP to act as a proton carrier inside a HBM can be controlled reversibly. The rate of proton transfer through the lipid layer in turn modulates the O_2 reduction activity of the embedded catalyst, which itself is the first example of a synthetic Cu O_2 reduction catalyst supported on a Au electrode. The rational design of the BTT ligand, which is tailored to form a HBM on Au, exhibits catalytic activity similar to that of synthetic Cu O_2 reduction catalysts supported on carbon. This electrochemical platform allows for the precise and independent control of both the thermodynamics and kinetics of proton transfer to a molecular catalyst. This approach ultimately can be used to acquire unique mechanistic insight

into PCET reactions in biological systems and energy conversion processes.

6.8 References

(1) Browne, W. R.; Feringa, B. L. *Nat. Nanotechnol.* **2006**, *1*, 25.
(2) Balzani, V.; Credi, A.; Raymo, F. M.; Stoddart, J. F. *Angew. Chem. Int. Ed.* **2000**, *39*, 3348.
(3) Hirjibehedin, C. F.; Lin, C.-Y.; Otte, A. F.; Ternes, M.; Lutz, C. P.; Jones, B. A.; Heinrich, A. J. *Science* **2007**, *317*, 1199.
(4) Fuentes, N.; Martin-Lasanta, A.; Alvarez de Cienfuegos, L.; Ribagorda, M.; Parra, A.; Cuerva, J. M. *Nanoscale* **2011**, *3*, 4003.
(5) Alberts, B.; Johnson, A.; Lewis, J.; Raff, M.; Roberts, K.; Walter, P. *Molecular Biology of the Cell*; 4th ed.; Garland Science: New York, 2002.
(6) von Lintig, J.; Kiser, P. D.; Golczak, M.; Palczewski, K. *Trends Biochem. Sci.* **2010**, *35*, 400.
(7) Donaldson, J.; Segev, N. *Trafficking Inside Cells: Pathways, Mechanisms and Regulation*; Landes Bioscience and Springer Science, 2009.
(8) Lee, H. J.; Gennis, R. B.; Ädelroth, P. *Proc. Natl. Acad. Sci. U.S.A.* **2011**, *108*, 17661.
(9) Mayer, J. M. *Annu. Rev. Phys. Chem.* **2004**, *55*, 363.
(10) Chen, Z.; Vannucci, A. K.; Concepcion, J. J.; Jurss, J. W.; Meyer, T. J. *Proc. Natl. Acad. Sci. U.S.A.* **2011**, *108*, E1461.
(11) Huynh, M. H. V.; Meyer, T. J. *Chem. Rev.* **2007**, *107*, 5004.
(12) Wenger, O. S. *Acc. Chem. Res.* **2013**, *46*, 1517.
(13) Thorseth, M. A.; Tornow, C. E.; Tse, E. C. M.; Gewirth, A. A. *Coor. Chem. Rev.* **2013**, *257*, 130.
(14) Nørskov, J. K.; Rossmeisl, J.; Logadottir, A.; Lindqvist, L.; Kitchin, J. R.; Bligaard, T.; Jónsson, H. *J. Phys. Chem. B* **2004**, *108*, 17886.
(15) Boulatov, R.; Collman, J. P.; Shiryaeva, I. M.; Sunderland, C. J. *J. Am. Chem. Soc.* **2002**, *124*, 11923.
(16) Thorseth, M. A.; Letko, C. S.; Rauchfuss, T. B.; Gewirth, A. A. *Inorg. Chem.* **2011**, *50*, 6158.
(17) Oberst, J. L.; Thorum, M. S.; Gewirth, A. A. *J. Phys. Chem. C* **2012**, *116*, 25257.
(18) Rosenthal, J.; Nocera, D. G. *Acc. Chem. Res.* **2007**, *40*, 543.
(19) Chng, L. L.; Chang, C. J.; Nocera, D. G. *Org. Lett.* **2003**, *5*, 2421.
(20) Thorseth, M. A.; Letko, C. S.; Tse, E. C. M.; Rauchfuss, T. B.; Gewirth, A. A. *Inorg. Chem.* **2013**, *52*, 628.
(21) Hosseini, A.; Barile, C. J.; Devadoss, A.; Eberspacher, T. A.; Decreau, R. A.; Collman, J. P. *J. Am. Chem. Soc.* **2011**, *133*, 11100.
(22) Plant, A. L. *Langmuir* **1993**, *9*, 2764.
(23) Plant, A. L. *Langmuir* **1999**, *15*, 5128.
(24) Twardowski, M.; Nuzzo, R. G. *Langmuir* **2003**, *19*, 9781.
(25) Twardowski, M.; Nuzzo, R. G. *Langmuir* **2004**, *20*, 175.
(26) Thorum, M. S.; Yadav, J.; Gewirth, A. A. *Angew. Chem. Int. Ed.* **2009**, *48*, 165.

(27) Devaraj, N. K.; Decreau, R. A.; Ebina, W.; Collman, J. P.; Chidsey, C. E. D. *J. Phys. Chem. B* **2006**, *110*, 15955.
(28) Inman, C. E.; Reed, S. M.; Hutchison, J. E. *Langmuir* **2004**, *20*, 9144.
(29) Ermakova, T. G.; Gritsa, A. I.; Deriglazov, N. M.; Tatarova, L. A.; Keiko, V. V.; Vakul'skaya, T. I.; Lopyrev, V. A. *Chem. Heterocyc. Compd.* **1980**, *16*, 313.
(30) Hosseini, A.; Collman, J. P.; Devadoss, A.; Williams, G. Y.; Barile, C. J.; Eberspacher, T. A. *Langmuir* **2010**, *26*, 17674.
(31) Rowe, G. K.; Creager, S. E. *J. Phys. Chem.* **1994**, *98*, 5500.
(32) Subczynski, W. K.; Hyde, J. S. *Biophys. J.* **1983**, *41*, 283.
(33) Windrem, D. A.; Plachy, W. Z. *Biochim. Biophys. Acta* **1980**, *600*, 655.
(34) Chang, P.; Wilke, C. R. *J. Phys. Chem.* **1955**, *59*, 592.
(35) Atkins, P. d. P., J. C. *Physical Chemistry*; W. H. Freeman and Company (New York), 2006.
(36) Subczynski, W. K.; Hyde, J. S. *Biochimica et Biophysica Acta (BBA) - Biomembranes* **1981**, *643*, 283.
(37) Jain, M. K. *Introduction to Biological Membranes*; 2nd ed.; Wiley: New York, 1988.
(38) Collman, J. P.; Devaraj, N. K.; Decréau, R. A.; Yang, Y.; Yan, Y.-L.; Ebina, W.; Eberspacher, T. A.; Chidsey, C. E. D. *Science* **2007**, *315*, 1565.
(39) Collman, J. P.; Decréau, R. A.; Lin, H.; Hosseini, A.; Yang, Y.; Dey, A.; Eberspacher, T. A. *Proc. Natl. Acad. Sci. U.S.A.* **2009**, *106*, 7320.
(40) Srivastava, A.; Singh, S.; Krishnamoorthy, G. *J. Phys. Chem.* **1995**, *99*, 11302.
(41) Schönfeld, P.; Schild, L.; Kunz, W. *Biochim. Biophys. Acta* **1989**, *977*, 266.
(42) McConnell, H. M.; Kornberg, R. D. *Biochemistry* **1971**, *10*, 1111.
(43) Palermo, E. F.; Lee, D.-K.; Ramamoorthy, A.; Kuroda, K. *J. Phys. Chem. B* **2010**, *115*, 366.
(44) Albrecht, O.; Gruler, H.; Sackmann, E. *J. Phys. France* **1978**, *39*, 301.
(45) John, K.; Schreiber, S.; Kubelt, J.; Herrmann, A.; Müller, P. *Biophys. J.* **2002**, *83*, 3315.
(46) Han, X.; Wang, L.; Qi, B.; Yang, X.; Wang, E. *Anal. Chem.* **2003**, *75*, 6566.

Chapter 7

Physical and Electrochemical Characterization of a Cu-based Analytical Platform Inside and Outside Lipid Membrane

The work in this chapter was accomplished in collaboration with Dr. Christopher J. Barile,[†] Nicholas A. Kirchschlager, Dr. Heng-Liang Wu, and Professor Andrew A. Gewirth.

[†] E. C. M. T. and C. J. B. and contributed equally.

7.1 Introduction

In a broad sense, proton-coupled electron transfer (PCET) refers to reactions that involve the addition or removal of both protons and electrons.[1-6] PECT reactions are ubiquitous in chemistry and biology and include N_2 fixation, CO_2 reduction, and H_2O oxidation.[7-11] One of the most studied PCET reactions is the O_2 reduction reaction (ORR),[12,13] which enables fuel cell catalysts and respiring enzymes such as cytochrome c oxidase.[14-17] Since the ORR to form H_2O involves the transfer of four electrons and four protons, there are many possible pathways by which this reaction can occur, making the ORR difficult to study.[18,19] Many different methods have been utilized to study ORR catalysts.[20-24] For example, by using a variety of spectroscopic techniques, multiple metal-O_2 binding motifs have been characterized.[25-28] Additionally, different derivatives in a class of catalysts have been synthesized in an effort to elucidate structure-activity relationships.[29-31] For example, the addition of pendant proton relays to ORR catalysts has been used to study the role of proton transfer in catalyst activity.[11,18,31-33] However, these

modifications frequently perturb other aspects of the catalyst including the redox potential of the metal ions and the steric environment surrounding the O_2 binding site.[30,31,34,35]

We recently pioneered the use of a hybrid bilayer membrane (HBM) to study the effect of proton transfer kinetics on ORR catalysts without altering their molecular structure.[36,37] A HBM consists of a lipid monolayer appended on top of a self-assembled monolayer (SAM).[38,39] We previously utilized a SAM of a dinuclear Cu complex (CuBTT: Cu complex of 6-((3-(benzylamino)-1,2,4-triazol-5-yl)amino)hexane-1-thiol) and a monolayer of 1,2-dimyristoyl-*sn*-glycero-3-phosphocholine (DMPC) lipid to form a HBM containing an ORR catalyst.[36] While CuBTT exposed to bulk aqueous solution is an active ORR catalyst, appending a lipid layer on top of CuBTT significantly inhibits the ORR activity.[36] This inhibition results from the inability of hydrophilic protons to diffuse across the hydrophobic interior of the lipid membrane.[36,40]

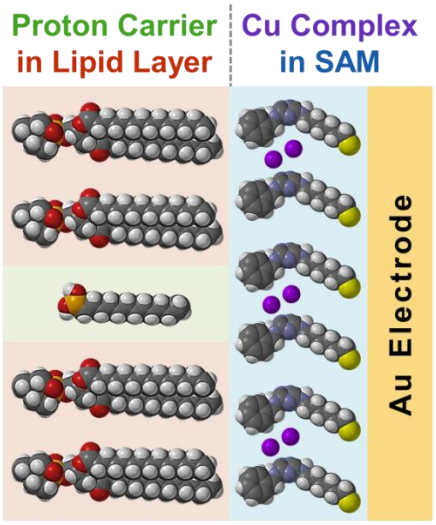

Figure 7.1. Schematic of the HBM electrochemical platform utilized in this study.

We discovered that the activity of the CuBTT catalyst inside a HBM is revived by the presence of a proton carrier in the lipid layer.[36] Furthermore, we designed proton carriers that switch on and off the ORR activity of CuBTT by either light or a pH change.[36,41] The ability of

these carriers to deliver protons across the lipid membrane of the HBM dictates the ORR activity of the underlying catalyst. Although the ORR switching behavior of these proton carriers has been demonstrated, the Cu(I)/Cu(II) couple of CuBTT that facilitates the ORR has not been studied in detail in this HBM framework. In this manuscript, we analyze the electrochemical behavior of BTT-modified electrodes inside and outside of lipid membranes under various pH regimes to gain mechanistic insight into this platform (Figure 7.1). We also further characterize the structure and composition of the HBM system using atomic force microscopy (AFM), electrochemical impedance spectroscopy (EIS), and X-ray photoelectron spectroscopy (XPS).

7.2 Results and Discussion

7.2.1 Characterization of the HBM Construct

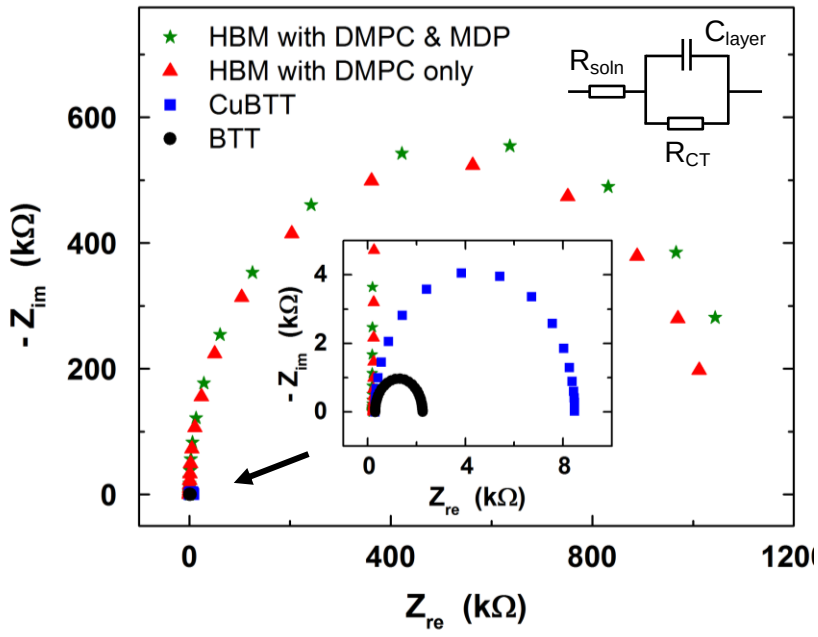

Figure 7.2. Nyquist plots of BTT on Au (inset, black circles), CuBTT on Au (inset, blue squares), HBM containing DMPC only (red triangles), and HBM containing DMPC with MDP added (green stars) with the Randles circuit used provided to the top-right of Figure 7.2. R_{soln} = solution resistance, R_{CT} = charge transfer resistance, C_{layer} = capacitance of the layer of interest.

We first characterize the thickness of our electrochemical platform using EIS.[42-45] Figure 7.2 displays the Nyquist plots of the electrochemical systems utilized in this study. Using the Randles circuit presented in Figure 7.2, we obtained the capacitance of each of the system studied using published modeling protocols (Table 7.1).[46,47] The capacitance observed for a SAM of BTT is comparable to the values obtained using C9 or C10 alkanethiolate-modified Au electrode.[47,48] Table 7.1 also lists the thicknesses of the SAMs and HBMs calculated from the capacitance (*C*) using Eq. 1:

$$C = \frac{\varepsilon\, \varepsilon_0}{d} \qquad \text{Eq. 1}$$

where ε is the dielectric constant of the layer of interest, ε_0 is the dielectric constant of vacuum, and *d* is the thickness.

Table 7.1. The thicknesses of the systems examined in this study. The layer thickness is calculated using Eq. 1 from the capacitance measured by EIS. The dielectric constant (ε) of the SAM is taken to be equal to that of alkanethiol SAMs (2.1),[49,50] while the ε of lipid membranes is about 2.7 (ranges from 2.1 to 3.2).[51-56] Since the literature values of the lengths of BTT and DMPC are comparable,[36] we estimated the average ε for a HBM containing a lipid monolayer appended onto a SAM to be 2.4.

System	Capacitance (μF)	Thickness (nm)
A SAM of BTT on Au	1.58 ± 0.20	1.17 ± 0.15
A SAM of CuBTT on Au	0.92 ± 0.14	2.01 ± 0.31
A HBM containing DMPC only	0.55 ± 0.06	3.88 ± 0.42
A HBM containing DMPC and MDP	0.52 ± 0.10	4.08 ± 0.81

The thicknesses found for a SAM of BTT, a SAM of CuBTT, a HBM containing DMPC, and a HBM containing DMPC with MDP incorporated are similar to those found previously using ellipsometry (Figure 7.3).[36] We further verify these experimentally-measured thicknesses by computing the lengths of BTT and DMPC using Spartan'08 v.1.2.0 (Wavefunction Inc.). The calculated length of BTT is ca. 0.8 nm longer than the measured thickness, indicating that for the

BTT-modified electrodes in aqueous environment, the benzyl arms of ca. 0.7 nm likely fold up to expose the hydrophilic N and maximize π-π stacking interactions. Upon the addition of Cu ions, the observed thickness (2.01 nm) of the CuBTT-modified system matches the length estimated computationally (2.0 nm). This result suggests that the benzyl arm unfolds to allow Cu coordination to the triazole rings to generate the dinuclear Cu electrocatalyst, which is the active site for O_2 reduction.[36,57] Upon appending a DMPC layer on top of CuBTT, the thickness almost doubles that of the CuBTT-only system. The increased thickness is 0.3 nm shorter than the literature reported length of DMPC with the discrepancy likely implying that either the lipid layer is formed at an angle or a small portion of the lipid tails overlaps with the benzyl arms of the CuBTT layer.[38] This finding indicates that the HBM consists of a SAM of CuBTT and a monolayer of DMPC appended on top. Upon incorporating MDP into the lipid monolayer, the thickness of the HBM remains relatively the same within error, signifying that MDP does not promote the formation of DMPC multilayers.

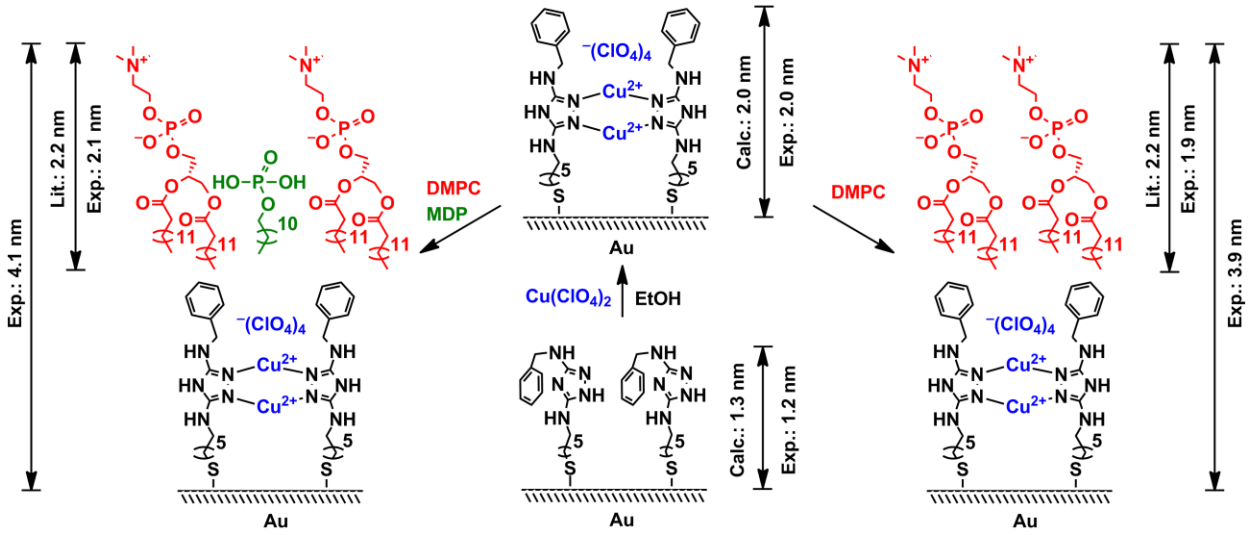

Figure 7.3. Calculated and measured thicknesses obtained from EIS of a SAM of BTT, a SAM of CuBTT, a HBM containing DMPC, and a HBM containing DMPC with MDP incorporated.

The surface morphology and surface roughness of a bare Au surface, a SAM of BTT, and a SAM of CuBTT have been previously reported.[36] However, the lipid layer of a HBM system is electrically insulating, preventing the use of scanning tunneling microscopy to probe the surface topology of a HBM containing a lipid monolayer. On the other hand, AFM is a well-established technique to interrogate supported lipid bilayers and HBMs.[58-61]

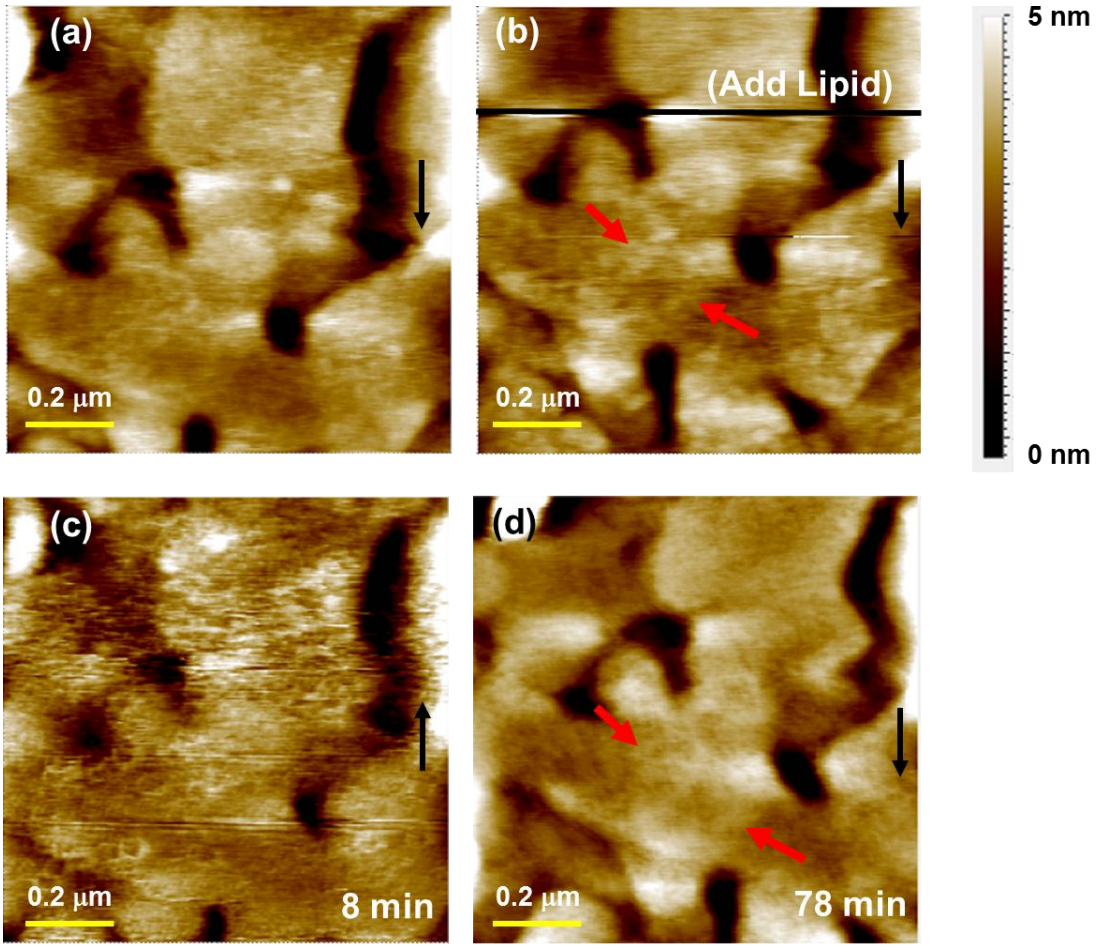

Figure 7.4. A set of sequential AFM images of the CuBTT SAM on Au acquired (a) before and (b)–(d) after the injection of DMPC vesicles at 3, 8, and 78 min. The black arrows indicate the scan direction. The black line in (b) denotes the moment when the DMPC vesicles were injected. The scanned area of the AFM images was 1 μm × 1 μm.

Figure 7.4 displays a series AFM images in chronological sequence recorded in pH 7 buffer solution with the black arrow showing the scan direction. Figure 7.4a shows the surface

condition of the CuBTT SAM prior to lipid addition. The thick black line in Figure 7.4b indicates the time point at which lipid-forming solution containing lipid vesicles is introduced to the AFM stage. During the vesicle fusion process to generate a monolayer of lipid on top of the CuBTT SAM, the AFM image becomes blurry (Figure 7.4c and lower part of Figure 7.4b). The blurred image is suggestive of a dynamic process that causes the AFM tip to be unstable. After the AFM tip stabilizes, we observed the formation of a lipid layer on top of the CuBTT SAM, which results in an AFM image that is less grainy (Figure 7.4d) than those obtained from the CuBTT SAM without lipid. This smoothing of the AFM image is possibly caused by the fluid nature of the DMPC lipid layer at this temperature. This set of experiment represents an important example to probe *in situ* the construction of a HBM containing a redox-active SAM.

7.2.2 pH Dependence of SAMs Containing BTT

After characterizing the structural attributes of the SAM and HBM systems, we investigated the pH-dependence of the voltammetry of a SAM of BTT. Figure 7.5a displays the cyclic voltammograms (CVs) of a SAM of BTT on Au in solutions ranging from pH 1 to 13. At all pH values, the ratio between the anodic and cathodic peak currents is approximately unity, indicating that BTT exhibits a reversible redox wave in acidic, neutral, and basic conditions. Figure 7.5b shows the pH dependence of the midpoint potentials ($E_{1/2}$) of a SAM of BTT on Au. The midpoint potentials decrease by (59 ± 2) mV per pH unit, indicating that according to the Nernst equation, the redox event involves the transfer of H^+ and e^- in a 1:1 ratio from pH 1 to 13. Previous studies have demonstrated that triazoles undergo a reversible 1 e^- couple, and we previously showed that 3,5-diamino-1,2,4-triazole, a compound structurally related to BTT, also possesses a reversible redox couple.[36]

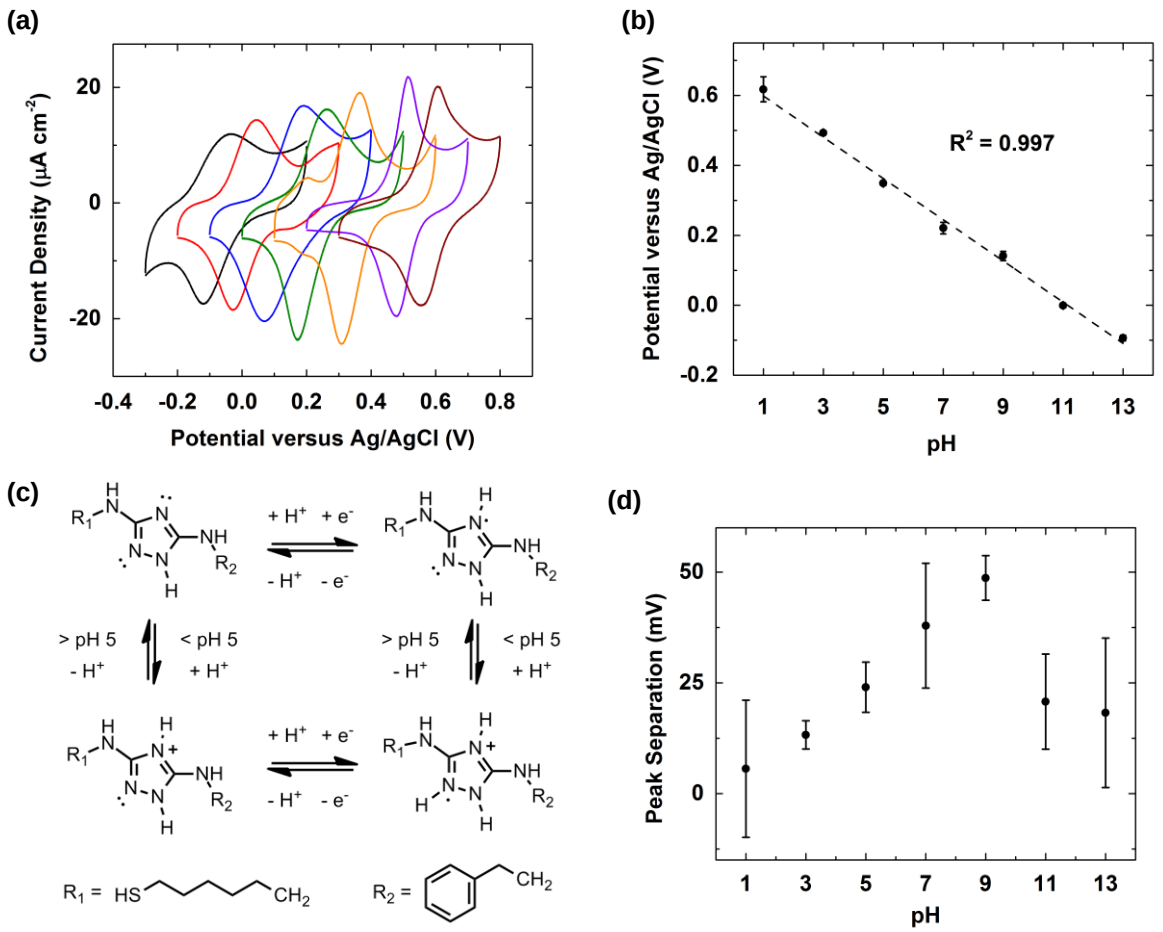

Figure 7.5. (a) Cyclic voltammograms (CVs) of SAMs of BTT on Au at pH 1 (brown), 3 (purple), 5 (orange), 7 (green), 9 (blue), 11 (red), and 13 (black) at a scan rate of 100 mV s^{-1}. (b) pH dependence of $E_{½}$ of the redox couple of a SAM of BTT on Au obtained from cyclic voltammograms at a scan rate of 100 mV/s. (c) Schematic of the BTT species involved in the redox process. (d) Peak separation of SAMs of BTT on Au as a function of solution pH.

Here, we add to this picture by demonstrating that 1 H^+ is also transferred in this process. Figure 7.5c shows a plausible schematic of the BTT species involved in this process based upon the pK_a of DAT.[62,63] We further note that in Figure 7.5a, the shape of the CVs changes as a function of pH. Figure 7.5d plots the peak separation values of BTT, which range from 0 to 50 mV, as a function of pH. The peaks separate more as the solution changes from pH 1 to pH 11, and separate less as the solution changes from pH 11 to pH 13. This inverted-V shaped behavior

has been observed before by Finklea et al. using a SAM-bound galvinol system, which like BTT, undergoes a reversible 1 e^-:1 H^+ PCET process.[64]

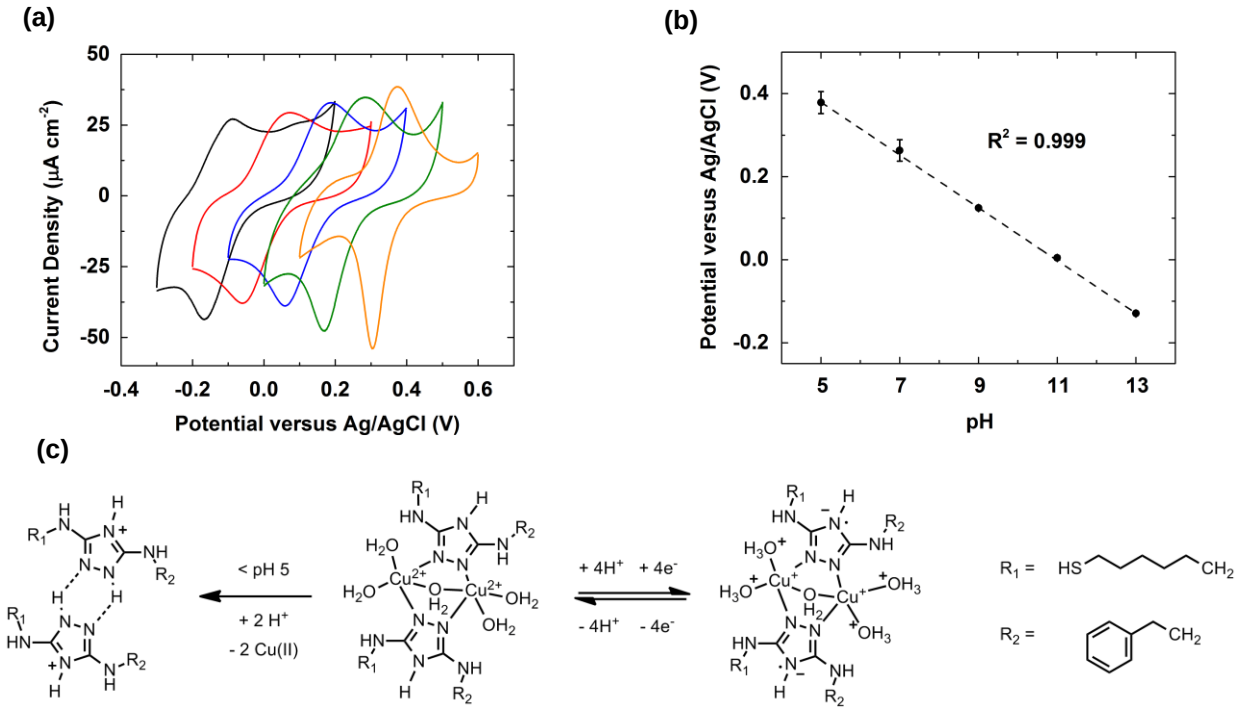

Figure 7.6. (a) CVs of SAMs of CuBTT on Au at pH 5 (orange), 7 (green), 9 (blue), 11 (red), and 13 (black) at a scan rate of 100 mV s^{-1}. (b) pH dependence of $E_{½}$ of the redox couple of a SAM of CuBTT on Au obtained from cyclic voltammograms at a scan rate of 100 mV/s. (c) Schematic of proton and electron transfer events of CuBTT.[65,66]

We next address the redox behavior of the BTT SAM after Cu incorporation to form the Cu(II) complex of BTT, CuBTT. Figure 7.6a displays CVs of CuBTT SAMs in solutions ranging from pH 5 to pH 13. Since the pK_a of the triazole ring in BTT is about 4.5, we find that Cu no longer binds to BTT below pH 5. Figure 7.6b displays the $E_{½}$ values of the redox couple of a SAM of CuBTT as a function of pH. The $E_{½}$ values decrease by (64 ± 0.5) mV per pH unit, a value close to the Nernstian prediction for a redox reaction involving H^+ and e^- in a 1:1 ratio. Upon addition of Cu, the integrated charge of the redox couple doubles,[36] signifying that the 1e^- Cu(I)/Cu(II) redox couple coincides with the 1 e^- redox couple of BTT. Here, we further

understand the CuBTT system by establishing that equal number of protons and electrons are transferred in this process. Figure 7.6c describes the protonation and redox events for the CuBTT system we hypothesize occur using the information we gained from Figures 7.6a and b.

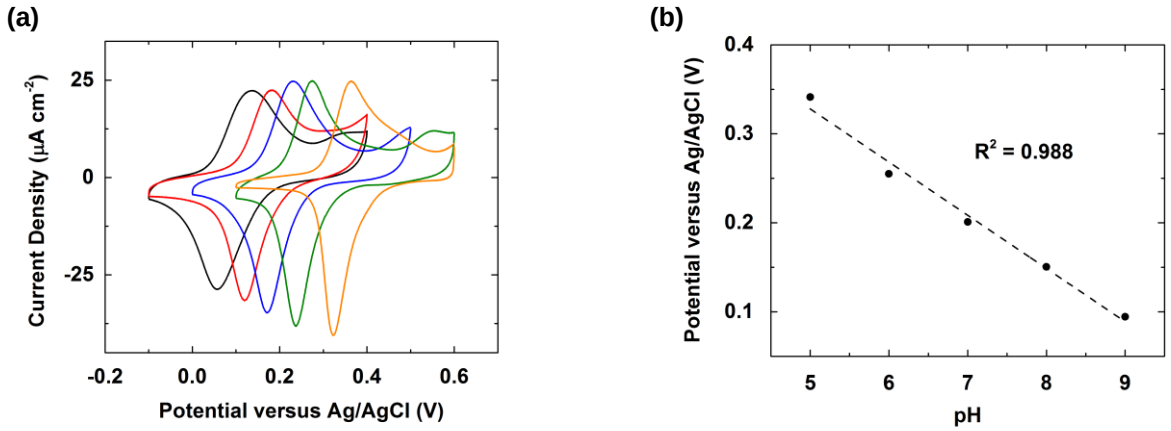

Figure 7.7. (a) CVs of SAMs of ZnBTT on Au at pH 5 (orange), 6 (green), 7 (blue), 8 (red), and 9 (black) at a scan rate of 100 mV s^{-1}. (b) pH dependence of the $E_{½}$ of the redox couple of a SAM of ZnBTT on Au obtained from cyclic voltammograms at a scan rate of 100 mV/s.

To verify that the BTT redox wave is not silenced upon complexation with a metal, we introduced Zn, a redox-inactive metal in the potential window used, to a BTT SAM. Figure 7.7a displays CVs of ZnBTT in solutions under varying pH regime. Figure 7.7b shows how the $E_{½}$ of the redox couple of a SAM of ZnBTT varies with pH. The $E_{½}$ decreases by (60 ± 4) mV per pH unit, which is expected for a process involving H^+ and e^- in a ratio of 1:1. Since Zn is redox-silent, the redox wave observed for ZnBTT must be due to the reduction of the triazole ring in BTT. In other words, metal binding to BTT does not suppress the BTT wave and does not affect the pH dependence of the BTT couple.

7.2.3 pH Dependence of HBMs Containing BTT SAMs

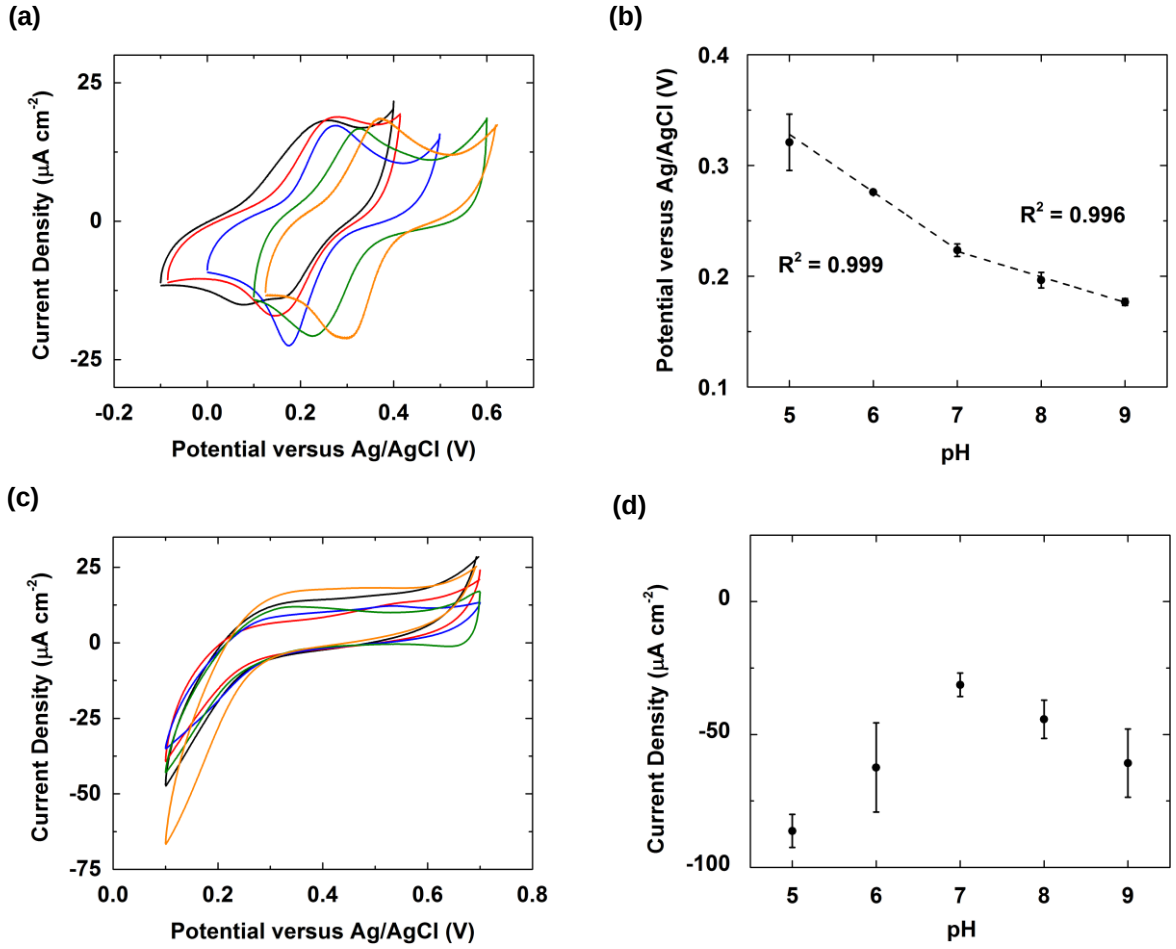

Figure 7.8. (a) CVs of SAMs of CuBTT covered by a monolayer of DMPC on Au at pH 5 (orange), 6 (green), 7 (blue), 8 (red), and 9 (black). (b) pH dependence of $E_{½}$ of a SAM of CuBTT covered by a monolayer of DMPC on Au obtained from cyclic voltammograms at a scan rate of 100 mV/s. (c) CVs of SAMs of CuBTT covered by a monolayer of DMPC on Au after running CVs at pH 5 (orange), 6 (green), 7 (blue), 8 (red), and 9 (black) in a solution of $K_3Fe(CN)_6$ (1 mM) and KCl (100 mM). (d) pH dependence of the maximum cathodic current densities of a SAM of CuBTT covered by a monolayer of DMPC on Au in a solution of $K_3Fe(CN)_6$ (1 mM) and KCl (100 mM).

To examine the effect of proton flux on PCET reactions, we utilized a HBM platform. This HBM platform consists of a BTT-modified electrode with a monolayer of DMPC appended

on top through van der Waal's interactions between the hydrophobic lipid tails and the lipophilic benzyl arm on BTT. We first studied the case without proton carriers in the lipid layer to understand how a lipid layer affects the behavior of a HBM-buried redox couple. Figure 7.8a displays the CuBTT redox wave inside a HBM from pH 5 to pH 9, the range in which DMPC is stable.[67,68] Previously, we determined that the BTT wave is silent when covered by a lipid monolayer inside a HBM.[39] The redox wave of CuBTT inside a HBM observed in Figure 7.8a is therefore due solely to the Cu(I)/Cu(II) couple. Figure 7.8b shows the $E_{½}$ of a SAM of CuBTT covered by a monolayer of DMPC in solutions of varying pH values. $E_{½}$ decreases by (52 ± 2) mV per pH unit from pH 5 to 7, while $E_{½}$ decreases by (23 ± 2) mV per pH unit from pH 7 to 9. Interestingly, this result suggests that the ratio of protons to electrons transferred switches from 1:1 at pH 5 to 7 to 1:2 at pH 7 to 9 according to the Nernst equation.

In an effort to determine the origin of this change in the number of protons transferred to CuBTT inside a lipid, we interrogated the integrity of the DMPC lipid layer by using blocking experiments in which a redox probe is added to bulk solution.[36,39] Figure 7.8c displays CVs obtained for CuBTT covered by a monolayer of DMPC with $K_3Fe(CN)_6$ in the bulk solution.In the absence of a lipid layer, the reversible Fe(II)/Fe(III) redox couple is observed. However, upon appending a monolayer of DMPC, electron transfer from the electrode to $K_3Fe(CN)_6$ is impeded by the insulating nature of the lipid. Figure 7.8d demonstrates that from pH 5 to 9, the current density for the blocking experiment is the least at pH 7. This result indicates that the lipid layer is most well-formed at pH 7, which is expected since at this pH stable zwitterionic ionic lipid species predominant. If the lipid layer had completely blocked access of protons in the bulk solution to CuBTT from pH 5 to 9, then $E_{½}$ of CuBTT would not depend upon pH. However, upon increasing the pH from 7 to 9, the amount of current density obtained in the blocking

experiment increases. This finding indicates that as the lipid layer becomes more anionic at higher pH values, it becomes more permeable to the redox probe and also protons in bulk solution. As a result, $E_{½}$ of CuBTT shifts negative with increasing pH, although to less of an extent as observed in the case of CuBTT without lipid. Upon decreasing the pH from 7 to 5, the amount of current density obtained in the blocking experiment increases more rapidly than from pH 7 to 9. This result indicates that the lipid layer becomes even more permeable to the redox probe and protons in bulk solution at pH 5. Correspondingly, $E_{½}$ of CuBTT is more sensitive to pH changes in the pH 5 to 7 range. In summary, the two different slopes observed in pH ranges 5-7 and 7-9 of the $E_{½}$ of CuBTT in Figure 7.8c correlate to the two slopes measured in the blocking experiments in Figure 7.8d.

To probe the effect of assisted proton transport on PCET reactions in a HBM, we incorporated mono-*N*-dodecylphosphate (MDP), a proton carrier utilized by our group previously,[36] into the lipid layer of the HBM. Figure 7.9a displays the CuBTT redox wave inside a HBM system with MDP incorporated in the DMPC layer from pH 5 to pH 9. The redox wave presented is sensitive to the pH of the bulk solution. Figure 7.9b displays the $E_{½}$ of a SAM of CuBTT covered by a monolayer of DMPC with 1 equivalent of MDP added to the DMPC layer from pH 5 to 9. The $E_{½}$ of CuBTT decreases by (46 ± 4) mV per pH unit across the entire pH range. In contrast to the DMPC only case, we observe only one slope in Figure 7.9c for the case with MDP added to the lipid layer.

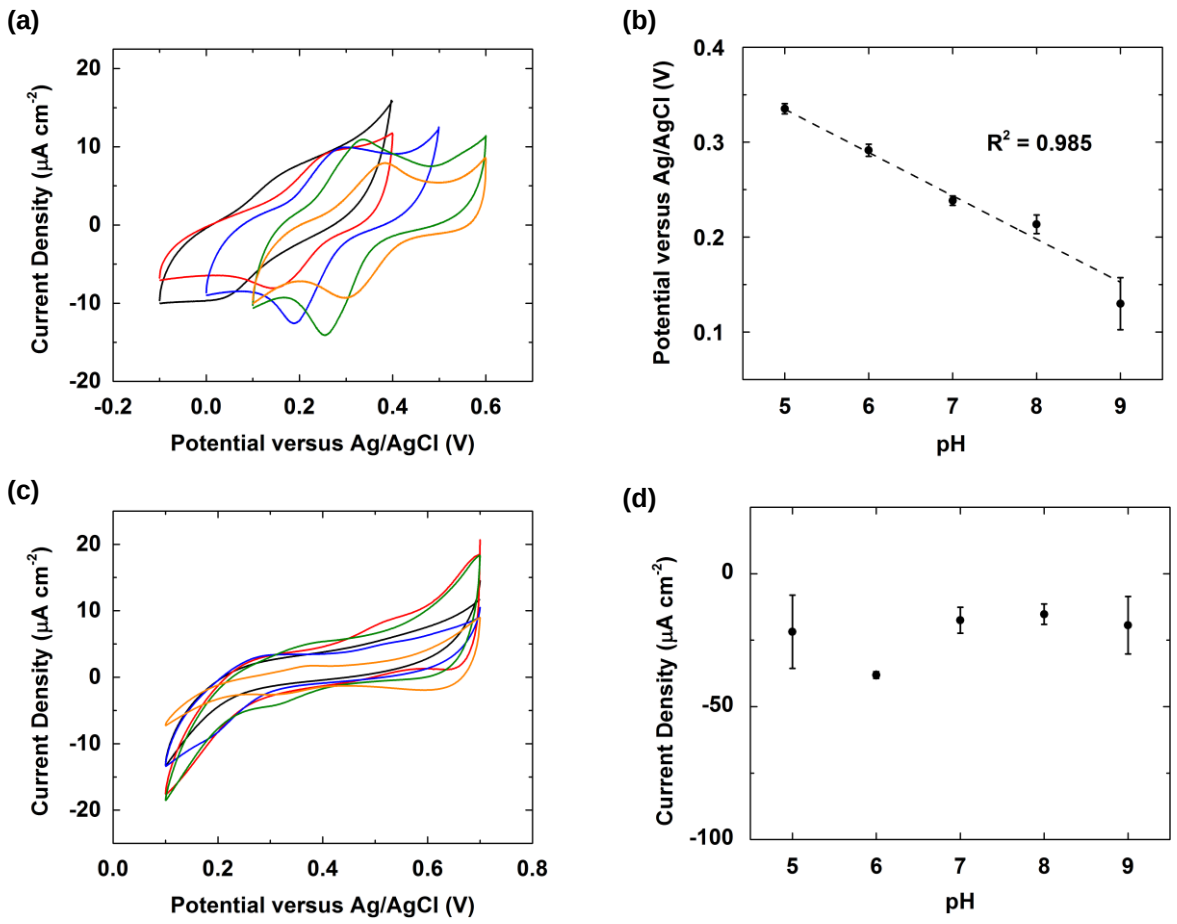

Figure 7.9. (a) CVs of SAMs of CuBTT covered by a monolayer of DMPC with 1 equivalent of MDP added to the lipid layer on Au at pH 5 (orange), 6 (green), 7 (blue), 8 (red), and 9 (black) at a scan rate of 100 mV s^{-1}. (b) pH dependence of $E_{½}$ of a SAM of CuBTT covered by a monolayer of DMPC with 1 equivalent of MDP added to the DMPC layer on Au obtained from cyclic voltammograms at a scan rate of 100 mV/s. (c) CVs of SAMs of CuBTT covered by a monolayer of DMPC with 1 equivalent of MDP added to the lipid layer on Au after running CVs at pH 5 (orange), 6 (green), 7 (blue), 8 (red), and 9 (black) in a solution of $K_3Fe(CN)_6$ (1 mM) and KCl (100 mM). (d) pH dependence of the maximum cathodic current densities of a SAM of CuBTT covered by a monolayer of DMPC with 1 equivalent of MDP added to the DMPC layer on Au in a solution of $K_3Fe(CN)_6$ (1 mM) and KCl (100 mM).

To understand the empirical difference between systems with and without MDP (Figure 7.9b vs. 7.8b), we conducted blocking experiments to the HBM with MDP added analogous to the case of lipid only. Figure 7.9c displays the CVs obtained for CuBTT covered by a MDP-

DMPC layer with $K_3Fe(CN)_6$ in the bulk solution. Similar to the case of DMPC only, the absence of a reversible Fe(II)/Fe(III) redox couple signifies the formation of a complete lipid monolayer with MDP incorporated. Figure 7.9d shows the maximum amounts of current density obtained from the blocking experiments with CuBTT in a HBM containing MDP. Across the pH range studied, the magnitudes of the blocking current density at 0.1 V vs. Ag/AgCl remain relatively constant at about -25 μA cm^{-2}. These current densities are comparable to the value obtained for CuBTT in a HBM without MDP at pH 7, indicating that the lipid effectively blocks access of the $K_3Fe(CN)_6$ redox probe in bulk solution to CuBTT from pH 5 to 9 when MDP is incorporated in the HBM. These results suggest that the presence of MDP increases the stability of the DMPC at pH 5, 6, 8, and 9, possibly in a manner analogous to cholesterol incorporation in other HBM systems.[38] However, since the $E_{½}$ of the CuBTT redox process shifts with pH (Figure 7.9c), CuBTT must still have access to protons from the bulk solution. This finding suggests that MDP delivers protons across the lipid membrane to CuBTT during cycling of the Cu(I)/Cu(II) redox couple.

7.2.4 pH dependence of O_2 Reduction by CuBTT inside a HBM

Having established that MDP delivers protons to CuBTT as it cycles between Cu(II) and Cu(I), we next studied the ability of CuBTT to catalyze the O_2 reduction reaction inside a HBM containing MDP as a function of pH. In prior work, we determined that a HBM containing MDP results in about 350% more current than a HBM without MDP at pH 5 at -0.5 V vs. Ag/AgCl. In contrast, at pH values greater than 5, the O_2 reduction current does not enhance the ORR current at similar overpotentials (Figure 7.10a), which means that at these pH values, there is very little to no enhancement of O_2 reduction current over the HBM case without proton carrier. Figure

7.10b shows the percent enhancement of O_2 reduction current by CuBTT-containing HBM with MDP added to the lipid layer compared to the lipid only case without MDP at various pH values. The ability of MDP to deliver protons changes based upon its protonation state. At pH 5, MDP exists primarily as $RHPO_4^-$ which can be protonated to RH_2PO_4. The neutral species RH_2PO_4 is hydrophobic enough to penetrate the hydrophobic lipid interior and deliver protons to CuBTT via flip-flop diffusion.[36] In contrast, from pH 6 to 9, the acid-base equilibrium of MDP shifts towards RPO_4^{2-}, which when protonated yields $RHPO_4^-$, a species too hydrophilic to undergo flip-flop diffusion across the lipid layer. The $RH_2PO_4/RHPO_4^-/RPO_4^{2-}$ equilibrium of MDP thus explains the pH dependence of the enhancement of O_2 reduction current density by CuBTT in HBM.

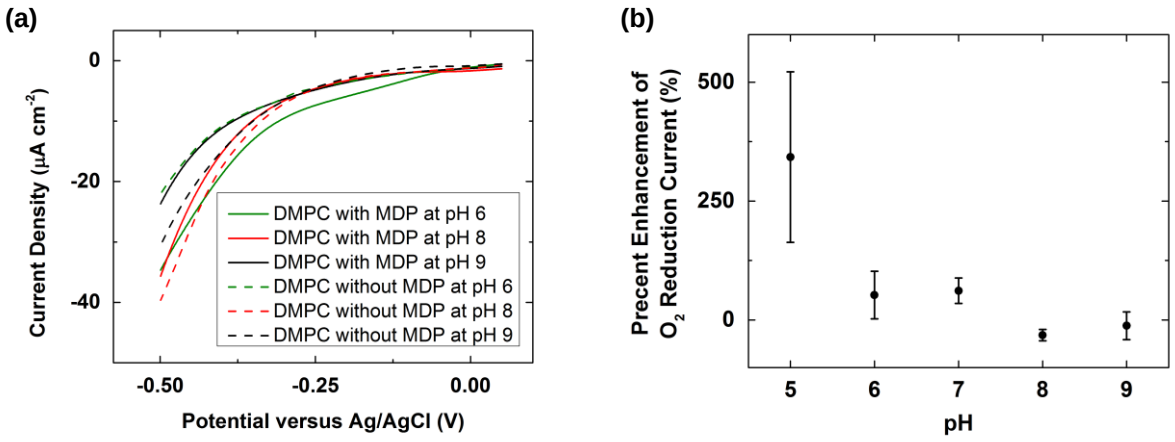

Figure 7.10. (a) Linear sweep voltammograms (LSVs) of SAMs of CuBTT covered by a monolayer of DMPC with 1 equivalent of MDP added to the lipid layer on Au in O_2-saturated pH 6 (green), 8 (red), and 9 (black) buffer solutions. (b) Percent enhancement of O_2 reduction current by a SAM of CuBTT covered by a DMPC layer with 1 equivalent of MDP added to the lipid layer as compared to the lipid only case as a function of pH.

Unlike the trend observed for O_2 reduction, the Cu(I)/Cu(II) couple of CuBTT in a HBM with MDP is not affected by the pH-controlled speciation of MDP (Figure 7.9a). This difference reflects the fact that during O_2 reduction, each MDP carrier delivers a catalytic amount of

protons to CuBTT, whereas during the Cu(I)/Cu(II) redox event, MDP transports only a stoichiometric quantity of protons. In other words, MDP still delivers enough protons to facilitate the PCET Cu(I)/Cu(II) couple despite the fact that its acid-base equilibrium implies that it is predominantly speciated as RPO_4^{2-} at high pH.

7.2.5 XPS of HBMs before and after ORR

To confirm that the integrity of the electrochemical platform is not compromised during O_2 reduction, we carried out post-mortem XPS measurements after ORR catalysis. Figure 7.11 compares the XPS spectra of HBMs before and after conducting electrocatalysis. The typical penetration depth using XPS is larger than 5 nm,[69] which is longer than the full thickness of a HBM, thus explaining the presence of Au peaks in the survey scan. All of the peaks observed in the high-resolution scans do not change or shift after O_2 reduction, suggesting that the surface species do not undergo chemical modifications during ORR. In particular, we do not observe any trace of Cu(0) signal, indicating that the formation of Cu metal or nanoparticles from Cu(II) ions does not occur in our HBM platform at these potentials.

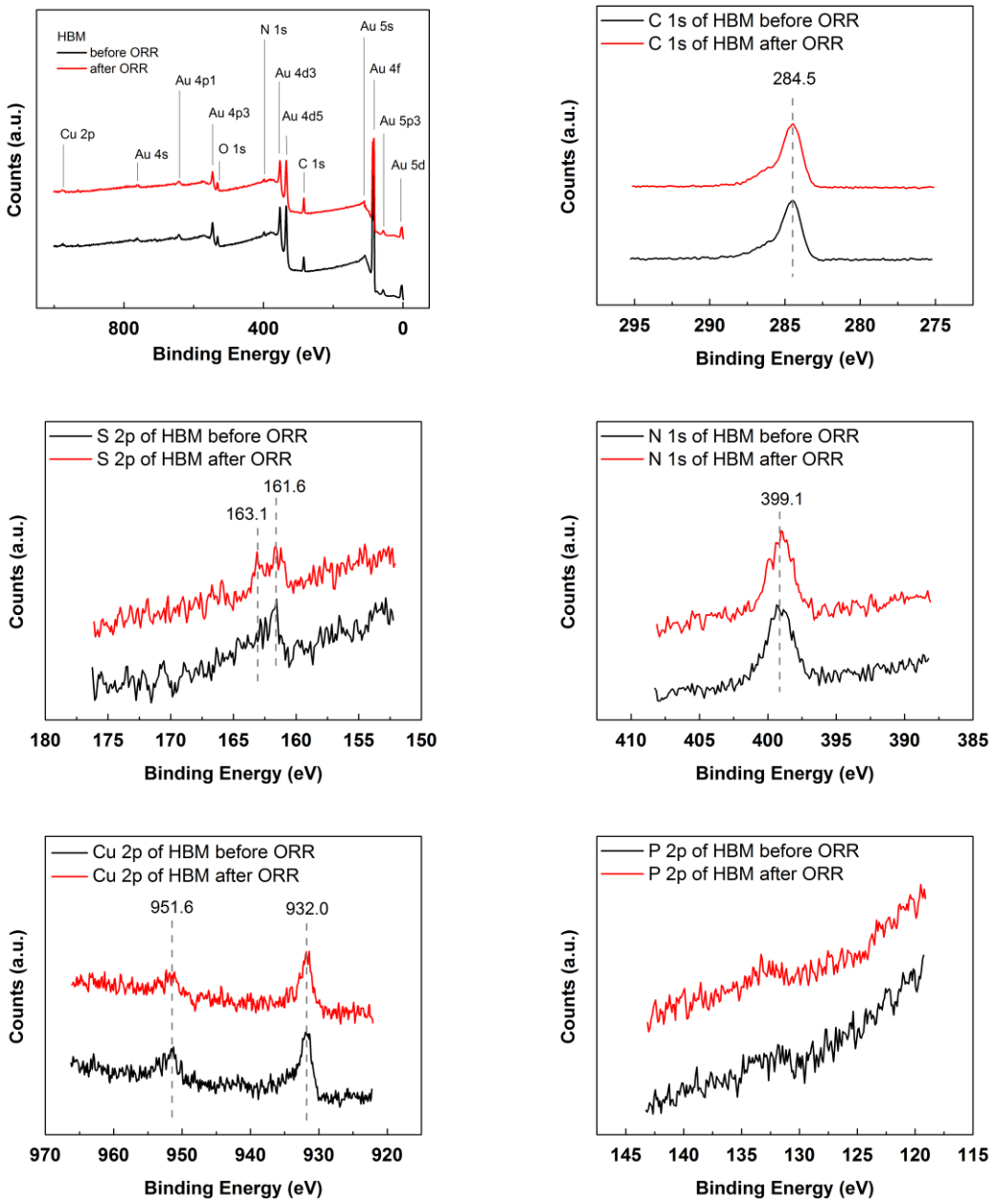

Figure 7.11. XPS (a) survey scan and high-resolution scans of (b) C 1s, (c) S 2p, (d) N 1s, (e) Cu 2p, and (f) P 2p obtained from HBMs before (black) and after (red) O_2 reduction.

7.3 Conclusions

In this chapter, we investigated the physical and electrochemical properties of a HBM electrochemical platform that is broadly useful to examine the role of proton transfer

kinetics in PCET reactions. In particular, we probed the surface structure of the lipid monolayer of the HBM using AFM and characterized the pH-dependent redox behavior of the underlying Cu(I)/Cu(II) couple of the CuBTT SAM covered by the lipid layer. We recorded a series of AFM images in a consecutive fashion to monitor the lipid formation process via a vesicle fusion process in a redox-active HBM system. In addition to surface examination, we determined the number of electrons transferred for each of the redox waves observed in a BTT SAM, a CuBTT SAM, a HBM containing lipid only, and a HBM containing a lipid monolayer with an alkyl phosphate proton carrier incorporated. The pH dependence of the redox wave correlates to the amount of current passed in the blocking experiment, suggesting the redox event is related to the state of the lipid layer. XPS data of the HBM collected before and after catalysis corroborates that Cu(II), but not Cu(0), is responsible for the ORR activity and is not degraded during the ORR process.

7.4 References

(1) Soudackov, A.; Hammes-Schiffer, S. *J. Chem. Phys.* **2000**, *113*, 2385.
(2) Horvath, S.; Fernandez, L. E.; Soudackov, A. V.; Hammes-Schiffer, S. *Proc. Natl. Acad. Sci. USA* **2012**, *109*, 15663.
(3) Hammes-Schiffer, S. *Acc. Chem. Res.* **2009**, *42*, 1881.
(4) Costentin, C.; Robert, M.; Savéant, J.-M. *Chem. Rev.* **2010**, *110*, PR1.
(5) Mayer, J. M.; Rhile, I. J. *BBA-Bioenergetics* **2004**, *1655*, 51.
(6) Mayer, J. M. *Annu. Rev. Phys. Chem.* **2004**, *55*, 363.
(7) Weinberg, D. R.; Gagliardi, C. J.; Hull, J. F.; Murphy, C. F.; Kent, C. A.; Westlake, B. C.; Paul, A.; Ess, D. H.; McCafferty, D. G.; Meyer, T. J. *Chem. Rev.* **2012**, *112*, 4016.
(8) Fecenko, C. J.; Meyer, T. J.; Thorp, H. H. *J. Am. Chem. Soc.* **2006**, *128*, 11020.
(9) Chen, Z.; Vannucci, A. K.; Concepcion, J. J.; Jurss, J. W.; Meyer, T. J. *Proc. Natl. Acad. Sci. USA* **2011**, *108*, E1461.
(10) Hammes-Schiffer, S.; Soudackov, A. V. *J. Phys. Chem. B* **2008**, *112*, 14108.
(11) Wenger, O. S. *Acc. Chem. Res.* **2013**, *46*, 1517.
(12) Zhang, J.; Xie, Z.; Zhang, J.; Tang, Y.; Song, C.; Navessin, T.; Shi, Z.; Song, D.; Wang, H.; Wilkinson, D. P.; Liu, Z.-S.; Holdcroft, S. *J. Power Sources* **2006**, *160*, 872.
(13) Jaouen, F.; Proietti, E.; Lefevre, M.; Chenitz, R.; Dodelet, J.-P.; Wu, G.; Chung, H. T.; Johnston, C. M.; Zelenay, P. *Energy Environ. Sci.* **2011**, *4*, 114.

(14) Collman, J. P.; Ghosh, S.; Dey, A.; Decréau, R. A.; Yang, Y. *J. Am. Chem. Soc.* **2009**, *131*, 5034.
(15) Collman, J. P.; Devaraj, N. K.; Decréau, R. A.; Yang, Y.; Yan, Y.-L.; Ebina, W.; Eberspacher, T. A.; Chidsey, C. E. D. *Science* **2007**, *315*, 1565.
(16) Collman, J. P.; Decréau, R. A.; Lin, H.; Hosseini, A.; Yang, Y.; Dey, A.; Eberspacher, T. A. *Proc. Natl. Acad. Sci. USA* **2009**, *106*, 7320.
(17) Boulatov, R.; Collman, J. P.; Shiryaeva, I. M.; Sunderland, C. J. *J. Am. Chem. Soc.* **2002**, *124*, 11923.
(18) Rosenthal, J.; Nocera, D. G. *Acc. Chem. Res.* **2007**, *40*, 543.
(19) Gewirth, A. A.; Thorum, M. S. *Inorg. Chem.* **2010**, *49*, 3557.
(20) Kim, J.; Gewirth, A. A. *J. Phys. Chem. B* **2006**, *110*, 2565.
(21) Erickson, E. M.; Thorum, M. S.; Vasić, R.; Marinković, N. S.; Frenkel, A. I.; Gewirth, A. A.; Nuzzo, R. G. *J. Am. Chem. Soc.* **2012**, *134*, 197.
(22) Erickson, E. M.; Oruc, M. E.; Wetzel, D. J.; Cason, M. W.; Hoang, T. T. H.; Small, M. W.; Li, D.; Frenkel, A. I.; Gewirth, A. A.; Nuzzo, R. G. *Anal. Chem.* **2014**, *86*, 8368.
(23) Muramoto, K.; Ohta, K.; Shinzawa-Itoh, K.; Kanda, K.; Taniguchi, M.; Nabekura, H.; Yamashita, E.; Tsukihara, T.; Yoshikawa, S. *Proc. Natl. Acad. Sci. USA* **2010**, *107*, 7740.
(24) Kieber-Emmons, M. T.; Qayyum, M. F.; Li, Y.; Halime, Z.; Hodgson, K. O.; Hedman, B.; Karlin, K. D.; Solomon, E. I. *Angew. Chem. Int. Ed.* **2012**, *51*, 168.
(25) Blackman, A.; Tolman, W. In *Metal-Oxo and Metal-Peroxo Species in Catalytic Oxidations*; Meunier, B., Ed.; Springer Berlin Heidelberg: 2000; Vol. 97, p 179.
(26) Karlin, K. D.; Gultneh, Y. In *Progress in Inorganic Chemistry*; John Wiley & Sons, Inc.: 2007, p 219.
(27) Solomon, E. I.; Heppner, D. E.; Johnston, E. M.; Ginsbach, J. W.; Cirera, J.; Qayyum, M.; Kieber-Emmons, M. T.; Kjaergaard, C. H.; Hadt, R. G.; Tian, L. *Chem. Rev.* **2014**, *114*, 3659.
(28) Solomon, E. I.; Chen, P.; Metz, M.; Lee, S.-K.; Palmer, A. E. *Angew. Chem. Int. Ed.* **2001**, *40*, 4570.
(29) Tse, E. C. M.; Schilter, D.; Gray, D. L.; Rauchfuss, T. B.; Gewirth, A. A. *Inorg. Chem.* **2014**, *53*, 8505.
(30) Thorseth, M. A.; Tornow, C. E.; Tse, E. C. M.; Gewirth, A. A. *Coord. Chem. Rev.* **2013**, *257*, 130.
(31) Thorseth, M. A.; Letko, C. S.; Tse, E. C. M.; Rauchfuss, T. B.; Gewirth, A. A. *Inorg. Chem.* **2012**, *52*, 628.
(32) Sjödin, M.; Styring, S.; Wolpher, H.; Xu, Y.; Sun, L.; Hammarström, L. *J. Am. Chem. Soc.* **2005**, *127*, 3855.
(33) Chng, L. L.; Chang, C. J.; Nocera, D. G. *Org. Lett.* **2003**, *5*, 2421.
(34) Hatcher, L.; Karlin, K. *J Biol Inorg Chem* **2004**, *9*, 669.
(35) McCrory, C. C. L.; Ottenwaelder, X.; Stack, T. D. P.; Chidsey, C. E. D. *J. Phys. Chem. A* **2007**, *111*, 12641.
(36) Barile, C. J.; Tse, E. C. M.; Li, Y.; Sobyra, T. B.; Zimmerman, S. C.; Hosseini, A.; Gewirth, A. A. *Nat. Mater.* **2014**, *13*, 619.
(37) Hosseini, A.; Barile, C. J.; Devadoss, A.; Eberspacher, T. A.; Decreau, R. A.; Collman, J. P. *J. Am. Chem. Soc.* **2011**, *133*, 11100.
(38) Hosseini, A.; Collman, J. P.; Devadoss, A.; Williams, G. Y.; Barile, C. J.; Eberspacher, T. A. *Langmuir* **2010**, *26*, 17674.

(39) Tse, E. C. M.; Barile, C. J.; Gewargis, J. P.; Li, Y.; Zimmerman, S. C.; Gewirth, A. A. *Anal. Chem.* **2015**, *87*, 2403.
(40) Jain, M. K. *Introduction to Biological Membranes*; 2nd ed.; Wiley: New York, 1988.
(41) Li, Y.; Tse, E. C. M.; Barile, C. J.; Gewirth, A. A.; Zimmerman, S. C. *J. Am. Chem. Soc.* **2015**, *137*, 14059.
(42) Bard, A. J.; Faulkner, L. R. *Electrochemical Methods: Fundamentals and Applications*; Wiley, 2000.
(43) Long, Y.-T.; Li, C.-Z.; Kraatz, H.-B.; Lee, J. S. *Biophys. J.* **2003**, *84*, 3218.
(44) Colonna, B.; Echegoyen, L. *Chem. Comm.* **2001**, 1104.
(45) Kim, K.; Kwak, J. *J. Electroanal. Chem.* **2001**, *512*, 83.
(46) Ding, S.-J.; Chang, B.-W.; Wu, C.-C.; Lai, M.-F.; Chang, H.-C. *Anal. Chim. Acta* **2005**, *554*, 43.
(47) Agonafer, D. D.; Chainani, E.; Oruc, M. E.; Lee, K. S.; Shannon, M. A. *J. Nanotechnol. Eng. Med.* **2013**, *3*, 0310061.
(48) Boubour, E.; Lennox, R. B. *J. Phys. Chem. B* **2000**, *104*, 9004.
(49) Damos, F. S.; Luz, R. C. S.; Kubota, L. T. *Langmuir* **2005**, *21*, 602.
(50) Slowinski, K.; Chamberlain, R. V.; Bilewicz, R.; Majda, M. *J. Am. Chem. Soc.* **1996**, *118*, 4709.
(51) Gramse, G.; Dols-Perez, A.; Edwards, M. A.; Fumagalli, L.; Gomila, G. *Biophys. J.* **2013**, *104*, 1257.
(52) Nymeyer, H.; Zhou, H.-X. *Biophys. J.* **2008**, *94*, 1185.
(53) Dilger, J.; McLaughlin, S.; McIntosh, T.; Simon, S. *Science* **1979**, *206*, 1196.
(54) Ohki, S. *J. Theor. Biol.* **1968**, *19*, 97.
(55) Huang, W.; Levitt, D. G. *Biophys. J.* **1977**, *17*, 111.
(56) Flewelling, R. F.; Hubbell, W. L. *Biophys. J.* **1986**, *49*, 541.
(57) Thorum, M. S.; Yadav, J.; Gewirth, A. A. *Angew. Chem. Int. Ed.* **2009**, *121*, 171.
(58) Mingeot-Leclercq, M.-P.; Deleu, M.; Brasseur, R.; Dufrene, Y. F. *Nat. Protocols* **2008**, *3*, 1654.
(59) Meuse, C. W.; Krueger, S.; Majkrzak, C. F.; Dura, J. A.; Fu, J.; Connor, J. T.; Plant, A. L. *Biophys. J.* **1998**, *74*, 1388.
(60) Plant, A. L. *Langmuir* **1999**, *15*, 5128.
(61) Twardowski, M.; Nuzzo, R. G. *Langmuir* **2003**, *19*, 9781.
(62) Efimenko, I. A.; Shishilov, O. N. *Russ. J. Inorg. Chem.* **2012**, *57*, 1695.
(63) Chernyshev, V. M.; Gaidukova, G. V.; Zemlyakov, N. D.; Taranushich, V. A. *Russ. J. Appl. Chem.* **2005**, *78*, 776.
(64) Finklea, H. O.; Haddox, R. M. *Phys. Chem. Chem. Phys.* **2001**, *3*, 3431.
(65) Hernández-Gil, J.; Ferrer, S.; Castiñeiras, A.; Liu-González, M.; Lloret, F.; Ribes, Á.; Čoga, L.; Bernecker, A.; Mareque-Rivas, J. C. *Inorg. Chem.* **2014**, *53*, 578.
(66) Pankratov, A. N.; Borodulin, V. B.; Chaplygina, O. A. *Russ. J. Coord. Chem.* **2005**, *31*, 660.
(67) Guha, M.; Gantz, D. L.; Gursky, O. *J. Lipid Res.* **2008**, *49*, 1752.
(68) Benjwal, S.; Jayaraman, S.; Gursky, O. *Biochemistry* **2005**, *44*, 10218.
(69) Leng, Y. *Materials Characterization: Introduction to Microscopic and Spectroscopic Methods*; Wiley, 2013.

Chapter 8

Proton Transfer Kinetics Control the Mechanism of O_2 Reduction by Non-Precious Metal Electrocatalysts

The work in this chapter was accomplished in collaboration with Dr. Christopher J. Barile,[†] Nicholas A. Kirchschlager, Dr. Ying Li, John P. Gewargis, Professor Steven C. Zimmerman, Dr. Ali Hosseini, and Professor Andrew A. Gewirth.

[†] E. C. M. T. and C. J. B. contributed equally.

8.1 Introduction

The successful commercialization of low-temperature fuel cells with high power densities requires substantially improving the cathode catalysts that reduce O_2 to H_2O via four electrons and four protons. State-of-the-art fuel cells utilize catalysts based on Pt and its alloys, but these materials are neither robust nor cost-effective and exhibit a substantial overpotential of ~300 mV for O_2 reduction reaction (ORR).[1] For these reasons, non-precious metal (NPM) alternatives based on Fe, Co, and Cu have been studied intensely.[2,3] Despite more than fifty years of effort, the design of robust and inexpensive catalysts with low overpotentials remains challenging.[4,5] One of the critical obstacles to developing NPM catalysts is their poor durability resulting in part from deleterious side reactions that produce H_2O_2 or O_2^{-}.[6] Here, we identify that a fundamental source of undesired side reactions for NPM catalysts is a mismatch between the rates of proton and electron transfer to catalysts. More importantly, we determine that by optimizing the proton

transfer rate, we can tune an O_2 reduction catalyst so that it achieves high selectivity for the four e^- reduction of O_2 to H_2O without generating H_2O_2 or O_2^-. These findings lead to new design rules for future NPM catalysts.

Many methods have been used to modulate the thermodynamics and kinetics of electron and proton transfer independently at the electrode-solution interface.[7,8] For example, electrode potential dictates the thermodynamics of electron transfer,[9] and self-assembled monolayers (SAMs) can be used to vary the kinetics of electron transfer.[10,11] For proton transfer, the pH of the bulk solution is commonly altered to affect the thermodynamics of proton transfer.[12-14] However, control of the kinetics of proton transfer has not been achieved in a straightforward way.

Present methods of controlling proton transfer kinetics involve the synthesis of a series of systematically-altered catalysts with pendant proton relays.[15-17] These syntheses can be burdensome, and the addition of proton relays frequently changes the redox properties of the catalyst through both electronic and steric effects. Alternatively, a hybrid bilayer membrane (HBM) is a unique electrochemical platform to control proton kinetics to a catalyst without changing the molecular structure of the catalyst or the nature of the bulk solution.[18,19] In this paper, we demonstrate the use of a HBM to modulate proton transport quantitatively to a Cu-based O_2 reduction catalyst (CuBTT: Cu complex of 6-((3-(benzylamino)-1,2,4-triazol-5-yl)amino)hexane-1-thiol) and observe how the regulation of proton kinetics affects the mechanism of O_2 reduction.

8.2 Materials and Methods

Chemicals were obtained from commercial sources and used without further purification

unless otherwise specified. Potassium phosphate buffer solutions (100 mM) were prepared using Milli-Q water (> 18 MΩ cm) or D_2O and adjusted to the desired pH using H_3PO_4 or D_3PO_4 and KOH or KOD. Experiments at pH 2−4 were performed in Britton-Robinson buffer consisting of H_3BO_3 (0.04 M, 99.999%, Sigma-Aldrich), CH_3COOH (0.04 M, 99.99%, Sigma-Aldrich), H_3PO_4 (0.04 M, 85 wt. % in H_2O, 99.99%, Sigma-Aldrich), and $NaClO_4$ (0.1 M, 99.9%, Sigma-Aldrich). The pH was adjusted using NaOH (10 M, analytical titration grade, Fisher Scientific). Solutions were sparged with Ar and O_2 for 30 min prior to each electrochemical experiment.

Caution! Perchlorate salts are potentially explosive. Only small amounts of materials should be prepared.

For rotation studies on glassy carbon electrodes, $Cu(ClO_4)_2 \cdot 6H_2O$ (0.35 mg, 0.92 μmol, Alfa Aesar) in EtOH (320 μL) was added to protected 6-((3-(benzylamino)-1,2,4-triazol-5-yl)amino)hexane-1-thiol (0.5 mg, 0.92 μmol), the synthesis of which was described previously (*18*). The solution was sonicated for 5 min, and finely ground Vulcan XC-72 (3 mg, Cabot Corp.) was added. The resulting mixture was sonicated for 15 min, and Nafion 117 solution (4 μL, 5 wt. % in alcohols, Sigma-Aldrich) was added. This mixture was sonicated for 30 min, and the resulting ink (10 μL) was deposited on a glassy carbon electrode, which was subsequently dried under a stream of Ar. PANI-Fe-C was synthesized according to a previous study and deposited on a glassy carbon electrode in an analogous manner.[4]

1-dodecylboronic acid (DBA) was incorporated into the lipid layer of the HBM using the same method as previously described for mono-*N*-dodecylphosphate (MDP).[18] All experiments performed were at least triplicated. Voltammograms shown are from representative trials. Error bars presented represent standard deviations of all trials.

Mass spectrometry (MS) experiments were performed using a Quattro Ultima (Waters) electrospray ionization (ESI) mass spectrometer. MS was performed in both positive and negative ionization modes. To quantify the amount of DBA in the HBM, the lipid layers of the surfaces were extracted using EtOH and $CHCl_3$, and the solvents were removed under reduced pressure. The solids were reconstituted in $CDCl_3$, and ^1H NMR spectroscopy studies were conducted with a 400 MHz spectrometer (Varian).

A working solution for dye-based spectroelectrochemistry was prepared by adding a DMSO solution of Amplex Red (10 mM, 50 µL) to a pH 7 potassium phosphate buffer solution (50 mM, 4.85 mL) containing horseradish peroxidase (HRP, 0.1 mg). The amount of H_2O_2 was quantified by placing the working solution (400 µL) in a quartz cuvette (Hellma Analytics, SUPRASIL®, 10 mm high precision cell) and scanning from 300 to 800 nm using an ultraviolet-visible (UV-Vis) spectrometer (Beckman Coulter, DU®250). A spectroelectrochemical cell was used to measure the amount of H_2O_2 generated during O_2 reduction. The colorimetric assay was added to the pH 7 phosphate buffer solution before the experiments were performed. After the voltammetry was completed, the solution was stirred with a glass pipette, and the absorbance of the solution was recorded.

The amount of H_2O_2 generated during the reduction of O_2 by CuBTT is calculated from Beer's Law. The extinction coefficient of resorufin is taken to be 58,000 cm^{-1} M^{-1} at 571 nm as reported previously.[20] The path length of the cuvettes used was 1 cm. By integrating the linear sweep voltammograms (LSVs) and dividing by the scan rate, the total charge during O_2 reduction is calculated. Buffer volumes ranged from 0.5 to 1.0 mL. The absorbance values measured are reported in terms of absorbance units per Coulomb of charge passed per milliliter

of buffer used. For a theoretical system producing 1 mole of H_2O_2 per mole of CuBTT catalyst, the calculated absorbance value is 29 C^{-1} mL^{-1}.

8.3 Results and Discussion

8.3.1 Lipid Permeability of DBA

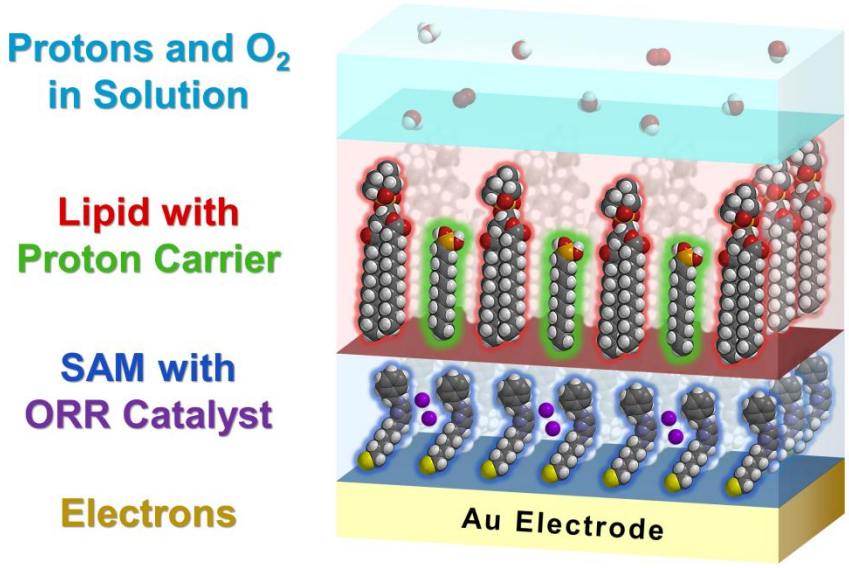

Figure 8.1. Schematic of a HBM that controls the thermodynamics and kinetics of protons and electrons. A Au electrode is modified with a SAM of CuBTT ORR catalyst (blue) and a monolayer of DMPC lipid (red) with DBA proton carrier (green).

The HBM used consists of a monolayer of lipid appended through van der Waals' forces to a SAM of CuBTT catalyst covalently attached to a Au electrode (Figure 8.1). We identify 1-dodecylboronic acid (DBA) to be a competent lipid-bound proton carrier due to its favorable acidity and dipole moment, attributes we previously determined dictate the permeability of species in HBMs.[21] Anions with larger LPP values diffuse across lipids more readily than anions with smaller LPP values (Figure 8.2a).

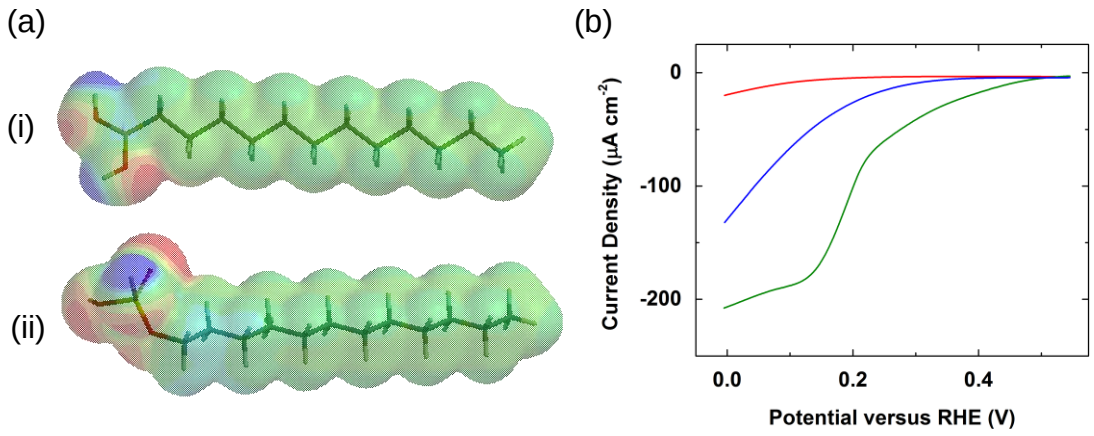

Figure 8.2. (a) Electrostatic potential maps of (i) 1-dodecylboronic acid (DBA) and (ii) mono-*N*-dodecylphosphate (MDP). (b) O_2 reduction LSVs of a SAM of CuBTT with a monolayer of DMPC appended (red) with DBA (green) or MDP (blue) added in the lipid layer in O_2-saturated pH 5 phosphate buffer at a scan rate of 10 mV s^{-1}.

The lipid permeability parameter (LPP) is defined as:

$$LPP(A^-) = 0.5\,\chi_{pk_a}(HA) + 0.5\,(1 - \chi_{dipole}(HA)) \quad \ldots (1)$$

where χ_{pKa} and χ_{dipole} is a scaling factor defined as:

$$\chi_{pKa}(HA) = \frac{pK_a(HA) - pK_a(HA')_{min}}{pK_a(HA'')_{max} - pK_a(HA')_{min}} \quad \ldots (2)$$

$$\chi_{dipole}(HA) = \frac{dipole(HA) - dipole(HA')_{min}}{dipole(HA'')_{max} - dipole(HA')_{min}} \quad \ldots (3)$$

The pK_a of DBA is about 9,[22] and the dipole moment of DBA is calculated using Spartan '08 (Wavefunction, Inc.) version 1.2.0 to be 1.94 D. Using equations 1, 2, and 3, the LPP of DBA is determined to be 1.11. The pK_a of MDP, a proton carrier used in a previous study,[18] is about 2,[23] and the dipole moment of MDP is calculated to be 4.53 D. The LPP of MDP is therefore 0.57, a value lower than that of DBA.

Figure 8.2b shows the LSVs of O_2 reduction by CuBTT in HBMs at pH 5. The incorporation of either MDP or DBA in the lipid layer of the HBM enhances the O_2 reduction current density as compared to the lipid only case. DBA, however, enhances the O_2 reduction current density more than MDP, indicating that DBA is a more effective proton carrier. These

observations match with the calculations below Figure 8.2a, which predict that DBA undergoes flip-flop diffusion across the lipid layer more readily than MDP.

We have tested a wide variety of other proton carrier chemistries in an effort to find a proton transport agent that undergoes more rapid flip-flop diffusion than DBA. In terms of proton transfer rate, DBA already represents a substantial improvement over a phosphate-based proton carrier (Figure 8.2b), which we previously published.[18] The proton transfer rate in bulk solution is many orders of magnitude faster than the flip-flop diffusion rate of DBA; it is unlikely that any proton carrier operating via a flip-flop mechanism could achieve comparable transfer rates. Indeed the flip-flop rate of DBA is 55 s^{-1} (see Section 8.3.8 for the calculation of this value), which is comparable to the flip-flop diffusion rates of proton carriers in biological lipid membranes.[44]

8.3.2 pH Depedence of DBA as a Proton Carrier in a HBM

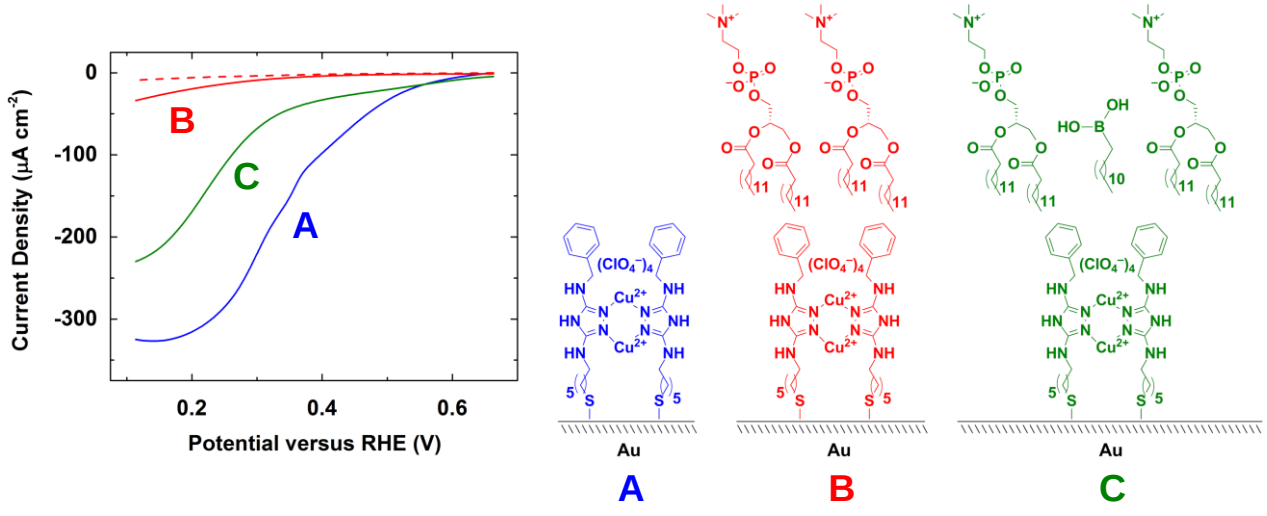

Figure 8.3. Electrochemistry of an O_2 reduction catalyst under varying regimes of proton transfer kinetics. LSVs of a SAM of CuBTT (blue) covered by a monolayer of DMPC lipid (red) with 10 mol% DBA proton carrier in the lipid layer (green) on Au electrodes in pH 7 phosphate buffer saturated with O_2 (solid lines) and Ar (dashed line) at a scan rate of 10 mV s^{-1}.

Figure 8.3 shows representative linear sweep voltammograms (LSVs) of the HBM system at pH 7. In the absence of a lipid layer, the O_2 reduction voltammetry by a SAM of CuBTT exhibits an O_2 diffusion-limited current density of ~325 μA cm^{-2} with an onset potential of 0.54 V versus the reversible hydrogen electrode (RHE) at pH 7 (Figure 8.3, blue line). Upon appending a monolayer of 1,2-dimyristoyl-*sn*-glycero-3-phosphocholine (DMPC) lipid, the O_2 reduction current density decreases substantially (Figure 8.3, red line). We hypothesize that the inhibition in O_2 reduction activity originates from the inability of hydrophilic protons to diffuse through the hydrophobic lipid layer. In Figure 8.3, the red dashed line shows that the current density obtained by a SAM of CuBTT covered by a lipid monolayer in an Ar-sparged solution is less than that obtained in an O_2-saturated solution. These results indicate that O_2 reduction occurs at the CuBTT-lipid interface despite the low availability of protons. Furthermore, the green line in Figure 8.3 demonstrates that incorporating 10 mol% DBA in the DMPC layer dramatically increases the O_2 reduction current compared to the lipid only case. DBA facilitates proton transport to CuBTT via flip-flop diffusion, thus reviving the O_2 reduction current to ~70% of that observed without lipid. The addition of a proton carrier inside the lipid layer of the HBM serves to increase the kinetics of proton transfer to the catalyst, not change the thermodynamic potential of the ORR process.

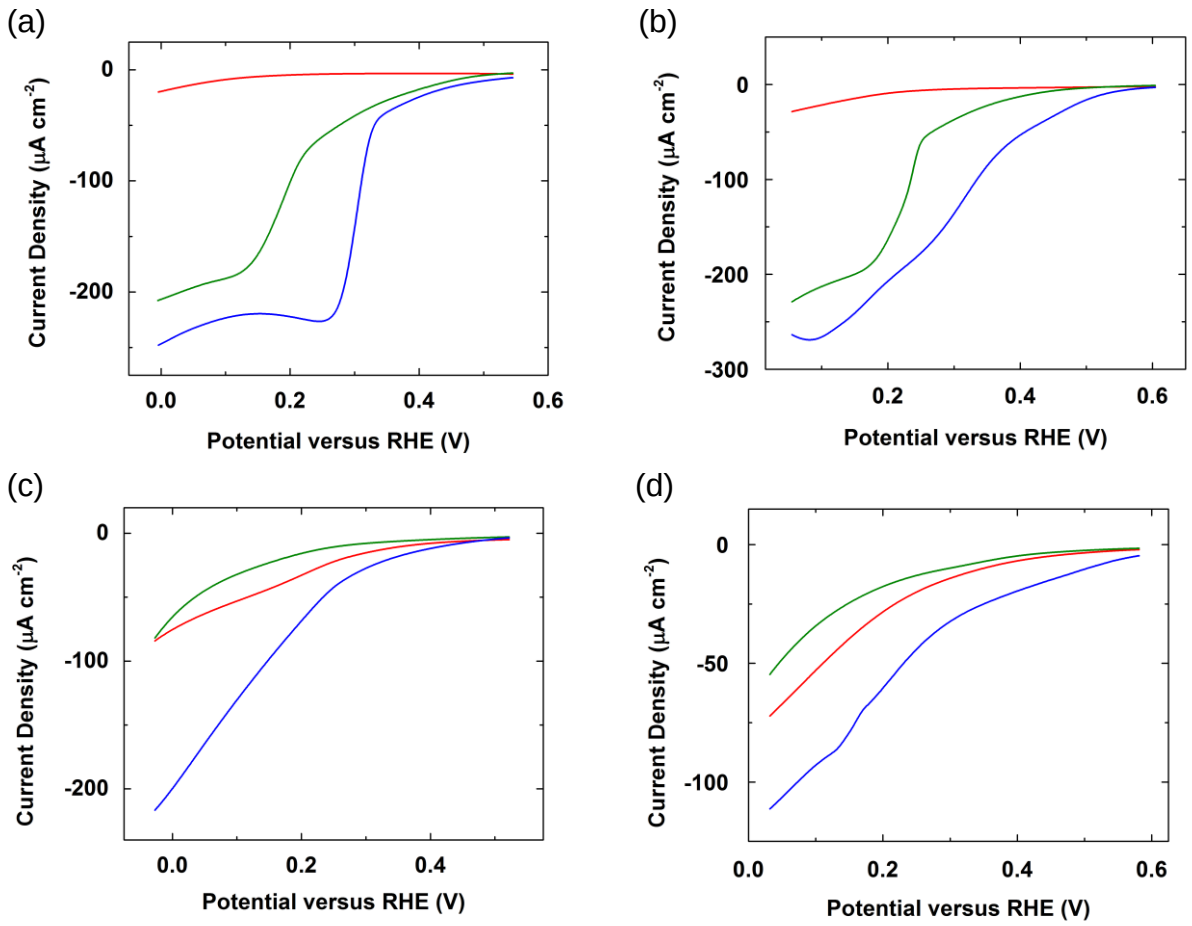

Figure 8.4. O_2 reduction LSVs of a SAM of CuBTT (blue), with a monolayer of DMPC appended (red), and with 10 mol% DBA in the lipid layer (green) in O_2-saturated pH (a) 5, (b) 6, (c) 8, and (d) 9 phosphate buffer at a scan rate of 10 mV s^{-1}.

Additionally, the ability of DBA to act as a proton carrier is dependent upon pH and its concentration in the DMPC layer (Figure 8.4). Previous studies demonstrate that aliphatic amphiphilic species deliver protons across lipid membranes via flip-flop diffusion. Aliphatic acids and amines are known to orient themselves with their polar head groups towards the lipid-water interface.[24] In the presence of a pH gradient or other driving force, these species deliver protons across the lipid membranes through a flip-flop diffusion process.[25] Additionally, previous work with proton carriers has established that these species also undergo flip-flop

diffusion in HBM systems.[18,19] To summarize the results presented in Figure 8.4, the onset potential for O_2 reduction by CuBTT inside lipid is shifted negative compared to the case without lipid due to the effect of the hydrophobic environment of the lipid as has been previously reported for this and other HBM systems[32,33]. Inside lipid with proton carrier, the maximum O_2 reduction current density is controlled in part by the acid-base equilibrium of the proton carrier.

One possible effect to consider is that the amount of O_2 present in bulk solution may be decreasing as the catalyst reduces O_2, and that this effect may convolute the interpretation of our voltammograms. The total integrated charge of the LSV of O_2 reduction by the SAM of CuBTT at pH 7 (the case where the current is the highest, so the system consumes the most O_2) is ~8 mC cm^{-2}. Based on our finding that for this case each O_2 molecule is reduced by an average of 3.79 e^- (Table 8.1) and since the surface area of the electrode used is 0.219 cm^2, we calculate that 4.9 nmol of O_2 are consumed during voltammetry. The solubility of O_2 in pH 7 buffer is 0.24 mM,[26] and we use ~3 mL of buffer solution in our experiments. Therefore, there are ~720 nmol of O_2 in the bulk solution. This calculation shows that at maximum, only 0.7% of the O_2 in bulk solution is consumed during O_2 reduction, and so this effect is considered negligible when interpreting O_2 reduction voltammetry.

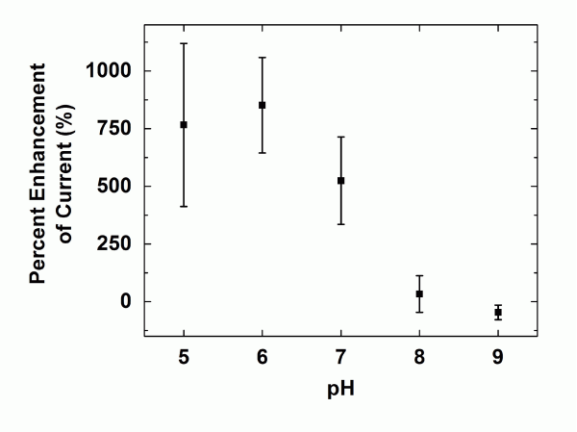

Figure 8.5. Percent enhancement of O_2 reduction current by a SAM of CuBTT covered by a DMPC layer with 10 mol% DBA as compared to the lipid only case as a function of pH.

A proton carrier must be sufficiently hydrophobic to undergo flip-flop diffusion and transfer protons across a hydrophobic lipid membrane in a HBM.[27] Figure 8.5 shows how the enhancement of O_2 reduction current by DBA as compared to the lipid only case varies as a function of pH. From pH 5 to pH 7, the O_2 reduction current with DBA is about 6 times greater than without DBA. However, at pH 8 and pH 9, the enhancement effect of DBA is negligible. At low pH, a greater proportion of DBA is in the neutral state and thus is hydrophobic enough to flip-flop through the hydrophobic lipid layer of the HBM. As the pH increases, more DBA carriers are deprotonated and so proton delivery to the CuBTT catalyst is suppressed, thus inhibiting O_2 reduction activity. The pK_a of a typical boronic acid is about 9 in aqueous solution,[22,28] which possibly explains the observation that the activity of DBA diminishes at pH 8. However, we note that the pK_a values of lipid-bound species often differ by several pH units as compared to their pK_a values in bulk aqueous solutions.[29-33]

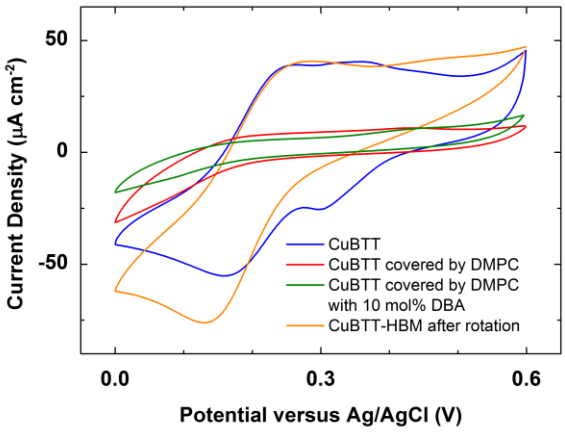

Figure 8.6. Cyclic voltammograms (CVs) of a SAM of the Cu complex (blue), the HBM containing the Cu complex (red), the HBM containing the Cu complex with 10 mol% DBA in the lipid layer (green), and the HBM-modified electrode after rotation at 200 rpm (orange) in a solution of $K_3Fe(CN)_6$ (1 mM) with KCl (100 mM) at a scan rate of 50 mV/s.

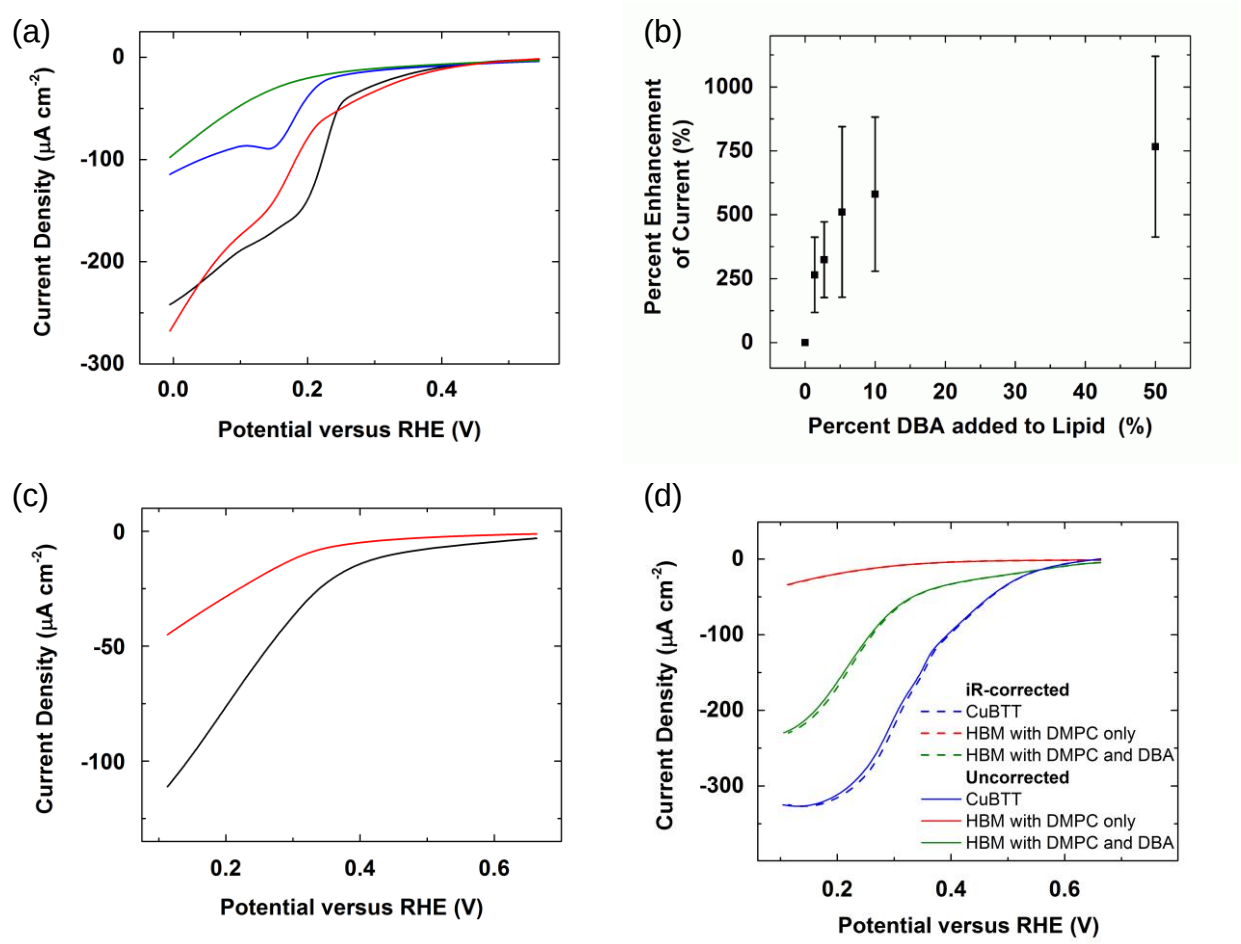

Figure 8.7. (a) O_2 reduction LSVs of a SAM of CuBTT covered by a monolayer of DMPC with 50 mol% (black), 5.3 mol% (red), 2.7 mol% (blue), and 1.4 mol% (green) DBA added in O_2-saturated pH 5 phosphate buffer at a scan rate of 10 mV s^{-1}. (b) Percent enhancement of O_2 reduction current by a SAM of CuBTT covered by a DMPC layer as a function of the amount of DBA added to the lipid layer at pH 5. (c) O_2 reduction LSVs of a SAM of CuBTT covered by a monolayer of DMPC with 2.7 mol% (black) and 1.4 mol% (red) DBA added in O_2-saturated pH 7 phosphate buffer at a scan rate of 10 mV s^{-1}. (d) O_2 reduction LSVs of a SAM of CuBTT (blue), with a monolayer of DMPC appended (red), and with 10 mol% DBA in the lipid layer (green) in O_2-saturated pH 7 phosphate buffer at a scan rate of 10 mV s^{-1}. The solid lines represent the raw data, and the dashed lines represent data that were iR-corrected. iR correction was conducted using impedance measurements.

To ensure a complete lipid layer is formed, we probe the electronic conductivity through the HBM using a solution of $K_3Fe(CN)_6$ as done previously.[18] The Fe(II)/Fe(III) redox couple from $K_3Fe(CN)_6$ is present when CuBTT is not covered by lipid. The disappearance of the

Fe(II)/Fe(III) couple upon formation of a lipid monolayer with and without DBA indicates that a compact lipid layer is formed (Figure 8.6, red and green lines). The reappearance of the Fe(II)/Fe(III) couple after rotating the HBM-modified electrode indicates that no useful information can be obtained from rotating ring-disk electrode experiments for lipid-modified systems (Figure 8.6, orange line).

Figures 8.7a-c show the effect of the concentration of DBA in the lipid layer of the HBM on the enhancement of O_2 reduction current of CuBTT at pH 5 and 7 by DBA as compared to the lipid only case. As the amount of DBA added increases from 0 to 10 mol%, the current enhancement correspondingly increases by about 500% due to an increase in proton flux through the lipid to CuBTT. The O_2 reduction current of CuBTT no longer increases once the amount of DBA added is greater than about 10 mol% (Figure 8.7b) because this is the maximum amount of DBA that can be incorporated into the lipid layer as determined by ^{1}H NMR spectroscopy (*vide infra*). These results suggest that we can modulate the proton transport rate in the HBM by changing the amount of DBA present in the lipid layer. We performed iR correction to the data shown in Figure 8.3 using electrochemical impedance spectroscopy (EIS). Figure 8.7d compares the iR-corrected and uncorrected voltammograms. Since iR correction does not significantly affect the voltammetry due to the low current passed in the CuBTT system, we conclude that it is valid to interpret the uncorrected voltammograms presented throughout the manuscript.

8.3.3 Dye-based Spectroelectrochemical Detection of H_2O_2

O_2 reduction can occur via one, two, or four e^- processes to generate O_2^-, H_2O_2, or H_2O, respectively. H_2O_2 can be formed directly from the O_2 reduction catalyst or through disproportionation of O_2^- to H_2O_2 and O_2. We quantified the H_2O_2 produced during O_2 reduction by CuBTT to probe the O_2 reduction pathways in a HBM. Previously, we used rotating ring-disk

electrode (RRDE) experiments to determine the amount of H_2O_2 generated by a SAM of CuBTT.[18] Unfortunately, we found that RRDE techniques cannot be used on HBM systems because of the limited mechanical stability of the lipid layer during electrode rotation (Figure 8.6, orange line). Therefore, we used dye-based spectroelectrochemistry to quantify the amount of H_2O_2 produced in a stationary environment (see Section 8.2 for experimental details). Upon reacting with H_2O_2 facilitated by horseradish peroxidase, Amplex red turns into resorufin, which in turn changes the color of the solution to red. We thus monitor the absorbance at 571 nm to quantify the amount of H_2O_2 generated by CuBTT inside a HBM with and without the addition of DBA. Figure 8.8 displays a representative set of UV-Vis data. A substantial amount of H_2O_2 is detected in the absence of DBA, while essentially no H_2O_2 is recorded with maximum amount of DBA incorporated in the lipid layer of a HBM. Table 8.1 summarizes the results of the spectroelectrochemical experiments.

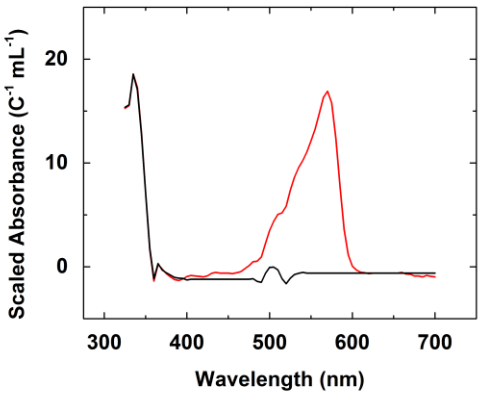

Figure 8.8. Representative UV-Vis spectra recorded after O_2 reduction by CuBTT with DMPC (red line) and DMPC with 10 mol% DBA in the lipid layer (black line) in O_2-sparged pH 7 buffer containing Amplex Red and HRP.

Table 8.1. Absorbances for resorufin measured at 571 nm and the amount of H_2O_2 detected.

Sample	Absorbance at 571 nm (C^{-1} mL^{-1})	mol H_2O_2 / mol CuBTT (x)	e^- consumed per O_2 (ϕ)[#]
No lipid	3.05 ± 0.09	0.105 ± 0.003	3.79 ± 0.01
DMPC	19.7 ± 2.0	0.68 ± 0.07	1.98 ± 0.10
DMPC with 1.4 mol% DBA	8.7 ± 2.6	0.30 ± 0.09	2.20 ± 0.54
DMPC with 2.7 mol% DBA	1.9 ± 0.8	0.066 ± 0.028	3.60 ± 0.17
DMPC with 10 mol% DBA	0[*]	< 0.003	> 3.98

[*] Within the detection limits of the experiment, no resorufin was measured by UV-Vis spectroelectrochemistry. Since the detection limit of the spectrometer is ~0.01 absorbance, the calculated maximum possible H_2O_2 produced is 0.003 mol per mol of O_2 consumed by CuBTT.

[#] To calculate ϕ from the amount of H_2O_2 detected, the mechanism by which O_2 reduction occurs must first be known. From the discussion in the main text, we found that in the absence of lipid, O_2 reduction occurs by a mixture of 2 and 4 e^- processes. In the absence of proton carrier with lipid, O_2 reduction occurs by mainly a 1 e^- process. In the presence of DBA in lipid, O_2 reduction occurs by a mixture of 1 and 4 e^- processes.

Equation to calculate ϕ for no lipid (mixture of 2 and 4 e^- processes):

$$\phi = \frac{x\ mol\ H_2O_2}{mol\ CuBTT}\left(\frac{mol\ CuBTT}{mol\ O_2}\ \frac{2\ mol\ e^-}{mol\ H_2O_2}\right) + \left(\frac{(1-x)\ mol\ H_2O}{mol\ CuBTT}\right)\left(\frac{mol\ CuBTT}{mol\ O_2}\ \frac{4\ mol\ e^-}{mol\ H_2O}\right)$$

Equation to calculate ϕ for lipid with DBA (mixture of 1 and 4 e^- processes):

$$\phi = \frac{2x\ mol\ O_2^-}{mol\ CuBTT}\left(\frac{mol\ CuBTT}{mol\ O_2}\ \frac{mol\ e^-}{mol\ O_2^-}\right) + \left(\frac{(1-2x)\ mol\ H_2O}{mol\ CuBTT}\right)\left(\frac{mol\ CuBTT}{mol\ O_2}\ \frac{4\ mol\ e^-}{mol\ H_2O}\right)$$

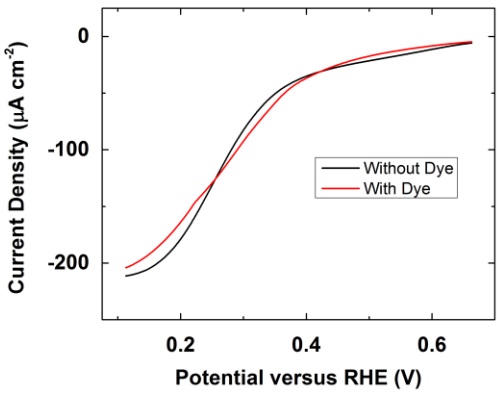

Figure 8.9. O_2 reduction LSVs of CuBTT covered by DMPC with 10 mol% DBA in the lipid layer with and without Amplex red/HRP solution at pH 7.

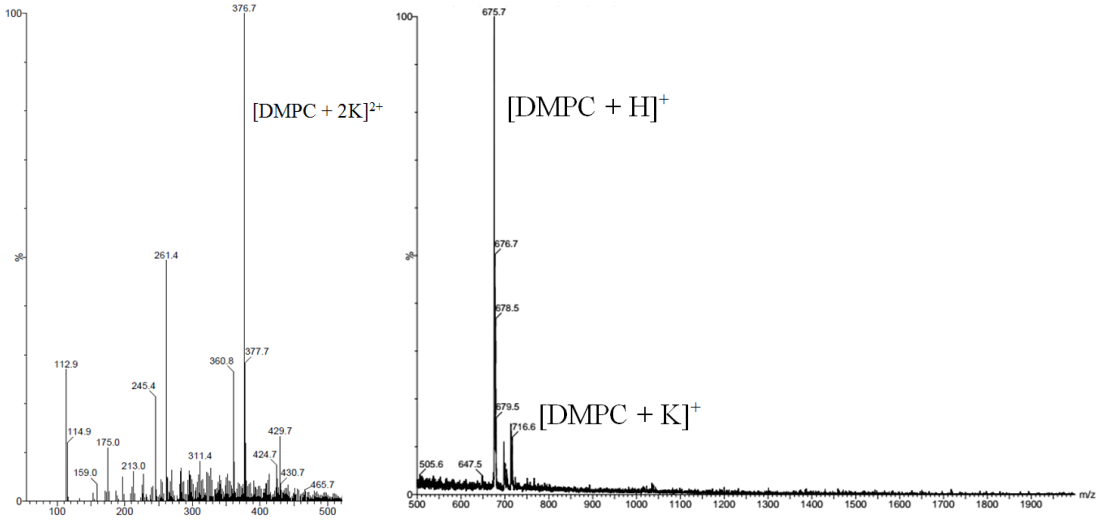

Figure 8.10. ESI-MS of extracted lipid surface after O_2 reduction by CuBTT covered by DMPC.

We conducted the following controls to verify that DBA and DMPC do not interfere with the spectroelectrochemical assay of H_2O_2. Upon combining DBA/DMPC solution with an equal amount of Amplex Red working solution, no peak at 571 nm was detected in the UV-Vis spectrum. The addition of KO_2 or H_2O_2 both resulted in a peak at 571 nm in the UV-Vis spectra, demonstrating that neither DBA nor DMPC interfere with the H_2O_2 assay. Figure 8.9 displays LSVs of O_2 reduction by a SAM of CuBTT covered by DMPC with 10 mol% DBA with and

without the H_2O_2 detection solution. The voltammetries are very similar, indicating that Amplex Red and HRP do not interfere with the O_2 reduction process by CuBTT. Furthermore, no Amplex Red, resorufin, or HRP is detected by ESI-MS in the solution obtained after extracting surfaces containing HBMs with EtOH and $CHCl_3$ (Figure 8.10). This control experiment indicates that Amplex Red, resorufin, and HRP do not readily incorporate into the lipid layer and that these species remain in bulk solution. Taken together, the results obtained from Figures 8.9 and 8.10 demonstrate that Amplex Red, resorufin, and/or HRP do not interfere with the ORR activity of CuBTT inside a HBM.

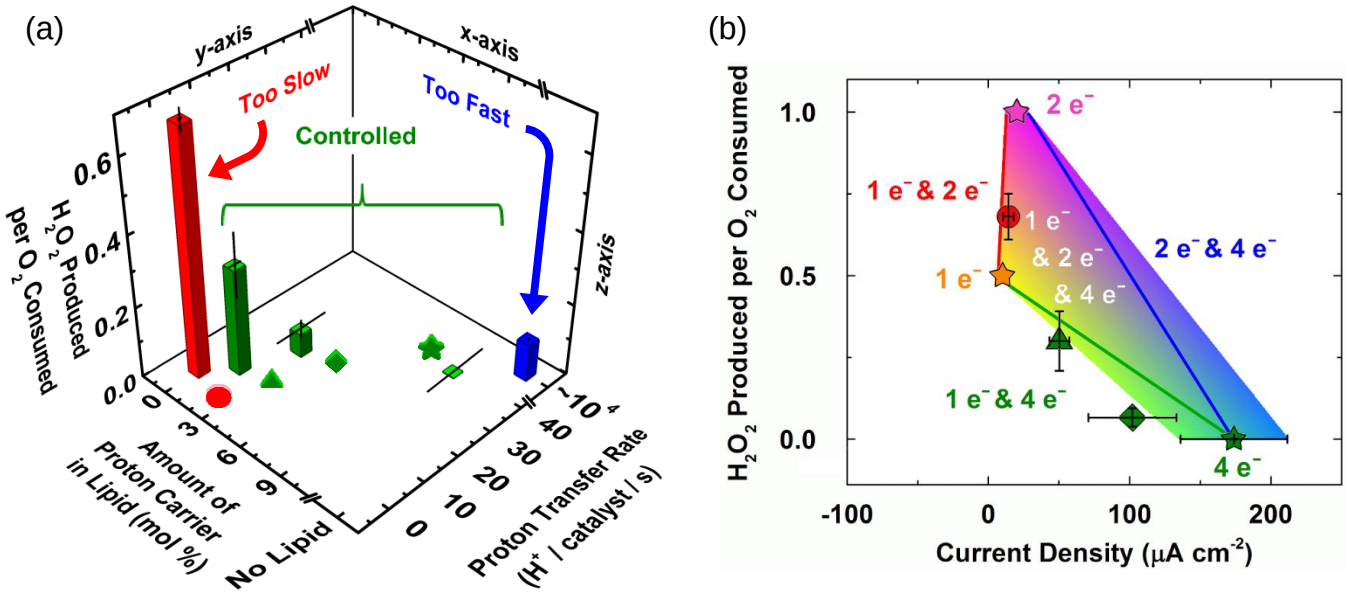

Figure 8.11. Control of proton transfer kinetics alters the pathways and product speciation of O_2 reduction. (A) The amount of H_2O_2 detected by dye-based spectroelectrochemistry during the O_2 reduction process by CuBTT at pH 7 (z-axis) versus the rate of proton transfer to CuBTT (y-axis) versus the amount of DBA proton carrier in the lipid layer of the HBM (x-axis). (B) Result of analysis showing a plot of moles of H_2O_2 detected per mole of O_2 consumed by CuBTT versus catalytic O_2 reduction current density by CuBTT in a HBM at pH 7 at 0.11 V versus RHE with various mol% of DBA (circle = 0%, triangle = 1.4%, diamond = 2.7%, green star = 10%). This analysis originates from data and calculations presented in Figure 8.3 and the mathematical modeling analysis in Section 8.3.3.

In Figure 8.11a, the z-axis shows the quantity of H_2O_2 detected spectroelectrochemically during the O_2 reduction process at pH 7. In the absence of a lipid layer, CuBTT produces 0.11 moles of H_2O_2 per mole of O_2 consumed (Figure 8.11a, blue bar). This result matches rotating ring-disk electrode experiments[18] and suggests that the four e^- reduction of O_2 to H_2O by the catalyst is the dominant process. Upon appending a monolayer of lipid without DBA on the CuBTT catalyst, the amount of H_2O_2 increases substantially to 0.68 moles of H_2O_2 per mole of O_2 consumed by CuBTT (Figure 8.11a, red bar), indicating a change in the pathway of O_2 reduction. In the xz-plane of Figure 8.11a, the red and green bars show that as the amount of DBA inside the lipid layer of the HBM increases from 0 to 10 mol%, the amount of H_2O_2 detected during O_2 reduction correspondingly decreases. Importantly, with 10 mol% DBA in the lipid layer of the HBM (green star), *no* H_2O_2 is detected: at this concentration of DBA, the four e^- reduction process of O_2 to H_2O occurs exclusively.

8.3.4 Studies in Deuterated Buffer Solutions

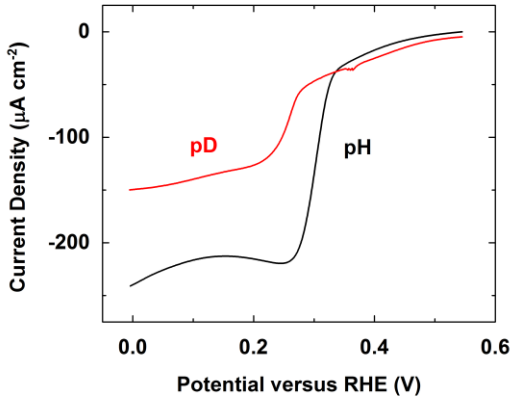

Figure 8.12. O_2 reduction LSVs of a SAM of CuBTT in O_2-saturated pH 5 (black) and pD 5 (red) phosphate buffer at a scan rate of 10 mV s^{-1}.

To interrogate the mechanism of O_2 reduction by CuBTT, we compare the voltammetry in proteo and deutero solutions. In the absence of a lipid layer, the O_2 reduction current by CuBTT in a pD 5 solution decreases by ~40% as compared to pH 5 (Figure 8.12). This kinetic

isotope effect (KIE) suggests that the rate-determining step (RDS) of O_2 reduction by CuBTT is likely the O-O bond breaking step which involves protons or deuterons.

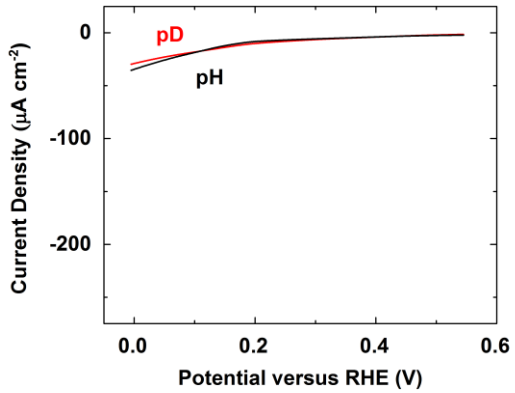

Figure 8.13. O_2 reduction LSVs of a SAM of CuBTT covered by a monolayer of DMPC in O_2-saturated pH 5 (black) and pD 5 (red) phosphate buffer at a scan rate of 10 mV s^{-1}.

In the presence of a DMPC monolayer, no KIE is observed suggesting that the RDS is electron transfer, and access of protons and deuterons to CuBTT is significantly hindered (Figure 8.13). This finding suggests that O_2 is predominantly reduced by 1 e^- to O_2^- by CuBTT in lipid without DBA. This interpretation is consistent with other studies that determine that a lack of a kinetic isotope effect coincides with O_2^- production from O_2 reduction.[34,35] Additionally, protons do not diffuse readily through lipid membranes,[36] and in a variety of aprotic solvents, where protons are unavailable, O_2 reduction produces O_2^-.[37,38]

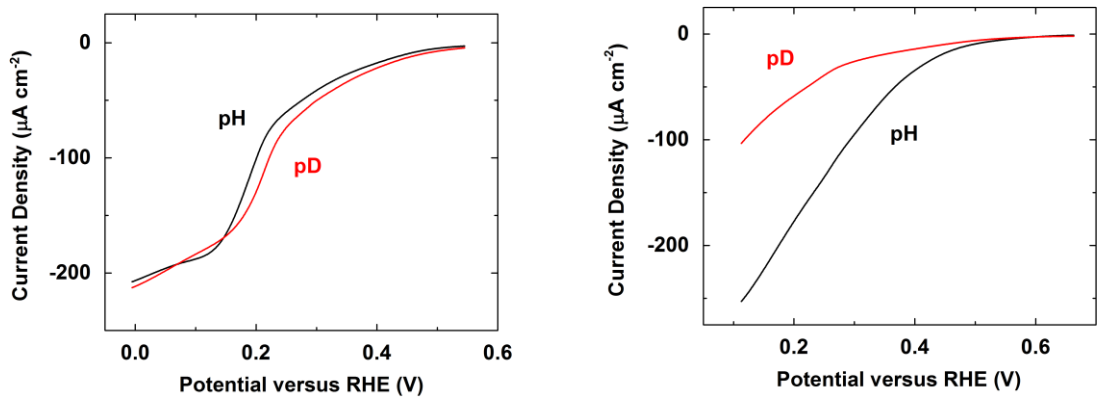

Figure 8.14. (a) O_2 reduction LSVs of a SAM of CuBTT covered by a monolayer of DMPC with 10 mol% DBA in O_2-saturated (a) pH 5 (black) and pD 5 (red) and (b) pH 7 (black) and pD 7 (red) phosphate buffer solutions at a scan rate of 10 mV s^{-1}.

We did not observe a significant KIE for O_2 reduction by CuBTT with DBA incorporated in the lipid layer at pH and pD 5 (Figure 8.14a). The lack of KIE with DBA inside the lipid layer suggests that the RDS in the presence of a proton carrier is a step slower than the O-O bond breaking event. Furthermore, according to rate law analysis, the absence of a KIE indicates that neither the RDS nor any steps prior to the RDS involve protons or deuterons. The only step in the ORR mechanism inside a HBM that fit these criteria is the flip-flop diffusion of DBA across the lipid layer. Slow electron transfer is ruled out as the RDS since a KIE is observed in pH and pD 7 solutions (Figure 8.14b).

In contrast to pH and pD 5, we observe a KIE at pH and pD 7 for O_2 reduction by CuBTT inside a HBM incorporated with DBA (Figure 8.15). Under these more basic conditions, DBA is in equilibrium with its conjugate base and so the requirement for the carrier to be protonated before undergoing flip-flop diffusion is embodied in the rate equation for O_2 reduction, thus resulting in the KIE observed. In other words, at pH or pD 7 (but not at pH or pD 5), a proton or deuteron must add to DBA before it can undergo flip-flop diffusion. This requirement results in the kinetic isotope effect observed at pH and pD 7.

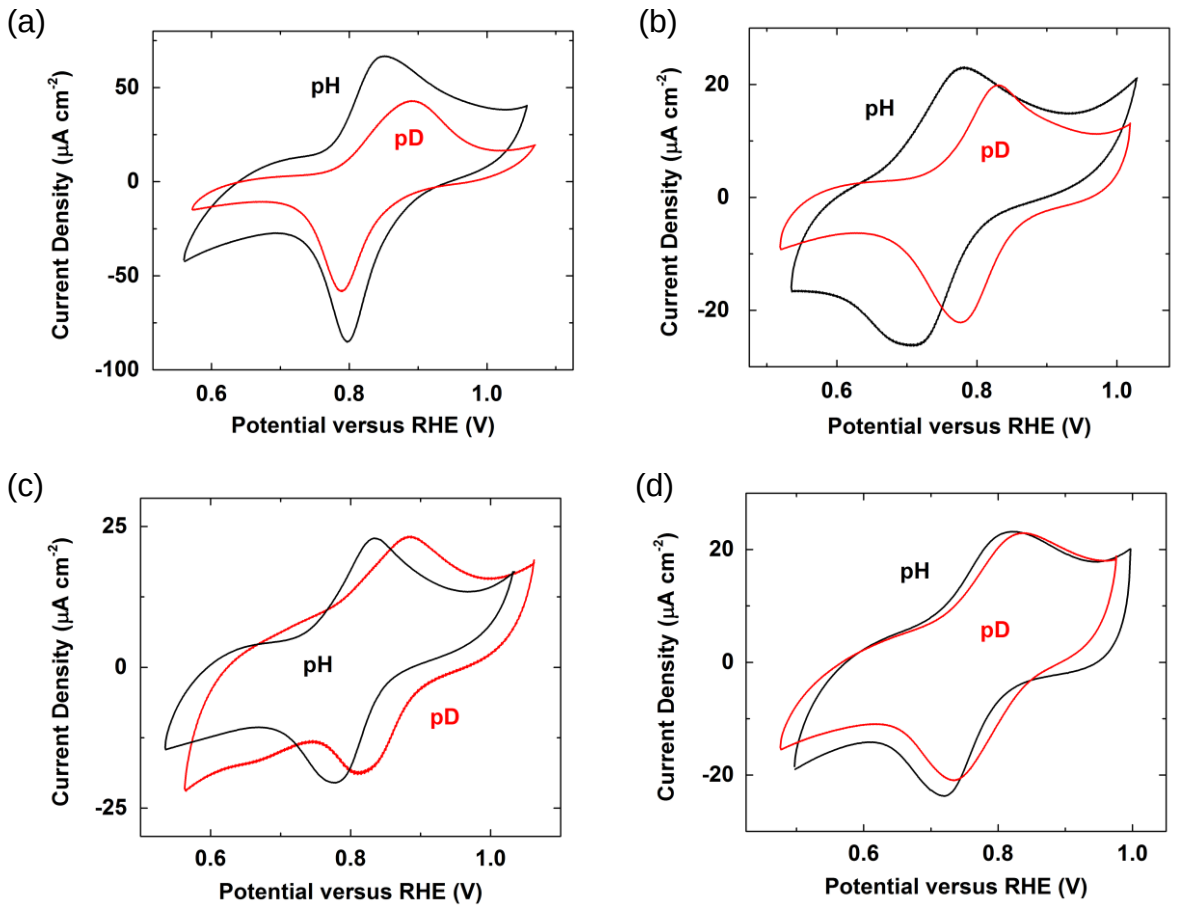

Figure 8.15. CVs of (a) a SAM of CuBTT (b) covered by a monolayer of DMPC in Ar-saturated pH 5 (black) and pD 5 (red) phosphate buffer at a scan rate of 100 mV s^{-1}. CVs of a SAM of CuBTT covered by a monolayer of DMPC with 10 mol% DBA in Ar-saturated (c) pH 5 (black) and pD 5 (red) and (d) pH 7 (black) and pD 7 (red) phosphate buffer at a scan rate of 100 mV s^{-1}.

Figures 8.15a-d show the cyclic voltammograms of a SAM of CuBTT with or without lipid in Ar-saturated pH/pD 5 and pH/pD 7 solutions. Previously, we determined that in the absence of lipid, the voltammetry observed is due to a combination of the Cu(I/II) couple and the 1 e^- redox wave associated with the triazole ring of BTT.[21] We also showed that inside lipid, the BTT wave becomes silent and only the Cu(I/II) couple is present. These results explain why the current densities measured for the cases inside lipid (Figures 8.15b-d) are about half of the current density observed for the system without lipid (Figure 8.15a). The voltammograms also

show that in all cases, the current densities obtained in deutero solutions are less than those in proteo solutions although to varying extents. This observation is likely due to the increased energy level of the transition state of the deuterated species as proposed by Weaver and coworkers.[39]

The redox waves in deutero solutions shift positive compare to those in proteo solution in all cases. These shifts are due to the more favorable change in entropy that occurs upon reducing Cu(II) to Cu(I) in deutero solutions. Cu(II) has a tighter solvation shell than Cu(I), and D_2O forms a stronger deuterium bonding network than the hydrogen bonding network of H_2O. Therefore, there is a greater increase in entropy when the deuterated solvent structure relaxes upon formation of Cu(I), resulting in a positive shift of the redox wave. Similar trends have been observed for a variety of cationic transition metal complexes.[40] We note that the magnitudes of the isotope effects are less for the cases inside lipid, likely due to a lack of an extended water network and solvation shell inside lipid. We also note that these shifts in potential are not due to reference electrode effects, as confirmed by experiments with $K_3Fe(CN)_6$ which demonstrated identical potentials for the Fe(II/III) wave in proteo and deutero solutions as expected.[41]

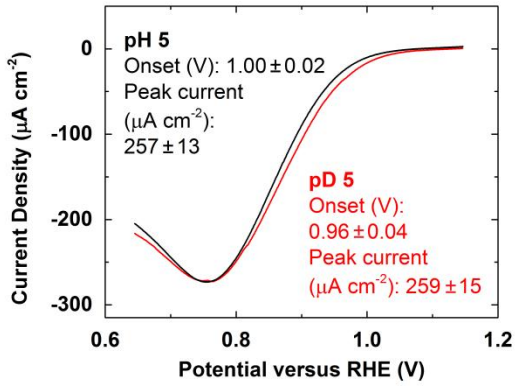

Figure 8.16. O_2 reduction LSVs of Pt in O_2-saturated pH 5 (black) and pD 5 (red) phosphate buffer at a scan rate of 10 mV s^{-1}.

To confirm that Pt does not exhibit a kinetic isotope effect under our experimental conditions, we measured the O_2 reduction activity by Pt in pH and pD 5 solutions (Figure 8.16). For the case of O_2 reduction on Pt, the kinetically-controlled RDS is electron transfer even though the overall reaction contains a thermodynamically-controlled pH-dependent component. The clearest evidence for this fact is the lack of a kinetic isotope effect for O_2 reduction on Pt. Previous studies have shown that Pt catalyzes the O_2 reduction reaction in electrolytes containing H_2O and D_2O with the same activity (Figure 8.16).[42] This finding necessitates that protons cannot be involved at or before the rate-determining step.

We observed an isotope effect in the absence of lipid, therefore we conclude that proton-mediated O-O bond breaking is the rate-determining step (RDS) in this case as has been proposed for many other O_2 reduction catalysts.[1] In contrast, the lack of an isotope effect in the presence of DMPC only corroborates our findings that the catalyst predominantly reduces O_2 by 1 e^- to O_2^- in the absence of proton carrier, a process that does not involve protons. Furthermore, we also do not observe an isotope effect for the case with 10 mol% DBA incorporated in the lipid layer. This result indicates that the RDS of O_2 reduction by CuBTT in a HBM is the delivery of protons across the lipid membrane via flip-flop diffusion, a step that does not involve protonation or deprotonation.

8.3.5 Analysis of O_2 Reduction Pathways in HBMs

The unique ability of the HBM system to modulate the kinetics of proton transport affords the first example of an O_2 reduction catalyst that switches between one, two, and four e^- reduction pathways with H_2O as the bulk solvent. We developed a model described below to analyze this data. Figure 8.11b, derived from this analysis and experiment, shows a plot of the quantity of H_2O_2 detected from CuBTT as a function of catalytic current density. Each star

represents a purely one, two, or four e^- pathway, each line represents a mixture of two pathways, and the shaded region represents cases in which all three pathways occur simultaneously. The circle, triangle, diamond, and green star correspond to the HBMs with 0, 1.4, 2.7, and 10 mol% DBA in the lipid layer, respectively. Because the data for the HBMs with DBA lie on the calculated line for a mixture of one e^- and four e^- processes within error, we conclude that the two e^- process does not occur in the presence of DBA.

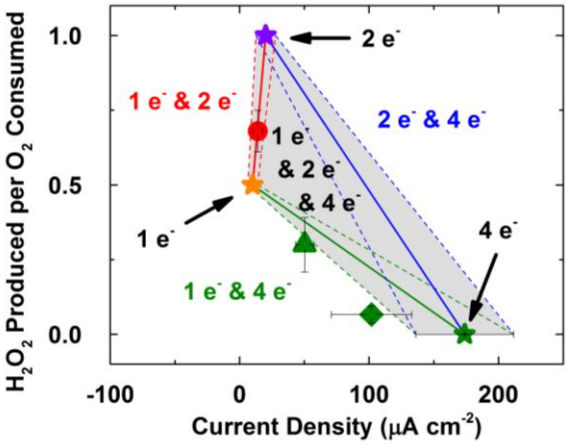

Figure 8.17. Plot of moles of H_2O_2 detected per mole of O_2 consumed by CuBTT versus catalytic O_2 reduction current density by CuBTT in a HBM at pH 7 with various mol% of DBA (circle = 0%, triangle = 1.4%, diamond = 2.7%, green star = 10%). Solid lines with dashed error bounds represent calculated regimes in which only two of the three proposed pathways occur.

Figure 8.17 shows a version with more details of the plot in Figure 8.11b. The y-axis on the plot in Figure 8.17 comes from the data described in Section 8.3.3. The x-axis is the catalytic current density for O_2 reduction recorded at 0.11 V versus RHE. Each vertex of the triangle represents a purely 1 e^-, 2 e^-, or 4 e^- pathway. The purely 4 e^- pathway point (green star) is taken from the data obtained for CuBTT with 10 mol% DBA in the DMPC layer since this system is found by dye-based spectroelectrochemistry to be a purely 4 e^- process. Although the presence of 10 mol% DBA in the lipid layer improves the selectivity of the catalyst compared to when

CuBTT is exposed directly to bulk solution, the maximum current density produced by CuBTT inside lipid with DBA is ~30% lower than the case without lipid. Compared to the lipid-only system, however, both the selectivity and the O_2 reduction current density increase upon the addition of the proton carrier. These findings demonstrate the interplay between catalyst activity and selectivity.

The purely 1 e^- (orange star) and purely 2 e^- (purple star) pathway points are calculated from the data obtained for CuBTT with DMPC without DBA (red circle). In this case, the catalyst reduces O_2 by predominantly 1 e^- as is evidenced by the large amount of H_2O_2 detected spectroelectrochemically and the lack of a KIE for O_2 reduction observed. If all of the CuBTT reduced O_2 by a 1 e^- process to form O_2^-, then due to the disproportionation of O_2^- to O_2 and H_2O_2, 0.5 moles of H_2O_2 per mole of O_2 consumed by CuBTT would be produced. Since we detected 0.68 moles of H_2O_2 per mole of O_2 consumed by CuBTT, the additional 0.18 moles of H_2O_2 indicate that the 2 e^- reduction of O_2 also occurs. This finding suggests that the DMPC lipid layer is not entirely impermeable to protons under the conditions of these experiments. We then proceed to calculate the expected current densities and coverages for the purely 1 e^- and purely 2 e^- processes from the HBM without DBA using the system of equations formulated below:

I. Known Quantities

Let n be the total number of CuBTT catalysts on the surface. By integrating the charge of the Cu(I)/Cu(II) couple under an Ar atmosphere, we determine that

$$n = 2.83 \times 10^{13} \text{ molecules CuBTT}$$

Let i be the total number of electrons passed per second in the case of DMPC without DBA. From the current at 0.11 V versus RHE, we determine that

$$i = 9.03 \times 10^{13} \frac{\mathrm{e}^-}{\mathrm{s}}$$

Let i_4^* be the number of electrons passed per second in the case of DMPC with 10% DBA. In this case, no H_2O_2 is produced, so only the 4 e^- process occurs. From the current at 0.11 V versus RHE, we determine that

$$i_4^* = 1.08 \times 10^{15} \frac{\mathrm{e}^-}{\mathrm{s}}$$

Let M be the number of H_2O_2 molecules produced per second in the case of DMPC without DBA as determined by dye-based spectroelectrochemistry.

$$M = 3.07 \times 10^{13} \frac{\text{molecules } \mathrm{H_2O_2}}{\mathrm{s}}$$

II. Fundamental Equations

Let n_1, n_2, and n_4 be the total number of CuBTT catalysts on the surface that reduce O_2 by 1 e^-, 2 e^-, and 4 e^-, respectively, in the case of DMPC without DBA. Therefore,

$$n = n_1 + n_2 + n_4$$

Let k_1, k_2, and k_4 be the pseudo-first-order rate constants of the 1 e^-, 2 e^-, and 4 e^- O_2 reduction reactions, respectively, in units of s^{-1} in the HBM.

k, the overall weighted average rate constant is therefore:

$$k = \frac{k_1 n_1 + k_2 n_2 + k_4 n_4}{n}$$

Let e_1, e_2, and e_4 be the number of electrons transferred in the 1 e^-, 2 e^-, and 4 e^- O_2 reduction reactions, respectively.

$$e_1 = 1\frac{e^-}{CuBTT}$$
$$e_2 = 2\frac{e^-}{CuBTT}$$
$$e_4 = 4\frac{e^-}{CuBTT}$$

e, the overall weighted average number of electrons transferred is therefore:

$$e = \frac{e_1 n_1 + e_2 n_2 + e_4 n_4}{n}$$

The total number of electrons passed per second, i, is equal to the sum of the number of electrons passed per second from 1 e^- (i_1) 2 e^- (i_2), and 4 e^- (i_4) processes.

$$i = i_1 + i_2 + i_4$$

The number of electrons passed due to the individual pathways is:

$$i_1 = n_1 k_1 e_1$$
$$i_2 = n_2 k_2 e_2$$
$$i_4 = n_4 k_4 e_4$$

In the case of DMPC with 10% DBA where only the 4 e^- process occurs:

$$i_4^* = n_4^* k_4 e_4$$
where $n_4^* = n$

Let m_1 and m_2 be the number of H_2O_2 molecules generated per CuBTT for the 1 e^- and 2 e^- O_2 reduction pathways, respectively. For the case of the 1 e^- pathway, 2 O_2^- molecules from 2 CuBTT catalysts generate 1 H_2O_2 molecule, giving:

$$m_1 = 0.5\frac{H_2O_2}{CuBTT}$$

For the case of the 2 e^- pathway, 1 H_2O_2 is generated directly from 1 CuBTT catalyst, giving:

$$m_2 = 1\frac{H_2O_2}{CuBTT}$$

The total amount of H_2O_2 generated per second in the case of DMPC without DBA is a summation of the amount coming from both 1 e^- and 2 e^- process because the 4 e^- process generates only H_2O without any H_2O_2.

$M = n_1k_1m_1 + n_2k_2m_2$

Summary of equations to solve for n_1, n_2 , k_1, k_2, k, and e:

$nk = n_1k_1 + n_2k_2 + n_4k_4$ (1)

$M = m_1n_1k_1 + m_2n_2k_2$ (2)

$i = e_1n_1k_1 + e_2n_2k_2 + e_4n_4k_4$ (3)

$en = e_1n_1 + e_2n_2 + e_4n_4$ (4)

$n = n_1 + n_2 + n_4$ (5)

III. Solving for Unknowns

Solve Equations 1, 2, and 3 for n_1k_1, n_2k_2, and n_4k_4 in terms of *n, k, M,* and *i.*

Rearranging (1) and (2) yields:

$n_2k_2 = nk - n_1k_1 - n_4k_4$ (6)

$n_2k_2 = \frac{M - m_1n_1k_1}{m_2}$ (7)

Combine (6) and (7) by equating both sides:

$$nk - n_1k_1 - n_4k_4 = \frac{M - m_1n_1k_1}{m_2}$$

Solve for n_1k_1:

$$\left(\frac{m_1}{m_2} - 1\right)n_1k_1 = \frac{M}{m_2} + n_4k_4 - nk$$

$$n_1k_1 = \frac{\frac{M}{m_2}+n_4k_4-nk}{\frac{m_1}{m_2}-1} = \frac{M+m_2n_4k_4-m_2nk}{m_1-m_2} \qquad (8)$$

Rearranging (3) yields:

$$n_2k_2 = \frac{i-e_1n_1k_1-e_4n_4k_4}{e_2} \qquad (9)$$

Combine (6) and (9) by equating both sides:

$$nk - n_1k_1 - n_4k_4 = \frac{i - e_1n_1k_1 - e_4n_4k_4}{e_2}$$

$$\frac{e_1n_1k_1}{e_2} - n_1k_1 = \frac{i - e_4n_4k_4}{e_2} - nk + n_4k_4$$

$$\left(\frac{e_1}{e_2} - 1\right)n_1k_1 = \frac{i - e_4n_4k_4}{e_2} - nk + n_4k_4$$

Solve for n_1k_1:

$$n_1k_1 = \frac{\frac{i-e_4n_4k_4}{e_2}-nk+n_4k_4}{\frac{e_1}{e_2}-1} = \frac{i-e_4n_4k_4-e_2nk+e_2n_4k_4}{e_1-e_2} \qquad (10)$$

Combine (8) and (10) by equating both sides:

$$\frac{i-e_4n_4k_4-e_2nk+e_2n_4k_4}{e_1-e_2} = \frac{M+m_2n_4k_4-m_2nk}{m_1-m_2}$$

Solve for n_4k_4:

$$(m_1 - m_2)(i - e_4n_4k_4 - e_2nk + e_2n_4k_4) = (e_1 - e_2)(M + m_2n_4k_4 - m_2nk)$$

$$(m_1 - m_2)i - (\boldsymbol{m_1 - m_2})\boldsymbol{e_4n_4k_4} - (m_1 - m_2)e_2nk + (\boldsymbol{m_1 - m_2})\boldsymbol{e_2n_4k_4} = (e_1 - e_2)M + (\boldsymbol{e_1 - e_2})\boldsymbol{m_2n_4k_4} - (e_1 - e_2)m_2nk$$

$$(\boldsymbol{m_1 - m_2})\boldsymbol{e_2n_4k_4} - (\boldsymbol{m_1 - m_2})\boldsymbol{e_4n_4k_4} - (\boldsymbol{e_1 - e_2})\boldsymbol{m_2n_4k_4} = (e_1 - e_2)M - (e_1 - e_2)m_2nk - (m_1 - m_2)i + (m_1 - m_2)e_2nk$$

$$[(\boldsymbol{m_1}-\boldsymbol{m_2})\boldsymbol{e_2}-(\boldsymbol{m_1}-\boldsymbol{m_2})\boldsymbol{e_4}-(\boldsymbol{e_1}-\boldsymbol{e_2})\boldsymbol{m_2}]n_4k_4 = (e_1-e_2)M-(e_1-e_2)m_2nk-(m_1-m_2)i+(m_1-m_2)e_2nk$$

$$\boldsymbol{n_4k_4}=\frac{(\boldsymbol{e_1}-\boldsymbol{e_2})\boldsymbol{M}-(\boldsymbol{e_1}-\boldsymbol{e_2})\boldsymbol{m_2nk}-(\boldsymbol{m_1}-\boldsymbol{m_2})\boldsymbol{i}+(\boldsymbol{m_1}-\boldsymbol{m_2})\boldsymbol{e_2nk}}{[(\boldsymbol{m_1}-\boldsymbol{m_2})\boldsymbol{e_2}-(\boldsymbol{m_1}-\boldsymbol{m_2})\boldsymbol{e_4}-(\boldsymbol{e_1}-\boldsymbol{e_2})\boldsymbol{m_2}]}$$

Simplify n_4k_4:

$$\boldsymbol{n_4k_4}=\frac{\boldsymbol{i}}{\boldsymbol{4}}-\frac{\boldsymbol{M}}{\boldsymbol{2}}$$

Use (8) and the solution of n_4k_4 to determine n_1k_1:

$$n_1k_1=\frac{M+m_2n_4k_4-m_2nk}{m_1-m_2}=\frac{M-m_2nk}{m_1-m_2}+\frac{m_2}{m_1-m_2}(n_4k_4)$$

$$n_1k_1=\frac{M-m_2nk}{m_1-m_2}+\frac{m_2}{m_1-m_2}\left(\frac{(e_1-e_2)M-(e_1-e_2)m_2nk-(m_1-m_2)i+(m_1-m_2)e_2nk}{[(m_1-m_2)e_2-(m_1-m_2)e_4-(e_1-e_2)m_2]}\right)$$

$$n_1k_1=\frac{M-m_2nk}{m_1-m_2}+m_2\left(\frac{\frac{(e_1-e_2)}{(m_1-m_2)}M-\frac{(e_1-e_2)}{(m_1-m_2)}m_2nk-i+e_2nk}{[(m_1-m_2)e_2-(m_1-m_2)e_4-(e_1-e_2)m_2]}\right)$$

Simplify n_1k_1:

$$n_1k_1=\frac{M-nk}{-0.5}+(-2)\left(\frac{i}{4}-\frac{M}{2}\right)$$

$$n_1k_1=-2M+2nk-\frac{i}{2}+M$$

$$\boldsymbol{n_1k_1}=\boldsymbol{2nk}-\frac{\boldsymbol{i}}{\boldsymbol{2}}-\boldsymbol{M}$$

Rearranging (1) and (2) yields:

$$n_1k_1=nk-n_2k_2-n_4k_4 \qquad (11)$$

$$n_1k_1=\frac{M-m_2n_2k_2}{m_1} \qquad (12)$$

Combining (11) and (12) yields:

$$nk - n_2k_2 - n_4k_4 = \frac{M - m_2n_2k_2}{m_1}$$

$$\frac{m_2n_2k_2}{m_1} - n_2k_2 = \frac{M}{m_1} - nk + n_4k_4$$

Solve for n_2k_2:

$$n_2k_2 = \frac{\frac{M}{m_1} - nk + n_4k_4}{\frac{m_2}{m_1} - 1} = \frac{M - m_1nk + m_1n_4k_4}{m_2 - m_1} = \frac{M - m_1nk}{m_2 - m_1} + \frac{m_1}{m_2 - m_1}(n_4k_4)$$

$$n_2k_2 = \frac{M - m_1nk}{m_2 - m_1} + \frac{m_1}{m_2 - m_1}\left(\frac{(e_1 - e_2)M - (e_1 - e_2)m_2nk - (m_1 - m_2)i + (m_1 - m_2)e_2nk}{[(m_1 - m_2)e_2 - (m_1 - m_2)e_4 - (e_1 - e_2)m_2]}\right)$$

Simplify n_2k_2:

$$n_2k_2 = \frac{M - 0.5nk}{0.5} + 1\left(\frac{i}{4} - \frac{M}{2}\right)$$

$$n_2k_2 = 2M - nk + \frac{i}{4} - \frac{M}{2}$$

$$\boldsymbol{n_2k_2 = \frac{3}{2}M + \frac{i}{4} - nk}$$

Summary:

$$\boldsymbol{n_1k_1 = 2nk - \frac{i}{2} - M}$$

$$\boldsymbol{n_2k_2 = \frac{3}{2}M + \frac{i}{4} - nk}$$

$$\boldsymbol{n_4k_4 = \frac{i}{4} - \frac{M}{2}}$$

Now use equations (4) and (5) to solve for n_1 and n_2 in terms of e, n, and n_4.

Solve for n_1 by rearranging (4) and (5):

$$en = e_1n_1 + e_2n_2 + e_4n_4 \quad (4)$$

$$n_2 = \frac{en - e_1n_1 - e_4n_4}{e_2} \quad (13)$$

$$n = n_1 + n_2 + n_4 \quad (5)$$

$$n_2 = n - n_1 - n_4 \quad (14)$$

Combining (13) and (14) yields:

$$\frac{en - e_1n_1 - e_4n_4}{e_2} = n - n_1 - n_4$$

$$\frac{en - e_4n_4}{e_2} - n + n_4 = \frac{e_1n_1}{e_2} - n_1$$

$$\frac{en - e_4n_4}{e_2} - n + n_4 = \left(\frac{e_1}{e_2} - 1\right)n_1$$

$$n_1 = \frac{\frac{en - e_4n_4}{e_2} - n + n_4}{\frac{e_1}{e_2} - 1} = \frac{en - e_4n_4 - e_2n + e_2n_4}{e_1 - e_2}$$

$$n_1 = \frac{en - e_4n_4 - e_2n + e_2n_4}{e_1 - e_2}$$

Simplify n_1:

$$n_1 = \frac{en - 4n_4 - 2n + 2n_4}{-1} = 2n_4 + 2n - en$$

$$\boldsymbol{n_1 = 2n_4 + 2n - en}$$

Solve for n_2 by rearranging (4) and (5):

$$en = e_1n_1 + e_2n_2 + e_4n_4 \quad (4)$$

$$n_1 = \frac{en - e_2n_2 - e_4n_4}{e_1} \quad (15)$$

$$n = n_1 + n_2 + n_4 \qquad (5)$$

$$n_1 = n - n_2 - n_4 \qquad (16)$$

Combining (15) and (16) yields:

$$\frac{en - e_2 n_2 - e_4 n_4}{e_1} = n - n_2 - n_4$$

$$\frac{en - e_4 n_4}{e_1} - n + n_4 = \frac{e_2 n_2}{e_1} - n_2$$

$$\frac{en - e_4 n_4}{e_1} - n + n_4 = \left(\frac{e_2}{e_1} - 1\right) n_2$$

$$n_2 = \frac{\frac{en - e_4 n_4}{e_1} - n + n_4}{\frac{e_2}{e_1} - 1} = \frac{en - e_4 n_4 \ - e_1 n + e_1 n_4}{e_2 - e_1}$$

$$n_2 = \frac{en - e_4 n_4 \ - e_1 n + e_1 n_4}{e_2 - e_1}$$

Simplify n_2:

$$n_2 = \frac{en - 4n_4 \ - n + n_4}{1} = en - 3n_4 - n$$

$$\boldsymbol{n_2 = en - 3n_4 - n}$$

Combine the above results to yield:

$$\boldsymbol{f(k, n_1) = k_1 = \frac{2nk - \frac{i}{2} - M}{n_1}}$$

$$\boldsymbol{g(k, n_2) = k_2 = \frac{\frac{3}{2}M + \frac{i}{4} - nk}{n_2}}$$

$$\boldsymbol{w(e) = n_1 = 2n_4 + 2n - en}$$

$$\boldsymbol{v(e) = n_2 = en - 3n_4 - n}$$

$$\boldsymbol{n_4 k_4 = \frac{i}{4} - \frac{M}{2}}$$

k_4 is known from:
$i_4^* = n_4^* k_4 e_4$

Since k_4, M, i are known then n_4 is also known.

Combine *f* and *w*:

$$\boldsymbol{f(k, e) = k_1 = \frac{2nk - \frac{i}{2} - M}{2n_4 + 2n - en}}$$

Combine *g* and *v*:

$$\boldsymbol{g(k, e) = k_2 = \frac{\frac{3}{2}M + \frac{i}{4} - nk}{en - 3n_4 - n}}$$

Now both $\boldsymbol{f}$ and $\boldsymbol{g}$ are in terms of $\boldsymbol{k}$ and $\boldsymbol{e}$. The resulting equations are solved numerically with different combinations of $\boldsymbol{k}$ and $\boldsymbol{e}$. The values of $\boldsymbol{k}$ and $\boldsymbol{e}$ that fit the system of equations will then determine $\boldsymbol{k_1}$ and $\boldsymbol{k_2}$ and from there $\boldsymbol{n_1}$ and $\boldsymbol{n_2}$ using the following constraints:
$0 \leq i_1, i_2, i_4 \leq i$
$0 \leq k_1, k_2$
$0 \leq n_1, n_2, n_4 \leq n$

The values of k_1 and k_2 cannot be determined exactly from the equations above, but must range from ~0.5 to ~5 given the constraints above and the values we determine experimentally for i and M. For all plots shown, we assume that k_1 and k_2 are equal and maximize n_1 within the bounds of the equations above, since isotope studies described in Section 8.3.4 suggest that mostly the 1 e^- reduction of O_2 occurs inside lipid without DBA. Since the range of valid values for k_1 and k_2 are narrow, regardless of what values we choose, the data for the HBM with 1.4% and 2.7% DBA (Figure 8.11b in main text) lie on the line for a mixture of 1 e^- and 4 e^- reduction processes within error.

From the equations described above, we calculate that inside lipid without DBA, ~95% of the CuBTT sites reduce O_2 by 1 e^-, ~2% of the CuBTT sites reduce O_2 by 2 e^-, and ~3% of the CuBTT sites reduce O_2 by 4 e^-. By combining these coverage values with the calculated rate constants for each of the three reduction pathways, the total number of electrons transferred per molecule of O_2 inside lipid without DBA is found to be 1.98 ± 0.10 (ϕ).

These results demonstrate that inside lipid without DBA, predominantly a 1 e^- process occurs, a consequence of limited proton availability inside the lipid. Since the 2 e^- and 4 e^- processes also occur although to a small extent, the lipid is not completely impermeable to protons. The leakage rate of protons through lipid is slow, however, and hence these processes, which require a high local concentration of protons, are statistically unlikely.

With the rate constants determined above, the current densities expected for the purely 1 e^- and purely 2 e^- processes are calculated. These values give the positions of the orange and purple stars presented in Figure 8.17, respectively. The current density of the 4 e^- process is known directly from the voltammetry obtained from O_2 reduction by CuBTT covered by a

DMPC monolayer with 10 mol% DBA. These three vertices map out the triangle of space in Figure 8.17 that describes all possible combinations of 1, 2, and 4 e^- pathways.

We plot the amount of H_2O_2 produced and the current densities of the HBMs containing 1.4 and 2.7 mol% DBA in Figure 8.17. Since the data obtained from these systems lie on the side of the triangle that describe a mixture of 1 and 4 e^- pathways, we conclude that DBA suppresses the 2 e^- pathway. This finding means that CuBTT sites near proton carriers undergo the 4 e^- O_2 reduction process, while those that do not have access to proton carriers undergo the 1 e^- O_2 reduction process. As the concentration of DBA increases inside the DMPC layer, the percentage of the 4 e^- process increases accordingly until all CuBTT sites have access to proton carriers.

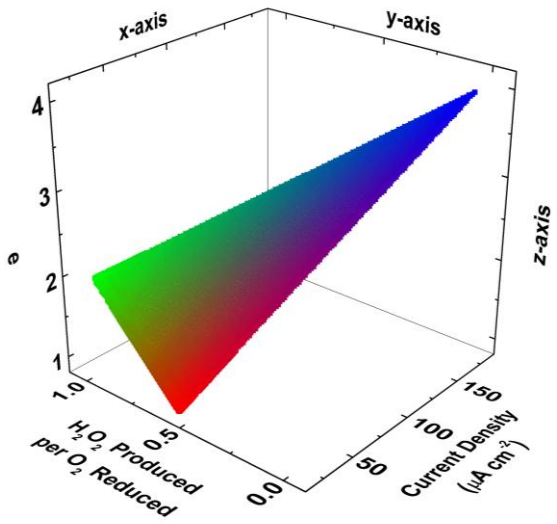

Figure 8.18. A six-dimensional plot showing theoretical current densities for O_2 reduction by CuBTT inside a HBM (x-axis) versus the expected amount of H_2O_2 produced per O_2 reduced (y-axis) versus calculated e values (z-axis) versus calculated n_1, n_2, and n_4 values (red, green, and blue, respectively).

Figure 8.18 shows a six-dimensional plot of the calculated current densities versus H_2O_2 produced per O_2 reduced versus the number electrons per O_2 reduced (e) versus coverage values

for the 1 e^- (n_1), 2 e^- (n_2), and 4 e^- (n_4) processes of the CuBTT system inside a HBM. e, as defined previously, is the average number of electrons each CuBTT site uses to reduce O_2. For example, if 50% of CuBTT sites reduce O_2 by 1 e^- ($\frac{n_1}{n} = 0.5$), 25% by 2 e^- ($\frac{n_2}{n} = 0.25$), and 25% by 4 e^- ($\frac{n_4}{n} = 0.25$), then e would be equal to 2 (0.5*1 + 0.25*2 + 0.25*4). n_1, n_2, and n_4 are graphically represented by the colors red, green, and blue, respectively. For instance, the color purple represents a 50%-50% mixture of n_1 and n_4.

We note the subtle but important difference between e and what we define as ϕ. ϕ (commonly referred in other works as n) is the number of electrons transferred per O_2 molecule. Frequently, ϕ is calculated by assuming a mixture of 2 e^- and 4 e^- processes because the 1 e^- process is usually not considered in aqueous systems. Here, we must consider all three processes due to the unique attributes of the HBM system. e describes the average O_2 reduction pathway performed by each catalytic site and is not convoluted by the rate constants for the individual pathways (k_1, k_2, and k_4). The value e is rarely discussed in literature, presumably because the rate constants for the individual reaction pathways are difficult to determine. However, the kinetic control imparted by the HBM system allows us to determine these rate constants and hence calculate values for e.

In other words, ϕ is defined as the average number of electrons consumed by a catalyst per O_2 on a current basis:

$$\phi = \frac{i_1}{i} e_1 + \frac{i_2}{i} e_2 + \frac{i_4}{i} e_4$$

However, if the rate constants are known as they are here, this equation can be further expanded to yield:

$$\phi = \frac{n_1 k_1 e_1}{i} e_1 + \frac{n_2 k_2 e_2}{i} e_2 + \frac{n_4 k_4 e_4}{i} e_4$$

Rearranging gives:

$$\phi = \frac{n_1 k_1 {e_1}^2 + n_2 k_2 {e_2}^2 + n_4 k_4 {e_4}^2}{i}$$

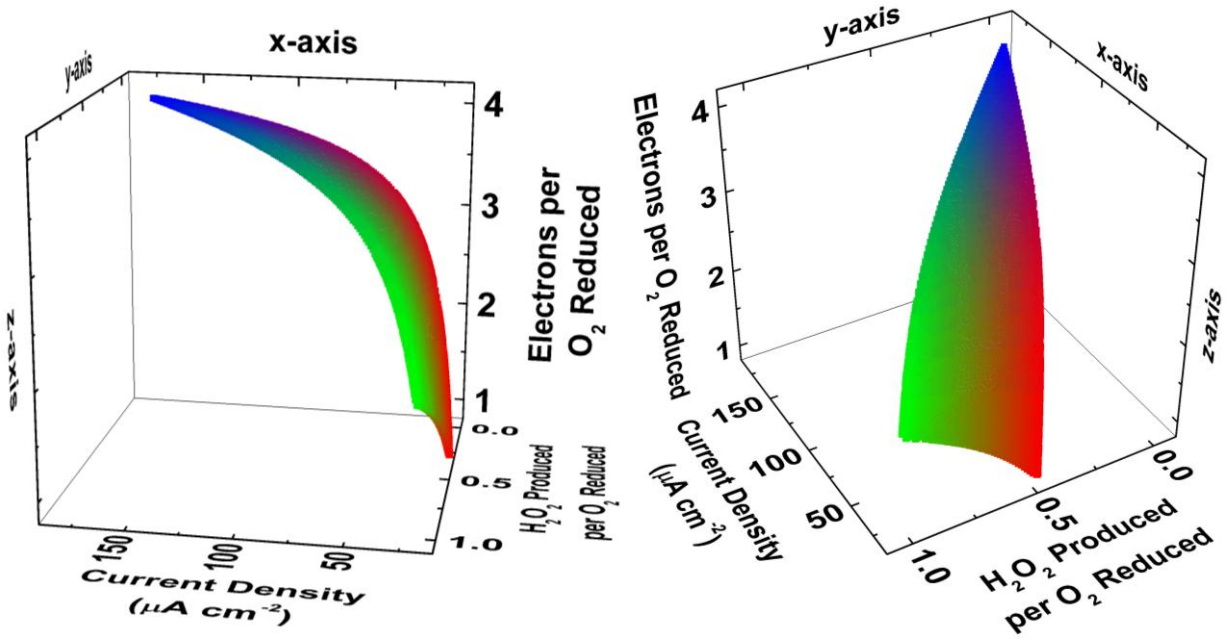

Figure 8.19. Two different perspectives of a six-dimensional plot showing the theoretical current densities for O_2 reduction by CuBTT inside a HBM (x-axis) versus expected amount of H_2O_2 produced per O_2 reduced (y-axis) versus calculated ϕ values (z-axis) versus calculated n_1, n_2, and n_4 values (red, green, and blue, respectively).

Figure 8.19 shows a six-dimensional plot of the calculated current densities versus H_2O_2 produced per O_2 reduced versus the number of electrons per O_2 reduced (ϕ) versus coverage values for the 1 e^- (n_1), 2 e^- (n_2), and 4 e^- (n_4) processes of the CuBTT system inside a HBM. Comparing the two equations for e and ϕ below demonstrates why the plot in Figure 8.18 is linear whereas those in Figure 8.19 are curved.

$$e = \frac{e_1 n_1 + e_2 n_2 + e_4 n_4}{n}$$

$$\phi = \frac{n_1 k_1 {e_1}^2 + n_2 k_2 {e_2}^2 + n_4 k_4 {e_4}^2}{i}$$

In the plots in Figure 8.19, there is only one point where $\phi = 1$. At this point, the current density is equal to that of the purely 1 e^- process and the amount of H_2O_2 produced per O_2 reduced is equal to 0.5 since the catalyst generates only O_2^- in this case which disproportionates to form O_2 and H_2O_2. Similarly, the plots only have one point where $\phi = 4$. At this point, the current density is equal to that of the purely 4 e^- process and there is no H_2O_2 produced since H_2O is the only product. However, there are multiple points on the plots where $\phi = 2$. These points form a curved line across the surface that include the purely 2 e^- case (green) and many different mixtures of multiple processes.

8.3.6 Analysis of O_2 Reduction Pathways without Lipid

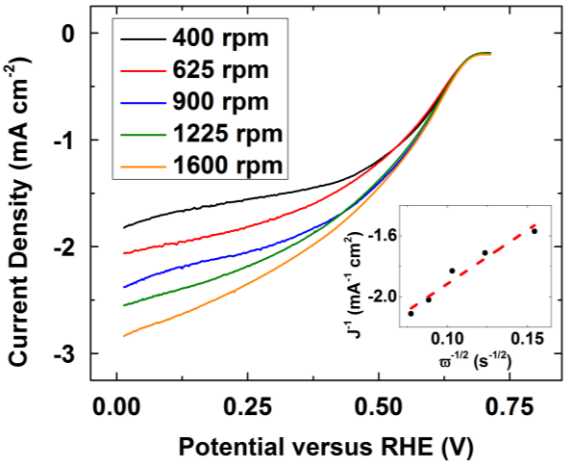

Figure 8.20. A set of O_2 reduction LSVs of the Cu complex of protected BTT supported on Vulcan carbon XC-72 with Nafion binder on glassy carbon at a scan rate of 10 mV s^{-1} with rotation rates of 400 (black), 625 (red), 900 (blue), 1225 (green), and 1600 (orange) rpm. The inset shows the corresponding Koutecky-Levich plot.

This finding is in contrast to most O_2 reduction catalysts that are directly exposed to bulk aqueous environments, which generally proceed via a mixture of two and four e^- pathways.[1]

Indeed, we find that in the absence of a lipid layer, Koutecky-Levich analysis and H_2O_2 detection studies indicate that CuBTT reduces O_2 by a mixture of two and four e^- processes (Figure 8.20).

Table 8.2. Total number of electrons transferred per O_2 for CuBTT without lipid obtained from three different methods.

Pathways	Dye-based spectroelectrochemistry	Rotating ring-disk electrode	Koutecky-Levich analysis
1 e^- & 4 e^-	3.37 ± 0.02	3.1 ± 0.4	
2 e^- & 4 e^-	3.79 ± 0.01	3.7 ± 0.2	3.7 ± 0.2

Table 8.2 shows the calculated number of electrons transferred per O_2 molecule using dye-based spectroelectrochemistry, rotating ring-disk electrode experiments, and Koutecky-Levich analysis. The first two of these methods cannot discriminate between 1 e^- and 2 e^- processes because detection occurs after the disproportionation of O_2^- to H_2O_2 and O_2, a process that occurs rapidly at pH 7.[26] Therefore we calculate the two extreme cases where only 1 e^- & 4 e^- and 2 e^- & 4 e^- pathways occur. Koutecky-Levich analysis, however, directly determines the total number of electrons transferred at the electrode. Hence, we can discriminate between 1 e^- & 4 e^- and 2 e^- & 4 e^- pathways. Because Koutecky-Levich analysis for the 2 e^- & 4 e^- pathways gives values that match with the other two techniques, we conclude that CuBTT without lipid reduces O_2 by a mixture of 2 e^- and 4 e^-.

8.3.7 Proton Transfer Rate Calculations

Because we have gained insight about O_2 reduction pathways, detected the amount of H_2O_2 generated, and calculated the surface coverage of CuBTT, it is possible to quantify the proton transfer rates in the HBM on a per catalyst basis, which increase with proton carrier

concentration (Figure 8.11a, xy-plane). Here, we describe calculations for proton transfer on a per catalyst basis for CuBTT inside a HBM at pH 7 (Figure 8.11a, y-axis). From the discussions in Section 8.3.5, we conclude that a mixture of 4 e^- and 1 e^- processes occur in these cases. Using the nomenclature in Section 8.3.5, we can write two equations describing this system.

$$i = n_1 k_1 e_1 + n_4 k_4 e_4$$

$$M = n_1 k_1 m_1$$

Rearranging yields:

$$\frac{M}{m_1} = n_1 k_1$$

$$i = \frac{M}{m_1} e_1 + n_4 k_4 e_4$$

Solving for $n_4 k_4 e_4$ yields:

$$n_4 k_4 e_4 = i - \frac{M}{m_1} e_1$$

The current produced by the 4 e^- process is $n_4 k_4 e_4$. For a 4 e^- process, 1 H^+ is transferred for every 1 e^-, so the quantity of the current is also equal to the number of protons consumed during the voltammetry. Finally, to determine the proton transfer rate per CuBTT catalyst, this number is divided by the total surface coverage of CuBTT (n), which has previously been reported to be 2.83×10^{13} CuBTT molecules cm^{-2},[18] giving $\frac{i - \frac{M}{m_1} e_1}{n}$.

8.3.8 Proton Carrier Quantification by NMR

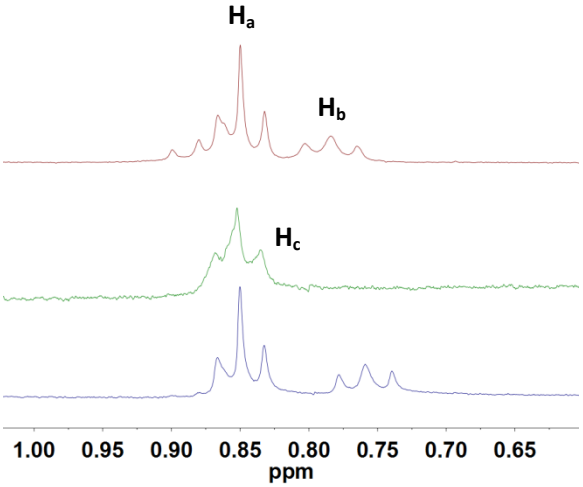

Figure 8.21. ^{1}H NMR spectra of DBA (red), DMPC (green), and DBA and DMPC (blue) in $CDCl_3$.

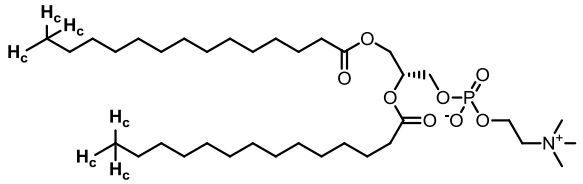

1,2-dimyristoyl-*sn*-glycero-3-phosphocholine (DMPC)

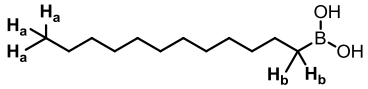

1-dodecylboronic acid (DBA)

Figure 8.22. Schematic of DMPC and DBA indicating the nuclei of interest.

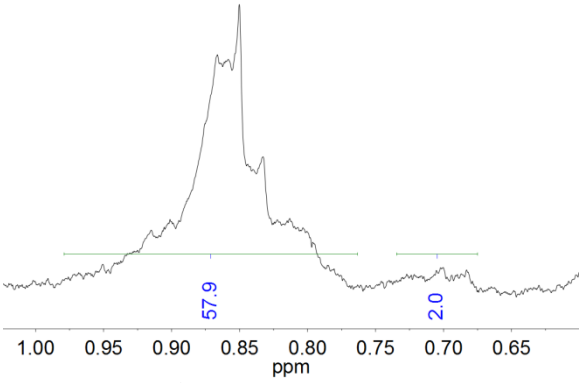

Figure 8.23. ^{1}H NMR spectrum with peak integration (blue numbers) of the lipid layer extracted from HBMs with 50 mol% DBA initially added to DMPC in $CDCl_3$.

Furthermore, by quantifying the amount of DBA in the lipid layer of the HBM using ^{1}H NMR spectroscopy, we also determine the proton transfer rates on a per proton carrier basis. To calculate the surface coverage of DBA in the HBM system, we use the ^{1}H NMR spectroscopy shown in Figures 8.21-23. Figure 8.21 shows the ^{1}H NMR spectra of DBA (red), DMPC (green), and a mixture of DBA and DMPC (blue) in $CDCl_3$. The protons on the methylene group adjacent to the B atom (H_b) in DBA can be distinguished from other proton resonances in the presence of DMPC because of the upfield shift of these resonances due to the electron-donating nature of the B atom (Figure 8.22). The protons on the methyl group of the lipid tails (H_c) and the protons on the methyl group on DBA (H_a) integrate to a relative value of 57.9 compared to the two H_b protons. Figure 8.21 shows that the resonances for H_a and H_c overlap at ~0.85 ppm, meaning that the contribution from the H_c protons must first be subtracted out from the H_a + H_c integration. This procedure then gives a DMPC:DBA ratio of [(57.9-3)/6]:(2/2) = 9.15:1, which corresponds to ~10 mol% DBA (Figure 8.23).

From this value, we proceed to calculate the number of protons transferred per proton carrier per second for the case where CuBTT is covered by DMPC with 10 mol% DBA. The lateral packing density of DMPC is 3.3×10^{-10} mol cm^{-2}.[43] Using the 9.15:1 ratio from above, the surface coverage of DBA is 3.3×10^{-11} mol cm^{-2}. The current density at 0.11 V versus RHE is (174 ± 38) μA cm^{-2}, which corresponds to $(1.82 \pm 0.39) \times 10^{-9}$ mol e^- s^{-1} cm^{-2}. Since dye-based spectroelectrochemistry shows that CuBTT covered by DMPC with 10 mol% DBA reduces O_2 exclusively by 4 e^- (see Section 8.3.3), 1 H^+ is transferred for every 1 e^-. Therefore the proton transfer rate is $(1.82 \pm 0.39) \times 10^{-9}$ mol H^+ s^{-1} cm^{-2}, which when considered with the DBA surface coverage, gives a proton transfer rate on a per proton carrier basis of (55 ± 12) H^+ per second per proton carrier at pH 7, values similar to those of proton carriers in lipid bilayers.[44]

8.3.9 O_2 Reduction Mechanism inside and outside a HBM

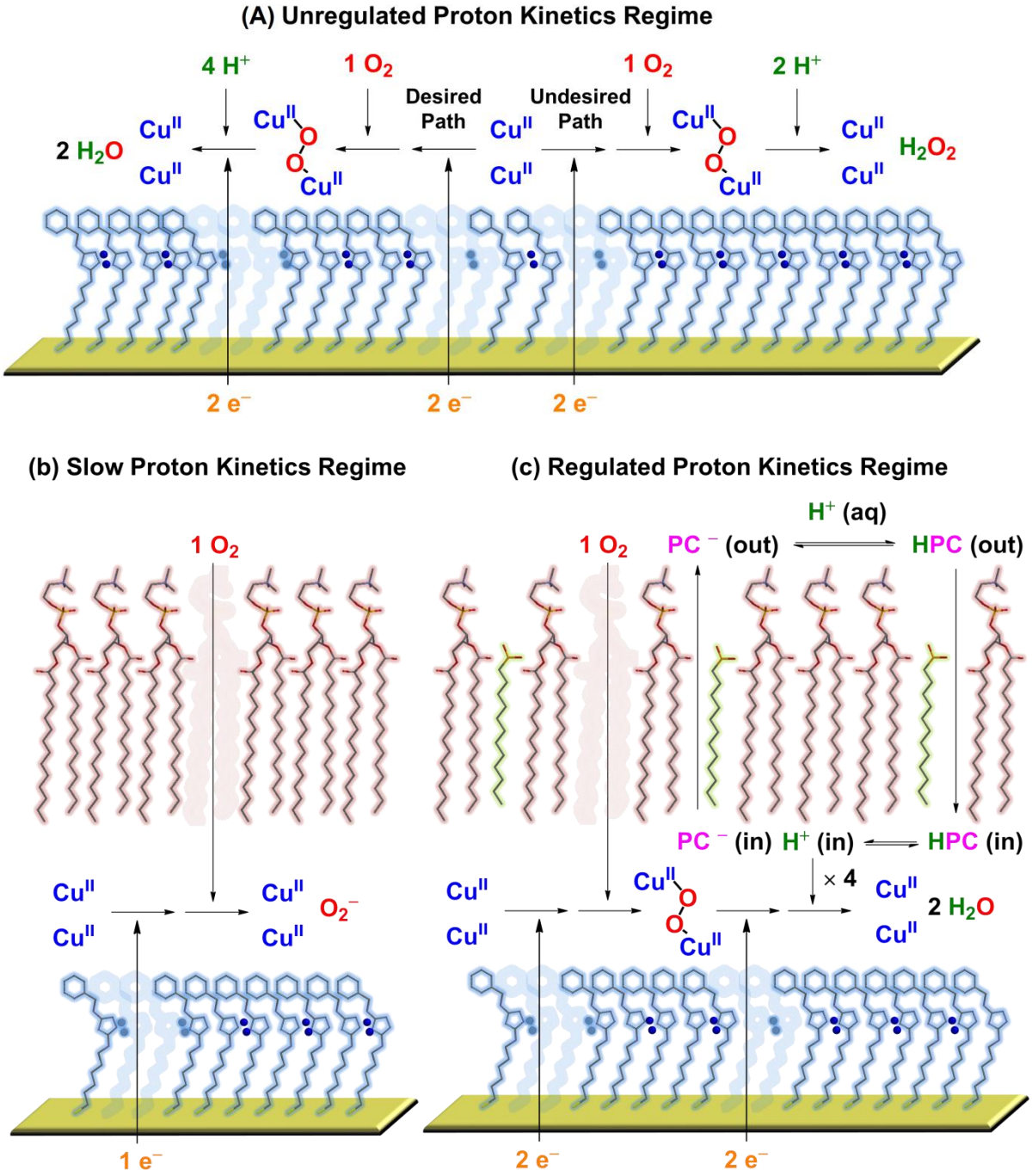

Figure 8.24. Regulation of proton transfer kinetics induces mechanistic changes of O_2 reduction, which dictate the selectivity of products. O_2 reduction pathways by CuBTT in the (a) unregulated, (b) slow, and (c) regulated proton transfer kinetics regimes, PC = proton carrier.

Figure 8.24 describes how the kinetics of proton delivery affect the mechanism of O_2 reduction by CuBTT. In the absence of a lipid layer (Figure 8.24a), CuBTT has free access to protons at a bulk proton transfer rate of ~10^4 s^{-1} at pH 7.[45] In this case, protonation of the Cu-O-O-Cu adduct to generate H_2O_2 as a side product occurs before the O-O bond breaking event. However, protonation of the Cu-O-O-Cu species outside lipid may enable faster O-O bond cleavage than inside lipid, thus explaining the higher maximum current density obtained in bulk solution compared to the case inside the lipid with proton carrier. Inside a lipid layer, as the amount of DBA increases, the rate of proton transfer to CuBTT increases accordingly and favors the four e^- pathway (Figure 8.24c) over the one e^- pathway (Figure 8.24b), the latter of which occurs when proton accessibility is completely restricted. Interestingly, at high DBA concentrations, the amount of H_2O_2 detected during O_2 reduction is even less than that produced by a SAM of CuBTT without lipid. Because the RDS in a HBM with DBA is proton transfer across the lipid layer (Section 8.3.4), not the O-O bond breaking step, the Cu-O-O-Cu adduct cannot prematurely protonate to generate H_2O_2. This finding demonstrates the importance of tuning the rate of proton transport to O_2 reduction catalysts. Faster proton transfer kinetics (e.g. those in bulk H_2O) do not necessarily yield the most selective catalyst, but rather the interplay between the rates of proton delivery, electron transfer, and O-O bond breaking dictates the O_2 reduction mechanism and consequently the products of the catalyst.

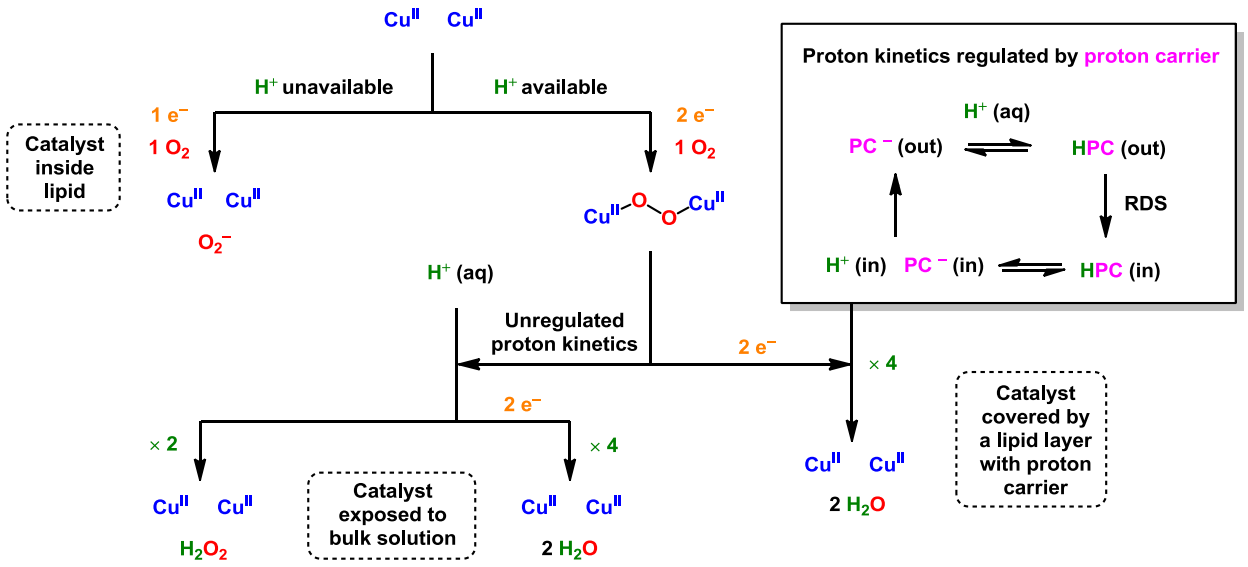

Figure 8.25. O_2 reduction pathways in a HBM, PC = proton carrier.

We examined three individual cases:

(i) CuBTT covered by DMPC without proton carrier

(ii) CuBTT covered by DMPC with proton carrier

(iii) CuBTT exposed to solution directly without lipid

For case (i) where CuBTT is covered by a monolayer of lipid without proton carrier, the mechanism of O_2 reduction to O_2^- is:

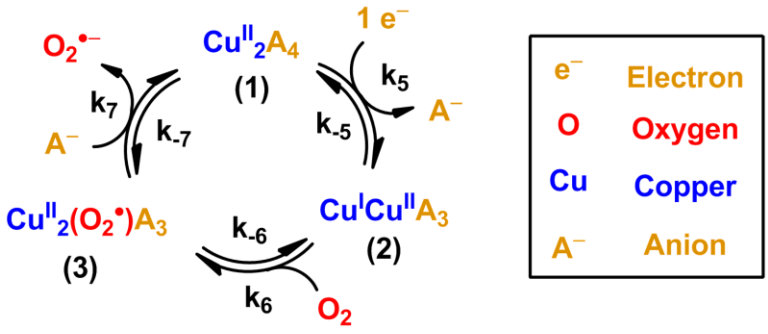

Figure 8.26. O_2 reduction by CuBTT in a HBM without proton carrier.

$$\frac{d[O_2^{\cdot-}]}{dt} = k_7[A^-][\mathbf{3}] - k_{-7}[\mathbf{1}][O_2^{\cdot-}] \qquad (17)$$

$$\frac{d[3]}{dt} = k_6[\mathbf{2}][O_2] - k_{-6}[\mathbf{3}] \qquad (18)$$

$$\frac{d[2]}{dt} = k_5[\mathbf{1}] - k_{-5}[\mathbf{2}][A^-] \qquad (19)$$

Figure 8.26 shows a mechanism by which CuBTT reduces O_2 covered by a lipid monolayer. The potentials at which catalytic currents are passed are about 200 mV more negative than the Cu(I)/Cu(II) couple, indicating that the Cu(II) is efficiently reduced to Cu(I). However, we did not observe a diffusion-limited current, suggesting that the uptake of O_2 is not limiting. Because the first two steps in the catalytic cycle are likely not rate-limiting, we hypothesize that the release of O_2^- is the RDS. As O_2^- is generated by a monolayer of CuBTT and released into the bulk solution, the concentration of O_2^- is assumed to be low. Taken together, we combine Eq. 17, 18, and 19 and apply steady-state assumptions on **2** and **3** to give:

$$\frac{d[O_2^{\cdot-}]_{lipid}}{dt} = \frac{k_7 k_6 k_5[\mathbf{1}][O_2]}{k_{-6}k_{-5}} \qquad (20)$$

For case (ii) where CuBTT is in a HBM with proton carrier incorporated in the lipid layer, the lack of a KIE means that the RDS is the flip-flop diffusion of the proton carrier across the lipid membrane (Figure 8.27 and see Section 8.3.4):

Figure 8.27. O_2 reduction by CuBTT in a HBM with proton carrier incorporated in the lipid layer, where z is the number of proton carriers that flip across the lipid membrane before the protons are added to the Cu_2O_2 adduct and can vary from 1 to 4.

$$\frac{d[H_2O]_{HBM}}{dt} = k_{flip}[PC_{out}]^z - k_{-flip}[PC_{in}]^z \qquad (21)$$

For case (iii) where CuBTT is exposed to the bulk solution, there are two products, which are generated from two different pathways of O_2 reduction. The pathways to generate H_2O_2 and H_2O are:

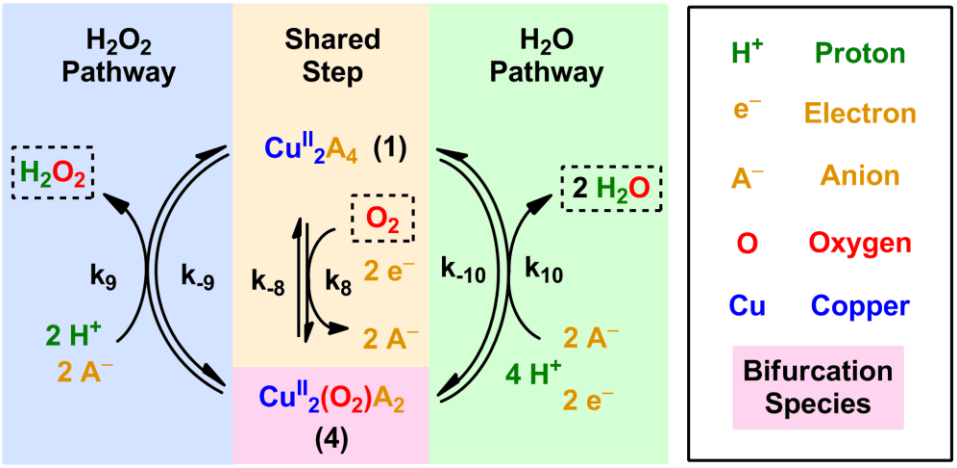

Figure 8.28. O_2 reduction by CuBTT in a HBM without proton carrier.

Figure 8.28 displays a mechanism by which CuBTT reduces O_2 when the catalyst has direct access to protons in the bulk solution. The potentials at which catalytic currents are passed are about 100 mV more negative than the Cu(I)/Cu(II) couple, suggesting the Cu(II) is efficiently reduced to Cu(I). O_2 binds to the reduced species to give **4**, which is then protonated. H_2O_2 is released while regenerating **1** to re-enter the catalytic cycle. **4** can undergo a different pathway to generate H_2O via multiple proton and electron transfer steps. Upon releasing two H_2O molecules, **1** is regenerated for use in the next catalytic cycle. We emphasize that other bifurcation pathways can be postulated to give the same mixture of products. We also stress that these steps can occur in a coupled, concerted, or consecutive fashion.

There are two key messages in the scheme presented in Figure 8.28. First, the two pathways to produce H_2O and H_2O_2 share an initial step and this step does not involve protons. Second, **4** is the putative bifurcation species. The pathway undergone by **4** dictates the product.

In essence, the product speciation stems from the relative rates of electron and proton transfer. Slow electron transfer hinders O-O bond scission, thus impeding H_2O generation and favoring H_2O_2 production.

At this stage, we know that protons are involved at or before the RDS, because we observe a KIE. Therefore, the O_2 reduction rate should scale with concentration of protons.

$$\frac{d[H_2O_2]_{no\ lipid}}{dt} \propto [H^+]^u$$

$$\frac{d[H_2O]_{no\ lipid}}{dt} \propto [H^+]^w$$

where *u* and *w* are the number of protons involved at or before the RDS.

In summary, the overall rate of O_2 reduction is:

$$-\frac{d[O_2]}{dt} = \frac{d[O_2^{\cdot-}]_{lipid}}{dt} + \frac{d[H_2O]_{HBM}}{dt} + \frac{d[H_2O]_{no\ lipid}}{dt} + \frac{d[H_2O_2]_{no\ lipid}}{dt} \qquad (22)$$

(i) In the extreme case where access to protons by CuBTT is constrained, i.e. the lipid only case with no proton carrier: $[PC_{out}]$, $[PC_{in}]$, $[H^+]$ and related terms = 0, so the second, third and fourth terms in Eq. (22) drop out of the equation, resulting in:

$$-\frac{d[O_2]}{dt} = \frac{d[O_2^{\cdot-}]_{lipid}}{dt} = \frac{k_7 k_6 k_5 [\mathbf{1}][O_2]}{k_{-6} k_{-5}}$$

Since the rate equation has no dependence on $[H^+]$, the equation above explains the observation that inside lipid, CuBTT reduces O_2 by mostly 1 e^- to generate O_2^-.

(ii) In the case where access to protons by CuBTT is controlled by the amount of DBA in the lipid layer, i.e. the HBM with DBA added to the lipid layer: terms containing $[H^+]$ = 0, so the third and fourth terms in Eq. (22) drop out of the equation, resulting in:

$$-\frac{d[O_2]}{dt} = \frac{d[H_2O]_{HBM}}{dt} = \frac{k_7 k_6 k_5[\mathbf{1}][O_2]}{k_{-6}k_{-5}} + \left(k_{flip}[PC_{out}]^z - k_{-flip}[PC_{in}]^z\right)$$

The equation above describes the situation that inside lipid with DBA, CuBTT reduces O_2 by 1 e^- and 4 e^- to generate O_2^- and H_2O. In the optimal case where there is sufficient DBA added to the lipid layer, i.e.

$$\left(k_{flip}[PC_{out}]^z - k_{-flip}[PC_{in}]^z\right) \gg \frac{k_7 k_6 k_5[\mathbf{1}][O_2]}{k_{-6}k_{-5}}$$

CuBTT reduces O_2 by 4 e^- to generate H_2O exclusively.

(iii) In the case where proton availability to CuBTT is unrestricted, i.e. CuBTT not covered by lipid: $[PC_{out}] = 0$, $[PC_{in}] = 0$ and $[H^+]$ and related terms dominate over the first and second terms in Eq. (22), resulting in:

$$-\frac{d[O_2]}{dt} = \frac{d[H_2O]_{no\ lipid}}{dt} + \frac{d[H_2O_2]_{no\ lipid}}{dt}$$

Therefore for the case of CuBTT, a mixture of H_2O_2 and H_2O is produced.

8.3.10 Comparison of O_2 Reduction Behavior to other Non-precious Metal Catalysts

To test the applicability of the finding that controlling proton transfer kinetics in a HBM model system to O_2 reduction catalysts affects their selectivity, we analyze practical fuel cell NPM catalysts under varying pH regimes. We find that these catalysts, including the NPM catalyst with the lowest overpotential to date,[4] generate lower amounts of H_2O_2 during O_2 reduction upon increasing the pH. Figures 8.29a and b show the percent H_2O_2 generated by the Fe-based catalyst (PANI-Fe-C) that exhibits the lowest overpotential for O_2 reduction out of all known non-precious metal catalysts. This catalyst was synthesized according to a recently published procedure by Wu and coworkers.[4] Wu et al. studied O_2 reduction by PANI-Fe-C under very acidic conditions (pH ≤ 1). Here, we study PANI-Fe-C in slightly more basic conditions. As

is common for NPM catalysts, the onset potential for O_2 reduction by PANI-Fe-C shifts negative as the pH of the solution increases (Figure 8.29c).

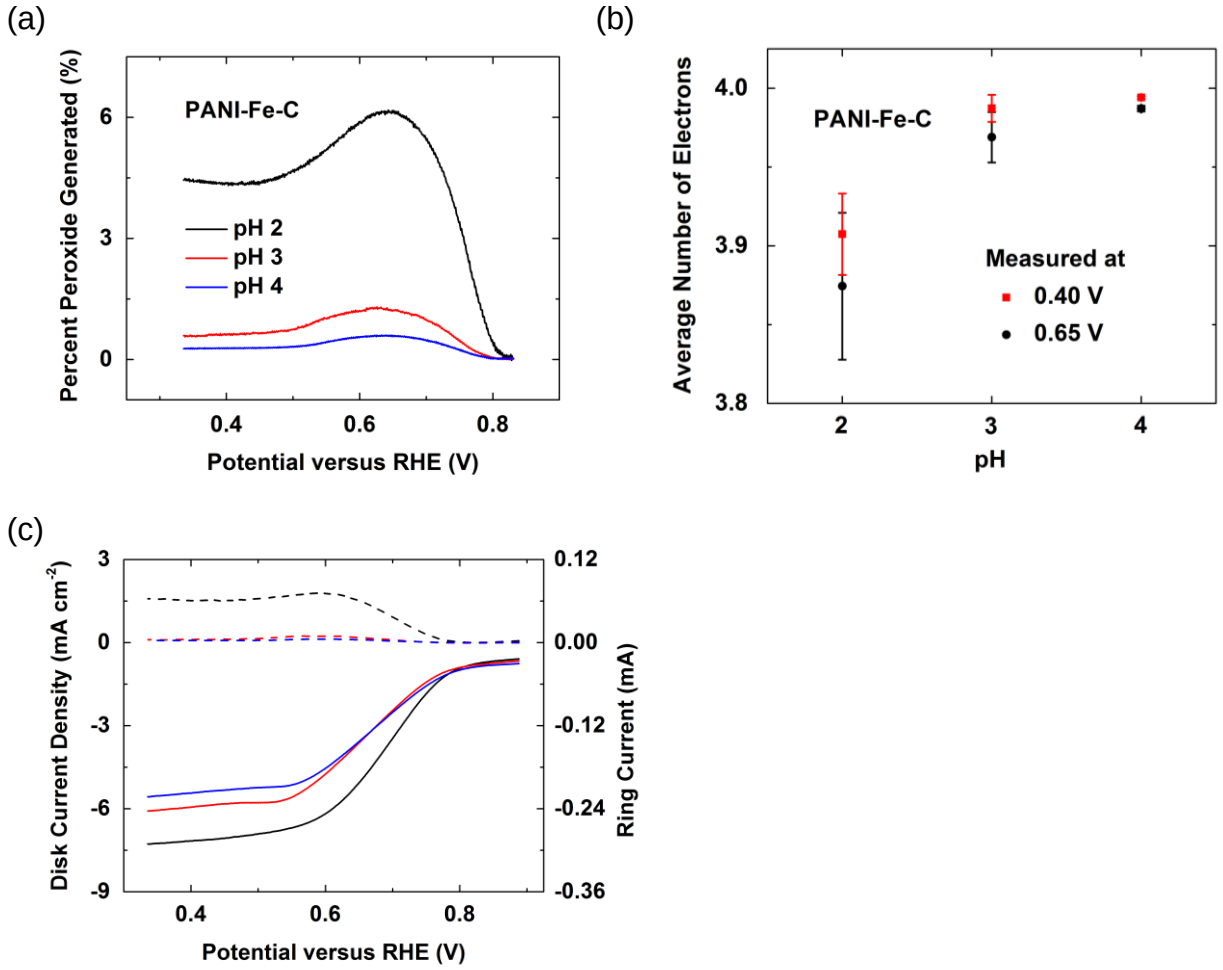

Figure 8.29. (a) Percent H_2O_2 generated as a function of potential by the Fe-based catalyst (PANI-Fe-C) that exhibits the lowest overpotential for O_2 reduction out of all known non-precious metal catalysts. (b) Average number of electrons transferred to O_2 at 0.65 V (black circles) and 0.4 V (red squares) by PANI-Fe-C. (c) O_2 reduction rotating ring-disk experiments (RRDE) of PANI-Fe-C at pH 2 (black), 3 (red), and 4 (blue). Solid line = disk current density. Dashed line = ring current.

We vary the pH from 2 to 4 and find that at higher pH values, the amount of H_2O_2 generated decreases. Similarly, we note that in several examples of molecular Cu and Fe ORR catalysts,[26,46,47] the amount of H_2O_2 generated is also suppressed as the pH of the bulk solution

increases. Based on the discussion in the main manuscript, we interpret these results as signifying that a decrease in proton transfer kinetics inhibits the pathway for H_2O_2 generation by decreasing the likelihood that protonation of a bound O_2 adduct occurs before O-O bond breaking. We conclude that a decrease in proton transfer rate at higher pH discourages the protonation of bound O_2 adducts before O-O bond breaking to generate H_2O_2. These results demonstrate that regulating proton transport is important in determining the selectivity of NPM catalysts in general, not just catalysts inside HBMs.

8.3.11 Comparison of O_2 Reduction Behavior to Non-precious Metal Catalysts

Previously, we studied the ORR activity of a catalyst bearing an Fe-N_4 core inside a HBM with various concentrations of proton carrier.[19] In that work, the Fe picket fence porphyrin outside of a lipid layer reduces O_2 by an average of ~3.5 electrons. Upon appending a monolayer of lipid on top of the catalyst, the catalyst produces solely O_2^- in a one electron reduction process due to the unavailability of protons. In a manner similar to the results found with the CuBTT system, the selectivity of the catalyst increases as the amount of proton carrier inside the lipid layer of the HBM increases. However, unlike the CuBTT HBM system, the selectivity of which can be increased to produce H_2O as the sole product, the average number of electrons for ORR by the Fe porphyrin inside the lipid layer with proton carrier reaches a value similar to the exposed open SAM catalyst (~3.5 electrons).

We hypothesize that the dinuclearity of CuBTT allows the O-O bond to break before protonation inside the lipid layer with proton carrier, and that this ability accounts for the high selectivity achievable with this system. In contrast, the O-O bond cannot break before protonation in the mononuclear Fe porphyrin case, and thus the selectivity of the catalyst cannot

be improved beyond the exposed open SAM case. In other words, inside the lipid with proton carrier, a protonated FeO_2 species can still bifurcate to produce either H_2O_2 or H_2O.

8.3.12 Comparison of O_2 Reduction Behavior to Pt-based Precious Metal Catalysts

The mechanism by which NPM catalysts reduce O_2 is in contrast to that of Pt. Pt neither exhibits a pH-dependent overpotential nor an isotope effect,[42,48] suggesting that the RDS is an electron transfer step. Nonetheless, Pt-based catalysts produce a small fraction of H_2O_2 regardless of pH, the production of which limits fuel cell lifetime.[1,6] Unlike NPM catalysts, regulating proton transfer to Pt does not improve its selectivity for the four e^- reduction of O_2 to H_2O since the RDS does not involve protons.

8.3.13 Comparison of O_2 Reduction Behavior to Naturally-occuring Enzymes

The knowledge we have gained about proton transfer kinetics and the mechanism of O_2 reduction provides new understanding into the performance of some of the best synthetic O_2 reduction catalysts. Equally interesting, it also provides insight into the structure-selectivity relationship of O_2 reduction enzymes. The enzymatic O_2 reduction catalysts laccase and cytochrome c oxidase reduce O_2 exclusively by four e^- to H_2O, thus avoiding the generation of H_2O_2 or O_2^-, which are toxic to cells.[49,50] These enzymes utilize complex proton channels to regulate proton transfer rates, so that each proton transfer is directly correlated with an electron transfer event.[51,52] Analogous considerations of the synergy between the electron and proton transfer rates are important in designing robust synthetic O_2 reduction catalysts.

Laccases typically are found to participate in the four electron reduction of O_2. However, the exact electron number and the presence or absence of peroxide is found to be dependent on the exact manner in which laccase is appended to the electrode. It has been suggested that the

production of H_2O_2 depends on the electron transfer rate from the electrode to laccase, which can vary depending upon the environment surrounding the enzyme.[53]

From the mechanistic framework proposed in our work, the effect of electron transfer rate on the selectivity of laccase can be rationalized. When the electron transfer rate to laccase is too slow, we hypothesize that O-O bond breaking cannot occur fast enough to produce H_2O before protonation of the O-O adduct to generate H_2O_2. Instead of tuning the electron transfer rate, the HBM system presented here allows for the control of the proton transfer rate to the O_2 reduction catalyst. Specifically, the amount of H_2O_2 generated decreases as the proton transfer rate is slowed down so that it is compatible with the O-O bond breaking rate.

Finally, we note that many laccase electrode constructs do not yield limiting current behavior in studies using rotating electrodes.[54,55] The origin of this behavior has been unclear over the past twenty years, but is possibly explained by our work. The lack of limiting current means that the laccase activity is not constrained by O_2 availability, as is the case with many other electrode materials. Rather, we suggest that the current is limited by proton availability at the active site.

8.3.14 H_2O_2 Experiments

The results in Figure 8.30a show that H_2O_2 oxidation occurs at ~0.9 V, a potential more positive than 0.68 V. At potentials negative of the thermodynamic potential (0.68 V), the Au electrode reduces H_2O_2 (Figure 8.30b).

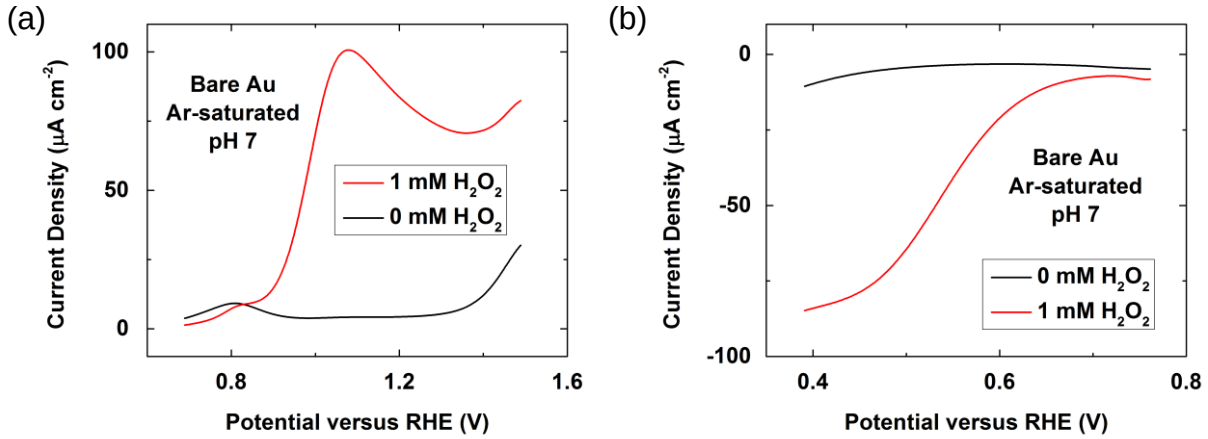

Figure 8.30. LSVs showing (a) anodic and (b) cathodic currents produced by a bare Au surface in the absence (black) and presence (red) of 1 mM H_2O_2 in Ar-saturated pH 7 phosphate buffer at a scan rate of 10 mV s^{-1}.

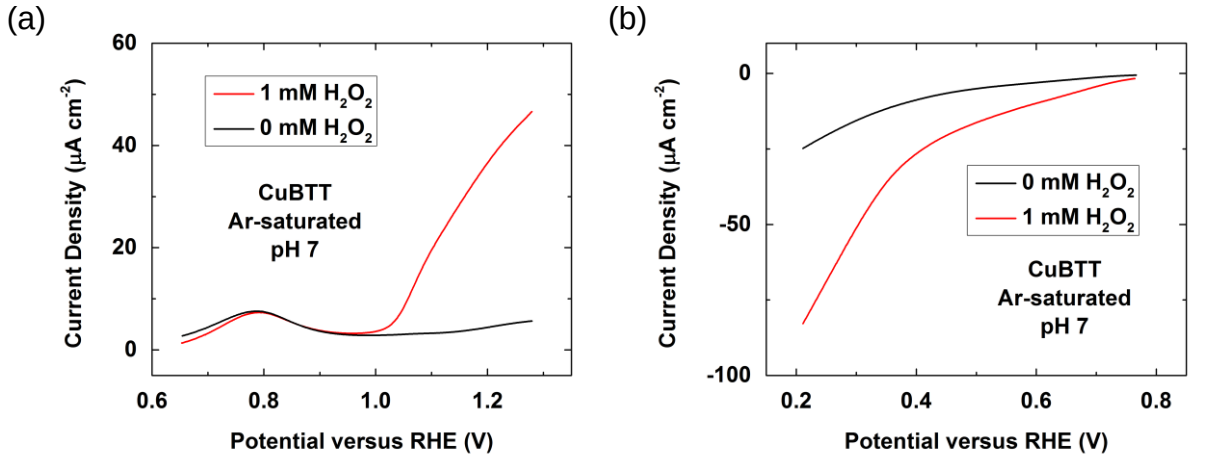

Figure 8.31. LSVs showing (a) anodic and (b) cathodic currents produced by a SAM of CuBTT in the absence (black) and presence (red) of 1 mM H_2O_2 in Ar-saturated pH 7 phosphate buffer at a scan rate of 10 mV s^{-1}.

We first consider a mechanism that only involves the stabilization of H_2O_2 by DBA without flip-flop diffusion of the proton carrier. To test this hypothesis, we performed experiments with CuBTT without lipid in the presence of H_2O_2. The LSVs in Figures 8.31a and b demonstrate that CuBTT oxidizes and reduces H_2O_2. Therefore, the first requirement of this

proposed mechanism, that CuBTT be able to catalytically reduce H_2O_2, is fulfilled (Figure 8.31b).

We next test if CuBTT catalyzes H_2O_2 reduction inside a lipid layer in the absence of a flipping proton carrier. The LSVs in Figure 8.32a below show that there is no enhancement of the reduction current by CuBTT inside lipid with H_2O_2 added to the bulk solution. This experiment proves that inside lipid, CuBTT cannot reduce H_2O_2 to H_2O because protons are not available inside the hydrophobic lipid environment, thus disproving the proposed mechanism of DBA stabilizing putatively-formed H_2O_2 so that H_2O_2 can be further reduced.

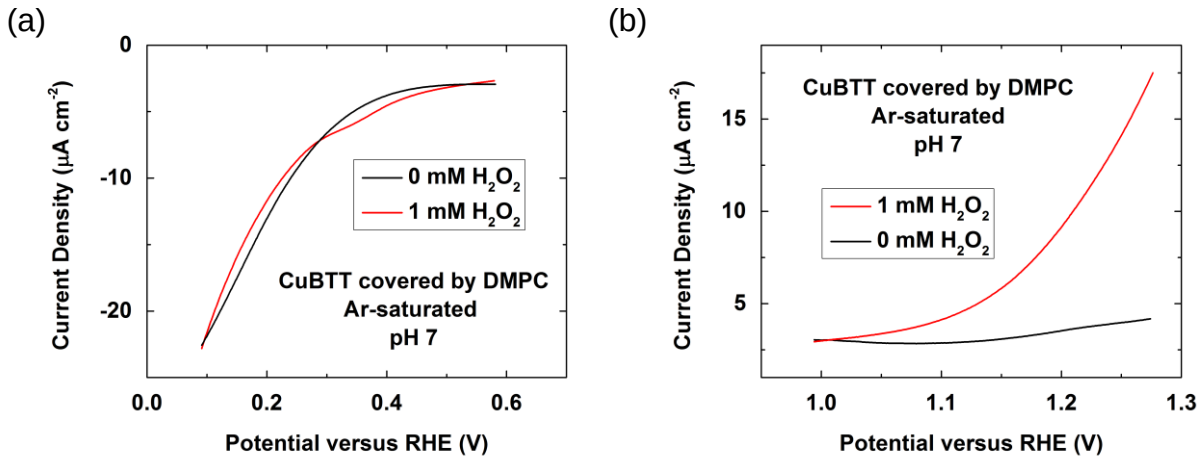

Figure 8.32. LSVs showing (a) cathodic and (b) anodic currents produced by a HBM containing CuBTT in the absence (black) and presence (red) of 1 mM H_2O_2 in Ar-saturated pH 7 phosphate buffer at a scan rate of 10 mV s^{-1}.

We now check the validity of an important assumption made in the previous paragraph. We assume that H_2O_2 can diffuse through the lipid layer of the HBM facilely so that it can reach the CuBTT SAM. We performed an additional experiment which definitively demonstrates that H_2O_2 does indeed permeate the lipid layer of our HBM system. The LSVs in Figure 8.32b above demonstrate that CuBTT can oxidize H_2O_2 when it is covered by a lipid layer, thus proving that H_2O_2 diffuses through the lipid layer to the CuBTT sites.

Unlike H_2O_2 reduction which cannot occur inside the lipid because it requires protons, H_2O_2 oxidation can occur inside the lipid layer because protons are expelled in the process, not consumed. As with all of our lipid experiments, we conducted blocking experiments with $K_3Fe(CN)_6$ to demonstrate that the lipid layer remains well-formed after H_2O_2 oxidation and present the data in Figure 8.33.

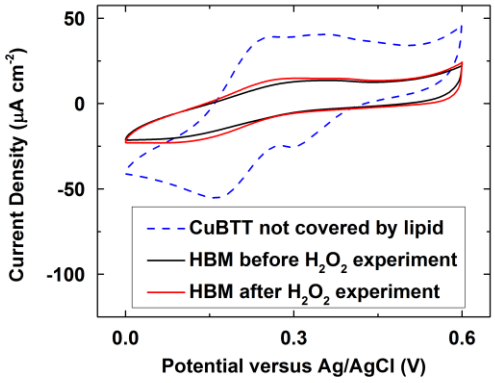

Figure 8.33. CVs of a SAM of CuBTT (blue dashed line), the HBM containing CuBTT covered by a DMPC monolayer before (black) and after (red) H_2O_2 experiments in a solution of $K_3Fe(CN)_6$ (1 mM) with KCl (100 mM) at a scan rate of 50 mV/s.

At this stage, we have ruled out the possibility that DBA acts as a static (does not undergo flip-flop diffusion) stabilizing agent for H_2O_2 inside the lipid layer. Since we know H_2O_2 rapidly permeates lipid layers, we can also demonstrate that it is unlikely for DBA to simultaneously act as a flip-flop delivery agent for protons and a stabilizing agent for H_2O_2. At high DBA concentrations (~10%), nearly every CuBTT site reduces O_2 by 4 e^- to form H_2O. If H_2O_2 is produced first and then is stabilized by DBA, there would have to be two DBA molecules per CuBTT to both stabilize the H_2O_2 and deliver the remaining two protons needed for H_2O_2 reduction to H_2O. However, there is < 1 equivalent of DBA per CuBTT inside the lipid layer. In this case, then, each DBA molecule would have to flip-flop back and forth between the lipid membrane at least two times before H_2O_2 diffusion away from the vicinity of the CuBTT

catalyst occurs. We consider this scenario highly unlikely given the ease of simple H_2O_2 diffusion compared to the energetic penalties associated with flip-flop diffusion.

8.3.15 Tafel Slope Analysis[56]

For the case of CuBTT catalyst in the absence of a lipid layer, the currents level out at higher overpotentials and then decrease due to limits in the diffusion of O_2 from bulk solution. Thus Tafel analysis is not applicable in the region where the current begins to level out. However, in the lower overpotential region, the Tafel slope at pH 7 for the open SAM catalyst is (140 ± 13) mV dec^{-1} (Figure 8.34a), which is close to the theoretical value (120 mV dec^{-1}) for a rate-limiting electron transfer step. This result implies that one or multiple chemical step(s) could be involved at or before a rate-determining electron transfer event. This measured Tafel slope agrees with our suggested mechanism that protonation and O_2 binding, both of which are chemical steps, are involved before the rate-limiting O-O bond breaking step.

For the case of CuBTT covered by a monolayer of DMPC only, the Tafel slope at pH 7 is (284 ± 24) mV dec^{-1} (Figure 8.34b), a value consistent with a rate-limiting chemical step. We hypothesize that this chemical step is the unfavorable dissociation of a charged superoxide species into the hydrophobic environment of the lipid interior. For the case of a HBM with DBA added to the lipid layer, the Tafel slope at pH 7 is (215 ± 31) mV dec^{-1} (Figure 8.34c), a value also consistent with a rate-limiting chemical step. This Tafel slope further supports our proposal that the flip-flop diffusion of DBA across the lipid membrane is the RDS for the case with DBA inside lipid.

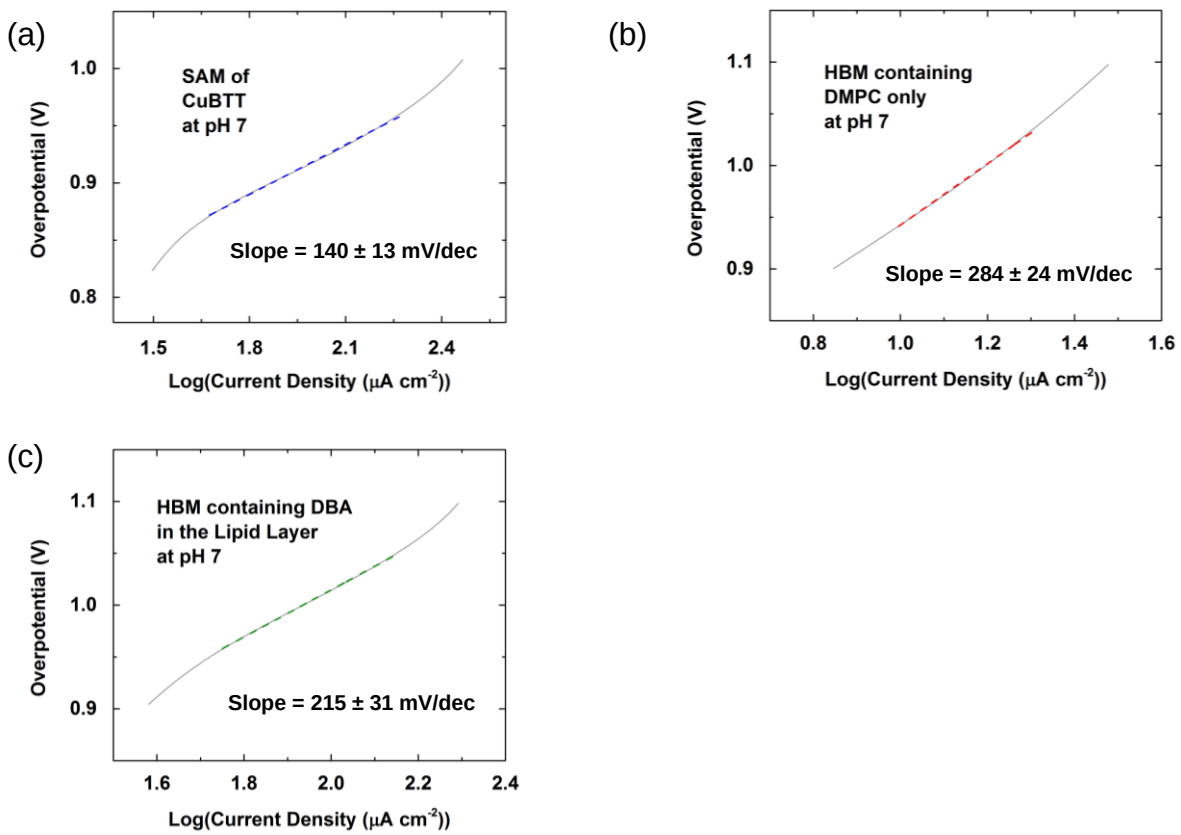

Figure 8.34. Tafel plot of (a) a SAM of CuBTT, (b) a HBM containing the CuBTT SAM, and (c) a CuBTT-HBM with DBA incorporated into the DMPC monolayer in O_2-saturated pH 7 phosphate buffer.

8.3.16 Effect of Proton Kinetics on the Selectivity of CuBTT

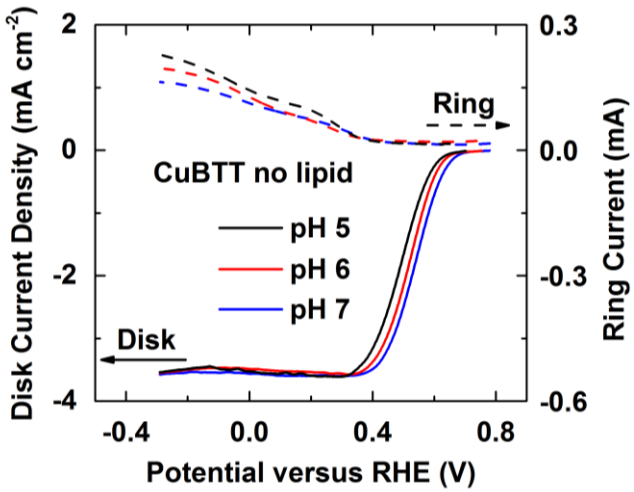

Figure 8.35. O_2 reduction RRDE LSVs of CuBTT on a glassy carbon electrode at pH 5 (black), 6 (red), and 7 (blue) with a rotation rate of 1600 rpm at a scan rate of 10 mV s^{-1}. Solid line = disk current density. Dashed line = ring current.

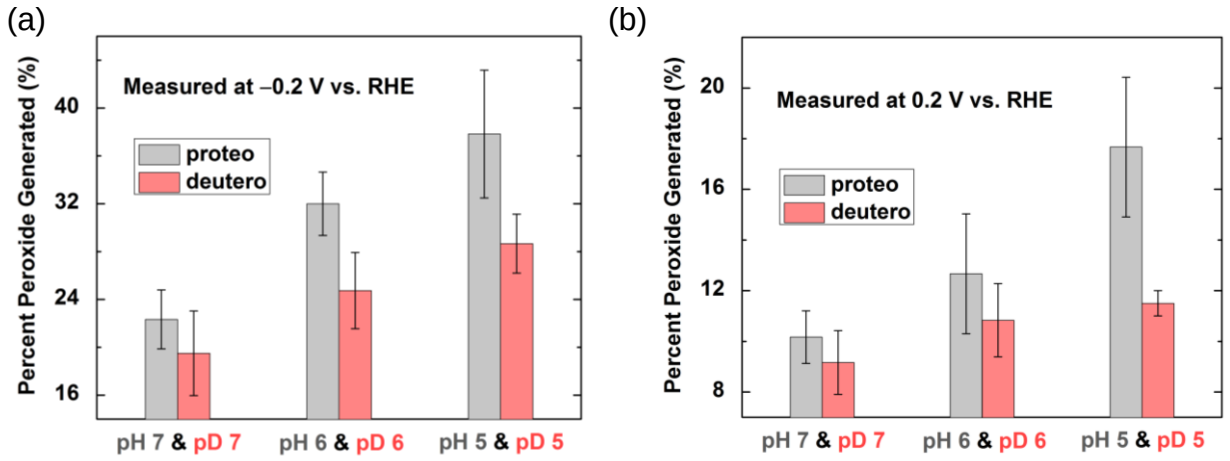

Figure 8.36. Percent peroxide generated by CuBTT on a glassy carbon electrode at pH (gray) and pD (red) 5, 6, and 7 measured at (a) –0.2 V and (b) 0.2 V versus RHE calculated from the RRDE data presented in Figure 8.35.

We measured the H_2O_2 (and D_2O_2) yields using rotating ring-disk electrodes (RRDE) for the CuBTT catalyst in the absence of lipid at pH (and pD) 5, 6, and 7. Figure 8.35 shows the ring and disk currents collected at pH 5, 6, and 7. Figures 8.36a and b display the percent peroxide produced from the RRDE experiments at two different potentials. As the pH increases, the H_2O_2 yield decreases, suggesting that a decrease in proton concentration suppresses the 2 e^- pathway. We hypothesize that at higher pH values, the kinetics of proton transfer to the CuOOCu species decreases, thus allowing more time for O-O bond cleavage without H_2O_2 release. These results are directly analogous to what we observed when the solution pH increases for the case using Fe/N/C NPM catalyst (see Section 8.3.10).

From pD 5 to 7, the amount of D_2O_2 decreases just like the pH cases. However, at all pD values, the D_2O_2 yield is lower than the H_2O_2 yield. These results also match the trend observed for the isotope effect on the peroxide yield for the Fe/N/C NPM catalyst. Deuteron transfer is kinetically slower than proton transfer, thus allowing more time for the 4 e^- pathway to occur.

8.4 Conclusions

Over the past fifty years, there has been an immense amount of effort aimed at developing active and selective O_2 reduction catalysts.[5,57,58] It may be that part of the reason why this goal has never been realized stems from the difficulty of designing and synthesizing proton relays with optimal proton transfer rates. The results of this manuscript suggest that a new strategy be employed for improving the selectivity of NPM catalysts, namely controlling proton transfer kinetics. In particular, this methodology might include slowing down proton transfer rates to match that of the O-O bond breaking rate. We have demonstrated in this report that if the proton transfer rate to NPM catalysts is properly tailored, the formation of H_2O_2 and O_2^- can be avoided. By establishing a framework for modulating both proton and electron transfer kinetics, the HBM platform developed here provides crucial insight needed to improve the performance of future O_2 reduction catalysts for fuel cell applications.

8.5 References

(1) Gewirth, A. A.; Thorum, M. S. *Inorg. Chem.* **2010**, *49*, 3557.
(2) Hatcher, L.; Karlin, K. *J. Biol. Inorg. Chem.* **2004**, *9*, 669.
(3) Jaouen, F.; Proietti, E.; Lefevre, M.; Chenitz, R.; Dodelet, J.-P.; Wu, G.; Chung, H. T.; Johnston, C. M.; Zelenay, P. *Energy Environ. Sci.* **2011**, *4*, 114.
(4) Wu, G.; More, K. L.; Johnston, C. M.; Zelenay, P. *Science* **2011**, *332*, 443.
(5) Thorseth, M. A.; Tornow, C. E.; Tse, E. C. M.; Gewirth, A. A. *Coord. Chem. Rev.* **2013**, *257*, 130.
(6) Higgins, D. C.; Chen, Z. *Can. J. Chem. Eng.* **2013**, *91*, 1881.
(7) Mayer, J. M. *Annu. Rev. Phys. Chem.* **2004**, *55*, 363.
(8) Costentin, C.; Robert, M.; Savéant, J.-M. *Chem. Rev.* **2010**, *110*, PR1.
(9) Bard, A. J.; Faulkner, L. R. *Electrochemical Methods: Fundamentals and Applications*; Wiley, 2000.
(10) Collman, J. P.; Devaraj, N. K.; Eberspacher, T. P. A.; Chidsey, C. E. D. *Langmuir* **2006**, *22*, 2457.
(11) Chidsey, C. E. D. *Science* **1991**, *251*, 919.
(12) Fecenko, C. J.; Meyer, T. J.; Thorp, H. H. *J. Am. Chem. Soc.* **2006**, *128*, 11020.
(13) Irebo, T.; Reece, S. Y.; Sjödin, M.; Nocera, D. G.; Hammarström, L. *J. Am. Chem. Soc.* **2007**, *129*, 15462.

(14) Chen, Z.; Vannucci, A. K.; Concepcion, J. J.; Jurss, J. W.; Meyer, T. J. *Proc. Natl. Acad. Sci. U.S.A.* **2011**, *108*, E1461.
(15) Rosenthal, J.; Nocera, D. G. *Acc. Chem. Res.* **2007**, *40*, 543.
(16) Wenger, O. S. *Acc. Chem. Res.* **2013**, *46*, 1517.
(17) Sjödin, M.; Styring, S.; Wolpher, H.; Xu, Y.; Sun, L.; Hammarström, L. *J. Am. Chem. Soc.* **2005**, *127*, 3855.
(18) Barile, C. J.; Tse, E. C. M.; Li, Y.; Sobyra, T. B.; Zimmerman, S. C.; Hosseini, A.; Gewirth, A. A. *Nat. Mater.* **2014**, *13*, 619.
(19) Hosseini, A.; Barile, C. J.; Devadoss, A.; Eberspacher, T. A.; Decreau, R. A.; Collman, J. P. *J. Am. Chem. Soc.* **2011**, *133*, 11100.
(20) Campillo-Brocal, J. C.; Lucas-Elio, P.; Sanchez-Amat, A. *MicrobiologyOpen* **2013**, *2*, 684.
(21) Tse, E. C. M.; Barile, C. J.; Gewargis, J. P.; Li, Y.; Zimmerman, S. C.; Gewirth, A. A. *Anal. Chem.* **2015**, *87*, 2403.
(22) Hall, D. G. In *Boronic Acids*; Wiley-VCH Verlag GmbH & Co. KGaA: 2006, p 1.
(23) Anslyn, E. V.; Dougherty, D. A. *Modern Physical Organic Chemistry*; University Science, 2006.
(24) Srivastava, A.; Singh, S.; Krishnamoorthy, G. *J. Phys. Chem.* **1995**, *99*, 11302.
(25) Schönfeld, P.; Schild, L.; Kunz, W. *BBA-Bioenergetics* **1989**, *977*, 266.
(26) Boulatov, R.; Collman, J. P.; Shiryaeva, I. M.; Sunderland, C. J. *J. Am. Chem. Soc.* **2002**, *124*, 11923.
(27) Walter, A.; Gutknecht, J. *J. Membrain Biol.* **1986**, *90*, 207.
(28) Babcock, L.; Pizer, R. *Inorg. Chem.* **1980**, *19*, 56.
(29) Kanicky, J. R.; Shah, D. O. *Langmuir* **2003**, *19*, 2034.
(30) Yoo, J.; Cui, Q. *Biophys. J.* **2008**, *94*, L61.
(31) Gómez-Fernández, J. C.; Villalaín, J. *Chem. Phys. Lipids* **1998**, *96*, 41.
(32) Chattopadhyay, A.; Mukherjee, S.; Rukmini, R.; Rawat, S. S.; Sudha, S. *Biophys. J.* **1997**, *73*, 839.
(33) Zhang, J.; Hadlock, T.; Gent, A.; Strichartz, G. R. *Biophys. J.* **2007**, *92*, 3988.
(34) Geletii, Y. V.; Hill, C. L.; Atalla, R. H.; Weinstock, I. A. *J. Am. Chem. Soc.* **2006**, *128*, 17033.
(35) Milstien, S.; Kapatos, G.; Levine, R. A.; Shane, B. *Chemistry and Biology of Pteridines and Folates*; Springer UC, 2002.
(36) Jain, M. K. *Introduction to Biological Membranes*; 2nd ed.; Wiley: New York, 1988.
(37) Maricle, D. L.; Hodgson, W. G. *Analytical Chemistry* **1965**, *37*, 1562.
(38) Laoire, C. O.; Mukerjee, S.; Abraham, K. M.; Plichta, E. J.; Hendrickson, M. A. *J. Phys. Chem. C* **2009**, *113*, 20127.
(39) Weaver, M. J.; Tyma, P. D.; Nettles, S. M. *J. Electroanal. Chem.* **1980**, *114*, 53.
(40) Frank, H. S.; Wen, W.-Y. *Discuss. Faraday Soc.* **1957**, *24*, 133.
(41) Weaver, M. J.; Nettles, S. M. *Inorg. Chem.* **1980**, *19*, 1641.
(42) Ghoneim, M. M.; Clouser, S.; Yeager, E. *J. Electrochem. Soc.* **1985**, *132*, 1160.
(43) Albrecht, O.; Gruler, H.; Sackmann, E. *J. Phys. France* **1978**, *39*, 301.
(44) Carley, A. N.; Kleinfeld, A. M. *Biochemistry* **2009**, *48*, 10437.
(45) Rose, M. C.; Stuehr, J. *J. Am. Chem. Soc.* **1968**, *90*, 7205.
(46) Thorseth, M. A.; Letko, C. S.; Tse, E. C. M.; Rauchfuss, T. B.; Gewirth, A. A. *Inorg. Chem.* **2012**, *52*, 628.

(47) Tse, E. C. M.; Schilter, D.; Gray, D. L.; Rauchfuss, T. B.; Gewirth, A. A. *Inorg. Chem.* **2014**, *53*, 8505.
(48) Li, M. F.; Liao, L. W.; Yuan, D. F.; Mei, D.; Chen, Y.-X. *Electrochim. Acta* **2013**, *110*, 780.
(49) Proshlyakov, D. A.; Pressler, M. A.; DeMaso, C.; Leykam, J. F.; DeWitt, D. L.; Babcock, G. T. *Science* **2000**, *290*, 1588.
(50) Nogala, W.; Szot, K.; Burchardt, M.; Jönsson-Niedziolka, M.; Rogalski, J.; Wittstock, G.; Opallo, M. *Bioelectrochemistry* **2010**, *79*, 101.
(51) Brändén, G.; Gennis, R. B.; Brzezinski, P. *BBA-Bioenergetics* **2006**, *1757*, 1052.
(52) Bento, I.; Silva, C.; Chen, Z.; Martins, L.; Lindley, P.; Soares, C. *BMC Struct. Biol.* **2010**, *10*, 28.
(53) Habrioux, A.; Servat, K.; Tingry, S.; Kokoh, B. *Performances of Enzymatic Glucose/O2 Biofuel Cells*, 2011.
(54) Blanford, C. F.; Foster, C. E.; Heath, R. S.; Armstrong, F. A. *Faraday Discuss.* **2009**, *140*, 319.
(55) Thorum, M. S.; Anderson, C. A.; Hatch, J. J.; Campbell, A. S.; Marshall, N. M.; Zimmerman, S. C.; Lu, Y.; Gewirth, A. A. *J. Phys. Chem. Lett.* **2010**, *1*, 2251.
(56) Fletcher, S. *J. Solid State Electrochem.* **2009**, *13*, 537.
(57) Kopf, M.-A.; Karlin, K. D. In *Biomimetic Oxidations Catalyzed by Transition Metal Complexes* 2000, p 309.
(58) Collman, J. P.; Devaraj, N. K.; Decréau, R. A.; Yang, Y.; Yan, Y.-L.; Ebina, W.; Eberspacher, T. A.; Chidsey, C. E. D. *Science* **2007**, *315*, 1565.

Chapter 9

The "Flip-flop" Diffusion Mechanism across Lipid Membranes

The work in this chapter was accomplished in collaboration with Dr. Christopher J. Barile,[†] Dr. Ying Li, John P. Gewargis, Nicholas A. Kirchschlager, Professor Steven C. Zimmerman, and Professor Andrew A. Gewirth.

[†] C. J. B. and E. C. M. T. contributed equally.

9.1 Introduction

Transmembrane diffusion across lipid layers is central to the understanding of fundamental biological transport processes and the development of drug delivery schemes.[1-4] In nature, organisms develop intricate ion channels and stimuli-responsive gating machineries for signal transduction, cell identification, and guarding against toxins, which still allow the uptake of compounds that are essential to survival.[5-8] Understanding membrane function is a crucial step in developing new drug therapies in a rational way.[9-13] Lipinski's rule of five describes the molecular properties crucial for the bioavailability and pharmacokinetics of candidate drugs inside human bodies and thus serves as a first-order principle for drug design.[14-17] Altering the length of an alkyl tail is a method to tune the lipophilicity of a drug, thus modifying the transport properties of the drug.[18-21]

Extensive computational efforts have been invested in studying the transport processes of drug-like compounds,[22-24] cholesterol in lipids,[25-27] and charged species through ion channels.[28,29]

While neutral amphiphilic molecules move through lipid bilayers with relative ease,[30] a multitude of pathways exist to expedite the transport process of ions across biological membranes. Ion channels gate the ion flux between intracellular and extracellular space for signaling purposes and other cellular events.[31] For transmembrane proton transport, energy-intensive proton pumps move protons against the concentration gradient.[32,33] A third mechanism to transport ions involves long-chain fatty acids which deliver protons via "flip-flop" diffusion spontaneously in the presence of a pH gradient.[34-37]

Fatty acids are known to transfer protons across lipid layers faster than unassisted proton diffusion.[30] Previous reports suggest that the length of the fatty acid plays an important role in determining the transmembrane properties of fatty acids.[38,39] The length-dependent diffusion rates across lipid membranes are thought to relate to the effective van der Waals interactions between the alkyl chains of the fatty acids and the phospholipids,[38,39] but mechanistic details of the "flip-flop" diffusion process on a molecular level are still lacking.

Experimentally, unilamellar vesicles[34] and black lipid membranes[35,36,40] are common methods utilized to mimic cell membranes. A less explored alternative is to use a hybrid bilayer membrane (HBM), which consists of a self-assembled monolayer (SAM) covered by a monolayer of lipid.[41] We previously utilized a HBM to assess anion permeability through lipids and to provide mechanistic insight into the unassisted anion transmembrane diffusion process.[42] Using the HBM construct, we also demonstrated that O_2 reduction ($O_2 + 4H^+ + 4e^- \rightarrow 2H_2O$) by CuBTT (CuBTT = copper complex of 6-((3-(benzylamino)-1,2,4-triazol-5-yl)amino)hexane-1-thiol) is kinetically limited by proton transfer kinetics, suggesting that the rate-determining step (RDS) of O_2 reduction is the "flip-flop" diffusion of a proton carrier across the lipid membrane.[43]

However, the precise details of the "flip-flop" diffusion cycle describing how proton carriers deliver protons across a lipid layer in a HBM are currently unknown.

In this paper, we gain mechanistic insight into the proton carrier diffusion pathway in a HBM during O_2 reduction. We systematically vary the composition of the proton carrier and the lipid in the HBM and model the resulting trends in O_2 reduction activity in terms of fundamental physicochemical parameters. Scheme 9.1 displays a HBM containing CuBTT with an overlaid O_2 reduction mechanism. The SAM consisting of CuBTT (blue) mediates the reduction of O_2 to H_2O. Electron transport occurs through the SAM from the Au electrode, while an amphiphilic proton carrier (green) incorporated in the lipid layer (red) transports the protons necessary for the O_2 reduction process.

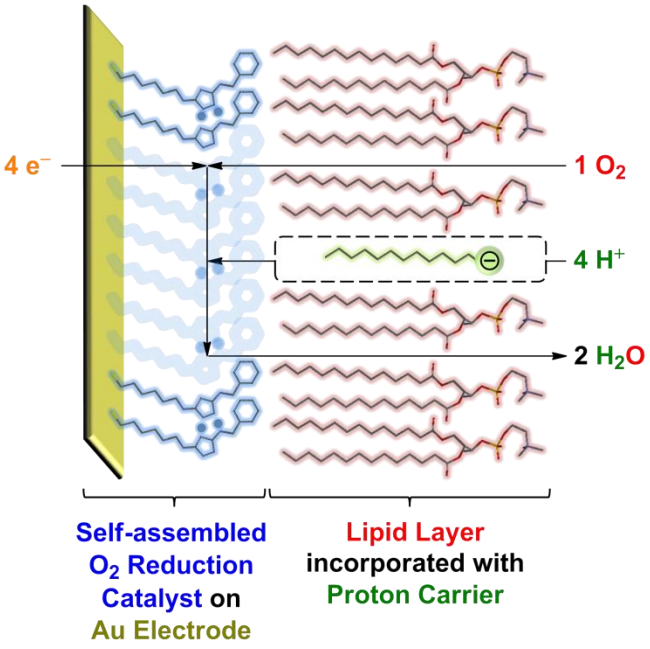

Scheme 9.1. Schematic of a hybrid bilayer membrane (HBM) containing an O_2 reduction electrocatalyst (blue) self-assembled on Au covered by a monolayer of lipid (red) incorporated with a proton carrier (green) which undergoes "flip-flop" diffusion (dashed box) to catalyze O_2 reduction to generate H_2O.

9.2 General Experimental Section

Chemicals were obtained from commercial sources and used without further purification unless otherwise specified. Lipids were purchased from Avanti Polar Lipids (Alabaster, AL) and mono-*N*-dodecylphosphate (MDP) was purchased from Sigma-Aldrich (St. Louis, MO). 1-octylboronic acid (C8-BA), 1-decylboronic acid (C10-BA), 1-dodecylboronic acid (C12-BA), and 1-tetradecylboronic acid (C14-BA) were purchased from Alfa Aesar (Ward Hill, MA). The synthesis procedure and characterization data of *N*-methyliminodiacetate (MIDA) protected 1-(MIDA boryl)undecane (C11-B-MIDA), 1-(MIDA boryl)tridecane (C13-B-MIDA), and (4-(*p*-tolylethynyl)phenethyl) MIDA boronate (rigid-B-MIDA) and the deprotection method to afford 1-undecylboronic acid (C11-BA), 1-tridecylboronic acid (C13-BA), and (4-(*p*-tolylethynyl)phenethyl)boronic acid (rigid-BA) are presented in Sections 9.3 and 9.4.

9.3 Synthetic Procedures of Proton Carriers

All reactions were carried out under a dry N_2 atmosphere. Chemicals were purchased from commercial sources and used without further purification. Dry dichloromethane (DCM), tetrahydrofuran (THF), and dimethyl sulfoxide (DMSO) were used directly from a solvent delivery system just prior to use. Freshly-purchased triethylamine (TEA) was dried and stored over 4 Å molecular sieves. All other solvents, like methanol (MeOH), were of reagent grade and used without further purification. Reported reaction temperatures refer to the temperature of the heating medium. The progress of reactions was monitored by silica gel thin layer chromatography (TLC) using 0.2 mm silica 60 coated, plastic plates with F254 indicator. Flash and gravity chromatography was performed using 230-400 mesh (40-63 μm) silica gel (SiO_2). Ratios of solvents for NMR solvents and flash chromatography are reported as volume ratios.

NMR spectra were performed in $CDCl_3$ and acquired using a Varian Unity 500 MHz instrument in the VOICE laboratory, University of Illinois at Urbana-Champaign, unless otherwise specified. Chemical shifts (δ) and coupling constants (J) are reported in parts per million (ppm) and hertz (Hz), respectively. For ^1H spectra, chemical shifts are referenced to the residual proton solvent peak: 7.26 ppm for $CDCl_3$ and 3.35 ppm for CD_3OD. For ^{13}C spectra, chemical shifts are referenced to the solvent peak at 77.5 ppm in $CDCl_3$ and 49.3 ppm for CD_3OD. Electrospray ionization mass spectrometry (ESI-MS) data were collected with a Quattro II instrument (Waters) at the University of Illinois at Urbana-Champaign.

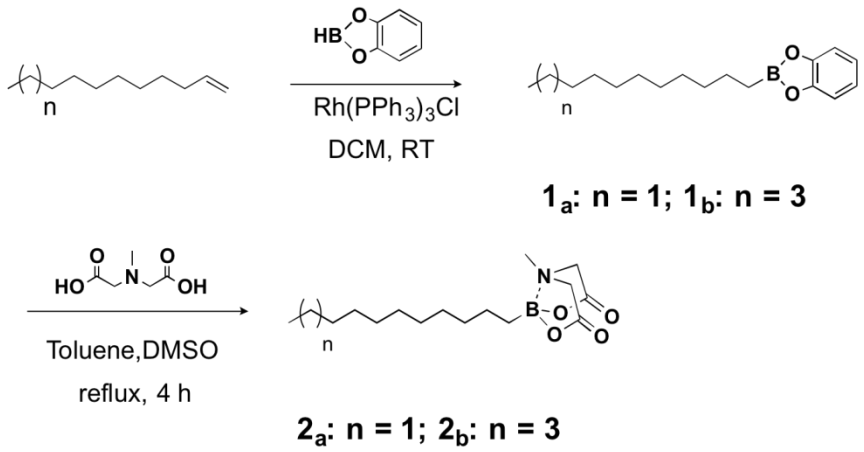

Scheme 9.2. Preparation of MIDA-protected C11- and C13- boronic acids.

C11-B-MIDA (2_a): To a solution of 1-undecene (463 mg, 3 mmol) in 3 mL of toluene, catecholborane (360 mg, 3 mmol) and $Rh(PPh_3)_3Cl$ (28 mg, 0.03 mmol) were added. The mixture was stirred at room temperature for 1 h. To the solution, 1 mL DMSO and *N*-methyliminodiacetic acid (441 mg, 3 mmol) were added. The suspension was refluxed for 4 h and became homogenous after 15 min. The solution was cooled to room temperature and concentrated down under reduced pressure. The solution was precipitated into 30 mL of diethyl

ether, and the precipitation was collected by vacuum filtration. The crude solid was further purified by gradient column chromatography (silica, hexanes:EtOAc:MeOH = 1:10:0 to 0:10:0 to 0:10:1) to give a white solid (yield: 234 mg, 25 %). ^{1}H NMR δ 3.81 (d, *J*=16.5, 2H), 3.67 (d, *J*=16, 2H), 2.91 (s, 3H), 1.42-1.20 (m, 18H), 0.878 (t, *J*=7, 3H), 0.64-0.57 (m, 2H). ^{13}C NMR (125 MHz): 167.0, 45.9, 33.1, 32.2, 30.0, 29.9, 29.8, 29.7, 29.6, 24.2, 22.9, 14.38. HR-ESI (*m/z*): $[M+H]^+$ calcd for $C_{16}H_{30}BNO_4$, 312.2346; found 312.2343 $[M+H]^+$.

C13-B-MIDA (2_b): Similar procedure gave an off-white solid (yield: 218 mg, 21 %). ^{1}H NMR (CD_3OD:$CDCl_3$=1:9): δ 3.86 (d, J= 16.5, 2H), 3.65 (d, J=16.5, 2H), 2.82 (s, 3H), 1.35-1.10 (m, 22H), 0.80 (t, J=7, 3H), 0.53 (m, 2H). ^{13}C NMR (125 MHz, CD_3OD:$CDCl_3$=1:9): 168.2, 61.9, 61.8, 61.7(5), 45.5(9), 45.5(4), 32.9, 31.9, 29.6(8), 29.6(4), 29.6(1), 29.5, 29.3, 24.0, 22.7, 14.0. HR-ESI (*m/z*): $[M+H]^+$ calcd for $C_{18}H_{34}BNO_4$, 340.2659; found 340.2662 $[M+H]^+$.

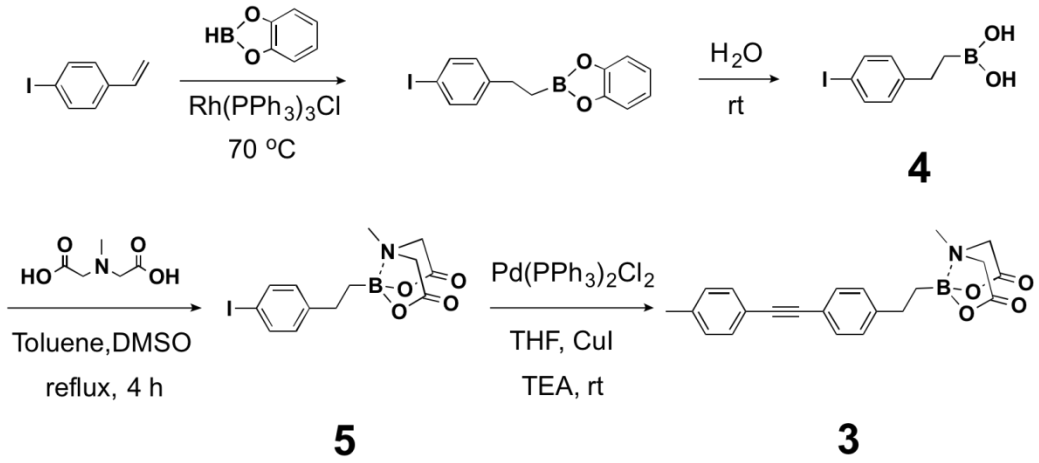

Scheme 9.3. Preparation of MIDA-protected rigid boronic acid.

4: To a 7-mL vial, 4-iodostyrene (200 mg, 0.87 mmol), catecholborane (106 μl, 1 mmol), and tris(triphenyl-phosphine)rhodium(I) chloride (2 mg, 2.2 μmol) were added. The mixture was

heated to 70 ^{o}C for 6 h. The reaction was cooled to room temperature and 2 mL of water was added. The mixture was stirred at room temperature for 2 h. The aqueous layer was extracted with DCM. The organic layers were combined and concentrated down under reduced pressure. The crude product was used in the next step without further purification.

5: To a solution of **4** (0.87 mmol, assuming full conversion from the first step) in 1 mL of toluene and 0.2 mL of DMSO, *N*-methyliminodiacetic acid (132 mg, 0.9 mmol) was added. The mixture was heated to 110 ^{o}C for 4 h. The reaction was cooled to room temperature, diluted with DCM, and washed with water. The organic layer was dried over Na_2SO_4, and the solvent was removed under reduced pressure. The crude product was purified by gradient column chromatography (silica, MeOH:DCM = 1:99 to 5:95) to give a brown solid (yield: 130 mg, 39%). ^{1}H NMR (CD_3OD:$CDCl_3$=1:9): δ 7.49 (d, *J*=8, 2H), 6.88 (d, *J*=8, 2H), 3.90 (d, *J*=16.5, 2H), 3.67 (d, *J*=17, 2H), 2.79 (s, 3H), 2.57 (m, 2H), 0.81 (m, 2H).

(4-(p-tolylethynyl)phenethyl) MIDA boronate (rigid-B-MIDA) (3): To a solution of **5** (20 mg, 0.05 mmol) and 4-ethynyltoluene (30 mg, 0.26 mmol) in 1 mL of THF, bis(triphenylphosphine)palladium(II) dichloride (2 mg, 2.8 μmol), copper iodide (2 mg, 10 μmol), and triethylamine (0.1 mL, 0.7 mmol) were added. The reaction was stirred at room temperature for 16 h. The mixture was diluted with DCM and washed with water. The organic layer was dried over Na_2SO_4, and the solvent was removed under reduced pressure. The crude product was purified by gradient column chromatography (silica, MeOH:DCM = 1:99 to 5:95) to give a light brown solid (yield: 11 mg, 59%). ^{1}H NMR δ 7.44 (d, *J*=8, 2H), 7.41 (d, *J*=8, 2H), 7.19 (d, *J*=8, 2H), 7.15 (d, *J*=8, 2H), 3.81 (d, *J*=16, 2H), 3.65 (d, *J*=16, 2H), 2.87 (s, 3H), 2.77

(m, 2H), 2.37 (s, 3H), 0.96 (m, 2H). ^{13}C NMR (125 MHz, CD_3OD:$CDCl_3$=1:9): δ 168.0, 145.0, 138.2, 131.5, 131.3, 129.0, 127.9, 120.5, 120.2, 88.9, 88.7, 61.8, 45.6, 30.0, 21.3. HR-ESI (*m*/*z*): $[M+H]^+$ calcd for $C_{22}H_{23}BNO_4$, 376.1720; found, 376.1736.

General deprotection scheme for protected alkylboronic acids: The *in situ* deprotection of **2$_a$, 2$_b$** or rigid-B-MIDA was performed by dissolving **2$_a$, 2$_b$** or rigid-B-MIDA (5.4 μmol) in THF (0.2 mL). NaOH (0.01 mL, 10 M) was added, and the resulting solution was stirred vigorously for 15 min at room temperature. NH_4Cl (9 mL, sat. aq.) was then added, and the mixture was stirred vigorously for 5 min. Diethyl ether (9 mL × 3) was added to extract the organic layer, which was then combined, dried, and concentrated down under reduced pressure to about 0.1 mL. The deprotected alkylboronic acid solutions were used to make lipid forming solutions without further purification.

9.4 NMR Spectra of the Proton Carriers

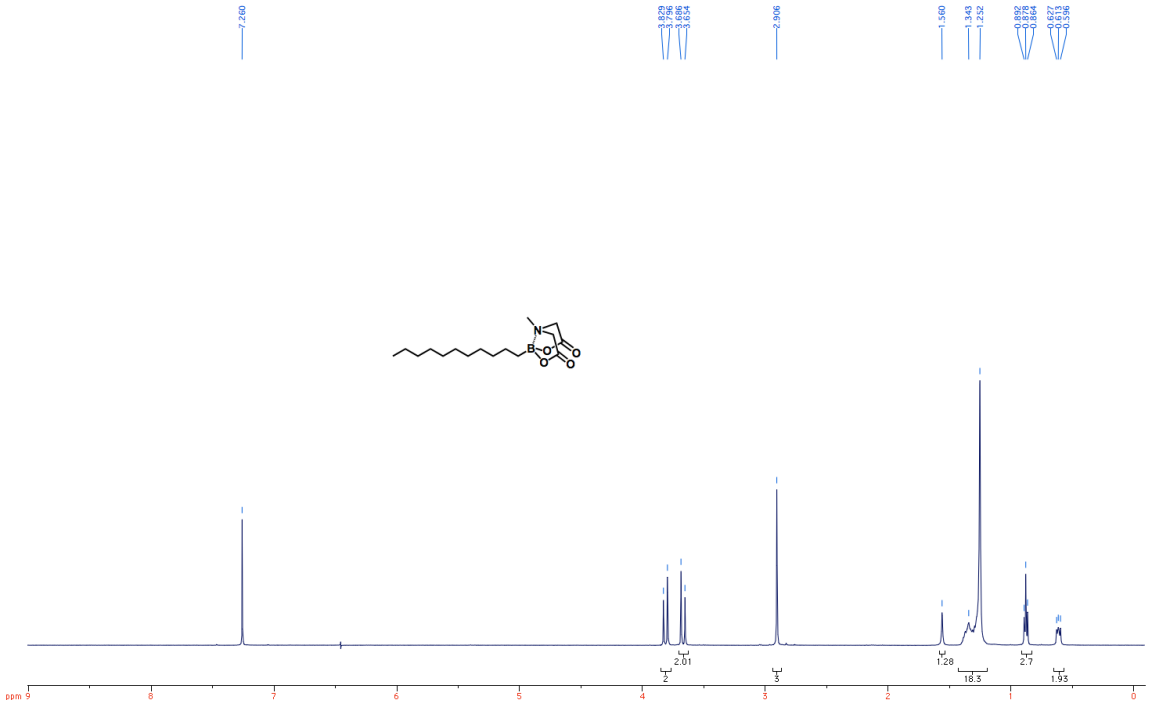

Figure 9.1. ^{1}H NMR spectrum of $\mathbf{2_a}$.

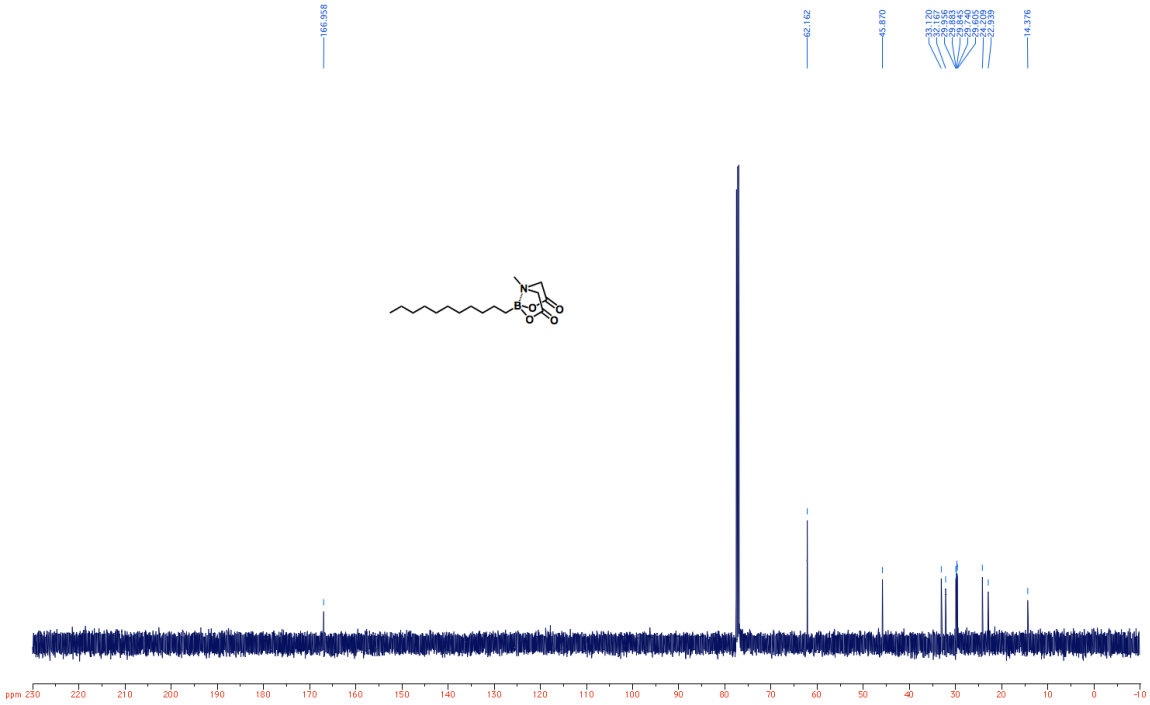

Figure 9.2. ^{13}C NMR spectrum of $\mathbf{2_a}$.

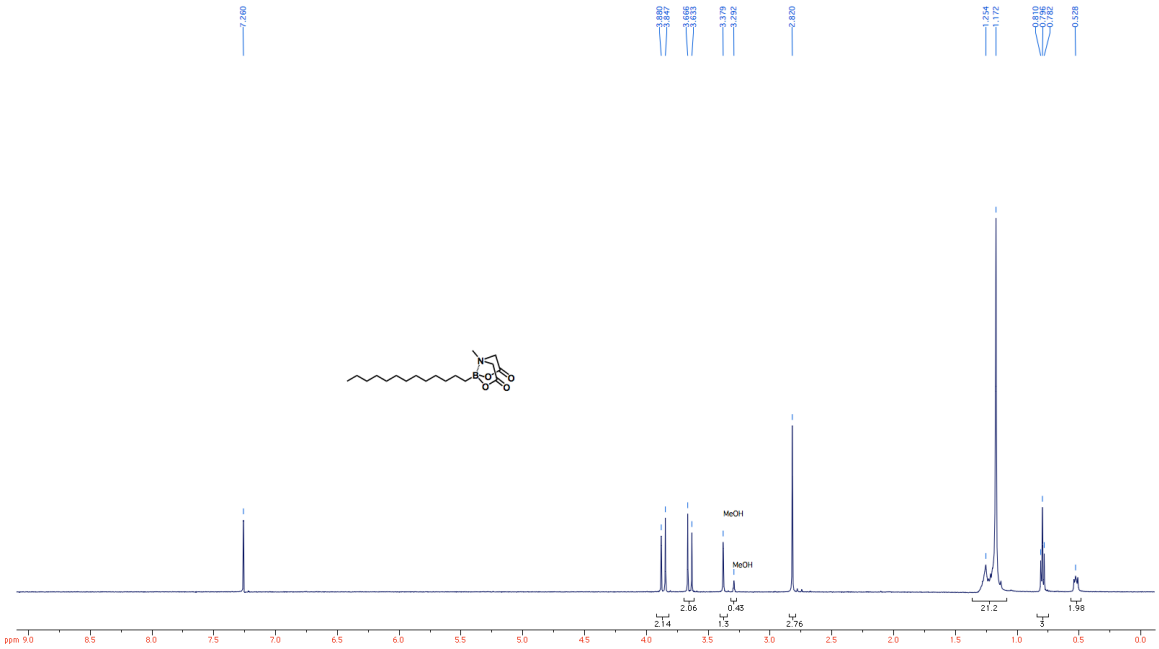

Figure 9.3. ^{1}H NMR spectrum of **2_b**.

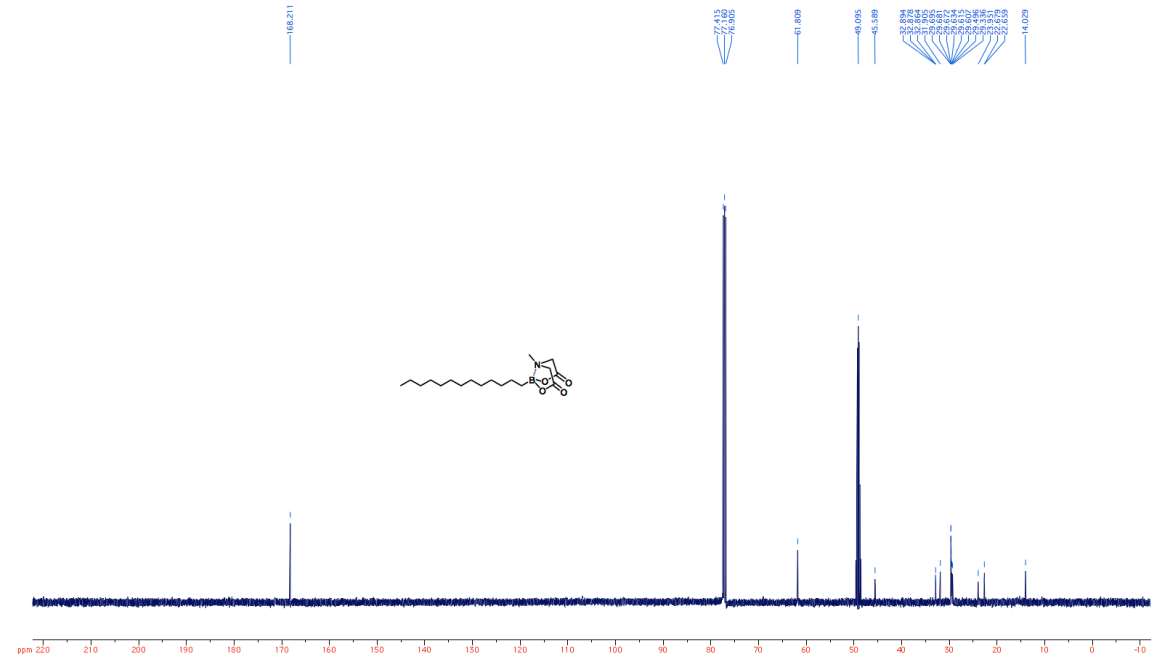

Figure 9.4. ^{13}C NMR spectrum of **2_b**.

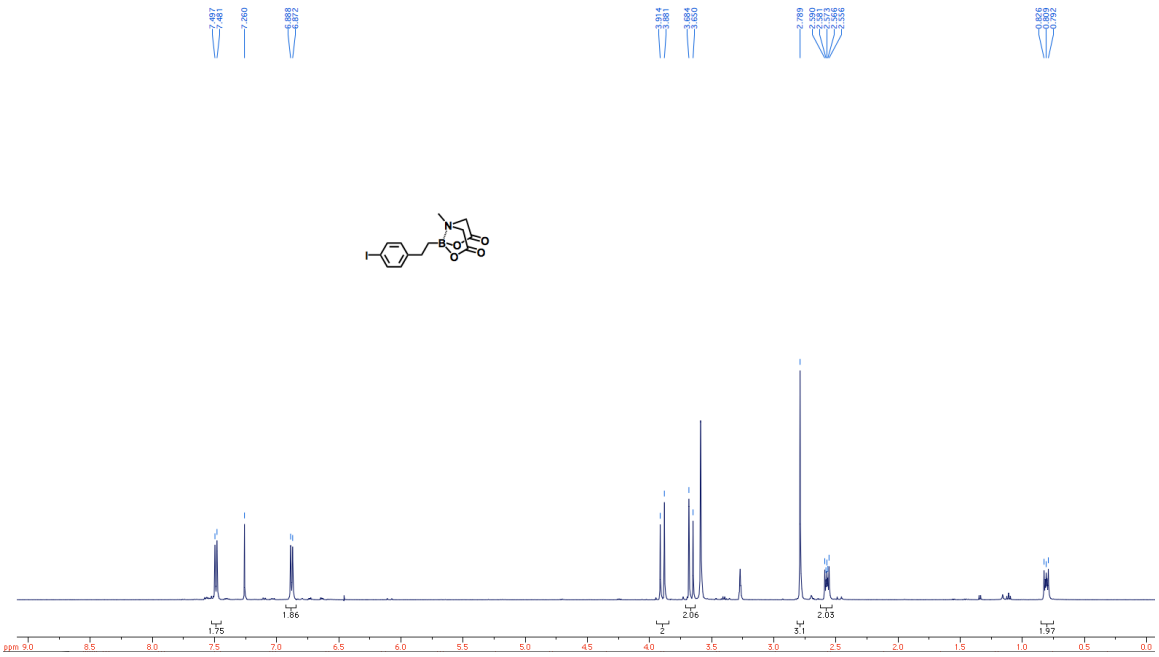

Figure 9.5. ^{1}H NMR spectrum of **5**.

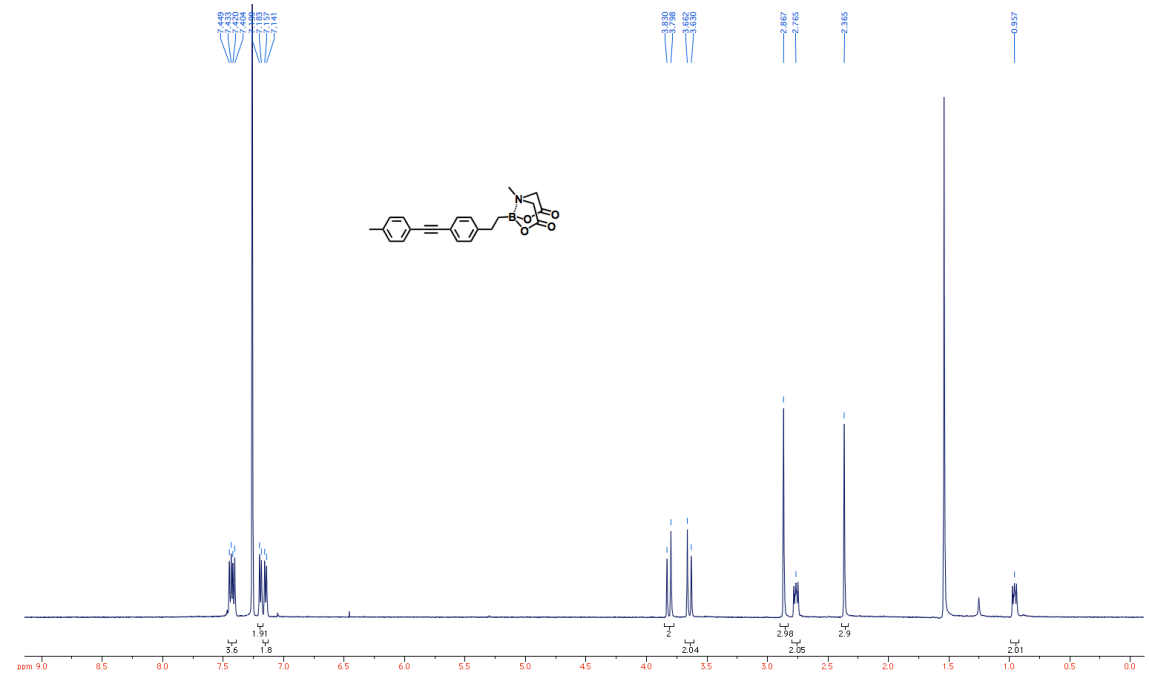

Figure 9.6. ^{1}H NMR spectrum of rigid-B-MIDA (**3**).

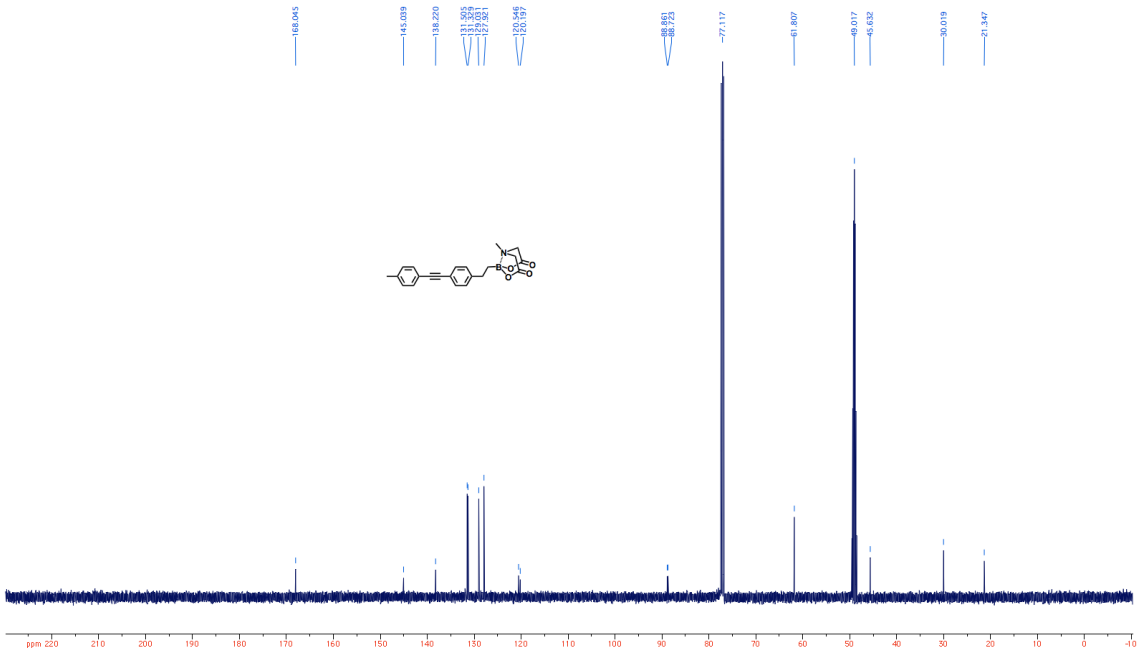

Figure 9.7. ^{13}C NMR spectrum of rigid-B-MIDA (**3**).

9.5 HBM Construction Procedures

Caution! Perchlorate salts are potentially explosive. Only small amounts of materials should be prepared.

Table 9.1. Comparison of lipids used in this study and their gel-phase transition temperatures.[44,45]

Lipid Name	Name based on the Number of Carbons in the Lipid Tail	Gel-phase Transition Temperature (°C)
1,2-dilauroyl-*sn*-glycero-3-phosphocholine (DLPC)	C12-PC	-2
1,2-ditridecanoyl-*sn*-glycero-3-phosphocholine	C13-PC	14
1,2-dimyristoyl-*sn*-glycero-3-phosphocholine (DMPC)	C14-PC	24
1,2-dipentadecanoyl-*sn*-glycero-3-phosphocholine	C15-PC	35
1,2-dipalmitoyl-*sn*-glycero-3-phosphocholine (DPPC)	C16-PC	41

Preparation of the HBM system was reported elsewhere.[43] In short, 6-((3-(benzylamino)-1,2,4-triazol-5-yl)amino)hexane-1-thiol (BTT) was synthesized and deposited as a SAM on a Au working electrode. Cu ions were incorporated into the BTT-modified Au surface using an ethanolic solution of $Cu(ClO_4)_2$. The BTT SAM was then covered by a monolayer of 1,2-dilauroyl-*sn*-glycero-3-phosphocholine (DLPC, C12-PC), 1,2-ditridecanoyl-*sn*-glycero-3-phosphocholine (C13-PC), 1,2-dimyristoyl-*sn*-glycero-3-phosphocholine (DMPC, C14-PC), 1,2-dipentadecanoyl-*sn*-glycero-3-phosphocholine (C15-PC), or 1,2-dipalmitoyl-*sn*-glycero-3-phosphocholine (DPPC, C16-PC) with and without 1 equivalent of proton carrier added as described previously for the MDP-(C14-PC) system [41,46]. To prepare the lipid-forming solution containing C15-PC or C16-PC, the solution was kept at ~50 °C or ~70 °C, respectively, during vesicle formation.

For experiments conducted at temperatures above the gel-phase transition temperatures (T_m) of lipids, the buffer solutions were kept at room temperature ((25 ± 1) °C) for C12-PC, C13-PC, and C14-PC, at (50 ± 1) °C for C15-PC, and at (60 ± 1) °C for C16-PC. For experiments conducted at temperatures below the T_m of lipids, the buffer solutions were kept at (5 ± 1) °C for C13-PC, (10 ± 1) °C for C14-PC, and room temperature ((25 ± 1) °C) for C15-PC and C16-PC.

9.6 Biophysical Modeling Methods

All length measurements of lipids and proton carriers were calculated using Spartan ’08 (Wavefunction, Inc.) version 1.2.0. The lengths of the negatively-charged head group of MDP and the boronic acid proton carriers were calculated to be 4.2 Å and 3.0 Å, respectively. The intermolecular distance between all proton carriers and neighboring lipids was taken to be 4.2 Å. The intermolecular distance between lipid molecules was taken to be 8.0 Å, a value derived from

the lateral packing density of phosphocholine lipids.[47-49] Figure 9.8 displays the lengths calculated for the different sections of lipids, total lengths of lipids, and lengths of MDP and BA proton carriers used in the modeling. The values for the elementary charge and permittivity of free space were taken to be 1.602 x 10^{-19} C and 8.854 x 10^{-12} F/m.[50] Professor Zaida Luthey-Schulten and Dr. Zhaleh Ghaemi provided inputs to our modeling methods.

9.7 Effect of Lipid Tail Length on O_2 Reduction by CuBTT inside a HBM

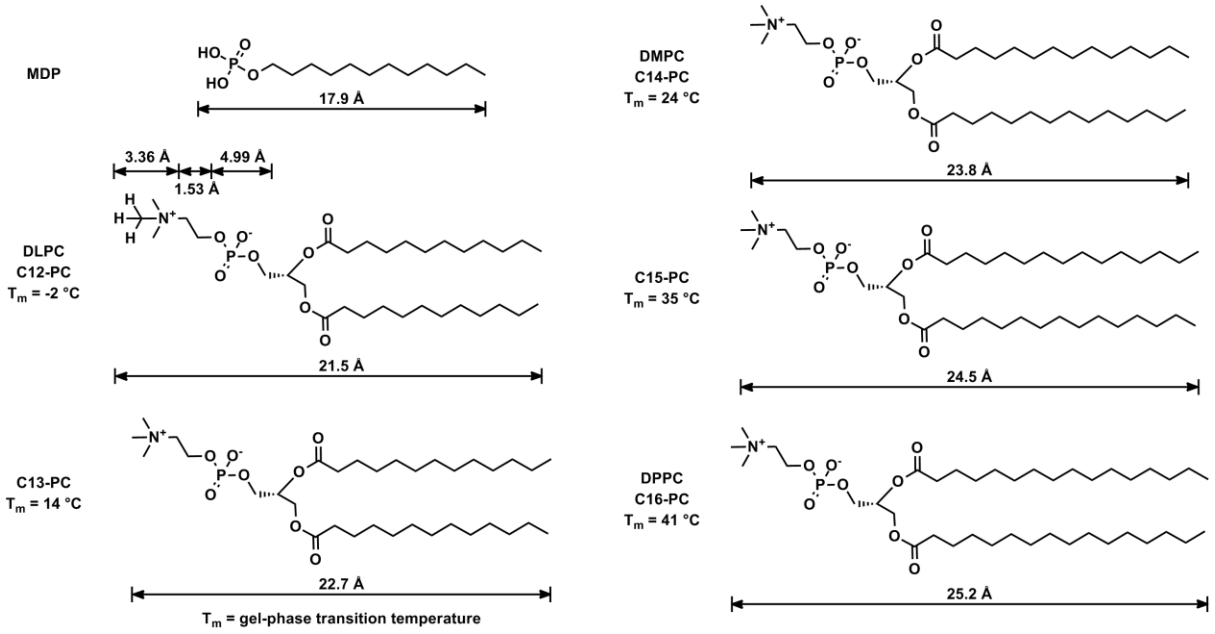

Figure 9.8a. Structures, numbers of carbons in the tail chain, gel-phase transition temperatures (T_m), and calculated lengths of MDP and lipids used in this study.[44,45]

To interrogate the "flip-flop" diffusion process of proton carriers across the lipid membrane of a HBM as indicated by the dashed box in Scheme 9.1, we first varied the chain length of the lipid used while holding the length of the proton carrier constant. As the length of lipid increases, the gel-phase transition temperature (T_m) of the lipid increases as well. Table 9.1 and Figure 9.8 show the T_m values and the number of carbon atoms in the tail of the lipids used

in the HBMs in this study. We previously determined that at temperatures below the T_m of lipids, proton carriers incorporated in the lipid layer of a HBM do not undergo "flip-flop" diffusion because the proton carrier is immobile in the solid lipid matrix.[43]

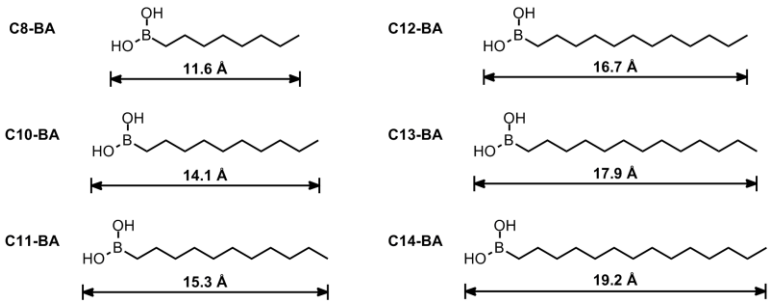

Figure 9.8b. Structures, numbers of carbons in the tail chain, and calculated lengths of boronic acids used in this study.

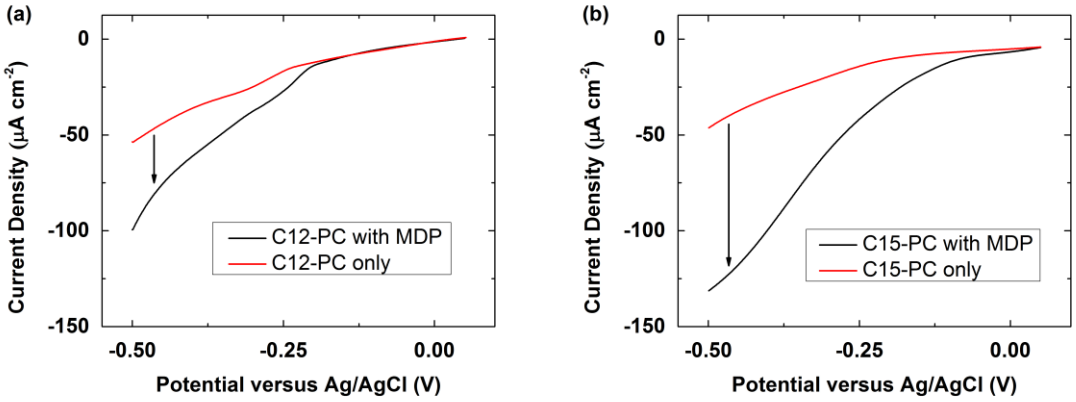

Figure 9.9. Linear sweep voltammograms (LSVs) of O_2 reduction by CuBTT covered by a monolayer of (a) C12-PC and (b) C15-PC (red lines) with 1 equivalent of MDP added (black lines) in O_2-saturated pH 5 phosphate buffer solution at temperatures above the gel-phase transition temperatures (T_m) of the corresponding lipids.

Figures 9.9a and b show linear sweep voltammograms (LSVs) of O_2 reduction by CuBTT with HBM with and without MDP incorporated in C12-PC and C15-PC, respectively. Above the T_m of C12-PC and C15-PC, the O_2 reduction current densities of CuBTT inside the HBM with

MDP are enhanced compared to the HBMs without proton carrier. The current enhancement (defined as the ratio of the O_2 reduction current with and without MDP obtained at -500 mV) with MDP incorporation observed in HBM containing C12-PC and C15-PC is (37 ± 41) % and (196 ± 76) %, respectively. Interestingly, we found that when C14-PC formed the HBM, the current enhancement is (343 ± 209) %,[43] which is greater than that measured using either the shorter or longer lipids. The decreased enhancement for C12-PC and C15-PC suggests that there is a mismatch between the chain lengths of the proton carrier and the lipid layer which changes the ability of MDP to transfer protons.

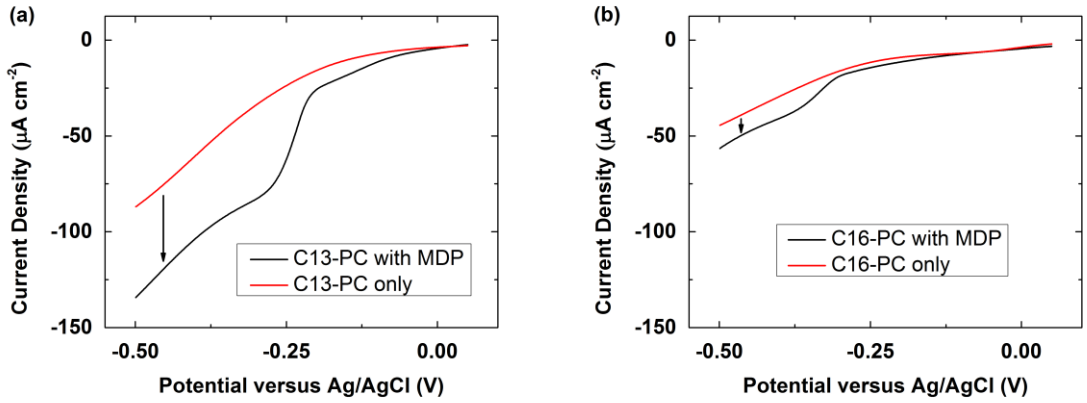

Figure 9.10. LSVs of O_2 reduction by CuBTT covered by a monolayer of (a) C13-PC and (b) C16-PC (red lines) with 1 equivalent of MDP added (black lines) in O_2-saturated pH 5 phosphate buffer solution at temperatures *above* the T_m of the corresponding lipids.

Figures 9.10a and b display LSVs of O_2 reduction by CuBTT in a HBM with and without MDP incorporated in C13-PC and C16-PC, respectively. At temperatures above the T_m of C13-PC and C16-PC, the O_2 reduction current is enhanced by the presence of MDP. However, the current enhancement by MDP observed in the HBM containing C16-PC is less than that of the HBM containing C13-PC, demonstrating that the chain length of the lipid modulates the

effectiveness with which MDP delivers protons to CuBTT. In these cases, as with C12-PC and C15-PC, less O_2 reduction current enhancement is seen in the presence of MDP than with C14-PC.

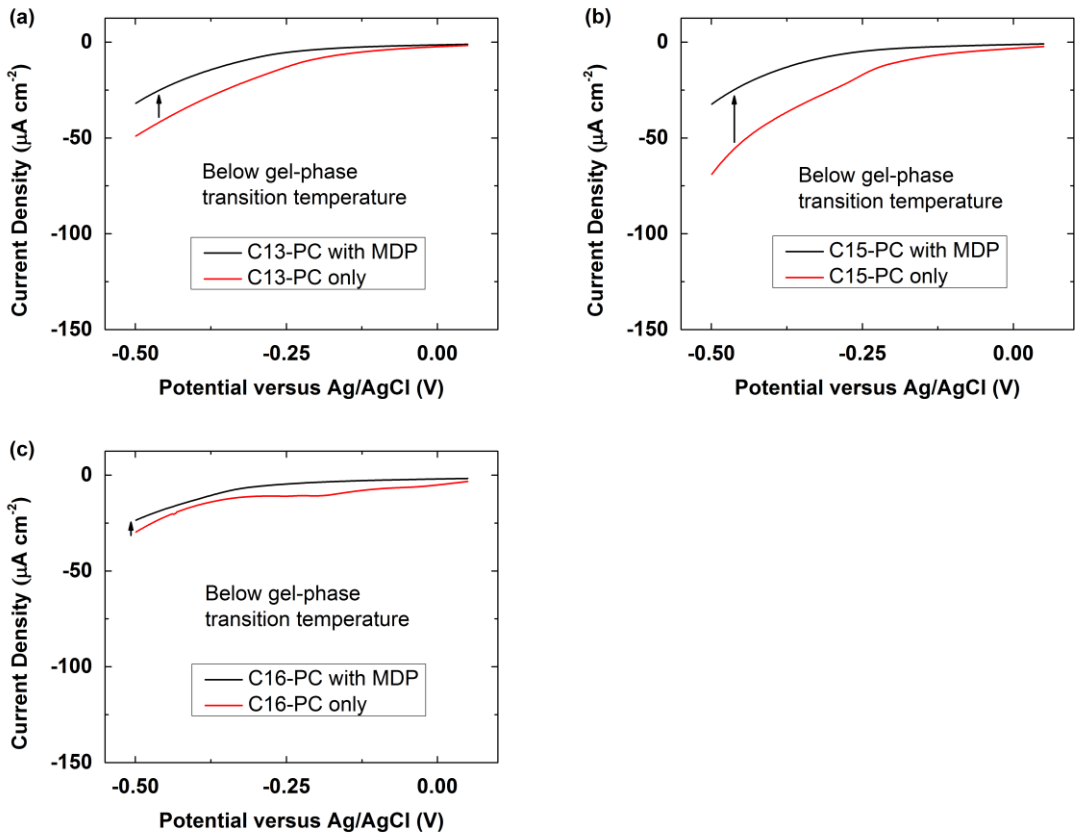

Figure 9.11. LSVs of O_2 reduction by CuBTT covered by a monolayer of (a) C13-PC, (b) C15-PC, and (c) C16-PC lipids (red lines) with 1 equivalent of MDP added (black lines) in O_2-saturated pH 5 phosphate buffer solution at temperatures *below* the T_m of the corresponding lipids.

Figures 9.11a-c show the change in O_2 reduction activity by the HBM containing CuBTT with and without proton carrier incorporated in the lipid layer at temperatures below the T_m of the lipids. Since the C12-PC-based HBM exhibits a T_m of -2 °C, we were not able to probe whether MDP enhances proton transport to CuBTT in gel-phase C12-PC. However, for the cases

with temperatures below the T_m of C13-PC, C15-PC and C16-PC, the O_2 reduction current densities of CuBTT inside the HBM with MDP is lower compared to the HBM without proton carrier. In the presence of MDP, the lipid layer is more densely pack, thus further inhibiting the O_2 reduction activity. This finding is similar to what we previously observed for MDP incorporated in C14-PC at 10 °C.[43]

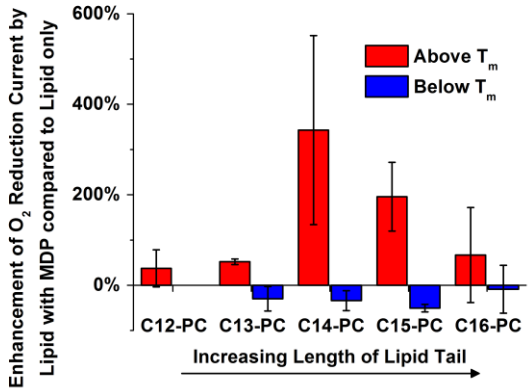

Figure 9.12. Summary of the percent enhancement of O_2 reduction current densities by CuBTT in HBMs containing MDP in the C12-PC, C13-PC, C14-PC, C15-PC, and C16-PC lipid layers above (red bars) and below (blue bars) the T_m of the lipids.

Figure 9.12 displays the percent enhancement of O_2 reduction current densities by CuBTT in HBMs with MDP in the C12-PC, C13-PC, C14-PC, C15-PC, and C16-PC lipid layers. For all lipids tested, at temperatures below the T_m of the lipids (Figure 9.12 blue bars and Figure 9.11), the presence of MDP does not enhance the O_2 reduction current density. Above the T_m of the lipids (Figure 9.12 red bars), however, MDP delivers protons to CuBTT via "flip-flop" diffusion, thus resulting in increased O_2 reduction current density. The HBM containing MDP in C14-PC exhibits the highest O_2 reduction current density compared to the HBMs with the other lipids, suggesting that the MDP proton carrier bearing a 12-carbon chain in a lipid layer with a

14-carbon tail provides the optimal condition for a proton carrier to undergo "flip-flop" diffusion to deliver protons for O_2 reduction in a HBM.

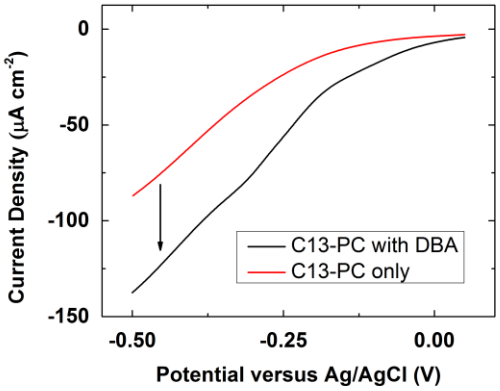

Figure 9.13. LSVs of O_2 reduction by CuBTT covered by a monolayer of C13-PC (red line) with 1 equivalent of C12-BA added (black line) in O_2-saturated pH 5 phosphate buffer solution at room temperature.

To demonstrate that the lipid chain length effect is independent of proton carrier identity, we repeated these measurements using 1-dodecylboronic acid (C12-BA), a proton carrier we found to exhibit large enhancements (ca. 750 %) at pH 5 (See Chapter 8). The black line in Figure 9.13 displays the LSV of O_2 reduction by CuBTT in a HBM containing C12-BA incorporated in C13-PC. Incorporation of C12-BA in C13-PC results in an enhancement of (42 ± 17) % in O_2 reduction current as compared to the C13-PC only case. In contrast, incorporation of C12-BA in C14-PC resulted in an enhancement of (524 ± 193) % in O_2 reduction current as compared to the C14-PC only case. Changing from C14-PC to C13-PC with C12-BA as the proton carrier results in a substantial decrease in the O_2 reduction current. The decline in O_2 reduction current enhancement upon decreasing the lipid length is also observed in the MDP-(C14-PC) system, suggesting that the current enhancement is independent of the identity of the

proton carrier head group, but instead is dependent on the lipid tail length and the proton carrier tail length.

9.8 Effect of Proton Carrier Length on O_2 Reduction by CuBTT inside a HBM

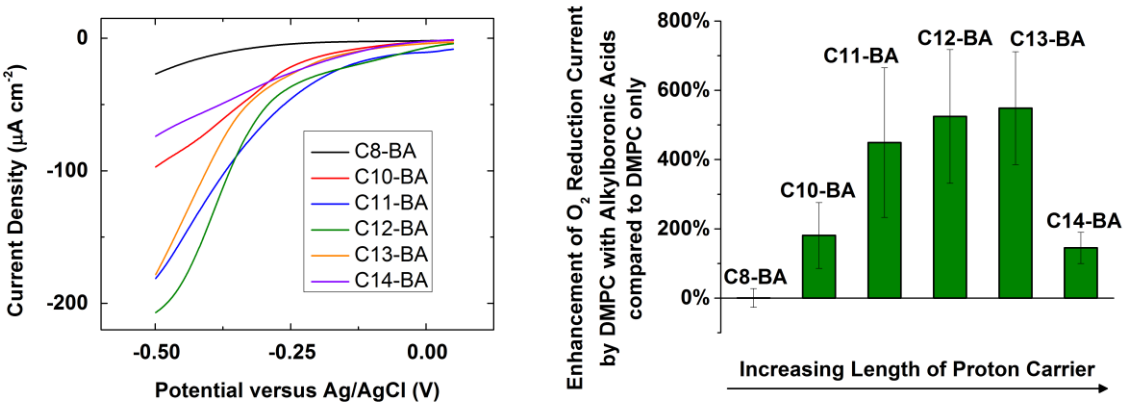

Figure 9.14. (a) LSVs of O_2 reduction by CuBTT in a HBM with 1 equivalent of C8- (black), C10- (red), C11- (blue), C12- (green), C13- (orange) and C14- (purple) BA added to the C14-PC layer at pH 7 at 26 °C. (b) Summary of the percent enhancement of O_2 reduction current densities by CuBTT in HBMs containing BA's of different lengths in the C14-PC lipid layer as compared to the HBMs without proton carrier.

Moving forward, we address the effect of proton carrier length on O_2 reduction by CuBTT in a HBM containing C14-PC. Figure 9.14a shows O_2 reduction LSVs of CuBTT in a HBM with alkylboronic acids of different lengths incorporated in C14-PC. The O_2 reduction current density increases as the chain length of the proton carrier increases from C8 to C12. Intriguingly, the O_2 reduction current density decreases as the chain length of the proton carrier increases from C13 to C14. Figure 9.14b summarizes the percent enhancement of the catalytic O_2 reduction current densities by CuBTT in a HBM using alkylboronic acids with various chain lengths, from 8-carbon to 14-carbon, as compared to the cases without proton carrier. Similar to the lipid chain length study, we find a proton carrier with about a 12- or 13-carbon chain in a

lipid layer with a 14-carbon tail to be the optimal pair to facilitate proton delivery to CuBTT via "flip-flop" diffusion for O_2 reduction.

9.9 Optimal Lengths of Lipids and Proton Carriers

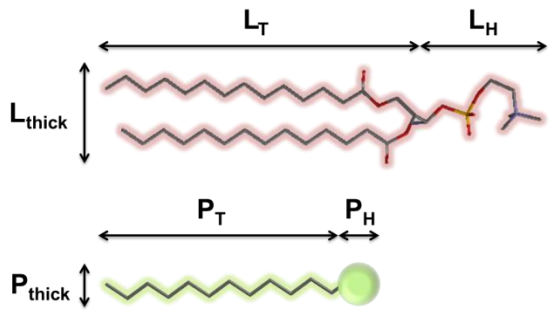

Figure 9.15. Definitions used for modeling studies of lipid and proton carrier: L_T = length of lipid tail, L_H = length of lipid head, L_{thick} = thickness of lipid, P_T = length of proton carrier tail, P_H = length of proton carrier head, and P_{thick} = thickness of proton carrier.

From the two sets of experiments described in sections 9.7 and 9.8, we determined that the O_2 reduction current density inside a HBM by CuBTT depends upon both the lengths of the proton carrier and lipid. This result demonstrates that for both sets of experiments, optimal O_2 reduction occurs when the HBM meets certain lipid-proton carrier length criteria. The results also indicate that this relative enhancement effect is independent of the identity of the head group and depends only on the difference between the lengths of the proton carrier and lipid. We thus consider the differences in lengths between the lipid tail (L_T) and the proton carrier tail (P_T) as shown in Figure 9.15.

Figure 9.16 compares the enhancement of O_2 reduction current by the lipid-embedded proton carriers as a function of $L_T - P_T$. For all values of $L_T - P_T$, the magnitudes of current enhancement by boronic acid proton carriers (blue) is greater than those by phosphate proton carriers (black). The results from Chapter 8 suggests that the BA-based proton carriers diffuse

more readily through lipid layers than their phosphate counterparts, a phenomenon likely due to the higher pK_a of the BA head group relative to that of MDP. Figure 9.16 shows that when the proton carrier tail length and lipid tail length are comparable ($L_T - P_T$ = 4 to 6 Å), the O_2 reduction current enhancement is low and thus proton transfer via the carrier is slow. Similarly, if the gap between the tail lengths of proton carrier and lipid is too large ($L_T - P_T$ = 10 to 14 Å), the proton carriers again do not substantially affect the O_2 reduction current. Intriguingly, in the regime of $L_T - P_T$ = 6 to 10 Å, there is significantly greater O_2 reduction current enhancement found with the addition of the proton carrier. These findings indicate that 6 to 10 Å is the optimal length difference between the tails of the proton carrier and the lipid to maximize the rate of transmembrane proton delivery.

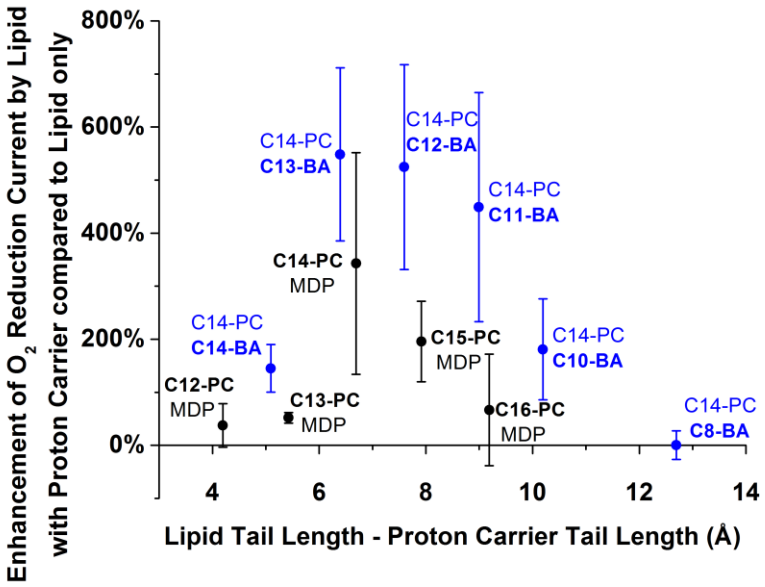

Figure 9.16. Summary of the percent enhancement of the O_2 reduction current by CuBTT in a HBM with boronic acids of different lengths added to a C14-PC layer (blue) and MDP added to lipids of different lengths (black) as compared to the HBM without proton carrier above the T_m of the lipids.

9.10 Energy Calculations and Mechanistic Modeling of the "Flip-flop" Diffusion Process

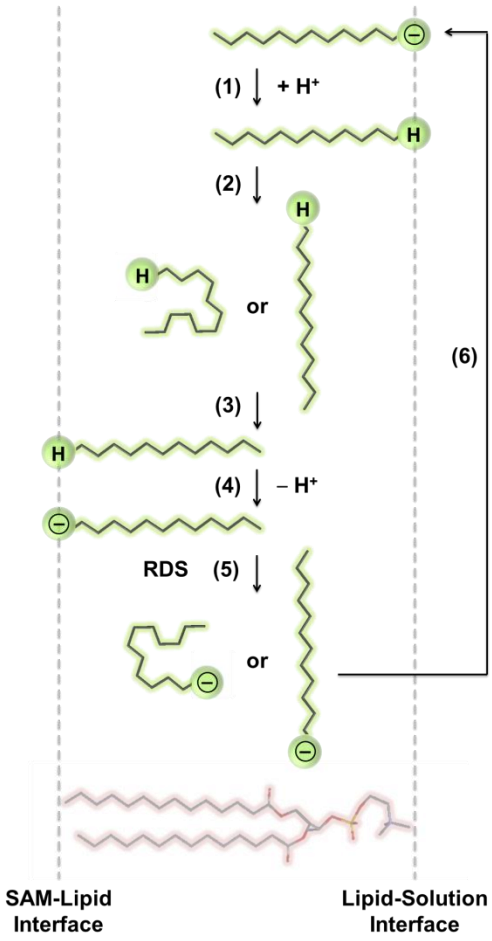

Figure 9.17. Detailed transmembrane "flip-flop" diffusion cycles of a proton carrier that involves bending and rotation or rotation only: (1) = protonation of anionic proton carrier, (2) & (3) = flipping of neutral proton carrier, (4) = deprotonation of neutral proton carrier, and (5) & (6) = flipping of anionic proton carrier.

To understand the empirical dependency of transmembrane proton transport on the chain lengths of proton carriers and lipids, we sought to gain mechanistic insight into the proton carrier diffusion pathway in a HBM during O_2 reduction. We first modeled the results by evaluating two different ways in which a proton carrier transfers a proton across a lipid monolayer. Figure 9.17 shows a detailed scheme of the proposed "flip-flop" diffusion processes of a proton carrier in a lipid monolayer in discrete steps. Similar mechanisms have been proposed for "flip-flop"

diffusion of lipids in lipid bilayers.[51,52] We evaluated each of these steps to ascertain where the maximum of proton transfer would occur as a function of $L_T - P_T$.

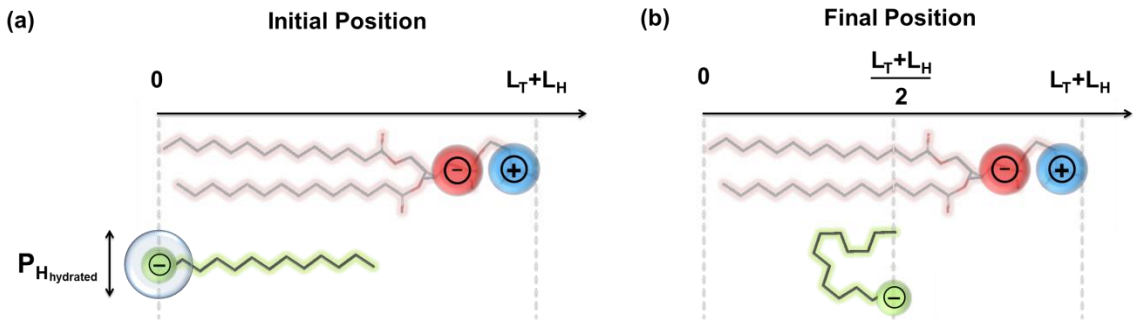

Figure 9.18. (a) Initial position and (b) final position at $(L_T+L_H)/2$ involved in the model of the RDS of "flip-flop" diffusion. Red structure = lipid with the negative and positive charges specified, green structure = proton carrier with the negatively-charged head surrounded by a blue halo representing a hydration sphere.

The anionic proton carrier is first protonated at the lipid-solution interface (step 1). The resulting neutral species then flips across the hydrophobic region of the lipid membrane either by a rotation motion only or by a combination of bending and rotation motions (steps 2 and 3). The proton carrier then delivers a proton at the SAM-lipid interface to CuBTT, becoming anionic in the process (step 4). Next, the deprotonated proton carrier flips back across the lipid either by a rotation motion only or by a combination of bending and rotation motions, and then the proton carrier can once again become protonated at the lipid-solution interface (steps 5 and 6). We expect step 5 to be the RDS since a hydrophilic, charged species must diffuse across the hydrophobic environment of the lipid tail. Additionally, the lipid-proton carrier system must reorganize to accommodate the strain built-up during the flipping process for which there will be an energetic penalty. The lipid-proton carrier system then releases this accumulated strain in step 6, and thus this step is energetically favorable. Note that step 2, although similar to step 5,

involves the transfer of a neutral proton carrier through the hydrophobic lipid layer. This process is more facile than transferring a charged proton carrier, and thus step 2 is not expected to be the RDS.

To ascertain the plausibility of the "flip-flop" mechanism proposed in Figure 9.17 and to understand the origin of the effects of lipid and proton carrier lengths on the O_2 reduction current by CuBTT, we modeled the "flip-flop" process with relevant physical parameters for step 5. We first address the mechanism that involves a combination of bending and rotation motions. The model considers four fundamental physical attributes of charged species moving across lipid membranes: electrostatic interactions between the lipid head group and the proton carrier, the membrane stress associated with motion of the proton carrier, surface tension of the hydration sphere of the proton carrier head group, and the polarization that occurs upon moving a charge between two dielectric media. Figure 9.18 illustrates one set of possible positions of the proton carrier at the initial and final stages of the RDS of "flip-flop" diffusion used in the modeling studies. Initially, the head group of the proton carrier lies at the lipid-SAM interface (Figure 9.18a) and is likely hydrated by water trapped at the interface, as is commonly observed in other lipid membrane systems.[53] At the final position of the RDS, the proton carrier has shed its water of hydration and orients itself in a folded fashion with the head group at the midpoint of the lipid layer (Figure 9.18b). The activation barrier for the RDS is calculated by subtracting the energy of the initial position from the final position ($E_{final} - E_{initial}$).

We calculate the electrostatic interaction between the deprotonated proton carrier and the lipid head group. The lipid head group consists of negatively and positively charged portions, each of which interacts with the deprotonated proton carrier. By applying Coulomb's law:

$$\Delta E = \frac{e^2}{4\pi\varepsilon_0\varepsilon_L}\left(\frac{1}{d_{final}} - \frac{1}{d_{initial}}\right) \qquad \text{Eq. 1}$$

where e is the elementary charge, ε_0 is the permittivity of free space, $\varepsilon_L = 2$ and is the dielectric constant of the lipid layer,[54] and d is the distance between the two charges considered, we compute the net difference in electrostatic energies between the final and initial positions. For all components and cases of the model, we assume that there are six nearest neighboring lipid molecules (n_L) and thus six head groups surrounding each proton carrier as has been shown before using atomic force microscopy.[55]

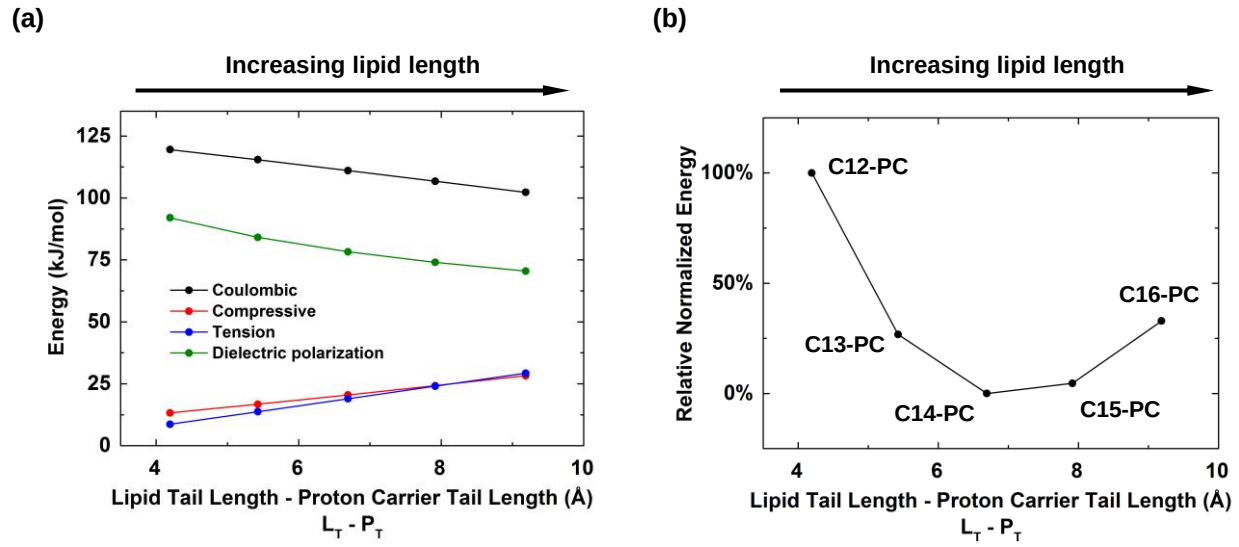

Figure 9.19. Calculated activation energies for "flip-flop" diffusion of MDP in HBMs with different lipid lengths. (a) Coulombic (black), compressive (red), surface tension (blue), and dielectric polarization (green) energies, and (b) total relative energy summing the four energy components of the model as a function of the differences in lengths between the tails of the lipid and proton carrier.

The calculated Coulombic energy barrier for the RDS of "flip-flop" diffusion of MDP in HBMs decreases with increasing lipid length (Figure 9.19a, black line). This trend can be rationalized as follows. The unfavorable interactions between the negatively charged proton carrier and the negative charges of the lipid head groups outweigh the favorable interactions between the negative charge of the proton carrier and the positive charges of the lipid head

groups. The negative-negative charge pairs have a stronger influence on the total Coulombic energy barrier because the distances between the sets of negative charges are shorter than the negative-positive charge pairs. Furthermore, because the negative charge of the proton carrier is closer to the negative lipid charges in the final RDS position than in the initial position, the interaction energy of the final position contributes most to the trend calculated. As the lipid length increases, the distance of this negative-negative pair increases, resulting in a decrease of the Coulombic interaction activation energy.

Second, we calculate the energy associated with the stress induced by the bending of the proton carrier during the RDS. We calculate the hydrated volume of the proton carrier head based upon the gap that is present in the HBM due to differences in the tail lengths of the lipid and the proton carrier ($L_T - P_T$). We assume the proton carrier bends over itself once during "flip-flop" diffusion, yielding a folded width that is equal to the diameter of the hydrated proton carrier head plus the width of the proton carrier tail (P_{thick}). By applying the equation for lateral membrane stress,[56]

$$\Delta E = \frac{1}{2} K \frac{(A-A_0)^2}{A_0} \qquad \text{Eq. 2}$$

where $A_0 = (P_{thick} + n_L L_{thick})(L_T)$ and is the initial area of the proton carrier-lipid unit cell, $A = (P_{H_{hydrated}} + P_{thick} + n_L L_{thick})(L_T)$ and is the final area of the stressed proton carrier-lipid unit cell, and K = 0.37 N/m and is the area compressibility modulus for lipid membranes,[57] we compute the net energy difference caused by folding-induced stress of the proton carrier in the lipid.

The calculated energy barrier associated with the stress induced by "flip-flop" diffusion of MDP in HBMs increases with increasing lipid length (Figure 9.19a, red line). The influence of the squared term in the numerator in Eq. 2, which can be decomposed into L_T and $P_{H_{hydrated}}$

terms, outweighs that of the denominator. The diameter of the hydrated proton carrier head group ($P_{H_{hydrated}}$) increases with lipid length because the increasing L_T – P_T gap accommodates more trapped water.

Third, we calculate the energy associated with changes in the surface tension upon breaking the hydration volume of the proton carrier head group during the RDS of "flip-flop" diffusion. By applying the surface tension equation for a cylinder,[54]

$$\Delta E = \left(2\pi\left(\frac{P_{thick}}{2}\right)(L_T - P_T - P_H) + 2\pi\left(\frac{P_{thick}}{2}\right)^2\right)\gamma_{L/W} \qquad \text{Eq. 3}$$

where $\gamma_{L/W}$ = 0.052 N/m and is the interfacial surface tension between lipid and water,[58] we compute the energy required to break the surface tension during "flip-flop". The calculated activation barrier associated with the surface tension induced by "flip-flop" diffusion of MDP in HBMs increases linearly with increasing lipid length (Figure 9.19a, blue line) because L_T is the only quantity in Eq. 3 that varies.

Lastly, we calculate the energy associated with moving the negative charge of the proton carrier across the lipid membrane during the "flip-flop" diffusion RDS. By applying the equation for moving a charged species across two dielectric media,[54]

$$\Delta E = \left(\frac{1}{4\pi\varepsilon_0}\right)\left(\frac{e^2}{2P_{H_{hydrated}}}\left(\frac{1}{\varepsilon_L} - \frac{1}{\varepsilon_E}\right) - \frac{e^2}{t\,\varepsilon_L}\ln\left(\frac{2\varepsilon_E}{\varepsilon_E + \varepsilon_L}\right)\right) \qquad \text{Eq. 4}$$

where ε_L = 2 and is the dielectric constant of lipid, $\varepsilon_E = \frac{((\varepsilon_W P_{thick}) + (\varepsilon_L n_L L_{thick}))}{P_{thick} + n_L L_{thick}}$ and is the effective dielectric constant at the SAM-lipid interface, ε_W = 80 and is the dielectric constant of water, and $t = \frac{L_T + L_H}{2}$ and is the distance travelled by the charged species across the membrane, we compute the energy associated with dielectric polarization.

The calculated activation barrier associated with the dielectric polarization caused by "flip-flop" diffusion of MDP in HBMs decreases with increasing lipid length (Figure 9.19a, green line). This trend can be understood as follows. Both the $P_{H_{hydrated}}$ and t terms increase with increasing lipid length in Eq. 4. Therefore, the $\frac{1}{P_{H_{hydrated}}}$ and $\frac{1}{t}$ terms decrease with increasing lipid length. However, whereas the t term is linear with respect to L_T, the $P_{H_{hydrated}}$ term varies as ${L_T}^{(\frac{1}{3})}$ due to a length-to-volume conversion. In the regime of $L_T - P_T$ = 4 to 10 Å, the influence of the ${L_T}^{(-\frac{1}{3})}$ term outweighs that of the $-\frac{1}{t}$ term, giving the computed trend of decreasing dielectric polarization energy with increasing lipid tail length.

Figure 9.19b displays the relative normalized energy barrier for "flip-flop" diffusion of MDP during the RDS combining the four components presented in Figure 9.19a. The model predicts the relative activation barrier is the lowest for the case of C14-PC, followed by C15-PC. The relative energy barrier increases significantly for the cases of C13-PC and C16-PC, and the barrier is the highest for the case of C12-PC. The black points of Figure 9.16 suggest that MDP delivers protons most effectively when it is in a HBM containing C14-PC. This observation matches the model which predicts that the energy barrier for "flip-flop" diffusion of MDP in C14-PC is lowest. Analogous comparisons reveal that the modeled trend (Figure 9.19b) matches well with the experimental data for all lipids studied (Figure 9.16, black points).

Next, we compute the energy associated with changes in the electrostatic interactions, induced stress to the lipid membrane, breaking the surface tension of the hydrated proton carrier head, and the dielectric polarization during the "flip-flop" diffusion process of boronic acids with different tail lengths in HBMs containing C14-PC using Eq. 1 to 4. Figure 9.20a displays the calculated energies as a function of proton carrier lengths. As the proton carrier length decreases,

the computed Coulombic energy remains the same (Figure 9.20a, black line). This trend is expected because neither the initial nor final positions of the negative charge on the proton carrier depends upon the length of the proton carrier tail.

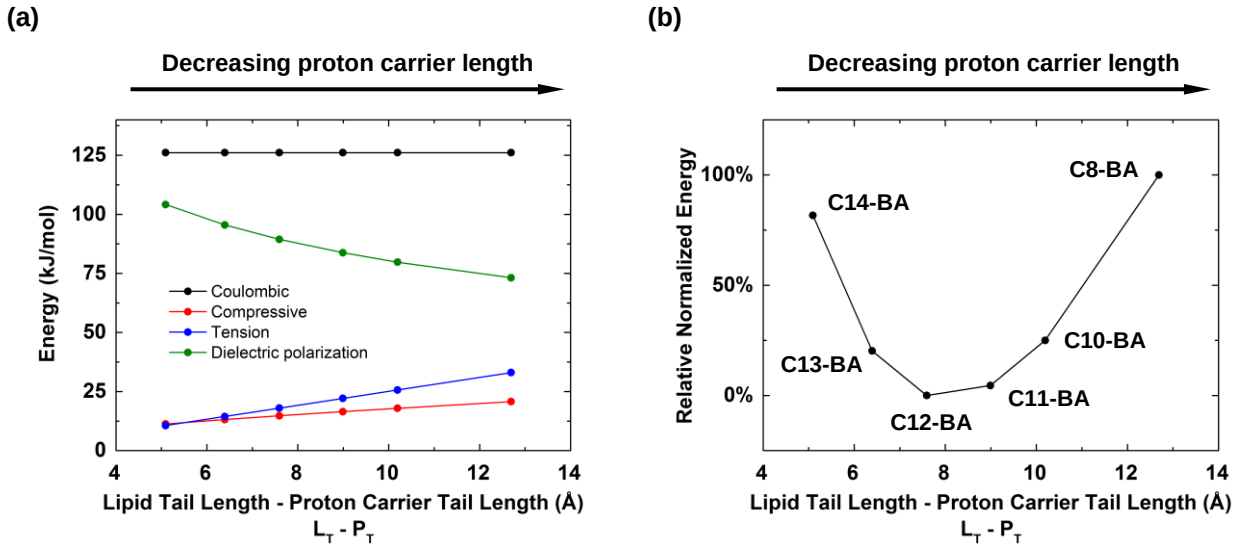

Figure 9.20. Calculated activation energies for "flip-flop" diffusion of boronic acids of different lengths in HBMs containing C14-PC lipid. (a) Coulombic (black), compressive (red), surface tension (blue), and dielectric polarization (green) energies, and (b) total relative energy summing the four energy components of the model as a function of the difference in length between the tails of the lipid and proton carrier.

The red line in Figure 9.20a shows the calculated energy associated with the stress induced during the RDS of proton carrier "flip-flop" diffusion. As the proton carrier length decreases, the lipid membrane must accommodate more stress. In Eq. 2, A is the only term that changes with proton carrier length. In particular, the $P_{H_{hydrated}}$ term within A increases as the proton carrier length decreases. Taking into account that in Eq. 2, A varies as its square and $P_{H_{hydrated}}$ varies as ${P_T}^{(\frac{1}{3})}$, the overall dependence of the energy related to stress scales as ${P_T}^{(\frac{2}{3})}$, explaining the slight curvature seen in the red line of Figure 9.20a.

The blue line of Figure 9.20a displays the calculated energy required to break the surface tension of the hydrated proton carrier head group. As the proton carrier length decreases, the barrier for this component of the model increases linearly because $-P_T$ is the only quantity in Eq. 3 that varies. Thus, as the proton carrier length decreases, the total calculation energy associated with surface tension increases.

The energy barrier due to the dielectric polarization as a function of proton carrier length is presented in the green line of Figure 9.20a. Upon decreasing the proton carrier length, the energy associated with moving the negative charge of the proton carrier head group across the C14-PC lipid layer decreases in a curved manner. In Eq. 4, $\frac{1}{P_{H_{hydrated}}}$ is the only term that changes as a function of the proton carrier length. Specifically, as the length of the proton carrier (P_T) decreases, the $P_{H_{hydrated}}$ term increases with its cube root. Therefore, with decreasing proton carrier length, the dielectric polarization energy of the "flip-flop" diffusion RDS decreases as ${P_T}^{(-\frac{1}{3})}$.

Figure 9.20b shows the relative normalized activation barrier for "flip-flop" diffusion of boronic acids with different tail lengths in HBMs containing C14-PC during the RDS after summing the four components presented in Figure 9.20a. The model predicts that the relative activation barriers in ascending order are: C11-BA ~ C12-BA < C13-BA < C10-BA << C14-BA < C8-BA. The blue points of Figure 9.16 indicate that C11-BA, C12-BA, and C13-BA deliver protons most rapidly in HBMs containing C14-PC as compared to boronic acids of other lengths. This observation qualitatively matches with the computed values for the energy barrier of the RDS during "flip-flop" diffusion (Figure 9.20b).

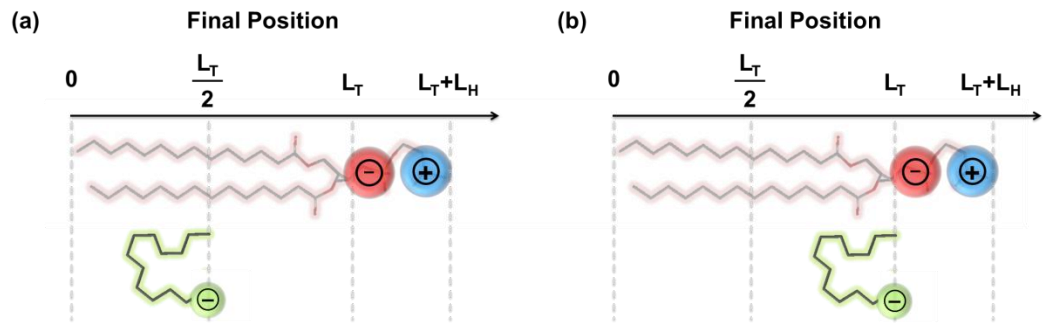

Figure 9.21. Final positions at (a) $L_T/2$ and (b) L_T involved in the model of the RDS of "flip-flop" diffusion. Red structure = lipid with the negative and positive charges specified, green structure = proton carrier with the negatively-charged head specified.

We next consider the final positions depicted in Figures 9.21a and b, and we present in Figure 9.22 the combined calculated energies for "flip-flop" diffusion summing the four components, namely the Coulombic, compressive, surface tension, and dielectric polarization energies. We first consider the case of MDP with changing lipid lengths. Figure 9.22a displays the relative normalized energy barrier for "flip-flop" diffusion of MDP during the RDS using $L_T/2$ (red) and L_T (blue) as the final positions. For a final position of $L_T/2$ (red), the model predicts that the relative activation barriers in ascending order are: C16-PC < C15-PC < C14-PC < C13-PC < C12-PC, suggesting that MDP delivers protons most effectively in C16-PC. For a final position of L_T (blue), the model predicts that the relative activation barriers in ascending order are: C12-PC < C13-PC < C14-PC < C15-PC < C16-PC, suggesting that MDP delivers protons most effectively in C12-PC. These two calculated trends depicted in Figure 9.22a do not match the experimental data shown in Figure 9.16, suggesting that the RDS of "flip-flop" diffusion across lipid membranes does not involve $L_T/2$ and L_T as the final positions.

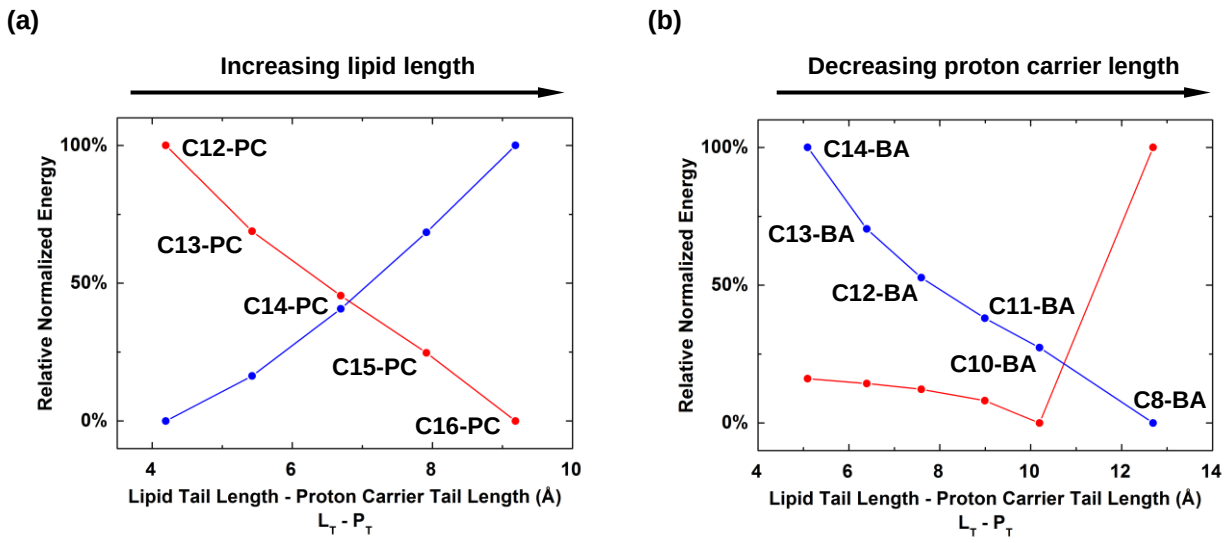

Figure 9.22. Calculated total relative energy for "flip-flop" diffusion using $L_T/2$ (red) and L_T (blue) as the final positions as a function of the differences in lengths between the tails of the lipid and proton carrier for the cases of (a) MDP in HBMs with different lipid lengths and (b) boronic acids of different lengths in HBMs containing C14-PC lipid.

We then consider the case of boronic acids of different lengths in C14-PC. Figure 9.22b displays the relative normalized energy barrier for "flip-flop" diffusion of boronic acids of different lengths during the RDS using $L_T/2$ (red) and L_T (blue) as the final positions. For $L_T/2$ (red), the model predicts that the relative activation barriers in ascending order are: C10-BA < C11-BA < C12-BA ~ C13-BA ~ C14-BA << C8-BA, suggesting that C10-BA delivers protons most effectively in C14-PC. For L_T (blue), the model predicts that the relative activation barriers in ascending order are: C8-BA < C10-BA < C11-BA < C12-BA < C13-BA < C14-BA, suggesting that C8-BA delivers protons most effectively in C14-PC. The experimental data shown in Figure 9.16 is in disagreement with the two computed trends depicted in Figure 9.22b, indicating that $L_T/2$ and L_T are not the highest energy points in the energy landscape of "flip-flop" diffusion across lipid membranes. Taken together, the modeling results indicate that a

position of $(L_T+L_H)/2$ is a plausible position for the proton carrier to reside in the final portion of the RDS.

In summary, the modeling results with a final position of $(L_T+L_H)/2$ for the proton carrier and a mechanism that involves bending of the alkyl chain of the proton carrier accurately predict the relative energy barriers for the RDS as experimentally determined. Previous studies with lipid bilayers without proton carriers suggest that concerted "flip-flop" diffusion of two lipid molecules may be more energetically favorable than isolated "flip-flop" events involving one lipid molecule.[51] However, our modeling and experimental results suggest that the "flip-flop" diffusion of proton carriers across lipid monolayers in HBMs occurs as individual unimolecular events. We hypothesize that the bimolecular nature of lipid "flip-flop" diffusion in lipid bilayers occurs because the diffusion of one lipid molecule must be compensated by the exchange of another lipid molecule in the opposing leaflet. This process ensures that the number of lipid molecules in each leaflet remains unchanged. In contrast, in the case of the HBM system, we suggest that unimolecular "flip-flop" diffusion occurs because transport takes place across a lipid monolayer and indeed, the modeling results support this hypothesis.

9.11 Mechanistic Implications of "Flip-flop" Diffusion in a HBM

We next address whether or not the "flip-flop" mechanism involves bending of the alkane chain, as depicted in Figure 9.17. Figure 9.23 plots the relative normalized energy barrier without bending for the "flip-flop" diffusion of a proton carrier across a lipid membrane during the RDS using $(L_T+L_H)/2$ as the final position. Figure 9.23a shows the results that involve MDP with changing lipid lengths. The model predicts that the relative activation barriers in ascending order are: C12-PC < C13-PC < C14-PC < C15-PC < C16-PC, suggesting MDP delivers protons most effectively in C12-PC. Figure 9.23b shows the results that involve boronic acids of different

lengths in C14-PC. The model predicts that the relative activation barriers in ascending order are: C8-BA < C10-BA < C11-BA < C12-BA < C13-BA < C14-BA, suggesting C8-BA delivers protons most effectively in C14-PC. The two calculated trends depicted in Figures 9.23a and b do not fit the experimental data shown in Figure 9.16, signifying that "flip-flop" diffusion across lipid membranes likely requires the proton carrier to bend, a motion that lowers the effective energy barrier for transmembrane movement. The origin of this behavior is that a model without alkane chain bending involves creation of too much stress during "flip-flop," and this stress inhibits the "flip-flop" process.

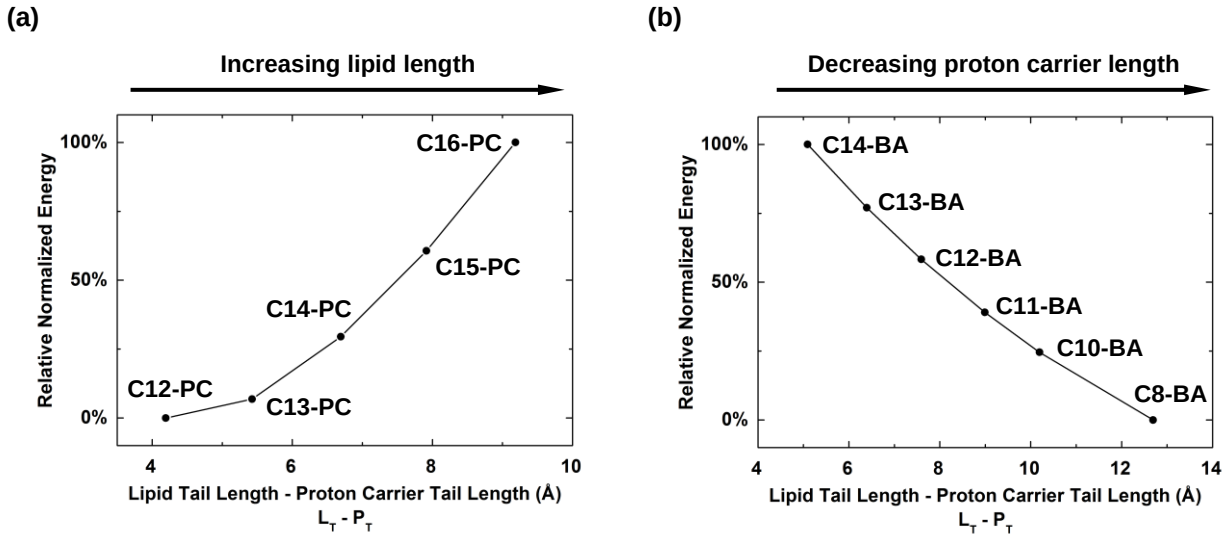

Figure 9.23. Calculated total relative energy for "flip-flop" diffusion assuming proton carrier does not bend during the process as a function of the difference in length between the tails of the lipid and proton carrier for the cases of (a) MDP in HBMs with different lipid lengths and (b) boronic acids of different lengths in HBMs containing C14-PC lipid.

To test the hypothesis that efficient "flip-flop" diffusion across lipid membranes requires the proton carrier to bend, we synthesized an unbendable boronic acid (rigid-BA) with a stiff carbon backbone. Figure 9.24 shows the structure of rigid-BA and the O_2 reduction LSVs of

CuBTT covered by a monolayer of C14-PC with rigid-BA. The calculated length of rigid-BA is 17.2 Å, which is similar to the length calculated for an effective proton carrier C12-BA (17.0 Å). The O_2 reduction current observed for the case with rigid-BA is (25 ± 7) μA cm^{-2} (black), which is even lower than the lipid only case (red). The incorporation of inactive proton carriers in the lipid layer results in a lower O_2 reduction current, a phenomenon observed previously and is likely due to the formation of a denser lipid layer (Figure 9.11).[43] The inability of rigid-BA to effectively deliver protons across lipid membranes demonstrates that a flexible backbone is necessary for the bending motion required during "flip-flop" diffusion. The results obtained from using rigid-BA support the "flip-flop" mechanism presented in Figure 9.17 that involves bending.

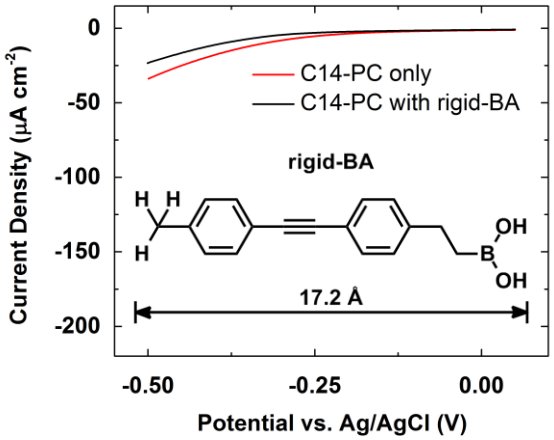

Figure 9.24. Structure of rigid-BA and O_2 reduction LSVs of CuBTT covered by a monolayer of C14-PC (red) with rigid-BA incorporated (black) in O_2-saturated pH 7 buffer at a scan rate of 10 mV/s.

9.12 Broader Impact of Mechanistic Findings

In this manuscript, we have gained mechanistic insight into the "flip-flop" diffusion of proton carriers across the lipid layer of HBM systems. In particular, our results suggest that

proton carriers must bend to minimize the accumulation of stress in the lipid layer and that the proton transfer rate is sensitive to the lengths of the alkyl tail of the proton carrier.

We now consider the applicability of the mechanistic findings in this study to drug delivery systems. Although drug delivery into cells can occur via a variety of different pathways which include mechanisms involving endocytosis, liposomes, and membrane channels, a growing number of drugs have been identified as reaching their targeted sites through passive "flip-flop" diffusion.[59-63] Notable examples of drugs that undergo "flip-flop" transport across cellular lipid bilayers are the anticancer drugs doxorubicin and mitoxantrone.[64,65] There are many factors which affect the pharmacokinetics of these drugs which include the binding rate of the drug to the outside of the lipid membrane,[66,67] the pumping of the drug out of the cell by proteins such as P-glycoprotein,[68-70] and the intrinsic "flip-flop" diffusion rate of the drug across the lipid membrane.[64] Our work here suggests that the rate of "flip-flop" diffusion across lipid membranes can be controlled by altering the length of the alkyl tail of the diffusing species. Similar methodologies to the one applied in this work may aid in future structure-activity relationships as applied to drug delivery.

9.13 Conclusions

In this report, we demonstrate that O_2 reduction by a Cu catalyst can be controlled by proton flux across the lipid layer of a HBM. "Flip-flop" diffusion of a lipid-embedded proton carrier dictates the proton transfer kinetics, and the rate of "flip-flop" diffusion depends on both the chain lengths of the proton carrier and the lipid. In particular, for maximum "flip-flop" rates, the length of the lipid tail must be 6 to 10 Å longer than the length of the proton carrier tail. We evaluate these empirical results with a biophysical model that contains parameters accounting for

changes in Coulombic interactions, stress accumulation, surface tension, and dielectric constants across the lipid-water interface. The model accurately reproduces the relative changes in energy barriers associated with the RDS for the "flip-flop" diffusion process. Studies with a rigid proton carrier corroborate findings that the RDS involves the bending of the alkyl tail of the proton carrier as it moves across the hydrophobic interior of the lipid layer. We envision that the methodologies developed here will lead to further understanding of the mechanism of "flip-flop" diffusion in lipid bilayers and aid in the development of drug delivery schemes.

9.14 References

(1) Karanth, H.; Murthy, R. S. R. *J. Pharm. Pharmacol.* **2007**, *59*, 469.
(2) Demarche, S.; Sugihara, K.; Zambelli, T.; Tiefenauer, L.; Voros, J. *Analyst* **2011**, *136*, 1077.
(3) Yatvin, M.; Kreutz, W.; Horwitz, B.; Shinitzky, M. *Science* **1980**, *210*, 1253.
(4) Dilger, J.; McLaughlin, S.; McIntosh, T.; Simon, S. *Science* **1979**, *206*, 1196.
(5) Engelman, D. M. *Nature* **2005**, *438*, 578.
(6) Saier, M. H. *Microbiol. Mol. Biol. Rev.* **2000**, *64*, 354.
(7) Alberts, B. *Molecular Biology of the Cell*; Garland Science, New York: New York, 2002.
(8) Denning, E. J.; Beckstein, O. *Chem. Phys. Lipids* **2013**, *169*, 57.
(9) Helm, F.; Fricker, G. *Pharmaceutics* **2015**, *7*, 27.
(10) Lian, T.; Ho, R. J. Y. *J. Pharm. Sci.* **2001**, *90*, 667.
(11) Maurer, N.; Fenske, D. B.; Cullis, P. R. *Expert Opin. Biol. Th.* **2001**, *1*, 923.
(12) Gabizon, A. A.; Shmeeda, H.; Zalipsky, S. *J. Liposome Res.* **2006**, *16*, 175.
(13) Allen, T. M.; Cullis, P. R. *Adv. Drug Deliver. Rev.* **2013**, *65*, 36.
(14) Lipinski, C. A.; Lombardo, F.; Dominy, B. W.; Feeney, P. J. *Adv. Drug Deliver. Rev.* **2001**, *46*, 3.
(15) Oprea, T. I.; Davis, A. M.; Teague, S. J.; Leeson, P. D. *J. Chem. Inf. Comp. Sci.* **2001**, *41*, 1308.
(16) Lipinski, C. A. *Drug Discov. Today Technol.* **2004**, *1*, 337.
(17) Leeson, P. D.; Springthorpe, B. *Nat. Rev. Drug Discov.* **2007**, *6*, 881.
(18) Kalgutkar, A. S.; Zhou, S.; Fahmi, O. A.; Taylor, T. J. *Drug Metab. Dispos.* **2003**, *31*, 596.
(19) Hoque, J.; Konai, M. M.; Samaddar, S.; Gonuguntala, S.; Manjunath, G. B.; Ghosh, C.; Haldar, J. *Chem. Comm.* **2015**, *51*, 13670.
(20) Bickerton, S.; Jiwpanich, S.; Thayumanavan, S. *Mol. Pharm.* **2012**, *9*, 3569.
(21) McCrary, P. D.; Beasley, P. A.; Gurau, G.; Narita, A.; Barber, P. S.; Cojocaru, O. A.; Rogers, R. D. *New J. Chem.* **2013**, *37*, 2196.
(22) Bemporad, D.; Essex, J. W.; Luttmann, C. *J. Phys. Chem. B* **2004**, *108*, 4875.

(23) Tepper, H. L.; Voth, G. A. *J. Phys. Chem. B* **2006**, *110*, 21327.
(24) Krämer, S. D.; Lombardi, D.; Primorac, A.; Thomae, A. V.; Wunderli-Allenspach, H. *Chem. Biodivers.* **2009**, *6*, 1900.
(25) Kučerka, N.; Perlmutter, J. D.; Pan, J.; Tristram-Nagle, S.; Katsaras, J.; Sachs, J. N. *Biophys. J.* **2008**, *95*, 2792.
(26) Ogushi, F.; Ishitsuka, R.; Kobayashi, T.; Sugita, Y. *Chem. Phys. Lett.* **2012**, *522*, 96.
(27) Hofsäß, C.; Lindahl, E.; Edholm, O. *Biophys. J.* **2003**, *84*, 2192.
(28) Aqvist, J.; Warshel, A. *Biophys. J.* **1989**, *56*, 171.
(29) Kim, I.; Warshel, A. *Proc. Natl. Acad. Sci. U.S.A.* **2014**, *111*, 2128.
(30) Hamilton, J. A. *Prostaglandins Leukot. Essent. Fatty Acids* **2007**, *77*, 355.
(31) Riquelme, G.; Lopez, E.; Garcia-Segura, L. M.; Ferragut, J. A.; Gonzalez-Ros, J. M. *Biochemistry* **1990**, *29*, 11215.
(32) Proshlyakov, D. A.; Pressler, M. A.; DeMaso, C.; Leykam, J. F.; DeWitt, D. L.; Babcock, G. T. *Science* **2000**, *290*, 1588.
(33) Hofacker, I.; Schulten, K. *Proteins* **1998**, *30*, 100.
(34) Kamp, F.; Hamilton, J. A. *Proc. Natl. Acad. Sci. U.S.A.* **1992**, *89*, 11367.
(35) Pohl, E. E.; Peterson, U.; Sun, J.; Pohl, P. *Biochemistry* **2000**, *39*, 1834.
(36) Pohl, E. E.; Voltchenko, A. M.; Rupprecht, A. *BBA-Biomembranes* **2008**, *1778*, 1292.
(37) Schönfeld, P.; Schild, L.; Kunz, W. *BBA-Bioenergetics* **1989**, *977*, 266.
(38) Disalvo, E. A.; Simon, S. A. *Permeability and Stability of Lipid Bilayers*; Taylor & Francis, 1995.
(39) Kampf, J. P.; Cupp, D.; Kleinfeld, A. M. *J. Biol. Chem.* **2006**, *281*, 21566.
(40) Winterhalter, M. *Curr. Opin. Colloid In.* **2000**, *5*, 250.
(41) Hosseini, A.; Collman, J. P.; Devadoss, A.; Williams, G. Y.; Barile, C. J.; Eberspacher, T. A. *Langmuir* **2010**, *26*, 17674.
(42) Tse, E. C. M.; Barile, C. J.; Gewargis, J. P.; Li, Y.; Zimmerman, S. C.; Gewirth, A. A. *Anal. Chem.* **2015**, *87*, 2403.
(43) Barile, C. J.; Tse, E. C. M.; Li, Y.; Sobyra, T. B.; Zimmerman, S. C.; Hosseini, A.; Gewirth, A. A. *Nat. Mater.* **2014**, *13*, 619.
(44) Mabrey, S.; Sturtevant, J. M. *Proc. Natl. Acad. Sci. U.S.A.* **1976**, *73*, 3862.
(45) John, K.; Schreiber, S.; Kubelt, J.; Herrmann, A.; Müller, P. *Biophys. J.* **2002**, *83*, 3315.
(46) Hosseini, A.; Barile, C. J.; Devadoss, A.; Eberspacher, T. A.; Decreau, R. A.; Collman, J. P. *J. Am. Chem. Soc.* **2011**, *133*, 11100.
(47) Albrecht, O.; Gruler, H.; Sackmann, E. *J. Phys. France* **1978**, *39*, 301.
(48) Lipowsky, R.; Sackmann, E. *Structure and Dynamics of Membranes: I. From Cells to Vesicles / II. Generic and Specific Interactions*; Elsevier Science, 1995.
(49) White, S. H.; King, G. I. *Proc. Natl. Acad. Sci. U.S.A.* **1985**, *82*, 6532.
(50) Atkins, P.; de Paula, J. *Atkins' Physical Chemistry*; OUP Oxford, 2014.
(51) McConnell, H. M.; Kornberg, R. D. *Biochemistry* **1971**, *10*, 1111.
(52) Anglin, T. C.; Conboy, J. C. *Biophys. J.* **2008**, *95*, 186.
(53) Zhou, Y. *Physics 1901 – 1921: Including Presentation Speeches and Laureates' Biographies*; Elsevier Science, 2013.
(54) MacDonald, R. C. *BBA-Biomembranes* **1976**, *448*, 193.
(55) Sheikh, K. H.; Giordani, C.; Kilpatrick, J. I.; Jarvis, S. P. *Langmuir* **2011**, *27*, 3749.
(56) Nagle, J. F.; Scott Jr, H. L. *BBA-Biomembranes* **1978**, *513*, 236.
(57) Waheed, Q.; Edholm, O. *Biophys. J.* **2009**, *97*, 2754.

(58) Mofrad, M. R. K.; Kamm, R. D. *Cellular Mechanotransduction: Diverse Perspectives from Molecules to Tissues*; Cambridge University Press, 2009.
(59) Bareford, L. M.; Swaan, P. W. *Adv. Drug Deliver. Rev.* **2007**, *59*, 748.
(60) Rajendran, L.; Knolker, H.-J.; Simons, K. *Nat. Rev. Drug Discov.* **2010**, *9*, 29.
(61) Xu, S.; Olenyuk, B. Z.; Okamoto, C. T.; Hamm-Alvarez, S. F. *Adv. Drug Deliver. Rev.* **2013**, *65*, 121.
(62) El-Sayed, A.; Harashima, H. *Mol. Ther.* **2013**, *21*, 1118.
(63) Coelho, J. *Drug Delivery Systems: Advanced Technologies Potentially Applicable in Personalised Treatment*; Springer Netherlands, 2013.
(64) Regev, R.; Eytan, G. D. *Biochem. Pharmacol.* **1997**, *54*, 1151.
(65) Regev, R.; Yeheskely-Hayon, D.; Katzir, H.; Eytan, G. D. *Biochem. Pharmacol.* **2005**, *70*, 161.
(66) Movileanu, L.; Popescu, D.; Victor, G.; Turcu, G. *Biosystems* **1997**, *40*, 263.
(67) Frézard, F.; Garnier-Suillerot, A. *BBA-Lipid Lipid Met* **1998**, *1389*, 13.
(68) Amin, M. L. *Drug Target Insights* **2013**, *7*, 27.
(69) Sharom, F.; Lugo, M.; Eckford, P. W. *J. Bioenerg. Biomembr.* **2005**, *37*, 481.
(70) Eytan, G. D. *Biomed. Pharmacother.* **2005**, *59*, 90.

Chapter 10

Photoresponsive Molecular Switch for Regulating Transmembrane Proton-Transfer Kinetics

Reprinted with permission from Li, Y; Tse, E. C. M.; Barile, C. J.; Gewirth, A. A.; Zimmerman, S. C.; *Journal of American Chemical Society* **2015**, *137*, 14059−14062.

10.1 Introduction

Precisely regulated proton transfer is essential to many biological reactions and alternative energy schemes.[1-3] Redox reactions with multiple proton-coupled electron transfer (PCET) steps have garnered a significant amount of interest over the past decades.[4,5] In particular, the oxygen reduction reaction to form water (ORR: $O_2 + 4e^- + 4H^+ \rightarrow 2H_2O$) is central to the development of energy conversion devices.[6] Currently however, the commercialization of fuel cells is impeded by the prohibitive cost, low abundance, and high overpotential of Pt, which is the current industrial cathode catalyst for the ORR.[7] Non-precious metal (NPM) ORR catalysts represent a class of promising alternatives to Pt.[8,9] However, a lack of comprehensive mechanistic understanding of the ORR and catalyst degradation pathways hampers the development of NPM catalysts with enhanced activity and durability.[10]

The ORR mechanism as with other multi-step PCET reactions is hard to decipher because of the intricate interplay between the thermodynamics and kinetics of electron and proton transfer.[2-5] The use of a self-assembled monolayer (SAM) can decouple the kinetics and

thermodynamics of electron transfer, the latter of which is dictated by the electrode potential.[11,12] We recently developed a new experimental framework, a hybrid bilayer membrane (HBM), to delineate between the effects of the kinetics and thermodynamics of proton transfer to a system that catalyzes PCET reactions.[13,14] A HBM consists of a SAM with a monolayer of lipid appended on top.[15] In one embodiment, a dinuclear Cu molecular ORR catalyst (CuBTT: Cu complex of 6-((3-(benzylamino)-1,2,4-triazol-5-yl)amino)hexane-1-thiol) forms the SAM.[14] We previously demonstrated that flip-flop diffusion of lipid-bound aliphatic acids can function as a pH-sensitive switch to turn on and off transmembrane proton delivery to the catalyst.[13]

Proton delivery via flip-flop diffusion of proton carriers happens spontaneously in the presence of a pH gradient.[16,17] It can be advantageous to regulate the transfer more precisely. Natural systems do execute exquisite control over proton and electron transfer steps by having specific functional groups that adopt precise conformational changes. For example, a 5 Å movement of an ubiquinone moiety accompanied by a 180° propeller twist of an isoprene chain upon illumination in the photosynthetic reaction center of *Rhodobacter sphaeroides* is a necessary prerequisite to proton uptake for photosynthesis.[18] The intricate photo-regulation of proton transport in nature has inspired a tremendous amount of effort towards mimicking these natural systems on the macromolecular level.[19,20] Despite decades of effort, the regulation has not been achieved with a small molecule. A HBM with a photo-responsive proton carrier could mimic the light-induced conformational gating found in nature and afford a new approach to tune transmembrane proton transfer kinetics with high temporal and spatial resolution as well as minimal input of chemicals or output of waste products.

Like many other photo-responsive chromophores,[21,22] a stiff stilbene moiety (1,1′-biindane) has either a Z or E configuration with respect to its central double bond upon

photoisomerization.[23-25] This chromophore has garnered increasing attention because of its scalable synthesis, easy derivatization, lack of thermal relaxation at room temperature,[26] high quantum yield (50%) for E to Z photoisomerization, and quantitative Z to E reversion. One application of light-driven conformational change is to utilize stiff stilbene as an internal molecular force probe.[27,28] Nevertheless, the gating ability of functional materials based on stiff-stilbene remains largely unexplored.

In this report, by utilizing the first artificial, membrane-bound, photo-responsive proton carrier, we regulate proton kinetics to a NPM ORR catalyst without perturbing the pH of the bulk solution. The new proton carrier features a boronic acid head-group for proton transfer, a stiff stilbene body for photoresponsiveness, and an alkyl tail for lipid incorporation. When this proton carrier isomerizes from E to Z, it decreases in length by ~10 Å and likely lowers the energy barrier for transmembrane flip-flop diffusion and thus induce proton delivery. In addition, we improved the synthesis of the ligand (BTT) of the copper catalyst to provide sufficient material for comprehensive HBM studies.[13]

10.2 Improved Preparation Scheme for the Synthesis of BTT in High Yield

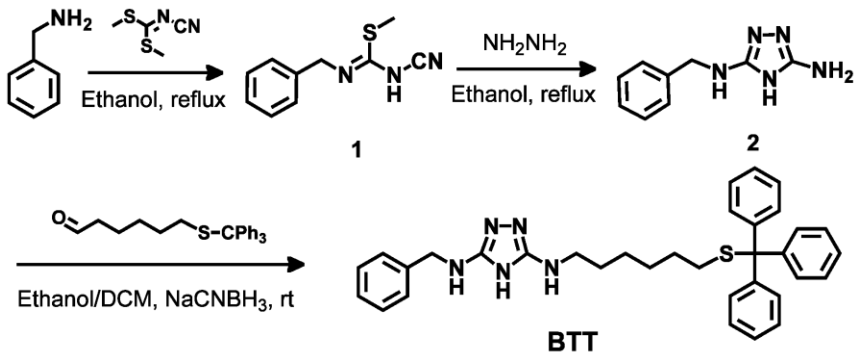

Scheme 10.1. Revamped procedure to prepare BTT in large quantities.

We first developed a new procedure for BTT preparation that afforded a significant 13-fold improvement in the overall yield. Although five instead of four synthetic steps are required, the new scheme (Scheme 10.1) eliminated one low-yield reductive amination step and one tedious chromatographic separation step. Partial aminolysis of dimethyl *N*-cyanodithio-carbonimidate with benzylamine first gives **1** (*N*-substituted *N'*-cyano-*S*-methylisothioureas), a key intermediate that readily cyclizes with hydrazine to afford **2**, which can be easily purified by filteration.[29] Reductive amination between the primary amine of **2** and the appropriate alkyl aldehyde was performed with $NaCNBH_3$ as the reducing agent in a one-pot reaction to prepare BTT on a large scale.

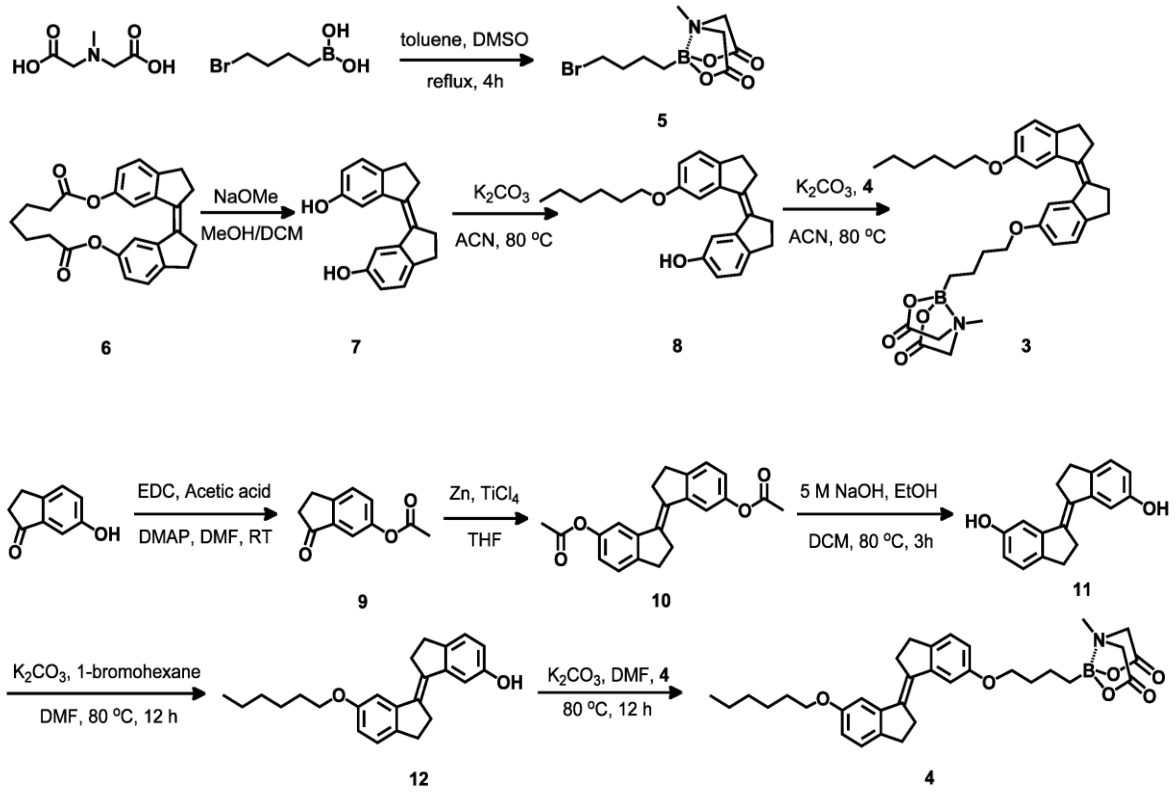

Scheme 10.2. Synthesis of protected photoswitch molecules: Z isomer (**3**) and E isomer (**4**).

With adequate BTT in hand, we proceeded to prepare the photo-responsive switch (both the Z and E forms) necessary for controlling transmembrane proton kinetics. The synthesis started from the photoreactive core, followed by the installation of the alkyl tail and the acid head-group sequentially (Scheme 10.2). The Z form core (**7**) was synthesized according to modified literature procedures via an intramolecular McMurry reaction under a high dilution condition.[27,28] Conversely, an *inter*molecular McMurry reaction of **9** afforded the E form (**10**) with high yield. The tail and head group were attached sequentially with K_2CO_3 as base at 80 ^oC. Other attempts to install the head group, such as with catecholborane, were unsuccessful due to their proneness to hydrolysis at elevated temperature even in a mildly basic environment.[30] In contrast, the MIDA-protected boronate ester (**4**) is easy to prepare from a commercially available starting material, able to survive harsh reaction conditions, and compatible with chromatography. In addition, the deprotection is easily achieved at room temperature with concentrated NaOH aqueous solution (a detailed procedure is available in the SI) to afford the photo-responsive boronic acid (**BA**) as proton carriers in the Z form (Z-**BA**) and E form (E-**BA**).[31,32]

[Ying Li in the Zimmerman group devised the synthesis schemes, prepared the molecules and collected the characterization data. See Ying Li's thesis dissertation for details.]

10.3 Photoswitching in Solution

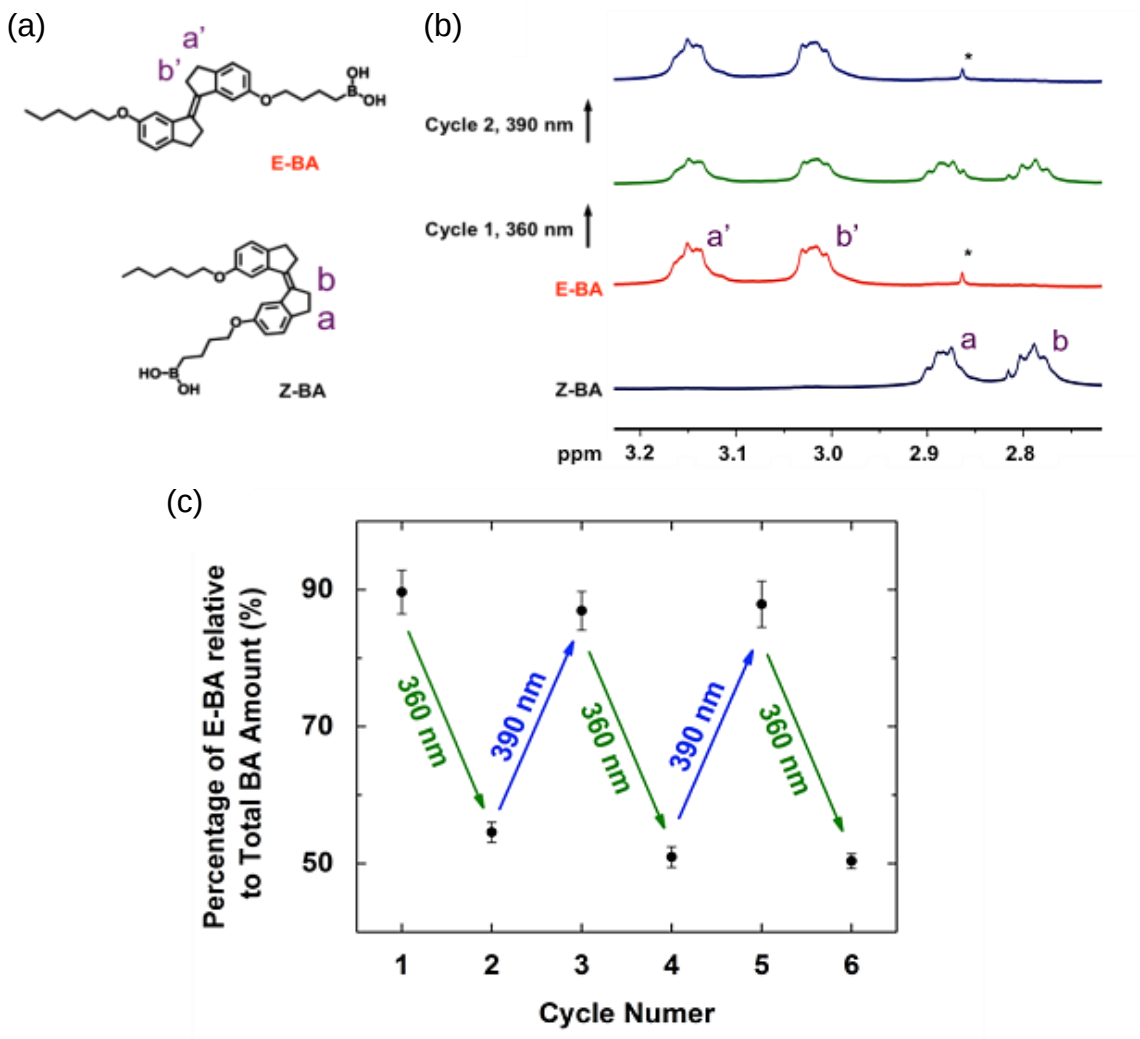

Figure 10.1. (a) Structures of E-**BA**, Z-**BA**, and the specific protons to be followed in ^{1}H NMR study. (b) Stacked truncated NMR spectra of BA (Z and E isomers) in CD_2Cl_2, indicating the corresponding proton signal shifts according to the irradiation cycles. * = ^{1}H resonance of the methyl group from MIDA after the deprotection step. (c) The percentage of E-**BA** relative to the total BA amount changes upon irradiation at 360 nm and 390 nm.

The light-induced E-Z isomerization of **BA** was first demonstrated in solution and followed by ^{1}H NMR spectroscopy. Figure 10.1a displays the structures of E-**BA** and Z-**BA**, and highlights the protons followed in the NMR study. Figure 10.1b shows an overlay of truncated ^{1}H NMR spectra: Z-**BA**, E-**BA** and one cycle of the E-Z-E conversion. The protons H_a and H_b in

Z-**BA** (Figure 10.1b, black line) appeared at 2.88 and 2.79 ppm, respectively. Their equivalent protons $H_{a'}$ and $H_{b'}$ in E-**BA** (red line) downshifted to 3.15 ppm ($\Delta\delta[H_a] = 0.27$ ppm) and 3.05 ppm ($\Delta\delta[H_b] = 0.26$ ppm), correspondingly. Upon UV irradiation at 360 nm, about 40% of E-**BA** was converted into Z-**BA** according to the ^{1}H NMR integration (green line). The mixture was exposed to UV irradiation at 390 nm and the Z isomer was almost quantitatively converted back to the E isomer (blue line). The complete Z-to-E and partial E-to-Z stilbene photo-isomerization is consistent with reported systems.[23,24] The full isomerization cycle was repeated two more times, and similar results were obtained. Figure 10.1c shows the percentage of E-**BA** versus the total **BA** plotted across sequential photo-irradiation events. Despite these observable changes in the ^{1}H NMR spectra, no significant changes are notable in the ^{11}B NMR spectra (Figure 10.2), suggesting that the boronic-acid group remains intact. The ability of this chromophore to cycle between two photo-distinguishable states allows us to construct a proof-of-concept, light-induced transmembrane proton delivery system in a HBM platform.

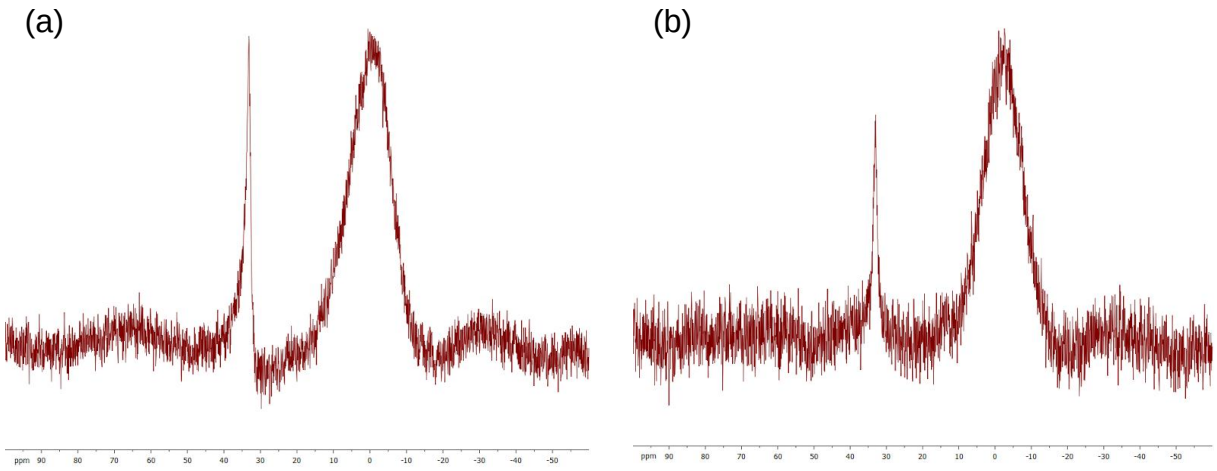

Figure 10.2. ^{11}B-NMR of **BA** (a) before irradiation and (b) after multiple cycles of irradiation.

10.4 Incorporating Photoswitches in the Lipid Layer of a HBM

Having demonstrated the reversible photo-responsiveness of E-**BA** and Z-**BA** in solution, we probed their ability to act as proton carriers in a HBM. Figure 10.3a displays the architecture of the three HBMs with and without the photo-responsive proton carriers incorporated in the lipid layer. Figure 10.3b shows linear sweep voltammograms (LSVs) of O_2 reduction by a SAM of CuBTT covered by a DMPC monolayer with and without the proton carriers added. In the absence of the proton carriers, the lipid layer blocks access of protons in bulk solution to CuBTT inside a HBM, resulting in a background O_2 reduction current density of about 40 μA cm^{-2} at -450 mV vs. Ag/AgCl (Figure 10.3b, black line). Upon incorporating Z-**BA**, the O_2 reduction current density at -450 mV increases by about 60% (blue line), indicating that Z-**BA** delivers protons from bulk solution across the lipid layer to the CuBTT catalyst for O_2 reduction as has previously been demonstrated for other proton carriers in HBM systems.[13,14] However, the O_2 reduction current density with E-**BA** added to the lipid layer (red line) is the same as the lipid only case, signifying that E-**BA** is incapable of transporting protons across the hydrophobic lipid layer.

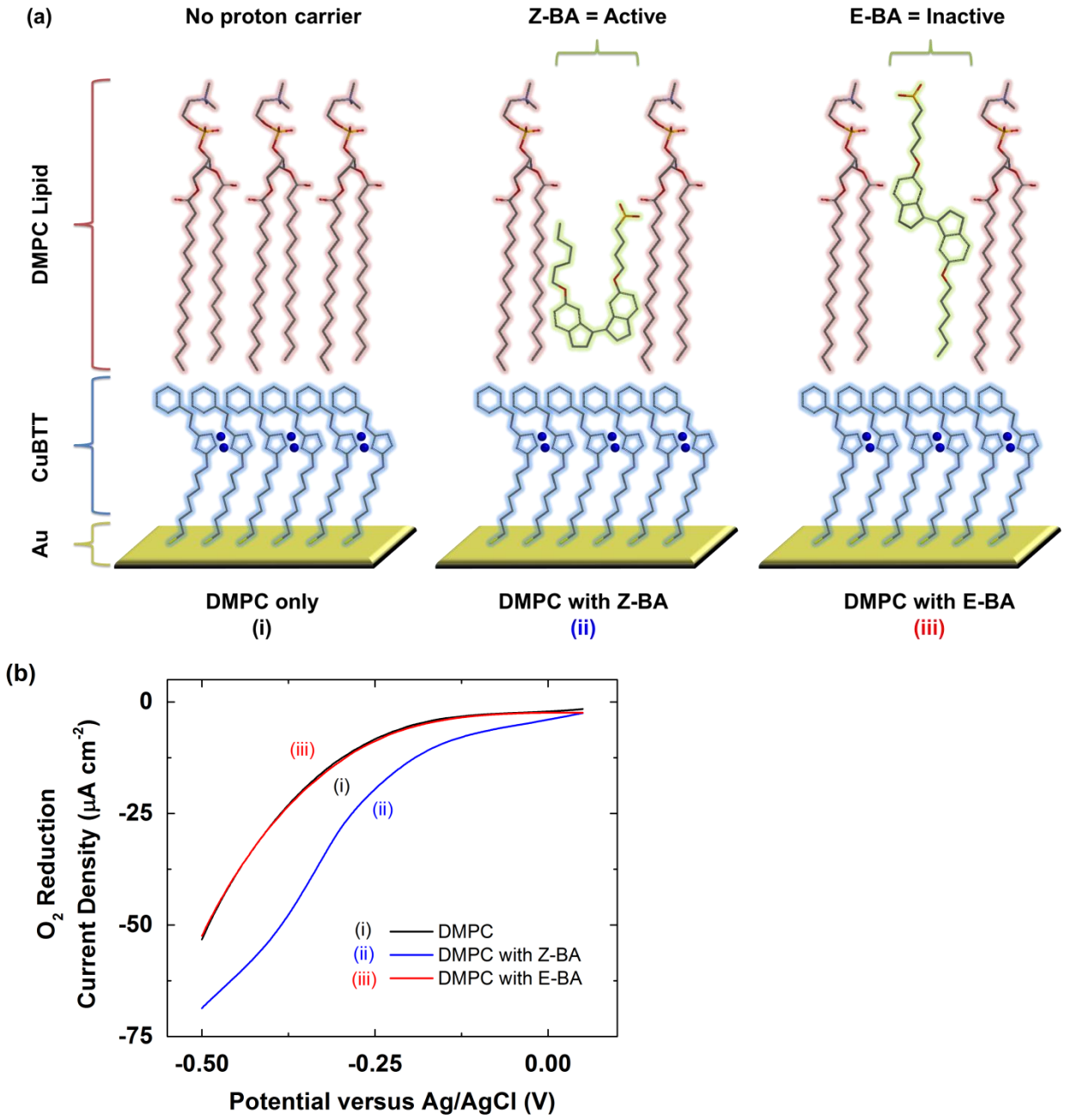

Figure 10.3. (a) Schematic of the HBMs studied: (i) DMPC only, (ii) DMPC with Z-**BA** incorporated, and (iii) DMPC with E-**BA** incorporated. (b) Linear sweep voltammograms (LSVs) of O_2 reduction catalyzed by CuBTT covered by a monolayer of DMPC (black) with Z-**BA** (blue) or E-**BA** (red) incorporated in the lipid layer in O_2-saturated pH 7 phosphate buffer at a scan rate of 10 mV/s.

10.5 Photoswitching on a Lipid-modified Electrode

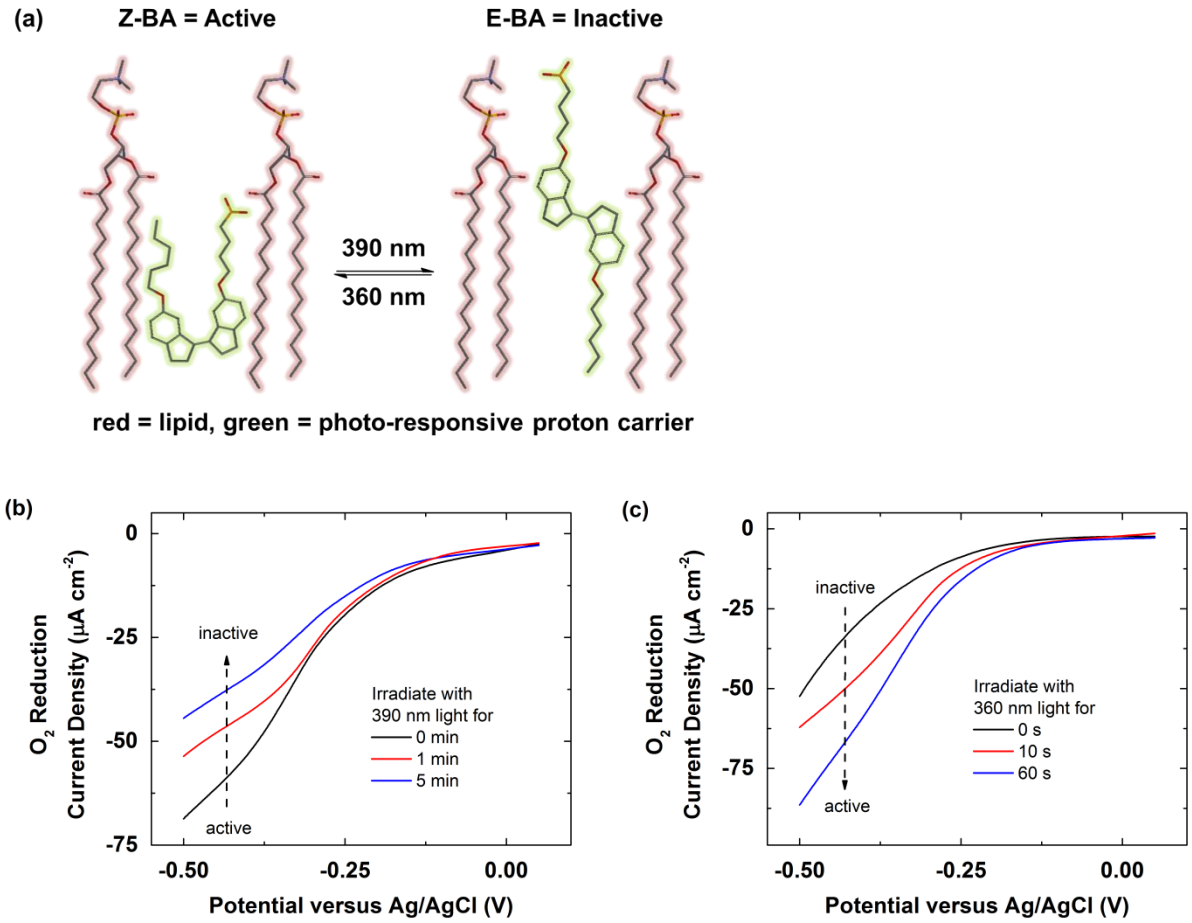

Figure 10.4. (a) Light-driven isomerization of Z-**BA** and E-**BA** inside the lipid layer of a HBM; the CuBTT SAM layer is omitted for clarity. (b) O_2 reduction LSVs in O_2-saturated pH 7 phosphate buffer at a scan rate of 10 mV/s by CuBTT covered by a monolayer of DMPC with Z-**BA** incorporated in the lipid layer irradiated with 390 nm light for 0 min (black), 1 min (red), and 5 min (blue), and (c) E-**BA** incorporated in the lipid layer irradiated with 360 nm light for 0 s (black), 10 s (red), and 60 s (blue).

We next explore the photo-switching behavior of E-**BA** and Z-**BA** in a HBM (Figure 10.4a). Figure 10.4b displays a set of LSVs of O_2 reduction by CuBTT covered by a DMPC monolayer with Z-**BA** added to the lipid layer with various irradiation periods. Upon irradiation with 390 nm for 1 and 5 min, the O_2 reduction current density at -450 mV drops by about 60% and 95%, respectively (Figure 10.4b, red and blue lines). As the irradiation time increases, the O_2

reduction current decreases until it reaches nearly the same value as the lipid only case or the case with E-**BA** added to the DMPC layer. These findings corroborate that as more of the proton carrier is converted to its inactive E-**BA** form, fewer protons are delivered across the lipid membrane, thus resulting in less catalytic O_2 reduction current. Figure 10.4c shows O_2 reduction LSVs by CuBTT covered by a DMPC monolayer with E-**BA** added to the lipid layer with various irradiation periods. Upon irradiation with 360 nm for 10 s, the O_2 reduction current density increases by about 65% (Figure 10.4b, red line). The O_2 reduction current reaches a value similar to the case with Z-**BA** added to the DMPC layer by irradiating for 1 min (blue line).

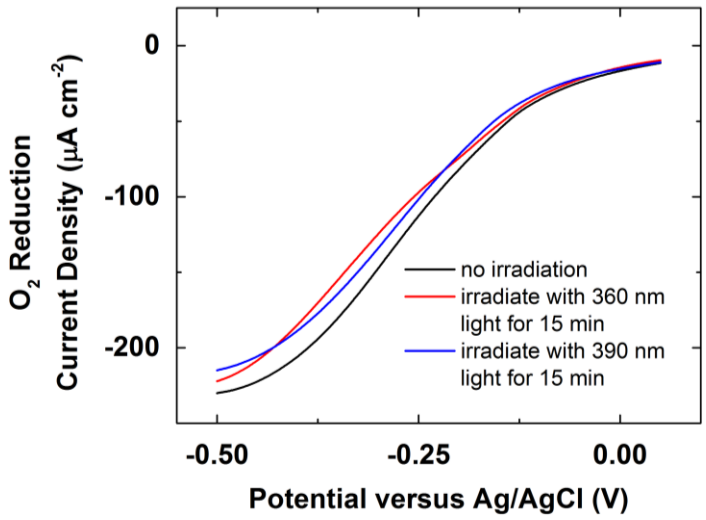

Figure 10.5. Linear sweep voltammograms (LSVs) of O_2 reduction catalyzed by CuBTT (black) irradiated with 360 nm light for 15 min (red) or 390 nm light for 15 min (blue) in O_2-saturated pH 7 phosphate buffer at a scan rate of 10 mV/s.

The black line of Figure 10.5 shows the LSV of CuBTT in O_2-saturated solution. The current density observed is similar to those observed previously,[13] suggesting that the new synthetic route of BTT does not perturb the O_2 reduction activity of CuBTT. The red and blue lines of Figure 10.5 show the LSVs of CuBTT in O_2-saturated solution after irradiating for 15

min with 360 nm and 390 nm light, respectively. These results demonstrate that both the Au-thiol linkage and the BTT-Cu bond are stable upon exposing to 360 nm or 390 nm light for 15 min.

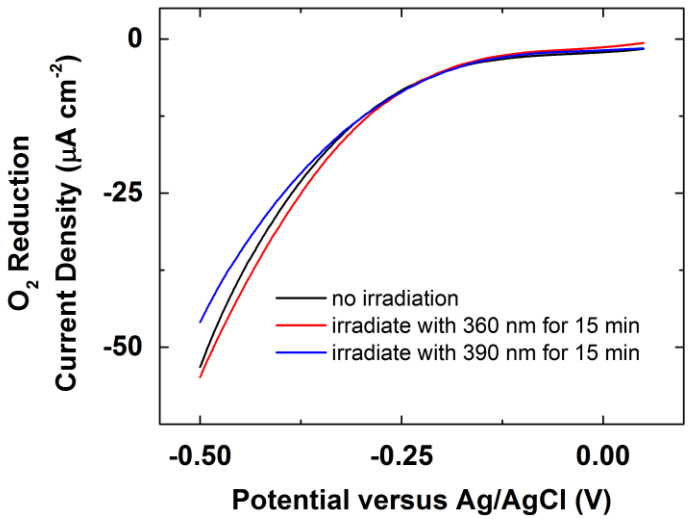

Figure 10.6. LSVs of O_2 reduction catalyzed by CuBTT covered by a monolayer of DMPC (black) irradiated with 360 nm light for 15 min (red) or 390 nm light for 15 min (blue) in O_2-saturated pH 7 phosphate buffer at a scan rate of 10 mV/s.

Figure 10.6 displays the LSVs of CuBTT covered by a monolayer of DMPC in O_2-saturated solution with and without irradiation. The current densities observed in all three cases are comparable, indicating that the integrity of the lipid layer is not perturbed by exposing to 360 nm or 390 nm light for 15 min.

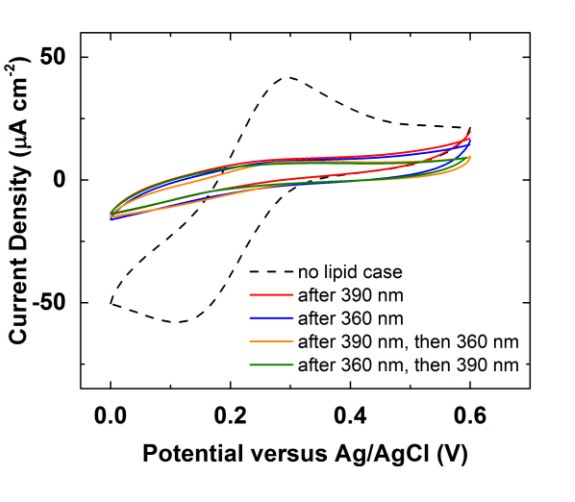

Figure 10.7. Representative cyclic voltammograms (CVs) of a SAM of CuBTT (black dashed line) and the HBMs containing CuBTT (solid lines) with E-BA incorporated in the lipid layer after irradiation with 360 nm light (blue) then with 390 nm light (green) and Z-BA incorporated in the lipid layer after irradiation with 390 nm light (red) then 360 nm light (orange) in a solution of $K_3Fe(CN)_6$ (1 mM) with KCl (100 mM) at a scan rate of 50 mV/s.

To further probe the integrity of the lipid layer, we subjected the surfaces to an electrochemical blocking experiment. We checked if the surfaces are blocked or not after O_2 reduction by conducting blocking experiments in a solution of $K_3Fe(CN)_6$. Figure 10.7 shows the CVs of blocked surfaces (solid lines) and an unblocked sample (dashed line). This experiment supports the notion that the lipid layer does not contain a pore or other defect following irradiation with light of 360 and 390 nm.

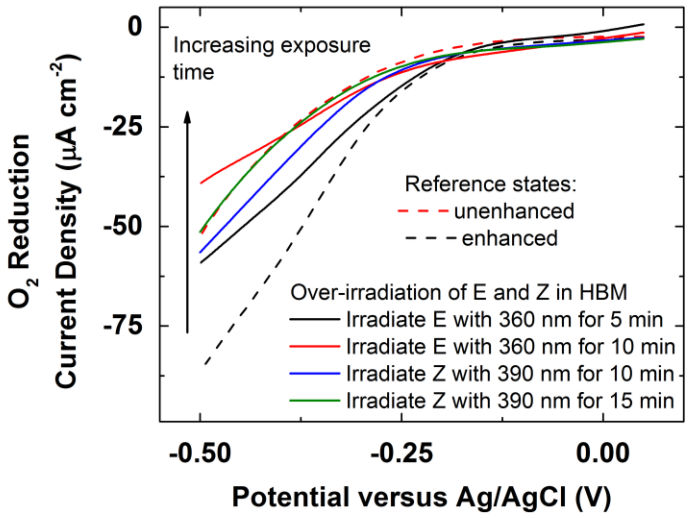

Figure 10.8. LSVs of O_2 reduction catalyzed by CuBTT covered by a monolayer of DMPC with Z-**BA** (black dashed line), E-**BA** (red dashed line), E-**BA** irradiated with 360 nm light for 5 min (black solid line), E-**BA** irradiated with 360 nm light for 10 min (red solid line), Z-**BA** irradiated with 390 nm light for 10 min (blue solid line), and Z-**BA** irradiated with 390 nm light for 15 min (blue solid line) in O_2-saturated pH 7 phosphate buffer at a scan rate of 10 mV/s.

Figure 10.8 shows the LSVs of CuBTT covered by a monolayer of DMPC with light-responsive proton carriers in O_2-saturated solution. Upon irradiating E-**BA** with 360 nm light for 5 and 10 min, the current densities observed are lower than the "enhanced" state. Furthermore, upon irradiating Z-**BA** with 390 nm light for 15 min, the current density observed is similar to the "unenhanced" state. The observed degradation after prolong exposure to light could be due to proton carriers leaching from the lipid layer or being damaged by light. Control experiments presented in Figures 10.5-10.8 demonstrate that the integrity of the CuBTT SAM and the lipid layer is not compromised by irradiating with light at 360 and 390 nm. Furthermore, we interrogate the content of the lipid layer using ESI-MS, which confirms the presence of proton carrier in the lipid layer (Figure 10.9). Taken together, these results represent the first example of using a molecular switch and light to deliver proton across intact membranes.

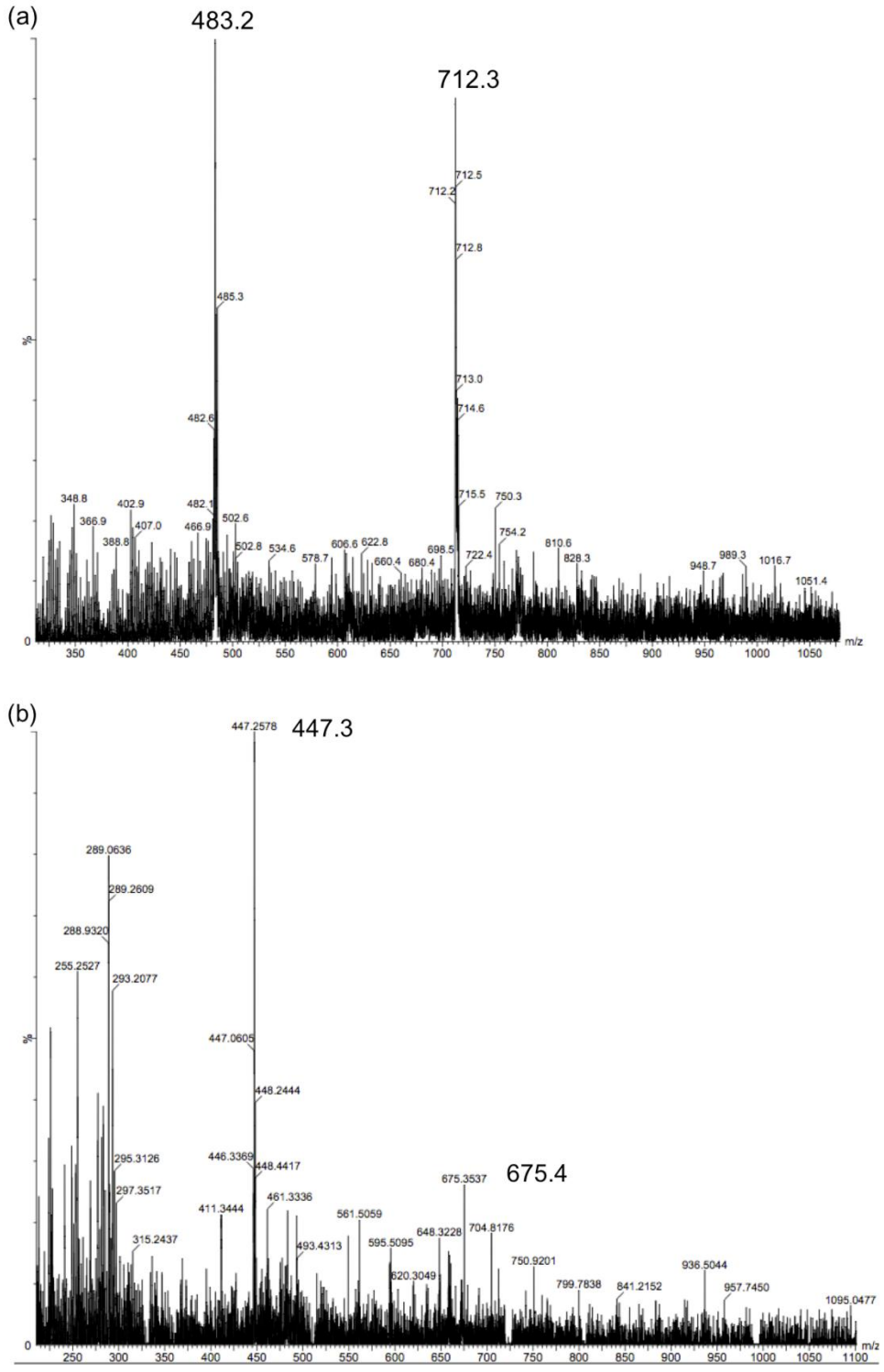

Figure 10.9. ESI-MS of extracted lipid layer of HBM with (a) E-**BA** and (b) Z-**BA** incorporated in the lipid layer.

10.6 Reversible Turning On and Off of a Photoswitch inside a Lipid Membrane

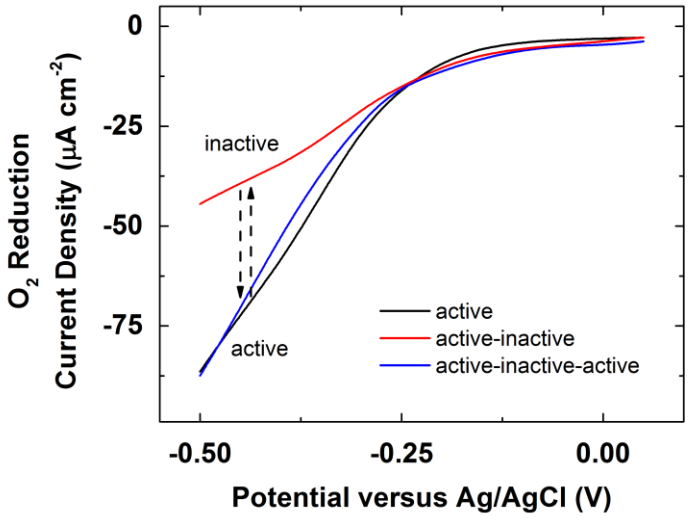

Figure 10.10. O_2 reduction LSVs in O_2-saturated pH 7 phosphate buffer at a scan rate of 10 mV/s by CuBTT covered by a monolayer of DMPC with Z-**BA** incorporated in the lipid layer (black) irradiated with 390 nm light for 5 min (red) followed by 360 nm light for 1 min (blue).

We further examined light-induced proton delivery in a HBM after a complete on-off-on cycle. Figure 10.10 displays LSVs of O_2 reduction by CuBTT covered by a DMPC monolayer with Z-**BA** added to the lipid layer with sequential irradiations. Upon irradiation with 390 nm light for 5 min and then 360 nm light for 1 min, we revived the O_2 reduction current density to within 10% of the current density of the initial on state (Figure 10.10, blue line), testifying to the reversibility of the system.

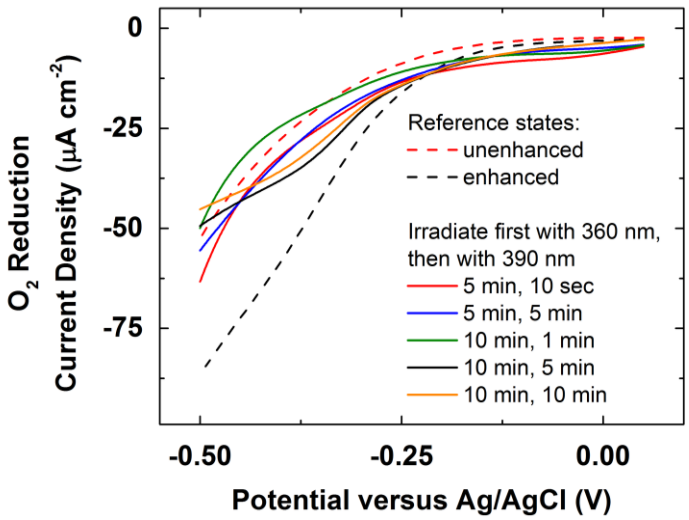

Figure 10.11. LSVs of O_2 reduction catalyzed by CuBTT covered by a monolayer of DMPC with Z-**BA** (black dashed line), E-**BA** (red dashed line), Z-**BA** irradiated with 390 nm light for 5 min followed by 360 nm light for 10 sec (red solid line), Z-**BA** irradiated with 390 nm light for 5 min followed by 360 nm light for 5 min (blue solid line), Z-**BA** irradiated with 390 nm light for 10 min followed by 360 nm light for 1 min (green solid line), Z-**BA** irradiated with 390 nm light for 10 min followed by 360 nm light for 5 min (black solid line), and Z-**BA** irradiated with 390 nm light for 10 min followed by 360 nm light for 10 min (orange solid line) in O_2-saturated pH 7 phosphate buffer at a scan rate of 10 mV/s.

Similar to the results obtained in Figure 10.8, Figure 10.11 shows that prolong exposure to 360 nm and 390 nm irradiation causes irreversible decrease in O_2 reduction current. Figure 10.11 red line shows that 10 sec is not enough to convert all the E-**BA** (the inactive form) into Z-BA (the active form), similar to the red line shown in Figure 10.8. Figure 10.11 blue line indicates that 5 min exceeds the irradiation time limit and results in lowered O_2 reduction current, similar to the black line shown in Figure 10.8. The green, orange, and black lines in Figure 10.11 together demonstrate that in the event of irradiation with 390 nm light for 10 min, subsequent irradiation with 360 nm light cannot fully recover the O_2 reduction current to the reference "enhanced" state, regardless of the length of irradiation with 360 nm light. This result is likely due to the irreversible leaching of the proton carrier from the lipid layer during

irradiation—an amplification of 10% dissolution of proton carrier in the on-off-on case shown in Figure 10.10. In summary, we achieve the first photo-responsive proton gate in a HBM and demonstrate the use of this photogate to successively turn off and back on an O_2 reduction catalyst without concomitant changes in solution pH.

10.7 Conclusions

In this chapter, we improved the synthesis of BTT, the ligand for assembling an active Cu ORR catalyst. More importantly, we designed the first synthetic photo-responsive proton gate incorporated in the lipid layer of a HBM. Upon irradiating the HBM with lights of different wavelengths temporally, the proton gate inside the lipid membrane adopts the Z or E conformation, which modulates the transmembrane proton flux and thus switches the lipid-covered O_2 reduction catalyst on and off on-demand. Further spatial regulation of this photo-responsive proton gate in the bio-inspired HBM platform could permit the development of more complex hybrid models for future biophotonics, optoelectronics, molecular switches, and memory elements.

10.8 References

(1) Chang, C. J.; Chang, M. C. Y.; Damrauer, N. H.; Nocera, D. G. *BBA-Bioenergetics* **2004**, *1655*, 13.
(2) Weinberg, D. R.; Gagliardi, C. J.; Hull, J. F.; Murphy, C. F.; Kent, C. A.; Westlake, B. C.; Paul, A.; Ess, D. H.; McCafferty, D. G.; Meyer, T. J. *Chem. Rev.* **2012**, *112*, 4016.
(3) Mayer, J. M.; Rhile, I. J. *BBA-Bioenergetics* **2004**, *1655*, 51.
(4) Hammes-Schiffer, S. *Acc. Chem. Res.* **2009**, *42*, 1881.
(5) Mayer, J. M. *Annu. Rev. Phys. Chem.* **2004**, *55*, 363.
(6) Jaouen, F.; Proietti, E.; Lefevre, M.; Chenitz, R.; Dodelet, J.-P.; Wu, G.; Chung, H. T.; Johnston, C. M.; Zelenay, P. *Energy Environ. Sci.* **2011**, *4*, 114.
(7) Gewirth, A. A.; Thorum, M. S. *Inorg. Chem.* **2010**, *49*, 3557.
(8) Thorseth, M. A.; Tornow, C. E.; Tse, E. C. M.; Gewirth, A. A. *Coord. Chem. Rev.* **2013**, *257*, 130.

(9) Tse, E. C. M.; Schilter, D.; Gray, D. L.; Rauchfuss, T. B.; Gewirth, A. A. *Inorg. Chem.* **2014**, *53*, 8505.
(10) Coms, F. D. *ECS Trans.* **2008**, *16*, 235.
(11) Chidsey, C. E. D. *Science* **1991**, *251*, 919.
(12) Bard, A. J.; Faulkner, L. R. *Electrochemical Methods: Fundamentals and Applications*; Wiley, 2000.
(13) Barile, C. J.; Tse, E. C. M.; Li, Y.; Sobyra, T. B.; Zimmerman, S. C.; Hosseini, A.; Gewirth, A. A. *Nat. Mater.* **2014**, *13*, 619.
(14) Hosseini, A.; Barile, C. J.; Devadoss, A.; Eberspacher, T. A.; Decreau, R. A.; Collman, J. P. *J. Am. Chem. Soc.* **2011**, *133*, 11100.
(15) Hosseini, A.; Collman, J. P.; Devadoss, A.; Williams, G. Y.; Barile, C. J.; Eberspacher, T. A. *Langmuir* **2010**, *26*, 17674.
(16) Schönfeld, P.; Schild, L.; Kunz, W. *BBA-Bioenergetics* **1989**, *977*, 266.
(17) McConnell, H. M.; Kornberg, R. D. *Biochemistry* **1971**, *10*, 1111.
(18) Stowell, M. H. B.; McPhillips, T. M.; Rees, D. C.; Soltis, S. M.; Abresch, E.; Feher, G. *Science* **1997**, *276*, 812.
(19) Muraoka, T.; Kinbara, K.; Aida, T. *Nature* **2006**, *440*, 512.
(20) Yagai, S.; Kitamura, A. *Chem. Soc. Rev.* **2008**, *37*, 1520.
(21) Beharry, A. A.; Woolley, G. A. *Chem. Soc. Rev.* **2011**, *40*, 4422.
(22) Klajn, R. *Chem. Soc. Rev.* **2014**, *43*, 148.
(23) Xu, J.-F.; Chen, Y.-Z.; Wu, D.; Wu, L.-Z.; Tung, C.-H.; Yang, Q.-Z. *Angew. Chem. Int. Ed.* **2013**, *52*, 9738.
(24) Yan, X.; Xu, J.-F.; Cook, T. R.; Huang, F.; Yang, Q.-Z.; Tung, C.-H.; Stang, P. J. *Proc. Natl. Acad. Sci. USA* **2014**, *111*, 8717.
(25) Wang, J.; Feringa, B. L. *Science* **2011**, *331*, 1429.
(26) Kucharski, T. J.; Boulatov, R. *J. Mater. Chem.* **2011**, *21*, 8237.
(27) Yang, Q.-Z.; Huang, Z.; Kucharski, T. J.; Khvostichenko, D.; Chen, J.; Boulatov, R. *Nat. Nano.* **2009**, *4*, 302.
(28) Akbulatov, S.; Tian, Y.; Boulatov, R. *J. Am. Chem. Soc.* **2012**, *134*, 7620.
(29) Dolzhenko, A. V.; Dolzhenko, A. V.; Chui, W.-K. *Heterocycles* **2007**, *71*, 429.
(30) Ketuly, K. A.; Hadi, A. H. A. *Molecules* **2010**, *15*, 2347.
(31) Uno, B. E.; Gillis, E. P.; Burke, M. D. *Tetrahedron* **2009**, *65*, 3130.
(32) Gillis, E. P.; Burke, M. D. *J. Am. Chem. Soc.* **2007**, *129*, 6716.

Chapter 11

Anion Transport through Lipids in a Hybrid Bilayer Membrane

† E. C. M. T. and C. J. B. contributed equally.

11.1 Introduction

Ion transport across cell membranes is a crucial aspect of many cellular functions. Frequently, cell membranes contain specific ion channels, mediators, or pumps which accelerate transmembrane ion transport.[1,2] However, even in the absence of transport assistance, ions, water, and other small molecules can permeate lipid layers.[3] Over the last few decades, there has been much interest in elucidating the mechanism of unassisted ionic transport across cell membranes.[4] This knowledge aids in the understanding of charge stabilization and distribution in cell membranes and in the development of drug delivery schemes, particularly those involving drugs encapsulated by liposomes.[5-8]

Two competing theories have emerged that describe how ions and small molecules permeate through lipid membranes: the solubility-diffusion mechanism and the pore mechanism. According to the solubility-diffusion mechanism, the lipid membrane is modeled as a thin hydrophobic layer that separates two aqueous phases.[9] Permeable species must first dissolve in

and diffuse across the hydrophobic phase and then dissolve in the aqueous phase. In contrast, the pore mechanism describes permeable species as diffusing through hydrophilic defects or transient channels in lipid layers that result from thermal fluctuations.[10] Although the solubility-diffusion and pore mechanisms make dramatically different predictions about ion permeability, there is substantial disagreement as to what factors determine when each mechanism is operative.[11-18]

Ion permeability through lipid bilayers is most commonly measured by first setting up a concentration gradient of the ion of interest across a liposome.[19] The ion concentration outside the liposome is then measured as a function of time using a variety of analytical techniques including dye-based fluorimetry, ion-specific electrodes, and radioactive tracing.[20,21] However, all of these techniques suffer from limited anion scope. For instance, *N*-(ethoxycarbonylmethyl)-6-methoxyquinolinium bromide is a dye that is used to measure Cl^-, Br^-, and I^- concentration, but it cannot be applied to other anions and even its sensitivity amongst these three anions varies substantially.[22] Permeability measurements utilizing ion-specific electrodes have been limited to H^+.[23] Radioactive tracing has been limited to mostly Cl^- and Br^- because the use and procurement of more complex radiolabeled ions can be difficult.[23]

In this paper, we develop a novel method of assaying relative anion permeability through lipids using electrochemistry. Whereas previous methods rely on a concentration gradient of anions across the aqueous phases of the lipid-water system, we assess anion permeability using an electrostatic gradient set up by metal cations on an electrode surface. This electrochemical method allows for a wide variety of anions to be tested without adding or altering any other components of the system.

The electrochemical platform utilized in this work to measure relative anion permeability consists of Cu-triazole-based molecules embedded in a hybrid bilayer membrane (HBM). Previously, we demonstrated how this system can be used to control proton flux to a molecular O_2 reduction catalyst.[24,25] A HBM consists of a lipid monolayer that is appended on top of a self-assembled monolayer (SAM) of molecules covalently bound to a Au surface.[26] In this work, we use cyclic voltammetry (CV) to cycle the redox state of the Cu inside the lipid layer of the HBM between Cu(I) and Cu(II). As each Cu(I) ion is oxidized to Cu(II), an anion must be transported from the bulk aqueous phase through the lipid layer and associated with Cu(II) to compensate for the change in charge.

We find that the voltammetric response of the HBM system varies as a function of anions present in bulk solution, and that these changes can be rationalized in terms of the ability of each anion to permeate through the lipid layer of the HBM. We interrogate two key attributes of the CVs—the peak position of the cathodic wave and the peak separation between the cathodic and anodic peaks, and develop a quantitative and predictive model for these attributes in terms of fundamental chemical trends. We discuss how these results can be viewed in light of the two leading theories describing ion permeability through lipids.

11.2 Factor Analysis Methodology

Factor analysis methodology was used to fit combinations of known trends to the experimental data. This technique has been widely used in a variety of chemical systems.[27-29] The general procedure is described below.

1. Chemical trends and experimental data are scaled (χ) from 0 to 1, with the maximum value in a given data series set as $\chi = 1$ and the minimum value set as $\chi = 0$. For example, in the

case of the pK_a of a given acid, HA, $\chi_{pKa}(HA)$ depends on the minimum pK_a in the data set ($pK_a(HA')_{min}$) and the maximum pK_a found in the data set ($pK_a(HA'')_{max}$).

$$\chi_{pKa}(HA) = \frac{pK_a(HA) - pK_a(HA')_{min}}{pK_a(HA'')_{max} - pK_a(HA')_{min}}$$

2. Weights (a_i) are assigned to trends and the weighted trends are summed together. For example, for a given anion A^-,

Model ***2b34*** $(A^-) = a_1\, \chi_{dipole}(HA) + a_2\, \chi_{pKa}(HA) + a_3\, \chi_{ligand\ strength}(A^-)$

where a_i ranges from 0 to 1, and $\Sigma\, a_i = 1$.

3. Trends in both ascending and descending order are examined. Arabic numerals with bars represent trends in descending order. For example,

Model ***2b34*** $(A^-) = a_1\, \chi_{dipole}(HA) + a_2\, \chi_{pKa}(HA) + a_3\, \chi_{ligand\ strength}(A^-)$

Model ***2b$\bar{3}$4*** $(A^-) = a_1\, \chi_{dipole}(HA) + a_2\, (1-\chi_{pKa}(HA)) + a_3\, \chi_{ligand\ strength}(A^-)$

4. The linear combinations of known trends are computed, and the differences between the known trends and the experimentally observed trend are calculated. For example, the fit of *Model* ***2b$\bar{3}$4*** to the experimental trend equals

$|$*Experimental* (Br^-) - *Model* ***2b$\bar{3}$4*** $(Br^-)\ |$ + $|$*Experimental* (Cl^-) - *Model* ***2b$\bar{3}$4*** $(Cl^-)\ |$ +

$|$*Experimental* (F^-) - *Model* ***2b$\bar{3}$4*** $(F^-)\ |$ + $|$*Experimental* $(H_2PO_4^-)$ - *Model* ***2b$\bar{3}$4*** $(H_2PO_4^-)\ |$ +

$|$*Experimental* (PF_6^-) - *Model* ***2b$\bar{3}$4*** $(PF_6^-)\ |$ + $|$*Experimental* (ClO_4^-) - *Model* ***2b$\bar{3}$4*** $(ClO_4^-)|$

5. The best-fit model is the model with the least difference calculated in #4.

11.3 Results and Discussion

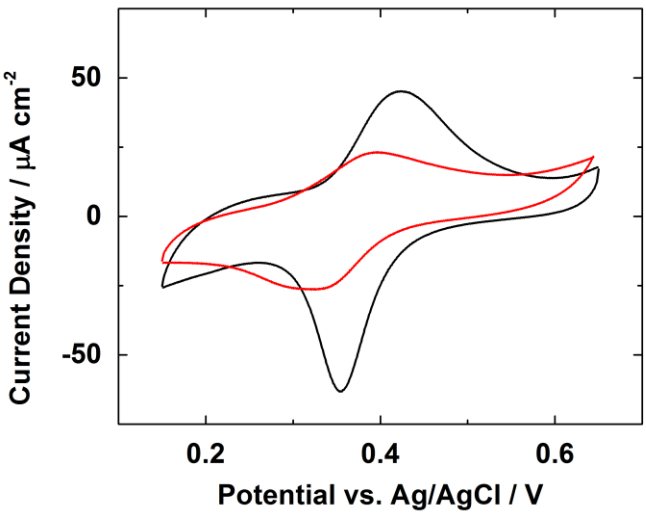

Figure 11.1. CVs of a SAM of Cu-BTT (black) and a SAM of Cu-BTT inside a monolayer of DMPC (red) on Au in Ar-sparged pH 5 KH_2PO_4 (100 mM).

The black line in Figure 11.1 shows a CV of a SAM of Cu-BTT. Previously, we demonstrated that the voltammetry contains both the Cu(I)/Cu(II) couple and a $1e^-$ redox couple associated with the triazole ring of BTT.[24] The two waves have very similar midpoint potentials ($E_{1/2}$), but different anodic-cathodic peak separations (ΔE_p), resulting in the asymmetric nature of the voltammetry.

The red line in Figure 11.1 shows a CV of a SAM of Cu-BTT inside a monolayer of DMPC. To ensure a well-packed lipid layer is formed, we probe its electronic conductivity using a solution of $K_3Fe(CN)_6$ as done previously.[24] In the absence of a lipid layer, the Fe(II)/Fe(III) redox couple from $K_3Fe(CN)_6$ is present. The disappearance of the Fe(II)/Fe(III) couple upon lipid formation indicates that a compact lipid layer is formed. The red line in Figure 11.1 shows that the $E_{1/2}$ of Cu-BTT inside a HBM shifts to more negative potentials compared to the open SAM case due to the hydrophobic environment of the lipid layer. More interestingly, the total integrated charge decreases by approximately half upon appending a lipid monolayer. This

observation suggests that one of the two redox couples seen in the open SAM case becomes silent in the HBM.

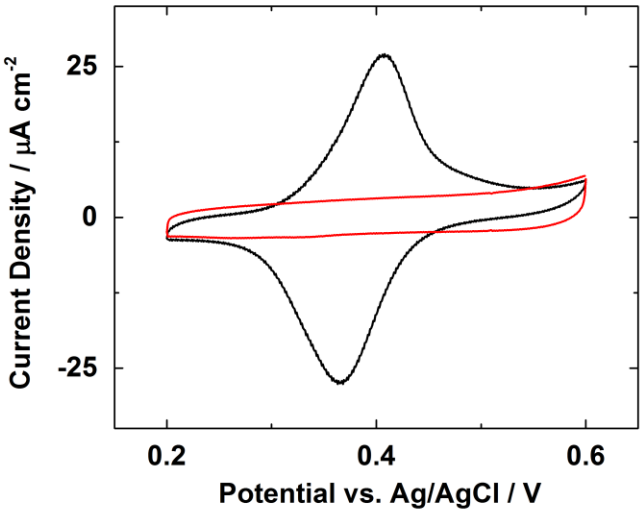

Figure 11.2. CVs of a SAM of Zn-BTT (black), and a SAM of Zn-BTT inside a monolayer of DMPC (red) on Au in Ar-sparged pH 5 KH_2PO_4 (100 mM).

To determine which redox couple disappears, we performed voltammetry of Zn-BTT. The black line in Figure 11.2 shows a CV of a SAM of Zn-BTT, which has a $E_{1/2}$ similar to that of Cu-BTT. Zn is redox-inactive in this potential range, so the resulting voltammetry is only due to the BTT wave. Therefore, the integrated charge of the Zn-BTT voltammetry is approximately half that of Cu-BTT. The red line in Figure 11.2 shows the CV of a SAM of Zn-BTT inside a monolayer of DMPC. The voltammetry does not show any redox couple, indicating that inside a monolayer of DMPC, the BTT couple becomes silent. By performing CVs of a SAM of Zn-BTT with and without lipid, we determined that the BTT wave is silent inside lipid, thus explaining the 50% decrease in charge seen in the Cu-BTT system upon lipid formation. In other words, we only observe the Cu(I)/Cu(II) couple in the Cu-BTT inside a HBM.

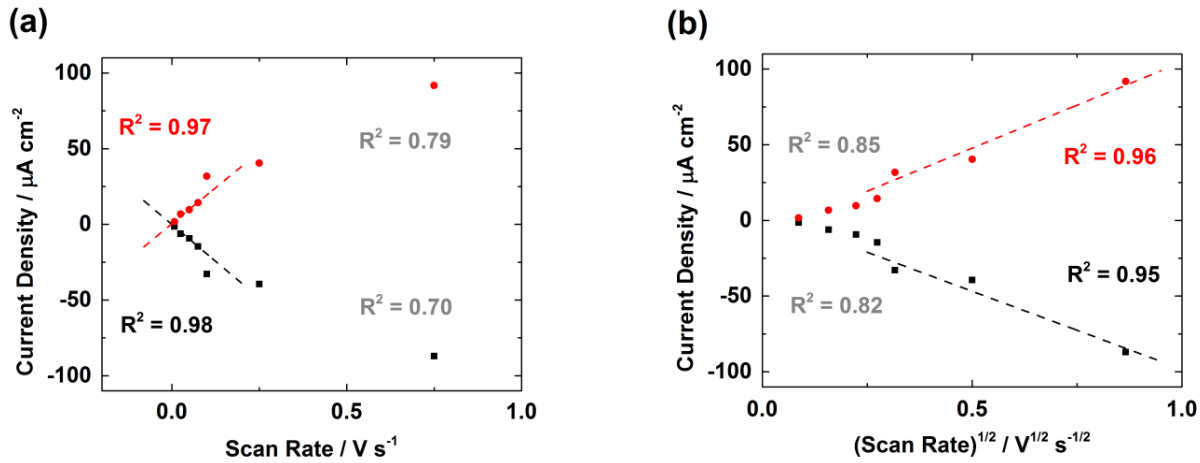

Figure 11.3. Peak cathodic (black) and anodic (red) current densities of a SAM of Cu-BTT inside a monolayer of DMPC on Au in Ar-sparged pH 5 KH_2PO_4 (100 mM) as a function of (a) scan rate and (b) the square root of scan rate. At relatively slow and fast scan rates, the best fit lines (R^2 values in red and black) vary as a function of scan rate and the square root of scan rate, respectively. R^2 values in grey with poor fits represent the *vice versa* cases.

Figure 11.3 shows the peak current densities of a SAM of Cu-BTT inside a DMPC monolayer as a function of scan rate. Typically for a SAM with covalently-bound redox centers, the peak current density increases linearly with scan rate. For electrochemical species in bulk solution, however, the peak current density is controlled by diffusion to the electrode surface and increases linearly with the square root of scan rate.[30] In the case of Cu-BTT in a HBM, we observe both diffusion-controlled and diffusionless regimes. Figure 11.3a shows that at scan rates below 100 mV/s, the peak current densities for both anodic and cathodic processes scale linearly with scan rate. However, Figure 11.3b shows that at scan rates at or above 100 mV/s, the peak current densities scale linearly with the square root of the scan rate. We hypothesize that at relatively fast scan rates, the voltammetry is limited by anion diffusion through the lipid layer of the HBM. Hence, although Cu-BTT is covalently bound to the electrode, its voltammetry is diffusion-controlled at fast scan rates. At slow scan rates, anions have sufficient time to diffuse across the lipid layer, and so the Cu-BTT system is in the diffusionless regime.

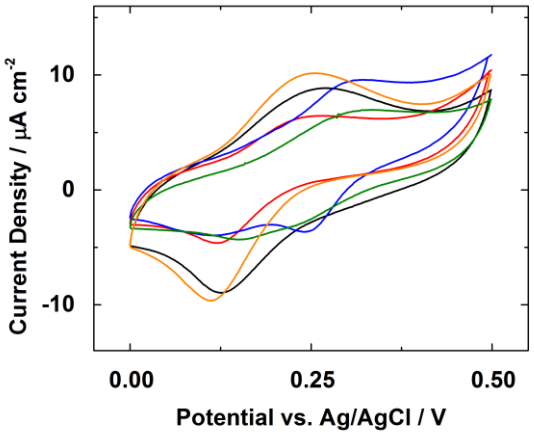

Figure 11.4. CVs of a SAM of Cu-BTT inside a monolayer of DMPC on Au in pH 5 100 mM KCl (black), KBr (red), KF (blue), KPF_6 (green), and $KClO_4$ (orange) at a scan rate of 100 mV/s.

Because the voltammetry of Cu-BTT inside a HBM at fast scan rates is controlled by anion diffusion, we decided to determine if the voltammetry would be sensitive to the identity of the anions present in the bulk solution. Figure 11.4 shows CVs of a SAM of Cu-BTT inside a monolayer of lipid in deoxygenated solutions containing different anions. We note that the CV has a positive slope centered around the $E_{1/2}$ of the Cu(I)/Cu(II) wave. This slope may be due to resistance in the system caused by slow anion diffusion through the lipid layer. Upon subtracting the slope from the voltammetry, the peak positions shift. However, the standard deviation of the shifts is only about 2 mV across all anions studied. Because the peak positions relative to each anion remain almost the same, this resistive behavior does not affect the subsequent quantitative analysis performed in this manuscript. More importantly, Figure 11.4 shows that there is a strong dependence of $E_{1/2}$ on the anions used with an average of (244 ± 73) mV.

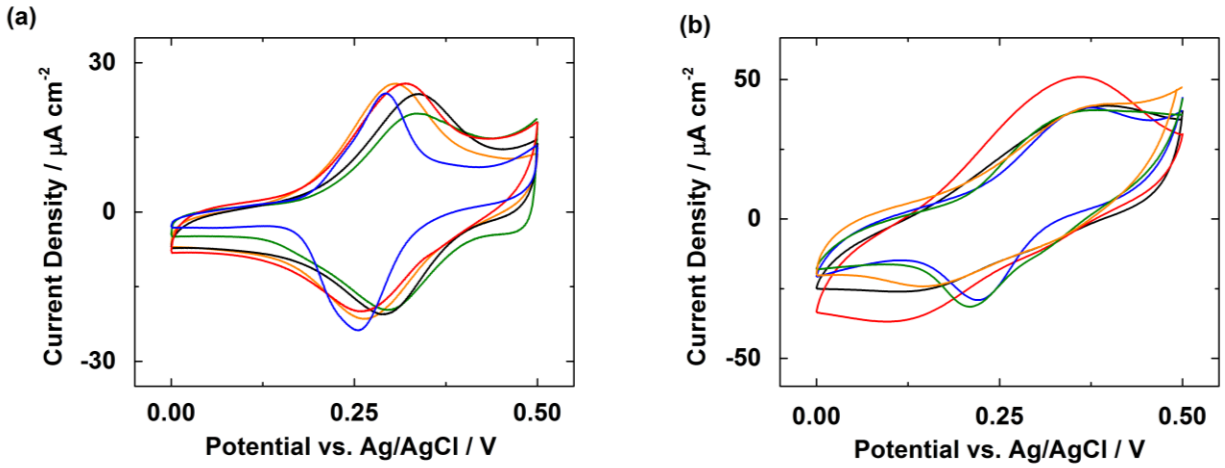

Figure 11.5. CVs of a SAM of (a) BTT and (b) Cu-BTT on Au in pH 5 100 mM KCl (black), KBr (red), KF (blue), KPF_6 (green), and $KClO_4$ (orange) at a scan rate of 100 mV/s.

Figure 11.5 shows the CVs of BTT and Cu-BTT SAMs in the absence of lipid. Unlike in the Cu-BTT lipid case, the redox couples of BTT and Cu-BTT are only modestly perturbed by the anions present in bulk solution as evidenced by the smaller standard deviations in $E_{1/2}$ [(295 ± 18) mV and (265 ± 26) mV, respectively]. These findings are consistent with previous studies that showed a relatively small anion effect on the voltammetry of Cr and Co complexes.[31,32]

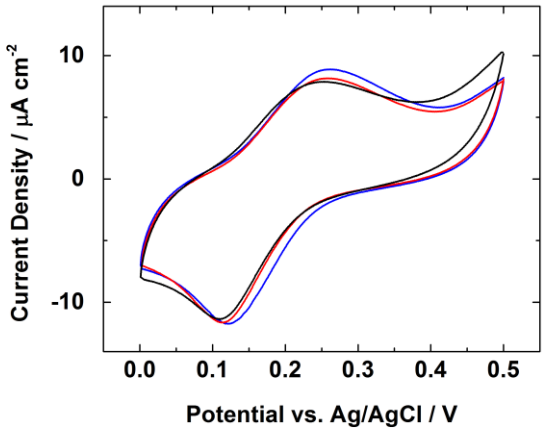

Figure 11.6. CVs of a SAM of Cu-BTT embedded in a monolayer of DMPC on Au in pH 5 50 mM (black), 100 mM (red), and 125 mM (blue) $KClO_4$ at a scan rate of 100 mV/s.

As presented in Figure 11.4, $E_{1/2}$ and ΔE_p of a SAM of Cu-BTT inside a lipid monolayer vary substantially depending upon the anion used. In the fast scan rate regime where the voltammetry is controlled by anion diffusion, $E_{1/2}$ and ΔE_p reflect the thermodynamics and kinetics of anion transport through the lipid membrane. We hypothesize that anion transport in a HBM is driven by an electrochemical gradient, not a concentration gradient. Figure 11.6 shows the CVs of a SAM of Cu-BTT inside a monolayer of DMPC in solutions with various concentrations of $KClO_4$. Figure 11.6 indicates that changing the electrolyte concentration does not significantly affect the voltammetry. This finding is consistent with our hypothesis that $E_{1/2}$ and ΔE_p only depend upon the nature of the anions, not the amount of anions present in the bulk solution.

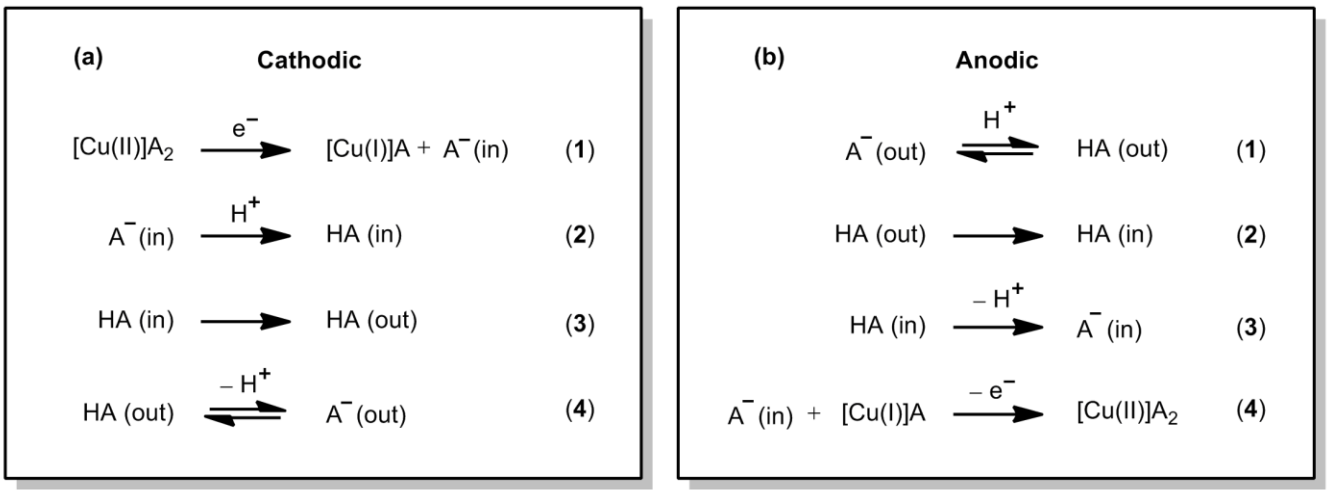

Scheme 11.1. Proposed elementary steps in the (a) cathodic and (b) anodic processes of a Cu-BTT SAM inside a monolayer of lipid undergoing a solubility-diffusion mechanism. The rate-determining steps for both processes are proposed to be steps 2.

We now address how the nature of the anions affects $E_{1/2}$ and ΔE_p of the Cu(I)/Cu(II) couple inside a HBM. For the cathodic process, we expect anions, which as relatively hydrophilic species, to be efficiently expelled from the hydrophobic interior of the lipid

membrane (i.e. Scheme 11.1a, step 3 is fast). Therefore the rate-determining step (RDS) in the cathodic process, reflected by the position of the cathodic peak (E_{pc}), is expected to be either the electron transfer step in the reduction of Cu(II) to Cu(I) with the dissociation of an anion from the Cu complex (Scheme 11.1a, step 1) or the protonation of the anion inside the lipid layer (Scheme 11.1a, step 2). More hydrophobic anions are more stable in the hydrophobic lipid layer, and therefore the cathodic process is expected to be more favorable with hydrophobic anions, and E_{pc} would shift positive accordingly.

However, the RDS of the anodic process is anion transport through the lipid layer (Scheme 11.1b, step 2), not electron transfer or anion association with the Cu complex (Scheme 11.1b, step 4). For example, anions with sluggish kinetics across the lipid membrane are expected to delay the anodic response. Taking into consideration that the anodic peak position is convoluted by shifts in the cathodic peak position, we instead use ΔE_p to measure the relative rates of anions diffusing through the lipid layer.

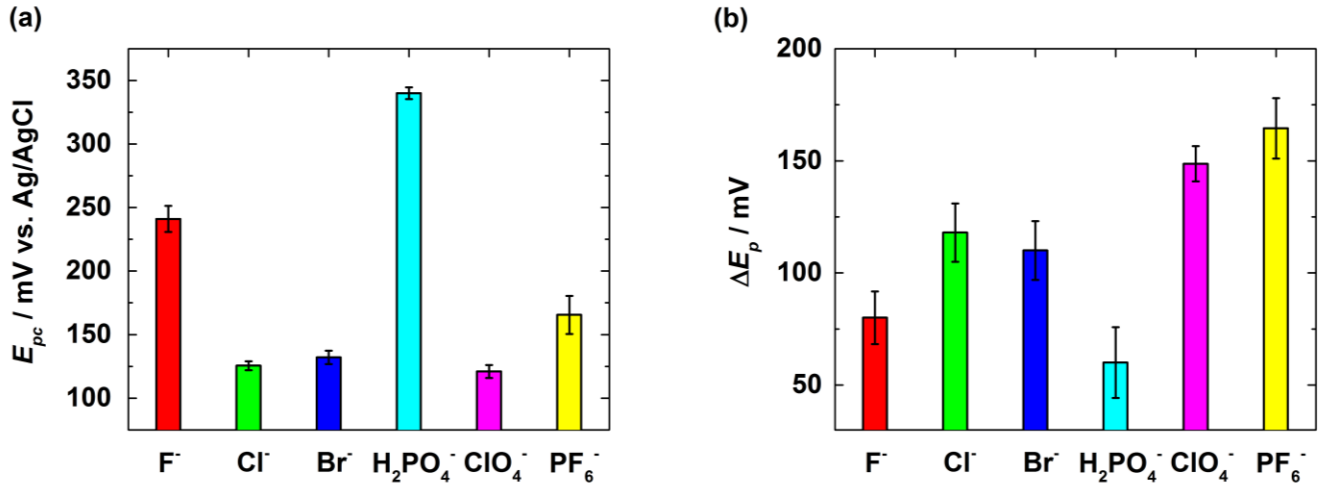

Figure 11.7. Plots of (a) E_{pc} and (b) ΔE_p versus anions tested in this study.

Figures 11.7a and 11.7b show that both E_{pc} and ΔE_p change as a function of anions used. ClO_4^- results in the most negative E_{pc}, indicating that the reduction of Cu(II) to Cu(I) is least favorable with ClO_4^- present. $H_2PO_4^-$ results in the smallest ΔE_p, indicating that $H_2PO_4^-$ diffuses the fastest across the lipid membrane to compensate for the change in Cu oxidation state.

We investigate if the observed E_{pc} and ΔE_p trends match any known chemical trends that are particularly important to the solubility-diffusion and pore mechanisms, the two main anion transport theories. We specifically compare four chemical trends: size, dipole moment, basicity, and ligand strength. According to the pore mechanism, in which anions diffuse through hydrophilic channels in the lipid layer, the ion size dramatically influences the rate of ion transport.[22] Smaller anions are predicted to diffuse across the lipid layer faster because they can more easily fit into transient pores. However, in the solubility-diffusion mechanism, anions must dissolve into the hydrophobic lipid layer. Therefore, the dipole moment should correlate with the rate of transmembrane migration, as stated by Meyer-Overton's rule.[33] Less polar anions will be transported across the lipid layer faster because they are more soluble in the hydrophobic lipid layer.

It is known that neutral molecules diffuse across lipid layers faster than charged species.[34] Weak acids diffuse faster than their deprotonated conjugate bases, and the conjugate bases of strong acids diffuse faster when their transport can be coupled to positively-charged carriers.[35] Because protonated anions are more hydrophobic, we expect anion basicity to influence the rate of anion transport through the lipid. The solubility-diffusion mechanism predicts that the rate of anion transport increases with more basic anions because species diffuse through a hydrophobic medium. However, the pore mechanism predicts the opposite because species diffuse through hydrophilic channels. We also consider the possibility that the anions can act as ligands to Cu.

To probe whether ligand binding or dissociation affects the electrochemical response of the redox wave, we compare our observed trends to the spectrochemical series. We also compare our results to the Hofmeister series, which describes the ability of anions to associate with water molecules, but we did not find any obvious correlation.[36]

Interestingly, we find that no single chemical trend matches well with the observed E_{pc} and ΔE_p series. We therefore suspect that multiple trends are operative in concert. We screen linear combinations of the four chemical trends using the quantitative data in Table 11.1 and determine the combination of trends that best fits our observed series.

Table 11.1. Input values of known chemical trends used in modeling studies.

Anion	Trend **1a,b** Size of A^-, $A^-_{(aq)}$ ($Å^3$) [a]	Trend **2a,b** Dipole moment of A^-, HA (D) [b]	Trend **3** pK_a of HA[37-40]	Trend **4** Ligand strength of A^- (cm^{-1}) [c]
Br^-	28.1, 266.1	1.16, 1.16	-9	12390
Cl^-	23.7, 235.3	1.69, 1.69	-8	13190
F^-	14.5, 166.1	2.32, 2.32	3	16090
$H_2PO_4^-$	62.7, 361.7	0.33, 0.33	2	14640
PF_6^-	72.4, 429.4	0, 5.62	-11	9000
ClO_4^-	53.6, 372.6	0, 4.05	-10	9000

[a] Sizes of bare anions[41-44] and anions with one hydration sphere[45-49]

[b] For monatomic anions, the dipole moment of HA is used as a surrogate for electronegativity. For symmetric polyatomic anions, the dipole moment of A^- is assumed to be zero. Dipole moments are calculated using Spartan '08 (Wavefunction, Inc.) v. 1.2.0.

[c] The ligand strengths of anions are estimated using the stretching frequencies of the metal-ligand bond in a series of vanadium complexes. PF_6^- and ClO_4^- are less coordinating than I^-, and thus are given a value smaller than I^-.[50] $H_2PO_4^-$ is known to have a binding affinity in between Cl^- and F^-, and thus its value is given as the average value of Cl^- and F^-.[51,52]

To find the best fit of the chemical trends to our observed series, we analyze a linear combination of three trends, giving us twelve models: **1a2a3**, **1a2a4**, **1a2b3**, **1a2b4**, **1a34**, **1b2a3**, **1b2a4**, **1b2b3**, **1b2b4**, **1b34**, **2a34**, and **2b34**. We consider both the ascending and descending combinations of the trends of each model. For example, model **1a2a3** considers the linear combinations of the size of A^-, the dipole moment of A^-, and the pK_a of HA in ascending order, whereas model $\overline{\mathbf{1}\boldsymbol{a}}\,\overline{\mathbf{2}\boldsymbol{a}}\,\overline{\mathbf{3}}$ considers the same trends in descending order. In total, we screened 96 ($=12\times2^3$) models.

For E_{pc}, the best fit model is $\overline{\mathbf{2}\boldsymbol{a}}\mathbf{34}$ with weighting coefficients of 0.4, 0.5, and 0.1 for each of the trends, respectively. Because the weighting coefficient for the ligand strength trend (trend **4**) is nearly zero, we conclude that there is no meaningful correlation between anion ligand strength and the cathodic peak position. However, the model demonstrates that as the peak position of the cathodic wave shifts more positive, the dipole moment of A^- becomes weaker and the pK_a of HA increases. In other words, as the anions become more nonpolar and more basic, the reduction of Cu(II) to Cu(I) becomes more facile. These findings are reasonable because the cathodic process generates anions inside the hydrophobic lipid layer. More nonpolar species are more stable in hydrophobic environments, and more basic anions are more readily converted to neutral HA species, which are more nonpolar than their corresponding deprotonated forms. Because both the basicity and dipole moment of the anions affect E_{pc}, we hypothesize that the RDS of the cathodic process is the protonation of A^- inside the lipid (Scheme 11.1a, step 2).

For ΔE_p, the best fit model is $\mathbf{2b}\overline{\mathbf{3}}\mathbf{4}$ with the same weighting coefficients of 0.4, 0.5, and 0.1 for each of the trends, respectively. Because the weighting coefficient for the ligand strength trend (trend **4**) is nearly zero, we also conclude that there is no meaningful correlation between anion ligand strength and ΔE_p. The model shows, however, that the pK_a of HA and the dipole

moment of HA correlate with ΔE_p. Specifically, the pK_a of HA decreases and the dipole moment of HA increases as ΔE_p increases. Changes in ΔE_p correlate with the kinetics of the RDS of the anodic process, which is anion transport from the bulk solution through the lipid layer. In other words, a smaller ΔE_p means faster anion transport kinetics. More basic anions are more likely to be protonated. Protonated species are more hydrophobic, and hence more readily permeate the hydrophobic lipid layer. We note that the best fit model uses the dipole moment of HA instead of A^-, which agrees with previous studies showing that anions diffuse faster through lipids when coupled to protons.[23] The model shows that less polar HA species diffuse across the hydrophobic lipid layer faster because they are relatively hydrophobic. In summary, the permeability of anions through the lipid layer depends on both the dipole moment and the pK_a of HA.

The modeling results suggest that the solubility-diffusion mechanism accurately describes anion transport in HBM systems because this mechanism predicts that more hydrophobic anions diffuse across the lipid layer faster. The pore mechanism is not operative because the model does not yield a strong correlation between size and anion transport kinetics. These conclusions agree with previous literature showing that in most cases, cations diffuse via the pore mechanism, whereas anions diffuse via the solubility-diffusion mechanism.[3,11,22] In addition, because our model finds almost no correlation between anion ligand strength and ΔE_p, we conclude that anion ligand binding to Cu does not convolute the interpretation of ΔE_p as a measure of anion transport kinetics through the lipid layer.

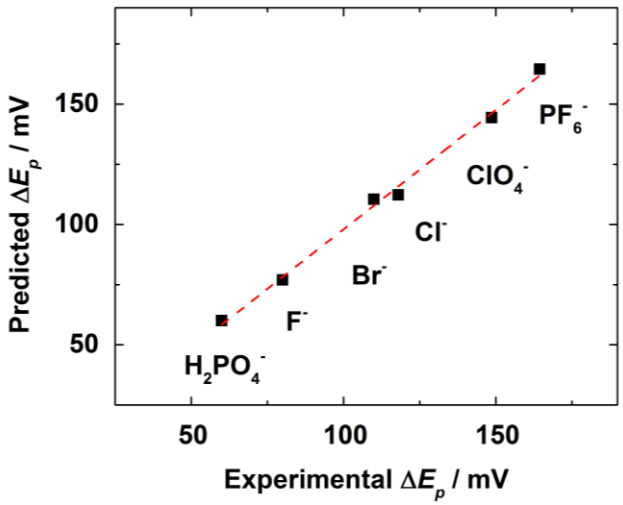

Figure 11.8. Experimental ΔE_p versus ΔE_p predicted by model $\mathbf{2b\overline{3}}$.

To simplify our model of anion transport kinetics, we eliminate the ligand strength trend because it has a weighting coefficient of almost 0 to yield the collapsed best-fit model $\mathbf{2b\overline{3}}$. We reevaluate the weighting coefficients for model $\mathbf{2b\overline{3}}$ and find that the best-fit model has coefficients of 0.5 for the dipole moment of HA and 0.5 for the pK_a of HA. Figure 11.8 shows that the predicted ΔE_p matches very well with the experimental ΔE_p with a R^2 value of 0.996 and a standard deviation of the errors of 2.5 mV. Figure 11.9 shows the relationship between the two trends used in model $\mathbf{2b\overline{3}}$. The very weak correlation (R^2 = 0.036) between the two trends demonstrates that the trends are independent of each other, and thus are good basis sets for this model.

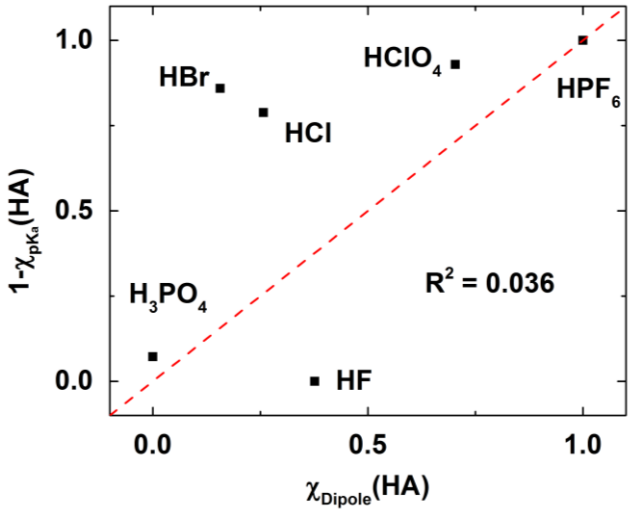

Figure 11.9. Relationship between the two trends used in model **2b$\overline{3}$**, the normalized pK_a and the dipole moment of the conjugate acids of the anions studied.

To evaluate the predictive capability of our model, for each anion studied we used the experimental data of the remaining five anions to calculate its ΔE_p using model **2b$\overline{3}$**. For example, to predict the ΔE_p of Br^-, we calculated the χ_{pKa} (HBr) and the χ_{dipole}(HBr) of Br^- using values in Table 11.1 and applied model **2b$\overline{3}$**. Figure 11.10 shows that the errors between the predicted ΔE_p values for each anion based upon the other five and the corresponding experimental ΔE_p values are within 6 mV except for PF_6^-. The large error associated with predicting the ΔE_p for PF_6^- is due to discrepancies in the literature regarding the pK_a of HPF_6.[39]

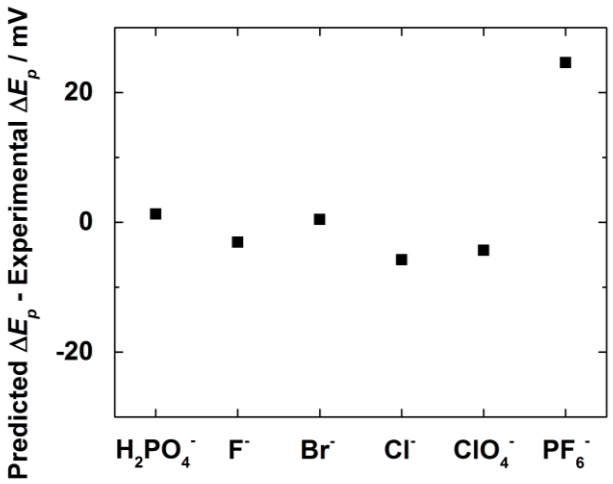

Figure 11.10. Difference between the experimental ΔE_p of an anion and the ΔE_p predicted from the remaining five anions using model **2b$\overline{3}$**.

We propose defining a new parameter, the lipid permeability parameter (LPP), to describe the relative ease of anion transport in HBMs. The LPP of an anion is easily calculated from fundamental chemical attributes, namely the pK_a and the dipole moment of the conjugate acid (Eq. 1). We assign $H_2PO_4^-$ and PF_6^- LPP values of 1 and 0 because they diffuse through the lipid layer the fastest and slowest, respectively. Table 11.2 lists the LPP values for all of the anions studied.

$$LPP(A^-) = 0.5\ \chi_{pKa}(HA) + 0.5\ (1-\chi_{dipole}(HA)) \qquad (1)$$

Table 11.2. LPP values.

Anion	PF_6^-	ClO_4^-	Cl^-	Br^-	F^-	$H_2PO_4^-$
LPP	0	0.19	0.50	0.52	0.84	1

11.4 Conclusions

We analyzed the effect of anions on the electrochemical response of a Cu-BTT SAM covalently bound to Au inside a lipid monolayer. The voltammetry is affected by the scan rate

and the identity of the anions, but not the bulk anion concentration. An increase in scan rate causes the HBM system to switch from a diffusionless regime to one controlled by anion diffusion. In the latter regime, we tested six anions that exhibit a wide range of E_{pc} and ΔE_p values, which reflect the differences in the thermodynamics and kinetics of anion diffusion across the lipid membrane. We then developed a simple model based on anion polarity and basicity that accurately predicts E_{pc} and ΔE_p of Cu-BTT inside a lipid with different anions present in bulk solution. Under this framework, we gained mechanistic information about the Cu(I)/Cu(II) couple inside lipid. In addition, our results suggest that the solubility-diffusion mechanism, not the pore mechanism, is operative for anion transport inside a HBM. Finally, we propose defining a new parameter, the lipid permeability parameter, to describe the relative ease of anion transport in HBMs.

11.5 References

(1) Denning, E. J.; Beckstein, O. *Chem. Phys. Lipids* **2013**, *169*, 57.
(2) Devaux, P. F. *Annu. Rev. Bioph. Biom.* **1992**, *21*, 417.
(3) Dilger, J.; McLaughlin, S.; McIntosh, T.; Simon, S. *Science* **1979**, *206*, 1196.
(4) Deamer, D. W.; Bramhall, J. *Chem. Phys. Lipids* **1986**, *40*, 167.
(5) Lian, T.; Ho, R. J. Y. *J. Pharm. Sci.* **2001**, *90*, 667.
(6) Maurer, N.; Fenske, D. B.; Cullis, P. R. *Expert Opin. Biol. Th.* **2001**, *1*, 923.
(7) Gabizon, A. A.; Shmeeda, H.; Zalipsky, S. *J. Liposome Res.* **2006**, *16*, 175.
(8) Allen, T. M.; Cullis, P. R. *Adv. Drug Deliver. Rev.* **2013**, *65*, 36.
(9) Finkelstein, A. *Water Movement through Lipid Bilayers, Pores, and Plasma Membranes: Theory and Reality*.; Wiley Interscience: New York, 1987.
(10) Bordi, F.; Cametti, C.; Naglieri, A. *Biophys. J.* **1998**, *74*, 1358.
(11) Deamer, D. W.; Volkov, A. G. *Proton permeation of lipid bilayers*; CRC Press: Boca Raton, Florida, 1995.
(12) Volkov, A. G.; Paula, S.; Deamer, D. W. *Bioelectroch. Bioenerg.* **1997**, *42*, 153.
(13) Bemporad, D.; Essex, J. W.; Luttmann, C. *J. Phys. Chem. B* **2004**, *108*, 4875.
(14) Tepper, H. L.; Voth, G. A. *J. Phys. Chem. B* **2006**, *110*, 21327.
(15) Gurtovenko, A. A.; Anwar, J. *J. Phys. Chem. B* **2007**, *111*, 13379.
(16) Lis, M.; Wizert, A.; Przybylo, M.; Langner, M.; Swiatek, J.; Jungwirth, P.; Cwiklik, L. *Phys. Chem. Chem. Phys.* **2011**, *13*, 17555.

(17) Przybyło, M.; Drabik, D.; Łukawski, M.; Langner, M. *J. Phys. Chem. B* **2014**, *118*, 11470.
(18) Vorobyov, I.; Olson, Timothy E.; Kim, Jung H.; Koeppe Ii, Roger E.; Andersen, Olaf S.; Allen, Toby W. *Biophys. J.* **2014**, *106*, 586.
(19) Nichols, J. W.; Deamer, D. W. *Proc. Natl. Acad. Sci. USA* **1980**, *77*, 2038.
(20) Kaplan, J. H. *BBA-Biomembranes* **1972**, *290*, 339.
(21) Bangham, A. D.; Standish, M. M.; Watkins, J. C. *J. Mol. Biol.* **1965**, *13*, 238.
(22) Paula, S.; Volkov, A. G.; Deamer, D. W. *Biophys. J.* **1998**, *74*, 319.
(23) Gutknecht, J.; Walter, A. *J. Membrane Biol.* **1979**, *47*, 59.
(24) Barile, C. J.; Tse, E. C. M.; Li, Y.; Sobyra, T. B.; Zimmerman, S. C.; Hosseini, A.; Gewirth, A. A. *Nat. Mater.* **2014**, *13*, 619.
(25) Hosseini, A.; Barile, C. J.; Devadoss, A.; Eberspacher, T. A.; Decreau, R. A.; Collman, J. P. *J. Am. Chem. Soc.* **2011**, *133*, 11100.
(26) Hosseini, A.; Collman, J. P.; Devadoss, A.; Williams, G. Y.; Barile, C. J.; Eberspacher, T. A. *Langmuir* **2010**, *26*, 17674.
(27) Burgard, D. R.; Perone, S. P.; Wiebers, J. L. *Anal. Chem.* **1977**, *49*, 1444.
(28) Liu, Z.; Patterson, D. G.; Lee, M. L. *Anal. Chem.* **1995**, *67*, 3840.
(29) Malinowski, E. R. *Factor Analysis in Chemistry*; Wiley, 2002.
(30) Bard, A. J.; Faulkner, L. R. *Electrochemical Methods: Fundamentals and Applications*; Wiley, 2000.
(31) Wakabayashi, N.; Kitamura, F.; Ohsaka, T.; Tokuda, K. *J. Electroanal. Chem.* **2001**, *499*, 161.
(32) Aikens, D. A.; Ross, J. W. *J. Phys. Chem.* **1961**, *65*, 1213.
(33) Meyer, H. *Arch. Exp. Pathol. Pharmakol.* **1899**, *42*, 109.
(34) Flewelling, R. F.; Hubbell, W. L. *Biophys. J.* **1986**, *49*, 541.
(35) Walter, A.; Gutknecht, J. *J. Membrane Biol.* **1986**, *90*, 207.
(36) Zhang, Y.; Cremer, P. S. *Annu. Rev. Phys. Chem.* **2010**, *61*, 63.
(37) Anslyn, E. V.; Dougherty, D. A. *Modern Physical Organic Chemistry*; University Science, 2006.
(38) Brownstein, S.; Stillman, A. E. *J. Phys. Chem.* **1959**, *63*, 2061.
(39) Koppel, I. A.; Burk, P.; Koppel, I.; Leito, I.; Sonoda, T.; Mishima, M. *J. Am. Chem. Soc.* **2000**, *122*, 5114.
(40) Schrödter, K.; Bettermann, G.; Staffel, T.; Wahl, F.; Klein, T.; Hofmann, T. In *Ullmann's Encyclopedia of Industrial Chemistry*; Wiley-VCH Verlag GmbH & Co. KGaA: 2000.
(41) Shannon, R. *Acta Crystallogr. A* **1976**, *32*, 751.
(42) Nomkoko, E. T.; Jackson, G. E.; Nakani, B. S.; Bourne, S. A. *Dalton T.* **2004**, 1789.
(43) Onoda, A.; Okamura, T.-a.; Yamamoto, H.; Ueyama, N. *Acta Crystallogr. E* **2001**, *57*, o1022.
(44) Murphy, B.; Roberts, G.; Tyagi, S.; Hathaway, B. J. *J. Mol. Struct.* **2004**, *698*, 25.
(45) Allen, F. H.; Kennard, O.; Watson, D. G.; Brammer, L.; Orpen, A. G.; Taylor, R. *J. Chem. Soc. Perk. T. 2* **1987**, S1.
(46) Nam, D.; Lee, C.; Park, S. *Phys. Chem. Chem. Phys.* **2014**, *16*, 21747.
(47) Habershon, S. *Phys. Chem. Chem. Phys.* **2014**, *16*, 9154.
(48) Tang, E.; Di Tommaso, D.; de Leeuw, N. H. *J. Chem. Phys.* **2009**, *130*.
(49) Eriksson, A.; Kristiansson, O.; Lindgren, J. *J. Mol. Struct.* **1984**, *114*, 455.

(50) Hoggard, P. In *Optical Spectra and Chemical Bonding in Inorganic Compounds*; Mingos, D., Schönherr, T., Eds.; Springer Berlin Heidelberg: 2004; Vol. 106, p 37.
(51) Ophardt, C. E. *J. Chem. Educ.* **1984**, *61*, 1102.
(52) Villeneuve, G.; Erragh, A.; Beltran, D.; Drillon, M.; Hagenmuller, P. *Mater. Res. Bull.* **1986**, *21*, 621.

Chapter 12

Proton Transfer Kinetics Dictate Quinone Speciation at Lipid-modified Electrodes

The work in this chapter was accomplished in collaboration with Dr. Christopher J. Barile,[†] Dr. Ying Li, Professor Steven C. Zimmerman, and Professor Andrew A. Gewirth.

[†] E. C. M. T. and C. J. B. contributed equally.

12.1 Introduction

Proton-coupled electron transfer (PCET) reactions are ubiquitous in natural and artificial energy conversion schemes.[1,2] In particular, PCET reactions mediated by quinones are of particular importance in biological studies and the pharmaceutical industry.[3,4] Quinones enable both the cellular respiration and photosynthesis processes.[5] Quinones also serve as the structural basis of many potent anti-tumor chemotherapeutic compounds and anti-Alzheimer lead drug candidates.[6,7] Apart from their application and utility in medicinal chemistry, quinone-based redox mediators facilitate the oxygen reduction reaction (ORR) in implantable biofuel cells.[8-10]

Unsurprisingly, these important quinone-mediated PCET reactions are studied by a multitude of computational and experimental methods.[3-13] Based on the pioneering work of Laviron, Finklea et al. later incorporated ideas from Marcus theory to examine the potential- and pH-dependent apparent transfer coefficient (α) of PCET reactions involving quinones.[14] The proton and electron transfer steps can occur in sequential steps or concerted steps,[15] rendering

these quinone systems difficult to study experimentally. While conventional studies of water-soluble quinones in buffered solutions provide insights into the PCET mechanism, surface-immobilized quinone systems result in cleaner electrochemical responses that allow for more accurate determination of apparent rate constants.[5,11-13] By combining the theoretical framework and the experimental efforts, the PCET process of quinones are now commonly described by a nine-membered square scheme.

The most common reaction pathway of simple quinones in aqueous solutions is the $2e^-$ $2H^+$ redox step that cycles between the fully-oxidized species "M" and the fully-reduced state "V", as evidenced by a typical 59 mV/pH shift that follows the ideal Nernstian behavior. There are reports that suggest flanking amines induce a $2e^-$ $3H^+$ pathway at low pH.[11] While a tremendous amount of effort has been reported to measure and calculate the apparent rate constants and α and examine their dependencies on pH and potential, a significantly less amount of effort is put in to observe the species other than "M" and "V" in the nine-membered square scheme.

There are two main impediments to access all nine members in the scheme. First, the relative energy species of some of these species such as the dianion "S" and the doubly-protonated species "Q" are likely too high and thus are unstable and unattainable. Second, the inability to independently control both electron transfer and proton transfer limits the chances to attain species when the ratio of electrons and protons transferred does not equal one. A self-assembled monolayer (SAM) on Au electrode is frequently used to address the energetics and fluxes of electron transfer to a redox-reporter positioned at the SAM-solution interface. However, proton thermodynamics and kinetics are much more difficult to modulate.

A hybrid bilayer membrane (HBM) offers an electrochemical platform to explore species

in the nine-membered scheme by delineating the effects of proton transfer from electron transfer. A HBM consists of a SAM covered by a lipid monolayer.[16,17] Previously, we explored the pH-responsiveness of a lipid-bound proton carrier to reversibly turn on and off an embedded ORR catalyst.[18] We further demonstrated the utility and practicality of our HBM system to assess the lipid permeability of anions.[19] Here, we demonstrate that by tethering quinone moieties at the SAM-lipid interface with and without proton carrier added to the lipid monolayer, we are able to access several species that are rarely observed for surface-confined quinone systems. We envision that the ability to modulate speciation across the nine-member square scheme will not only provide unique mechanistic insight into the intricate PCET pathway of quinones, but lay a foundation for new understanding of PCET reactions in both chemistry and biology.

12.2 Synthesis Procedures of Redox Probes

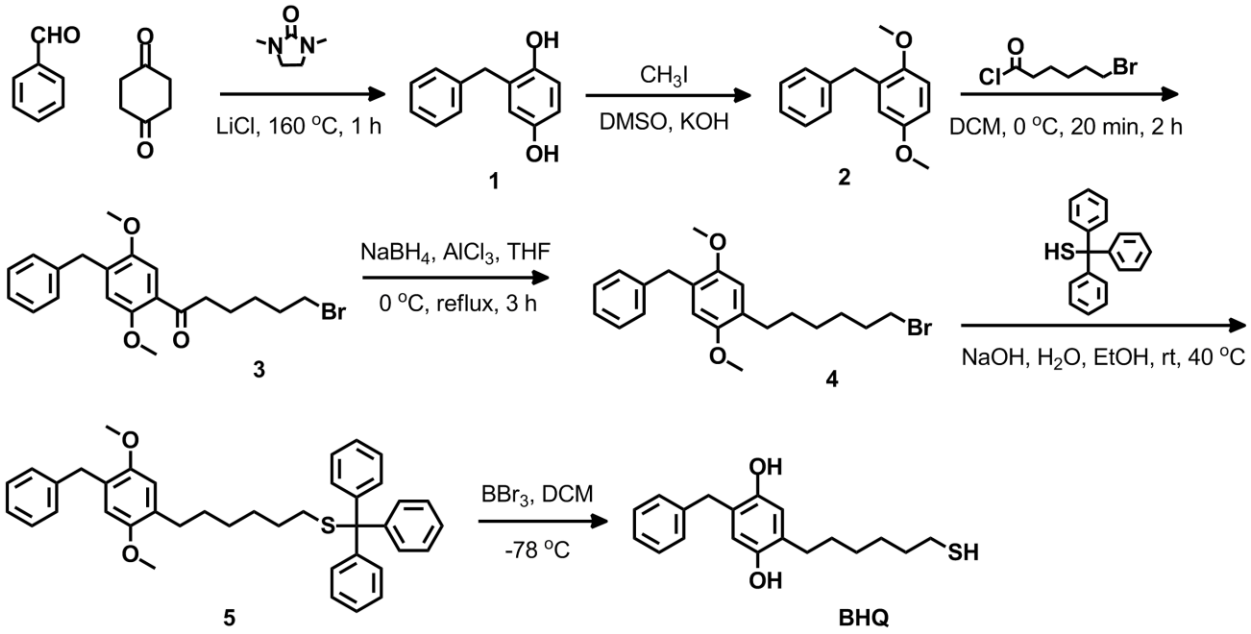

Scheme 12.1. Preparation of BHQ.

1: To a solution of 1,4-cyclohexanedione (2.8 g, 25 mmol) and benzaldehyde (2.65g, 25 mmol) in 10 mL of 1,3-dimethyl-2-imidazolidinone, lithium chloride (1.2 g, 28 mmol) was added. The mixture was heated to 160 $^{\circ}$C for 1 h, cooled to room temperature, poured into 50 mL of water and extracted twice with 50 mL of diethyl ether. The organic layers were combined, dried with anhydrous Na_2SO_4 and concentrated down under reduced pressure. The crude product was purified by gradient column chromatography (silica, EtOAc/hexanes: 1/4 to 1/1) to give a white solid (yield: 3.72 g, 82%). ^{1}H NMR (500 MHz, $CDCl_3$): δ 7.30 (m, 2H), 7.22 (m, 3H), 6.67 (m, 1H), 6.60 (m, 1H), 6.59 (s, 1H), 4.37 (b, 1H), 4.34 (b, 1H), 3.94 (s, 2H).

2: To 30 mL of DMSO, potassium hydroxide (6.4 g, 0.11 mol) was added. The mixture was stirred at room temperature for 10 min. To the suspension, **1** (3 g, 15 mmol) and methyl iodide (4 mL, 64 mmol) were added. The mixture was stirred at room temperature for 1 h, poured into 30 mL of water, and extracted twice with 50 mL of DCM. The organic layers were combined, dried with anhydrous Na_2SO_4, concentrated down under reduced pressure to give an off-white solid without further purification (yield: 3.2g, 93 %). ^{1}H NMR (500 MHz, $CDCl_3$): δ 7.27 (m, 2H), 7.19 (m, 3H), 6.80 (d, J=8.5, 1H), 6.72 (dd, J=8.5,3, 1H), 6.66 (d, J=3, 1H), 3.95 (s, 2H), 3.78 (s, 3H), 3.72 (s, 3H).

3: A solution of **2** (1.7 g, 7.4 mmol) in 15 mL of DCM was cooled to 0 °C and $AlCl_3$ (1.34 g, 10 mmol) was added portion-wise over 20 min. To the mixture, 6-bromocaproyl chloride (1.12 mL, 7.3 mmol) was added dropwise and the suspension was stirred at 0 °C for 2 h. The reaction was quenched by adding 10 mL of aqueous HCl solution (0.1 M) and washed with 20 mL of saturated aqueous $NaHCO_3$ solution. The organic layer was dried with anhydrous Na_2SO_4 and

concentrated down under reduced pressure. The crude product was purified by gradient column chromatography (silica, EtOAc/hexanes: 1/10 to 1/4) to give an off-white solid (yield: 3.72 g, 82%). ^{1}H NMR (500 MHz, $CDCl_3$): δ 7.28 (m, 2H), 7.26 (s, 1H), 7.20 (m, 3H), 6.68 (s, 1H), 3.99 (s, 2H), 3.81 (s, 3H), 3.78 (s, 3H), 3.42 (t, J=7, 2H), 2.98 (t, J=7, 2H), 1.90 (m, 2H), 1.70 (m, 2H), 1.50 (m, 2H). ESI (m/z): calculated for $C_{21}H_{25}BrO_3$, 404.1 $[M]^+$; found, 405.2 $[M+H]^+$.

4: To 6 mL of THF at 0 °C, $AlCl_3$ (4.3 g, 32 mmol) and $NaBH_4$ (1.3 g, 34 mmol) were added portion-wise. To this suspension, a solution of **3** (1.19 g, 2.9 mmol) in 3 mL of THF at 0 °C was added dropwise. The mixture was warmed to room temperature and heated to reflux for 3 h. The reaction was carefully quenched by 1 ml of acetone and 10 ml of ice water. The aqueous layer was extracted three times with 15 mL of ethyl acetate. The organic layers were combined, dried with anhydrous Na_2SO_4, and concentrated down under reduced pressure. The crude product was used without further purification. ^{1}H NMR (500 MHz, $CDCl_3$): δ 7.27 (m, 2H), 7.21 (M, 2H), 7.17 (m, 2H), 6.68 (s, 1H), 6.59 (S, 1H), 3.95 (s, 2H), 3.77 (s, 3H), 3.70 (s, 3H), 3.41 (t, J=7, 2H), 2.57 (t, J=7, 2H), 1.87 (m, 2H), 1.58 (m, 2H), 1.48 (m, 2H), 1.38 (m, 2H).

5: To a solution of triphenylmethanethiol (1.17 g, 4.2 mmol) in 10 mL of 95% EtOH, a solution of NaOH (0.6 g, 15 mmol) in 2 mL of water was added. The suspension was stirred at room temperature for 15 min and a solution of **4** (1.1g, 2.8 mmol) in 10 mL of ethanol was added. The mixture was vigorously stirred at 40 °C for 4 h and filtered. The solvent of the filtrate was evaporated under reduced pressure and the oily residue was combined with the filtered residue and dissolved in 20 mL DCM. The organic layer was washed with 20 mL of water, 20 mL of saturated brine solution, dried over anhydrous Na_2SO_4, and concentrated down under reduced

pressure. The crude product was purified by gradient column chromatography (silica, EtOAc/hexanes: 1/10 to 1/4) to give a white solid (yield: 1.2 g, 73%). ^{1}H NMR (500 MHz, $CDCl_3$): δ 7.45 (m, 6H), 7.31 (m, 8H), 7.25 (m, 4H), 7.21 (m, 2H), 6.70 (s, 1H), 6.62 (S, 1H), 3.99 (s, 2H), 3.79 (s, 3H), 3.72 (s, 3H), 32.56 (t, J=8, 2H), 2.19 (t, J=8, 2H), 1.53 (m, 2H), 1.45 (m, 2H), 1.34 (m, 2H), 1.27 (m, 2H). ^{13}C NMR (125 MHz, $CDCl_3$): δ 151.4, 151.3, 145.2, 144.1, 141.4, 130.3, 130.0, 129.8, 129.0, 128.4, 127.9, 127.5, 126.6, 125.9, 113.6, 113.5, 113.3, 113.2(5), 66.5, 56.4, 56.4, 56.3, 56.2, 36.0, 32.2, 30.2, 30.1, 29.3, 29.0(3), 29.0(1), 28.7.

BHQ: To a solution of **5** (20 mg, 0.034 mmol) in 2 mL of DCM at -78 °C, BBr_3 (0.2 mL, 1 M solution in DCM) was added dropwise. The mixture was slowly warmed to room temperature and stirred for 2 h. The reaction was cooled to 0 °C and quenched with 0.2 mL of water. The organic layer was washed with 2 mL of saturated brine solution, dried over anhydrous Na_2SO_4, and concentrated down under reduced pressure. The crude product was purified by gradient column chromatography (silica, MeOH/DCM: 1/99 to 5/95) to give a white oil (yield: 10 mg, 93%). ^{1}H NMR (500 MHz, $CDCl_3$): δ 7.29 (m, 3H), 7.22 (m, 2H), 6.57 (s, 1H), 6.49 (s, 1H), 4.30 (b, 1H), 3.91 (s, 2H), 3.40 (t, J=7, 2H), 2.53 (t, J=7.5, 2H), 1.86 (m, 2H), 1.60 (m, 2H), 1.47 (m, 2H), 1.40 (m, 2H).

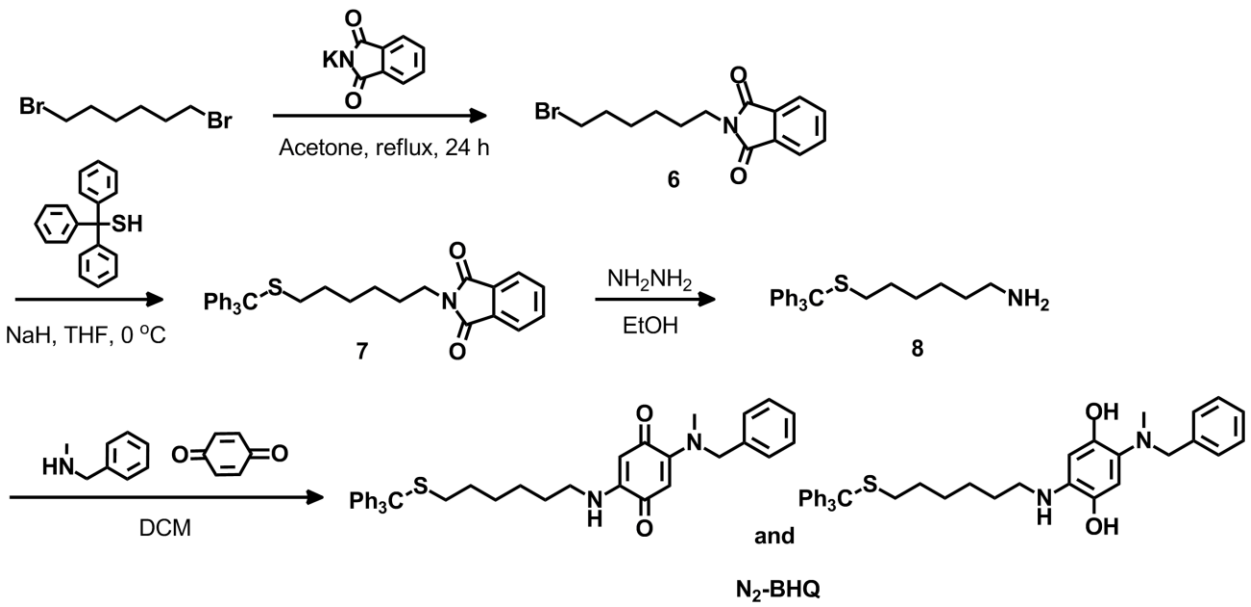

Scheme 12.2. Synthesis of N_2-BHQ.

6, **7**, and **8**: Products were obtained according to reported procedures.[20,21] ESI (m/z): calculated for $C_{25}H_{29}NS$, 375.2 $[M]^+$; found, 376.2 $[M+H]^+$.

N_2-BHQ: To a solution of benzylquinone (10.8 mg, 0.1 mmol) in 2 mL of DCM, *N*-methylbenzylamine (12.1 mg, 0.1 mmol) was added. The mixture was stirred at room temperature for 1 h and **4** (37.5 mg, 0.1 mmol) was added. The reaction was stirred at room temperature for 12 h. The organic layer was diluted with 10 mL of DCM, washed with 15 mL of saturated brine solution, dried over anhydrous Na_2SO_4, and concentrated down under reduced pressure. The crude product was purified by gradient column chromatography (silica, MeOH/DCM: 0/100 to 5/95) to give a red wax-like solid (yield: 26 mg, 43%, containing both the hydroquinone and benzylquinone forms, a mixture of products does not affect the electrochemical analysis because the molecules tethered to the surface are under potential-control upon redox cycling).

12.3 NMR Spectra of Redox Probes

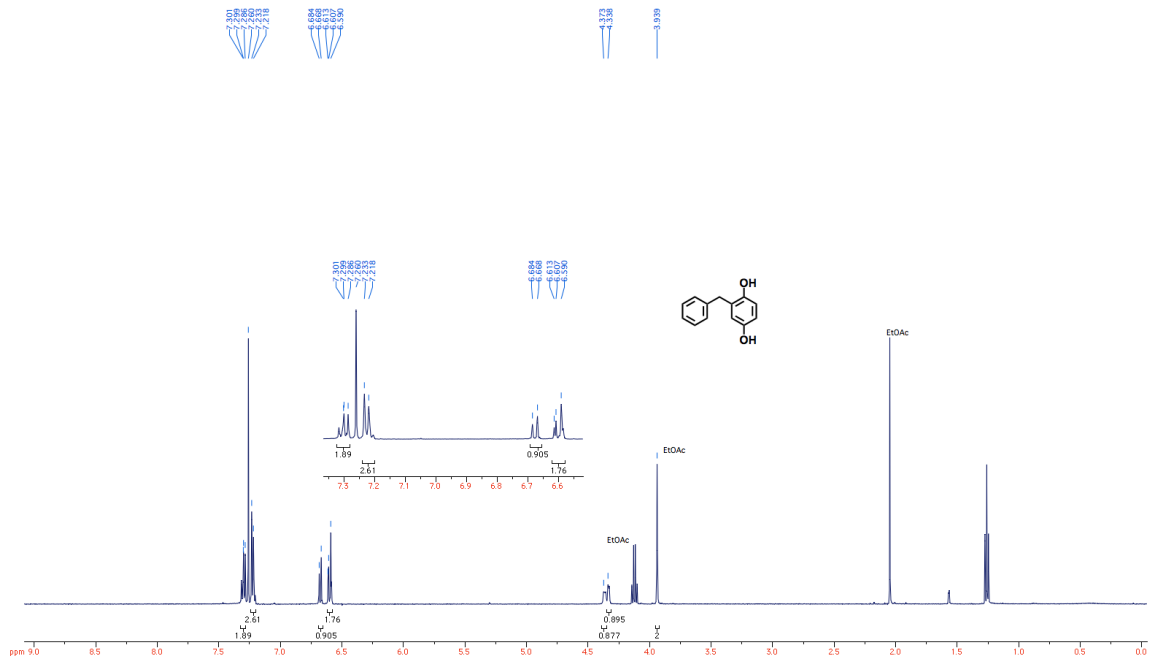

Figure 12.1. ^{1}H NMR spectrum of **1**.

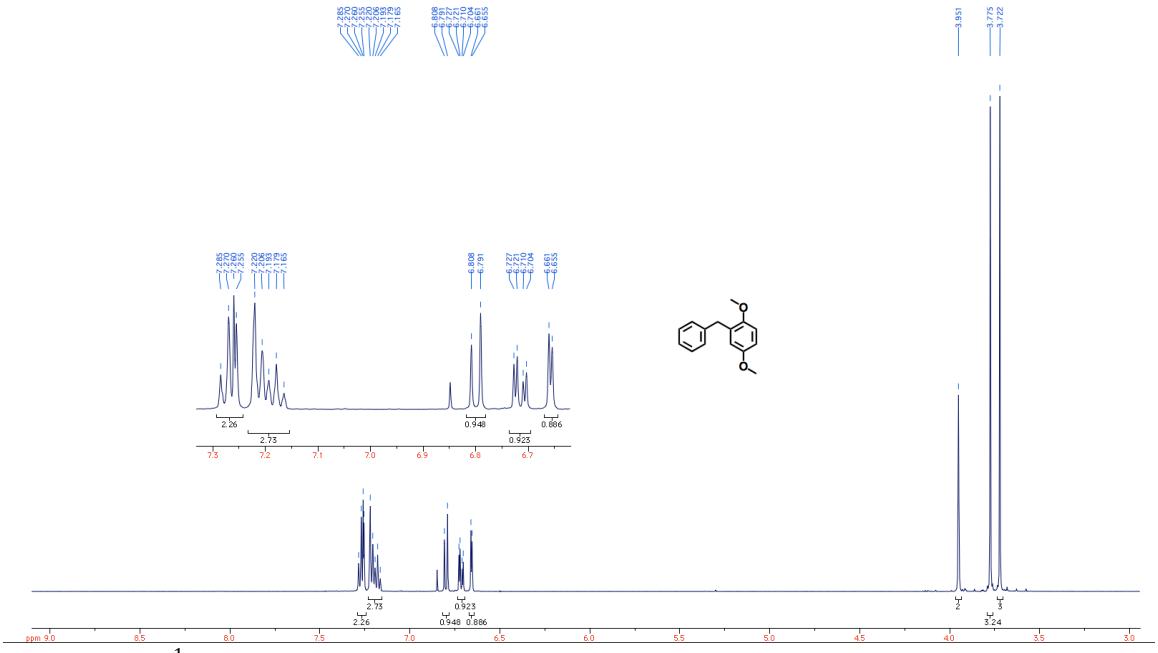

Figure 12.2. ^{1}H NMR spectrum of **2**.

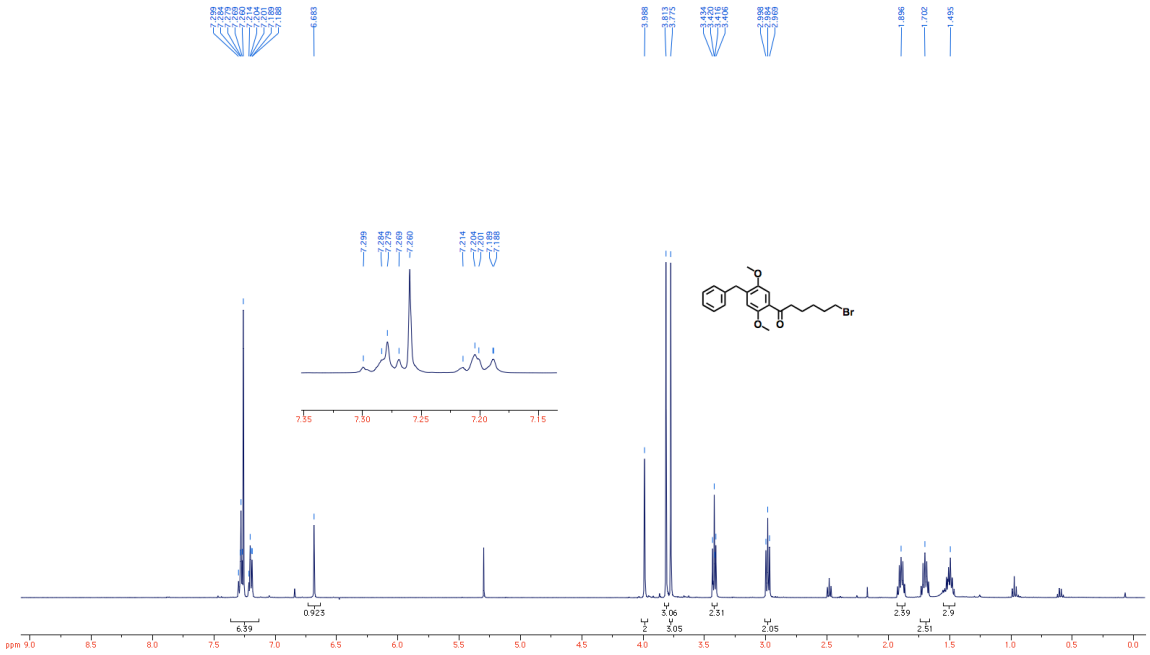

Figure 12.3. ^{1}H NMR spectrum of **3**.

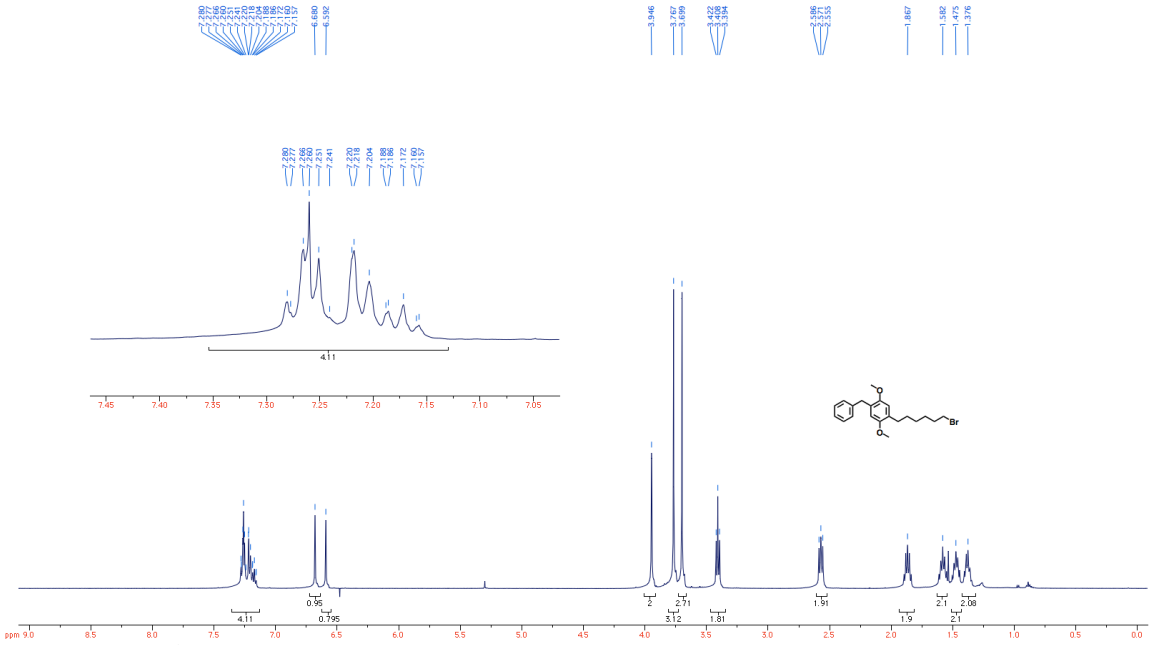

Figure 12.4. ^{1}H NMR spectrum of **4**.

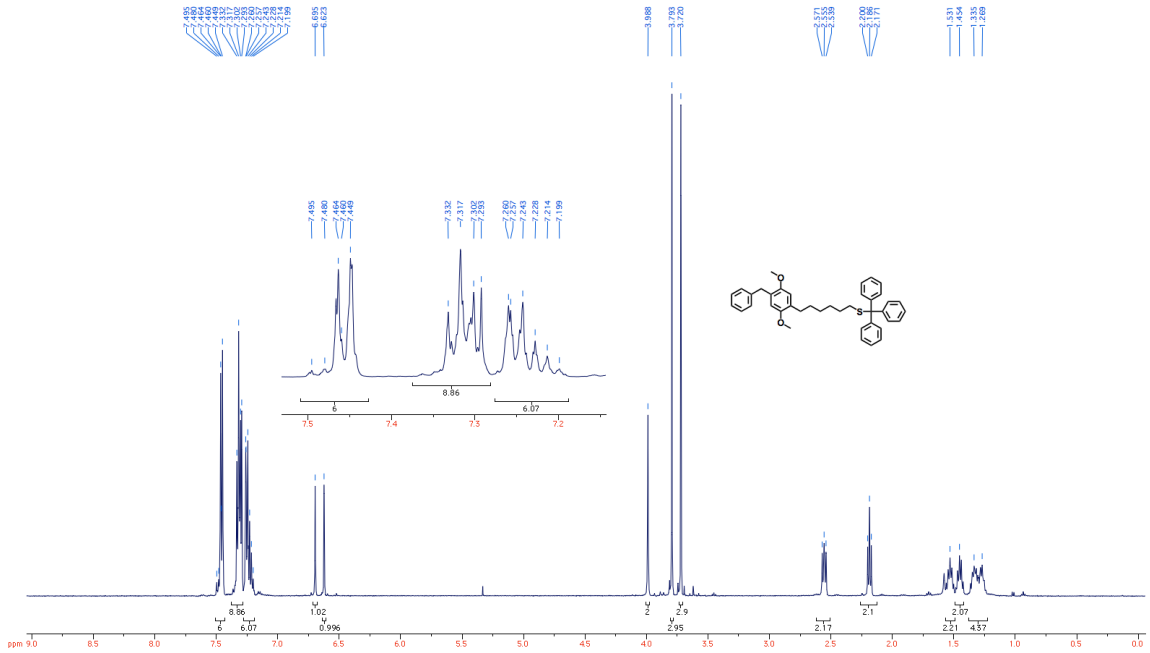

Figure 12.5. ^{1}H NMR spectrum of **5**.

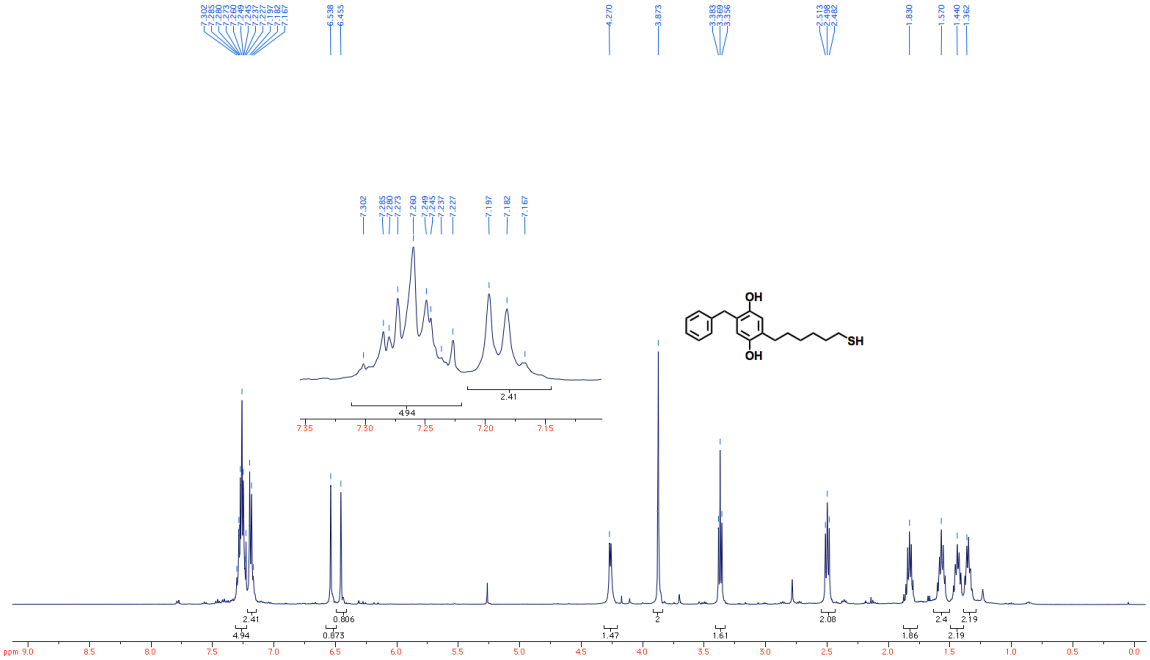

Figure 12.6. ^{1}H NMR spectrum of **BHQ**.

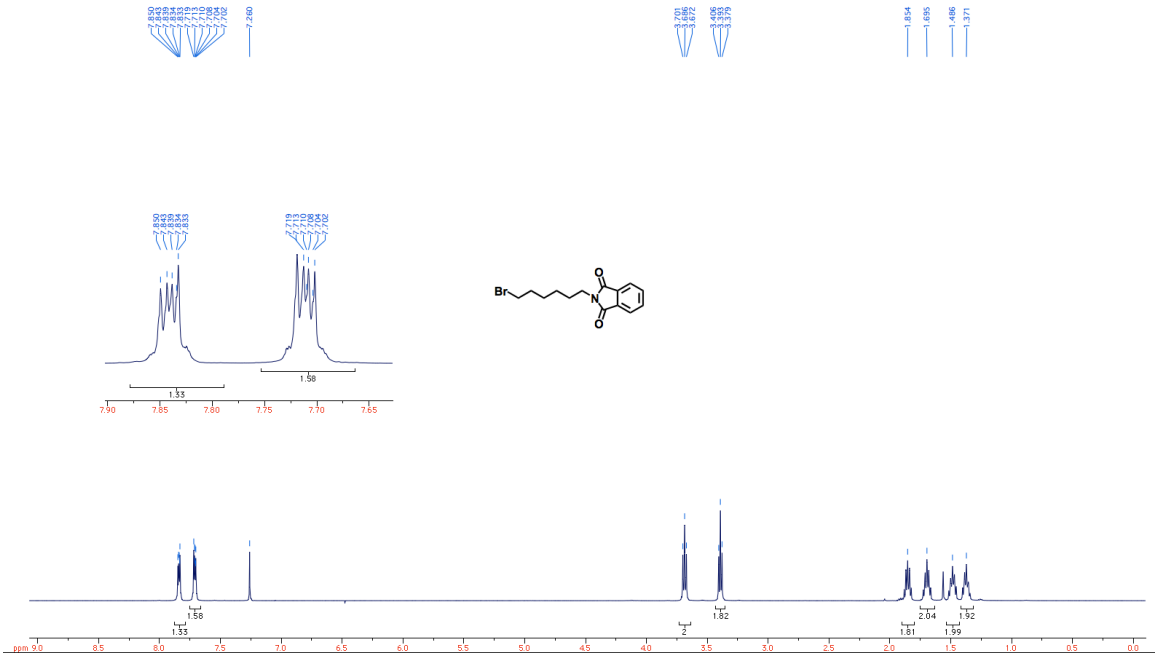

Figure 12.7. ^{1}H NMR spectrum of **6**.

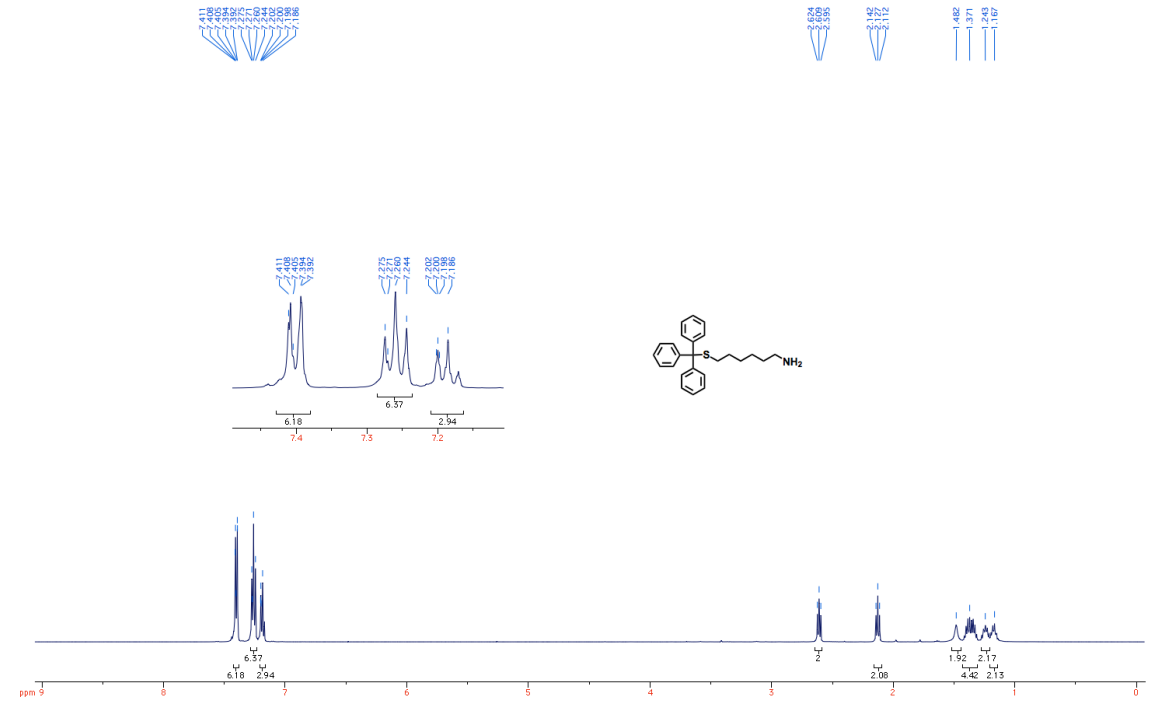

Figure 12.8. ^{1}H NMR spectrum of **8**.

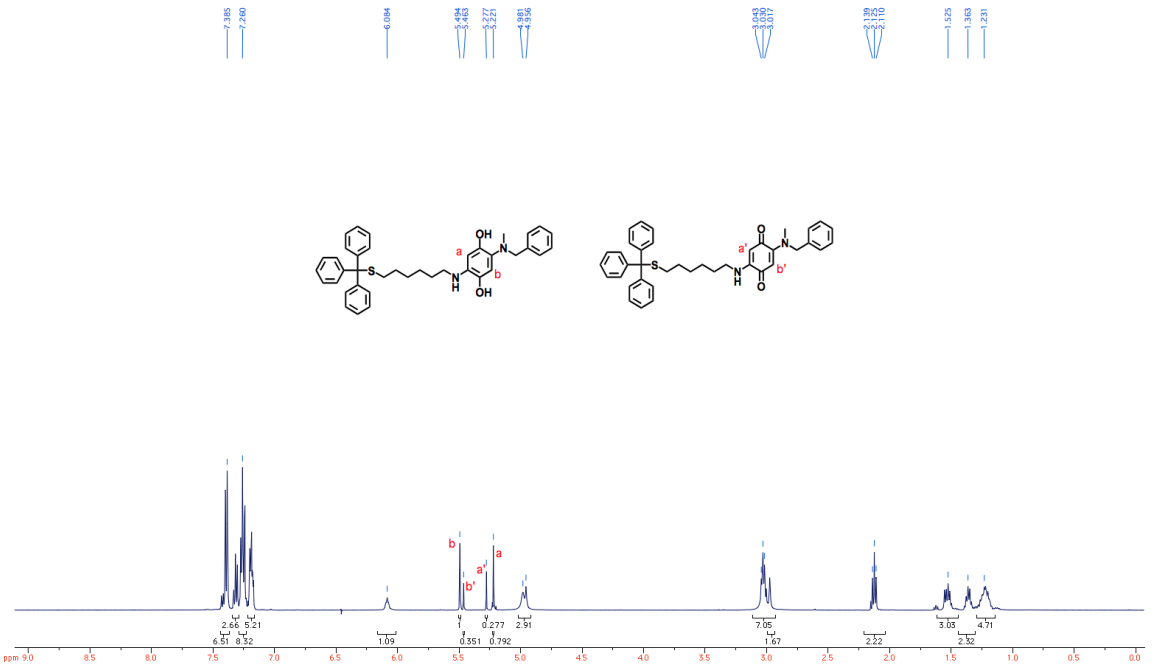

Figure 12.9. ^{1}H NMR spectrum of **N_2-BHQ**.

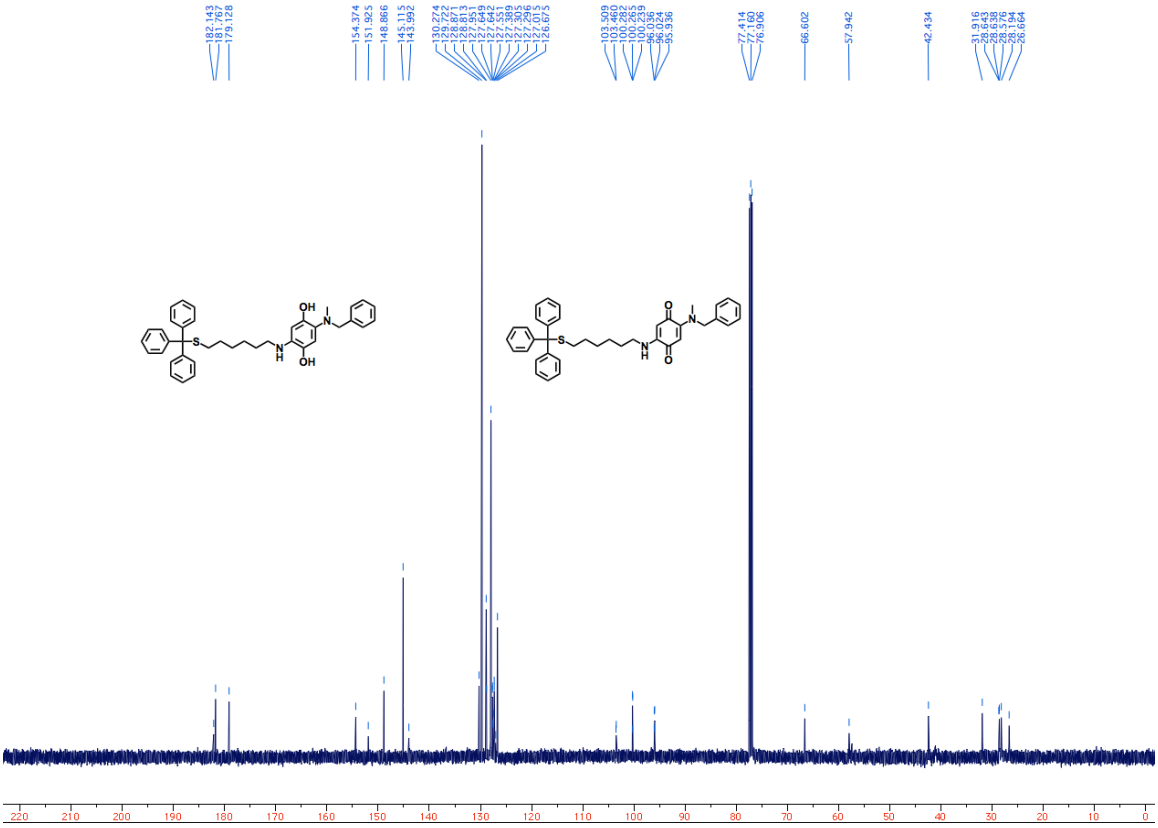

Figure 12.10. ^{13}C NMR spectrum of **N_2-BHQ**.

12.4 Results and Discussion

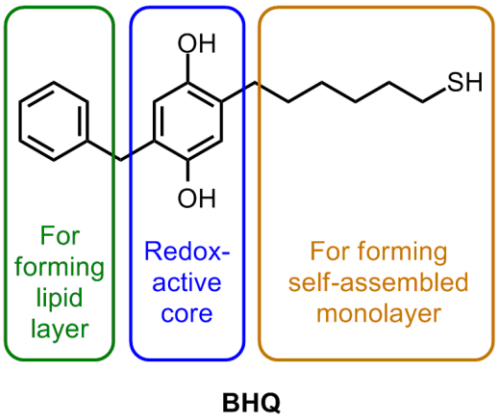

Figure 12.11. Functional and structural features of BHQ.

Figure 12.11 displays the structure of 2-benzyl-5-(6-mercaptohexyl)hydroquinone (BHQ), one of the two quinone derivatives synthesized and utilized in this work. In addition to its redox-active core, the BHQ molecule features two important regions, which both have a specific function. First, we equipped BHQ with a hexylthiol chain to allow for the formation of a well-packed SAM on Au electrodes. Electron transfer through this short-chained thiol is facile, thus ensuring that it is not the rate-determining step (RDS) in the quinone PCET reaction. Second, BHQ contains a terminal benzyl moiety. We previously determined that this group allows for a lipid monolayer to be appended to a SAM through van der Waals forces.[18]

Figure 12.12a shows representative cyclic voltammograms (CVs) of a SAM of BHQ at pH 7 at various scan rates. At all scan rates measured, the ratio between the anodic and cathodic peak currents is approximately unity, indicating that the redox system is reversible. Furthermore, both the peak anodic or cathodic currents increase linearly with increasing scan rate (Figure 12.12b), which is expected for a surface-confined redox species.

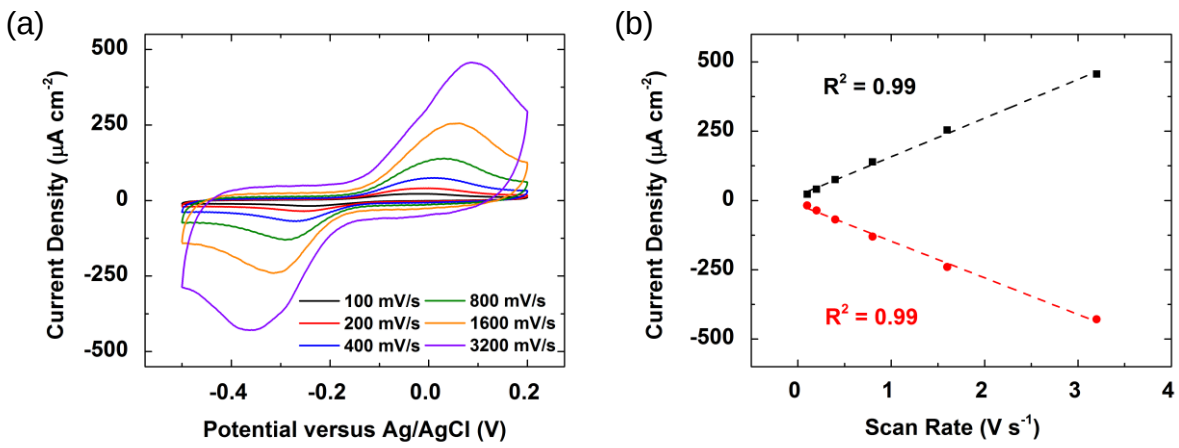

Figure 12.12. (a) CVs of a SAM of BHQ on Au in pH 7 Ar-saturated solution at scan rates of 100 (black), 200 (red), 400 (blue), 800 (green), 1600 (orange), and 3200 (purple) mV/s. (b) Randles-Sevcik plot of the peak anodic (black) and cathodic (red) current densities of a SAM of BHQ versus scan rate.

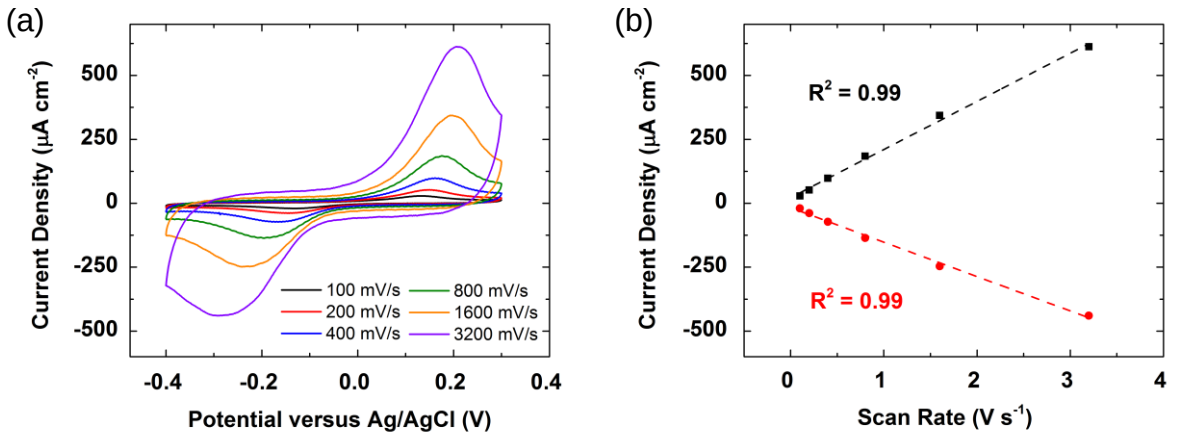

Figure 12.13. (a) CVs of a SAM of BHQ on Au in pH 3 Ar-saturated solution at scan rates of 100 (black), 200 (red), 400 (blue), 800 (green), 1600 (orange), and 3200 (purple) mV/s. (b) Randles-Sevcik plot of the peak anodic (black) and cathodic (red) current densities of a SAM of BHQ versus scan rate.

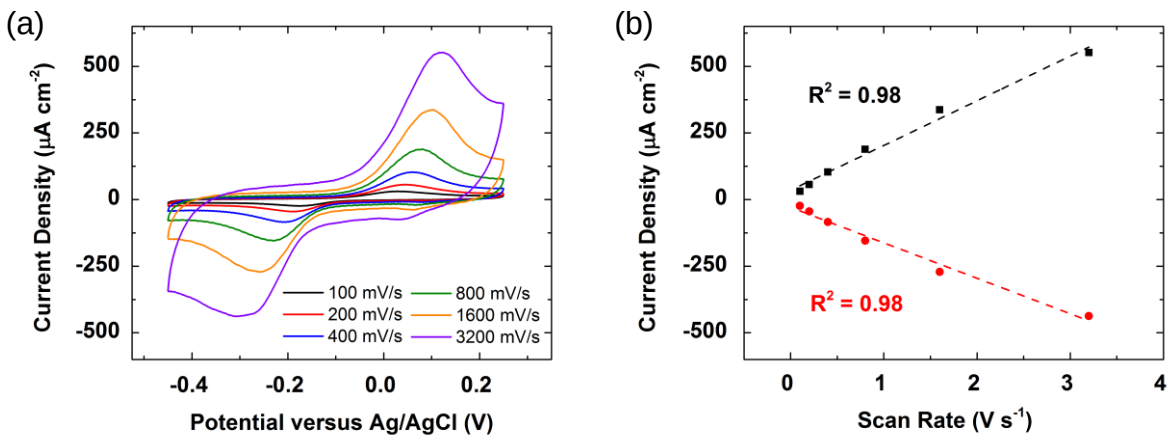

Figure 12.14. (a) CVs of a SAM of BHQ on Au in pH 5 Ar-saturated solution at scan rates of 100 (black), 200 (red), 400 (blue), 800 (green), 1600 (orange), and 3200 (purple) mV/s. (b) Randles-Sevcik plot of the peak anodic (black) and cathodic (red) current densities of a SAM of BHQ versus scan rate.

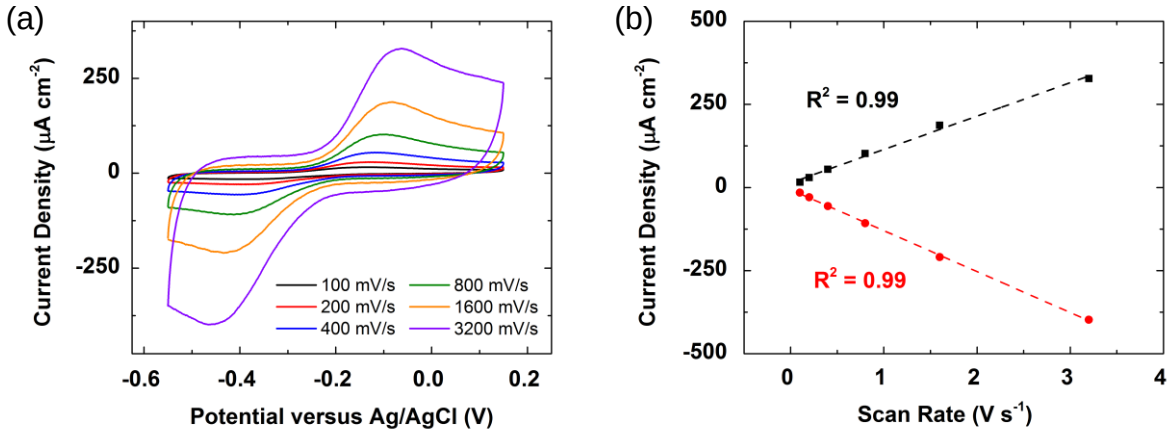

Figure 12.15. (a) CVs of a SAM of BHQ on Au in pH 9 Ar-saturated solution at scan rates of 100 (black), 200 (red), 400 (blue), 800 (green), 1600 (orange), and 3200 (purple) mV/s. (b) Randles-Sevcik plot of the peak anodic (black) and cathodic (red) current densities of a SAM of BHQ versus scan rate.

Figures 12.13-15 show CVs of BHQ at various scan rates and the corresponding Randles-Sevcik plots in pH 3, 5, and 9 solutions. The results show that BHQ is bound to the surface at these pH values as well. However, in all cases, the peak-to-peak separation values (ΔE_p) of the voltammograms are large and non-zero, in contrast to what is observed for surface-confined

redox species that demonstrate fast electron transfer such as simple ferrocene derivatives.[22] This finding indicates that the overall redox transformation of BHQ occurs relatively slowly likely due to the presence of multiple proton and electron transfer events.

Table 12.1. Apparent rate constants of a SAM of BHQ or N_2-BHQ and BHQ- or N_2-BHQ-containing HBMs with and without MDP.

System	Cathodic Rate (s^{-1})	Anodic Rate (s^{-1})
BHQ SAM	3.0 ± 1.0	3.9 ± 1.8
BHQ covered by DMPC	3.0 ± 1.4	3.9 ± 1.0
BHQ covered by DMPC with MDP	3.7 ± 0.5	4.4 ± 1.6
N_2-BHQ SAM	2.2 ± 1.1	2.5 ± 0.5
N_2-BHQ covered by DMPC	2.0 ± 0.2	2.3 ± 0.9
N_2-BHQ covered by DMPC with MDP	1.2 ± 1.0	3.6 ± 1.9

Indeed, we determined the apparent rate constants of the cathodic and anodic reactions to be (3.0 ± 1.0) s^{-1} and (3.9 ± 1.8) s^{-1}, respectively, using the Laviron equation (See Chapter 3).[23] Table 12.1 lists the apparent rate constants of the BHQ-containing systems used in this study. These values are similar to those obtained for SAMs of other quinones and metal complexes on carbon electrodes and are much less than those found for SAMs containing simple ferrocenes.[24,25]

To probe the PCET process of the BHQ SAM, we obtained CVs of a SAM of BHQ from pH 3 to 9 (Figure 12.16). For the cathodic wave, the potential of the peak current (E_{pc}) shifts positive by an average of 32 mV per pH unit as the pH increases (see inset). This value is close to the 30 mV per pH unit predicted by the Nernst equation for a process involving the transfer of protons and electrons in a 1:2 ratio. Considering the nine-membered square scheme shown in

Figure 12.17, we designate the cathodic process as converting the starting quinone, **M**, to a monodeprotonated hydroxyquinone species, **T**. In contrast to this finding, most quinone species are electrochemically reduced to their 2 H^+/2 e^- hydroquinone products. However, previous reports demonstrate that hydrophobic moieties on quinones can lead to reduction products in which fewer than two protons are transferred.[11] The data suggest that the phenyl groups of BHQ create a hydrophobic enough monolayer so that only one proton per BHQ is transferred upon reduction. For the anodic wave, the potential of the peak current (E_{pa}) shifts positive with increasing pH by 48 mV per pH unit. This number is in between the 59 mV/pH unit and 30 mV/pH unit values predicted by the Nernst equation for 2 H^+/2 e^- and 1 H^+/1 e^- processes, respectively. We hypothesize that after reduction to **T** occurs, protons from bulk solution slowly diffuse into the hydrophobic interior of the SAM, resulting in the protonation of **T** to **Q**. Therefore, a mixture of **T** and **Q** is oxidized back to the starting quinone, **M**, explaining the intermediate value witnessed for the pH dependence of anodic wave.

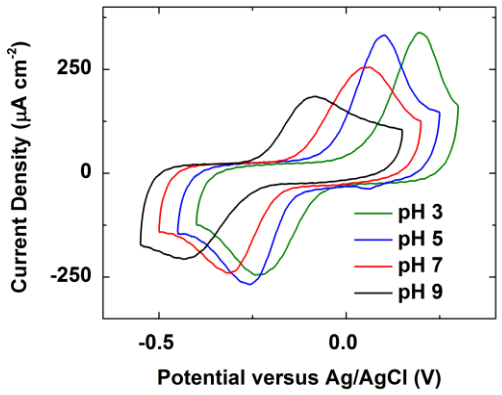

Figure 12.16. CVs of a SAM of BHQ on Au in pH 3 (green), 5 (blue), 7 (red), and 9 (black) Ar-saturated solutions at a scan rate of 1600 mV/s.

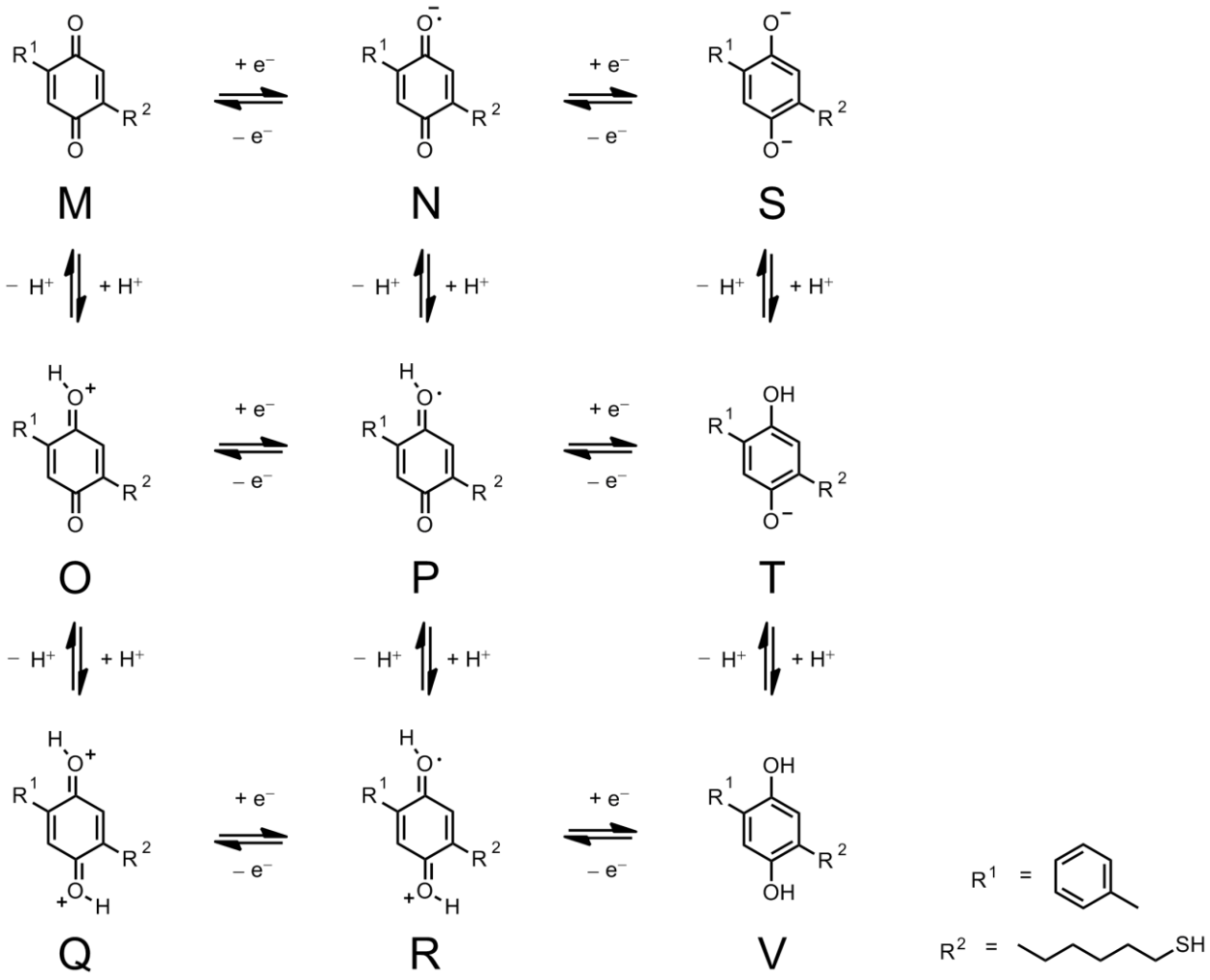

Figure 12.17. Nine-member square scheme for the BHQ system.

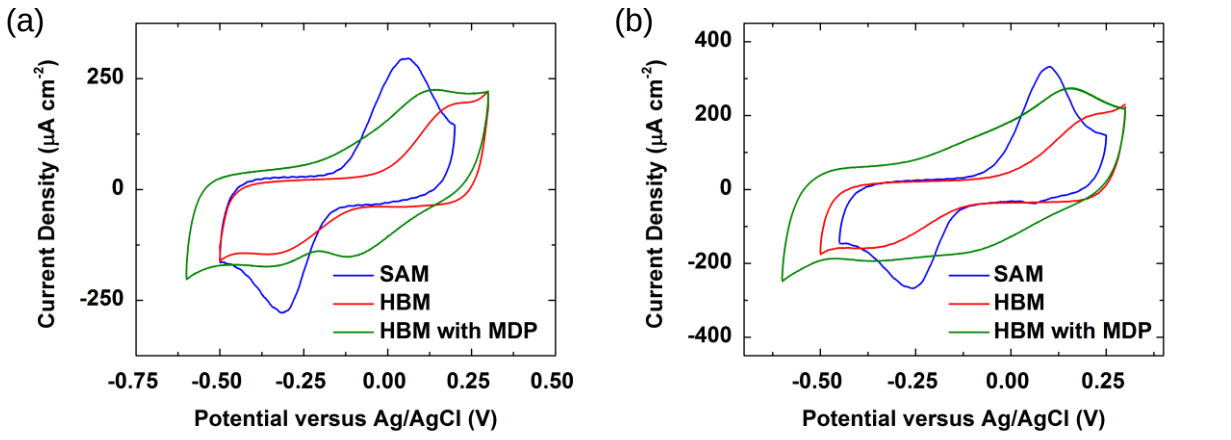

Figure 12.18. CVs of a SAM of BHQ (blue) covered by a monolayer of DMPC (red) with MDP added (green) in an Ar-saturated pH (a) 7 and (b) 5 solutions at a scan rate of 1600 mV/s.

Figure 12.18a shows cyclic voltammograms at pH 7 of a SAM of BHQ, a HBM containing BHQ and a DMPC lipid monolayer, and a HBM containing BHQ with the MDP proton carrier incorporated in the lipid layer. For three cases, the voltammetric response of the quinone varies dramatically. Table 12.2 lists the integrated charges for the cathodic and anodic waves of each of the three voltammograms. For a SAM of BHQ, the cathodic and anodic waves have an average integrated charge of 33 and 31 $\mu C\ cm^{-2}$, respectively, and since it is known that quinone SAMs undergo 2 e^- reduction, this amounts to a BHQ surface coverage of about 180 $pmole/cm^2$. Our modeling of this surface coverage determines that the intermolecular diameter of the BHQ SAM is 10.8 Å, which compares well with other reported quinone systems.[13]

Table 12.2. The integrated charges for the cathodic and anodic waves of a SAM of BHQ, the HBM containing BHQ, and the BHQ-HBM with MDP added to the lipid layer.

	pH	Integrated Charges ($\mu C\ cm^{-2}$)	
		Anodic	Cathodic
SAM	3	33 ± 3	33 ± 1
	5	36 ± 3	36 ± 2
	7	33 ± 3	31 ± 2
	9	28 ± 1	32 ± 1
HBM	5	18 ± 1	17 ± 1
	7	17 ± 1	17 ± 2
HBM with MDP	5	34 ± 8	35 ± 5
	7	34 ± 2	(i) 17 ± 2, (ii) 14 ± 3

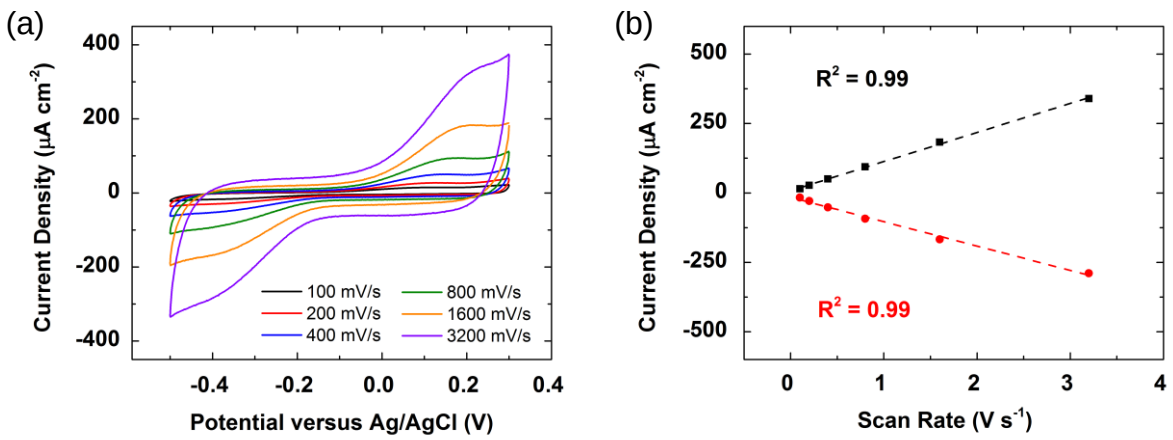

Figure 12.19. (a) CVs of a SAM of BHQ covered by a DMPC monolayer in pH 7 Ar-saturated solution at scan rates of 100 (black), 200 (red), 400 (blue), 800 (green), 1600 (orange), and 3200 (purple) mV/s. (b) Randles-Sevcik plot of the peak anodic (black) and cathodic (red) current densities of a SAM of BHQ covered by a DMPC monolayer versus scan rate.

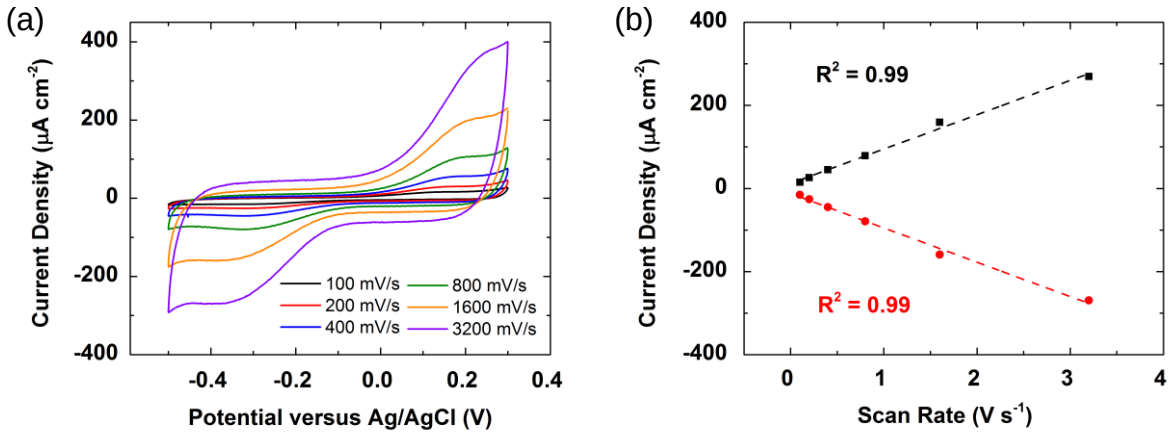

Figure 12.20. (a) CVs of a SAM of BHQ covered by a DMPC monolayer in pH 5 Ar-saturated solution at scan rates of 100 (black), 200 (red), 400 (blue), 800 (green), 1600 (orange), and 3200 (purple) mV/s. (b) Randles-Sevcik plot of the peak anodic (black) and cathodic (red) current densities of a SAM of BHQ covered by a DMPC monolayer versus scan rate.

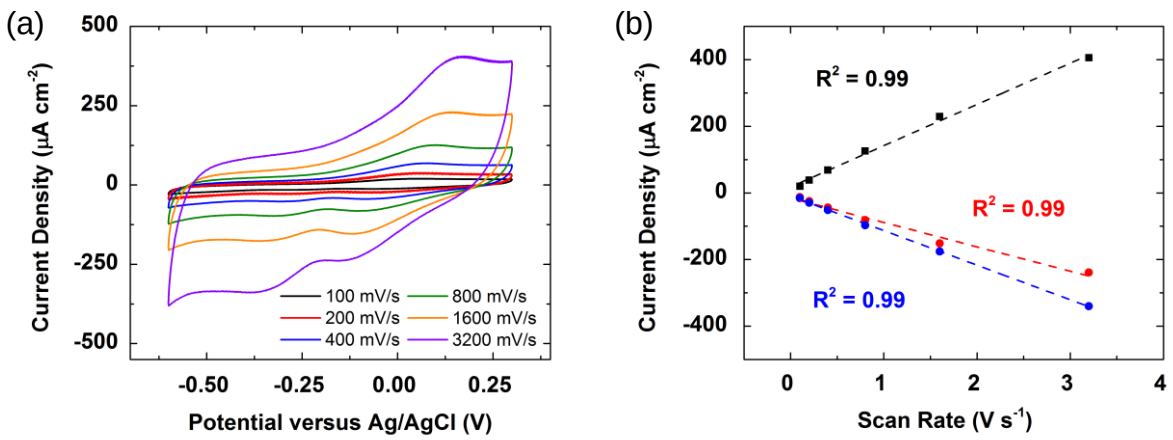

Figure 12.21. (a) CVs of a SAM of BHQ covered by a DMPC monolayer with MDP incorporated in the lipid layer in pH 7 Ar-saturated solution at scan rates of 100 (black), 200 (red), 400 (blue), 800 (green), 1600 (orange), and 3200 (purple) mV/s. (b) Randles-Sevcik plot of the peak anodic (black) and cathodic (red) current densities of a SAM of BHQ covered by a DMPC monolayer with MDP incorporated in the lipid layer versus scan rate.

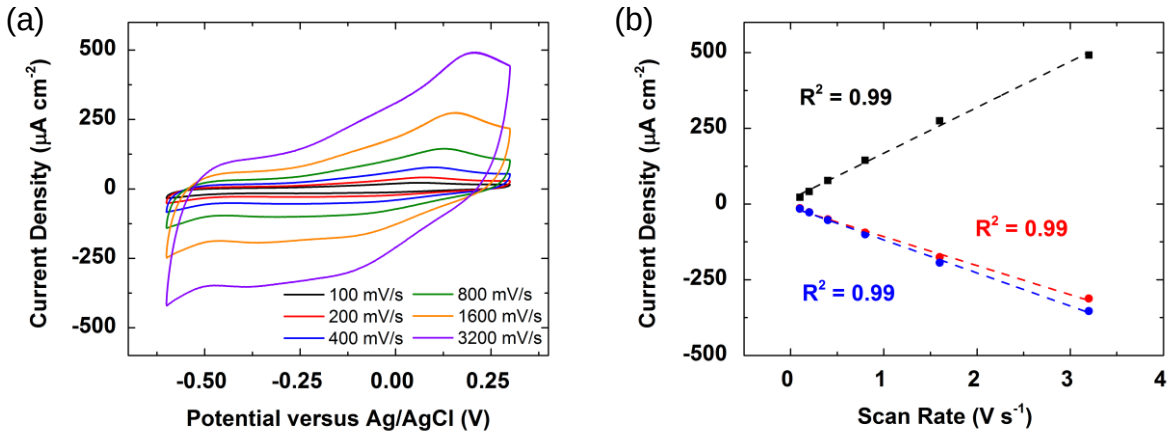

Figure 12.22. (a) CVs of a SAM of BHQ covered by a DMPC monolayer with MDP incorporated in the lipid layer in pH 5 Ar-saturated solution at scan rates of 100 (black), 200 (red), 400 (blue), 800 (green), 1600 (orange), and 3200 (purple) mV/s. (b) Randles-Sevcik plot of the peak anodic (black) and cathodic (red) current densities of a SAM of BHQ covered by a DMPC monolayer with MDP incorporated in the lipid layer versus scan rate.

Figures 12.19-22 display the CVs of BHQ covered by a DMPC monolayer with and without MDP at various scan rates and the corresponding Randles-Sevick plots. The results

indicate that the quinone moiety is surface-bound in the presence of lipid with and without proton carrier. Figure 12.23 summarizes the quantitative analysis of the BHQ voltammetry in HBM systems.

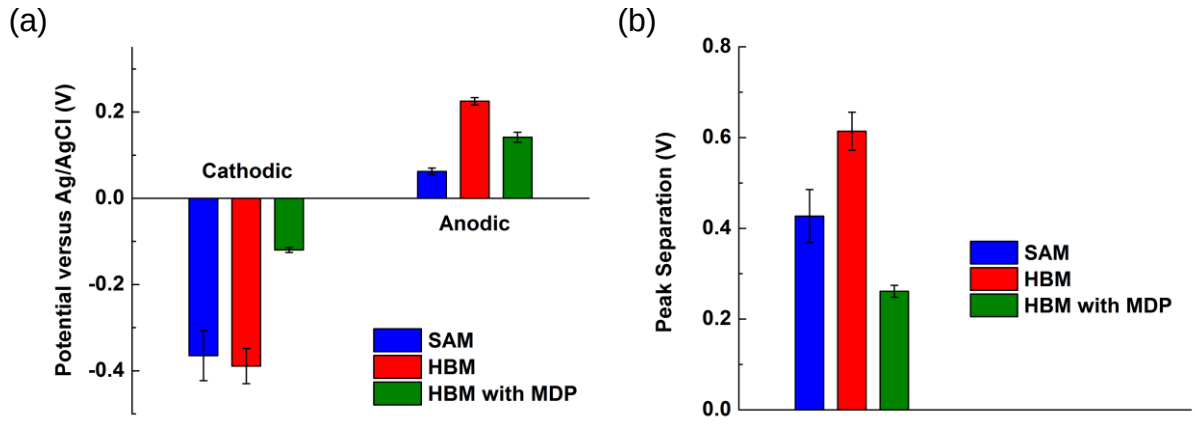

Figure 12.23. Bar graphs showing BHQ (a) cathodic and anodic peak positions and (b) peak separations at pH 7. Each graph has three sets of bars: open SAM, HBM, and HBM with MDP. For HBM with MDP, the cathodic peak position of the more negative cathodic wave is -0.374 ± 0.022 V versus Ag/AgCl. The cathodic process has two waves with the first wave (i) occurring at a more positive potential than the second (ii).

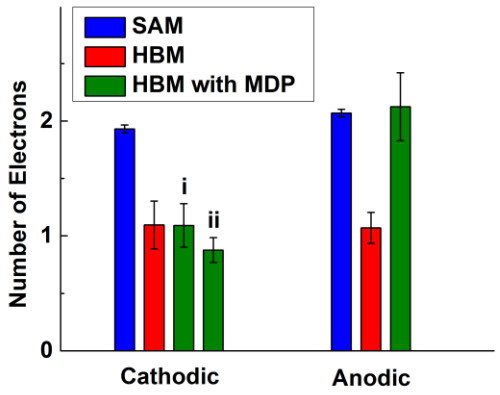

Figure 12.24. Bar graphs showing the number of electron transferred for the (a) cathodic and (b) anodic processes of BHQ in pH 7 Ar-saturated solution. Each graph has three sets of bars: open SAM, HBM, and HBM with MDP. The cathodic process has two waves with the first wave (i) occurring at a more positive potential than the second (ii).

When the BHQ SAM is covered by a monolayer of lipid to form a HBM (Figure 12.18, red line), the integrated charges for the cathodic and anodic processes decrease by approximately half (Figure 12.24, red bars). This result suggests that inside the lipid, the quinone undergoes a one electron reduction process.

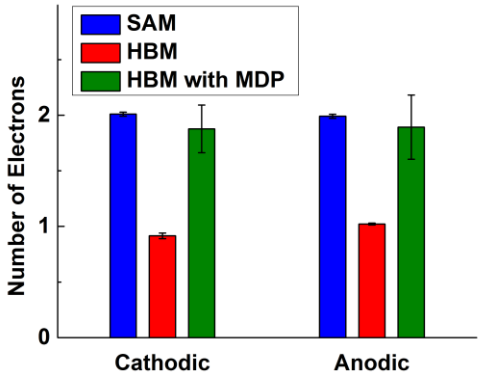

Figure 12.25. Bar graphs showing the number of electrons transferred for the cathodic and anodic processes of a SAM of BHQ (blue) covered by a monolayer of DMPC (red) with MDP incorporated in the lipid layer (green) in pH 5 Ar-saturated solution.

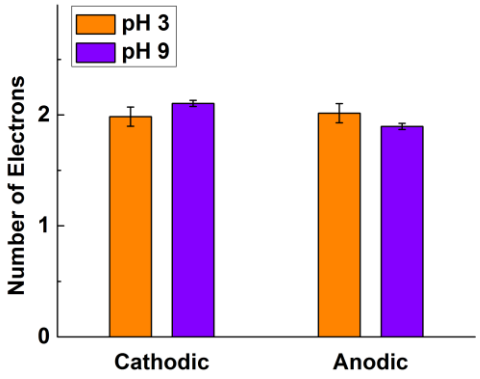

Figure 12.26. Bar graphs showing the number of electrons transferred for the cathodic and anodic processes of a SAM of BHQ in pH 3 (orange) and 9 (purple) Ar-saturated solutions.

Figures 12.25 and 12.26 display the number of electrons transferred for the cathodic and anodic processes of a SAM of BHQ and BHQ-containing HBMs with and without MDP in

various pH solutions. The red lines of Figures 12.18a and b display CVs of the HBM system with a SAM of BHQ covered by a monolayer of DMPC at pH 7 and 5, respectively. Unlike the open SAM case, the cathodic and anodic waves of the BHQ voltammetry increase an average of only 6 mV and 16 mV, respectively (Figure 12.27, red bars), indicating that the redox activity of BHQ inside the lipid layer does not depend strongly on the concentration of protons in bulk solution. This finding is consistent with the observation that protons diffuse relatively slowly through lipid layers in biological systems.[26-29] Taken together, these results indicate that inside a HBM, BHQ (**M**) undergoes a 1 e^-/0 H^+ reduction process to give the free radical species, **N** (Figure 12.17). In other words, the mechanism of the BHQ redox event changes from a PCET reaction involving 2 e^-/1 H^+ to single electron transfer in the presence of a lipid layer. In a directly analogous manner, we previously determined that a SAM of an O_2 reduction catalyst switches its mechanism from primarily producing H_2O by a 4 H^+/4 e^- process to reducing O_2 by 1 e^- to O_2^- when it is covered by a lipid monolayer (see Chapter 8). Our findings demonstrate that in the proton-constrained environment created by the lipid layer, redox systems that proceed by PCET in bulk solution occur by single electron transfer. Multiple electron transfer, for example, to produce the dianionic species **S** in the case of BHQ, is too thermodynamically unfavorable to occur. The production of such a highly charged hydrophilic species is energetically too costly in the hydrophobic environment of the HBM.

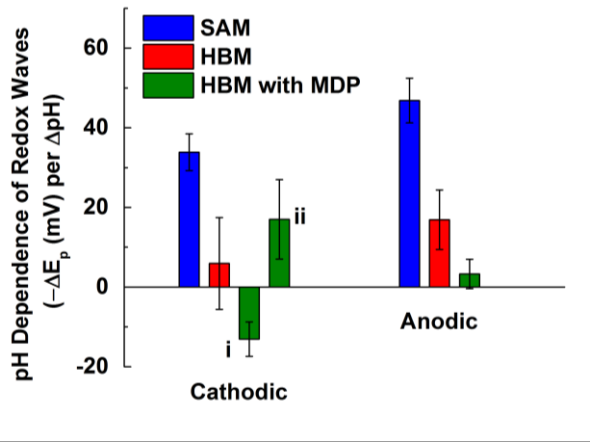

Figure 12.27. Bar graphs showing the average shifts in the cathodic and anodic peak positions of BHQ as the pH increases. Each graph has three sets of bars: open SAM, HBM, HBM with MDP. The cathodic process has two waves with the first wave (i) occurring at a more positive potential than the second (ii).

Upon incorporation of the MDP proton carrier into the lipid layer of the HBM, the voltammetric response changes even further (Figures 12.18a and b, green lines). Strikingly, two cathodic peaks appear in the response, each with an amount of integrated charge corresponding to a 1 e^- process (Figure 12.24). One wave remains for the anodic process, but its integrated charge indicates a 2 e^- process. These findings demonstrate that in the presence of the HBM with the MDP proton carrier, BHQ is reduced stepwise to **P** and then to the final **Q** hydroquinone process. MDP only transfer one proton at a time and thus facilitates two individual 1 H^+/1 e^- PCET steps through flip-flop diffusion across the lipid membrane. Because flipping of the proton carrier is relatively slow,[26-29] it kinetically controls the cathodic response of the BHQ system in discrete steps and serves as the only source of protons to the quinone in the proton-constrained environment of the lipid. For O_2 reduction catalysts inside HBMs with lipid-bound proton carriers, we previously determined that O_2 reduction proceeds by a mixture of four- and two-electron reduction pathways depending on the proton transfer rate through the lipid layer (see

Chapter 8). In a HBM absent a proton carrier, however, O_2 reduction occurs by single electron transfer to produce superoxide. Similarly, the BHQ system switches from a single electron transfer mechanism inside a HBM to one involving 2 H^+/2 e^- PCET in the presence of a proton carrier in a HBM.

Figure 12.27 green bars, shows how the potential of the BHQ voltammetry inside an HBM with MDP changes as a function of increasing pH. Interestingly, the position of both the cathodic and anodic peak potentials do not shift significantly with pH, indicating that the thermodynamics of BHQ reduction does not depend strongly on the concentration of protons in bulk solution. Instead, MDP delivers protons to BHQ in a kinetically-controlled fashion via flip-flop diffusion across the lipid layer of the HBM. Therefore, the potential of the BHQ redox process is not very sensitive to the concentration of protons in bulk solution.

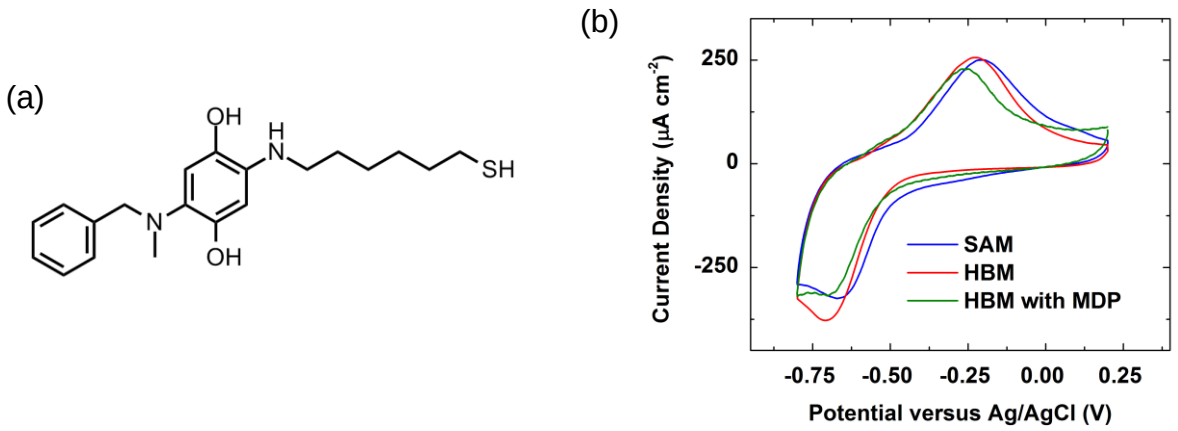

Figure 12.28. (a) Structure of N_2-BHQ and (b) CVs of a SAM of N_2-BHQ (blue) covered by a monolayer of DMPC (red) with MDP added (green) in an Ar-saturated pH 7 solutions at a scan rate of 1600 mV/s.

We further study 2-(benzyl(methyl)amino)-5-((6-mercaptohexyl)amino)hydroquinone (N_2-BHQ), a derivative of BHQ with two amines adjacent to the redox active core. Figure 12.28a

displays the structure of N_2-BHQ, the synthesis and characterization data of which are presented in Sections 12.2 and 12.3. Similar to BHQ, N_2-BHQ also features functional units to allow facile electron transfer, SAM formation, and favorable interaction with hydrocarbons on the lipid tail. We perform experiments on N_2-BHQ-modified Au surfaces in an analogous manner to BHQ-system. Figure 12.29 compares the redox waves of a SAM of BHQ and a SAM of N_2-BHQ. Due to the electron-donating nature of the amine groups, the midpoint potential of N_2-BHQ is more negative than that of BHQ, a similar phenomenon observed when comparing ferrocene to decamethyl-ferrocene.[30] Figure 12.30 displays the scan-rate dependence and Randles-Sevcik plot of a SAM of N_2-BHQ. The results show that N_2-BHQ is indeed surface-bound.

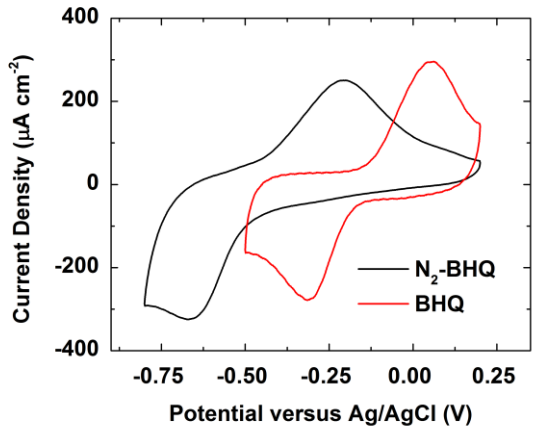

Figure 12.29. CVs of a SAM of BHQ (red) and a SAM of N_2-BHQ (black) on Au in pH 7 Ar-saturated solution at scan rates of 1600 mV/s.

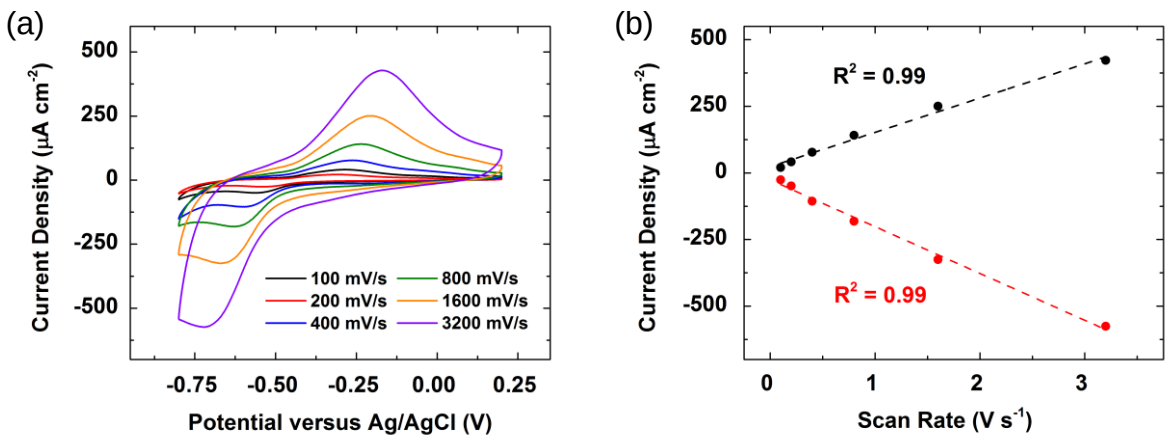

Figure 12.30. (a) CVs of a SAM of N_2-BHQ on Au in pH 7 Ar-saturated solution at scan rates of 100 (black), 200 (red), 400 (blue), 800 (green), 1600 (orange), and 3200 (purple) mV/s. (b) Randles-Sevcik plot of the peak anodic (black) and cathodic (red) current densities of a SAM of N_2-BHQ versus scan rate.

Figure 12.28b shows CVs of a SAM of N_2-BHQ, a N_2-BHQ-containing HBM, and the N_2-BHQ-HBM with MDP added to the lipid layer. Figure 12.31 summarizes the peak information of the redox waves of the three systems studied. In short, the three systems behave very similarly. To confirm the presence of a complete lipid layer on the SAM, we performed blocking experiments with $K_3Fe(CN)_6$ in the bulk solution. Figure 12.32 shows the results from the blocking experiments using the three systems. An absence of the Fe(II/III) wave and a decrease in the capacitance are indicative of a well-formed lipid layer, a phenomenon observed previously.[18]

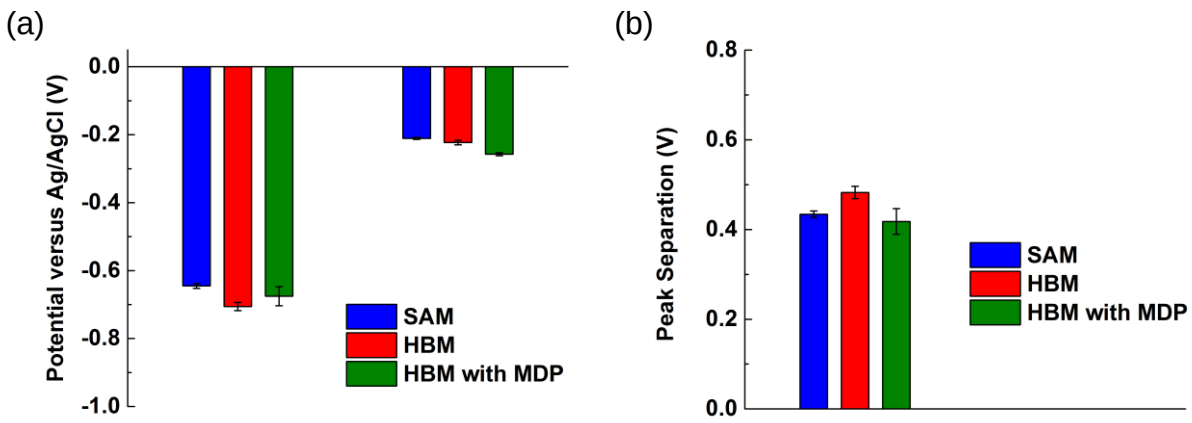

Figure 12.31. Bar graphs showing N_2-BHQ (a) cathodic and anodic peak positions and (b) peak separations at pH 7. Each graph has three sets of bars: open SAM, HBM, and HBM with MDP.

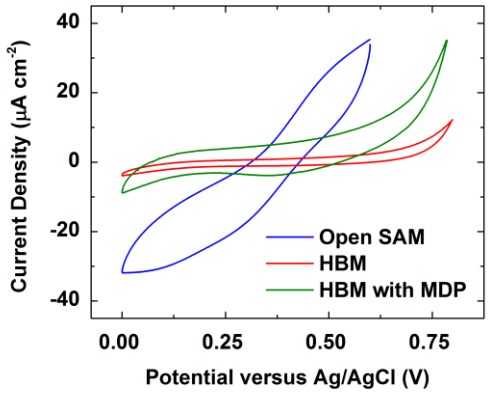

Figure 12.32. CVs of a SAM of N_2-BHQ (blue), the N_2-BHQ-containing HBM (red), and the N_2-BHQ-HBM with MDP incorporated in the lipid layer (green) in a solution of $K_3Fe(CN)_6$ (1 mM) with KCl (100 mM) at a scan rate of 50 mV/s.

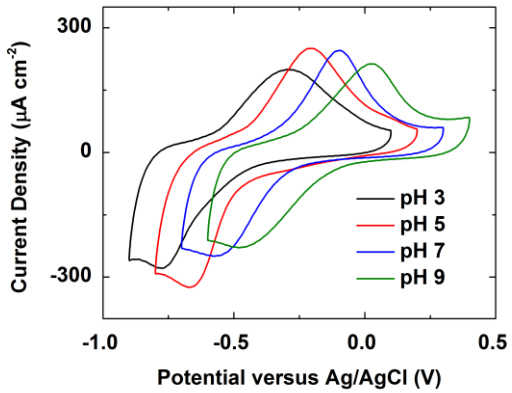

Figure 12.33. CVs of a SAM of N_2-BHQ on Au in pH 3 (green), 5 (blue), 7 (red), and 9 (black) Ar-saturated solutions at a scan rate of 1600 mV/s.

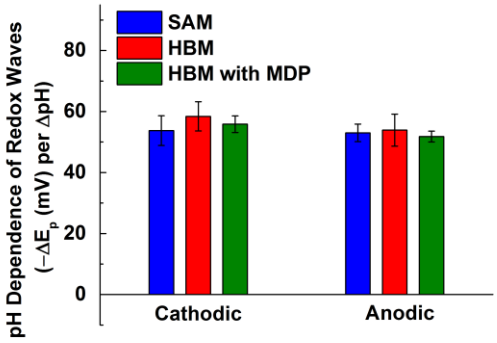

Figure 12.34. Bar graphs showing the average shifts in the cathodic and anodic peak positions of N_2-BHQ as the pH increases. Each graph has three sets of bars: open SAM, HBM, HBM with MDP.

To study the mechanism by which the quinone moiety in N_2-BHQ undergoes during redox cycling, we varied the pH of the bulk solution in an analogous manner to the BHQ case. Figure 12.33 shows CVs of a SAM of N_2-BHQ in solutions of various pH, and Figure 12.34 summarizes the pH dependence of the SAM of N_2-BHQ, the N_2-BHQ-containing HBM, and the N_2-BHQ-HBM with MDP incorporated in the lipid layer. The results show that N_2-BHQ exhibits a ca. 59 mV/pH shift in the three cases, indicating that a $2H^+/2e^-$ pathway is operational in all three systems. Figure 12.35 displays a nine-member square scheme of N_2-BHQ. A $2H^+/2e^-$

pathway means that BHQ cycles between species M and V regardless of the presence of a lipid layer or the incorporation of a proton carrier in the lipid layer. Comparing the N_2-BHQ results to the BHQ results, we hypothesize that trapped water bound to the amino groups flanking the redox core of N_2-BHQ are causing the redox response to be insensitive to the changes in the surrounding environment. However, the observation that a quinone-terminated SAM exhibiting a 59 mV/pH shift is common.[11] In short, the lipid-modified electrodes behave normally when there are pendant proton relays. By eliminating the effect originating from the amino groups, we are able to observe several other species on the nine-member square scheme.

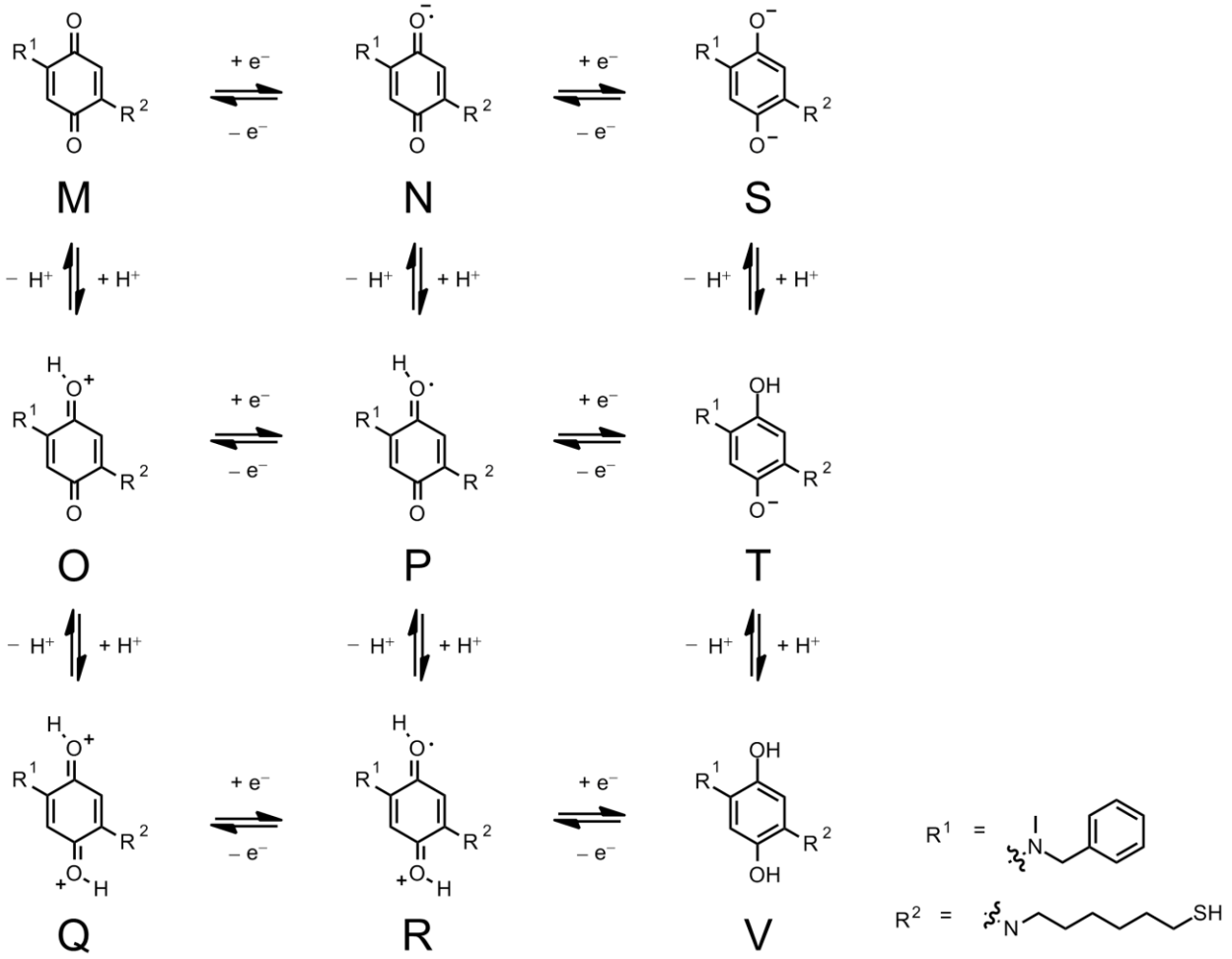

Figure 12.35. Nine-member square scheme for the N_2-BHQ system.

12.5 Conclusions

In this work, we prepared a quinone moiety that can self-assemble on a Au surface and allow a lipid monolayer to form on top. The addition of a hydrophobic lipid layer on top of the surface-bound quinone changes the reaction pathway from a proton-coupled electron transfer process to a pure electron transfer step. Upon incorporation of a proton carrier in the lipid layer, the mechanism of quinone redox switched to stepwise PCET. We demonstrate that regulating the flux of proton transfer dictates the reaction pathway of PCET processes. The ability to control the rate of proton delivery to a quinone moiety paves the way to a unified understanding of the interplay between the thermodynamics and kinetics of protons and electrons.

12.6 References

(1) Warren, J. J.; Tronic, T. A.; Mayer, J. M. *Chem. Rev.* **2010**, *110*, 6961.
(2) Hammes-Schiffer, S. *Acc. Chem. Res.* **2001**, *34*, 273.
(3) Nohl, H.; Jordan, W.; Youngman, R. J. *Adv. Free Radical Bio.* **1986**, *2*, 211.
(4) Santhamma, K. R.; Raj, R. K. *Biochem. Biophys. Res. Comm.* **1993**, *190*, 201.
(5) Coates, C. S.; Ziegler, J.; Manz, K.; Good, J.; Kang, B.; Milikisiyants, S.; Chatterjee, R.; Hao, S.; Golbeck, J. H.; Lakshmi, K. V. *J. Phys. Chem. B* **2013**, *117*, 7210.
(6) Faig, M.; Bianchet, M. A.; Winski, S.; Hargreaves, R.; Moody, C. J.; Hudnott, A. R.; Ross, D.; Amzel, L. M. *Structure* **2001**, *9*, 659.
(7) Nepovimova, E.; Uliassi, E.; Korabecny, J.; Peña-Altamira, L. E.; Samez, S.; Pesaresi, A.; Garcia, G. E.; Bartolini, M.; Andrisano, V.; Bergamini, C.; Fato, R.; Lamba, D.; Roberti, M.; Kuca, K.; Monti, B.; Bolognesi, M. L. *J. Med. Chem.* **2014**, *57*, 8576.
(8) Milton, R. D.; Hickey, D. P.; Abdellaoui, S.; Lim, K.; Wu, F.; Tan, B.; Minteer, S. D. *Chem. Sci.* **2015**, *6*, 4867.
(9) Giroud, F.; Milton, R. D.; Tan, B.-X.; Minteer, S. D. *ACS Catal.* **2015**, *5*, 1240.
(10) Cinquin, P.; Gondran, C.; Giroud, F.; Mazabrard, S.; Pellissier, A.; Boucher, F.; Alcaraz, J.-P.; Gorgy, K.; Lenouvel, F.; Mathé, S.; Porcu, P.; Cosnier, S. *PLoS ONE* **2010**, *5*, e10476.
(11) Kim, R. S.; Park, W.; Hong, H.; Chung, T. D.; Kim, S. *Electrochem. Commun.* **2014**, *41*, 39.
(12) Ma, W.; Long, Y.-T. *Chem. Soc. Rev.* **2014**, *43*, 30.
(13) Wieckowska, A.; Braunschweig, A. B.; Willner, I. *Chem. Comm.* **2007**, 3918.
(14) Hammes-Schiffer, S.; Soudackov, A. V. *J. Phys. Chem. B* **2008**, *112*, 14108.
(15) Mayer, J. M.; Rhile, I. J. *BBA-Bioenergetics* **2004**, *1655*, 51.

(16) Hosseini, A.; Barile, C. J.; Devadoss, A.; Eberspacher, T. A.; Decreau, R. A.; Collman, J. P. *J. Am. Chem. Soc.* **2011**, *133*, 11100.
(17) Hosseini, A.; Collman, J. P.; Devadoss, A.; Williams, G. Y.; Barile, C. J.; Eberspacher, T. A. *Langmuir* **2010**, *26*, 17674.
(18) Barile, C. J.; Tse, E. C. M.; Li, Y.; Sobyra, T. B.; Zimmerman, S. C.; Hosseini, A.; Gewirth, A. A. *Nat. Mater.* **2014**, *13*, 619.
(19) Tse, E. C. M.; Barile, C. J.; Gewargis, J. P.; Li, Y.; Zimmerman, S. C.; Gewirth, A. A. *Anal. Chem.* **2015**, *87*, 2403.
(20) Choi, K.; Mruk, R.; Moussa, A.; Jonas, A. M.; Zentel, R. *Macromolecules* **2005**, *38*, 9124.
(21) Moreno, A. Y.; Mayorov, A. V.; Janda, K. D. *J. Am. Chem. Soc.* **2011**, *133*, 6587.
(22) Eckermann, A. L.; Feld, D. J.; Shaw, J. A.; Meade, T. J. *Coord. Chem. Rev.* **2010**, *254*, 1769.
(23) Laviron, E. *J. Electroanal. Chem. Interfacial Electrochem.* **1979**, *101*, 19.
(24) Smalley, J. F.; Feldberg, S. W.; Chidsey, C. E. D.; Linford, M. R.; Newton, M. D.; Liu, Y.-P. *J. Phys. Chem.* **1995**, *99*, 13141.
(25) Tse, E. C. M.; Schilter, D.; Gray, D. L.; Rauchfuss, T. B.; Gewirth, A. A. *Inorg. Chem.* **2014**, *53*, 8505.
(26) John, K.; Schreiber, S.; Kubelt, J.; Herrmann, A.; Müller, P. *Biophys. J.* **2002**, *83*, 3315.
(27) McConnell, H. M.; Kornberg, R. D. *Biochemistry* **1971**, *10*, 1111.
(28) Srivastava, A.; Singh, S.; Krishnamoorthy, G. *J. Phys. Chem.* **1995**, *99*, 11302.
(29) Schönfeld, P.; Schild, L.; Kunz, W. *BBA-Bioenergetics* **1989**, *977*, 266.
(30) Connelly, N. G.; Geiger, W. E. *Chem. Rev.* **1996**, *96*, 877.

Appendix A

Heterogenizing Molecular Catalysts for the Hydrogen Evolution Reaction

The work in this appendix was accomplished in collaboration with Geoffrey M. Chambers, Professor Thomas B. Rauchfuss, and Professor Andrew A. Gewirth.

A.1 Introduction

Immense amount of effort has been invested to prepare catalysts to replace Pt and other precious metal based materials as catalyst for the hydrogen evolution reaction (HER).[1,2] Several solid-state non-precious materials (Ni, Co, W, chalcogenides, P, S, Se) are capable of reducing protons in acid, with varying degree of activity (onset potential, Tafel slope, turnover frequency (TOF), turnover number (TON)).[3-8] On the other hand, the HER activity of a major class of non-precious catalysts (molecular complexes) is largely unexplored.[9] Molecular catalysts are typically studied mostly in the context of homogeneous catalysis mostly in organic solvents, and various equivalences of acids are introduced into the solution. An efficient method to heterogenize these catalysts provides a new strategy to search for new durable, active HER catalysts in practical conditions, such as those in PEM electrolyzers.

Here, we devise a simple strategy to screen a library of HER catalysts without modification of both the catalyst and the carbon support for fair comparison between the heterogeneous and homogeneous cases. Figure A.1 shows the molecular catalysts utilized in this study. We next utilize this electrochemical platform to examine the HER performance of these molecular catalysts and provide viable strategies to stabilize catalysts that degrade in acidic

conditions.

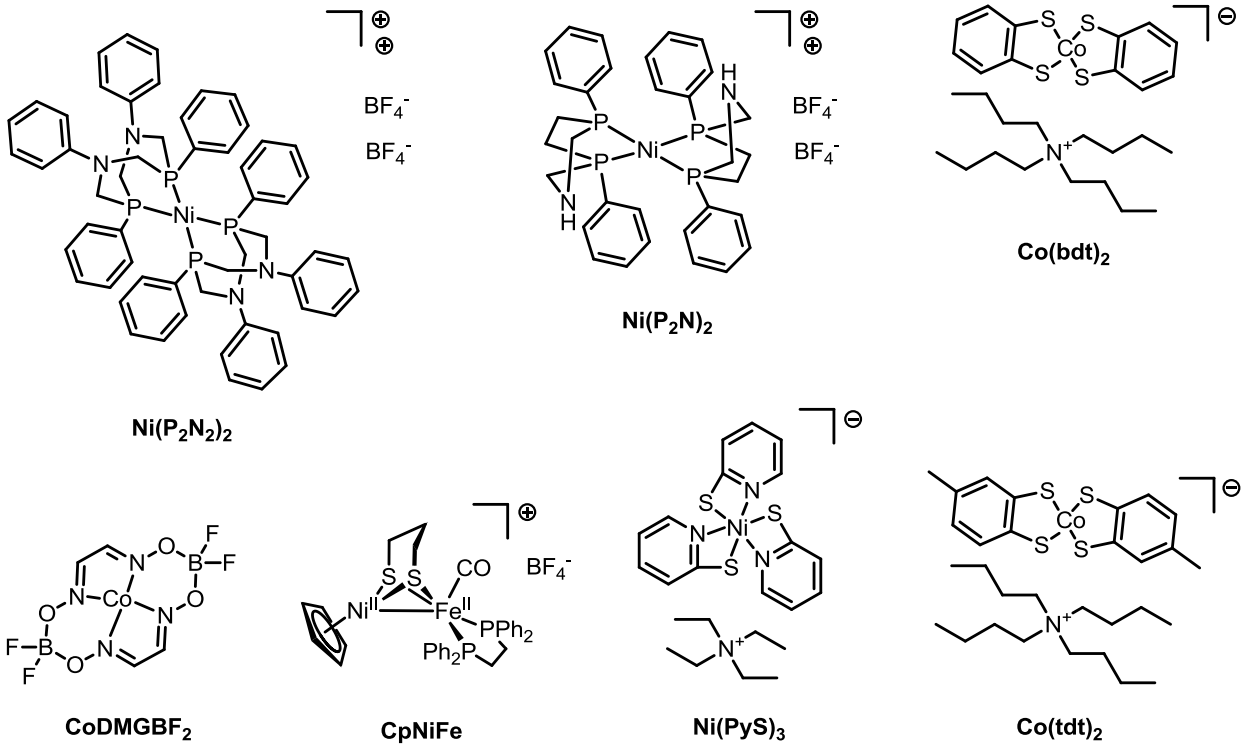

Figure A.1. HER catalysts utilized in this study.

A.2 Experimental Methods

A.2.1 General Procedures

Chemicals were obtained from commercial sources and used without further purification unless otherwise specified. Aqueous solutions were prepared using Milli-Q purified water (>18 MΩ cm) and the respective concentrated acids: perchloric acid (optima grade $HClO_4$, Fisher Scientific), sulfuric acid (AR® ACS grade H_2SO_4, Macron Fine Chemicals), phosphoric acid (ACS grade H_3PO_4, J.T. Baker), hydrochloric acid (AR® ACS grade HCl, Macron Fine Chemicals), hexafluorophosphoric acid (HPF_6, Sigma-Aldrich), tetrafluoroboric acid (HBF_4, Sigma-Aldrich), trifluoroacetic acid (spectrophotometric grade TFA, Sigma-Aldrich), and *p*-toluenesulfonic acid (reagent grade TsOH, Sigma-Aldrich). Solutions were sparged with Ar for 1

h prior to each experiment.

Caution! Perchlorate salts are potentially explosive. Only small amounts of materials should be prepared.

A.2.2 Catalytic Activity Assay

Unless otherwise stated, all rotating disk electrode (RDE) experiments were conducted at 2500 rpm to get rid of bubbles formed at the electrode surface. A suspension of finely ground Vulcan XC-72 (9 mg, Cabot Corp.) in DCM or EtOH (1.5 mL) was treated with one of the HER catalysts (10.3 μmol) in DCM or EtOH (1.5 mL). The mixture was sonicated for 15 min and treated with Et_2O (3 mL), and the solids were isolated by centrifugation before being dried in vacuo overnight. The resulting carbon-supported catalyst was suspended in EtOH (500 μL) and treated with Nafion (20 μL, 5 wt % in alcohols, Sigma-Aldrich), the resulting slurry being sonicated for 30 min. This ink (5 μL) was then deposited on a glassy carbon (GC) electrode, which was dried under a stream of Ar.

A.3 Results and Discussion

A.3.1 Quantification of $Ni(P_2N_2)_2$ Immobilized on Carbon using Spectroscopic, Spectrometric, and Analytical Techniques

We first study $Ni(P_2N_2)_2$, an active HER catalyst first established by a group of investigators in PNNL. This $Ni(P_2N_2)_2$ complex contains a single Ni center with pendant amine functionalities as efficient proton relays. Figure A.2a displays the LSVs of HER catalyzed by $Ni(P_2N_2)_2$ and relevant controls in acid medium. The almost identical HER traces by $Ni(P_2N_2)_2$ across two cycles suggest that $Ni(P_2N_2)_2$ is stable when subjected to potentials at which HER occurs in 1 M $HClO_4$ (solid lines in Figure A.2a).

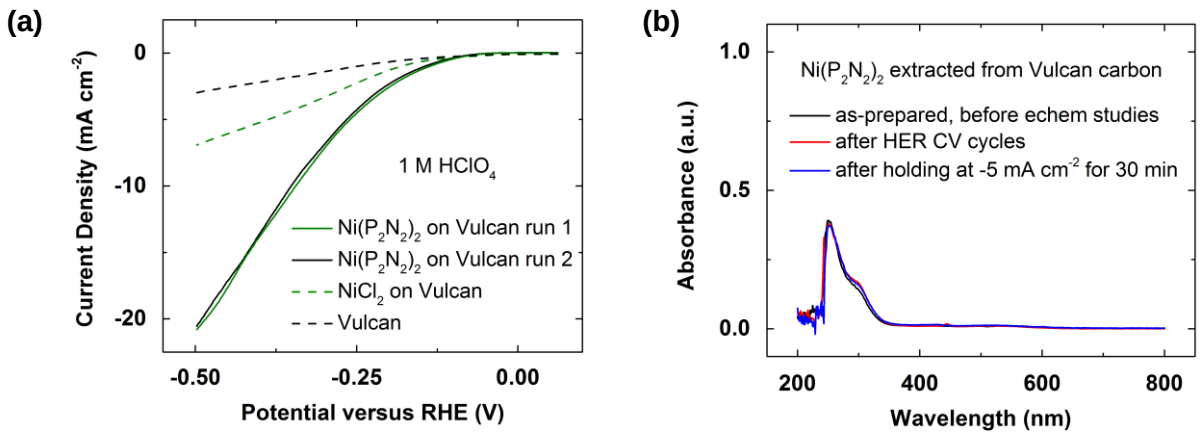

Figure A.2. (a) Linear sweep voltammograms (LSVs) of HER catalyzed by $Ni(P_2N_2)_2$ in the first scan (green solid line) and the second scan (black solid line) in 1 M $HClO_4$ at a scan rate of 10 mV/s and a rotation rate of 2500 rpm. Control experiments using $NiCl_2$ (green dashed line) and Vulcan carbon only (black dashed lines) are also shown in the Figure. (b) UV-Vis spectra of $Ni(P_2N_2)_2$ before electrochemical studies (black), after potential cycling (red), and after passing cathodic current for 30 min (blue).

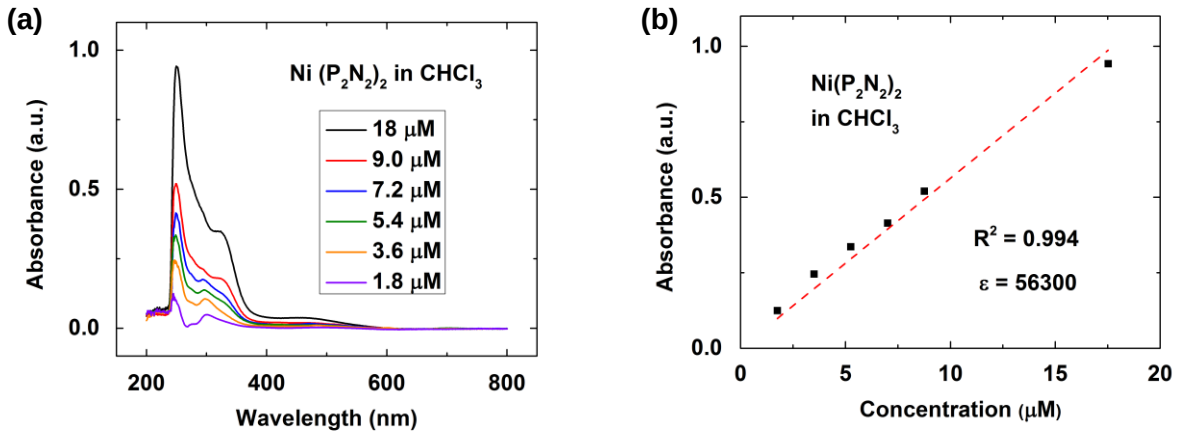

Figure A.3. (a) UV-Vis spectra and (b) the corresponding calibration curve of $Ni(P_2N_2)_2$.

To verify that the complex remains intact after catalysis, we extracted the catalyst from the electrode surface using $CHCl_3$ and conducted post-mortem experiments using ultraviolet-visible spectroscopy (UV-Vis) and mass spectrometry (MS). Figure A.3 shows the calibration curve of $Ni(P_2N_2)_2$ in $CHCl_3$ and the determination of its molar absorption coefficient (ε) using

the Beer-Lambert law. Figure A.2b shows the UV-Vis data of $Ni(P_2N_2)_2$ before and after electrochemical studies. The matching UV-Vis spectra of $Ni(P_2N_2)_2$ for cases before and after HER catalysis in Figure A.2b demonstrate that the catalyst remains unchanged during the course of electrochemical studies. Figure A.4 compares the MS results of $Ni(P_2N_2)_2$ before and after electrocatalytic reduction of H^+. The presence of the parent ion peak and other peaks related to $Ni(P_2N_2)_2$ before and after electrochemical experiments further confirms that the integrity of the catalyst is not perturbed by the HER process.

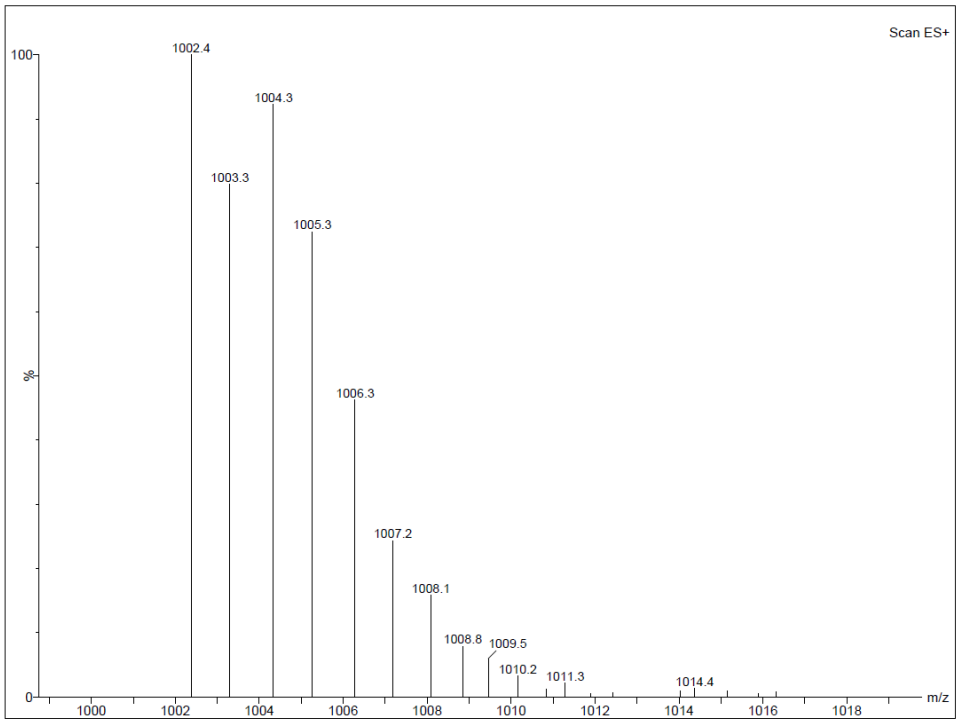

Figure A.4a. MS spectrum of $Ni(P_2N_2)_2$ extracted from carbon surface before HER.

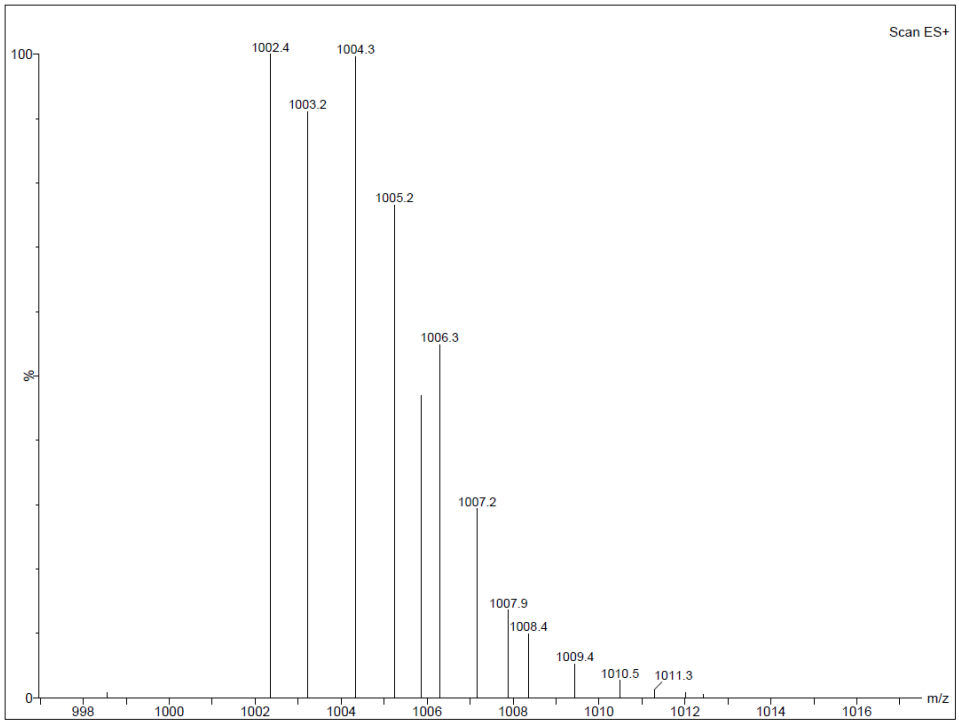

Figure A.4b. MS spectrum of $Ni(P_2N_2)_2$ extracted from carbon surface after HER.

Table A.1. EA of HER catalysts supported on Vulcan XC-72 carbon.

Catalysts	Weight %					
	Ni	**Co**	**P**	**S**	**B**	**F**
$Ni(P_2N_2)_2$	1.13	-	2.48	-	-	-
$Ni(P_2N)_2$	2.82	-	5.83	-	-	-
$Co(tdt)_2$	-	3.56	-	7.16	-	-
$Co(bdt)_2$	-	3.28	-	8.36	-	-
$Co(DMGBF_2)$	-	3.99	-	-	0.66	3.63
CpNi	1.49	-	-	-	-	-

Table A.2. CHN of HER catalysts and controls supported on Vulcan XC-72 carbon.

Catalysts	Weight %		
	C	H	N
$Ni(P_2N_2)_2$	88.49	0.95	1.48
$Ni(P_2N)_2$	72.35	2.31	1.68
$Co(tdt)_2$	83.49	2.65	1.06
$Co(bdt)_2$	79.18	2.54	1.05
$Co(DMGBF_2)$	80.30	0.87	3.64
$CoCl_2$	94.23	0.15	0.27
$FeCl_3$	90.72	0.07	0.28
$NiCl_2$	93.59	0.11	0.26

Table A.3. EA of controls supported on Vulcan XC-72 carbon.

Catalysts	Weight %			
	Ni	Co	Fe	Cl
$CoCl_2$	-	0.88	-	1.1
$FeCl_3$	-	-	0.85	1.74
$NiCl_2$	0.96	-	-	1.17

Table A.4. The amount of controls in a 5 μL cast from a 500 μL ink solution with 9 mg of carbon-supported catalysts calculated using the weight % of a particular element obtained from EA results shown in Table A.3.

Catalysts	Amount of complex (μg) calculated using weight % of a particular element			
	Ni	Co	Fe	Cl
$CoCl_2$	-	3.2	-	3.3
$FeCl_3$	-	-	3.7	4.0
$NiCl_2$	3.5	-	-	3.5

Table A.5. The amount of complex in a 5 μL cast from a 500 μL ink solution with 9 mg of carbon-supported catalysts calculated using the weight % of a particular element obtained from EA results shown in Table A.1.

Catalysts	Amount of complex (μg) calculated using weight % of a particular element					
	Ni	Co	P	S	B	F
$Ni(P_2N_2)_2$	19.8	-	20.6	-	-	-
P_2N	43.3	-	42.4	-	-	-
$Co(tdt)_2$	-	33.1	-	30.7	-	-
$Co(bdt)_2$	-	29.1	-	34.1	-	-
$Co(DMGBF_2)$	-	27.5	-	-	24.8	38.8
CpNi	18.23	-	-	-	-	-

We next quantify the amount of $Ni(P_2N_2)_2$ adsorbed on the Vulcan carbon surface. Using the UV-Vis calibration curve set up in Figure A.3, the amount of $Ni(P_2N_2)_2$ supported on Vulcan is about 20 μg and remains almost unaffected after HER. We further measure the amount of $Ni(P_2N_2)_2$ captured on carbon surfaces using elemental analysis (EA). Tables A.1 to 4 show the EA results of all the catalysts utilized in this study. Table A.5 displays the amount of catalysts immobilized on Vulcan XC-72 carbon calculated using the EA results. The amount of $Ni(P_2N_2)_2$ supported on carbon is about 20 μg, a value comparable to that found using UV-Vis techniques.

A.3.2 Comparing the Turnover Frequency and Tafel Slope of $Ni(P_2N_2)_2$ to Homogeneous Cases and Heterogeneous Catalysts

TOF is calculated using the following equation:

$$TOF = \frac{I}{2nF}$$

with I = current taken at a selected overpotential (C/s), 2 = 2 electron reduction of H^+, n = moles of catalysts (mol), and F = Faraday's constant (C/mol).

Equipped with the knowledge of the amount of catalyst used in the electrochemical studies, we assessed the turnover frequency (TOF) for HER of $Ni(P_2N_2)_2$. $Ni(P_2N_2)_2$ reaches a TOF of 1.86 s^{-1} at an overpotential of 600 mV. The TOF value measured for $Ni(P_2N_2)_2$ immobilized on carbon surface in aqueous acidic medium is drastically smaller than that reported for homogeneous catalysis by $Ni(P_2N_2)_2$. The difference likely stems from the environment surrounding the catalyst. Several literature reports suggest that a hydrophobic aprotic environment, such as one found in the active site of an enzyme isolated from the hydrophilic protic medium by a thick protein coat, is favorable for catalysis. It is possible that the inability to stabilize charged species in non-aqueous organic solvents raises the energy of the ground or resting state of the catalyst, thus lowering the effective energy barrier of the RDS.

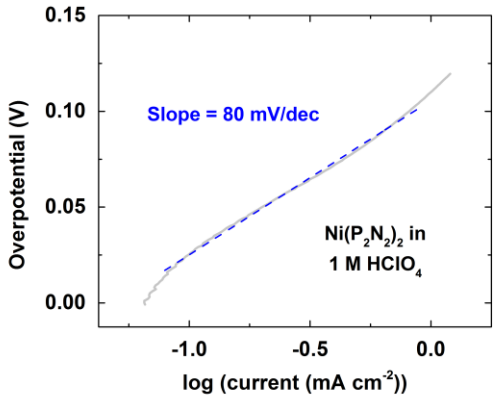

Figure A.5. Tafel plot of HER electrocatalysis by $Ni(P_2N_2)_2$ in 1 M $HClO_4$.

We next characterize the HER activity of $Ni(P_2N_2)_2$ and compare that to the activity of known solid-state HER catalysts. Tafel analysis is a typical method to interrogate the catalytic performance of heterogeneous materials absent mass transport limitations.[10] A Tafel slope of 120 and 60 mV/dec is indicative of a 1 e^- and 2 e^- rate-determining step (RDS), respectively.[10]

$Ni(P_2N_2)_2$ exhibits a Tafel slope of 80 mV/dec, a value suggestive of a possible involvement of a chemical step.

A.3.3 Medium-dependent HER Activity of $Ni(P_2N_2)_2$

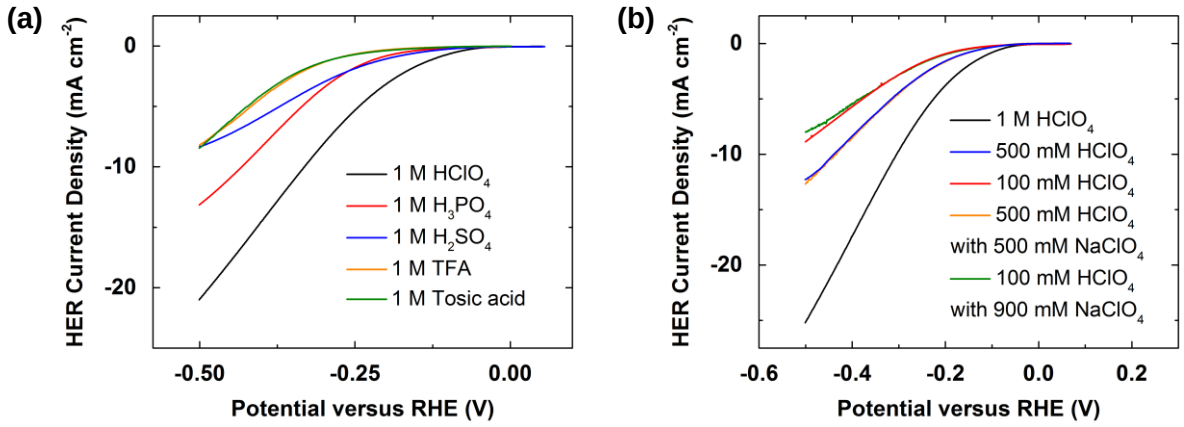

Figure A.6. LSVs of HER catalyzed by $Ni(P_2N_2)_2$ in (a) 1 M $HClO_4$ (black), 1 M H_3PO_4 (red), 1 M H_2SO_4 (blue), 1 M TFA (orange), 1 M Tosic acid (green), and (b) 500 mM $HClO_4$ (blue), 100 mM $HClO_4$ (red), 500 mM $HClO_4$ with 500 mM $NaClO_4$ added (orange), and 100 mM $HClO_4$ with 900 mM $NaClO_4$ added (green) at a scan rate of 10 mV/s with a rotation rate of 2500 rpm.

Moving forward, we investigated the electrocatalytic behavior of $Ni(P_2N_2)_2$ in aqueous media containing different acids. Figure A.6 displays the electrochemical characterization data of HER catalyzed by $Ni(P_2N_2)_2$ in various aqueous media. Interestingly, we found that both the onset potential and the potential-dependent current behavior of $Ni(P_2N_2)_2$ vary as a function of the identity of the electrolyte present in solution (Figure A.6a). The HER performance of $Ni(P_2N_2)_2$ in descending order is: (best) $HClO_4$ > H_3PO_4 > H_2SO_4 > TFA ≈ Tosic acid (worst). We rationalize the observed trend by the anion binding affinity. ClO_4^- is a non-coordinating anion that does not bind tightly to the positively charged $Ni(P_2N_2)_2$ during HER catalysis as compared to phosphate and sulfate anions. TFA and Tosic acids are organic acids commonly utilized in homogeneous HER catalysis in organic solvents. $Ni(P_2N_2)_2$ performs worse in organic

acids relative to in mineral acids possibly due to the relatively low solubility and ionic conductivity of organic acids in aqueous media.

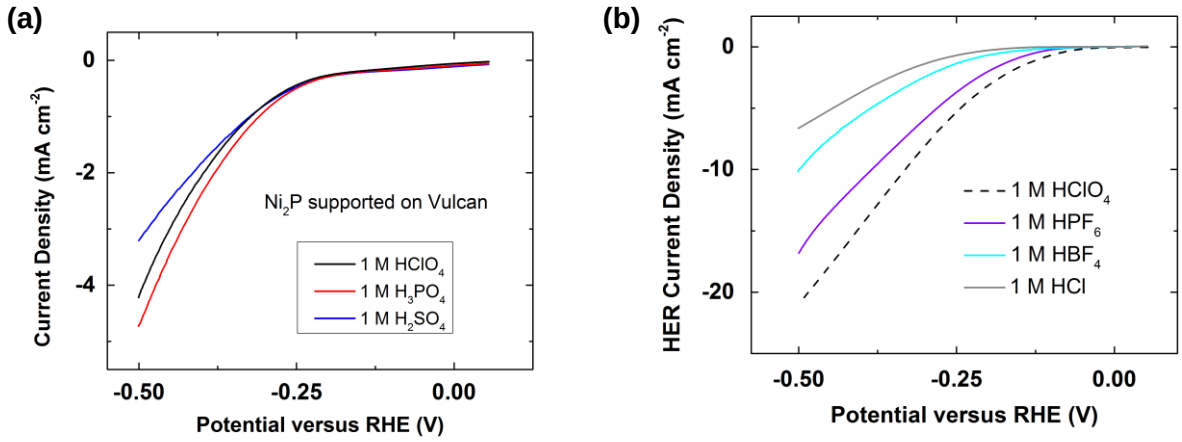

Figure A.7. LSVs of HER catalyzed by (a) Ni_2P in 1 M $HClO_4$ (black line), 1 M H_3PO_4 (red), and 1 M H_2SO_4 (blue) and (b) $Ni(P_2N_2)_2$ in 1 M $HClO_4$ (dashed black line), 1 M HPF_6 (purple), 1 M HBF_4 (cyan), and 1 M HCl (gray) at a scan rate of 10 mV/s with a rotation rate of 2500 rpm.

Figure A.7a shows the LSVs of HER catalyzed by Ni_2P, a typical heterogeneous solid material for proton reduction. Comparing to the molecular catalyst $Ni(P_2N_2)_2$, the HER activity of Ni_2P is affected by the electrolyte present in solution to a relatively minor extent. The high sensitivity towards electrolyte in solution suggests that the metal center of molecular catalysts such as $Ni(P_2N_2)_2$ operates at or involves a positively-charged state during the HER catalytic cycle. In contrast, heterogeneous solid materials exhibit weakly electrolyte-dependent activity, a behavior likely reflecting that the metal in the bulk material remains in the metallic state during proton reduction. The activity of bulk Ni_2P presented here is worse relative to rationally-designed Ni_2P in published work (Figure A.7a). Nano-sized and carefully-structured Ni_2P materials exhibit enhanced activity as compared to bulk Ni_2P. Here, we used commercially available bulk Ni_2P, a heterogeneous solid material for HER, as a standard to understand the

effect of electrolyte towards HER activity. We do not intend to conduct any quantitative analysis on the HER activity of bulk Ni_2P. HPF_6, HBF_4, and HCl are likely plagued or contaminated by halides which are known poisons to electrocatalysts (Figure A.7b). Therefore, we do not attempt to obtain any quantitative insight from this experiment. We hereby provide the data collected for the benefit of the readers.

We next examine the effect of concentration of electrolyte on the HER activity using molecular catalyst and solid material. Figure A.6b shows the LSVs of HER catalyzed by $Ni(P_2N_2)_2$ in aqueous media containing various concentrations of electrolytes. As the concentration of $HClO_4$ decreases, the HER activity of $Ni(P_2N_2)_2$ falls accordingly. To verify that the diminished HER activity does not originate from the change in ionic conductivity in solution, we conducted the same experiment with $NaClO_4$ as supporting electrolyte added to the solution to maintain the ionic conductivity. With $NaClO_4$ added to the solution, $Ni(P_2N_2)_2$ exhibits HER activity similar to cases without supporting electrolyte added. This result suggest that the HER activity is the related to the availability of protons to the molecular catalyst immobilized at the electrode surface. Figure A.8 displays LSVs of HER catalyzed by Ni_2P in acidic media at various pH. The HER activity of Ni_2P is also dependent on the proton availability. Taking together these results from a molecular catalyst and a solid heterogeneous material, we deduce that the pH-dependent HER activity is general.

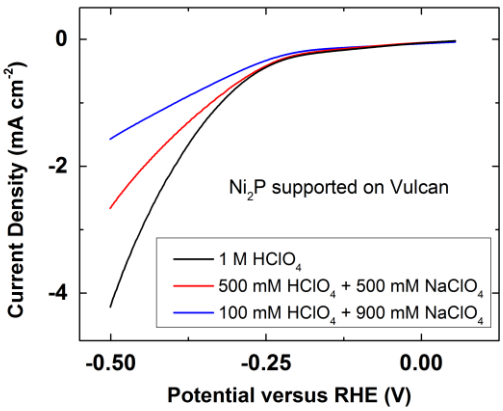

Figure A.8. LSVs of HER catalyzed by Ni_2P in 1 M $HClO_4$ (black line), 500 mM $HClO_4$ with 500 mM $NaClO_4$ added (red), and 100 mM $HClO_4$ with 900 mM $NaClO_4$ added (blue) at a scan rate of 10 mV/s with a rotation rate of 2500 rpm.

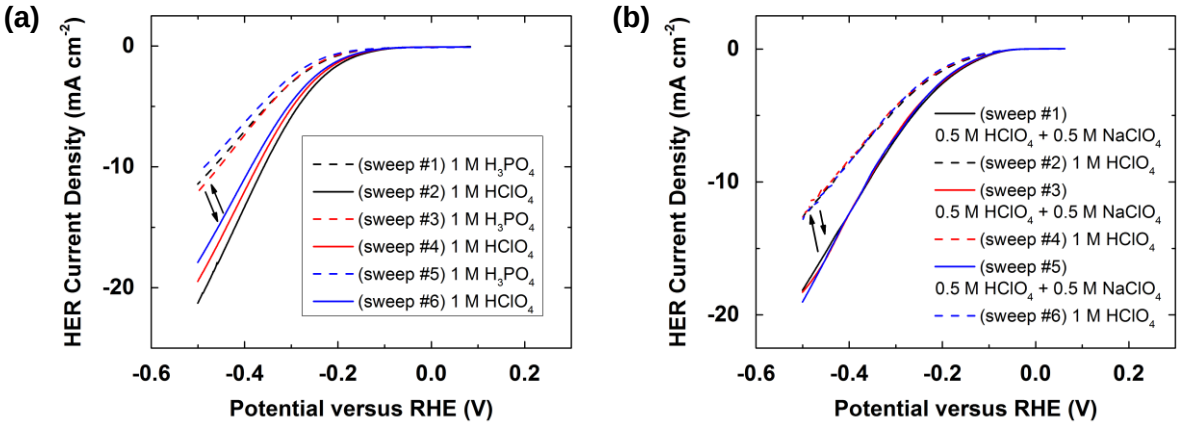

Figure A.9. LSVs of HER catalyzed by $Ni(P_2N_2)_2$ switching between solutions of (a) 1 M $HClO_4$ (solid lines) and 1 M H_3PO_4 (dashed lines), and (b) 1 M $HClO_4$ (solid lines) and 500 mM $HClO_4$ with 500 mM $NaClO_4$ (dashed lines). First, second, and third scans in each solution are denoted in black, red, and blue, respectively.

We next address the possible role of electrolyte in HER catalysis by $Ni(P_2N_2)_2$. Perchlorate, phosphate, and sulfate anions can bind reversibly to the cationic complex or poison the catalytic site irreversibly. Leveraging on the stability of the $Ni(P_2N_2)_2$, we conducted a series of experiments studying one cast of the molecular catalyst upon switching between solutions. Figure A.9 displays LSVs of HER catalyzed by $Ni(P_2N_2)_2$ conducted in different aqueous

solutions in an alternating fashion. In Figure A.9a, the HER activity of $Ni(P_2N_2)_2$ decreases upon switching from 1 M $HClO_4$ to 1 M H_3PO_4. The HER activity is almost fully rescued by switching back to 1 M $HClO_4$. The reversible inhibition and recovery of HER activity is further demonstrated for two more cycles. The slight change in the HER current density over time likely originates from the cross contamination between solutions or the loss of carbonaceous materials upon removal and reinsertion into the acidic solutions. Figure A.10a shows the LSVs of HER catalyzed by $Ni(P_2N_2)_2$ conducted in 1 M $HClO_4$ and 1 M H_2SO_4. Similar to the result obtained from the switching experiment between 1 M $HClO_4$ and 1 M H_3PO_4, the HER activity of $Ni(P_2N_2)_2$ reversibly switches between 1 M $HClO_4$ and 1 M H_2SO_4, demonstrating that perchlorate, phosphate, and sulfate anions likely reversibly binds to the metal ion in $Ni(P_2N_2)_2$ during catalytic cycle.

We further investigate whether reversible HER activity can be extended to solutions containing different concentrations of protons. Figure A.9b and Figures A.10 display the LSVs of HER catalyzed by $Ni(P_2N_2)_2$ switching between aqueous media of varying pH. In Figure A.9b, the HER current density obtained using $Ni(P_2N_2)_2$ decreases upon switching from 1 M $HClO_4$ to 500 mM $HClO_4$ with 500 mM $NaClO_4$ added. The HER activity is fully reactivated by switching back to 1 M $HClO_4$. The reversible suppression and recovery of HER activity is further demonstrated for two more cycles. $Ni(P_2N_2)_2$ also exhibits similar reversible alternating HER behavior in three other cases (Figure A.10b-d). These experiments highlight the durability of $Ni(P_2N_2)_2$ and demonstrate the possibility of using carbon-supported molecular complexes as HER catalyst candidates.

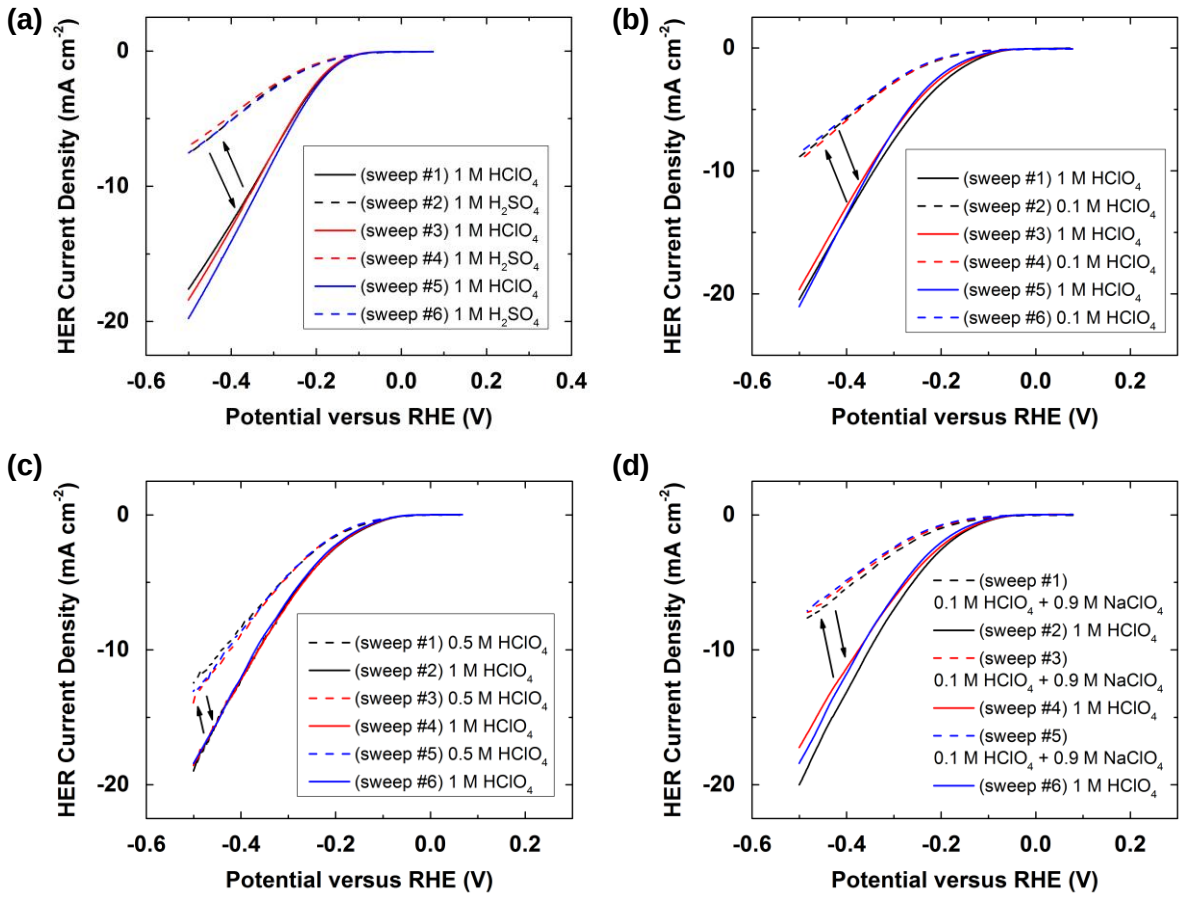

Figure A.10. LSVs of HER catalyzed by $Ni(P_2N_2)_2$ switching between solutions of (a) 1 M $HClO_4$ (solid lines) and 1 M H_2SO_4 (dashed lines), (b) 1 M $HClO_4$ (solid lines) and 100 mM $HClO_4$ (dashed lines), (c) 1 M $HClO_4$ (solid lines) and 500 mM $HClO_4$ (dashed lines), and (d) 1 M $HClO_4$ (solid lines) and 100 mM $HClO_4$ with 900 mM $NaClO_4$ (dashed lines). First, second, and third scans in each solution are denoted in black, red, and blue, respectively.

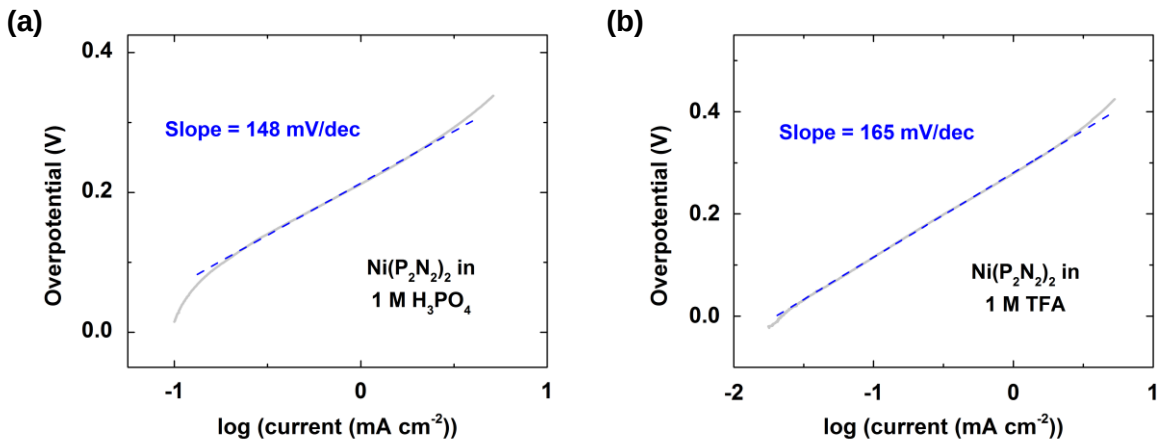

Figure A.11. Tafel slopes of HER catalyzed by $Ni(P_2N_2)_2$ in (a) 1 M H_3PO_4 and (b) 1 M TFA.

The different HER current density attained by $Ni(P_2N_2)_2$ in various acidic media prompts us to further characterize the electrochemical reduction of protons by the molecular catalyst immobilized on carbon surface. By utilizing Tafel analysis, we characterize the HER activity of $Ni(P_2N_2)_2$ in the regime absent mass transport limitations. Figure A.11 presents the Tafel slopes obtained from analyzing the LSVs of HER by $Ni(P_2N_2)_2$ in different electrolyte conditions. In 1 M H_3PO_4 shown in Figure A.11a, $Ni(P_2N_2)_2$ exhibits a Tafel slope of 148 mV/dec, a value significantly different from that obtained in 1 M $HClO_4$. $Ni(P_2N_2)_2$ achieves a Tafel slope of 165 mV/dec in 1 M TFA (Figure A.11b). Figures A.12 and A.13 display the Tafel plots of HER catalyzed by $Ni(P_2N_2)_2$ in other acidic conditions varying both the identity and the concentration of the electrolyte. Table A.6 summarizes the Tafel slopes obtained by $Ni(P_2N_2)_2$ in all the conditions considered in this study. While non-coordinating electrolytes enable $Ni(P_2N_2)_2$ to undergo a HER pathway close to 2 e^-, strongly bound anions facilitate a mechanism with a RDS of about 1 e^-. These Tafel slopes deviate slightly from the ideal values expected for purely $2e^-$ and $1e^-$ pathways, likely suggesting that these RDS are associated to a chemical step.[10] A low Tafel slope is desirable for electrocatalysis because less overpotential is needed to attain more

current.[10] Using terminologies relating thermodynamics and kinetics, a higher rate is achieved with a lower driving force. Pt is a classic example of a HER catalyst displaying a desirable Tafel slope of 60 mV/dec, an ideal value for a purely 2 e^- transfer step not affected by the kinetics of any chemical steps. With elaborate designs, the Tafel slopes attained by heterogeneous solid NPM materials approaches that of 60 mV/dec. Molecular catalysts such as $Ni(P_2N_2)_2$ allows for a high degree of tunability in the ligand design. Proton relays such as pendant amines installed at the second coordination sphere of the ligand framework enables a Tafel slope of 80 mV/dec, a feat exhibited by a molecular catalyst that may rival the performance of Pt and NPM solid materials.

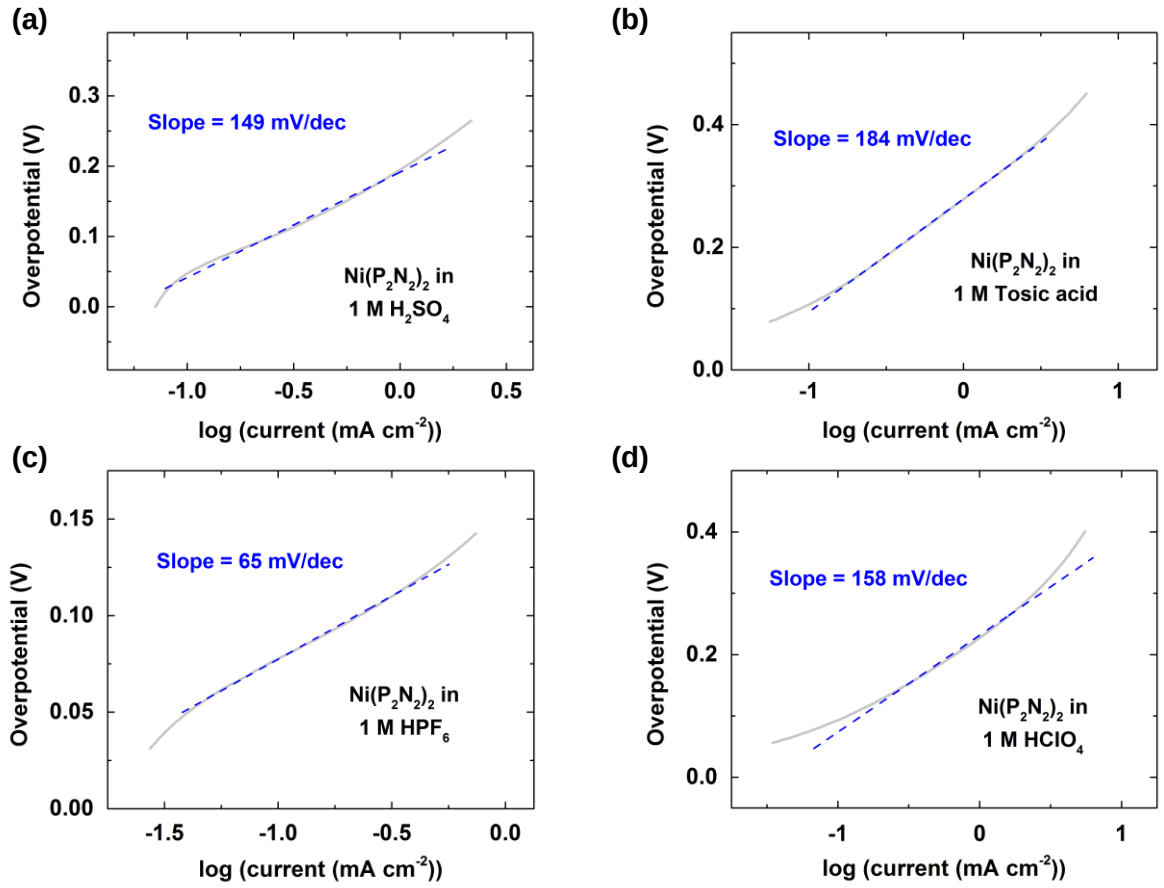

Figure A.12. Tafel slope of HER catalyzed by $Ni(P_2N_2)_2$ obtained in (a) 1 M H_2SO_4, (b) 1 M Tosic acid, (c) 1 M HPF_6, and (d) 1 M HBF_4.

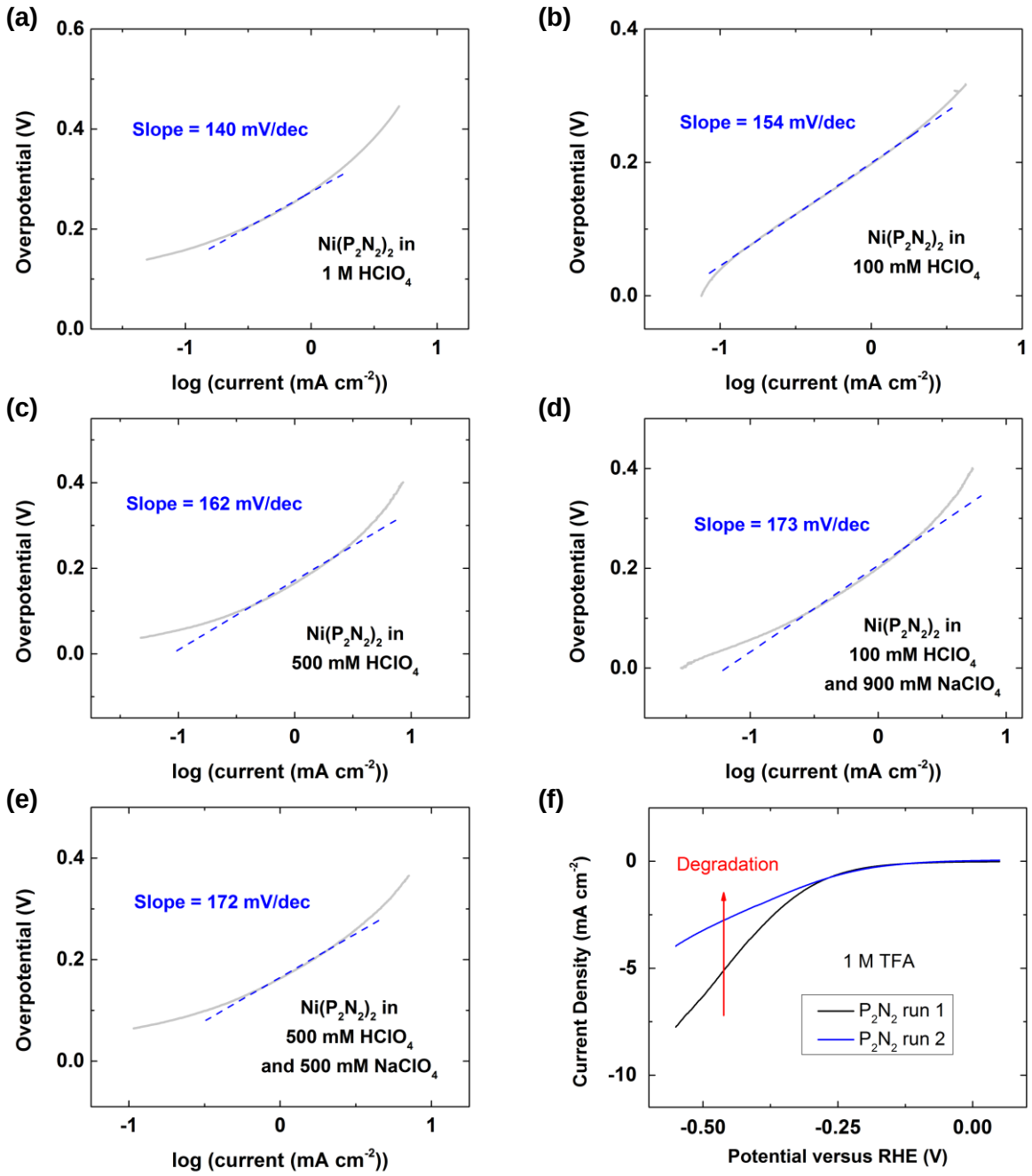

Figure A.13. Tafel slope of HER catalyzed by $Ni(P_2N_2)_2$ obtained in (a) 1 M HCl, (b) 100 mM $HClO_4$, (c) 500 mM $HClO_4$, (d) 100 mM $HClO_4$ with 900 mM $NaClO_4$, and (e) 500 mM $HClO_4$ with 500 mM $NaClO_4$. (f) LSVs of $Ni(P_2N_2)_2$ before (black) and after (blue) running HER in 1 M TFA.

Table A.6. Summary of HER performance of P_2N_2 on Vulcan in different conditions.

Acid Solution	Tafel Slope of $Ni(P_2N_2)_2$
1 M $HClO_4$	80
1 M H_3PO_4	148
1 M H_2SO_4	149
1 M TFA	165
1 M Tosic acid	184
1 M HPF_6	65
1 M HBF_4	158
1 M HCl	140
100 mM $HClO_4$	154
500 mM $HClO_4$	162
500 mM $HClO_4$ with 500 mM $NaClO_4$	172
100 mM $HClO_4$ with 900 mM $NaClO_4$	173

A.3.4 Ligand-dependent HER Performance of a $Ni(P_2N_2)_2$ Derivative

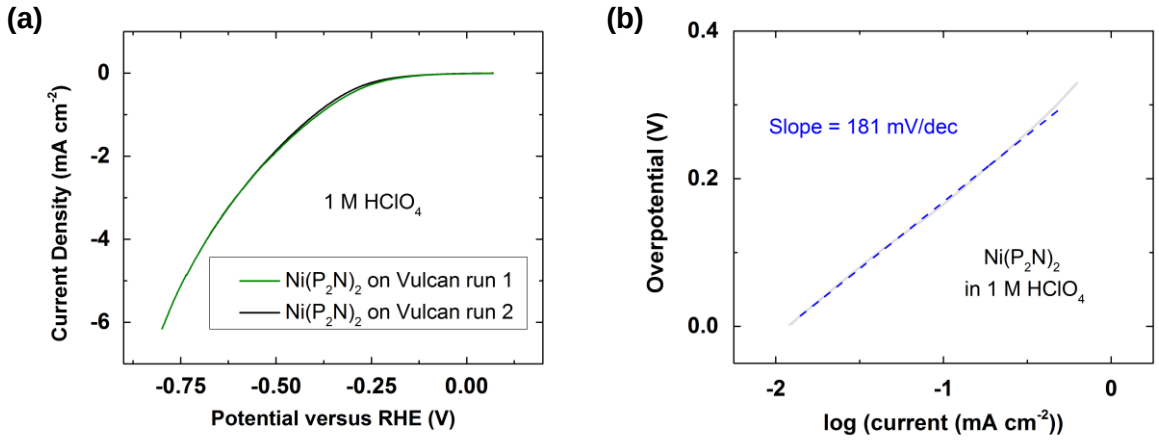

Figure A.14. (a) First (green) and second (black) scans of LSVs and (b) Tafel plot of HER catalyzed by $Ni(P_2N)_2$ acquired in 1 M $HClO_4$.

We next explore the impact of the supporting ligand set on the proton reduction activity of a molecular catalyst adsorbed on carbon surfaces. P_2N exceeds the performance of $Ni(P_2N_2)_2$ in homogeneous proton reduction in organic solvents.[11] We therefore prepared $Ni(P_2N)_2$ immobilized on Vulcan carbon and then conducted electrochemical characterization of the HER activity of $Ni(P_2N)_2$ in 1 M $HClO_4$, an aqueous acidic medium where $Ni(P_2N_2)_2$ exhibits the best HER performance. Figure A.14a displays the HER LSVs of $Ni(P_2N)_2$ recorded in aqueous acidic medium. $Ni(P_2N)_2$ exhibits an onset potential of about -200 mV vs RHE for HER, 100 mV more negative relative to the onset measured for $Ni(P_2N_2)_2$. The almost identical voltammograms with similar HER onsets and potential-dependent current responses indicate that $Ni(P_2N)_2$ is a stable catalyst for proton reduction in 1 M $HClO_4$ at these reducing potentials. Figure A.14b presents the HER Tafel plot of $Ni(P_2N)_2$. $Ni(P_2N)_2$ exhibits a Tafel slope of 181 mV/dec, a value much larger than that obtained by $Ni(P_2N_2)_2$.

We next address the different HER activities between $Ni(P_2N)_2$ and $Ni(P_2N_2)_2$, two closely-related molecular catalysts. Literature report discusses multiple forms of the $Ni(P_2N)_2$ molecular catalyst. The conformer with the pendant amine in the conformation to interact with the bound Ni-H adduct is an active catalyst for proton reduction. For homogeneous proton reduction in organic solvent, $Ni(P_2N)_2$ outperforms $Ni(P_2N_2)_2$ likely because more rigid ligand in $Ni(P_2N)_2$ holds the pendant amine in close proximity to allow for efficient proton transfer kinetics in a relatively non-polar aprotic environment. However for heterogeneous HER catalysis in aqueous media, $Ni(P_2N_2)_2$ outperforms $Ni(P_2N)_2$ instead. We rationalize the opposing trend observed in organic and aqueous media in two ways. First, proton is readily available to the catalyst in aqueous acids, therefore the enhancement effect of pendant proton relays on the rate

of proton reduction is significantly lowered. Unlike in organic solvents where protons are relatively less accessible, proton relays thus play a major role in preloading protons in the second coordination sphere and dictating the catalytic activity in homogeneous proton reduction. Second, pendant amines likely form an extensive H-bonding network with surrounding water and acid. By possessing two more pendant amines than $Ni(P_2N)_2$, $Ni(P_2N_2)_2$ has a higher probability to access a state with a pendant amine free from H-bonding to participate in HER catalysis.

A.3.5 A Survey of the HER Performance of a Library of HER Molecular Catalysts

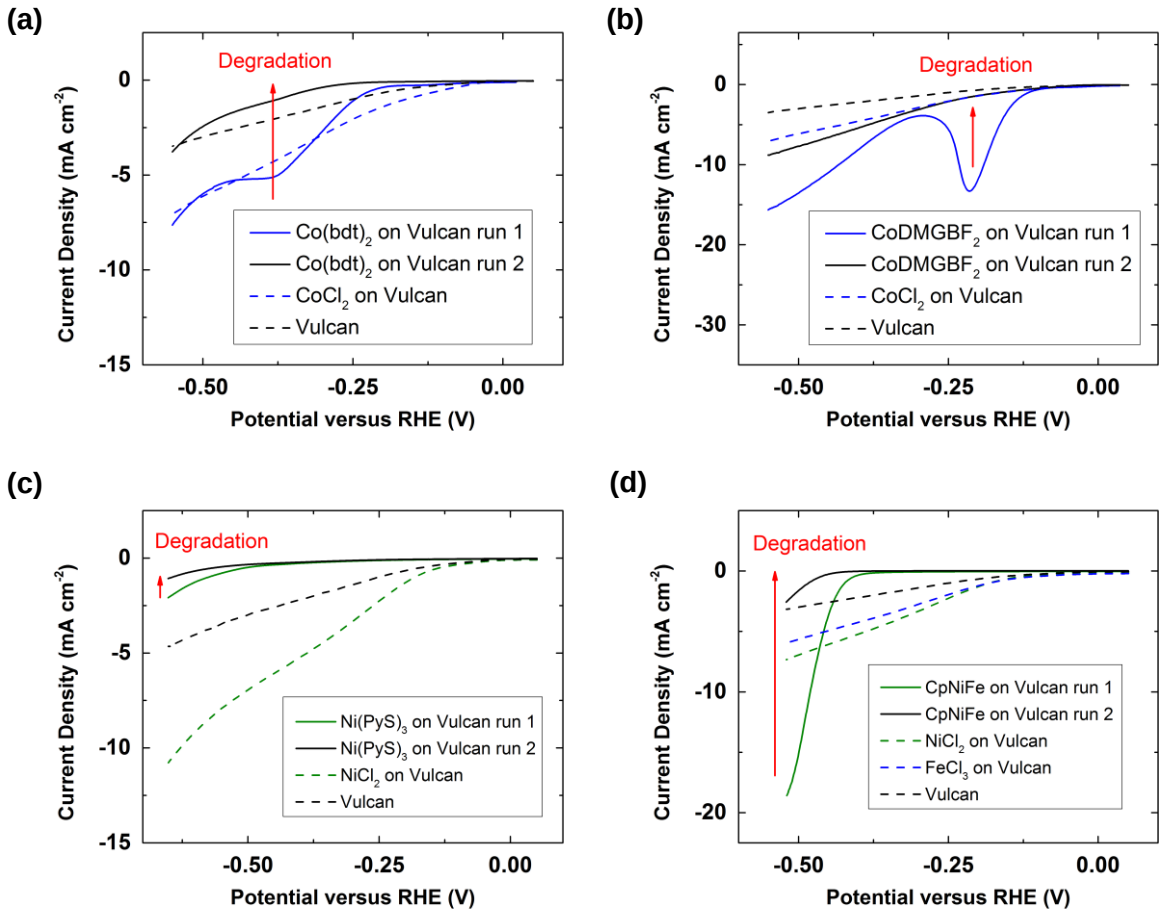

Figure A.15. HER LSVs of (a) $Co(bdt)_2$, (b) $CoDMGBF_2$, (c) $Ni(PyS)_3$, and (d) CpNiFe recorded in 1 M $HClO_4$ at a scan rate of 10 mV/s with a rotation rate of 2500 rpm.

Going beyond the idea to improve the HER performance of a specific molecular catalyst by altering the proton relays in the second coordination sphere, we next examine other classes of HER molecular catalysts bearing completely different supporting ligand sets and metal ions. Figure A.15 displays the LSVs of HER catalyzed by four known HER molecular catalysts supported on carbon. $Co(bdt)_2$ exhibits a HER onset potential of about -200 mV vs. RHE and the HER wave plateaus at about -370 mV vs. RHE (Figure A.15a). In the second scan, the HER current density significantly decreases. The solution around the electrode surface turned blue during HER, suggesting that the degradation in HER activity likely results from the leaching of $Co(bdt)_2$ into the acidic aqueous solution at reducing potentials. The addition of more Nafion binder and scanning to less negative potentials do not inhibit the degradation of HER activity by $Co(bdt)_2$. The onset of HER catalyzed by $CoDMGBF_2$ occurs at about -100 mV vs. RHE and the HER current density peaks at about -200 mV vs. RHE. Peaking behavior under rotation regime is uncommon; instead a phenomenon associated to the degradation of the catalyst is likely. In the second scan, the HER activity of $CoDMGBF_2$ diminishes significantly to a level similar to the Co^{2+} control, suggesting that Co^{2+} ions likely dissociates from the ligand $DMGBF_2$ under acidic reduction conditions and contributes to the HER current observed. We further verify the degradation in HER activity of $CoDMGBF_2$ by holding at -5 mA cm^{-2} and monitoring the change in electrode potential over time (Figure A.16). Within 1 min of operation, the potential shifts negative by 200 mV, signifying the degradation of the catalyst at reducing potential over time.

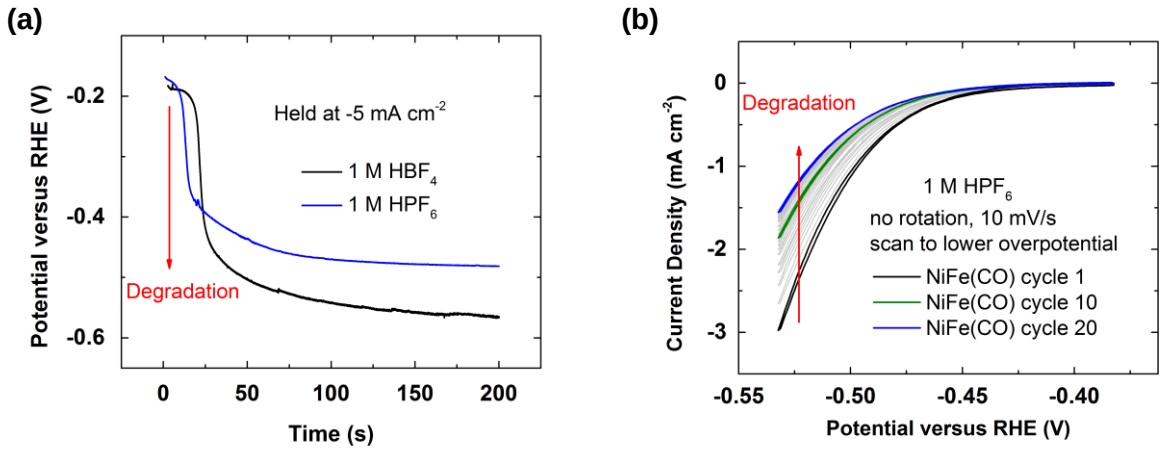

Figure A.16. (a) Representative chronopotentiometry of $CoDMGBF_2$ in 1 M HBF_4 and 1 M HPF_6. (b) CVs of CpNiFe in 1 M HPF_6.

After examining Co complexes, we next interrogate the HER activity of other first row transition metal complexes. Presented in Figure A.15c, $Ni(PyS)_3$ displays an onset potential for proton reduction at about -500 mV vs. RHE, a value significantly more negative relative to the other catalysts studied. The amount of HER current density extracted from $Ni(PyS)_3$ by applying a 500 mV driving force is much lower than that obtained from the Vulcan carbon only control. Therefore, $Ni(PyS)_3$ adsorbed on carbon surfaces is not an active HER catalyst in aqueous acidic media. CpNiFe is a competent molecular catalyst for proton reduction for the homogeneous case in organic solvent. We next recorded the HER performance of CpNiFe immobilized on carbon surfaces in aqueous acidic medium and presented the result in Figure A.15d. CpNiFe exhibits an onset potential for HER at about -400 mV vs. RHE. However, the amount of proton reduction current density significantly decreases, indicating that CpNiFe either decomposes or leaches to solution.

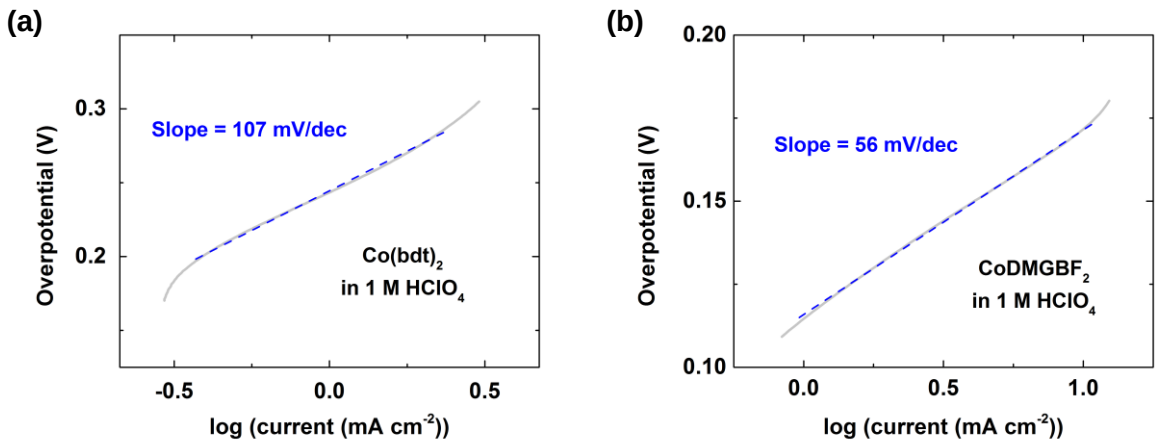

Figure A.17. Tafel plots of HER catalyzed by (a) $Co(bdt)_2$ and (b) $CoDMGBF_2$ in 1 M $HClO_4$ at a scan rate of 10 mV/s with a rotation rate of 2500 rpm.

We next conducted Tafel analysis on these catalysts. Figure A.17 and Figure A.18 show the Tafel plots of the four catalysts studied in this section and the measured Tafel slopes are reported in Table A.7. $Co(bdt)_2$ exhibits a Tafel slope of 107 mV/dec, while $CoDMGBF_2$ exhibits a Tafel slope of 56 mV/dec, a value that corresponds to an ideal 2 e^- RDS. $Ni(PyS)_3$, the least active catalyst tested, exhibits a Tafel slope of 237 mV/dec, indicating the involvement of a chemical step with slow kinetics. CpNiFe exhibits exceptional high proton reduction rate in organic solvents. Here in aqueous medium, CpNiFe demonstrates the lowest Tafel slope among other catalysts considered in this study. However considering HER is a 2 e^- reduction process, a Tafel slope below 60 mV/dec is perplexing, likely suggesting that CpNiFe complex undergoes another reaction during at HER potentials. Figure A.16b shows 20 HER cycles of CpNiFe in aqueous acidic solution in the absence of rotation. The use of a static electrode slows down but does not completely suppress the degradation rate of HER activity of CpNiFe. Combining the finding in Figure A.16b and the Tafel analysis, the origin of degradation of CpNiFe is likely a combination of both a reductive decomposition process and leaching of the catalyst into solution.

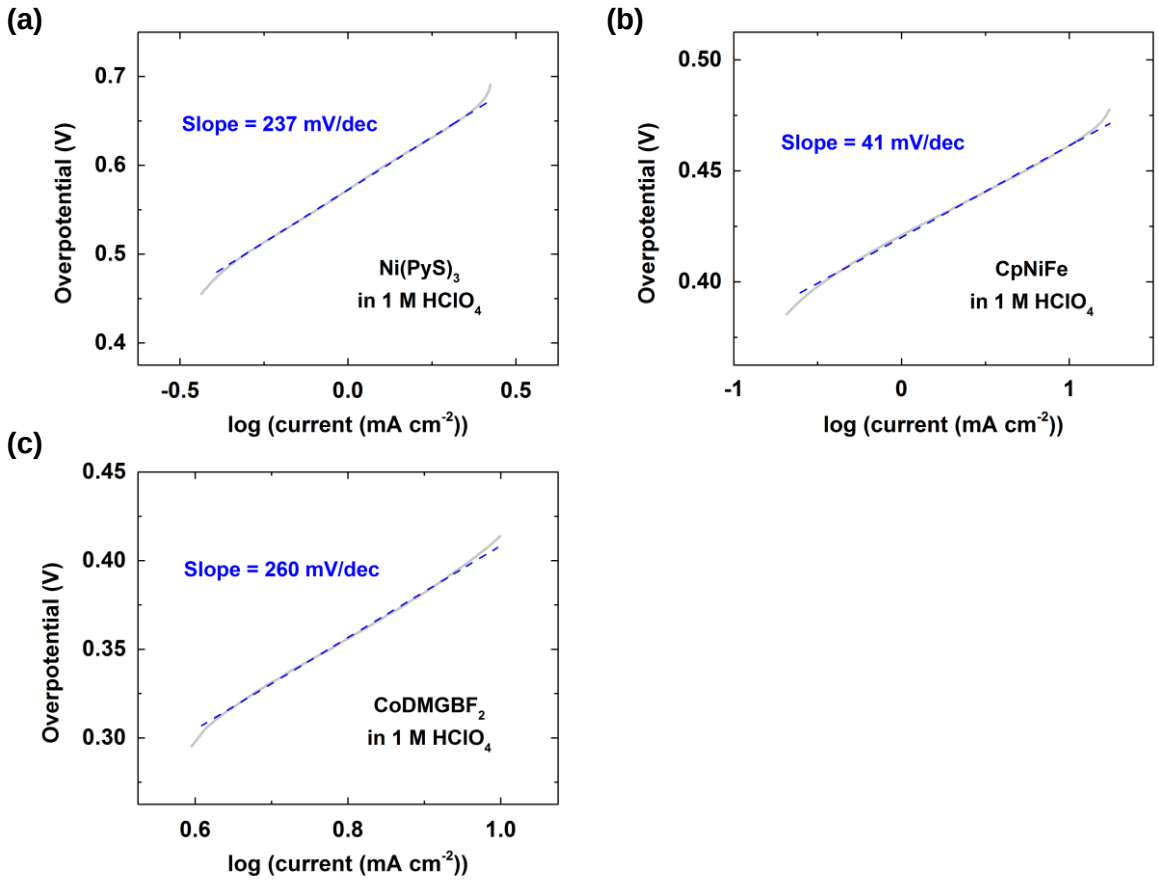

Figure A.18. Tafel plots of (a) $Ni(PyS)_3$ and (b) NiFe(CO) in 1 M $HClO_4$ and (c) $CoDMGBF_2$ after degradation in 1 M $HClO_4$.

Table A.7. Summary of the HER activity of the catalysts studied.

Catalysts	**Onset vs. RHE in 1 M $HClO_4$ (mV versus RHE)**	**Tafel Slope in 1 M $HClO_4$ (mV/dec)**
$Co(bdt)_2$	-200	107
$CoDMGBF_2$	-100	56
$Ni(PyS)_3$	-500	237
NiFe(CO)	-400	41

A.3.6 Methods to Prevent Degradation of Unstable Molecular HER Catalysts

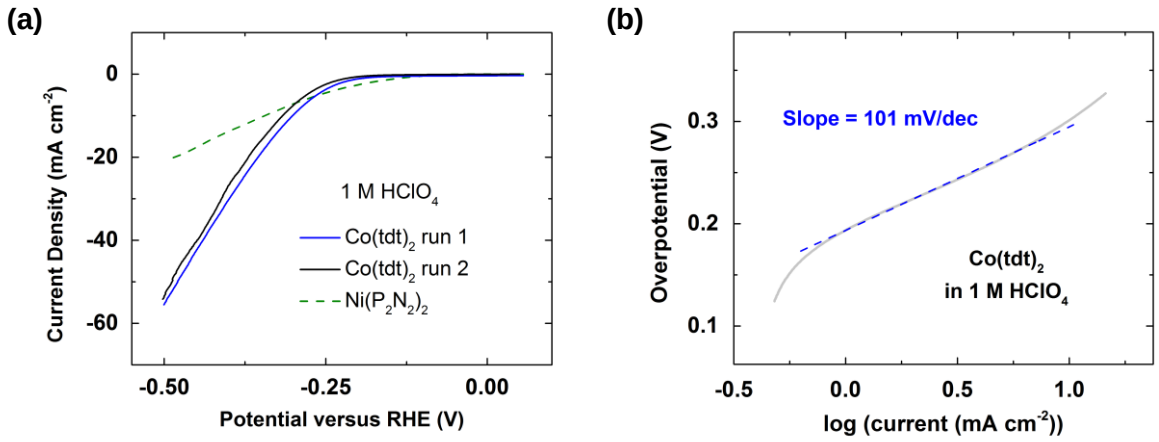

Figure A.19. (a) First run (blue) and second run (black) of HER LSVs and (b) Tafel plot of $Co(tdt)_2$ obtained in 1 M $HClO_4$ at a scan rate of 10 mV/s with a rotation rate of 2500 rpm.

In order to carry out further detailed electrochemical characterization of molecular HER catalysts, we first tackle the stability issue by preventing the catalyst from degrading in aqueous media. Taking $Co(bdt)_2$ as an example, the likely cause of the degradation in HER activity of $Co(bdt)_2$ is the leaching of the catalyst in aqueous acids. A viable strategy previously demonstrated to avoid the dissolution of molecular catalysts to bulk solution is through the covalent attachment of catalytic site onto the electrode surface.[12] However, even with the use of high-yielding click reactions under benign conditions, multi-step preparation is synthetically cumbersome and undoubtedly leads to waste generation. Here, we address the issue of leaching by adding a methyl group to the benzene ring of the supporting ligand tuning to enhance its hydrophobicity and lower its solubility in aqueous media. The resulting complex $Co(tdt)_2$ possesses a lower solubility in 1 M $HClO_4$ relative to $Co(bdt)_2$. Figure A.19a shows the LSVs of HER catalyzed by $Co(tdt)_2$ with an onset potential of about -200 mV vs. RHE, a value similar to the case of $Co(bdt)_2$ but about 100 mV more negative relative to that of $Ni(P_2N_2)_2$ (green dashed line). In between the first and second runs, $Co(tdt)_2$ was held at -5 mA cm^{-2} for 15 min. The

second scan of HER catalyzed by $Co(tdt)_2$ shifted negative only by a slight amount relative to that of the first scan, a behavior signifying that $Co(tdt)_2$ is more stable than $Co(bdt)_2$ in 1 M $HClO_4$. Figure A.19b shows the Tafel plot of $Co(tdt)_2$ with a Tafel slope of 101 mV/dec. Both $Co(tdt)_2$ and $Co(bdt)_2$ exhibit similar Tafel slopes, suggesting that the installation of a methyl group to the supporting ligand remote from the metal ion center does not interfere with the mechanism of proton reduction. The methyl group tunes the solubility of the molecular complex to prevent $Co(tdt)_2$ from leaching off the carbon surface. $Co(tdt)_2$ outperforms $Ni(P_2N_2)_2$ in the sense that more current is drawn at -0.5 mV vs. RHE.

Table A.8. Summary of stability of HER catalysts studied.

Catalysts	**$Ni(P_2N_2)_2$**	**CpNiFe**	**$CoDMGBF_2$**	**$Co(bdt)_2$**	**$Ni(PyS)_3$**
1 M $HClO_4$	stable	unstable	unstable	unstable	unstable
100 mM $HClO_4$	stable	unstable	unstable	unstable	unstable
1 M HCl	stable	unstable	unstable	unstable	unstable
1 M H_2SO_4	stable	unstable	unstable	unstable	unstable
1 M H_3PO_4	stable	unstable	unstable	unstable	unstable
1 M HBF_4	stable	unstable	unstable	unstable	unstable
1 M HPF_6	stable	unstable	unstable	unstable	unstable
1 M Tosic acid	stable	unstable	unstable	unstable	unstable
1 M TFA	unstable	unstable	unstable	unstable	unstable

We next tackle the stability issue of other catalysts using strategies that do not involve chemical modification of the molecular catalyst. We attempt to raise the stability of these molecular catalysts by using less acidic solutions and aqueous media containing electrolytes

other than perchlorates. Table A.8 summaries the HER results of molecular catalysts being subjected to multiple LSV cycles or chronopotentiometric conditions. Unfortunately, the HER activity of all four molecular catalysts degrades over time.

A.4 References

(1) Conway, B. E.; Bockris, J. O.; Apos, M. *J. Chem. Phys.* **1957**, *26*, 532.
(2) Conway, B. E.; Tilak, B. V. *Electrochim. Acta* **2002**, *47*, 3571.
(3) Lu, Q.; Hutchings, G. S.; Yu, W.; Zhou, Y.; Forest, R. V.; Tao, R.; Rosen, J.; Yonemoto, B. T.; Cao, Z.; Zheng, H.; Xiao, J. Q.; Jiao, F.; Chen, J. G. *Nat. Commun.* **2015**, *6*.
(4) Zheng, Y.; Jiao, Y.; Jaroniec, M.; Qiao, S. Z. *Angew. Chem. Int. Ed.* **2015**, *54*, 52.
(5) Safizadeh, F.; Ghali, E.; Houlachi, G. *Int. J. Hydrogen Energy* **2015**, *40*, 256.
(6) Vesborg, P. C. K.; Seger, B.; Chorkendorff, I. *J. Phys. Chem. Lett.* **2015**, *6*, 951.
(7) Zou, X.; Zhang, Y. *Chem. Soc. Rev.* **2015**, *44*, 5148.
(8) Zeng, M.; Li, Y. *J. Mat. Chem. A* **2015**, *3*, 14942.
(9) Wilson, A. D.; Newell, R. H.; McNevin, M. J.; Muckerman, J. T.; Rakowski DuBois, M.; DuBois, D. L. *J. Am. Chem. Soc.* **2006**, *128*, 358.
(10) Fletcher, S. *J. Solid State Electrochem.* **2009**, *13*, 537.
(11) Brown, H. J. S.; Wiese, S.; Roberts, J. A. S.; Bullock, R. M.; Helm, M. L. *ACS Catal.* **2015**, *5*, 2116.
(12) Das, A. K.; Engelhard, M. H.; Bullock, R. M.; Roberts, J. A. S. *Inorg. Chem.* **2014**, *53*, 6875.

Appendix B

Non-precious Metal Complexes of Pyrazolyl-, Imidazolyl-, and Triazolyl-based Ligands as Active Electrocatalysts for the Oxygen Reduction Reaction

The work in this appendix was accomplished in collaboration with Dr. Andrey Tregubov, Professor Thomas B. Rauchfuss, and Professor Andrew A. Gewirth.

B.1 Introduction

Based on our previous successful attempt to use of Cu complex of 3,5-diamino-1,2,4-triazole (DAT) as an efficient oxygen reduction reaction (ORR) catalyst for fuel cell applications,[1] we spearheaded a follow-up study on utilizing Cu complexes of Schiff base derivatives of DAT as cathode catalysts (Figure B.1). Our group also launched an investigation to use Cu complexes bound by pyridinyl-based and alkyl-amine-based ligands as ORR catalysts (Figure B.2). As an on-going effort, we further develop systems involving non-precious metal (NPM) complexes of ligands possessing pyrazole, imidazole, and triazole synthons (Figure B.3).

B.2 Results and Discussion

B.2.1 Cu complexes of Schiff Bases of DAT

Cu complexes of Schiff base of DAT essentially perform analogously to CuDAT, suggesting the addition of flanking electron-donating, electron-withdrawing, and proton-relay groups does not significantly perturb the dinuclear Cu core as the ORR reaction center. This is not the first example that ligand modification does not impact the electrocatalytic activity. For

the tri- and di-pyridyl amine ligand scaffolds (TPA and DPA), tweaking the sterics, electronics, and contiguity of the framework has no effect on the ORR onset and diffusion-limited current achieved across a wide range of pH units (pH 1-13).[2-4] All these experiments strongly indicates that the electron transfer energetics is likely primarily dictated by the electrode potential at the glassy carbon surface and the proton transfer dynamics is predominantly controlled by the solution pH. Another possible explanation is the newly-installed functionality degrades during electrocatalytic activity assay to produce the unmodified parent Cu complex *in situ*.

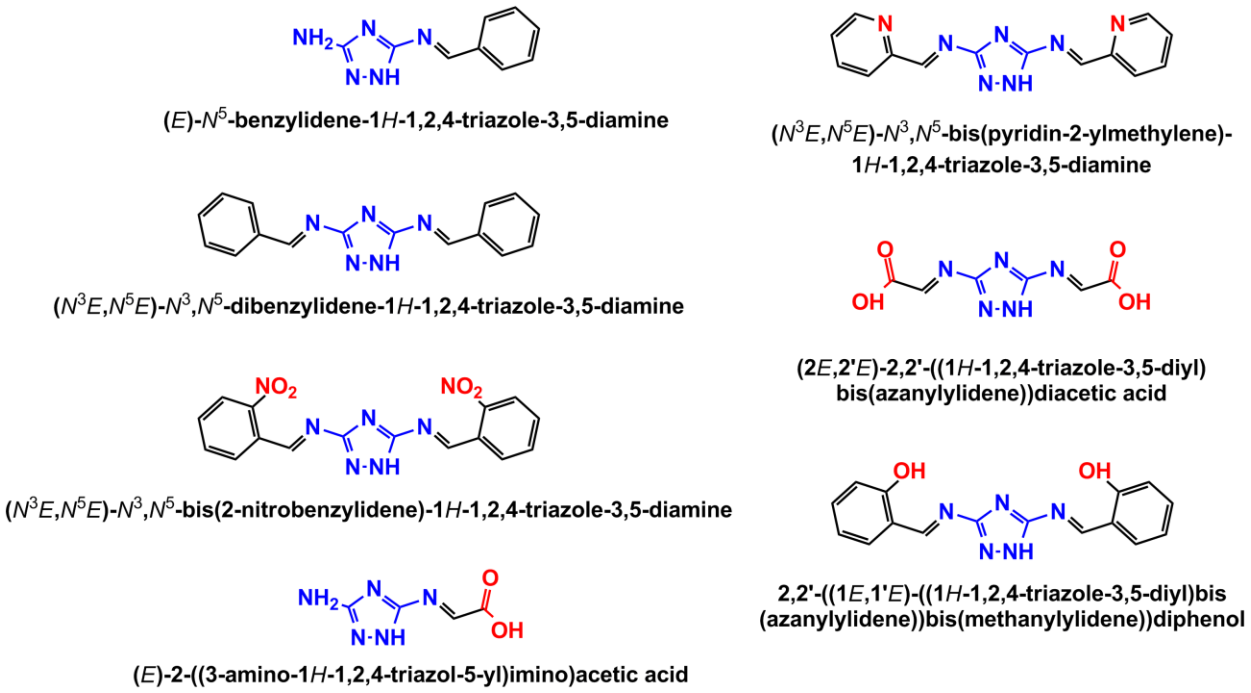

Figure B.1. A selective list of triazolyl-based ligands used.

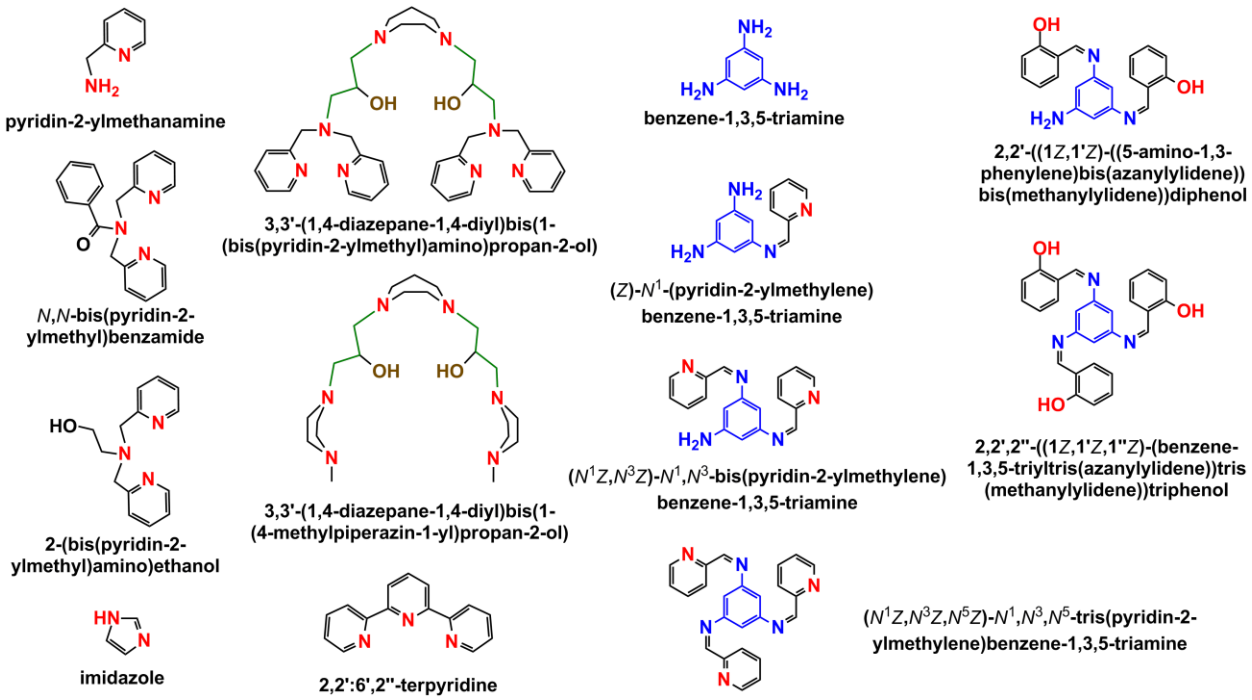

Figure B.2. A selective list of pyridinyl-, imidazolyl-, and alkyl-amine-based ligands used.

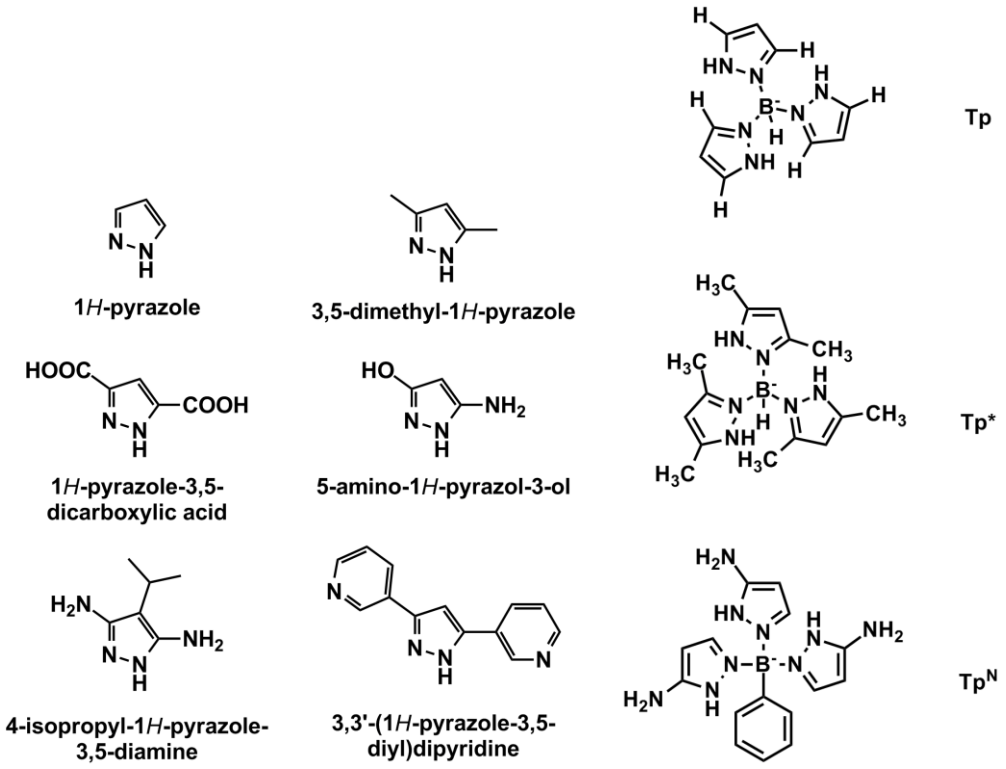

Figure B.3. A selective list of pyrazole-based ligands used.

B.2.2 Cu Complexes of Pyrazolyl-based Derivatives

In our continue effort to improve the performance of NPM catalysts for fuel cell technology, we prepared Cu complexes of pyrazole derivatives (substituents at the 3 and 5 positions) and trispyrazolylborate analogues (substituents at the 3 and 5 positions) shown in Figure B.3. We further tested these earth-abundant catalysts on inexpensive carbon support as electrocatalysts for the ORR and compared their performance to that of the benchmark catalysts in this field (Tables B.1 and B.2).[5] The information in Table B.1 came from detailed analyses of the raw data presented in Figure B.4 to B.9.

Table B.1. ORR onsets of Cu complexes utilized in this study versus record holders in literature. ORR onsets are defined as the potential at which 5% of the i_{lim} is reached. See Table B.2 for an extended list of reported ORR onsets of molecular ORR Cu electrocatalysts.[1,3]

pH	Record	Onset	HO-py-NH_2	py-$(py)_2$	Tp^N
1	Cu-TPA	0.530 V			0.510 V
4	Cu-DAT	0.580 V			0.580 V
7	Cu-DAT	0.690 V	0.704 V	0.706 V	0.720 V
10	Cu-DAT	0.760 V			0.830 V
13	Cu-DAT	0.820 V			0.860 V

Table B.2. An updated literature review on reported ORR onsets of non-heat-treated Cu catalysts.[4-6]

Catalyst	ORR Onset (V vs. RHE)	pH, solution
[Cu-Cu-2,9-Me_2-phen]$^{2+}$	0.610	pH 5, Britton-Robinson
[CuTPA]$(ClO4)_2$ and TPA-derivatives	0.690	pH 7, Britton-Robinson
[Cu-hexaazamac]Cl_4	0.670	pH 7.3, Borate Buffer

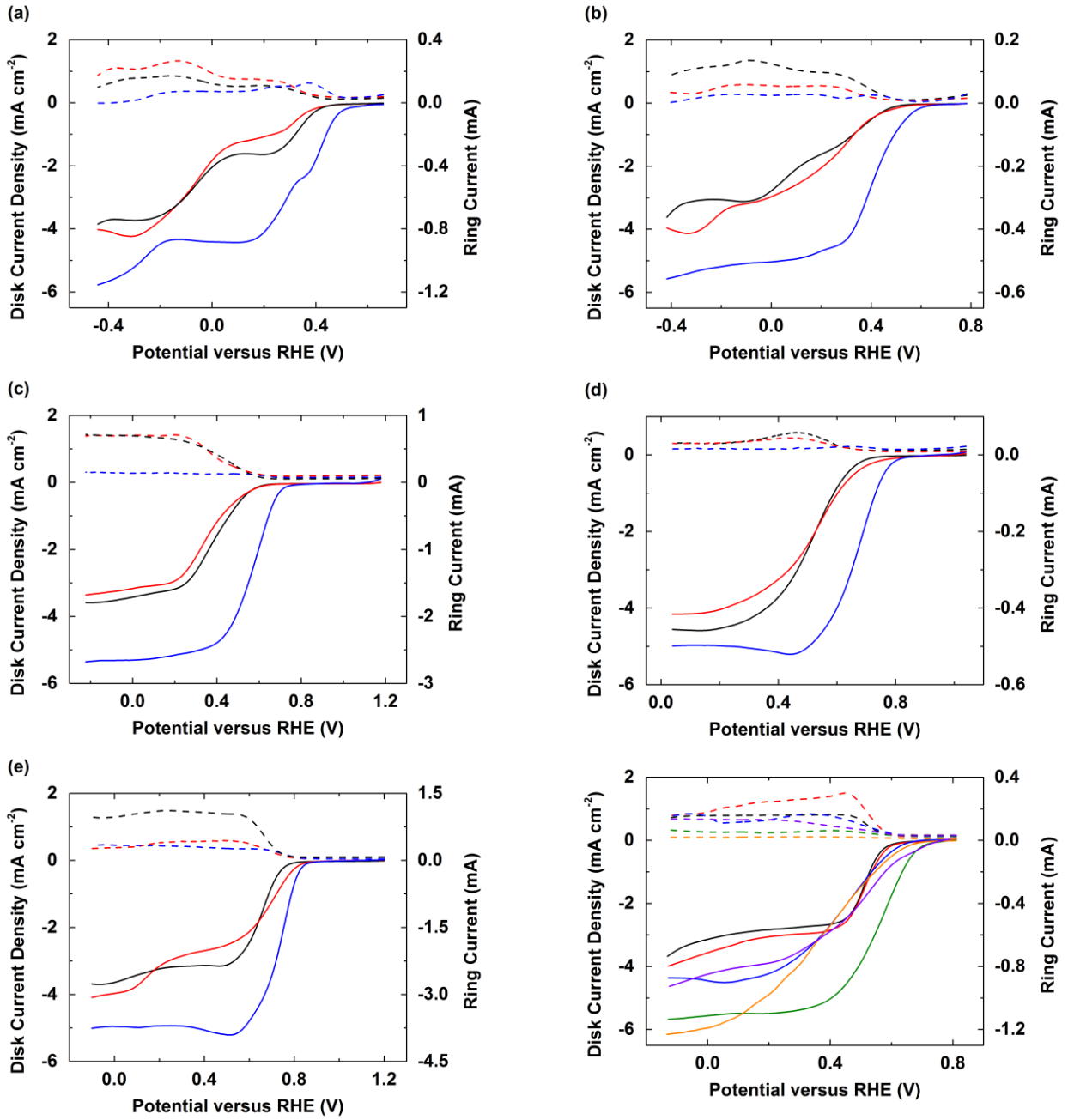

Figure B.4. Linear sweep voltammograms (LSVs, solid lines) and ring currents (dashed lines) of $[Cu(Tp)]^{2+}$ (black), $[Cu(Tp^{*})]^{2+}$ (red), and $[Cu(TpN)]^{2+}$ (blue) supported on Vulcan XC-72 in (a) pH 1, (b) pH 4, (c) pH 7, (d) pH 10, and (e) pH 13 O_2-saturated Britton-Robinson buffer solutions with a scan rate of 10 mV/s at 1600 rpm. (f) LSVs (solid lines) and ring currents (dashed lines) of $[Cu(pr)]^{2+}$ (black), $[Cu(py\text{-}(CH_3)_2)]^{2+}$ (red), $[Cu(py\text{-}(COOH)_2)]^{2+}$ (blue), $[Cu(py\text{-}(NH_2)_2)]^{2+}$ (orange), $[Cu(py\text{-}(py)_2)]^{2+}$ (purple), and $[Cu(HO\text{-}py\text{-}NH_2)]^{2+}$ (green) supported on Vulcan XC-72 in (a) pH 1, (b) pH 4, (c) pH 7, (d) pH 10, and (e) pH 13 O_2-saturated Britton-Robinson buffer solutions with a scan rate of 10 mV/s at 1600 rpm.

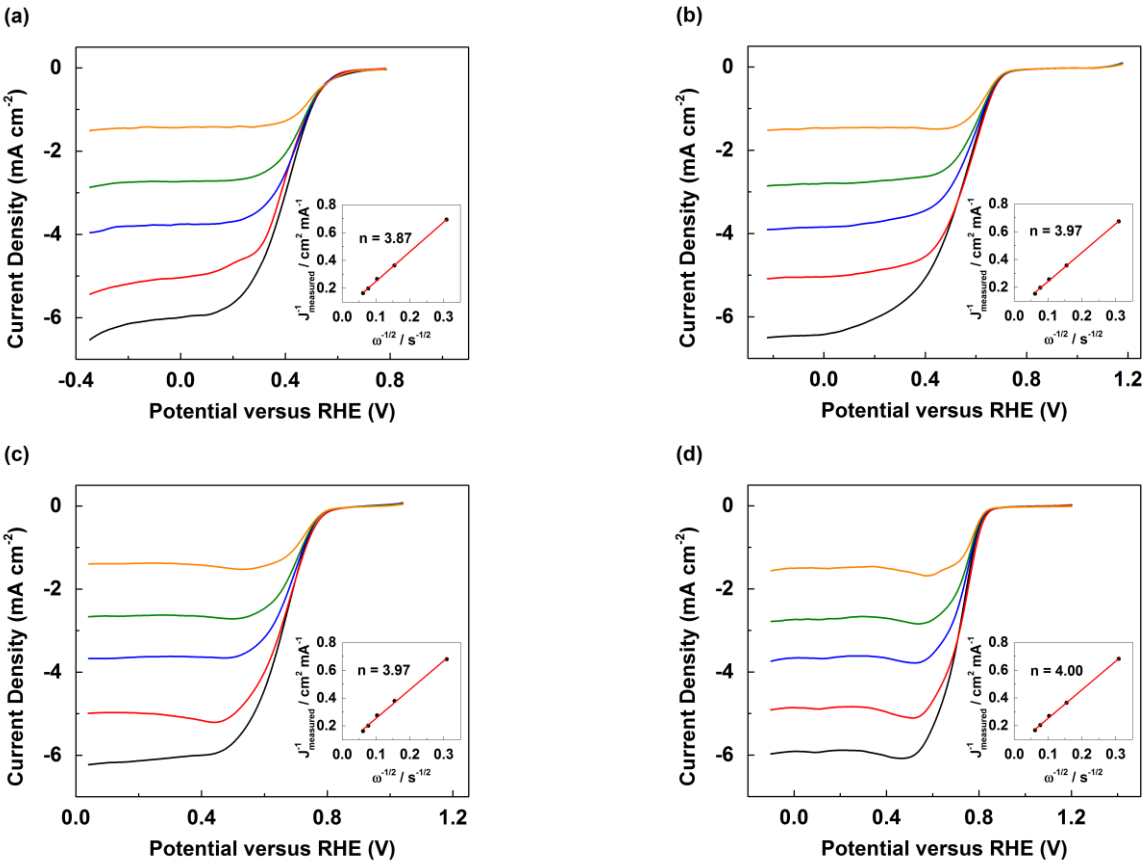

Figure B.5. Rotating disk electrode (RDE) LSVs and Koutecky-Levich plots (inset) of $[Cu(TpN)]^{2+}$ supported on Vulcan XC-72 in (a) pH 4, (b) pH 7, (c) pH 10, and (d) pH 13 O_2-saturated solutions with a scan rate of 10 mV/s at 100 (red), 400 (blue), 900 (green), 1600 (violet), and 2500 rpm (orange).

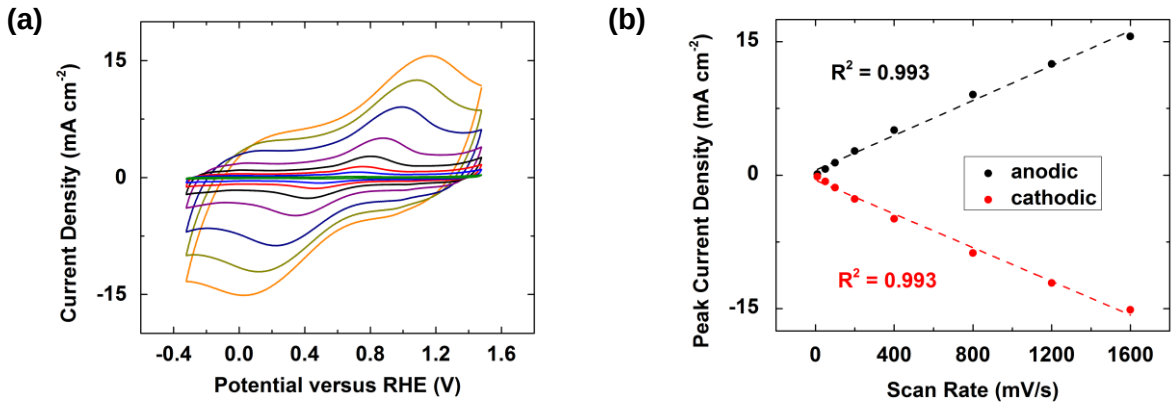

Figure B.6. (a) Cyclic voltammograms (CVs) of $[Cu(TpN)]^{2+}$ with scan rates of 10 (green), 50 (blue), 100 (red), 200 (black), 400 (purple), 800 (navy), 1200 (yellow), and 1600 (orange) mV/s in Ar-saturated pH 7 Britton-Robinson buffer solution. (b) Randles−Sevcik plot of $[Cu(TpN)]^{2+}$ obtained from the cathodic (red circles) and anodic (black circles) peak current densities.

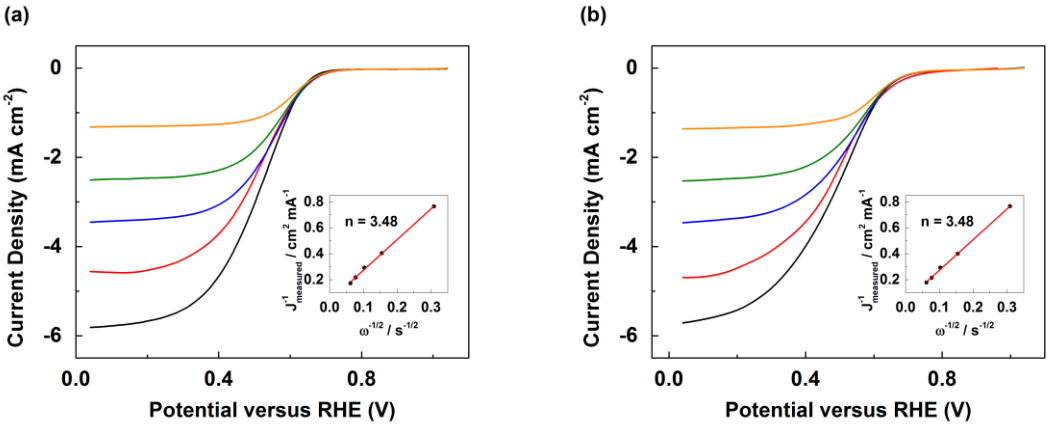

Figure B.7. Rotating disk electrode (RDE) LSVs and Koutecky-Levich plots (inset) of (a) $[Cu(Tp)]^{2+}$ and (b) $[Cu(Tp^{*})]^{2+}$ supported on Vulcan XC-72 in pH 10 O_2-saturated Britton-Robinson buffer solution with a scan rate of 10 mV/s at 100 (red), 400 (blue), 900 (green), 1600 (violet), and 2500 rpm (orange).

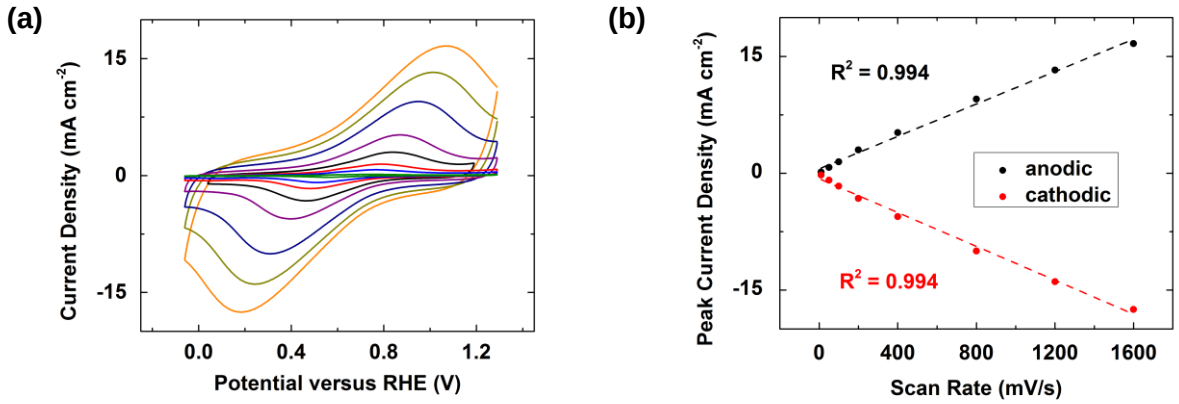

Figure B.8. (a) CVs of $[Cu(TpN)]^{2+}$ with scan rates of 10 (green), 50 (blue), 100 (red), 200 (black), 400 (purple), 800 (navy), 1200 (yellow), and 1600 (orange) mV/s in Ar-saturated pH 10 Britton-Robinson buffer solution. (b) Randles−Sevcik plot of $[Cu(TpN)]^{2+}$ obtained from the cathodic (red circles) and anodic (black circles) peak current densities.

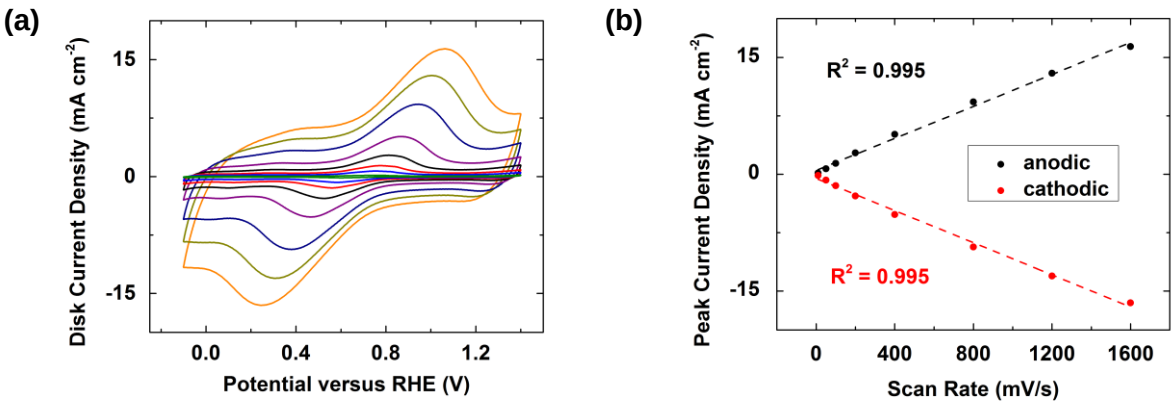

Figure B.9. (a) CVs of $[Cu(TpN)]^{2+}$ with scan rates of 10 (green), 50 (blue), 100 (red), 200 (black), 400 (purple), 800 (navy), 1200 (yellow), and 1600 (orange) mV/s in Ar-saturated pH 13 Britton-Robinson buffer solution. (b) Randles−Sevcik plot of $[Cu(TpN)]^{2+}$ obtained from the cathodic (red circles) and anodic (black circles) peak current densities.

B.2.3 NPM Catalysts that involve Pyridinyl-, Imidazolyl-, and Alkyl-amine-based Ligands

Our preliminary screening tests corroborate that Cu complexes of melamine derivatives in general are ineffective ORR catalysts relative to other classes of Cu complexes, likely because the geometric constraints by melamine inhibited the formation of a multi-nuclear active site that enforces cooperativity among the three Cu ions. Alkyl-amine-based ligands are typically inactive electrocatalysts, likely due to the unfavorable electronic coupling between the resultant Cu complex and the graphitic-like electrode surface.[4] Although imidazole is structurally closest to histidine, the eight residues that assemble the three Cu in place in laccase, the basicity of pyridine resembles that of histidine more closely than imidazole.[7,8] In order to realize a functional analogue of laccase, we used pyridinyl-based ligands as surrogates of histidines in hope to achieve more faithful mimicry. Building upon the T3-T2-T3 paradigm developed by our group using the Cu-DPA platform (Figure B.10), we further investigated first-row transition metal complexes of these linked DPA ligands.

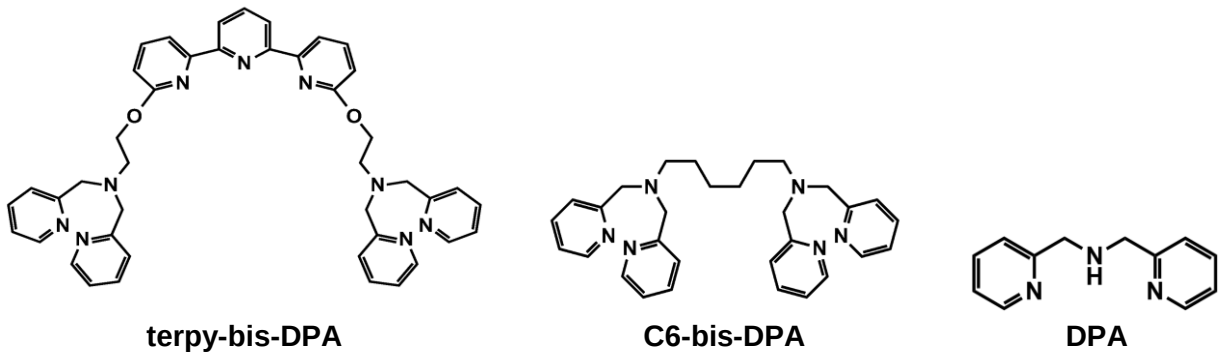

Figure B.10. A selective list of linked-DPA ligands used.

Table B.3. Elemental analysis of 1st row transition metal complexes of C6-bis-DPA.

EA Results	**Weight %**				**Mole %**		**Ratio**	
C6-bis-DPA complex	**C**	**H**	**N**	**M**	**N**	**M**	**N:M**	**Lig:M**
$MnCl_2$	85.16	1.34	2.94	3.64	0.21	0.07	3.17	1.06
$FeCl_3$	89.52	0.92	2.00	1.94	0.14	0.03	4.11	1.37
$CoCl_2$	87.27	1.13	2.34	3.07	0.17	0.05	3.21	1.07
$NiCl_2$	88.04	0.97	1.86	2.36	0.13	0.04	3.30	1.10
$ZnCl_2$	81.31	1.73	3.80	5.98	0.27	0.09	2.97	0.99

Here, we prepared dinuclear complexes of Mn, Fe, Co, Ni, Cu, and Zn supported on Vulcan XC-72 carbon powder and characterized these earth-abundant materials using elemental analysis (EA) techniques (Table B.3). We first investigated the redox response of the dinuclear complexes of C6-bis-DPA containing Mn, Fe, Co, Ni, Cu, and Zn in pH 7 buffer using CV and differential pulse voltammetry (DPV, for weak signal). Each of the di-Fe and di-Cu complexes of C6-bis-DPA shows a distinct redox peak (Figure B.11a). The di-Co complex of C6-bis-DPA exhibits multiple redox waves, likely suggesting that several Co complexes are present or various Co redox states are accessible under these conditions. Multiple Co species were observed under similar conditions used for oxygen evolution reaction (OER) studies. However, we were not able to observe any redox response for the cases involving the dinuclear Mn, Ni, and Zn complexes

using CV techniques. Therefore, we employed DPV in an effort to reveal weak redox signals. The orange line in Figure B.11b reveals a weak redox wave of the di-Ni complex. However, the di-Zn and di-Mn complexes are redox silent under these conditions, consistent to previous reports of other Zn and Mn complexes.

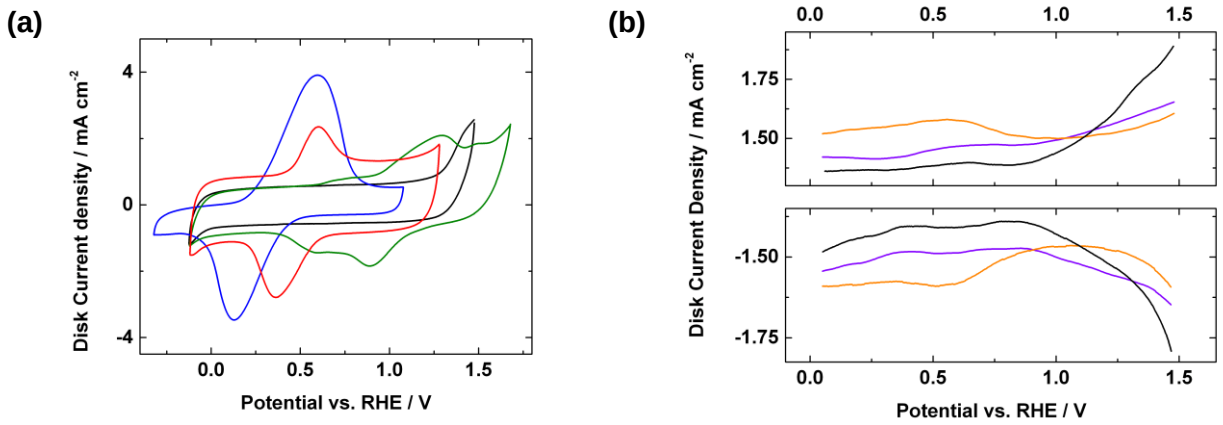

Figure B.11. (a) CV of the Fe (red), Co (green), Cu (blue), and Zn (black) complexes of C6-bis-DPA in an Ar-sparged pH 7 Britton-Robinson buffer solution with a scan rate of 200 mV/s. (b) Differential pulse voltammograms of Ni (orange), Mn (purple), and Zn (black) complexes of C6-bis-DPA in an Ar-sparged pH 7 Britton-Robinson buffer solution.

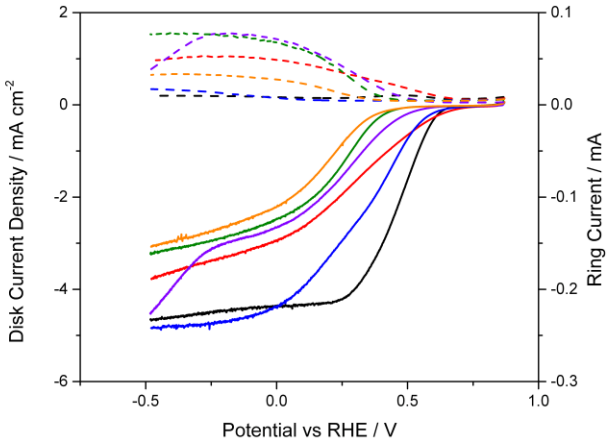

Figure B.12. Rotating ring-disk electrode (RRDE) LSVs of $[Cu_2(C6\text{-bis-DPA})Cl_4]$ (black), $[Co_2(C6\text{-bis-DPA})(H_2O)_2Cl_4]$ (red), $[Fe_2(C6\text{-bis-DPA})Cl_6]$ (blue), $[Ni_2(C6\text{-bis-DPA})Cl_4]$ (green), $[Zn_2(C6\text{-bis-DPA})Cl_4]$ (violet), and $[Mn_2(C6\text{-bis-DPA})(H_2O)_2Cl_4]$ (orange) supported on Vulcan XC-72 in pH 7 O_2-saturated Britton-Robinson buffer solution at 1600 rpm.

The ORR activity of mononuclear first-row transition metal complexes of TPA was reported previously.[9] However, the use of dinuclear and trinuclear first-row transition metal complexes as ORR catalysts remains an uncharted area. Here, we investigated the ORR activity of these inexpensive carbon-supported catalysts in pH 7 solutions using rotating ring-disk electrode (RRDE) experiments (Figure B.12). Table B.4 summarizes the number of electrons transferred during the ORR process for the cases of the six dinuclear complexes using data from Figure B.12. Results in Figure B.12 and Table B.4 demonstrate that only dinuclear complexes of C6-bis-DPA containing Fe and Cu reduce O_2 by almost 4 e^-. The di-Cu complex exhibits an onset potential more positive than the di-Fe complex, indicating the di-Cu complex is a better ORR catalyst candidate. The corresponding C6-bis-DPA complexes of Ni, Mn, Co, and Zn produce significant amounts of H_2O_2, as detected by the concentric Pt ring around the glassy carbon working electrode. The di-Co complex exhibits the lowest ORR onset potential, albeit undergoing a mixture of 2 e^- and 4 e^- process to reduce O_2. Experiments involving the trinuclear complexes of terpy-bis-DPA are underway.

Table B.4. Number of e^- transferred, calculated from the percent yield of H_2O_2 obtained from RRDE experiments presented in Figure B.12, catalyzed by various 1st row transition metal complexes of C6-bis-DPA ligand.

Complexes supported on Vulcan XC-72	Number of e^-
$[Cu_2(C6\text{-}bis\text{-}DPA)Cl_4]$	3.78
$[Co_2(C6\text{-}bis\text{-}DPA)(H_2O)_2Cl_4]$	2.72
$[Fe_3(C6\text{-}bis\text{-}DPA)Cl_6]$	3.76
$[Ni_2(C6\text{-}bis\text{-}DPA)Cl_4]$	2.28
$[Zn_2(C6\text{-}bis\text{-}DPA)Cl_4]$	2.98
$[Mn_2(C6\text{-}bis\text{-}DPA)(H_2O)_2Cl_4]$	2.26

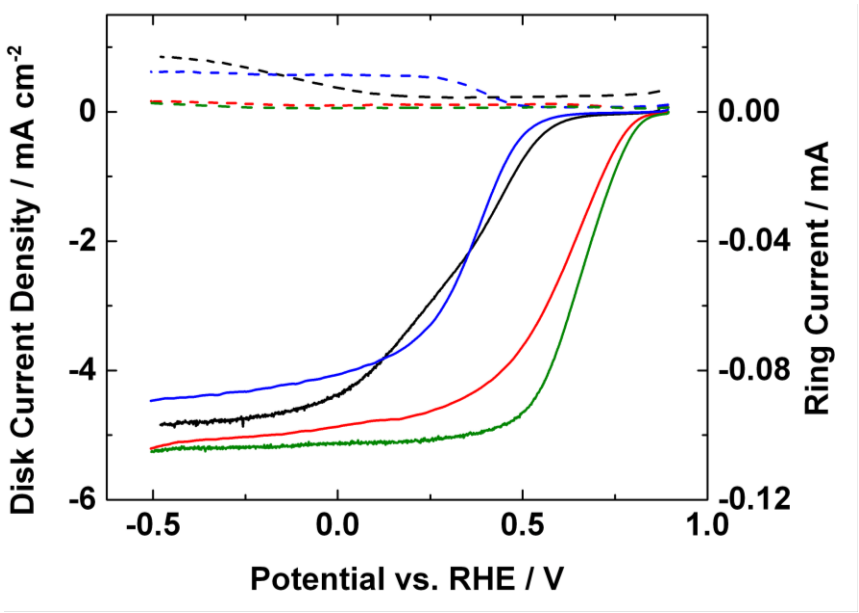

Figure B.13. RRDE linear sweep voltammograms and ring currents of [Fe_2(C6-bis-DPA)Cl_6] (black), pyrolyzed [Fe_2(C6-bis-DPA)Cl_6] (red), [Fe_3(terpy-bis-DPA)Cl_6] (blue), and pyrolyzed [Fe_3(terpy-bis-DPA)Cl_6] (green) supported on Vulcan XC-72 in pH 7 O_2-saturated Britton-Robinson buffer solution at 1600 rpm.

Pyrolysis of first-row transition metal complexes commonly results in heterogeneous materials that exhibit enhanced ORR activity relative to that of the parent unpyrolyzed discrete small molecules.[10] In particular, pyrolyzed Fe materials are the most active among catalysts that contain first-row transition metals. Here, we prepared pyrolyzed materials using multi-nuclear Fe complexes of C6-bis-DPA and terpy-bis-DPA as starting materials. Figure B.13 displays the RRDE results of pyrolyzed and unpyrolyzed Fe catalysts using DPA with C6 and terpy linker as the starting material. The unpyrolzyed di-Fe complex of C6-bis-DPA might feature a Fe_2-core resembling that of hemerythrin, a class of naturally-occurring non-heme iron proteins found in deep-ocean invertebrates that possesses rich O_2 chemistry.[11-28] Interestingly, the tri-Fe complex produces more H_2O_2 and exhibits a more negative ORR onset potential compared to the di-Fe complex. This empirical observation may stem from the terpy-bound Fe, a non DPA-bound Fe that contributes to the unfavorable effect observed. However, upon subjecting the di-Fe and tri-

Fe complexes to a pyrolysis treatment at 900 °C for 30 min, the amount of H_2O_2 detected decreases substantially and the ORR onset potential shifts positive by a significant amount, observations that are consistent with publish reports on using mononuclear Fe macrocycles and Fe-containing N-rich polymers as precursors. Taken together our preliminary results using di-Fe and tri-Fe as precursors and a vast library of published data, the active site of all these pyrolyzed materials likely does not resemble the precursors introduced prior to the pyrolysis step. In other words, the commonly-perceived Fe-N_4 core as the active site is highly likely a misconception due to the severe degree of heterogeneity as a result of the harsh condition utilized during the preparation step. Efforts to elucidate the active site are currently underway. Once we identify the structure and nature of the active site, we will construct the active site using a bottom-up method, tune the electronics and sterics of the site, and devise a simpler fabrication scheme in order to reduce the amount of waste during the preparation step.

B.3 References

(1) Thorum, M. S.; Yadav, J.; Gewirth, A. A. *Angew. Chem. Int. Ed.* **2009**, *48*, 165.
(2) Tse, E. C. M.; Schilter, D.; Gray, D. L.; Rauchfuss, T. B.; Gewirth, A. A. *Inorg. Chem.* **2014**, *53*, 8505.
(3) Thorseth, M. A.; Letko, C. S.; Rauchfuss, T. B.; Gewirth, A. A. *Inorg. Chem.* **2011**, *50*, 6158.
(4) Thorseth, M. A.; Letko, C. S.; Tse, E. C. M.; Rauchfuss, T. B.; Gewirth, A. A. *Inorg. Chem.* **2013**, *52*, 628.
(5) Thorseth, M. A.; Tornow, C. E.; Tse, E. C. M.; Gewirth, A. A. *Coor. Chem. Rev.* **2013**, *257*, 130.
(6) McCrory, C. C. L.; Ottenwaelder, X.; Stack, T. D. P.; Chidsey, C. E. D. *J. Phys. Chem. A* **2007**, *111*, 12641.
(7) Company, C. R. *CRC Handbook of Chemistry and Physics*; CRC Press, 1981.
(8) Sorrell, T. N. *Tetrahedron* **1989**, *45*, 3.
(9) Ward, A. L.; Elbaz, L.; Kerr, J. B.; Arnold, J. *Inorg. Chem.* **2012**, *51*, 4694.
(10) Chen, Z.; Higgins, D.; Yu, A.; Zhang, L.; Zhang, J. *Energy Environ. Sci.* **2011**, *4*, 3167.
(11) Wirstam, M.; Lippard, S. J.; Friesner, R. A. *J. Am. Chem. Soc.* **2003**, *125*, 3980.
(12) Sessler, J. L.; Sibert, J. W.; Lynch, V.; Markert, J. T.; Wooten, C. L. *Inorg. Chem.* **1993**, *32*, 621.
(13) Pulver, S.; Froland, W. A.; Fox, B. G.; Lipscomb, J. D.; Solomon, E. I. *J. Am. Chem. Soc.* **1993**, *115*, 12409.

(14) Plowman, J. E.; Loehr, T. M.; Schauer, C. K.; Anderson, O. P. *Inorg. Chem.* **1984**, *23*, 3553.
(15) Mizoguchi, T. J.; Lippard, S. J. *J. Am. Chem. Soc.* **1998**, *120*, 11022.
(16) Mizoguchi, T. J.; Kuzelka, J.; Spingler, B.; DuBois, J. L.; Davydov, R. M.; Hedman, B.; Hodgson, K. O.; Lippard, S. J. *Inorg. Chem.* **2001**, *40*, 4662.
(17) Mauerer, B.; Crane, J.; Schuler, J.; Wieghardt, K.; Nuber, B. *Angew. Chem. Int. Ed.* **1993**, *32*, 289.
(18) Mahapatra, S.; Kaderli, S.; Llobet, A.; Neuhold, Y. M.; Palanche, T.; Halfen, J. A.; Young, V. G.; Kaden, T. A.; Que, L.; Zuberbuhler, A. D.; Tolman, W. B. *Inorg. Chem.* **1997**, *36*, 6343.
(19) He, C.; Barrios, A. M.; Lee, D.; Kuzelka, J.; Davydov, R. M.; Lippard, S. J. *J. Am. Chem. Soc.* **2000**, *122*, 12683.
(20) Fernandes, C.; Neves, A.; Vencato, I.; Bortoluzzi, A. J.; Drago, V.; Weyhermuller, T.; Rentschler, E. *Chem. Lett.* **2000**, 540.
(21) Das, S.; Bhattacharyya, J.; Mukhopadhyay, S. *Dalton Trans.* **2008**, 6634.
(22) Brunold, T. C.; Solomon, E. I. *J. Am. Chem. Soc.* **1999**, *121*, 8277.
(23) Brunold, T. C.; Solomon, E. I. *J. Am. Chem. Soc.* **1999**, *121*, 8288.
(24) Brown, C. A.; Remar, G. J.; Musselman, R. L.; Solomon, E. I. *Inorg. Chem.* **1995**, *34*, 688.
(25) Bossek, U.; Hummel, H.; Weyhermuller, T.; Bill, E.; Wieghardt, K. *Angew. Chem. Int. Ed.* **1995**, *34*, 2642.
(26) Armstrong, W. H.; Lippard, S. J. *J. Am. Chem. Soc.* **1984**, *106*, 4632.
(27) Arii, H.; Nagatomo, S.; Kitagawa, T.; Miwa, T.; Jitsukawa, K.; Einaga, H.; Masuda, H. *J. Inorg. Biochem.* **2000**, *82*, 153.
(28) Arii, H.; Funahashi, Y.; Ozawa, T.; Jitsukawa, K.; Masuda, H. *J. Organomet. Chem.* **2007**, *692*, 343.

Appendix C

Epilogue

My five-year journey as a PhD student at UIUC came to an end. Just like any other trips, I came across bright, stimulating, inspiring days when everything went as planned and stumbled upon dull, bleak, dreary, depressing, lifeless nights when the door was slammed shut but the window was nowhere to be found. I learned how to appreciate the day and survive the night. With my PhD training, I am ready to embark on a new journey and start a new episode in my life.

"Why do we fall?

So we can learn to pick ourselves up."

I always wonder what I can do to influence the world, but unknowingly my thoughts have been shaped by the events occurring around me. I first aimed to be a translator to bridge the language barrier between people across national boundaries, and then I was mesmerized by the magic of chemistry. Eventually I decided to contribute my time and effort to solving the energy crisis. However, a series of unfortunate events that happened to my family and friends has changed my mind yet again. My grandpa and a friend of mine passed away because of cancer. A friend of mine who leads a healthy lifestyle struggled against cancer last year. At one point in life, I thought cancer is like terrorism or exploring life forms on Mars that is distal from my vicinity, but I was terribly wrong. More and more people around me are drawn into this battle against cancer. I too shall utilize my research background and scientific training to fight alongside our community as a whole against cancerous diseases.

"Life is priceless.

Make every moment count."